Medical Radiology
Diagnostic Imaging

M.F. Reiser
H. Hricak
M. Knauth

Andrea Baur-Melnyk
Editor

Magnetic Resonance Imaging of the Bone Marrow

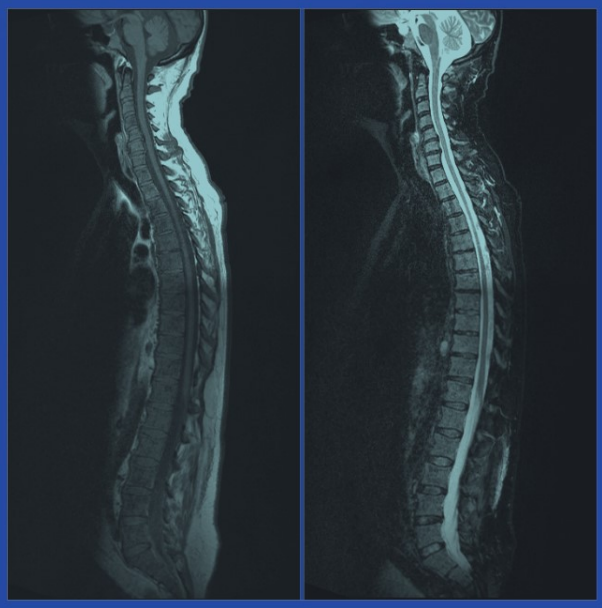

Springer

Medical Radiology

Diagnostic Imaging

For further volumes:
http://www.springer.com/series/4354

Andrea Baur-Melnyk
Editor

Magnetic Resonance Imaging of the Bone Marrow

Foreword by
Maximilian F. Reiser

Springer

Editor
Andrea Baur-Melnyk
Institut für Klinische Radiologie
Klinikum der Universität München (Großhadern)
Munich
Germany

ISBN 978-3-642-17859-7 ISBN 978-3-642-17860-3 (eBook)
DOI 10.1007/978-3-642-17860-3
Springer Heidelberg New York Dordrecht London

Library of Congress Control Number: 2012949706

Cover illustration: 63-year-old male with systemic mastocytosis

Printed on acid-free paper

Springer is part of Springer Science+Business Media (www.springer.com)

To my husband, Robert, and my parents

Andrea Baur-Melnyk

Foreword

The bones of birds contain gas instead of bone marrow in order to reduce their weight and allow them to fly. Since mammalians developed later in evolution than birds it can be assumed that the bone marrow is not just an atavism, even if air crafts were invented at a much later date. In humans and other mammalians, the bone marrow is one of the largest organs and the importance of this organ is also reflected in the Latin word "medulla" which is part of the term "medullary cavity" in which the bone marrow is located. Figuratively, this "medulla" has another meaning in the Latin language: "the dearest, the heart" indicating that back in ancient times the most important role of the bone marrow had been recognized.

For modern diagnostic imaging, especially MRI, the bone marrow plays a crucial role enabling the radiologist to detect a large variety of different disorders. Not only diseases originating from the bone marrow such as leukemia, myeloproliferative disorders, diseases of the reticuloendothelial system and anemias can be detected and characterized with MRI. In oncologic imaging metastatic spread to the skeleton plays a key role and multiple myeloma is an oncological disease originating from the bone marrow.

The bone marrow is also an area in which diseases of other organs may manifest so that their detection contributes to elucidate the health status of a patient. Bone infarction and bone marrow alterations in non-infective inflammatory bone marrow diseases such as Bechterew's disease and Sapho may provide direction in the further diagnostic work-up of a particular patient.

MRI opened the eyes of radiologists for a previously completely unknown or at least neglected entity, the bone marrow edema syndrome and understandably radiologists love this entity. Bone marrow edema can be seen as the footprint of injuries and disorders and could not be depicted with any other imaging modality. The visualization of bone marrow edema allows diagnosing a plethora of diseases and injuries and contributed to the elucidation of the natural history of various lesions.

All this would not be possible if humans would have bones filled with air. Alike the antique Romans, radiologists would therefore translate "medulla" as "the dearest".

On behalf of the editorial board of "Medical Radiology" I would like to express my sincere gratitude to Professor Baur-Melnyk and the eminent authors of this monograph for their time and expertise. We are confident that the reader will welcome this state-of-the-art reference book on the fascinating topic of MRI of the bone marrow. It provides at the same time comprehensive and compressed information on this topic of utmost clinical importance.

Munich, November 2012 Maximilian F. Reiser

Preface

The bone marrow is one of the largest organs of the human body. In almost every MR image the bone marrow or parts of it are displayed. MRI is the most sensitive imaging modality to display the marrow and its components, mainly consisting of fat and water bound protons. The exact knowledge of the normal marrow distribution as well as marrow variants in MRI is important for specific diagnoses. Benign variants often constitute mimickers of malignant diseases. Pathologies that may arise from bone marrow and marrow components are numerous. In this book haematological bone marrow malignancies, bone metastases, multiple myeloma as malignant causes for bone marrow alterations are presented. MRI can also be used as a tool for the assessment of treatment response in oncologic marrow involvement. The differentiation of benign and malignant vertebral compression fractures is an common clinical challenge which is discussed in detail in one separate chapter. Benign processes can also affect the bone marrow, such as diseases of the reticuloendothelial system, anemias and marrow insufficiency. Osteonecrosis and bone marrow infarction is another common clinical problem in musculoskeletal imaging which will be presented in detail. It has to be differentiated from bone marrow edema syndromes which may have multiple underlying causes. Bone marrow changes are frequently found in acute and chronic trauma and their patterns are often specific for a particular type of injury. Infective and non infective bone marrow diseases have to be differentiated from bone marrow edema syndromes. At the end technical aspects and new techniques for bone marrow imaging in MRI, such as diffusion and perfusion as well as contrast media application are discussed.

We hope that this book will aid in clinical practise and can aid in patient care. We want to thank all contributing authors, who are internationally known experts in their field, for their great efforts and for their outstanding contributions. We would also like to acknowledge the continuous support and encouragement by Springer.

Andrea Baur-Melnyk

Contents

Contributors

Reiner Bartl Center of Osteoporosis, Kaufingerstr. 15 5. OG, 80331 Munich, Germany, e-mail: Reiner.Bartl@osteologie-online.de

Andrea Baur-Melnyk Institut für Klinische Radiologie, Klinikum der Universität München-Großhadern, Marchioninistraße 15, 81377 Munich, Germany; Department of Clinical Radiology, University Hospitals Munich/Grosshadern, LMU, Marchioninistr. 15, 81377 Munich, Germany, e-mail: Andrea.Baur@med.uni-muenchen.de

Alain Blum Service d'Imagerie Guilloz, CHU de Nancy, 29 av du Maréchal de Lattre de Tassigny, 54035 Nancy, France, e-mail: alain.blum@gmail.com

Klaus Bohndorf Department of Radiology, Klinikum Augsburg, Stenglinstr. 2, 86156 Augsburg, Germany, e-mail: Klaus.bohndorf@klinikum-augsburg.de

Kathleen Carrigan Department of Radiology, UMMC, 22 South Greene St, Baltimore, MD 21201, USA

Victor N. Cassar-Pullicino Department of Radiology, Robert Jones and Agnes Hunt Orthopaedic Hospital, Oswestry SY10 7AG, Shropshire, UK

Melvin D'Anastasi Institut für Klinische Radiologie, Klinikum der Universität München-Großhadern, Marchioninistraße 15, 81377 München, Germany

Heike E. Daldrup-Link Department of Radiology, Lucile Packard Children's Hospital, Stanford University, 725 Welch Road, Stanford, CA 94305, USA, e-mail: H.E.Daldrup-Link@stanford.edu

Annick Demeyere General Hospital Imelda, Bonheiden, Belgium

Olaf Dietrich Josef Lissner Laboratory for Biomedical Imaging, Department of Clinical Radiology-Großhadern, Ludwig Maximilian University (LMU) of Munich, Munich, Germany, e-mail: od@dtrx.net

Hassan Douis Royal National Orthopaedic Hospital NHS Trust, Stanmore, UK

Michiel Eyselbergs University Hospital Antwerp, University of Antwerp, Rooienberg 25, 2570 Duffel, Belgium

Anastasia Fotiadou Department of Radiology, Hinchingbrooke Hospital, Huntingdon, Cambridgeshire, PE29 6NT, UK

C. Galant Department of Pathology, Université catholique de Louvain, Saint Luc University Hospital, Hippocrate Avenue 10/2942, 1200 Brussels, Belgium

Tobias Geith Institut für Klinische Radiologie, Klinikum der Universität Munchen-Großhadern, Marchioninistraße 15, 81377 Munich, Germany

Daniel Golovko Department of Internal Medicine, University of Colorado Hospital, Aurora, CO, USA

Robert Hemke Department of Radiology, Academic Medical Center, University of Amsterdam, Meibergdreef 9, Amsterdam, The Netherlands

Apostolos Karantanas Department of Medical Imaging, University Hospital, University of Crete, Heraklion, Greece, e-mail: akarantanas@gmail.com

Sung Kim Department of Radiology, UMMC, 22 South Greene St, Baltimore, MD 21201, USA

A. Larbi Department of Radiology, Cliniques Universitaires Saint-Luc, UCL Université de Louvain, Hippocrate Avenue 10/2942, 1200 Brussels, Belgium

Sophie Lecocq Service d'Imagerie Guilloz, Hopital Central, CHU Nancy, 54000 Nancy, France

F. Lecouvet Department of Radiology, Cliniques Universitaires Saint-Luc, UCL Université de Louvain, Hippocrate Avenue, 10/2942, 1200 Brussels, Belgium, e-mail: lecouvet@yahoo.fr

F. E. Lecouvet Department of Musculoskeletal Imaging, Université catholique de Louvain, Saint Luc University Hospital, Brussels, Belgium; Department of Radiology, Université catholique de Louvain, Saint Luc University Hospital, Hippocrate Avenue 10/2942, 1200 Brussels, Belgium

M. Lonneux Department of Radiology, Cliniques Universitaires Saint-Luc, UCL Université de Louvain, Hippocrate Avenue 10/2942, 1200 Brussels, Belgium

Matthias Louis Service d'Imagerie Guilloz, Hopital Central, CHU Nancy, 54000 Nancy, France

Mario Maas Department of Radiology, Academic Medical Center, University of Amsterdam, Meibergdreef 9, Amsterdam, The Netherlands, e-mail: m.maas@amc.uva.nl

J. Malghem Department of Radiology, Cliniques Universitaires Saint-Luc, UCL Université de Louvain, Hippocrate Avenue 10/2942, 1200 Brussels, Belgium

N. Michoux Department of Musculoskeletal Imaging, Université catholique de Louvain, Saint Luc University Hospital, Brussels, Belgium; Department of Radiology, Cliniques Universitaires Saint-Luc, UCL Université de Louvain, Hippocrate Avenue 10/2942, 1200 Brussels, Belgium

Michael Mulligan Department of Radiology, UMMC, 22 South Greene St, Baltimore, MD 21201, USA, e-mail: mmulligan@umm.edu

Iris-Melanie Noebauer-Huhmann Division of Neuroradiology and Musculoskeletal Radiology, Department of Radiology, Medical University of Vienna/Vienna General Hospital, Waerhringer Guertel 18-20, 1090 Vienna, Austria, e-mail: iris.noebauer@meduniwien.ac.at

P. Omoumi Department of Musculoskeletal Imaging, Université catholique de Louvain, Saint Luc University Hospital, Brussels, Belgium; Department of Radiology, Université catholique de Louvain, Saint Luc University Hospital, Hippocrate Avenue 10/2942, 1200 Brussels, Belgium; Department of Radiology, Cliniques Universitaires Saint-Luc, UCL Université de Louvain, Hippocrate Avenue 10/2942, 1200 Brussels, Belgium

Gerwin Paul Schmidt Department of Clinical Radiology, University Hospitals Munich/Grosshadern, LMU, Marchioninistr. 15, 81377 Munich, Germany, e-mail: gerwin.schmidt@med.uni-muenchen.de

Elizabeth Sutton Department of Radiology, Memorial Sloan-Kettering Cancer Center, New York, USA

Pedro Teixeira Service d'Imagerie Guilloz, Hopital Central, CHU Nancy, 54000 Nancy, France

Bernhard J. Tins Department of Radiology, Robert Jones and Agnes Hunt Orthopaedic Hospital, Oswestry SY10 7AG, Shropshire, UK, e-mail: Bernhard.Tins@rjah.nhs.uk

B. Tombal Department of Urology, Cliniques Universitaires Saint-Luc, UCL Université de Louvain, Hippocrate Avenue 10/2942, 1200 Brussels, Belgium

Martin Uffmann Landesklinikum Neunkirchen, Peischingerstrasse 19, 2620, Neunkirchen, Austria

B. Vande Berg Department of Radiology, Cliniques Universitaires Saint-Luc, UCL Université de Louvain, Hippocrate Avenue 10/2942, 1200 Brussels, Belgium

Bruno C. Vande Berg Department of Musculoskeletal Imaging, Université catholique de Louvain, Saint Luc University Hospital, Brussels, Belgium; Department of Radiology, Université catholique de Louvain, Saint Luc University Hospital, Hippocrate Avenue 10/2942, 1200 Brussels, Belgium, e-mail: bruno.vandeberg@uclouvain.be

Filip M. Vanhoenacker Department of Radiology, General Hospital Sint-Maarten Duffel-Mechelen, Rooienberg 25, 2570 Duffel, Belgium; University Hospital Antwerp, University of Antwerp, Rooienberg 25, 2570 Duffel, Belgium; Faculty of Medicine and Health Sciences, University of Ghent, Rooienberg 25, 2570 Duffel, Belgium, e-mail: filip.vanhoenacker@telenet.be

Part I

Histology and Normal Bone Marrow

Histology of Normal Bone and Bone Marrow, and Their Main Disorders

Reiner Bartl

Contents

Abstract

The unique attraction of a bone and bone marrow biopsy is that it allows direct visualisation of bone and its cells, as well as the bone marrow, i.e., haematopoiesis and all elements of the stromal compartment. The trephine biopsy has also some main advantages over the aspirate specimens. The most important is to enable examination of the topographic distribution of the cellular constituents of the marrow, their relationships to the bone trabeculae and an absolute assessment of cellularity. Furthermore in diseases which produce fibrosis, an aspirate often fails to produce an adequate diagnostic specimen (a "dry tap"). The procedure of taking a trephine biopsy ("Jamshidi needle") is relatively simple and is accomplished without complications in the vast majority of cases. Modern techniques of fixation, embedding and staining for conventional histology as well as immunohistology and histomorphometry enable accurate assessment of bone and bone marrow structure, architecture and cells. Today bone and bone marrow biopsies are widely used for investigation of unclear and malignant conditions of bone and bone marrow.

1 Introduction

Magnetic resonance imaging (MRI) is a worldwide used radiological method which has the advantage of displaying directly the bone marrow and its components. Fat as well as water bound protons deliver the contrast on MR sequences. It offers the advantage to examine the bone marrow without ionised radiation

R. Bartl (✉)
Center of Osteoporosis,
Kaufingerstr. 15 5. OG,
80331 Munich, Germany
e-mail: Reiner.Bartl@osteologie-online.de

A. Baur-Melnyk (ed.), *Magnetic Resonance Imaging of the Bone Marrow*, Medical Radiology. Diagnostic Imaging,
DOI: 10.1007/174_2011_442,

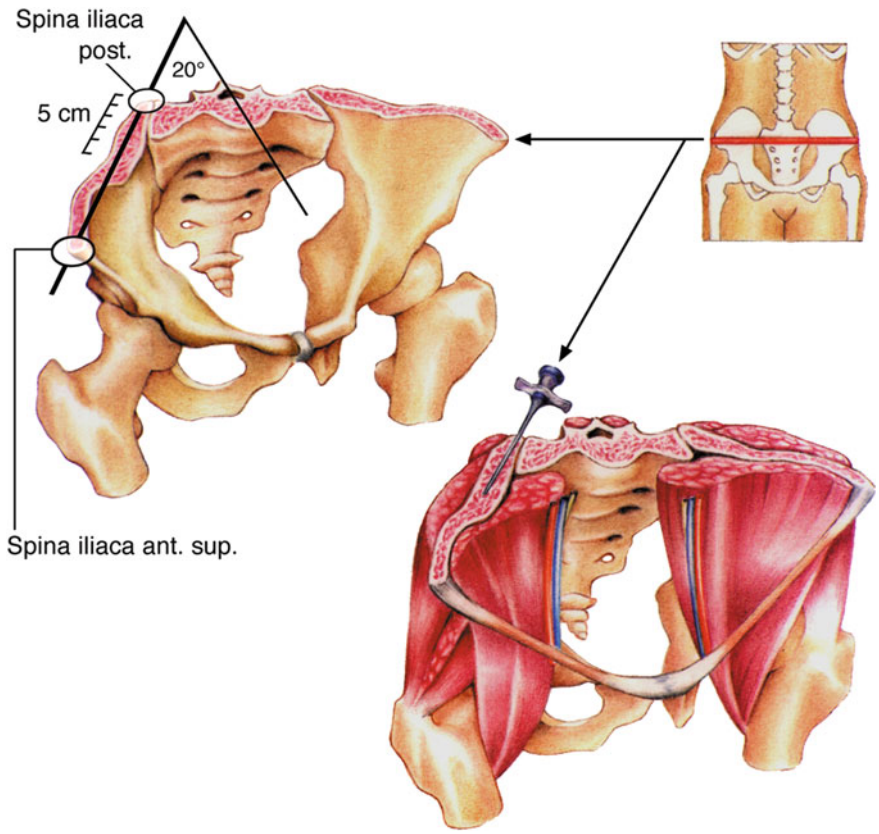

Fig. 1 Anatomy of the pelvis at the level of the usual biopsy site (manual trephine). Biopsies up to 6 cm can be taken safely. The iliac bone at the biopsy site is enclosed and protected by groups of broad muscles. Arteries, veins and nerves in the pelvis are located at a safe distance

and is especially suited to screen the complete bone marrow in a whole body approach. The bone marrow is one of the largest organs of the body. MRI offers the possibility of identifying both haematopoietic and fatty bone marrow, as well as inflammatory and neoplastic infiltrates. It is the method of choice for demonstrating myeloma, lymphoma and metastases, as well as localised oedematous processes. However, the limitations of MRI in these disorders are well known, particularly the difficulties of the detection of a small amount of pathologic cells and the limitation of specificity of MRI. A wide variety of haematologic and osseous disorders can produce similar abnormalities in MRI. The combination of MRI and histology is attractive by selecting the ideal puncture site. It is reasonable to take a biopsy:

- When the diagnosis is in doubt,
- When confirmation is sought of a specific process,
- When further categorisation is required for therapeutic decisions, and
- When follow-up and monitoring of therapy is necessary.

2 Biopsy of Bone and Bone Marrow

In recent years there has been a great increase in the number of bone and bone marrow biopsies (BMB) taken because the indications have broadened in direct proportion to improvements in

- Biopsy needles
- Methods of processing and therefore diagnostic reliability and
- The number and range of additional investigative techniques available and applicable to bone and bone marrow sections.

Consequently, the indications for taking biopsies have increased especially in internal medicine, haematology, oncology and osteology. Biopsies can be obtained from patients of all ages, and therefore the differences in skeletal structure and bone marrow in different bones, as well as the age-related alterations in both osseous and haematopoietic components must be taken into account, particularly with respect to histomorphometric measurements.

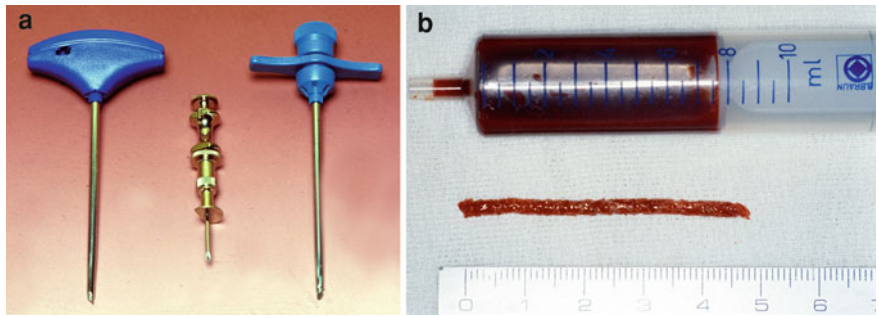

Fig. 2 Bone and marrow biopsy instruments. **a** Types of manual trephines and aspirate needle. **b** Biopsy and aspirate taken with them

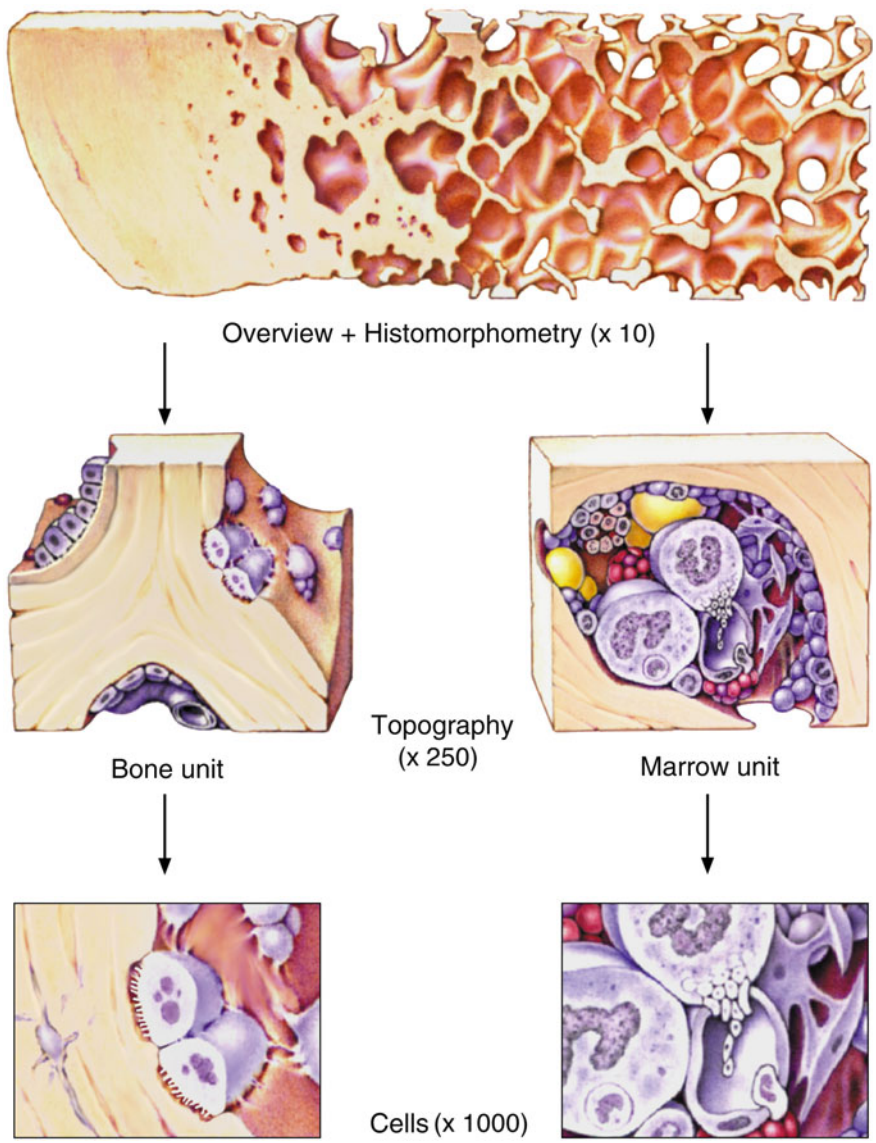

Fig. 3 Systematic evaluation of bone and bone marrow components and structures in iliac crest biopsies. The four topographic regions of the biopsy and their approximate sizes are: (1) Cortical space 2 mm, (2) Subcortical region 4 mm, (3) Central region 4–8 mm and (4) "Deeper" region 4 mm

Table 1 Histomorphometry of bone and bone marrow[a]

Variables	Mean value (SD)	Dimension
Haematopoietic tissue	40(9)	Vol%
Fatty tissue	28(8)	
Trabecular bone	26(5)	
Osteoid	0.3(0.2)	
Sinusoids	4.5(2.1)	
Lymphocytes (diffuse)	20(12)	/mm^2
Mast cells	2(1)	
Megakaryocytes	8(4)	
Macrophages (containing iron)	16(10)	
Plasma cells	21(18)	
Lymphoid nodules[b]	2	%
Arteries	3(4)	/100 mm^2
Arterioles	26(18)	
Capillaries	101(61)	
Sinusoids	1700(825)	
Osteoblastic index (OB)[c]	5(5)	%
Osteoclastic index (OC)[d]	4(3)	/100 mm

[a] These values are derived from 158 biopsies of healthy individuals
[b] When present (seen more in older individuals)
[c] OB = percentage of trabecular circumference covered by cuboidal osteoblasts
[d] OC = number of osteoclasts per 100 mm trabecular circumference

2.1 Biopsy Sites

In determining the choice of site, four main considerations apply:

- It should easily be accessible, involving a minimum of trauma and danger to the patient
- It should contain cortical and trabecular bone
- It should provide representative bone structure and turnover, and contain red haematopoietic marrow
- Repeat biopsies with minimal variability should be possible at this site.

The posterior iliac crest is the preferred site from which bone marrow biopsies are obtained under local anaesthesia (Fig. 1). But BMB can also be obtained in the operating theatre under radiological guidance from almost any skeletal area, depending on the indications and the diagnostic requirements. There are differences in the amounts of cortical and trabecular bone and marrow in different regions of the ilium, but these have no practical significance. Likewise, the proportion of bone, haematopoiesis and fat vary in different parts of the skeleton containing the red marrow, but the basic constituents are the same. For example, the volume percentages of trabecular bone are less, and those of the marrow cavities are greater in sternum and vertebral bodies than in the ilium.

2.2 Biopsy Needles

- The needle most commonly used (especially by the haematologist) is the 11–8 gauge "disposable" needle ("Jamshidi needle") which provides biopsies 2 mm in diameter while the length varies (1–6 cm) according to the depth to which the needle is introduced in the posterior iliac crest (Fig. 2a, b).
- The transilial needle used for horizontal cortex-to-cortex biopsies, 8 mm in diameter and taken from the anterior iliac crest is often used by the osteologist.
- The electric drill used for vertical biopsies from the anterior iliac crest is used by some clinicians when the bone is expected to be very soft or very hard and is suitable for histomorphometric requirements.

Table 2 Normal range of histomorphometric values at different skeletal sites (mean ± SD)

			Skeletal sites					
Parameters	Abbreviation	Units	Anterior iliac crest	Posterior iliac crest	Lumbar vertebra	Sternum	Calcaneus	Radius
Bone structure								
Bone volume	BV/TV	%	22 ± 4	22 ± 4	16 ± 4	15 ± 4	20 ± 6	19 ± 5
Bone surface	BS/BV	mm^2/mm^3	2.8 ± 0.7	2.6 ± 0.8	2.3 ± 0.6	2.7 ± 0.6	3.5 ± 0.8	3.2 ± 1.8
Trabecular thickness	TB.Th	µm	175 ± 42	181 ± 40	178 ± 48	155 ± 42	157 ± 50	161 ± 44
Mineralisation								
Osteoid volume	OV/BV	%	2.5 ± 2.2	2.8 ± 2.1	2.3 ± 1.8	1.6 ± 1.8	1.7 ± 1.4	1.3 ± 0.9
Osteoid surface	OS/BV	mm^2/mm^3	0.6 ± 0.4	0.6 ± 0.4	0.5 ± 0.3	0.4 ± 0.4	0.3 ± 0.2	0.4 ± 0.3
Osteoid thickness	O.Th	µm	4.1 ± 3.4	4.6 ± 3.3	5.4 ± 2.1	4.9 ± 3.5	4.0 ± 3.0	3.5 ± 3.6
Bone cells								
Osteoclasts	N.Ocl/B.Ar	per mm^2	1.0 ± 0.9	0.9 ± 0.7	0.9 ± 0.7	1.0 ± 0.8	0.5 ± 0.4	0.4 ± 0.2
Osteoblasts	N.Obl/B.Ar	per mm^2	2.5 ± 1.8	3.2 ± 1.1	2.6 ± 1.4	4.1 ± 1.6	2.2 ± 1.1	1.3 ± 0.4
Lining cells	N.Lin/B.Ar	per mm^2	2.0 ± 1.3	1.9 ± 1.0	2.0 ± 1.1	1.8 ± 1.0	0.8 ± 0.6	0.9 ± 0.3
Osteocytes	N.Ocy/B.Ar	per mm^2	32 ± 6	30 ± 5	24 ± 6	25 ± 6	32 ± 7	28 ± 6
Blood vessels								
Arteries	N.Art/M.Ar	per mm^2	0.4 ± 0.4	0.5 ± 0.3	0.6 ± 0.4	0.5 ± 0.5	0.5 ± 0.4	0.4 ± 0.4
Arterioles	N.Aio/M.Ar	per mm^2	1.3 ± 0.4	1.4 ± 0.5	1.4 ± 0.6	1.4 ± 0.9	1.4 ± 1.0	1.2 ± 0.9
Capillaries	N.Cap/M.Ar	per mm^2	17 ± 5	16 ± 5	16 ± 5	16 ± 5	11 ± 3	11 ± 4
Sinusoids	N.Sin/M.Ar	per mm^2	33 ± 7	35 ± 8	36 ± 9	36 ± 8	11 ± 4	11 ± 5
Endosteal sinusoid volume	ESV/TV	%	2.0 ± 1.3	2.1 ± 1.4	2.2 ± 1.4	2.3 ± 1.1	1.8 ± 0.9	1.8 ± 1.0
Stroma								
Fatty tissue volume	FV/MV	%	26 ± 8	25 ± 6	23 ± 7	28 ± 19	96 ± 4	96 ± 5
Mast cells	N.Mas/M.Ar	per mm^2	2.3 ± 1.8	2.2 ± 1.9	3.7 ± 3.1	1.9 ± 2.8	0	0
Plasma cells	N.Pia/M.Ar	per mm^2	30 ± 12	29 ± 10	31 ± 24	29 ± 14	0	0
Haematopoiesis								
Haematopoiesis volume	HV/MV	%	60 ± 6	62 ± 7	64 ± 7	61 ± 8	0	0
Megakaryocytes	N.Meg/M.Ar	per mm^2	14 ± 4	13 ± 4	15 ± 8	16 ± 7	0	0

TV = Total volume, BV = Bone volume, MV = Marrow volume, B.Ar = Bone area (2D), M.Ar = Marrow area (2D). Histomorphometry was performed in collaboration with Dr B. Mallmann

Once the sterile pad is removed, an aspiration needle is introduced, preferable at about 1 cm from the spot where the bone marrow biopsy was taken, and marrow is aspirated into sterile test tubes with the appropriate anticoagulant or culture media.

Biopsies may be cut and pieces used for different purposes: fixation for both plastic and paraffin embedding, and fresh frozen for cryostat sections and immunohistology. In this survey on bone and bone marrow histology the following stainings were used: Giemsa, Gomori and Ladewig.

Table 3 Histomorphometric parameters measured in posterior iliac crest biopsies according to age groups

			Age groups, years							
Parameters	Abbreviation	Units	−9	10–19	20–29	30—39	40–49	50–59	60–69	70–
Bone structure										
Bone volume	BV/TV	%	20 ± 4	25 ± 5	24 ± 5	22 ± 4	21 ± 5	20 ± 5	17 ± 3	13 ± 1
Bone surface	BS/BV	mm^2/mm^3	2.9 ± 0.4	2.8 ± 0.6	3.1 ± 0.3	2.9 ± 0.6	3.0 ± 0.6	3.0 ± 0.9	2.6 ± 0.7	2.1 ± 0.5
Trabecular thickness	TB.Th	µm	172 ± 30	222 ± 53	195 ± 44	73 ± 52	179 ± 49	177 ± 39	173 ± 33	171 ± 44
Mineralsation										
Osteoid volume	OV/BV	%	7.7 ± 2.4	5.2 ± 4.8	3.4 ± 3.4	2.0 ± 2.4	1.0 ± 1.1	1.9 ± 1.5	2.3 ± 2.3	1.7 ± 2.0
Osteoid surface	OS/BV	mm^2/mm^3	0.8 ± 0.4	0.9 ± 3.7	0.9 ± 0.5	0.5 ± 0.4	0.3 ± 0.2	0.5 ± 0.5	0.4 ± 0.4	0.5 ± 0.4
Osteoid thickness	O.Th	µm	11 ± 4	6 ± 4	4 ± 3	4 ± 9	4 ± 2	4 ± 5	5 ± 3	3 ± 3
Bone cells										
Osteoclasts	N.Ocl/B.Ar	per mm^2	3.1 ± 1.3	1.2 ± 1.0	0.7 ± 0.4	1.0 ± 0.8	0.8 ± 0.5	1.0 ± 0.9	2.1 ± 0.9	1.3 ± 0.9
Osteoblasts	N.Obl/B.Ar	per mm^2	3.6 ± 2.9	4.0 ± 2.6	1.7 ± 0.9	1.5 ± 1.3	0.7 ± 0.6	1.7 ± 2.0	1.6 ± 2.1	1.1 ± 1.2
Lining cells	N.Lin/B.Ar	per mm^2	5.4 ± 2.8	2.0 ± 1.2	1.9 ± 1.3	1.8 ± 0.9	1.0 ± 0.8	0.9 ± 0.7	1.4 ± 1.0	1.8 ± 1.3
Osteocytes	N.Ocy/B.Ar	per mm^2	24 ± 5	18 ± 5	17 ± 6	20 ± 8	8 ± 8	16 ± 6	18 ± 6	13 ± 3
Blood vessels										
Arteries	N.Art/M.Ar	per mm^2	0.3 ± 0.4	0.5 ± 0.6	0.4 ± 0.4	0.4 ± 0.4	0.4 ± 0.4	0.4 ± 0.4	0.5 ± 0.6	0.3 ± 0.4
Arterioles	N.Aio/M.Ar	per mm^2	1.3 ± 1.2	1.7 ± 0.9	1.3 ± 0.7	1.3 ± 0.7	1.0 ± 1.0	0.8 ± 0.7	1.2 ± 0.8	1.4 ± 1.2
Capillaries	N.Cap/M.Ar	per mm^2	13 ± 4	17 ± 6	18 ± 6	18 ± 6	18 ± 4	20 ± 7	18 ± 8	19 ± 5
Sinusoids	N.Sin/M.Ar	per mm^2	37 ± 5	31 ± 8	30 ± 7	34 ± 10	31 ± 7	33 ± 9	39 ± 5	36 ± 7
Endosteal sinusoids	ESV/TV	%	2.5 ± 0.9	2.7 ± 1.0	2.5 ± 1.5	3.0 ± 3.3	1.7 ± 1.7	1.8 ± 0.7	1.7 ± 0.7	1.5 ± 0.5
Stroma										
Fatty tissue	FV/MV	%	12 ± 7	17 ± 5	19 ± 9	26 ± 9	28 ± 11	30 ± 10	31 ± 9	44 ± 14
Mast cells	N.Mas/M.Ar	per mm^2	0.4 ± 0.7	0.7 ± 0.8	2.1 ± 1.9	2.2 ± 1.9	2.2 ± 2.4	2.2 ± 1.4	2.6 ± 2.1	3.9 ± 3.8
Plasma cells	N.Pla/M.Ar	per mm^2	19 ± 6	32 ± 11	30 ± 9	31 ± 9	29 ± 9	33 ± 9	34 ± 8	30 ± 9
Haematopoiesis										
Haematopoiesis	HV/MV	%	78 ± 13	72 ± 11	70 ± 12	62 ± 11	61 ± 14	59 ± 13	58 ± 11	45 ± 14
Megakaryocytes	N.Meg/M.Ar	per mm^2	20 ± 8	16 ± 4	15 ± 6	14 ± 6	15 ± 4	14 ± 5	13 ± 5	10 ± 6

Terminology, abbreviations and units see Table 2 Histomorphometry was performed in collaboration with Dr. B. Mallmann
Post-mortem biopsies taken with the electric drill from 100 normal subjects, 10 or more cases in each age group

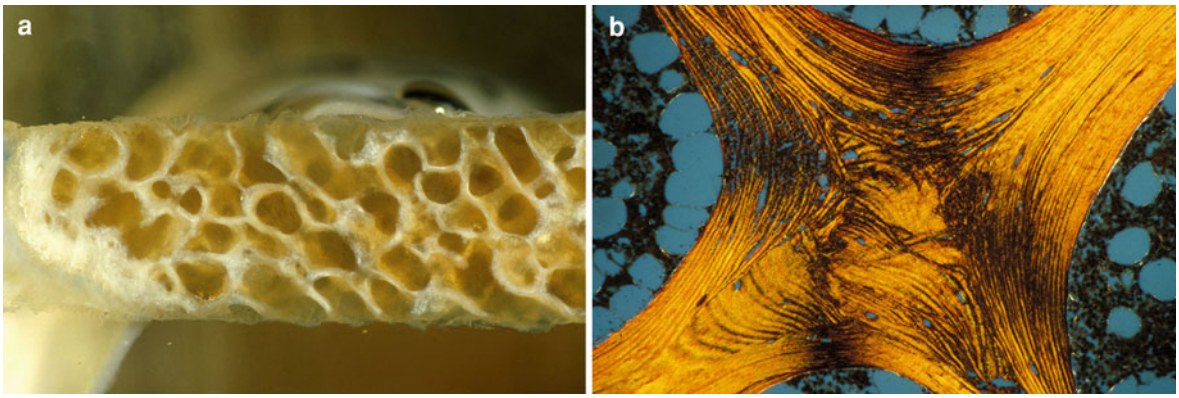

Fig. 4 Normal bone and bone marrow biopsy. **a** Cut surface of a bone marrow biopsy showing compacta, trabecular network and intertrabecular spaces. **b** Trabecular node consisting of parallel layers of collagen fibrils. These lamellae ensure flexibility of bone

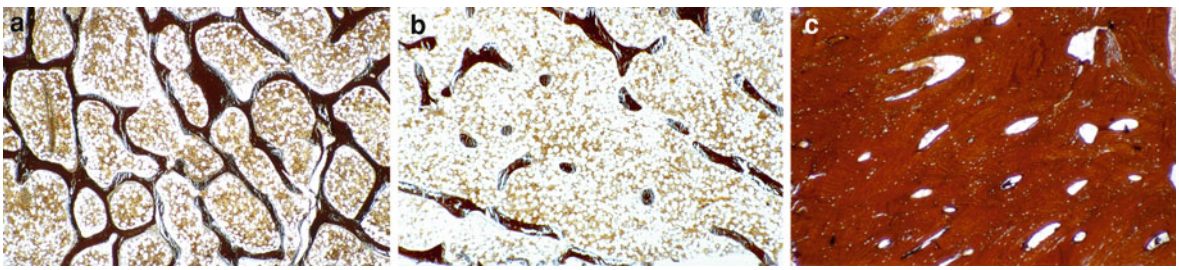

Fig. 5 Abnormalities of bone mass: **a** Normal bone mass and trabecular structure. **b** Osteoporosis. **c** Osteopetrosis

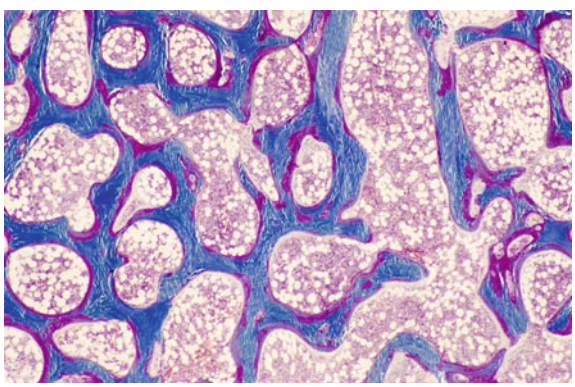

Fig. 6 Osteomalacia with abnormal bone mineralisation (vitamin D-deficiency). The trabecular bone volume is not increased, but extensive broad osteoid seams (*red*) are present

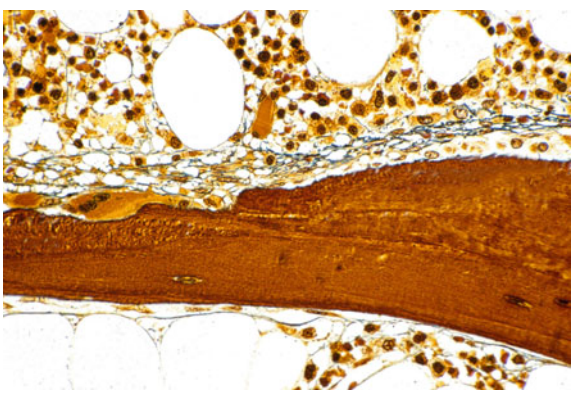

Fig. 7 Osseous remodelling with balance between osteoblastic bone formation (*right*) and osteoclastic bone resorption (*left*)

2.2.1 Biopsy Evaluation

A systemic survey is made, beginning with a scan of the whole biopsy section at low power and ending with examination at high power, under oil if necessary, of individual cells and structures (Fig. 3). Though this book is concerned with the bone marrow it is important to consider the bone and bone marrow together as a single system because alterations in the one are almost invariably accompanied by changes in the other. Diagnostic evaluation is made in the first

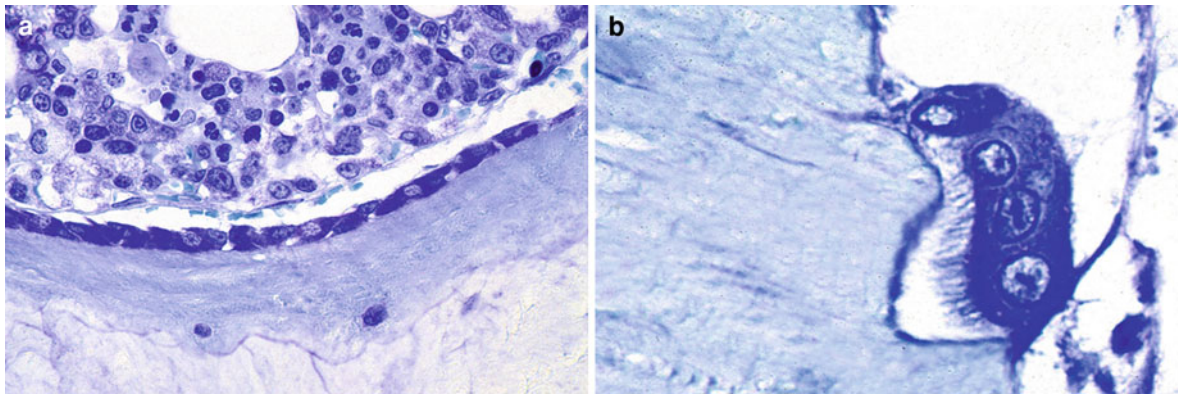

Fig. 8 Bone cells. **a** Layer of osteoblasts and paratrabecular sinus, with presence of two osteocytes in the osteoid seam. **b** Active osteoclast on bone with "ruffled border"

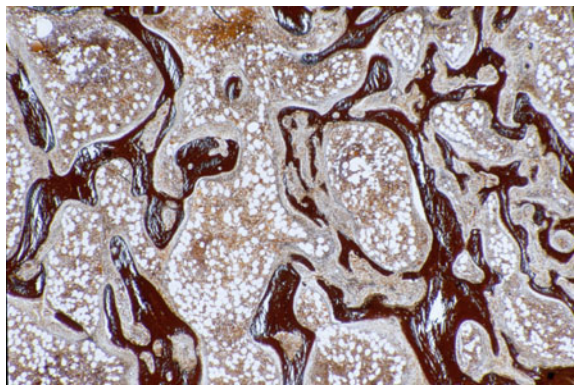

Fig. 9 Marked osteitis fibrosis generalisata, with destruction of trabecular network (dissecting osteoclasia) and extensive paratrabecular fibrosis in a young patient with renal bone disease

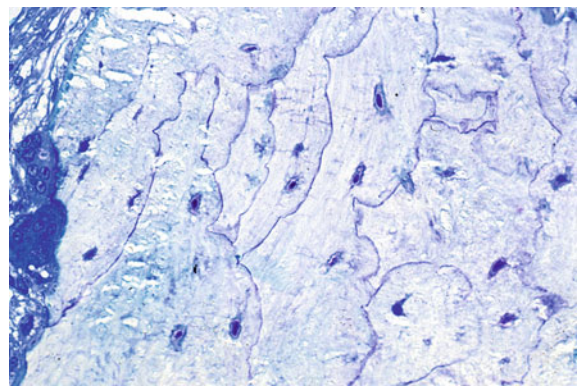

Fig. 10 Paget's disease of bone with cement lines and active, partly nucleolated osteoclasts (*left*)

instance with respect to the histological and histopathological findings and, where appropriate, immunohistological results. Then, taking account of the patient's clinical status and the results of other diagnostic procedures (CT, MRI, scans), and thirdly together with the peripheral blood picture and the smears of the bone marrow aspirate. Occasionally chromosome analysis, enzyme and marker studies are useful in the confirmation of a diagnosis.

2.2.2 Histomorphometry

Quantitative histology comprises three main types of primary measurements, expressed in three-dimensional terminology: volume surface and thickness. Number, the fourth type of primary measurements can only be expressed two-dimensionally, if serial sections are not examined. Other rare sophisticated parameters can be derived from combinations of these primary variables. The main variables we used are summarised in Table 1. The normal values given for different skeletal sites are derived from post-mortem biopsies taken with the electrical drill from 100 normal subjects who died suddenly but had no evidence of bone or marrow disease (Table 2). We also investigated age-related changes of bone and bone marrow in posterior iliac crest biopsies. The most important histomorphometric parameters are given in Table 3.

3 Normal Bone and its Main Disorders

3.1 Bone Structure

The ilium along with other flat bones consists of an outer frame—the cortex—and an interior network of ossicles—the trabecular, spongy or cancellous bone

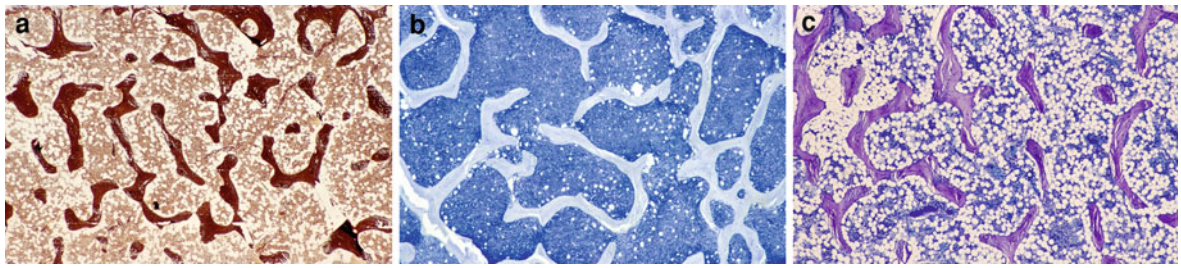

Fig. 11 Variants of marrow cellularity. **a** Normocellular marrow. **b** Hypercellular marrow. **c** Hypocellular marrow

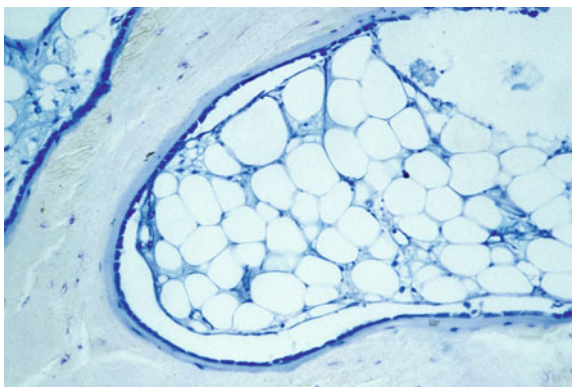

Fig. 12 Aplastic anaemia with oedema and absence of haematopoietic cells

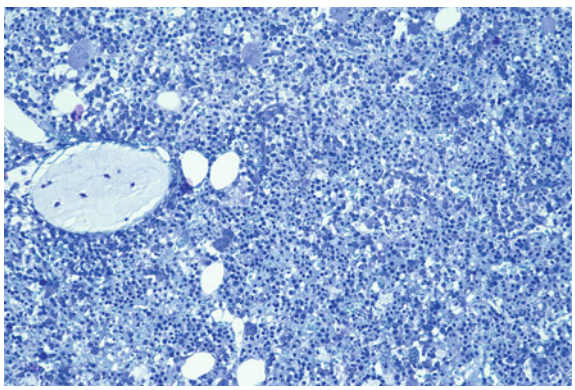

Fig. 13 Haemolytic anaemia with massive hyperplasia of erythropoiesis

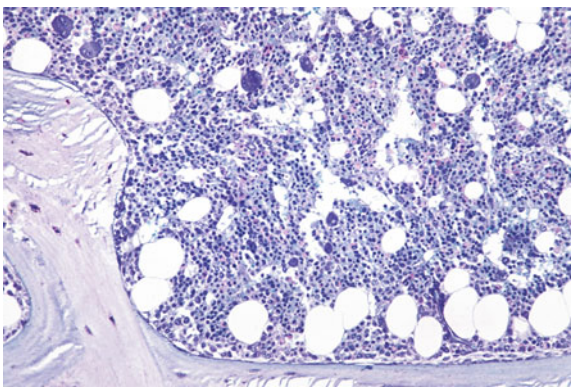

Fig. 14 Histotopography of normal haematopoiesis in the bone marrow: In bone marrow sections the erythroid precursors usually appear in small clusters, "erythrons". Megakaryocytes are present in relatively small numbers, but are prominent because of their size. Histotopographically erythrons and megakaryocytes are associated with the central marrow sinusoids, early granulopoietic precursors are situated in proximity to the trabeculae and the arterial vessels, while the more mature granulocytes are located in the central intertrabecular regions

(Fig. 4a, b). Undecalcified biopsies embedded in plastic are the most suitable for bone and its cells and for histomorphometry. About 80% of the total bone volume is cortical compact bone and about 20% is cancellous bone. Over 90% of compact bone consists of matrix and <10% is soft tissue. Bone matrix consists mainly of fibres of collagen type I and the amorphous ground substance between them contains proteins and proteoglycans specific for bone. About 65% of normal bone is mineral, mainly hydroxyapatite. Osteons are the functional units of compact bone. They are cylindrical structures composed of concentric layers (lamellae) of bone disposed around a central canal within are capillaries and venules. Osteons are the units responsible for the maintenance and remodelling of cortical bone. Trabecular bone refers to the honeycomb of bones that partitions the space enclosed by the cortical bone and which is lined by the endosteum. Most trabeculae are <0.2 mm thick and consist of segments formed by parallel layers—lamellae. About 10% of the trabecular surface is covered by osteoid.

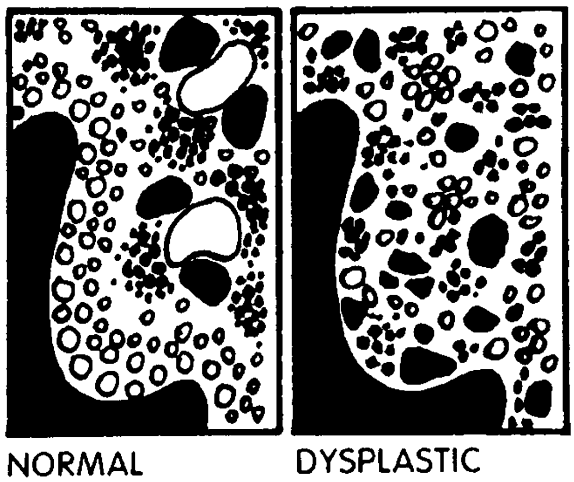

Fig. 15 Schematic representation of architectural disorganisation in myelodysplastic syndrome (MDS): on the *left* normal architecture of the bone marrow, with granulopoietic precursors at endosteal surface, erythrons and megakaryocytes around the central sinusoids. In MDS there is topographic distortion, with precursors of the three cell lines found in all marrow regions. There is no stromal organisation

Main disorders of bone mass and structure (Figs. 5a–c, 6): *Osteoporotic syndrome, osteogenesis imperfecta, osteosclerosis, osteopetrosis, osteomalacia*

3.2 Bone Cells

Osseous remodelling is characterised by the presence of osteoclasts in the scalloped niches (Howship's lacunae) and by a row of cuboidal osteoblasts on a layer of osteoid (unmineralised bone) is often present in the subcortical regions even when the deeper cancellous bone is almost devoid of it. There is a delicate balance between bone formation and resorption of bone in which highly complex regulatory mechanisms are involved (Fig. 7).

3.2.1 Osteoblasts

These are the cells that produce bone matrix. They arise out of progenitor cells in the stroma of the bone marrow and also from the endosteal lining cells of the endosteum. When activated they become cuboidal, and fibres and blood vessels in the vicinity appear more prominent (Fig. 8a, b).

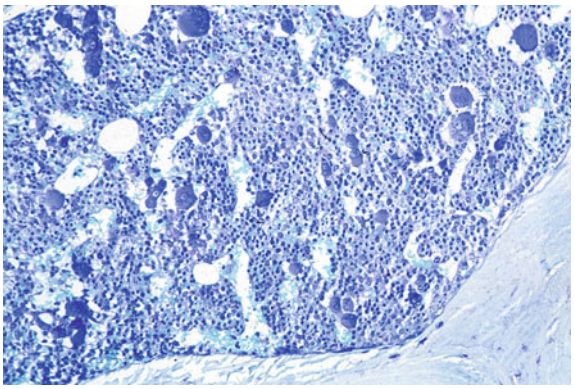

Fig. 16 Polycythaemia vera with almost complete replacement of the fat cells, and hypercellular erythropoiesis and megakaryocytes around the hyperplastic sinusoids

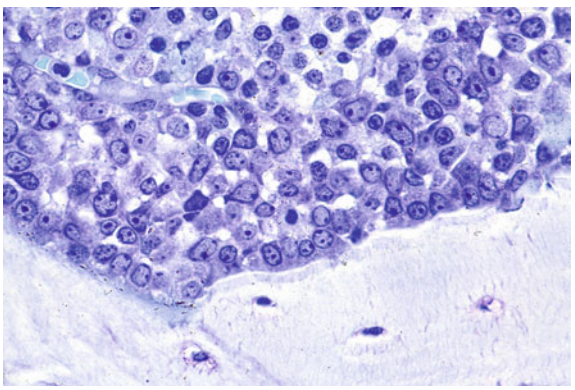

Fig. 17 Acute myeloid leukaemia in hypercellular marrow showing exclusively immature myeloid precursors

3.2.2 Osteocytes

Following deposition of osteoid and its mineralisation, the osteoblasts in that layer are enclosed and embedded in their own matrix and thus become osteocytes with lacunae whose processes connect by means of the canaliculi with those of other osteocytes and with the osteoblasts on the surface of the bone.

3.2.3 Osteoclasts

These are cells that resorb bone. They are multinucleated giant cells and range from 20 to 100 μm in diameter and may have 2–100 nuclei. Osteoclasts derive from the monocytic system and are formed by cell fusion. They are found on the trabecular and cortical surfaces in erosion cavities. The average life span of a labelled nucleus in osteoclasts is 11 days. Deregulated and overactive osteoclasts are the main

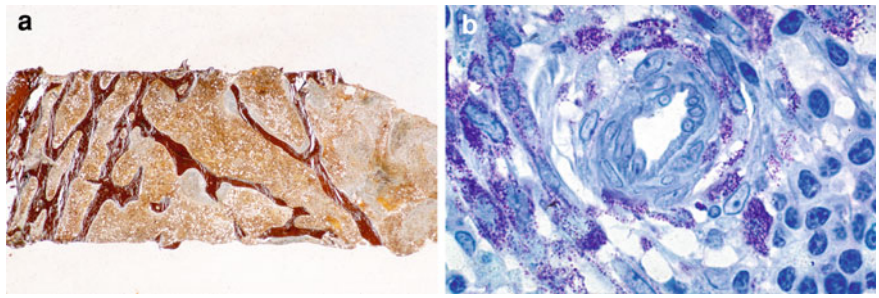

Fig. 18 Systemic mastocytosis in the bone marrow. **a** Multiple paratrabecular mast cell granulomas with osteolytic lesion (*right*). **b** Perivascular mastocytosis

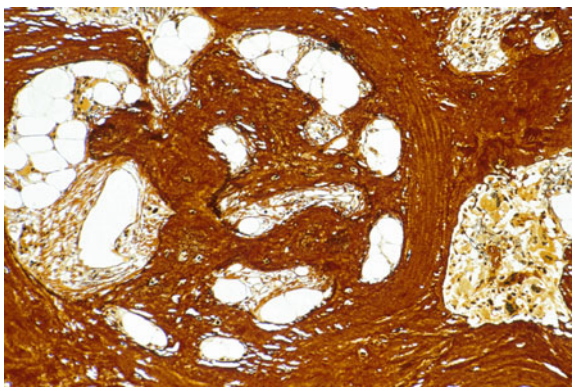

Fig. 19 Osteomyelosclerosis in case of PV with megakaryocytic hyperplasia (*right*)

cause of nearly all osteopathies (about 90%), such as osteoporosis (systemic) or osteolysis (local). There are only two osteopathies in which increased osteoclastic activity is primarily not involved: osteopetrosis and osteomalacia.

3.2.4 The Concept of Bone Remodelling

Remodelling involves a balanced sequence of resorption and formation. Overall, 5–10% of the existing bone is replaced annually, though the turnover of trabecular bone is probably nearer 20%. Remodelling is not uniform and varies greatly throughout the skeleton. A complete trabecular remodelling cycle takes about 200 days, and there are about 35 million basic multicellular units (BMUs) operative at any given time in the skeleton.

Main disorders of bone remodelling (Figs. 9, 10): *Osteitis fibrosa generalisata, subtype of renal bone disease, Paget's disease*

4 Normal Bone Marrow and its Main Disorders

4.1 Definition and Biology

The term "bone marrow" is generally used to refer to the tissue occupying the cavities between the trabecular bone. Normal marrow is either red, containing the haematopoietic elements, or yellow, composed mainly of adipose tissue (fat cells). In the adult, red marrow is found in the cavities of the skull, sternum, scapulae, vertebrae, ribs, pelvic bones and the proximal ends of the long bones. The red marrow is the organ that produces the mature blood cells, which have a finite life span and must be constantly replenished. The weight of the bone marrow is about 1600–3700 g, approximately the same as that of the liver. Why haematopoiesis in the adult is normally confined to these bones is not clear. A continuous supply of precursor cells is provided by the pluripotent stem cell compartment capable of self-renewal and having the ability to differentiate into the progenitor cells committed to erythro-, granulo-, mono- and megakaryopoiesis. The bone marrow is also a site for lymphopoiesis and maturation of plasma cells.

Main disorders of the pluripotent stem cell system: *Aplastic anaemia*, *myelodysplastic syndrome*, *myeloproliferative syndrome*

4.2 Age-Related Changes and Marrow Cellularity

With advancing age there is a reduction in the trabecular bone volume (osteopenia) and the numbers of associated endosteal cells, osteocytes and paratrabecular sinusoids.

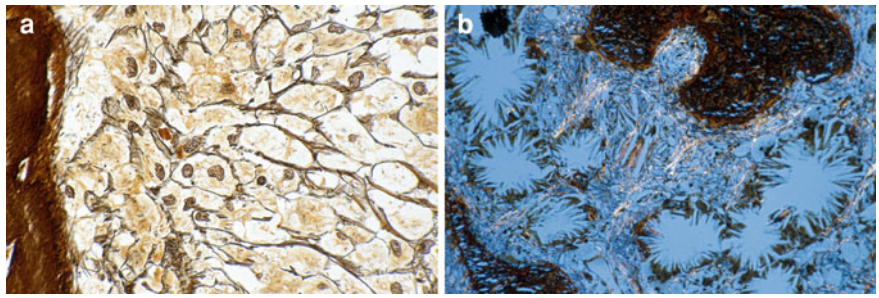

Fig. 20 Storage disorders. **a** Morbus Gaucher. **b** Hereditary oxalosis

Haematopoietic tissue is also decreased, accompanied by an increase in fat cells (hypoplasia, hypocellularity) (Table 3), particularly in the subcortical regions. However, there is great individual variability in these age (and sex)-related changes. In addition, other cells normally present in the bone marrow, such as lymphocytes, plasma cells and mast cells, may show increases in the bone marrow of older people. Stromal changes are also found: increase in fibers and changes in walls of blood vessels especially sclerosis.

Main disorders of marrow cellularity (Figs. 11a–c, 12, 13): *Aplastic anaemia*, *anaemias with hyperplastic marrow (haemolytic anaemias)*

4.3 Topography and Bone Marrow Architecture

The haematopoietic tissue is distributed in the marrow spaces in the extravascular compartment. Erythropoietic islands ("erythrons") and megakaryocytes are associated with the marrow sinusoids in the central regions of the marrow cavities, early myeloid precursors lie close to the endosteal surfaces and to the arterioles, while the more mature forms of the granulocytic series are also found in the central intertrabecular areas (Fig. 14). Alterations and variations of this topography are especially prone to occur in hyper- and hypo-plastic conditions, and when osseous or metastatic changes are present. Selective hypoplasia in the iliac crest has also been observed in certain conditions such as autoimmune and bone marrow oedema states, and it may be seen after radiotherapy to that region.

Main disorder of marrow topography (Fig. 15): *Myelodysplastic syndrome, toxic damage of the bone marrow*

4.4 Cellular Constituents of the Marrow

4.4.1 Erythropoiesis

The nucleated precursors of the red cells are found in clusters of cells exhibiting the range of maturational sequences from the earliest recognisable proerythroblast to normoblast. A macrophage with long cytoplasmic processes is usually located in the middle of each cluster. The myeloid–erythroid ratio is 1.5:1–3:1 in BMB.

Main disorders of erythropoiesis (Fig. 16): *Polycythaemia vera, anaemias with disturbances of maturation and prolifertion in the bone marrow*

4.4.2 Myelopoiesis—Granulocytes

The granulocytic series consists of neutrophils, eosinophils and basophils. The paratrabecular regions constitute the granulocytic generation zones, but precursors are also scattered throughout the rest of the marrow. Mature granulocytes migrate through the endothelium into the sinusoids.

Main disorders of granulopoiesis (Fig. 17): *Acute and chronic myeloid leukaemias, agranulocytosis*

4.4.3 Mast Cells—Basophils

These are best recognised in plastic embedded biopsies (Giemsa staining). Mast cells lie adjacent to the endothelial cells of sinusoids, at the endosteal surface of the trabecular bone and at the edges of lymphoid

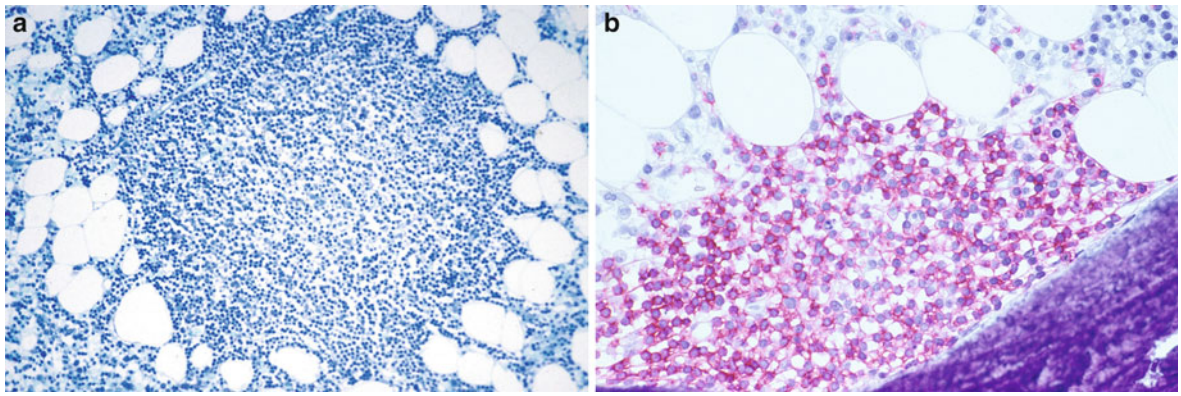

Fig. 21 Lymphoid nodules. **a** Non-neoplastic, large lymphoid nodule (about 0.4 mm in diameter) occupying much of the marrow space. **b** Neoplastic lymphoid nodule in the paratrabecular region in a case of low grad lymphoma. Immunohistology showing exclusively B cells

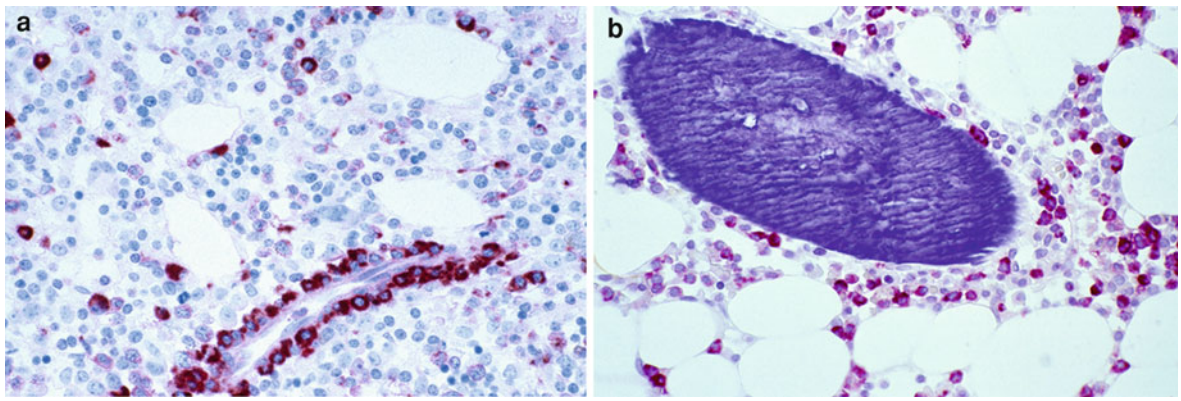

Fig. 22 Topographic significance of reactive and neoplastic plasmacytosis. **a** Reactive with mature plasma cells located around small blood vessels. **b** Neoplastic with random interstitial infiltration among fat cells, an important diagnostic parameter in early stage of myeloma

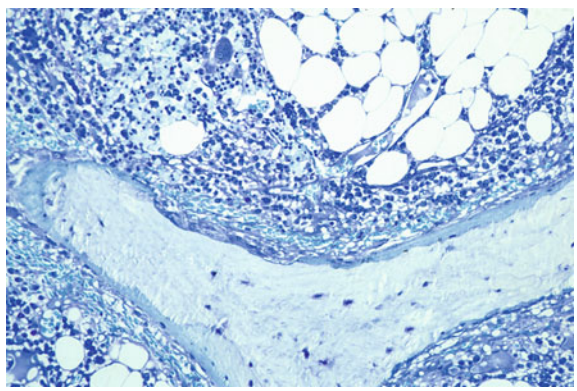

Fig. 23 Multiple myeloma with predominantly paratrabecular infiltration and high osteoclastic activity. Marked marrow atrophy in the central part of the marrow space

aggregates. They may be increased in infections, bone marrow oedema syndromes and occur as reactions to drugs.

Main disorders of basophils and mast cells (Fig. 18a, b): *Basophilic leukaemias, mastocytosis*

4.4.4 Megakaryocytes and Thrombopoiesis

These are the largest cells normally present in the bone marrow. Their size ranges from 12 to 150 μm and show considerable variation in shape as well as in nuclear configuration. Three stages of maturation are recognised: megakaryoblast, promegakaryocyte and mature megakaryocyte. Megakaryocytes typically project into the sinusoids and the platelets are shed directly into their lumina.

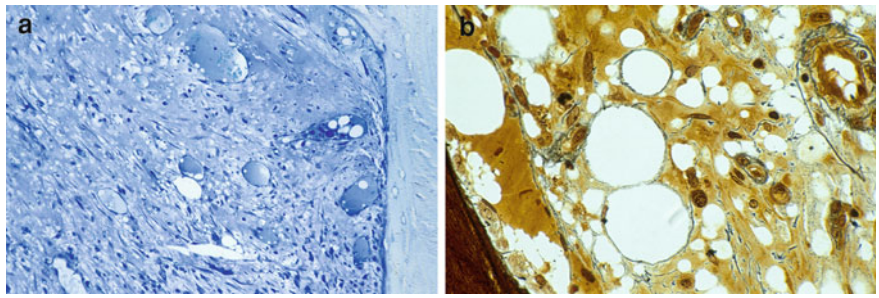

Fig. 24 Bone marrow oedema syndrome. **a** With marked oedema in the marrow space and loss of haematopoietic as well as fat cells. **b** Moderate fibrosis

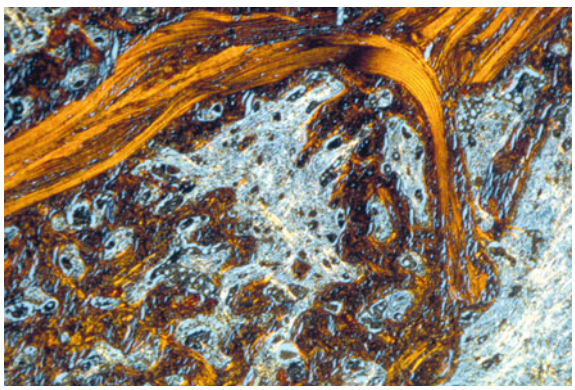

Fig. 25 Massive fibrosis and woven bone in a patient with bone metastases (prostate cancer)

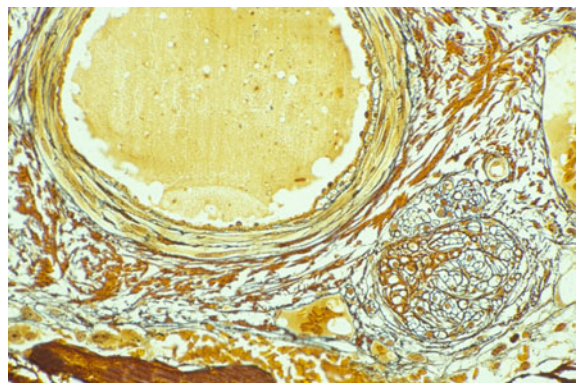

Fig. 27 Large artery and nerves (*lower right*) in the bone marrow

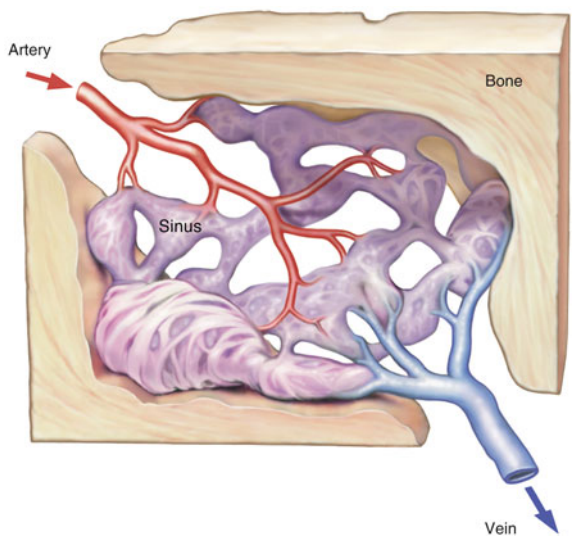

Fig. 26 Large blood vessel accompanied by nerve (*lower right*)

Main disorders of megakaryocytes (Fig. 19): *Idiopathic thrombocythaemia, myelofibrosis/osteomyelosclerosis, Werlhof's syndrome*

4.4.5 Monocytes, Macrophages and Iron-Containing Reticular Cells

Monocytes (though produced in the bone marrow) are not often encountered, even in optimal histological sections. They are recognised in greater quantities in immune histology than in conventionally stained sections. Macrophages appear to be a heterogeneous population and form part of the reticuloendothelial system, which is responsible for the breakdown of senescent red cells and the storage of iron.

Main disorders of monocytes and macrophages (Fig. 20a, b): *Monocytic leukaemia, storage disorders, granulomatous disorders, infectious disorders, iron overload*

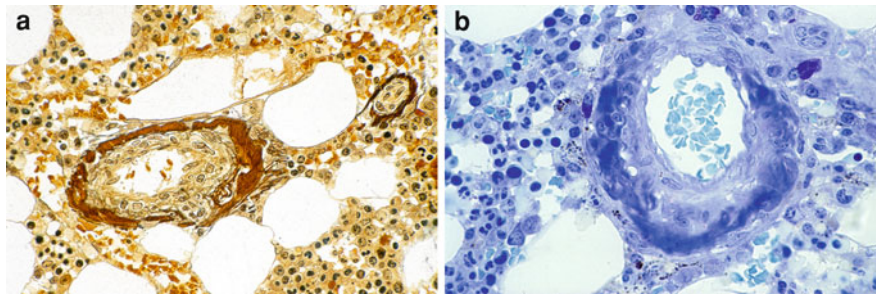

Fig. 28 Vascular disorders. **a** Calcified wall of blood vessel in a patient with primary HPT. **b** Blood vessel with deposition of amorphous material in their walls (amyloidosis)

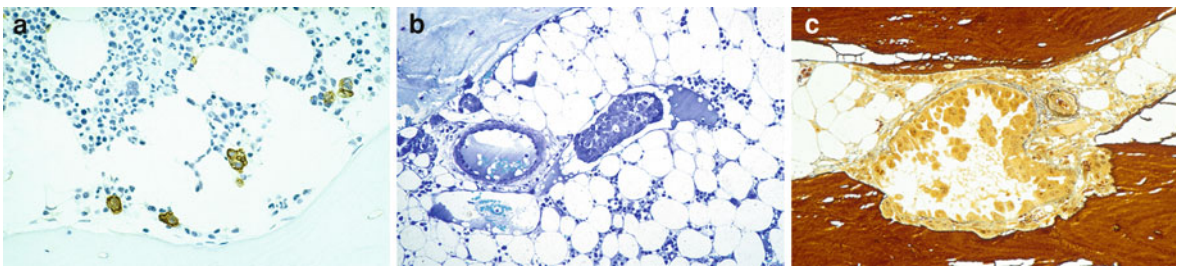

Fig. 29 Initial stages of process of establishment of metastases in the bone marrow. **a** Dissemination of tumour cells in the marrow (immunohistology) and beginning adhesion to the surface of the bone. **b** Tumour cell embolus in a sinus of the bone marrow and on the surface of a trabecula. **c** Development of a micrometastasis with induction of stroma and vessels

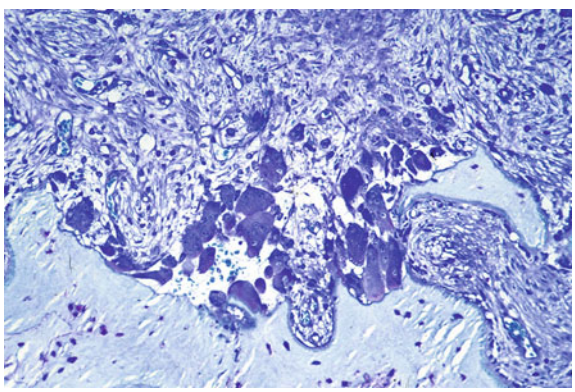

Fig. 30 Massive osteoclastic destruction of bone induced by cancer cells in the bone marrow

4.4.6 Lymphocytes and Lymphopoiesis

Lymphoid cells may constitute up to 15–20% of the nucleated cell population of the bone marrow. On immunohistology, most are T cells, reflecting the proportions in the peripheral blood. They are dispersed among the haematopoietic and fat cells, or aggregated as lymphoid nodules, whose incidence increases with age. Such nodules are found in 1 to >40% of bone marrow biopsies with the higher incidence in the older age groups. On immunohistology the nodules consist of a heterogeneous population of T and B cells, though mainly T cells. Four configurations of lymphoid aggregates have been described:

- Nodules with germinal centres
- Sharply demarcated nodules (Fig. 21a)
- Nodules with irregular borders, and
- Small aggregates of lymphoid cells.

In benign conditions, lymphoid nodules are found mainly in the intertrabecular (central) and perivascular regions.

Main disorders of lymphocytes (Fig. 21b): *Acute and chronic lymphoid leukaemias, malignant lymphomas*

4.4.7 Plasma Cells

These belong to the normal cell population of the bone marrow and represent the final developmental stage of

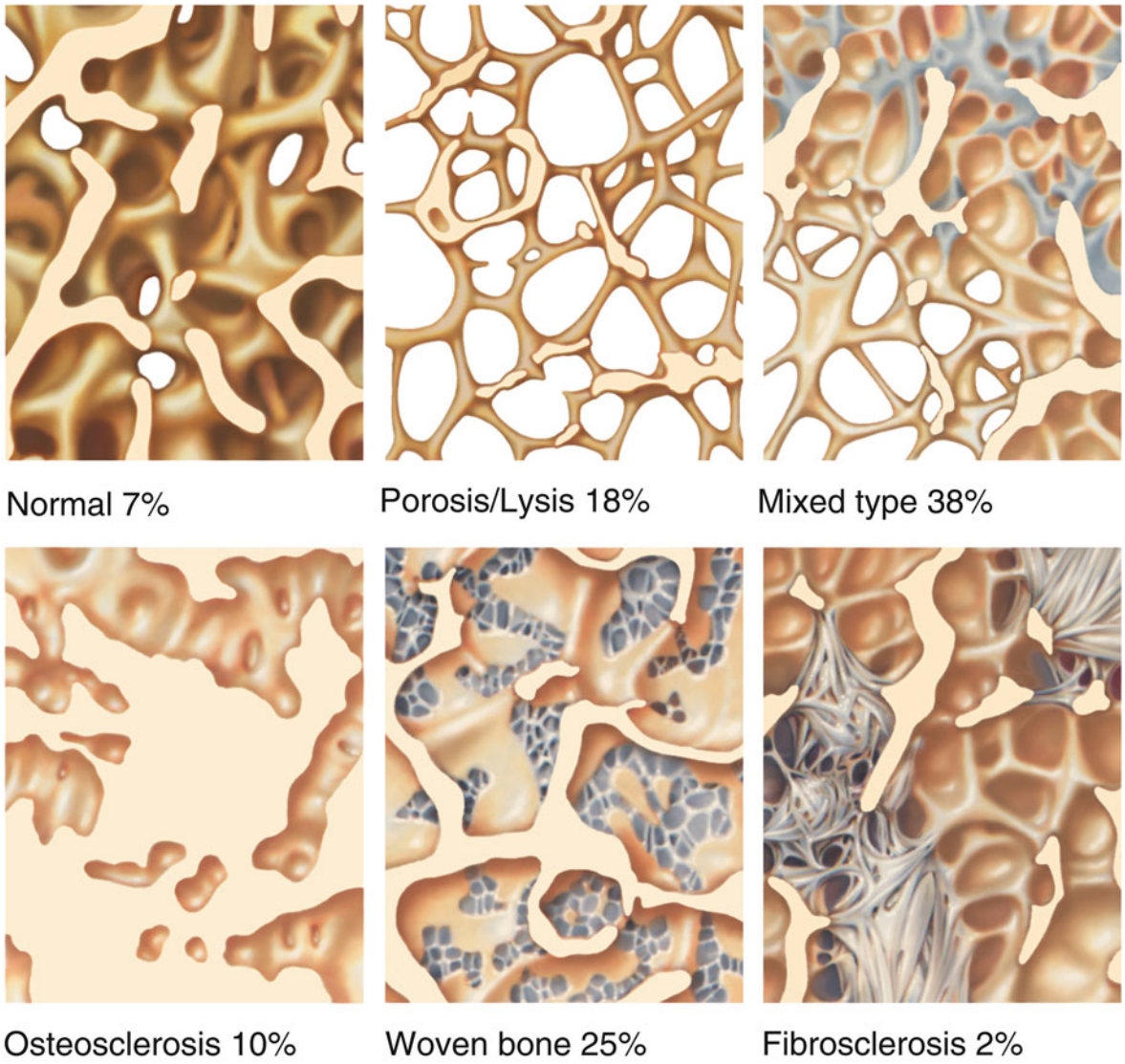

Fig. 31 Histologic types of osseous reactions near the metastases

the B cell lineage. They constitute about 1% of the nucleated cells of aspirates of normal adult marrow, with a range of 0.5–4.0%. Plasma cells are equally distributed throughout the red marrow with no significant differences between skeletal sites. These data imply that there are >100 million plasma cells in the red marrow, producing >90% of the serum immunoglobulins. Plasma cells are normally found in close apposition to capillaries and small vessels as well as singly and in clusters of two or three within the bone marrow.

Main disorders of plasma cells (Figs. 22a, b, 23): *Multiple myelomas, MGUS*

4.4.8 Stromal Cells

The stroma provides the supporting framework for haematopoiesis and is supported by the reticular cells, fat cells, fibroblasts and their fibrils and by the extensive network of blood vessels, including the sinusoids and their accompanying nerves. Together, these components constitute the bone marrow haematopoietic

microenvironment. Adhesion molecules are responsible for stem cell adherence to stromal cells. Fat cells occupy about one-third of the marrow volume in the iliac crest biopsy. They serve as a supporting, filling and metabolic function. There are close associations between the mesenchymal elements—the endothelium, the adventitial cells, fibroblasts and osteoblasts, and the endosteal lining cells as well as macrophages. Fibroblasts produce the reticular fibres of which the normal bone marrow has few, mainly in association with blood vessels and endosteum.

Main disorders of the bone marrow stroma: *Toxic damage and radiation of the bone marrow*

4.4.9 Extracellular Matrix

This consists of a variety of components, produced by the stromal cells. These proteins include adhesion molecules, collagen, fibronectin, proteoglycans as well as growth factors.

Main disorders of the extracellular compartment (Fig. 24a, b): *Bone marrow oedema syndrome*

4.4.10 Fibres

The normal bone marrow contains only thin reticular fibres near bone and blood vessels best visualised by the Gomori stain. They mainly consist of collagen type III.

Main disorders of fibres (Fig. 25): *Myelofibrosis and osteomyelofibrosis (myeloproliferative syndrome), inflammatory-associated fibrosis of the bone marrow, metastatic- induced fibrosis of the bone marrow (e.g. in prostate cancer)*

4.4.11 Blood Vessels and Nerves

The medullary arteries enter via the cortical bone and branch within the marrow and the trabeculae, accompanied by nerves. The smaller branches divide into arterioles and then into capillaries which frequently have a cuff of plasma cells around them, and lead into the sinusoids (Fig. 26). These form a system of channels of variable width and length whose walls consist of a single layer of endothelial cells. The sinusoids in turn drain into the periosteal veins. Nerves are rarely found, and occasionally may be seen next to blood vessels or in the periosteum (Fig. 27).

Main disorders of blood vessels (Fig. 28a, b): *Arteriosclerosis, vasculitis, amyloidosis*

5 Metastatic Bone Disease

5.1 Mode of Spread of Metastases

Evidence has accumulated that any primary malignant tumour has the ability to spread as soon as it is established and has access to lymphatic and blood vessels. The sinusoidal system of the red marrow is lined by a thin endothelial layer, has no tight junctions, and has a low perfusion rate but large blood flow thus facilitating passage of tumour cell emboli into the extravascular space. Moreover, the haematopoietic and stromal cells of the bone marrow probably provide the tumour cells with growth factors, including adhesion molecules required for their survival, establishment and expansion. Since bone and bone marrow have no lymphatics, metastatic cells reach the bone marrow via the blood stream or by contiguous spread. Bone metastases start in the red bone marrow. The incidence of involvement of the thoracic and lumbar spine and pelvis is statistically equal, 70% each, due not only to their anatomical mass, but also to the role of the vertebral venous system in conveying metastases to the bones, especially retrograde flow in Batson's vertebral plexus. Other bones are less frequently affected. The complex series of interactions between cancer cells and host tissue (bone marrow) may be summarised as follows (Fig. 29a–c):

- Invasion of blood and lymph vessels at site of origin, and single cells or clusters split off into the circulation (sinusoid system) ("tumour cell emboli")
- Extravasation out of the blood stream into the interstitium (using collagenases) ("tumour cells in the bone marrow")
- Adherence to stromal tissues (by adhesion molecules) ("fixed tumour cells" in the bone marrow, especially in the paratrabecular regions)
- Growth with induction of connective tissue and blood vessels (by growth factors) (birth of "micrometastases" in the bone marrow)

- Osseous reactions with bone destruction (osteolyses/osteoporosis) and/or formation (osteosclerosis/woven bone) ("bone metastases"). Osteoclastic bone resorption and osteoblastic bone formation is stimulated by cytokines produced by the neighbouring tumour cells (Fig. 30).

Five different histologic patterns can be distinguished in bone marrow biopsies: normal, osteoporosis/osteolysis, mixed, trabecular sclerosis and woven bone (Fig. 31).

Main primary tumours developing bone metastases: *Breast cancer, prostate cancer, bronchogenic cancer, renal cancer*

5.2 Pitfalls in Histological Diagnosis

The most important pitfalls in histological diagnosis are

- Histological variation within the biopsy: subcortical hypoplasia, alternating fatty and hyperplastic areas in deeper parts of the biopsy
- Non-representative tangentially taken biopsies
- Presence of misleading artefacts. Pieces of epidermis, muscles, cartilage and blood clots
- Swelling or shrinkage of cells due to inadequate fixation, embedding or staining.

Literature

Books Dealing With Bone and Bone Marrow Histology

Bartl R (1998) Bone marrow biopsy and aspiration for diagnosis of multiple myeloma. In: Malpas J, Bergsagel D, Kyle R, Anderson K (eds) Myeloma: biology and management. Oxford University Press, Oxford, pp 89–121

Bartl R, Frisch B (1993) Biopsy of bone in internal medicine. Kluwer, Dordrecht

Bartl R, Frisch B, Burkhardt R (1982) Bone marrow biopsies revisited. A new dimension for haematologic malignancies. Karger, Basel

Burkhardt R (1971) Bone marrow and bone tissue. Springer, Heidelberg

Duhamel G (1974) Histopathologie Clinique de la Moelle Osseuse. Masson, Paris

Frisch B, Bartl R (1990) Atlas of bone marrow pathology. Kluwer, Dordrecht

Frisch B, Bartl R (1999) Biopsy interpretation of bone and bone marrow. Arnold, London

Frisch B, Lewis SM, Burkhardt R, Bartl R (1985) Biopsy pathology of bone and bone marrow. Chapman & Hall, London

Gatter K, Brown D (1997) An illustrated guide to bone marrow diagnosis. Blackwell Science, Oxford

Krause JR (1981) Bone marrow biopsy. Churchill Livingstone, Edinburgh

Rywlin AM (1976) Histopathology of the bone marrow. Little Brown, Boston

MR Imaging of the Normal Bone Marrow and Normal Variants

Bruno C. Vande Berg, P. Omoumi, C. Galant, N. Michoux, and F. E. Lecouvet

Contents

Abstract

The MR appearance of the normal marrow shows important variations not only with age and gender but also among individuals of the same age range and sex. On the contrary, marrow distribution and signal intensity patterns show little variation among similar bones of the same subject. Focal alterations in signal intensity can be observed as normal findings, reflecting local variations in the amount of normal expected medullary space components (including fat, hematopoietic or bone cells and vessels). Several variations from the normal age-related expected appearance have been recognized including focal or diffuse red marrow hyperplasia, enchondromas, hemangiomas, and marrow changes related to the presence of notochordal cells. Important limitations in the characterization potentials of MR imaging should also be kept in mind.

1 Introduction

The understanding of MR imaging of the normal bone marrow should belong to the basic ground knowledge shared by all radiologists given the everyday use of

B. C. Vande Berg · P. Omoumi · N. Michoux · F. E. Lecouvet
Department of Musculoskeletal Imaging, Université catholique de Louvain, Saint Luc University Hospital, Brussels, Belgium

C. Galant
Department of Pathology, Université catholique de Louvain, Saint Luc University Hospital, Hippocrate Avenue 10/2942, 1200 Brussels, Belgium

B. C. Vande Berg (✉) · P. Omoumi · F. E. Lecouvet
Department of Radiology, Université catholique de Louvain, Saint Luc University Hospital, Hippocrate Avenue 10/2942, 1200 Brussels, Belgium
e-mail: bruno.vandeberg@uclouvain.be

A. Baur-Melnyk (ed.), *Magnetic Resonance Imaging of the Bone Marrow*, Medical Radiology. Diagnostic Imaging,
DOI: 10.1007/174_2012_574, © Springer-Verlag Berlin Heidelberg 2013

MR imaging for the assessment of the entire body. It is frequently the radiologist's cornerstone to decide whether imaging findings are normal or abnormal and to differentiate between clinically significant or non-significant fortuitous findings. This challenge is extremely common in routine clinical practice given the high sensitivity of MR imaging for the detection of subtle focal marrow changes that are frequently clinically irrelevant. The purposes of this chapter are to focus on basic imaging principles of MR imaging of the bone marrow and to highlight the normal MR appearance of the bone marrow, normal variants, and frequent marrow alterations including benign bone tumors and hamartomas that can simulate significant lesions.

2 Anatomy and Physiology of Normal Bone Marrow

Red and yellow marrows that occupy the medullary cavity of the adult human skeleton differ in composition and distribution (Vogler and Murphy 1988; Vande Berg et al. 1998a) (Table 1). Red marrow contains about 50% of fat cells and 50% of hematopoietic cells embedded in a network of highly permeable sinusoids. The relative proportion of fat and non-fat cells varies with age and sex (Cristy 1981). It also depends on the bone considered and on the anatomic region of each individual bone. In adults, red marrow occupies the cranial vault, the spine, the ribs, the sternum, the pelvic region and the proximal aspects of the femur and humerus.

Yellow marrow almost exclusively contains fat cells and very few capillaries (Vogler and Murphy 1988; De Bruyn et al. 1970; Weiss 1965). In adult humans, it is mainly found in the appendicular skeleton. All long bones epiphyses contain yellow marrow, except the proximal ends of the humeri and femurs, mainly in women, in whom red marrow is frequently observed at MR imaging located adjacent to the subchondral bone plate (Vande Berg et al. 1997; Mirowitz 1993).

The possibility of red marrow to convert to yellow marrow and, reversely, of yellow marrow to transform into red marrow is a remarkable feature of bone marrow (Vogler and Murphy 1988; Vande Berg et al. 1998a; Weiss 1965). Conversion of red to yellow marrow occurs as a physiological process during growth and until adulthood (Fig. 1). At birth, red marrow occupies almost the entire skeleton (Vogler and Murphy 1988). It progressively converts to yellow marrow, starting distally in the limbs and centrally in the long bones (Cristy 1981). Reconversion of yellow to red marrow can occur in case of demand of more hematopoietic cells. In this case, the central red marrow becomes more cellular. In other words, it contains less fat cells. Simultaneously, red marrow expands in the peripheral skeleton and progressively replaces yellow marrow. These changes occur in a well-organized and predictable manner probably related to the underlying vasculature of each concerned bone area.

3 MR Sequences for Imaging of the Bone Marrow

3.1 T1- and T2-Weighted SE Sequences

The T1-weighted SE sequence is the most important sequence for bone marrow imaging simply because it is extremely accurate (high sensitivity and specificity) for the depiction of lipids that are contained within the adipocytes of both red and yellow marrow (Vogler and Murphy 1988; Vande Berg et al. 1998a). Many reasons account for the unparalleled robustness of the SE T1-weighted sequence for the assessment of the bone marrow (Table 2). First, it is the only MR imaging sequence for which a reliable criterion for signal normality of the red marrow has been described and consistently validated (Vogler and Murphy 1988; Carroll et al. 1997; Levine et al. 1994; Vande Berg et al. 1998b; Hanrahan 2011) (Fig. 2). Second, it is sensitive to focal alterations in marrow content that are observed in the vast majority of marrow lesions and it can be used to categorize these lesions (Vande Berg et al. 1998b). Third, it is widely available in all imaging centers. Finally, it shows limited variability over time and among magnets of different vendors. However, two significant weaknesses of the T1-weighted SE sequences must be stressed, keeping in mind its sensitivity and specificity when imaging fat. First, the T1-weighted SE sequence lacks specificity when categorizing a bone marrow lesion because it only depicts the disappearance of marrow fat and not the appearance of abnormal cells that

Table 1 Composition and distribution of the red and yellow marrow in young adults

	Red marrow	Yellow marrow
Adipocytes	50%	95%
Hematopoietic cells	50%	0%
Other cells	5%	5%
Vasculature	Rich network of capillaries with permeable walls (sinusoids)	Limited number of capillaries with continuous parietal membranes
Distribution	Cranial vault, spine, ribs, scapular and pelvic girdle, proximal humerus femurs	Bones distal to the humerus and femurs, all epiphyses

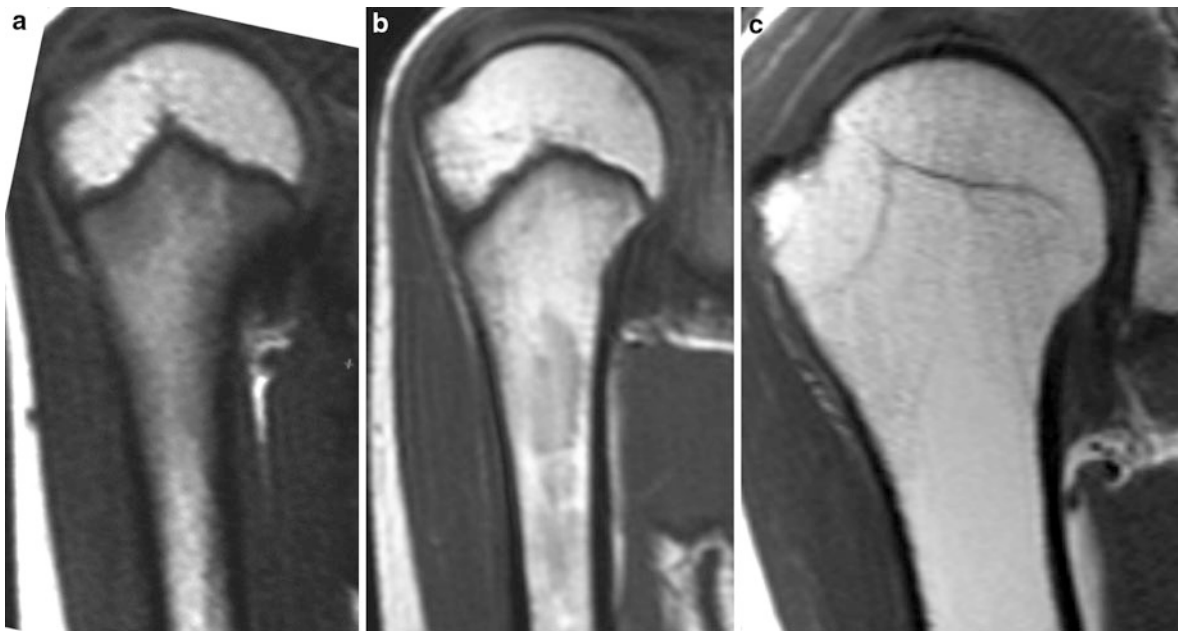

Fig. 1 Changes over years of the MR appearance of the proximal humerus on coronal T1-weighted SE MR images from subjects of 4-, 10- and 54 years of age. **a** At 4 years of age, the metaphysis and the diaphysis of the humerus contain red marrow that shows intermediate signal intensity and homogeneous signal. Normally, the red marrow signal intensity is higher than that of adjacent muscles (criterion for signal intensity normality). The humeral epiphysis contains fatty marrow that shows high signal intensity and homogeneous signal. **b** At 10 years of age, the signal intensity of the medullary cavity has increased with respect to **a**. **c** At 54 years of age, fatty marrow is present. A thin line of low signal intensity is located at the interface between the epiphysis and the metaphysis (physeal scar)

Table 2 Strengths and weaknesses of the T1-weighted SE sequence for the assessment of the bone marrow

Strengths	Weaknesses
Available criterion for signal normality	Lack of specificity
Available definitions for lesion patterns	Overestimation of the amount of fat
Availability in all imaging centers	
Reproducibility over time and among vendors	
Limited artefacts	

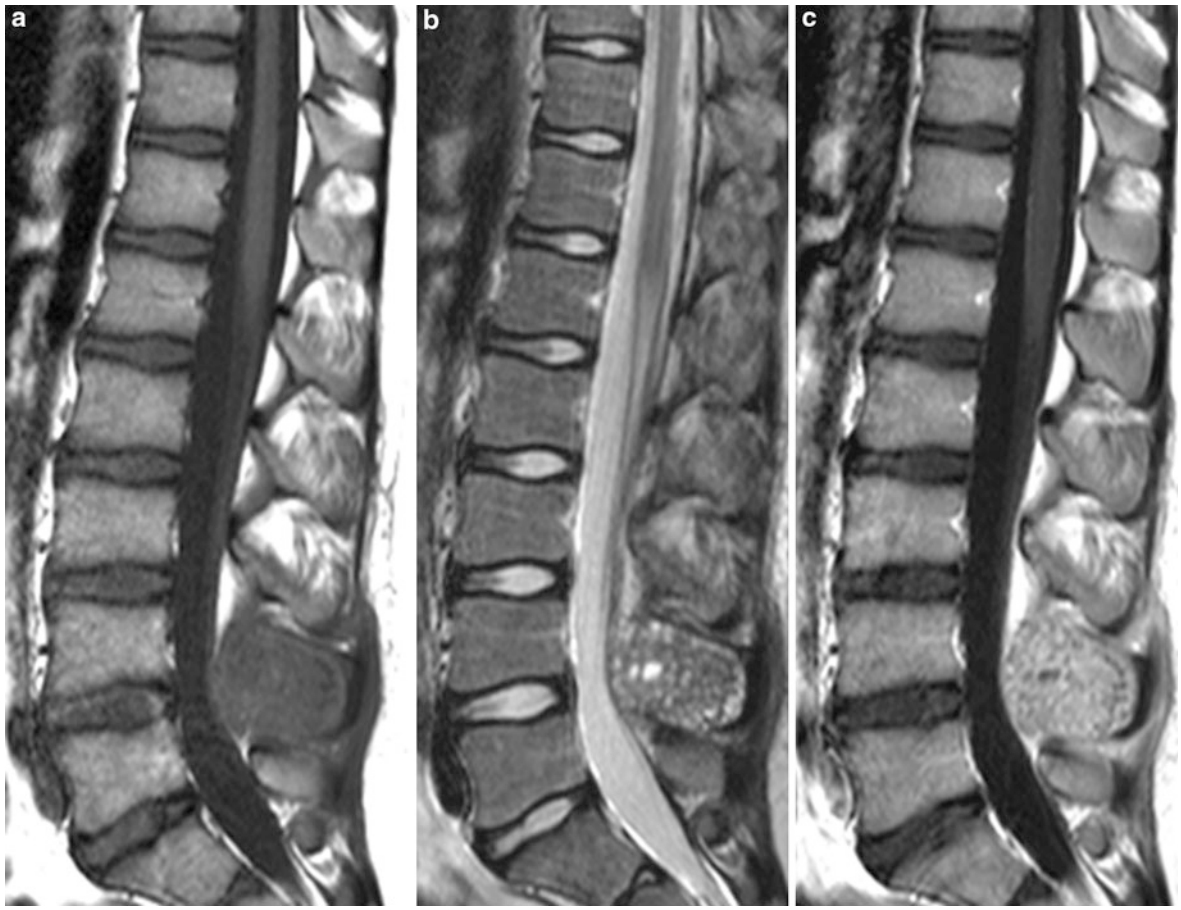

Fig. 2 Normal vertebral marrow in a 13-year-old boy with a lesion in the L5 spinous process. **a** On the sagittal T1-weighted SE image, the signal of red marrow is homogeneous and its intensity is higher than that of the adjacent intervertebral discs. **b** On the corresponding fat-saturated intermediate-weighted image, the signal of red marrow is homogeneous and its intensity is intermediate. However, it is not possible to assess the normality of the signal intensity on that sequence. **c** On the corresponding T1-weighted SE image obtained after intravenous injection of gadolinium, signal intensity enhancement is moderate and homogeneous

simultaneously occurs in abnormal conditions (Vogler and Murphy 1988; Vande Berg et al. 1998a). Second, the T1-weighted SE sequence is too sensitive to the presence of fat (Waitches et al. 1994). In other words, in some situations, the signal intensity remains within normal limits on T1-weighted images despite the presence of abnormal marrow components because of the presence of residual fat. Therefore, it is of the utmost importance to keep in mind that even a normal looking T1-weighted SE image of the bone marrow does not enable to exclude discrete marrow infiltration by abnormal cells or substances.

The non-fat-suppressed T2-weighted fast SE sequence has limited value in bone marrow imaging. It cannot be used to check the overall normality of the marrow signal intensity due to the lack of internal standard for normal signal intensity. It also has limited sensitivity for the detection of focal bone marrow lesions. Actually, in many marrow lesions, the amount of water is altered in a limited and variable way. On the contrary, the fatty content, which can be best assessed on SE T1-weighted sequences, is rapidly modified in any abnormal conditions. This variable behavior of fat and water could be related to the fact that the medullary cavity is a closed and non-expansible space that does not allow for important volume changes. However, the contribution of non-fat-suppressed T2-weighted sequence in marrow lesion characterization has been demonstrated in many conditions (Vogler and Murphy 1988; Vande Berg et al. 1998a).

Table 3 Clinical situations in which fat-saturated intermediate-weighted sequences may complement the T1-weighted SE sequence for lesion detection

Focal lesion with increased signal intensity on T1-W SE images	Background marrow with decreased signal intensity on T1-W SE images
Multiple myeloma	Children and teenagers
Hemangioma	Use of marrow stimulating drugs
Treated lesions	Serous conversion of marrow
Paget's disease	Multiple myeloma

Two opposed situations are encountered: focal lesion with only slight decrease in signal intensity on T1-W SE or background marrow with decreased signal intensity on T1-W SE

3.2 Fat-Saturated Sequences

Fat-saturation plays a crucial role in musculoskeletal MR imaging. It can be used as an adjunct to fluid-sensitive sequences (typically proton density- or T2-weighted sequences) or to enhanced T1-weighted sequences (Delfaut et al. 1999). The main added value of fat-saturation in marrow imaging derives from an increase in sensitivity for the detection of marrow lesions with fluid-sensitive sequences (Table 3) due to several reasons. First, signal intensity contrast between focal lesions and adjacent marrow may be decreased because of either an unusual high signal intensity of the focal lesion or of an unusual low signal intensity of the adjacent marrow (Fig. 3). Second, some marrow areas are poorly depicted on non-fat-saturated images because of their closed proximity to the receiving coils as in the posterior elements of the spine and they may become more easily detected on fat-saturated images (Fig. 4). Finally, on fluid-sensitive fat-saturated sequences, marrow lesions consistently demonstrate high signal intensity on a background of decreased signal intensity, which is favorable for their detection. These observations are the rationale for the use of fat-saturation in combination with fluid-sensitive sequences when the sensitivity of MR imaging for lesion detection must be optimized (Table 3); (Fig. 5). It should be kept in mind that the T1-weighted SE sequence may not be systematically replaced by fat-saturated fluid-sensitive sequences for marrow lesion detection because of the lack of criterion for normal marrow signal intensity on these sequences. In addition, the increase in sensitivity for lesion detection on fluid-sensitive sequences occurs at the expense of specificity. Actually, fat, compact bone and fibrous tissue consistently demonstrate low signal intensity on fat-saturated fluid-sensitive sequences although they differ in signal on T1-weighted SE images. Similarly, several lesion components of decreased signal intensity on non-fat-saturated fluid-sensitive sequences that could have contributed to lesion characterization will be lost on the corresponding fat-saturated images because of their intermediate or high signal intensity on these sequences (Simpfendorfer et al. 1996, 2008).

Fat-saturation can also be used with T1-weighted SE sequences generally after intravenous injection of gadolinium-based contrast material. This sequence contributes to a better depiction of the enhanced tissue and of normal red marrow enhancement. However, enhancement of strictly normal fatty marrow cannot be detected with these sequences. A drawback of the use of fat-saturation with fat-saturated T1-weighted sequences may be a decrease in specificity. For example, reappearance of normal signal intensity on non-fat-saturated T1-weighted images in a marrow lesion after contrast injection has been shown to be indicative of reactional marrow edema (Cuénod et al. 1996). This feature is not available on fat-saturated sequences because all enhanced areas will demonstrate high signal intensity.

3.3 Gadolinium-Enhanced MR Imaging

Red marrow is a highly vascularized tissue, thanks to the dense network of capillaries and their high permeability. However, its enhancement after gadolinium IV injection is only moderate on SE T1-weighted images (Vogler and Murphy 1988) (Fig. 2). This paradoxical observation can be partly explained as follows: the presence of gadolinium leads to a shortening of T1 relaxation times, explaining the signal enhancement on T1-weighted images. Considering that the T1 value of red marrow is physiologically relatively short because of the presence of fat, the shortening of the T1 relaxation time induced by gadolinium injection is relatively limited and will be barely visible at visual analysis. Quantitative techniques can help to detect the signal enhancement of red marrow (Baur et al. 1997). Normal fatty marrow generally shows no detectable enhancement.

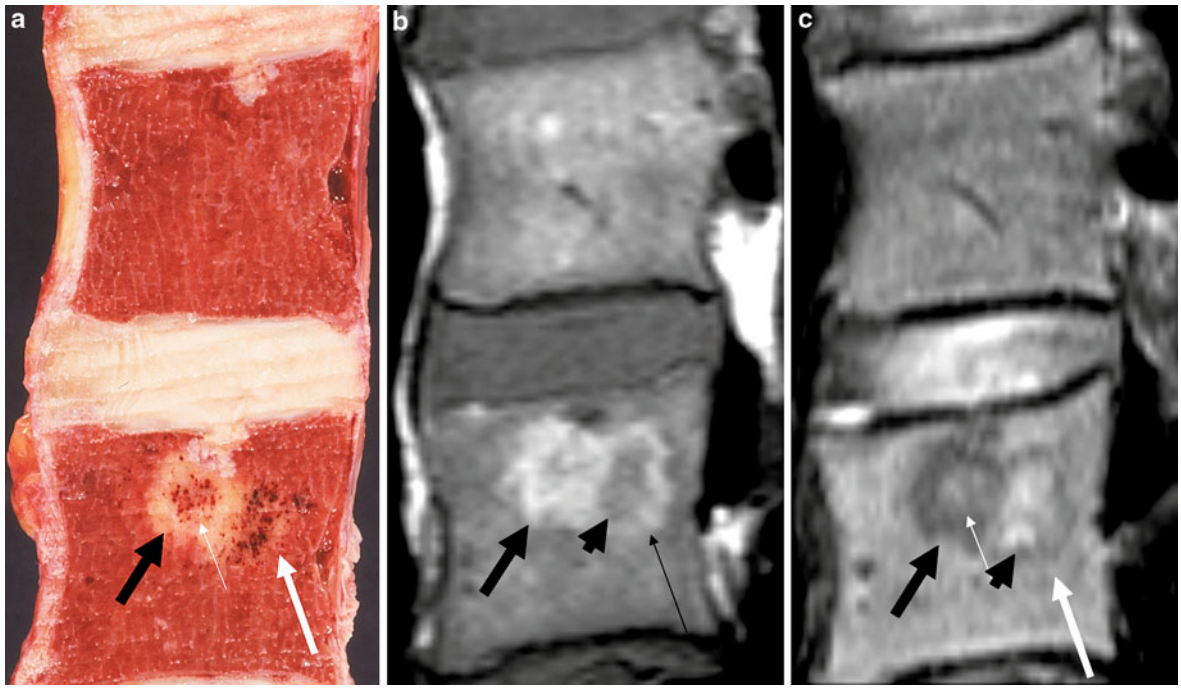

Fig. 3 Overestimation of fat on T1-weighted images and value of fat-saturated intermediate-weighted SE sequence. **a** Photograph of the macroscopic section of a cadaver spine with a vertebral hemangioma. At visual inspection, fat predominates and surrounds sparse central dilated vessels (*thin white arrow*) in the lesion's anterior aspect (*large black arrow*) whereas more vessels are detected posteriorly (*thick white arrow*). **b** On the corresponding T1-weighted SE image, the amount of fat is overestimated with respect to visual analysis and the lesion's anterior aspect seems to contain fat only (*large black arrow*) and a rim of fat is seen in the lesion's posterior aspect (*thin black arrow*). Note that the central component of the lesion's posterior aspect (*arrowhead*) has a signal intensity equivalent to that of the upper vertebral body. **c** The corresponding fat-saturated intermediate-weighted image seems to more closely reflect the distribution of the fat and non-fat components with some central components (*thin white arrow*) within the lesion's anterior aspect (*thick black arrow*). Note that the central component (*arrowhead*) of the lesion's posterior aspect has a higher signal intensity than that of the upper vertebral body

Dynamic contrast-enhanced MR imaging of the normal bone marrow has gained more attention as this technique is used for the assessment of bone lesions. In several studies, bone marrow perfusion appeared to decrease with age (Chen et al. 2001; Montazel et al. 2003; Griffith et al. 2005) as well as with an increasing fat content (Montazel et al. 2003; Griffith et al. 2005, 2006). More recently, quantitative analysis of normal marrow perfusion showed that the water/fat ratio had to be known for an accurate interpretation of perfusion parameters (Biffar et al. 2010).

3.4 Diffusion-Weighted MR Imaging

Diffusion-weighted imaging of the bone marrow slowly gains acceptance in the evaluation of bone marrow even though significant variations among techniques and results are observed in the literature (Dietrich et al. 2009; Khoo et al. 2011). Diffusion-weighted MR imaging is an established imaging technique in which the MRI signal intensity is influenced by the self-diffusion of water molecules, therefore, providing information about the microscopic structure and organization of biological tissues (Dietrich et al. 2009). It also yields numerical variables like the apparent diffusion coefficient (ADC) that reflects the degree of restriction of diffusion of free water molecules (Dietrich et al. 2001; Buyn et al. 2002; Raya et al. 2007). Typical ADCs of normal vertebral marrow are relatively low (between 0.2 and 0.5 $\times$ 10^{-3} mm^{-2}/s) (Dietrich et al. 2009; Li et al. 2011). Pathological bone marrow exhibits much higher diffusivities, ranging from 0.7 to 1.0 $\times$ 10^{-3} mm^{-2}/s in metastases as well as in malignant fractures and from 1.0 to

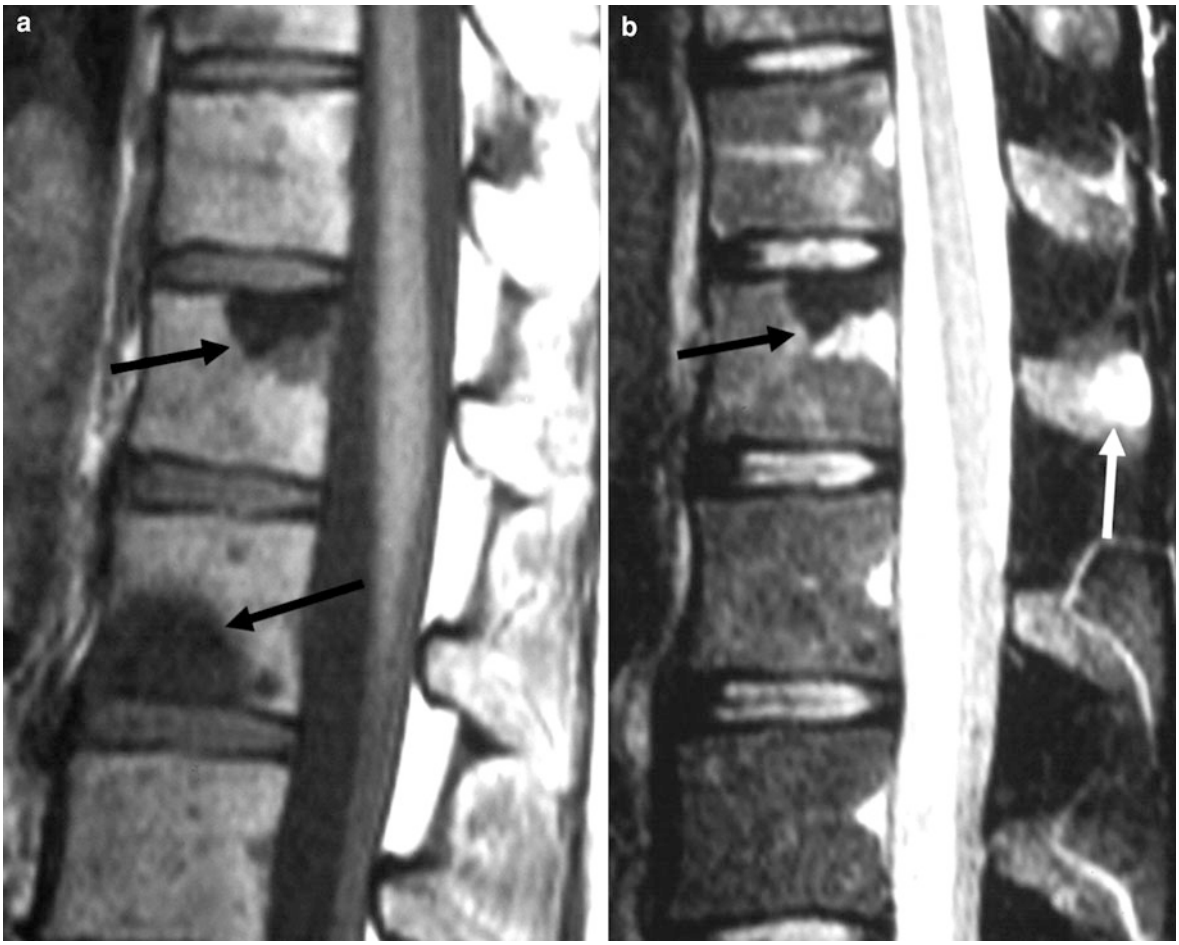

Fig. 4 Strengths and weaknesses of the T1-weighted and fat-saturated intermediate-weighted SE sequences. **a** On the Sagittal T1-weighted image, at least two lesions of low signal intensities (*arrows*) are detected. Other small lesions are also visible. **b** On the corresponding fat-saturated intermediate-weighted image, one lesion (*arrow*) is visible. The other lower lesion has a signal intensity similar to that of the presumed normal marrow and is not detected. An additional lesion (*white arrow*) is detected in a spinous process. The fat-saturated intermediate-weighted SE sequence does not replace but may complement the T1-weighted SE sequence for lesion detection

2.0×10^{-3} mm^{-2}/s in osteoporotic or traumatic fractures. A considerable overlap has been described in several studies.

3.5 Gradient-Echo MR Imaging

The network of trabecular bone that occupies most of the medullary space in vertebral bodies and in long bone epiphyses is responsible for local field inhomogeneities (Vogler and Murphy 1988). These inhomogeneities have very limited impact on marrow signal intensity on SE sequences but can be significant on gradient-echo sequences. The signal of the vertebral bone marrow on these sequences is therefore more influenced by the presence or trabecular bone than by its fat content. Initially, gradient-echo sequences were largely used to complement SE sequences for the depiction of trabecular bone destruction (lesion characterization).

On gradient-echo sequences, the selection of appropriate echo times enables to create images on which fat and water protons are either additive (in-phase images) or subtractive (opposed-phase images). On out-of-phase images, the signal of water and fat null out compared to the in-phase images. So in tissues with an equal amount of water and fat, such as normal red marrow, the signal intensity will drop between in-phase and out-phase images. The disappearance of this decreases in signal

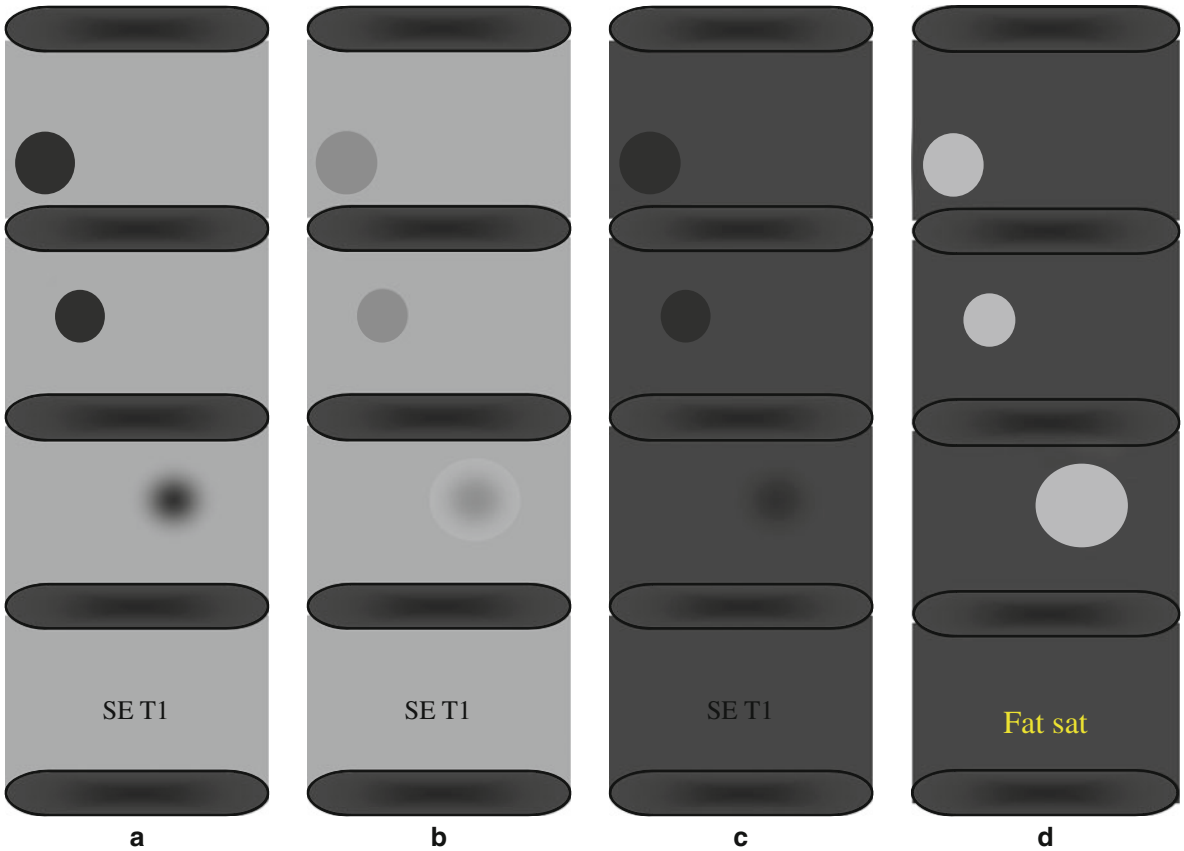

Fig. 5 Variable focal lesion conspicuity on T1-weighted SE images. **a** Normally, focal lesion conspicuity is elevated because of the marked intensity difference between the low signal lesions and the intermediate signal marrow. **b** In some situations, focal lesion conspicuity is decreased because the lesions have relatively high signal intensity. **c** In other situations, focal lesion conspicuity is decreased because the normal background marrow has a decreased signal intensity. **d** In situations (**b**) and (**c**), fat-saturated intermediate SE sequence may increase focal lesion conspicuity because of the high signal intensity of the lesion and the low signal intensity of the background marrow

intensity on opposed-phase images in vertebral red marrow reflects an imbalance between fat and water protons which occurs in abnormal conditions (Zampa et al. 2002).

3.6 Whole-Body MR Imaging

Recent development in MR imaging techniques has given the opportunity to image the entire body and therefore the entire skeleton (Eustace et al. 1997). These techniques can be combined with many sequences including the SE T1-weighted sequence, fat-saturated fluid-sensitive sequences and diffusion imaging (Dietrich et al. 2010). The understanding of marrow appearance remains unchanged with respect to standard acquisition protocols (Dietrich et al. 2009).

3.7 Field Strengths

The development of high field strength in clinical imaging has been the source of controversies about the value of these high fields for MR imaging of the bone marrow (Bolog et al. 2006; Vande Berg et al. 2005). On 3 T imagers, the signal intensity contrast between marrow lesions and adjacent red marrow is decreased with respect to lower field strengths (Bolog et al. 2006). However, this limitation does not seem to

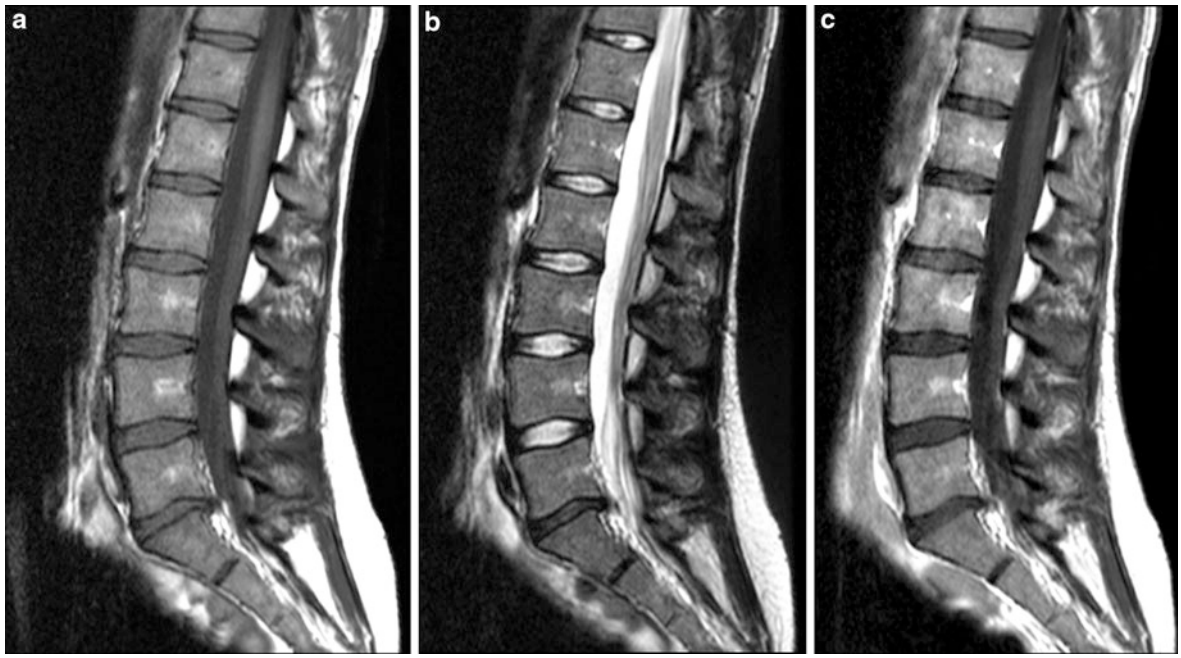

Fig. 6 Normal vertebral marrow in a 23-year-old woman. **a** Sagittal T1- and **b** T2-weighted spin-echo (SE) of the lumbar spine of a 23-year-old woman shows homogeneous marrow appearance with more fatty marrow around the vertebral veins. As a rule, the signal intensity of the red marrow is higher than that of the adjacent intervertebral discs on the SE T1-weighted sequence. **c** On the gadolinium-enhanced sagittal T1-weighted image, moderate signal intensity enhancement can be seen, merely by noting the artefactual decrease in signal intensity of the intervertebral disc. Enhancement percentage was 70%, as determined on quantitative dynamic MR study (not shown)

interfere with the accuracy of MR imaging of the bone marrow at 3 T (Vande Berg et al. 2005).

4 MR Imaging Appearance of Normal Vertebral Marrow

4.1 Normal Vertebral Marrow in Young Adults

The normal vertebral marrow of young adults shows both intermediate and homogeneous signal intensity on both T1- and T2-weighted SE images (Fig. 2). As a rule, the signal intensity of normal lumbar vertebral bodies on T1-weighted SE images must be higher than that of adjacent intervertebral disc in an adult patient (Carroll et al. 1997). In the thoracic spine of adults, marrow signal intensity can also be lower than that of THE disc because of the high signal intensity of intervertebral discs of the thoracic spine. On T2-weighted SE images, it is unreliable to assess the marrow status because of the lack of recognized internal standard with which marrow signal intensity can be compared. On fat-saturated intermediate- or T2-weighted fast SE images, the signal intensity of vertebral marrow normally ranges from intermediate to moderately elevated. After intravenous injection of gadolinium-containing contrast material, enhancement of marrow signal intensity is barely visible at visual inspection on T1-weighted SE images (Fig. 2). Signal intensity enhancement of the intramedullary and perivertebral veins should be visible after contrast injection and can be looked for to confirm accurate contrast material injection. Signal enhancement becomes more obvious on fat-saturated T1-weighted SE images or can be quantitatively assessed by performing dynamic MR studies (Chen et al. 2001; Montazel et al. 2003). Usually, the signal intensity of the normal marrow should not increase by more than 35% in adults above 35 years of age (Baur et al. 1997).

Along the spine, variations in the amount of fat can be observed as high fat content areas can be seen in the anterior aspects of C2 and C3 as well as in the sacro-coccygeal region below S3.

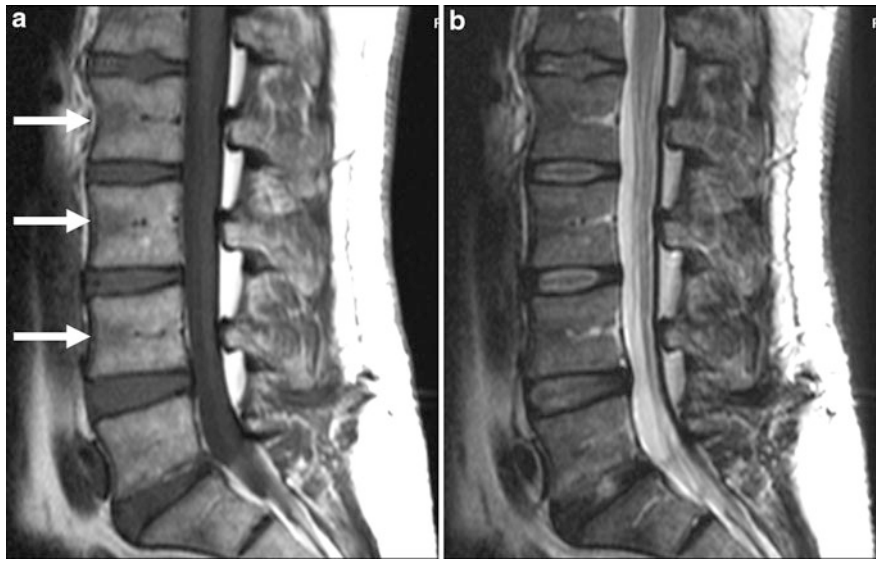

Fig. 7 Normal vertebral marrow in a 44-year-old man. **a** Sagittal T1- and **b** T2-weighted SE of the lumbar spine show moderate decrease in signal intensity in the anterior aspect of the vertebral bodies on both sequences (*arrows*). Note that the same pattern of more cellular red marrow distribution is present in all vertebral bodies

There is limited variation in the appearance of vertebral marrow among the vertebral bodies of the same region of normal subjects although several distribution patterns are observed in different individuals (Vande Berg et al. 2005; Ricci et al. 1990). Red marrow is generally distributed in a homogeneous pattern within the vertebral body (Fig. 2). Occasionally, red marrow is more cellular near the vertebral end-plate which is a metaphyseal equivalent, an area where the vasculature is generally more developed (Ricci et al. 1990; Hajek et al. 1987). Red marrow can also be more cellular in the anterior aspects of the vertebral bodies (Fig. 7) or less cellular around the vertebral basilar veins (Carroll et al. 1997) (Fig. 6).

4.2 Normal Variations According to Age and Gender

Age profoundly affects vertebral marrow signal intensity and homogeneity at MR imaging (Fig. 8). At birth, vertebral marrow shows homogeneous low MR signal intensity, mainly before the age of 2 years. During growth, the proportion of marrow fat cells increases in a diffuse and homogeneous manner, a process called fatty marrow conversion of red marrow, which results in a progressive increase in marrow signal intensity on T1-weighted images with age (Vogler and Murphy 1988). During adulthood, conversion of red to yellow marrow continues at a lower pace and in a more heterogeneous manner than during growth. Therefore, the marrow signal intensity on T1-weighted MR images is frequently higher and more heterogeneous in elderly than in young adult subjects. These signal heterogeneities might be considered to be normal in an elderly patient but not in a young adult.

Gender plays a rather limited role in vertebral marrow appearance although quantitative studies have shown that vertebral fat content is lower in females than in males before the age of 65 (Vande Berg et al. 1997; Liney et al. 2007).

4.3 Diffuse Normal Marrow Heterogeneities

Occasionally, vertebral marrow shows, at first glance, a heterogeneous pattern that alerts the radiologist about the existence of diffuse marrow infiltration. Patient's age is a very important parameter to take into account because this heterogeneous pattern is frequent in subjects after the fourth decade of life. To such a point that similar marrow heterogeneities may be considered to be normal in an elderly patient and abnormal in a young patient. This statement indirectly indicates the occasional difficulty in deciding whether an MR appearance is normal or abnormal.

A careful analysis of the MR images is needed to recognize the origin of vertebral marrow heterogeneities because two opposed situations can be observed. In the most frequent situation, dissemination of foci of high signal intensity (less cellular

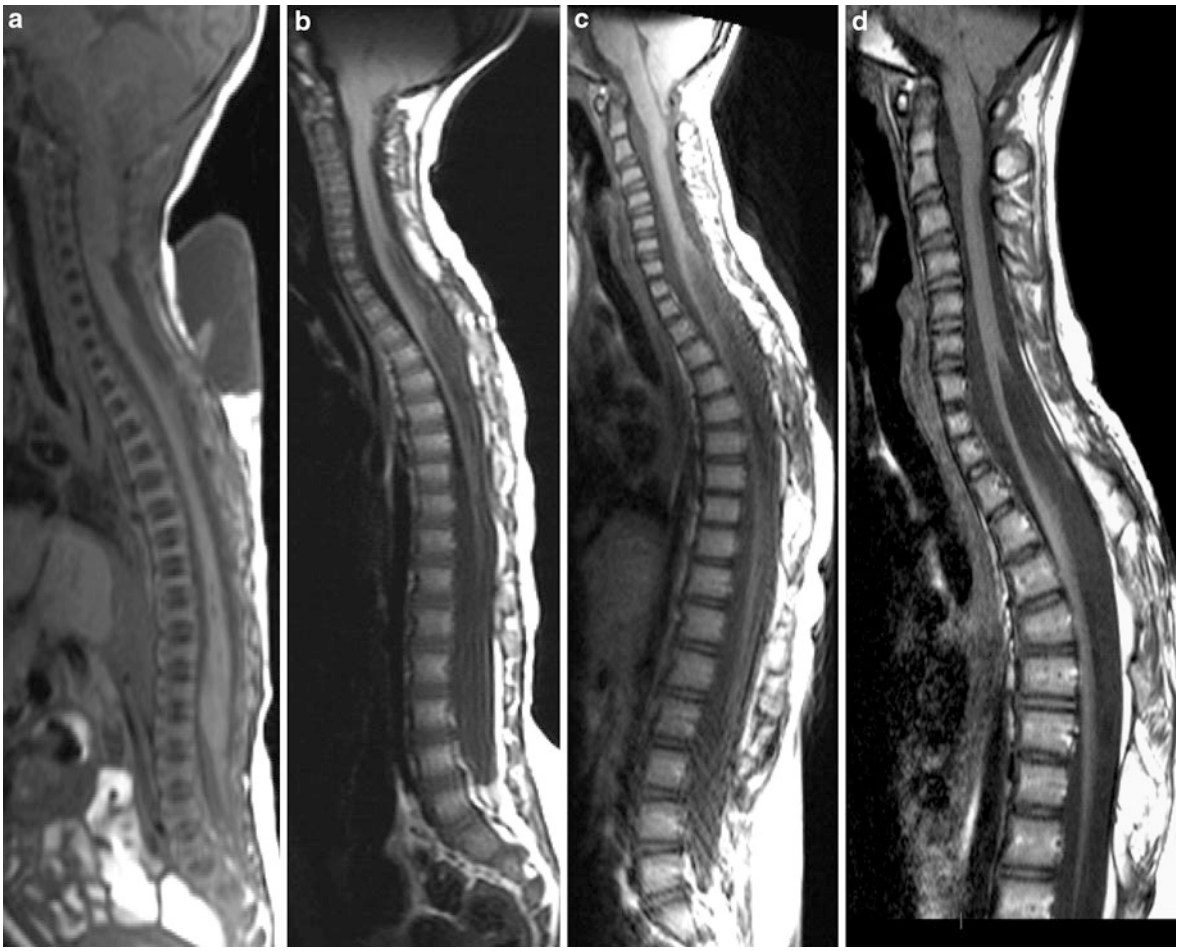

Fig. 8 Change over time of marrow MR appearance in a boy with spinal dysraphism. **a** At 3 days of age, the vertebral marrow shows very low signal intensity resulting from the absence of medullary fat and from the numerous iron-loaded red cell lineage. **b** At 3 years of age, the vertebral marrow has intermediate and homogeneous signal intensity. **c** At 6 years of age, the signal intensity is unchanged but fatty marrow starts to appear in the upper and lower spine extremities. **d** At 11 years of age, the signal intensity is similar but more fat is present around the vertebral veins

marrow) generates the heterogeneous pattern (Hajek et al. 1987) (Fig. 9). Consequently, foci of adjacent normal red marrow appear with concave margins because these contours are created by the presence of fat nodules. This heterogeneous pattern related with the presence of less cellular marrow can easily be recognized as a non-significant finding.

In a second less frequent pattern, dissemination of foci of decreased signal intensity (more cellular marrow) generates marrow heterogeneities (Fig. 10). In this condition, low signal intensity foci have convex and ill-delimited margins (Levine et al. 1994). This heterogeneity pattern is more troublesome than the previous one because its differential diagnosis includes diffuse marrow infiltration by neoplastic cells (Table 4). The corresponding histopathological picture is not known. At a microscopic level, hematopoietic cells have the propensity to form nodules in the medullary cavity. If large enough, these confluent nodules of red marrow cells could become visible at MR imaging which would lead to the appearance of areas of more pronounced decrease in signal intensity than adjacent marrow on T1-weighted SE MR images. These presumed red marrow foci occur in a non-predictable manner although they frequently involve the peripheral aspects of the vertebral bodies. Their

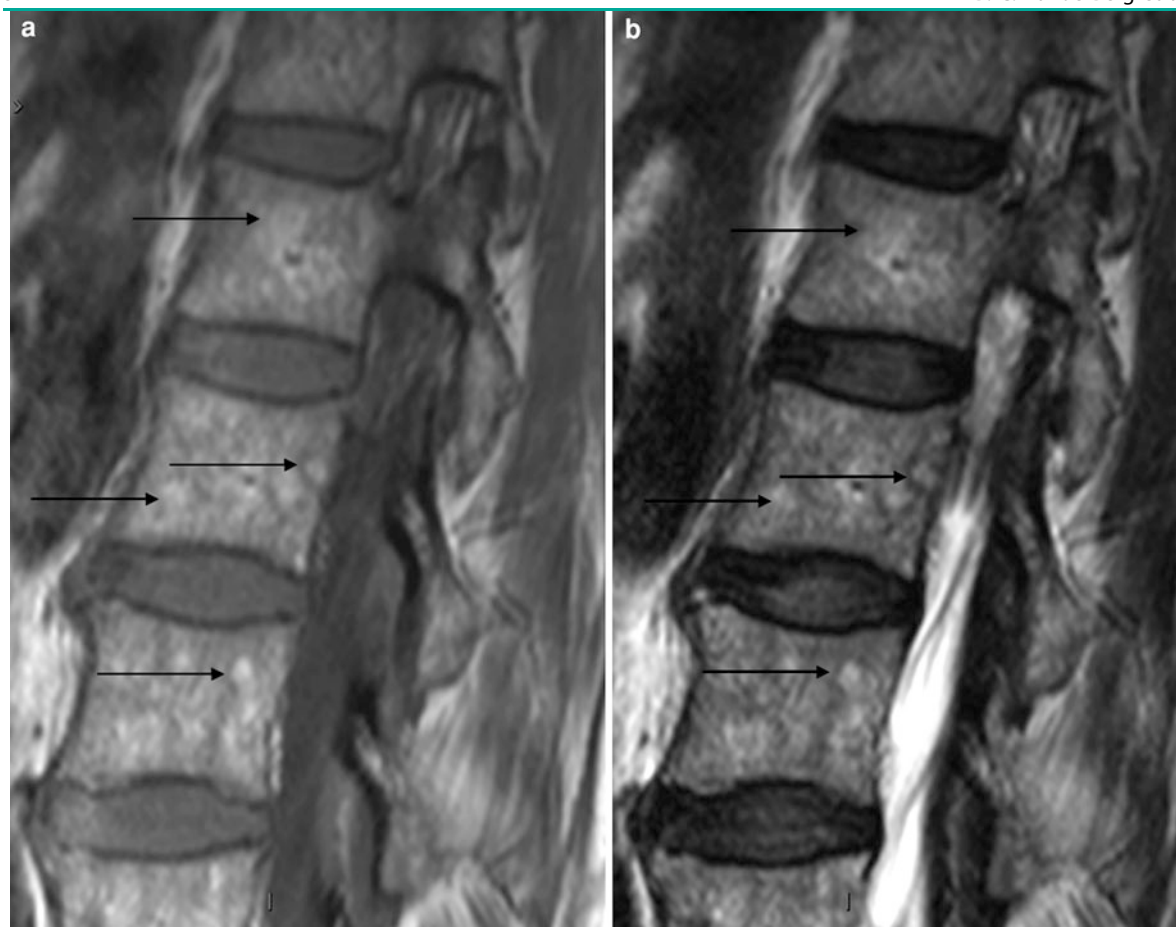

Fig. 9 Benign marrow heterogeneities in an elderly patient due to the dissemination of infracentimeric nodules of increased signal intensity. **a** Sagittal T1-weighted SE image of the spine of a 61-year-old woman shows disseminated foci (*arrows*) of increased signal intensity. The adjacent more cellular marrow shows concave margins in between the nodules. **b** On the corresponding T2-weighted SE image, the heterogeneities are similar because of the relatively high signal intensity of fat nodules

margins are sharp if the marrow conversion process is advanced and fuzzier if the marrow conversion process is limited (Levine et al. 1994). Occasionally, central areas of high signal intensity on T1-weighted images are present, which are an additional argument in favor of a normal variant. The presence of a low to intermediate signal intensity on T2-weighted, the lack of evident signal enhancement on T1-weighted images after gadolinium injection, the lack of trabecular bone changes on CT images and the lack of changes at follow-up studies generally help to differentiate these benign heterogeneities from clinically relevant abnormalities (Vogler and Murphy 1988). However, these heterogeneities may remain undistinguishable from significant marrow lesions.

4.4 Focal Normal Variants and Incidental Findings

4.4.1 Nodules of Fatty Marrow

Occasionally, large marrow foci of high signal intensity are present on T1-weighted SE images (Hajek et al. 1987) (Fig. 11). Their frequency increases with age. In subjects without previous medical history, the presence of fat lesions generally lacks clinical significance. Confusion may arise if the radiologist focuses on fast SE T2-weighted images because these fatty foci also show high signal intensity on this sequence. Analysis of the corresponding T1-weighted SE images or of fat-saturated images enables to recognize their fat content, and therefore their lack of clinical significance.

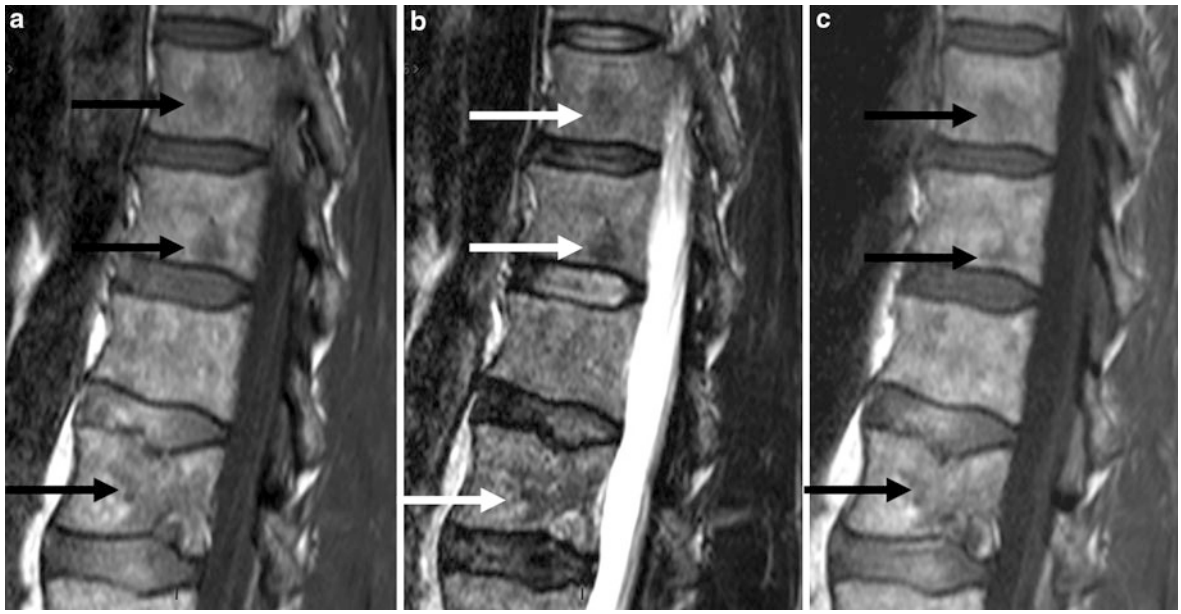

Fig. 10 Marrow heterogeneities in an elderly patient due to the dissemination of infracentimeric nodules of decreased signal intensity. **a** Sagittal T1-weighted SE image of the spine of a 60-year-old man shows dissemination of infracentimetric nodules (*arrows*) of decreased signal intensity. These foci show moderate decrease in signal and unsharp margins. **b** On the corresponding T2-weighted SE image, the nodules (*white arrows*) also demonstrate decreased signal intensity which remains compatible with cellular red marrow. **c** Similar sagittal T1-weighted SE image of the same patient obtained 3 years later demonstrates similar heterogeneities without any increase in nodule size (*black arrows*)

Table 4 Imaging features observed in benign heterogeneities in elderly patients and in significant focal lesions (metastasis, multiple myeloma, lymphoma)

	Green flags	Red flags
Signal intensity (T1 SE)	Moderate decrease	Marked decrease
Signal homogeneity (T1 SE)	Heterogeneous with central high signal	Homogeneous low
Margins (T1 SE)	Ill-delimited	Sharp
Enhancement (T1 SE)	Subtle (disappearance)	Obvious
Enhancement (Fat-sat T1 SE	Obvious	Obvious
Signal intensity (T2 SE)	Moderate decrease	High
Signal intensity (FS PD)	Not seen	High
Follow-up MR	No change in size/number	Increase in size/number
CT	No change in trabecular or cortical bone	Any change in trabecular or cortical bone

Green flags suggest irrelevant changes. Red flags suggest significant conditions. The absence of red flags decreases but does not exclude the likelihood of a significant condition

The demonstration of a very low signal intensity on fat-saturated images and of a normal trabecular bone pattern enables to exclude alternative diagnoses including vertebral hemangioma, Paget's disease and healed bone lesions.

4.4.2 Nodules of Hypercellular Red Marrow

Occasionally, one or multiple nodules of slightly decreased signal intensity can be observed in vertebral bodies on T1-weighted images (Fig. 12). Typically, the signal of these areas remains compatible with that of a

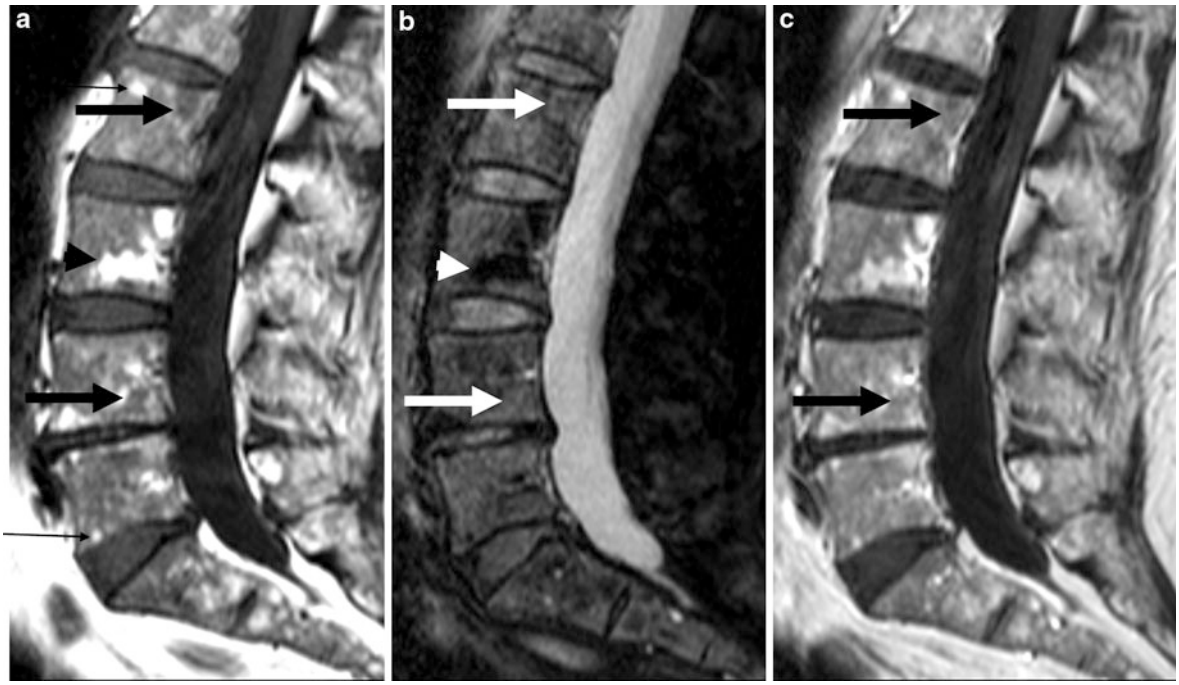

Fig. 11 Intricated marrow heterogeneities in a 73-year-old woman. **a** On the sagittal T1-weighted SE image, marrow heterogeneity results from infracentimetric nodules of decreased signal intensity (*large arrows*), infracentimetric nodules of increased signal intensity (*thin arrows*) and large regions of increased signal intensity (*arrowhead*). **b** On the corresponding fat-saturated intermediate-weighted SE image, areas of pure fat demonstrate low signal intensity (*arrowhead*) and areas of presumed more cellular marrow fade away (*white arrows*), without any increase in signal intensity. **c** On the corresponding enhanced T1-weighted SE image, the areas of decreased signal intensity (*arrows*) tend to fade away

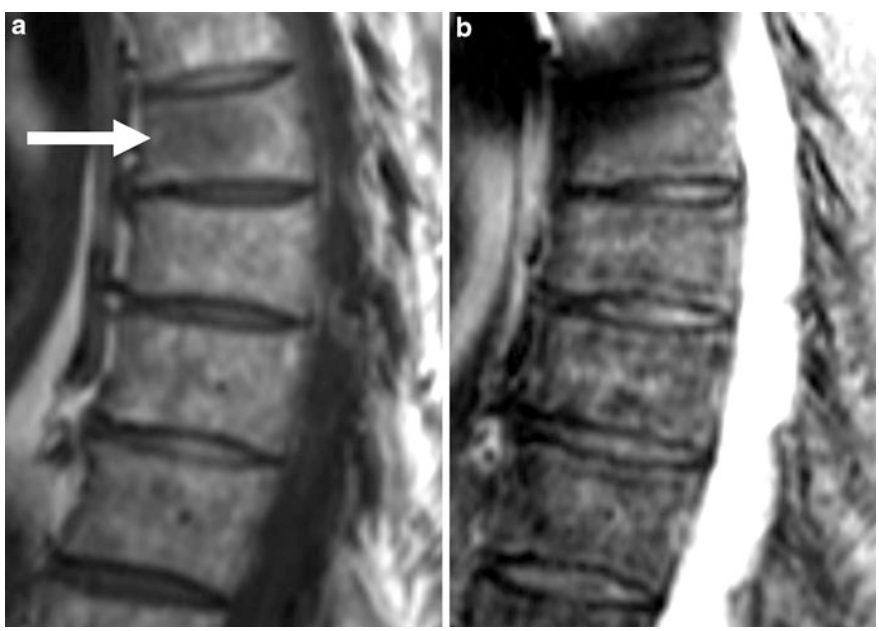

Fig. 12 Red marrow nodule. **a** A focal marrow area of moderate decrease in signal intensity (*arrow*) is visible on the sagittal T1-weighted SE image of the thoracic spine of a patient with bronchial carcinoma. **b** The abnormality shows intermediate signal intensity of the corresponding fat-saturated intermediate-weighted SE image. At biopsy hypercellular red marrow was demonstrated without any neoplastic cells

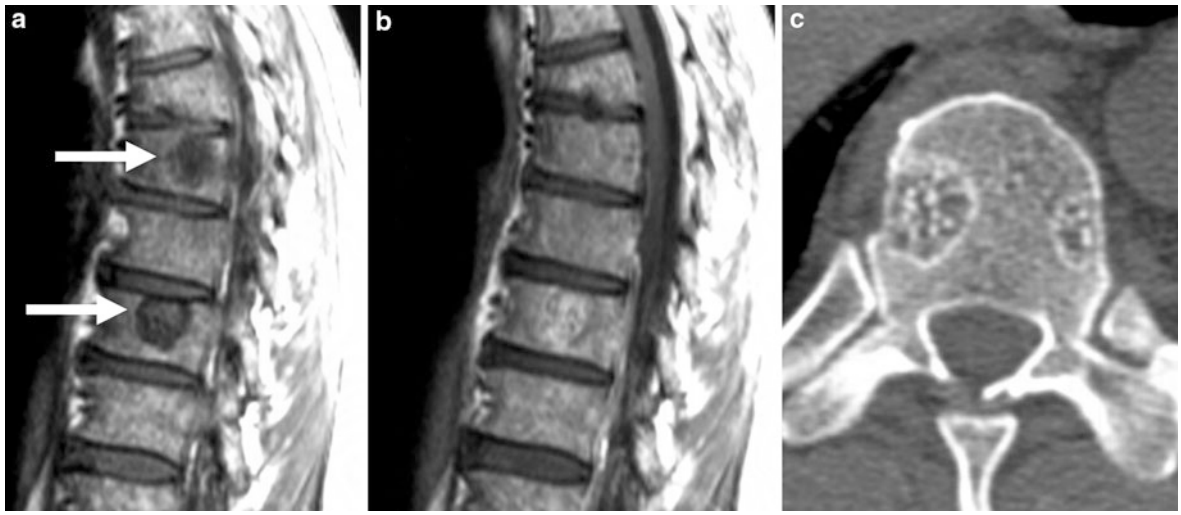

Fig. 13 Atypical vertebral hemangioma. **a**, **b** Pre- and post-contrast sagittal T1-weighted SE images of the thoracic spine of a 69-year-old man show two areas of low signal intensity (*arrows*) that enhances after contrast injection. **c** Axial CT image shows the typical appearance of a vertebral hemangioma. Rarely hemangioma can show a non-specific pattern of decreased signal on T1-weighted SE images

normal red marrow on all sequences including a moderate decrease in signal intensity on T1-weighted SE images, intermediate to low signal intensity of T2-weighted fast SE images, moderate increase in signal intensity on fat-saturated intermediate- or T2-weighted fast SE images, and no or moderate enhancement after gadolinium injection (Fig. 7). Most frequently, the signal intensity of the nodule is similar or slightly lower than that of the adjacent intervertebral disk (Bordalo-Rodrigues et al. 2003). Short-term follow-up MR studies demonstrate no change in the MR imaging appearance. CT and bone scans should be normal. Experience with G6 PD-FDG-PET imaging is limited but these areas may show slight increased hypermetabolic uptake in comparison to adjacent red marrow (Bordalo-Rodrigues et al. 2003). This observation occurs relatively rarely in normal individuals but it is frequent in patients with regenerating hematopoietic marrow after marrow aplasia or in response to the administration of hematopoietic growth factors.

4.4.3 Benign Vertebral Tumors and Hamartomas

4.4.3.1 Vertebral Hemangioma

Vertebral hemangioma is a common vertebral lesion with a frequency of 12% in women and 9% in men (Waitches et al. 1994) (Fig. 3). Hemangiomas are multiple in about one-third of cases (Schmorl et al. 1956). They are generally asymptomatic. Histologically, they correspond to cavernous hemangiomas and contain dilated, blood-filled vascular spaces lined by flat endothelial cells, set in a stroma containing large amounts of adipose tissue and no hematopoietic cells (Murphey et al. 1995; Wilner 1982). On T1-weighted SE images, the signal intensity of asymptomatic vertebral hemangiomas is higher to that of adjacent marrow (Ross et al. 1987) (Fig. 4), although it can also be equivalent and therefore not visible on T1-weighted images (Fig. 5). On T2-weighted SE images, its signal is consistently high (Fig. 4). The presence of fat cells and dilated vessels with interstitial edema most likely accounts for its high signal intensity on T1- and T2-weighted images, respectively (Baudrez and Galant 2001). Frequently, punctuated or linear areas of low signal intensity are also seen on T1- and T2-weighted images, probably due to the presence of thickened trabeculae. The signal enhancement of hemangiomas after gadolinium injection is variable, depending on its appearance on T1-weighted images and the type of sequence that is obtained after contrast injection. The enhancement pattern can be homogeneous or peripheral.

Occasionally, asymptomatic vertebral hemangiomas show low signal intensity on T1-weighted images, with marked enhancement on post-contrast T1-weighted SE images (Fig. 13). These hemangiomas

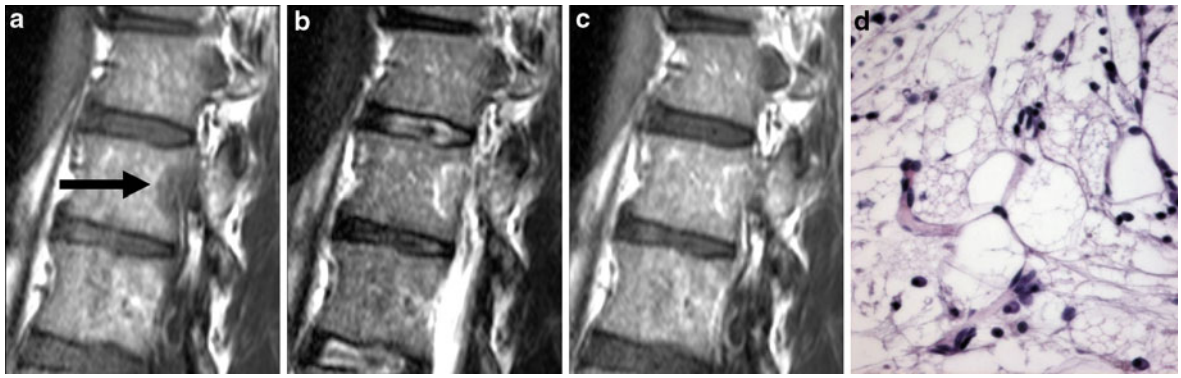

Fig. 14 Intraosseous benign notochordal cell tumor. **a** Sagittal T1-weighted SE image of the spine of a 45-year-old man with renal cancer shows an area of moderate decrease in signal intensity (*arrow*). **b** On the corresponding T2-weighted image, the lesion shows intermediate signal intensity with a peripheral rim of increased signal. **c** On the corresponding T1-weighted image obtained after contrast injection, the lesion shows homogeneous enhancement. **d** At microscopic examination of the biopsy specimen, the presence of adipocyte-like vacuolated eosinophilic cells indicates the diagnosis of an intraosseous benign notochordal cell tumor

can be confused with significant marrow lesions. CT images generally show a rather specific trabecular bone pattern suggestive of vertebral hemangioma (Wilner 1982; Laredo et al. 1986) (Fig. 6), although small hemangiomas with a diameter below 1 cm can remain occult on corresponding CT images. Symptomatic vertebral hemangiomas generally demonstrate low signal intensity on T1-weighted images with extra-osseous component (Wilner 1982; Laredo et al. 1986).

4.4.3.2 Vertebral Enostosis—Compact Bone Island

A compact bone island consists of lamellar cortical bone embedded within the trabecular network of the medullary cavity (Murphey et al. 1996). In a radiological study of cadaveric spines, their frequency was 14% and their size varied between 2 and 10 mm (Kroon et al. 1994). They frequently involve the periphery of the vertebral bodies and spare the central area (Resnick et al. 1983). Their signal intensity is very low on all sequences and adjacent marrow has generally a normal appearance (Murphey et al. 1996) (Fig. 8). Rarely, a peripheral high signal intensity rim surrounding a central low signal intensity area has been reported on STIR images of some unusually large compact bone islands (Seymour 1997) (Fig. 9). This pattern must be considered to be exceedingly rare and is therefore more frequently suggestive of sclerotic metastases than an uncommon bone island.

4.4.3.3 Benign Notochordal Cells Tumors

Intraosseous benign notochordal cell tumors are recently recognized conditions and were observed in a preliminary study in 14% of spines and 11.5% of the clivus (Yamaguchi et al. 2004; Kyriakos 2011). The average size of lesions found at autopsy was 4 × 2 mm. At histology, these lesions are characterized by well-demarcated encapsulated sheets of adipocytes-like vacuolated eosinophilic cells with subtle thickening of the adjacent trabeculae (Yamaguchi et al. 2004). The link between these lesions, notochordal remnants and chordoma is currently under investigation, as well as their risk of malignant transformation.

At MR imaging of biopsy-proven cases, lesions showed a slight decrease in signal intensity on T1-weighted and high signal intensity on T2-weighted images (Yamaguchi et al. 2002; Nishiguchi et al. 2011). Yamaguchi reported the lack of enhancement in all lesions in which contrast-enhanced MR images had been obtained (three out of nine MR investigated lesions), but a slight signal enhancement in other biopsy-proven lesions can be observed (Fig. 14). On CT images, subtle to marked bone sclerosis can be observed. In our experience, confusion with foci of red marrow is likely to occur on T1-weighted SE images. The presence of high signal intensity on T2-weighted images and of sclerosis on corresponding CT images might become features indicative of benign notochordal cell lesions in the future. Several reasons may account for their rare observation at MR imaging:

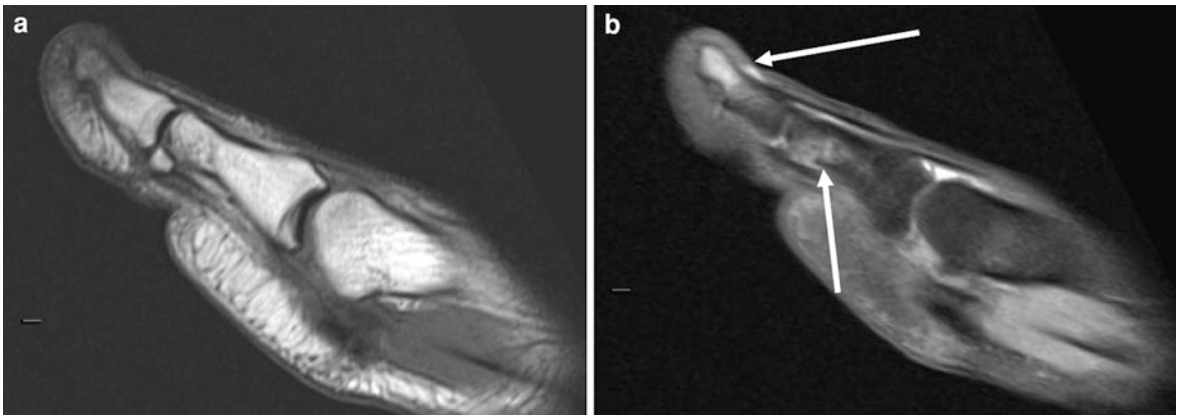

Fig. 15 Presumed serous atrophy in distal toes. **a** Sagittal SE T1 and **b** fat-saturated images of the first toe of a 24-year-old active woman with ankle pain shows no significant marrow alteration on T1-weighted image and high signal intensity (*arrow*) on the fat-saturated image. This alteration is not rare in young women and most likely corresponds to serous transformation of fatty marrow

limited size, limited decrease in signal intensity on T1-weighted SE images, limited recognition of this lesion at histology and lack of biopsy of suspected lesions. Given the high frequency of these lesions at autopsy, it is likely that more information will become available in the literature, including better understanding of differential diagnosis (Mirra and Brien 2001).

5 MR Appearance of the Normal Appendicular Skeleton

5.1 Normal Appendicular Marrow in Young Adults

The MR imaging appearance of any given bone merely depends on the macroscopic distribution of yellow and red marrow in this bone with little or no influence of the trabecular network on the MR image. Usually, almost exclusively fatty marrow is observed in the distally located bones within the upper or lower limbs. In the humerus and femur, red marrow is found in the proximal and, less frequently, in the distal metaphyses (Fig. 15). The diaphyses of these bones contain a mixture of yellow and red marrow. The epiphyses and apophyses also contain yellow marrow except in the proximal femur and humerus where red marrow can be observed, generally near the subchondral bone plate or the cortex (Vande Berg et al. 1997; Mirowitz 1993). Red marrow should not be present in distal femoral and humeral epiphyses.

Normal red marrow in the appendicular skeleton of young adult humans shows both intermediate and homogeneous signal intensity on both T1- and T2-weighted SE images. As a rule, the signal intensity of red marrow areas on T1-weighted SE images must be higher than that of adjacent muscles in a young adult patient (Carroll et al. 1997).

In the pelvis, as elsewhere in the appendicular skeleton, the marrow signal intensity should be higher than that of adjacent normal muscles on T1-weighted SE images (Levine et al. 1994). Other sequences are unreliable to decide whether red marrow has a normal or abnormal signal intensity.

5.2 Normal Variations According to Age, Gender and Body Habitus

During growth, conversion of red to yellow marrow starts at the most distal aspects of the limbs and proceeds centripetally. In any individual long bone, the same conversion process also follows a well-defined sequence, occurring first in the proximal and distal epiphyses, followed then by the diaphysis and distal metaphysis, and finally the proximal metaphysis. Although initially described as a homogeneous process, it seems that high signal intensity fatty marrow can be seen within the femoral diaphysis as early as 3 months of age and that fatty marrow with various degrees of heterogeneity is routinely seen in this region by 12 months of age. After five years of age, the femoral diaphysis showed

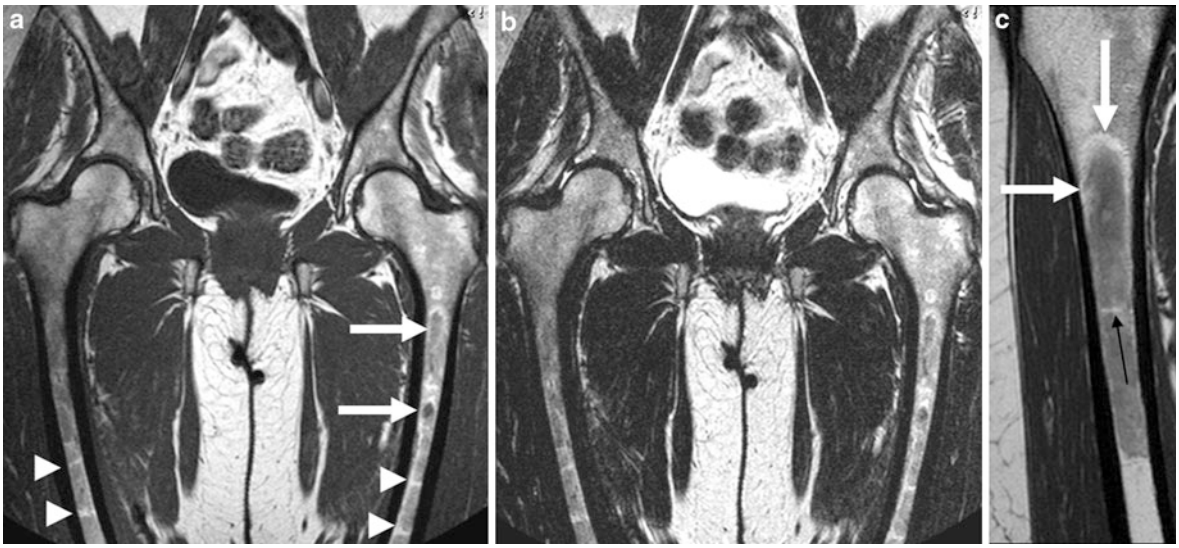

Fig. 16 Normal marrow patterns in proximal femurs. **a** Coronal T1-weighted SE image of a 52-year-old woman shows several variations in marrow appearance including transverse linear areas of increased signal intensity (*arrowheads*) and central areas of presumed more cellular marrow (*arrows*). **b** The foci of presumed red marrow show low signal intensity on T2-weighted SE images. **c** A close-up coronal T1-weighted SE image of a femur shows a normal appearance with a central area of more cellular marrow with less cellular marrow around (*large arrows*) and within (*thin arrow*) that region

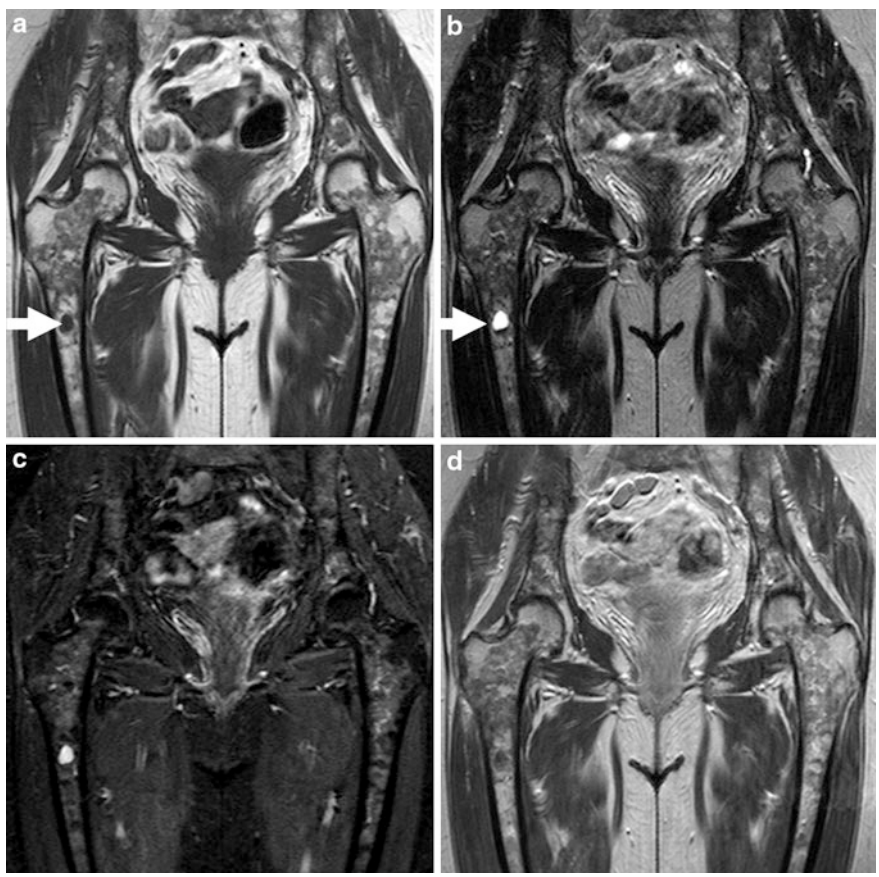

Fig. 17 Marrow heterogeneities. Coronal **a** T1-weighted, **b** T2-weighted, **c** fat-saturated intermediate-weighted and **d** enhanced T1-weighted SE images of the pelvis of an elderly woman with breast cancer demonstrate heterogeneous marrow. The presence of an intermediate signal intensity and the moderate signal enhancement is compatible with red marrow. A foci of fluid-like signal intensity (*arrow*) was seen in the right diaphysis. Radiographs and bone scan were normal. The lesion showed no change over time. A blind iliac crest biopsy of the bone marrow demonstrated the absence of abnormal cells within hypercellular hematopoietic marrow

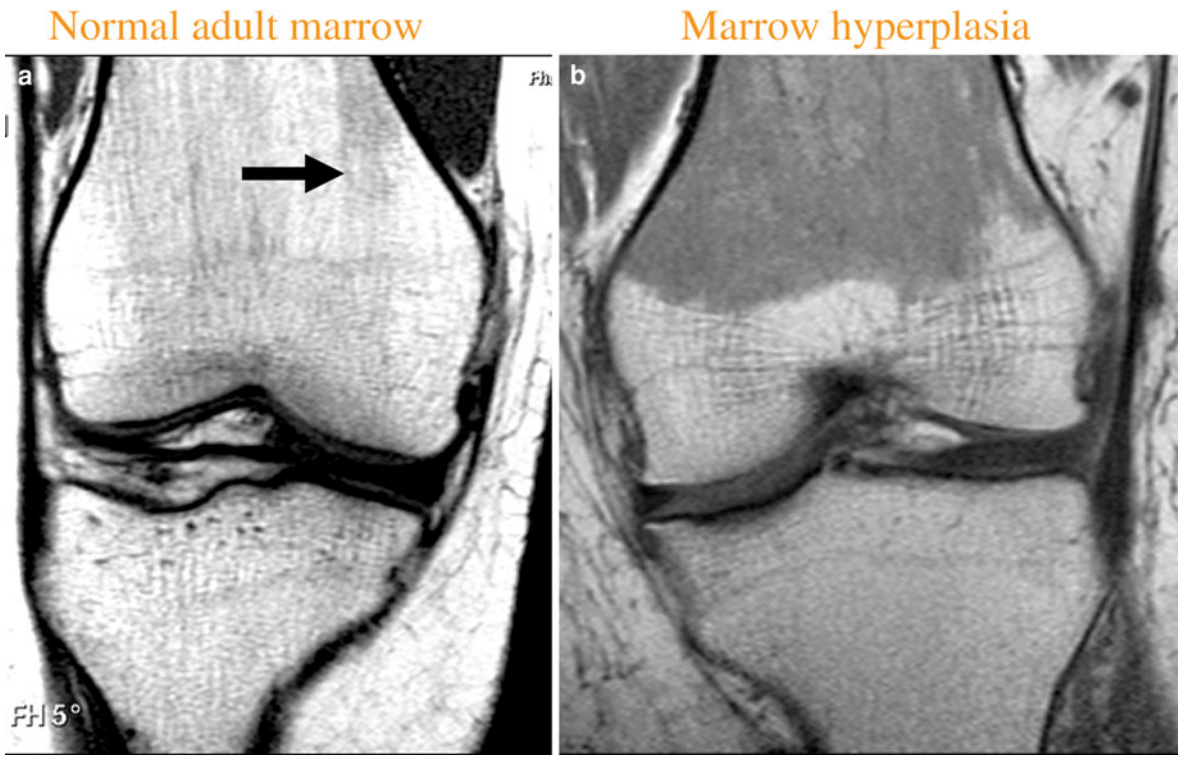

Fig. 18 Coronal T1-weighted SE images of the distal femurs of two 44-year-old women. **a** The expected marrow pattern shows only discrete areas of moderate decrease in signal intensity (*arrow*). **b** In a case of benign red marrow hyperplasia, the metaphyseal marrow shows decreased signal intensity that remains superior to that of adjacent muscles. Note the lack of red marrow in the epiphysis and the abrupt transition zone between the metaphysis and the epiphysis

Table 5 Imaging features observed in benign hematopoietic marrow hyperplasia at knee MR imaging (green flags)

	Green flags	Red flags
Signal intensity (T1 SE)	Moderate decrease, higher than that of muscles	Marked decrease lower than that of muscles
Signal homogeneity (T1 SE)	Homogeneous with serpinginous vessels	Homogeneous low
Topography	Dia-metaphyseal	Epiphyseal
Distribution	Bilateral, symmetrical	Unilateral, asymmetrical
Enhancement (T1 SE)	Subtle (disappearance)	Obvious
Enhancement (Fat-sat T1 SE	Obvious	Obvious
Signal intensity (T2 SE)	Moderate decrease	High or low
Signal intensity (FS PD)	Intermediate	High or low
Cortical bone, soft tissues	No change	Any change
Follow-up MR	No change	Any change

The presence of red flags suggests a significant condition and is not compatible with benign hematopoietic marrow hyperplasia. The absence of red flags decreases but does not exclude the likelihood of a significant condition

homogeneous high signal intensity. The apparent red marrow distribution within the body at MR imaging differs from that observed in cadavers because the T1-weighted sequence creates an overestimation of fat because of its sensitivity to the presence of fat.

In fit and active young females with body mass index at the lower limit, serous marrow may appear distally in the toes (Vande Berg et al. 1996) (Fig. 15). This process is reminiscent of that of red to yellow marrow conversion during growth as it follows the same body distribution.

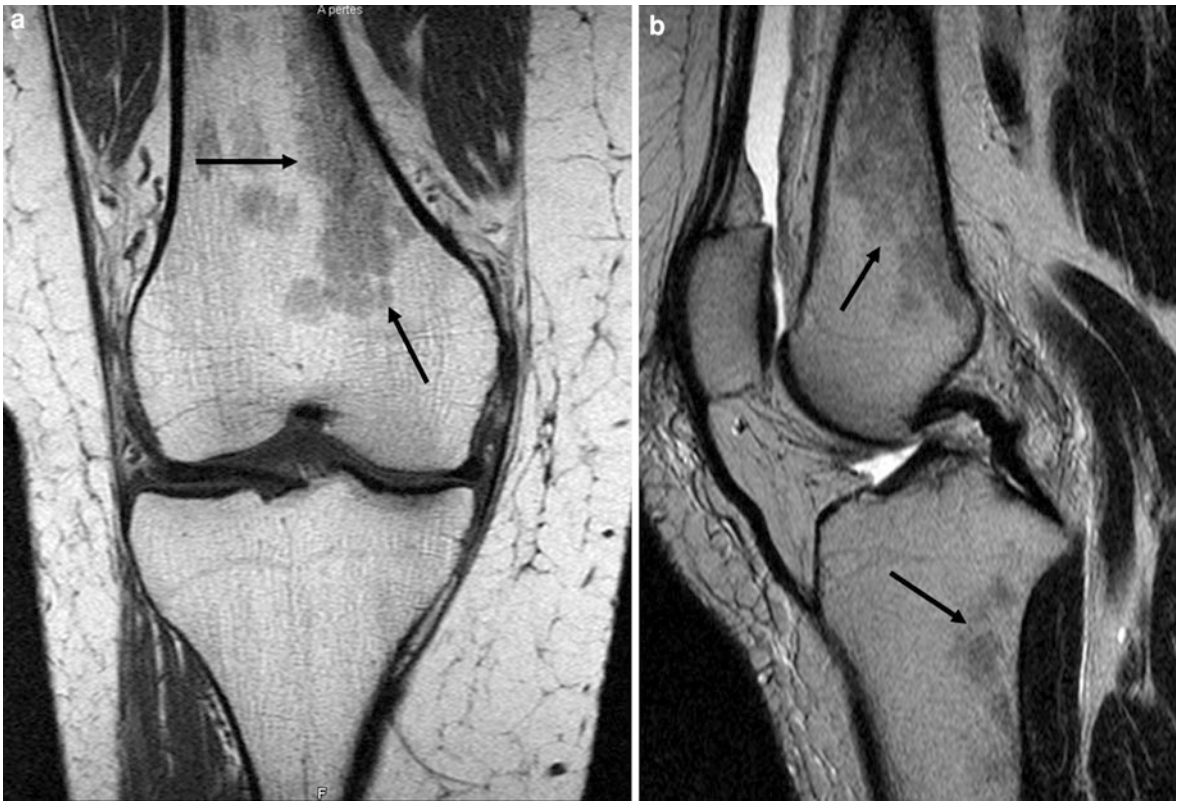

Fig. 19 Benign hematopoietic marrow hyperplasia. **a** Coronal T1-weighted SE image of an obese 64-year-old female demonstrate multiple areas of decreased signal intensity (*arrows*) in the distal femur metaphysis. **b** On the sagittal T2-weighted SE image, the non-fatty marrow (*arrow*) shows intermediate signal intensity, compatible with red marrow. Note the presence of similar changes in the posterior aspect of the tibial metaphysis (*arrow*) and the lack of epiphyseal marrow changes

Serous marrow is responsible for a moderate decrease in signal intensity on T1-weighted images and fairly high signal intensity on T2-weighted images. These changes can be extensive in cachectic patients with anorexia nervosa, hyperthryroidism or cancer (Vande Berg et al. 1994; García et al. 2011). Conversion of yellow to serous marrow reflects the disappearance of intracellular fat from adipocytes and the accumulation of hyaluronic acid in extracellular marrow spaces. This process is rapidly reversible, depending on the overall body status of the subject. In obese middle-aged women, an opposed situation with hematopoietic marrow hyperplasia can be observed (see below).

In elderly subjects, numerous variations in the MR appearance of the femur (Figs. 16, 17) can be observed: linear area of high signal intensity on T1-weighted images, areas of presumed coalescing red marrow with decreased signal intensity on T1- and T2-weighted images, and fluid-containing areas of low signal intensity on T1-weighted images and high signal intensity on T2-weighted images. These variations are generally similar in paired bones and imaging of the contralateral paired bone may occasionally contribute to decrease the degree of suspicion when the same local alteration is also present.

5.3 Benign Red Marrow Hyperplasia

Benign red marrow hyperplasia was defined initially by the presence of hypercellular hematopoietic marrow in the distal femur of a subject older than 25 years of age (Deutsch et al. 1989). This definition lacks precision because some red marrow can be present in many adults (Fig. 18) and because the detection of red marrow highly depends on the used sequence. Initially, this condition was recognized on SE T1-weighted images of the knee of adult without recognized medical condition (Deutsch et al. 1989).

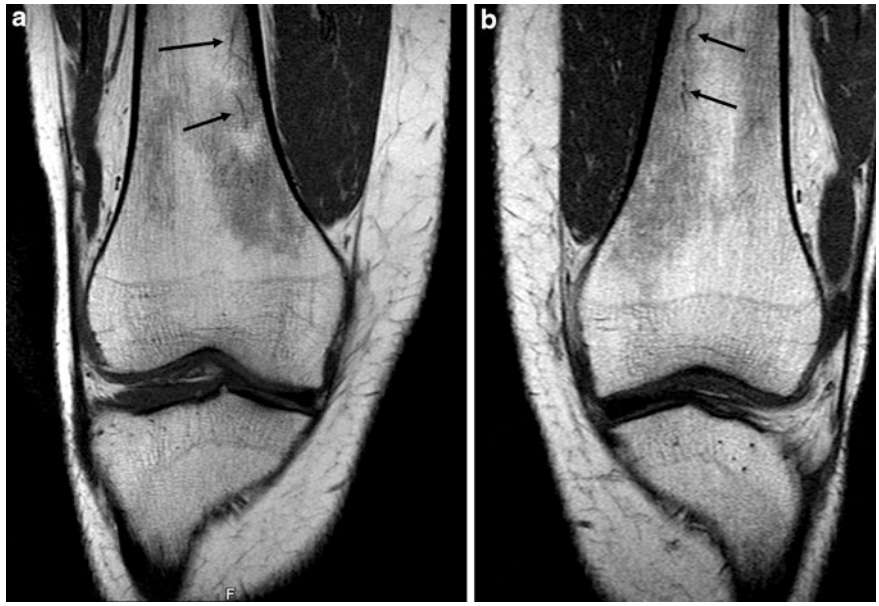

Fig. 20 Coronal T1-weighted SE images of the knees of a 62-year-old show symmetrical distribution of red marrow. The serpiginous lines (*arrows*) of low signal intensity are likely to correspond to intra-osseous veins

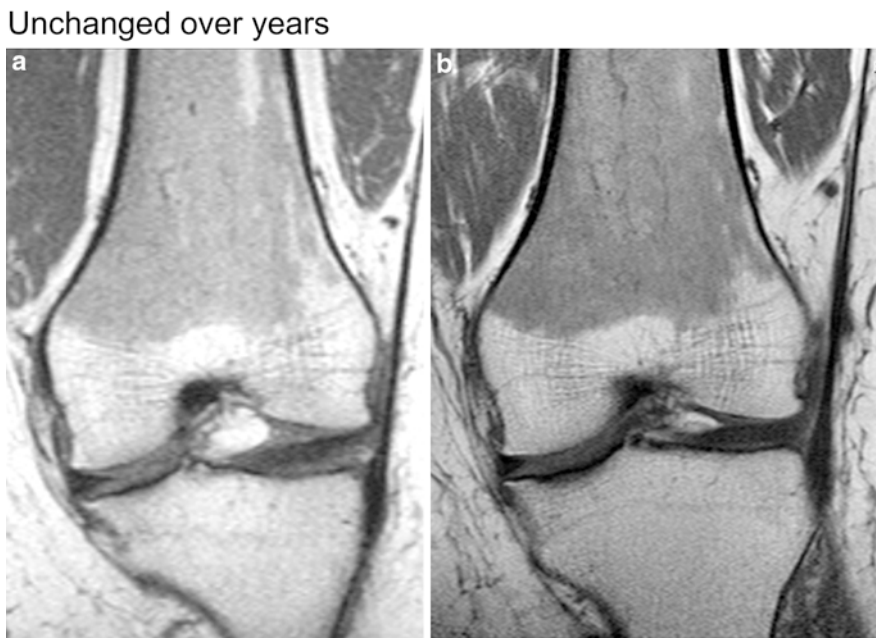

Fig. 21 Lack of significant change over time in benign red marrow hyperplasia. **a** Coronal T1-weighted SE images of the left knee of a 59-year-old woman show benign red marrow hyperplasia. **b** On the same image obtained 5 years later, benign red marrow hyperplasia with no change with respect to initial image

It reflects expansion of hematopoietic marrow in the appendicular skeleton (marrow reconversion). Primary idiopathic benign red marrow hyperplasia is fortuitously observed in middle-aged obese woman, in heavy smokers and in subjects with intensive sports activities such as long distance running (Shellock et al. 1992; Poulton et al. 1993). A secondary form of red marrow hyperplasia can be observed in association with abnormal situations that stimulate the production of hematopoietic cells including the use of hematopoietic growth factors during chemotherapy, and in several chronic disorders that are associated

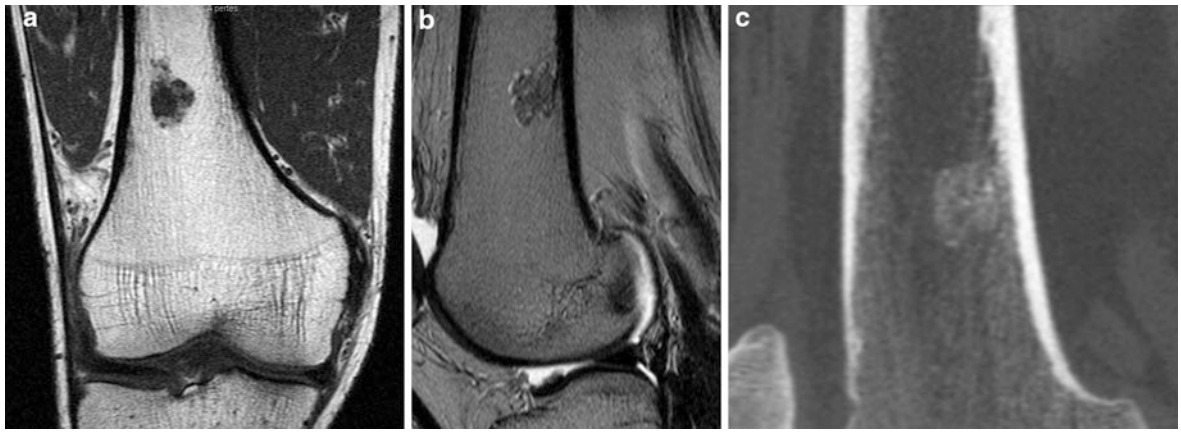

Fig. 22 Enchondroma. **a** Coronal T1-weighted SE image of the right knee shows a metaphyseal lesion of low signal intensity with lobulated contours and sharp margins. **b** On the sagittal T2-weighted SE image, the lesion has intermediate signal intensity with some punctated areas of high or low signal intensity. **c** On a sagittal CT reconstruction form, the lesion shows discrete calcification suggestive of an enchondroma

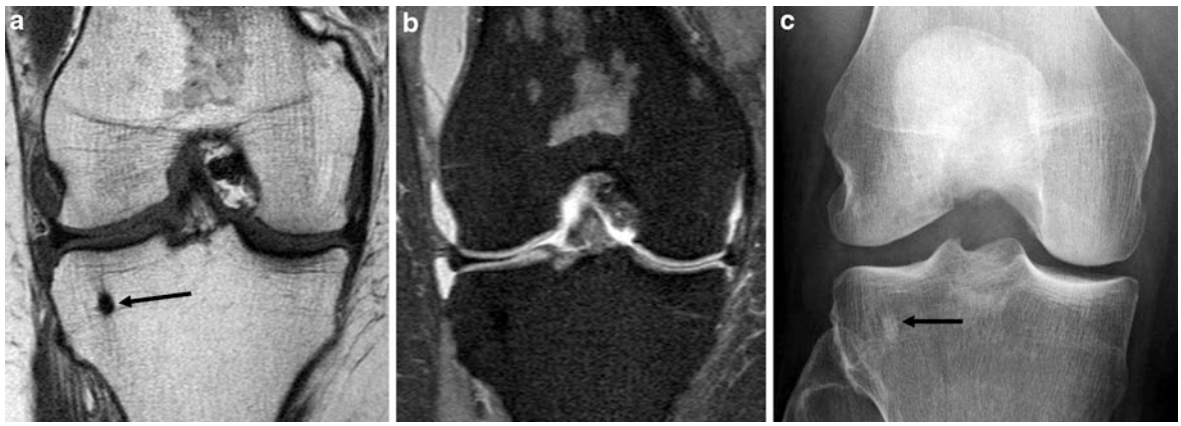

Fig. 23 Enostosis. **a** A lesion of very low signal intensity (*arrow*) is visible in the epiphyseal marrow of the proximal tibia on the coronal T1-weighted SE image. **b** No signal abnormality is seen on the corresponding STIR image. **c** A compact bone island (*arrow*) is visible on the AP radiograph

with anemia including hereditary hemoglobinopathies and chronic infections (Stabler et al. 2000; Altehoefer et al. 2001; Ciray et al. 2003).

Several MR features should be present in benign hematopoietic marrow hyperplasia at MR imaging of the knee whereas other features should not be observed (Table 5). When benign red marrow hyperplasia is observed around the knees, decreased signal intensity on T1-weighted images should be seen in the metaphyses but not in the epiphyses. It should predominate in the posterior aspect of the femur. It should also predominate in the femur with respect to the tibia where red marrow can be seen near the posterior aspect of the proximal metaphysis (Fig. 19). The bone marrow appearance should be symmetrical (Fig. 20) and unchanged over years (Fig. 21). On other sequences, the signal intensity of the presumed red marrow should behave like that of normal red marrow (Fig. 19). Cortical, periosteal and soft tissue changes should be absent. Benign hematopoietic marrow hyperplasia is frequent in middle-aged women but unusual in men with normal physical activities.

In this condition, both the appendicular and the axial bone marrow should be considered. In the vertebral marrow, hematopoietic marrow hyperplasia is

associated with a marked decrease in signal intensity on T1-weighted images and it may become lower than that of adjacent disk. It can also be heterogeneous due to the presence of residual fatty marrow and foci of red marrow. On T2-weighted SE images, the vertebral signal intensity can also be reduced, probably because of an increase in the intracellular iron. After intravenous gadolinium injection, signal intensity enhancement is moderate but can increase up to 80% on dynamic T1-weighted SE images.

Diffuse hematopoietic marrow hyperplasia can be confused with diffuse marrow infiltration in the spine and with focal metastases in the limbs when they take a nodular appearance, which rarely occurs in benign red marrow hyperplasia and is observed in the secondary form (Ciray et al. 2003). As a rule, marrow hyperplasia shows a signal similar to that of red marrow but this may also be observed in diffuse marrow infiltration by neoplastic cells. Several techniques can be used in an attempt to differentiate the two conditions. In- and out-phase gradient-echo images, T1 relaxation time determination, Hydrogen proton spectroscopy, dynamic contrast MR studies, diffusion-weighted images have all shown to be of some help but none has demonstrated definite conclusive results. FDG-PET imaging has also shown limitation in this setting because diffuse increased uptake can be observed in red marrow hyperplasia as in neoplastic medullary infiltration (Hollinger et al. 1998; Elmstrom et al. 2004). Therefore, obtention of a blind iliac crest biopsy may ultimately remain the more accurate technique to definitely address this occasionally difficult problem.

5.4 Focal Normal Variants and Incidental Findings

5.4.1 Benign Bone Tumors and Hamartomas

It is beyond the scope of this chapter to focus on benign bone tumors and the differential diagnosis with their malignant counterparts. However, the intensive practice of knee and shoulder MR imaging has changed the frequency with which these benign lesions are seen. Actually, medullary-based lesions including enchondromas (Fig. 22) and enostosis (Fig. 23) are frequently seen on MR images with a frequency varying from 2 to about 10% (Kransdorf et al. 2007; Walden et al. 2008; Subhas et al. 2009; Hong et al. 2011). Typically, enchondromas should be located within the metaphysis or the diaphysis but not in the epiphysis. On the contrary, enostoses predominate in the epiphysis where the trabecular network is denser than in the dia-metaphyseal regions. Cortically based benign lesions including cortical defect and non-ossifying fibromas are more easily detected on radiographs than on MR images.

5.4.2 Growing Skeleton

In growing skeleton, marrow heterogeneities are also present in some specific areas including the feet (Pal et al. 1999; Shabshin et al. 2006), the hands (Müller et al. 2011) and the physeal regions. Their clinical significance is ignored but the existence of these marrow heterogeneities should be kept in mind to avoid confusion with clinically significant lesions.

6 Conclusions

The analysis of bone marrow on MR images is based on the analysis of both its signal intensity and homogeneity on T1-weighted sequence taking into account the topography of the considered marrow area and the patient's age.

In young adults, the vertebral red marrow shows a homogeneous appearance and an intermediate signal intensity on T1-, T2- and fat-saturated intermediate-weighted images, with little signal intensity enhancement after intravenous injection of contrast material on non-fat-saturated T1-weighted SE images. A reproducible pattern of red and yellow marrow distribution is observed in the appendicular skeleton. In elderly patients, diffuse alteration in the signal homogeneity of bone marrow can be observed due to the presence of small infra-centimetric foci of high or low signal intensity.

The MR imaging appearance of the normal marrow shows important variations with age and also among individuals of the same age range. However, within a single individual, marrow signal intensity and homogeneity as well as red marrow distribution show little variation among each vertebral body or each paired bones.

Diffuse alteration in the signal intensity of bone marrow is observed in the condition named benign red marrow hyperplasia. Focal alterations in signal intensity can be observed that reflect local variations in the amount of normal expected vertebral components, including yellow and red marrow. Benign bone tumors and hamartomas must be known because of

their high frequency in the normal population. A more recently recognized condition related to the presence of notochordal cells deserves further study as it could account for some frequent tiny marrow changes.

MR imaging shows important limitations in characterizing diffuse and focal marrow changes that can be observed in healthy subjects and in patients. It can be difficult—and occasionally impossible to differentiate irrelevant changes from clinically significant marrow alterations, given the lack of specificity of MR imaging.

References

Altehoefer C, Bertz H, Ghanem NA, Langer M (2001) Extent and time course of morphological changes of bone marrow induced by granulocyte-colony stimulating factor as assessed by magnetic resonance imaging of healthy blood stem cell donors. J Magn Reson Imaging 14(2):141–146

Baudrez V, Galant C, Vande Berg BC (2001) Benign vertebral hemangioma: MR-histological correlation. Skeletal Radiol 30(8):442–446

Baur A, Stäbler A, Bartl R, Lamerz R, Scheidler J, Reiser M (1997) MRI gadolinium enhancement of bone marrow: age-related changes in normals and in diffuse neoplastic infiltration. Skeletal Radiol 26(7):414–418

Biffar A, Sourbron S, Schmidt G et al (2010) Measurement of perfusion and permeability from dynamic contrast-enhanced MRI in normal and pathological vertebral bone marrow. Magn Reson Med 64(1):115–124

Bolog N, Nanz D, Weishaupt D (2006) Muskuloskeletal imaging at 3.0 T: current status and future perspectives. Eur Radiol 16(6):1298–1307

Bordalo-Rodrigues M, Galant C, Lonneux M, Clause D, Vande Berg BC (2003) Focal nodular hyperplasia of the hematopoietic marrow simulating vertebral metastasis on FDG positron emission tomography. Am J Roentgenol 180(3):669–671

Buyn WM, Shin SO, Chang Y, Finsterbusch J, Frahm J (2002) Diffusion-weighted MR imaging of metastatic disease of the spine: assessment of response to therapy. Am J Neuroradiol 23:906–912

Carroll KW, Feller JF, Tirman PF (1997) Useful internal standards for distinguishing infiltrative marrow pathology from hematopoietic marrow at MRI. J Magn Reson Imaging 7(2):394–398

Chen WT, Shih TT, Chen RC, Lo SY, Chou CT, Lee JM et al (2001) Vertebral bone marrow perfusion evaluated with dynamic contrast-enhanced MR imaging: significance of aging and sex. Radiology 220(1):213–218

Ciray I, Lindman H, Astrom GK, Wanders A, Bergh J, Ahlstrom HK (2003) Effect of granulocyte colony-stimulating factor (G-CSF)-supported chemotherapy on MR imaging of normal red bone marrow in breast cancer patients with focal bone metastases. Acta Radiol 44(5):472–484

Cristy M (1981) Active bone marrow distribution as a function of age in humans. Phys Med Biol 26(3):389–400

Cuénod CA, Laredo JD, Chevret S, Hamze B, Naouri JF, Chapaux X, Bondeville JM, Tubiana JM (1996) Acute vertebral collapse due to osteoporosis or malignancy: appearance on unenhanced and gadolinium-enhanced MR images. Radiology 199(2):541–549

De Bruyn PPH, Breen PC, Thomas TB (1970) The microcirculation of the bone marrow. Anat Rec 168:55–68

Delfaut EM, Beltran J, Johnson G, Rousseau J, Marchandise X, Cotten A (1999) Fat suppression in MR imaging: techniques and pitfalls. Radiographics 19(2):373–382

Deutsch AL, Mink JH, Rosenfelt FP, Waxman AD (1989) Incidental detection of hematopoietic hyperplasia on routine knee MR imaging. Am J Roentgenol 152(2):333–336

Dietrich O, Herlihy A, Danneels WR et al (2001) Diffusion-weighted imaging of the spine using radial K-space trajectories. Magn Reson Mater Phys Biol Med 12:23–31

Dietrich O, Biffar A, Reiser MF, Baur-Melnyk A (2009a) Diffusion-weighted imaging of the bone marrow. Semin Musculoskelet Radiol 13(2):134–144

Dietrich O, Biffar A, Reiser MF, Baur-Melnyk A (2009b) Diffusion-weighted imaging of bone marrow. Semin Musculoskelet Radiol 13(2):134–144

Dietrich O, Biffar A, Baur-Melnyk A, Reiser MF (2010) Technical aspects of MR diffusion imaging of the body. Eur J Radiol 76(3):314–322

Elmstrom RL, Tsai DE, Vergilio JA, Downs LH, Alavi A, Schuster SJ (2004) Enhanced marrow [18F]fluorodeoxyglucose uptake related to myeloid hyperplasia in Hodgkin's lymphoma can simulate lymphoma involvement in marrow. Clin Lymphoma 5(1):62–64

Eustace S, Tello R, DeCarvalho V, Carey J, Wroblicka JT, Melhem ER, Yucel EK (1997) A comparison of whole-body turboSTIR MR imaging and planar 99mTc-methylene diphosphonate scintigraphy in the examination of patients with suspected skeletal metastases. Am J Roentgenol 169(6):1655–1661

García AI, Milinkovic A, Tomás X, Rios J, Pérez I, Vidal-Sicart S, Pomés J, DelAmo M, Mallolas J (2011) MRI signal changes of the bone marrow in HIV-infected patients with lipodystrophy: correlation with clinical parameters. Skeletal Radiol 40(10):1295–1301

Griffith JF, Yeung DK, Antonio GE et al (2005) Vertebral bone mineral density, marrow perfusion, and fat content in healthy men and men with osteoporosis: dynamic contrast enhanced MR imaging and spectroscopy. Radiology 236:945–951

Griffith JF, Yeung DK, Antonio GE et al (2006) Vertebral marrow fat content and diffusion and perfusion indexes in women with varying bone density: MR evaluation. Radiology 241:831–938

Hajek PC, Baker LL, Goobar JE, Sartoris DJ, Hesselink JR, Haghighi P et al (1987) Focal fat deposition in axial bone marrow: MR characteristics. Radiology 162:245–249

Hanrahan CJ, Shah LM (2011) MRI of spinal bone marrow: part 2, T1-weighted imaging-based differential diagnosis. Am J Roentgenol 197(6):1309–1321

Hollinger EF, Alibazoglu H, Ali A, Green A, Lamonica G (1998) Hematopoietic cytokine-mediated FDG uptake simulates the appearance of diffuse metastatic disease on whole-body PET imaging. Clin Nucl Med 23(2):93–98

Hong ED, Carrino JA, Weber KL, Fayad LM (2011) Prevalence of shoulder enchondromas on routine MR imaging. Clin Imaging 35(5):378–384

Khoo MM, Tyler PA, Saifuddin A, Padhani AR (2011) Diffusion-weighted imaging (DWI) in musculoskeletal MRI: a critical review. Skeletal Radiol 40(6):665–681

Kransdorf MJ, Peterson JJ, Bancroft LW (2007) MR imaging of the knee: incidental osseous lesions. Radiol Clin North Am 45(6):943–954

Kroon HM, Bloem JL, Holscher HC, van der Woude HJ, Reijnierse M, Taminiau AH (1994) MR imaging of edema accompanying benign and malignant bone tumors. Skeletal Radiol 23(4):261–269

Kyriakos M (2011) Benign notochordal lesions of the axial skeleton: a review and current appraisal. Skeletal Radiol 40(9):1141–1152

Laredo JD, Reizine D, Bard M, Merland JJ (1986) Vertebral hemangiomas: radiologic evaluation. Radiology 161(1):183–189

Levine CD, Schweitzer ME, Ehrlich SM (1994) Pelvic marrow in adults. Skeletal Radiol 23(5):343–347

Li Q, Pan SN, Yin YM, Li W, Chen ZA, Liu YH, Wu ZH, Guo QY (2011) Normal cranial bone marrow MR imaging pattern with age-related ADC value distribution. Eur J Radiol 80(2):471–477

Liney GP, Bernard CP, Manton DJ, Turnbull LW, Langton CM (2007) Age, gender, and skeletal variation in bone marrow composition: a preliminary study at 3.0 Tesla. J Magn Reson Imaging 26(3):787–793

Mirowitz SA (1993) Hematopoietic bone marrow within the proximal humeral epiphysis in normal adults: investigation with MR imaging. Radiology 188(3):689–693

Mirra JM, Brien EW (2001) Giant notochordal hamartoma of intraosseous origin: a newly reported benign entity to be distinguished from chordoma. Report of two cases. Skeletal Radiol 30(12):698–709

Montazel JL, Divine M, Lepage E, Kobeiter H, Breil S, Rahmouni A (2003) Normal spinal bone marrow in adults: dynamic gadolinium-enhanced MR imaging. Radiology 229(3):703–709

Müller LS, Avenarius D, Damasio B, Eldevik OP, Malattia C, Lambot-Juhan K, Tanturri L, Owens CM, Rosendahl K (2011) The paediatric wrist revisited: redefining MR findings in healthy children. Ann Rheum Dis 70(4):605–610

Murphey MD, Fairbain KJ, Parman L, Baxter KG, Parsa MB, Smith WS (1995) Muskuloskeletal angiomatous lesions: radiologic–pathologic correlation. Radiographics 15:893–917

Murphey MD, Andrews CL, Flemming DJ, Temple HT, Smith WS, Smirniotopoulos JG (1996) Primary tumors of the spine: radiologic–pathologic correlation. Radiographics 16:1131–1158

Nishiguchi T, Mochizuki K, Ohsawa M, Inoue T, Kageyama K, Suzuki A, Takami T, Miki Y (2011) Differentiating benign notochordal cell tumors from chordomas: radiographic features on MRI, CT, and tomography. Am J Roentgenol 196(3):644–650

Pal CR, Tasker AD, Ostlere SJ, Watson MS (1999) Heterogeneous signal in bone marrow on MRI of children's feet: a normal finding? Skeletal Radiol 28(5):274–278

Poulton TB, Murphy WD, Duerk JL, Chapek CC, Feiglin DH (1993) Bone marrow reconversion in adults who are smokers: MR imaging findings. Am J Roentgenol 161:1217–1221

Raya JG, Dietrich O, Birkenmaier C, Sommer J, Reiser MF, Baur-Melnyk A (2007) Feasability of a RARE-based sequence for quantitative diffusion-weighted MR imaging of the spine. Eur Radiol 17:2872–2879

Resnick D, Nemcek AA Jr, Haghighi P (1983) Spinal enostoses (bone islands). Radiology 147(2):373–376

Ricci C, Cova M, Kang YS, Yang A, Rahmouni A, Scott WW Jr et al (1990) Normal age-related patterns of cellular and fatty bone marrow distribution in the axial skeleton: MR imaging study. Radiology 177(1):83–88

Ross JS, Masaryk TJ, Modic MT, Carter JR, Mapstone T, Dengel FH (1987) Vertebral hemangiomas: MR imaging. Radiology 165(1):165–169

Schmorl G, Junghans H, Doin G (1956) Clinique et radiologie de la colonne vertébrale normale et pathologique. In: Doin G (ed) Lésion du rachis osseux, Paris, pp 71–140

Seymour R, Davies AM, Evans N, Mangham DC (1997) Diagnostic problems with atypical bone islands. Br J Radiol 70:87–88

Shabshin N, Schweitzer ME, Morrison WB, Carrino JA, Keller MS, Grissom LE (2006) High-signal T2 changes of the bone marrow of the foot and ankle in children: red marrow or traumatic changes? Pediatr Radiol 36(7):670–676

Shellock FG, Morris E, Deutsch AL, Mink JH, Kerr R, Boden SD (1992) Hematopoietic bone marrow hyperplasia: high prevalence on MR images of the knee in asymptomatic marathon runners. Am J Roentgenol 158(2):335–338

Simpfendorfer CS, Ilaslan H, Davies AM, James SL, Obuchowski NA, Sundaram M (1996) Does the presence of focal normal marrow fat signal within a tumor on MRI exclude malignancy? An analysis of 184 histologically proven tumors of the pelvic and appendicular skeleton. Radiology 199(2):541–549

Simpfendorfer CS, Ilaslan H, Davies AM, James SL, Obuchowski NA, Sundaram M (2008) Does the presence of focal normal marrow fat signal within a tumor on MRI exclude malignancy? An analysis of 184 histologically proven tumors of the pelvic and appendicular skeleton. Skeletal Radiol 37(9):797–804

Stabler A, Doma AB, Baur A, Kruger A, Reiser MF (2000) Reactive bone marrow changes in infectious spondylitis: quantitative assessment with MR imaging. Radiology 217(3):863–868

Subhas N, Bui KL, Sundaram M, Ilaslan H, Recht MP (2009) Incidental tumor and tumor-like lesions around the knee. Semin Musculoskelet Radiol 13(4):353–370

Vande Berg BC, Malghem J, Devuyst O, Maldague BE, Lambert MJ (1994) Anorexia nervosa: correlation between MR appearance of bone marrow and severity of disease. Radiology 193(3):859–864

Vande Berg BC, Malghem J, Lecouvet FE, Lambert M, Maldague BE (1996) Distribution of serous-like bone marrow changes in the lower limbs of patients with anorexia nervosa: predominant involvement of the distal extremities. Am J Roentgenol 166(3):621–625

Vande Berg BC, Lecouvet FE, Moysan P, Maldague B, Jamart J, Malghem J (1997) MR assessment of red marrow distribution and composition in the proximal femur: correlation with clinical and laboratory parameters. Skeletal Radiol 26(10):589–596

Vande Berg BC, Malghem J, Lecouvet FE, Maldague BE (1998a) Magnetic resonance imaging of the normal bone marrow. Skeletal Radiol 27:471–483

Vande Berg BC, Malghem J, Lecouvet FE, Maldague B (1998b) Classification and detection of bone marrow lesions with magnetic resonance imaging. Skeletal Radiol 27(10): 529–545

Vande Berg BC, Lecouvet FE, Galant C, Maldague BE, Malghem J (2005) Normal variants and frequent marrow alterations that simulate bone marrow lesions at MR imaging. Radiol Clin North Am 43(4):761–770

Vogler JBI, Murphy WA (1988) Bone marrow imaging. Radiology 168(3):679–693

Waitches G, Zawin JK, Poznanski AK (1994) Sequence and rate of bone marrow conversion in the femora of children as seen on MR imaging: are accepted standards accurate? Am J Roentgenol 162(6):1399–1406

Walden MJ, Murphey MD, Vidal JA (2008) Incidental enchondromas of the knee. Am J Roentgenol 190(6):1611–1615

Weiss L (1965) The structure of bone marrow functional interrelationships of vascular and hematopoietic compartments in experimental hemolytic anemia: an electron microscopic study. J Morph 117:467–538

Wilner D (1982) Radiology of bone tumors and allied disorders. Benign vascular tumors and allied disorders of bone. WB Saunders, Philadelphia, pp 660–782

Yamaguchi T, Yamato M, Saotome K (2002) First histologically confirmed case of a classic chordoma arising in a precursor benign notochordal lesion: differential diagnosis of benign and malignant notochordal lesions. Skeletal Radiol 31(7):413–418

Yamaguchi T, Suzuki S, Ishiiwa H, Ueda Y (2004a) Intraosseous benign notochordal cell tumours: overlooked precursors of classic chordomas? Histopathology 44(6):597–602

Yamaguchi T, Suzuki S, Ishiiwa H, Shimizu K, Ueda Y (2004b) Benign notochordal cell tumors: a comparative histological study of benign notochordal cell tumors, classic chordomas, and notochordal vestiges of fetal intervertebral discs. Am J Surg Pathol 28(6):756–761

Zampa V, Cosottini M, Michelassi C, Ortori S, Bruschini L, Bartolozzi C (2002) Value of opposed-phase gradient-echo technique in distinguishing between benign and malignant vertebral lesions. Eur Radiol 12(7):1811–1818

Part II

Bone Marrow Neoplasia

Haematological Bone Marrow Malignancies

Sung Kim, Kathleen Carrigan, and Michael Mulligan

Contents

Abstract

Lymphoproliferative disorders and myeloproliferative disorders frequently involve the skeletal system. Lymphoma of bone might occur as primary lymphoma of bone or as secondary involvement in Hodgkin or Non-Hodgkin disease. Lymphoma of bone usually occurs as an area of osteolysis or as a focal sclerotic lesion with tumor-like signal behavior in MRI. Leukemias as well as chronic myeloproliferative diseases usually show homogeneous diffuse hypercellularity with low signal intensity on T1-w SE images and diffuse hyperintensity in fat-suppressed images. Usually the lesions show marked contrast enhancement. After systemic chemotherapy or in the later stages of disease, due to myelofibrosis, the signal might become more patchy. The findings are nonspecific, however with the knowledge of the clinical data they can be interpreted correctly. Osteomyelosclerosis has a different signal behavior with low signal intensity in all sequences. However, due to enlarged sinusoids contrast enhancement might be intense.

1 Introduction

Lymphoproliferative disorders and myeloproliferative disorders frequently involve the skeletal system. Skeletal involvement may be the initial manifestation of the disorder and the dominant aspect of the clinical presentation (Fig. 1). While its imaging expression is often nonspecific in its appearance, these disorders comprise a specific subgroup of the malignant bone

S. Kim · K. Carrigan · M. Mulligan (✉)
Department of Radiology,
UMMC, 22 South Greene St,
Baltimore, MD 21201, USA
e-mail: mmulligan@umm.edu

A. Baur-Melnyk (ed.), *Magnetic Resonance Imaging of the Bone Marrow*, Medical Radiology. Diagnostic Imaging,
DOI: 10.1007/174_2011_522,

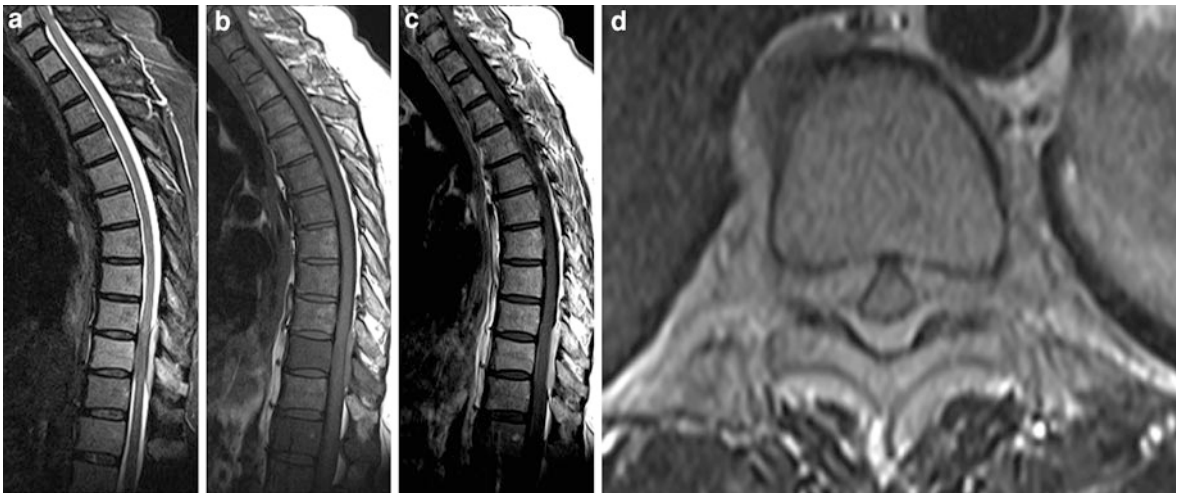

Fig. 1 A 70-year-old woman with CLL who presented with back pain. Matched sagittal spine MR images with **a** T2-weighting, **b** T1-weighting, and **c** T1-weighted SE post-contrast **d** axial T1-weighted fat saturated post-contrast, demonstrate abnormal marrow signal and enhancement in the T10 and T12 vertebrae and an enhancing soft tissue mass in the epidural space, centered at T10. Abnormal soft tissue also extended through the neural foramina and into the paravertebral soft tissues. Severe thecal sac narrowing and cord edema was noted at T10. A diffuse lymphoid infiltrate was identified at surgery. Subsequent bone marrow biopsy led to the diagnosis of CLL

lesions, which have an unusually favorable prognosis. This chapter will focus specifically on the skeletal manifestations of leukemias and lymphomas, as well as on chronic myeloproliferative diseases, with a review of the relevant literature. The discussion of the imaging features will include findings from conventional radiography, computed tomography, and nuclear scintigraphy, with an emphasis on magnetic resonance imaging.

2 Leukemias

2.1 Epidemiology and Clinical Background

Leukemias are a heterogeneous group of disorders which diffusely involve the bone marrow. By convention, they are grouped into acute and chronic forms. Acute leukemias are the result of defects in the blast cell maturation process that lead to an accumulation of immature cells within the bone marrow. Chronic forms, on the other hand, are characterized by marked overgrowth of mature cells within the marrow. Both acute and chronic leukemias may arise from a clonal expansion of myeloid or lymphoid cell lines (Bennet et al. 1976, 1989). The 2002 World Health Organization (WHO) classification system uses the combination of the cellular morphology, the immunophenotype, the cytogenetics and increasingly the gene expression profile, to classify the diverse array of leukemic disorders (Swerdlow et al. 2008; Yeoh et al. 2002).

Acute leukemias that affect children are typically of lymphocytic cell origin, accounting for three quarters of pediatric cases, which is in contrast to predominantly myelogenous acute leukemias that are seen in adults (Smith et al. 1999; Van Slyck 1972). Chronic leukemias may be granulocytic or lymphocytic in origin and typically present during the fourth to sixth decades of life (O'Hara 1967).

As leukemias involve the bone marrow by definition, osseous changes are almost always present, even if they may not be conspicuous on routine radiographic examinations. More pronounced imaging abnormalities are associated with the more aggressive types of leukemia and are more often seen in the pediatric age group.

The clinical manifestations of leukemic disorders can be explained by the underlying pathophysiology. The abnormal proliferation and accumulation of pathologic cells within the bone marrow suppresses the normal marrow elements, resulting in anemia, neutropenia, and thrombocytopenia. Fever, petechiae,

lethargy, and pallor are common signs and the patient with leukemia is frequently prone to bleeding episodes and recurrent infections. The structural integrity of the involved bones also is compromised. Not surprisingly, bone pain, pathologic fracture, and osteonecrosis are commonly associated with leukemia (Sinigaglia et al. 2008). The high cellular turnover leads to an accumulation of uric acid, a byproduct of nucleic acid breakdown. Thus, in advanced disease, gout and renal failure may be seen. Cardiac and neurologic complications can also be seen.

2.2 Acute Leukemia

Acute leukemia is the most common form of childhood malignancy. Its peak prevalence is typically in early childhood. Acute lymphoblastic leukemia (ALL) peak incidence occurs at 2–3 years of age, with evidence that ALL begins in utero (Greaves 2005). Acute myeloid leukemia (AML) rates also are highest in the first 2 years of life (Guillerman et al. 2011). The vast majority of acute leukemias are lymphoblastic in origin, with approximately 10% of cases myeloid, and 10% of other cell origin (Parker et al. 1980). The WHO classification subtypes are based on B-cell or T-cell origin. Precursor B-cell ALL accounts for 80–85% of cases. About 12% of ALL is of T-cell origin, and these may represent a disseminated form of T-cell lymphoblastic lymphoma. They are associated with older age, male gender, leukocytosis, and a mediastinal mass. Subtyping of AML is moving away from the traditional French-American-British (FAB) system to the WHO classification system, which incorporates cytogenetic and specific gene mutation information (Bennett et al. 1976; Swerdlow et al. 2008).

2.2.1 Findings in Radiographs

Radiographic skeletal changes are encountered in approximately 50–70% of patients and have been recognised since the 1950s (Wilson 1959; Resnick and Haghighi 2002). The number of bones involved correlates with the bone pain severity (Hann et al. 1979). Symptoms, however, localize poorly with the site of the actual skeletal lesions that are detected on radiographs. Asymptomatic radiographic findings, especially in the non-weight bearing areas, are also common (Sinigaglia et al. 2008). Skeletal radiographic findings of leukemia include diffuse demineralization, transverse lucent metaphyseal bands, subperiosteal cortical bone erosions, periosteal reaction, focal lytic bone lesions, osteonecrosis, and pathologic fractures.

The most commonly seen, although the least specific, finding is diffuse demineralization (Fig. 2). Diverse biochemical mechanisms likely contribute to the bone changes and hypercalcemia seen in childhood ALL. Some of the bone changes may be a result of altered calcium metabolism, such as that resulting from ectopic PTH production as well as ectopically produced fragments of PTH that were found in several children with ALL in one report (Cohn et al. 1987) or they may arise directly from marrow infiltration by the leukemic cells. Corticosteroid therapy also can lead to this finding in patients receiving chemotherapy. Typically, cortical thinning and medullary widening are noted in the long bones and complications such as vertebral compression fractures (Fig. 3) may occur (Ribeiro et al. 1988).

Metaphyseal band-like lucencies are frequently seen in patients with acute leukemia. While this finding is relatively nonspecific, in patients older than 2 years of age it is more frequently associated with leukemia than with any other condition (Wilson 1959). Nutritional deficiencies are thought to be responsible for these changes, resulting in abnormal endosteal mineralization and small trabeculae adjacent to the zone of provisional calcification. As a consequence, this finding is seen most commonly at the sites of rapid bone growth (around the knee, the proximal humerus, and the distal radius), although it can occur at other sites as well. These areas may be complicated by fractures, epiphyseal separation, and displacement, or even epiphyseal destruction (Manson et al. 1989). There is a wide differential diagnosis for metaphyseal band-like lucencies, especially in children less than 2 years of age. TORCH infections, healing rickets, scurvy, and metastatic disease (especially from neuroblastoma) are some conditions which also must be considered in addition to acute leukemia.

Parallel dense growth recovery lines of Harris can be seen in up to 50% of children with leukemia (Benz et al. 1976). These are presumed to be related to alternating periods of arrest and acceleration of bone growth. These types of changes may be seen in the vertebral endplates, where growth disturbances may lead to platyspondyly, brachyspondyly, and wedge-shaped vertebrae.

Solitary or multiple lytic osseous lesions also are frequently seen in the setting of acute leukemia

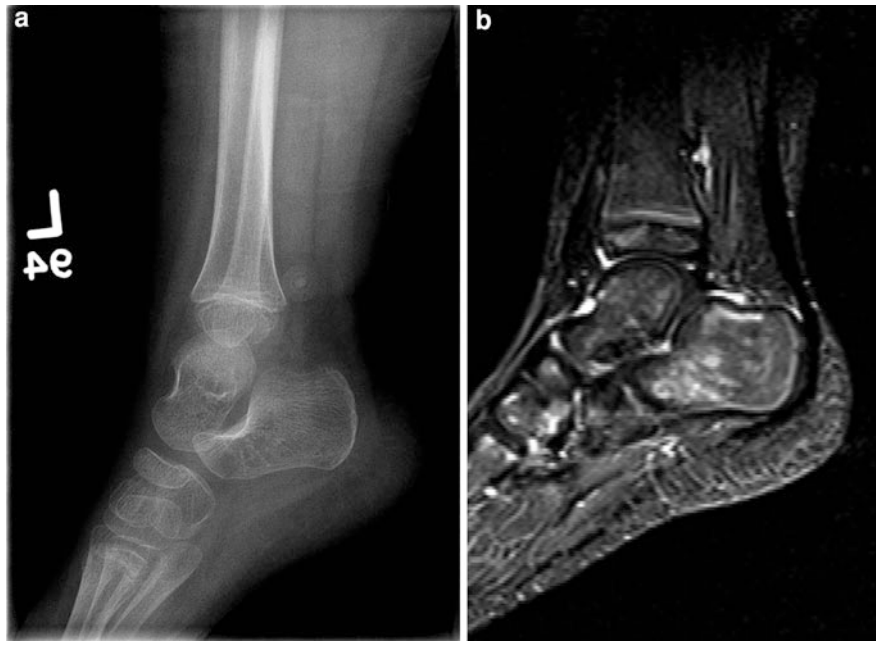

Fig. 2 A 3-year-old girl with ALL. **a** Lateral ankle radiograph shows diffuse demineralization. **b** Sagittal STIR MR image shows multiple small focal spots of bright signal intensity throughout the tarsal bones and in the distal tibia that are characteristic of hyperemic osteoporosis

(Fig. 4). They may involve both tubular and flat bones, affecting the long bones, skull, pelvis, ribs, and shoulder girdle. The medial cortex of the proximal humerus is a characteristic, if somewhat nonspecific, site of involvement that may be visible on a chest radiograph (Melhem and Saber 1980). Aggressive periostitis and subperiosteal haemorrhage may be associated with these lesions. Symmetric periosteal new bone formation simulating hypertrophic osteoarthropathy also may be seen in the long bones (Resnick and Haghighi 2002).

While many of the osseous findings seen with leukemia are nonspecific, their combination may increase the suspicion for the diagnosis of leukemia. Joint involvement is common, with arthralgia and arthritis having been reported in 12–65% of pediatric leukemic patients (Evans et al. 1994). The joint involvement is typically asymmetric and pauciarticular, with periarticular osseous involvement as well as intra-articular leukemic cell infiltration that sometimes is complicated by intra-articular or subperiosteal hemorrhage. Clinically, severe pain, tenderness, swelling, and effusion are common. The disappearance of joint complaints is an early indication of improvement following chemotherapy (Costello et al. 1983).

Other less common findings include osteosclerosis, especially in the epiphyses of long bones, cranial sutural diastases resulting from increased intracranial pressure that is typically due to meningeal infiltration of leukemic cells (Nixon and Gwinn 1973), and soft tissue epidural masses (Higashida et al. 2007).

2.2.2 Findings in Scintigraphy

Tc-99 m bone scintigraphy is abnormal in 75% of patients with ALL at diagnosis. The most common abnormality is symmetric increased uptake in the metadiaphyses of the lower extremities. Other patterns, like a superscan with further increased uptake in the long bone metaphyses, or focal increased uptake at sites of cortical bone destruction, or pathologic fracture or focal decreased uptake at sites of osteonecrosis, may be seen (Bernard et al. 1998).

2.2.3 Prognosis and Therapy

The prognostic significance of radiographic findings of leukemia is unclear. In one study, a poorer prognosis was shown to be associated with the presence of multiple bone lesions (Masera et al. 1977) while another study found that the absence of radiographic abnormalities was associated with more aggressive forms of leukemia (Heinrich et al. 1994). Other studies have shown no correlation of radiographic findings and duration of remission or survival (Hann et al. 1979; Appell et al. 1985; Révész et al. 1985).

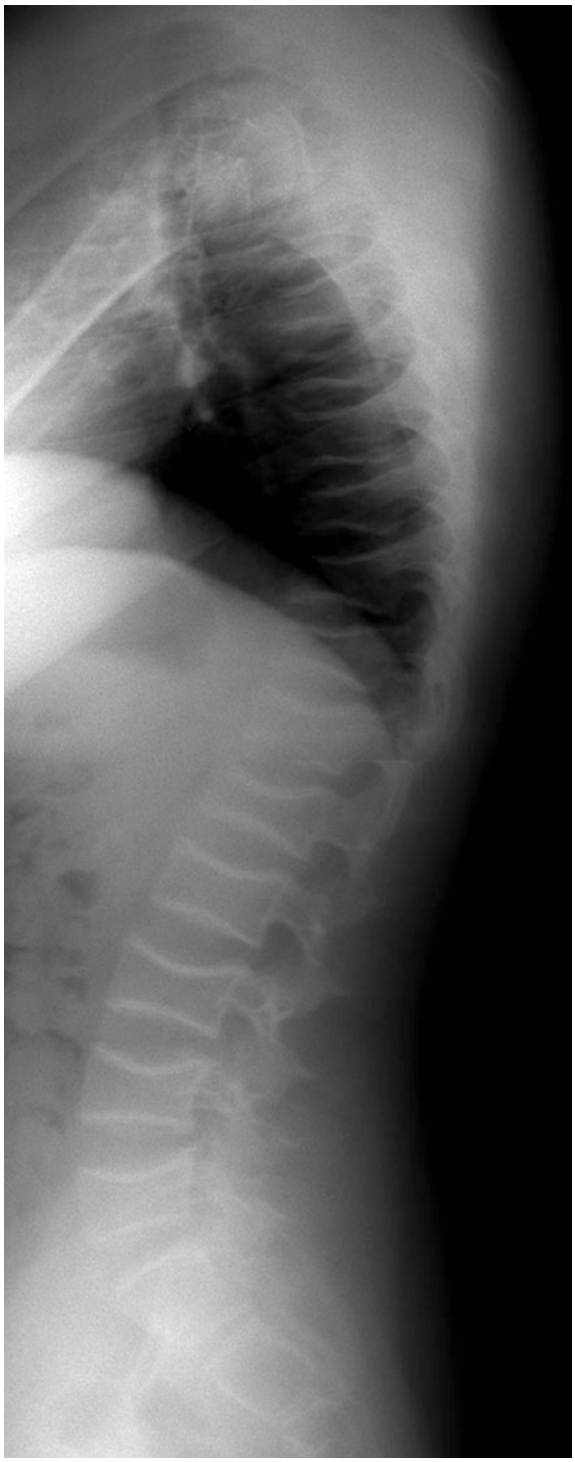

Fig. 3 A 17-year-old man with T-cell ALL. Lateral spine radiograph shows multiple vertebral body compression fractures

On the other hand, skeletal abnormalities have been observed to resolve with treatment (Rosenfield and McIntosh 1977). Nevertheless, due to the highly variable response of skeletal lesions to therapy, imaging follow-up studies are generally not recommended. Imaging of the skeleton should, therefore, be performed to evaluate new and specific symptoms rather than on a routine basis. The overall cure rate for children with acute lymphoblastic leukemia approaches 80% (Pui et al. 2008).

2.3 Chronic Leukemia

Chronic leukemias are classified based on their predominant cellular origin, according to WHO criteria (Swerdlow et al. 2008). Lymphocytic and myelogenous types both predominantly affect the adult population. The myelogenous subtype usually affects the middle-aged and the elderly, while the lymphocytic form typically affects only the elderly population. Chronic leukemia is rarely seen in the pediatric population (Guillerman et al. 2011). Clinically, the patient initially may be asymptomatic or may have nonspecific constitutional symptoms. The radiographic osseous changes of chronic leukemia are generally less common and less severe than those of acute leukemia.

Chronic lymphocytic leukemia (*CLL*) is classified as a form of low grade lymphocytic non-Hodgkin lymphoma, and it is the most common form of leukemia in the elderly. Two-thirds of patients are older than 60 years, while the peak incidence is in patients greater than 80 years of age (Baur-Melnyk and Reiser 2008). Monoclonal duplication of mature B lymphocytes, and less commonly T lymphocytes, is the underlying cause of this disorder. With replacement of the bone marrow elements, anemia, leukopenia, and thrombocytopenia may occur, manifesting clinically as weakness, bruising, and recurrent infections. The leukemic cells also may infiltrate other visceral organs, with splenomegaly and lymphadenopathy as common physical exam findings.

2.3.1 Findings in Radiographs and CT

The marrow replacement process is seen radiographically as nonspecific diffuse osteopenia. Small osteolytic

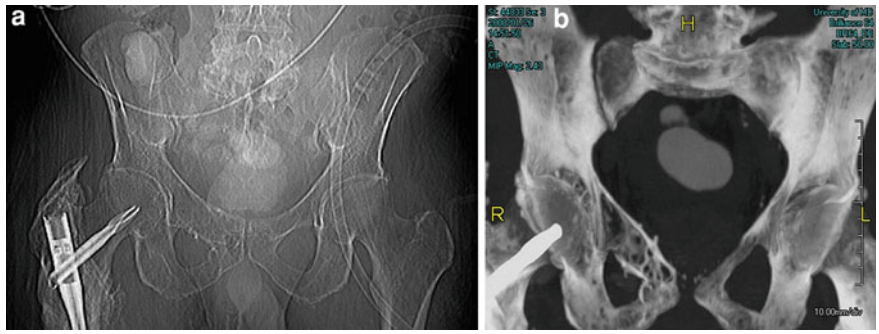

Fig. 4 A 64-year-old man with ALL. **a** Anteroposterior CT scout image shows a bubbly lytic lesion in the right superior pubic ramus, better depicted on **b** 3D CT image

lesions can be seen (Fig. 5), as well as more mass-like bony erosions due to the accumulation of leukemic cells. The small bones of the hands may become involved, and bone destruction, clubbing and soft tissue oedema can occur. With this combination of findings, called 'leukemic acropachy,' the metacarpals are more frequently affected when compared to the phalanges (Glatt and Weinstein 1969). Leukemia-related arthritis is observed in approximately 12% of patients with chronic leukemia (Spilberg and Meyer 1972). The knee, shoulder, and ankle joints are affected most commonly, and the pain is commonly polyarticular and migratory. Secondary gout is a common and well documented complication of chronic leukemia. Osteonecrosis secondary to steroid therapy and osteomyelitis are other common secondary complications of chronic leukemia.

Chronic myelogenous leukemia (*CML*) is a distinct entity, with a different cellular origin and pathophysiology. Formerly it has been subsummarised under the group of chronic myeloproliferative syndromes, however, to date it should be differentiated as a distinct entity. CML is characterized by the unregulated clonal expansion of myeloid elements, consisting of neutrophils, eosinophils or basophils. The patients are often asymptomatic, so the diagnosis results from findings detected on analysis of "routine" blood work. Similar to its lymphocytic cousin, nonspecific constitutional symptoms may ensue. Ultimately, myelofibrosis and death ensue in untreated individuals. Osseous radiographic manifestations are similar to those of CLL, as discussed above.

2.3.2 Prognosis and Therapy

Ninety-five percent of CML is associated with a single characteristic chromosomal translocation event that results in the so-called Philadelphia chromosome

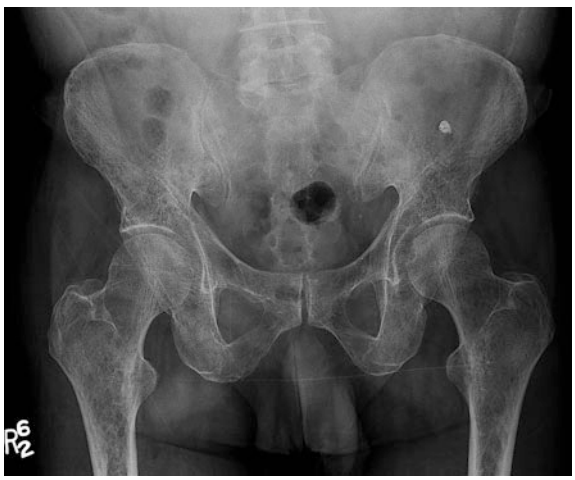

Fig. 5 A 55-year-old man with CLL. Anteroposterior pelvic radiograph shows multiple small focal lytic lesions throughout the pelvis and proximal femurs that mimic the appearance of multiple myeloma

t(9:22) (Nowell and Hungerford 1960). The resulting bcr-abl oncogene activation bypasses the normal cell cycle regulatory mechanism, leading to unchecked proliferation of the pathologic cell lines. The mutant gene product is a tyrosine kinase (Hehlmann et al. 2007). The recent targeted therapy approach using recombinant DNA technology and a monoclonal antibody has led to the development of the tyrosine kinase inhibitor class of drugs which has revolutionized the treatment of this disease. One recent study showed 95% survival after 8 years for patients treated with imatinib for CML (Gambacorti-Passerini et al. 2011).

2.4 Special Types of Leukemia

Hairy cell leukemia accounts for 2% of all leukemia cases. This entity was named for its microscopic

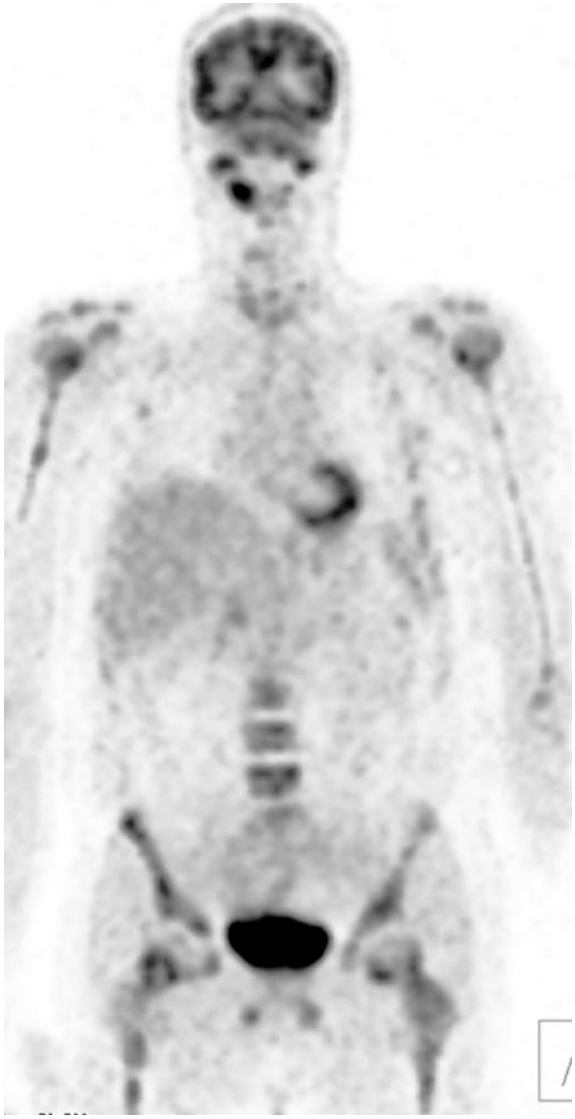

Fig. 6 A 60-year-old man with history of hairy cell leukemia diagnosed 20 years previously who presented with multiple new complaints. Coronal FDG PET image shows multiple FDG avid foci throughout the skeleton as well as multiple soft tissue masses in the neck. Biopsy of neck mass confirmed recurrent hairy cell leukemia

appearance of numerous hair-like villi on the lymphocyte's membrane (Schrek and Donnelly 1966). It most commonly affects middle-aged adults; males are affected three times more frequently than females (Fig. 6). An insidious onset with nonspecific constitutional symptoms is often evident retrospectively. The disease progresses slowly, but most patients succumb in the first 5 years, frequently due to atypical infections. Bone involvement is relatively uncommon. When present, however, early and severe pain is characteristic. One or two osteolytic lesions are typical, occurring most frequently in the spine or the head/neck region of the proximal femur (Herold et al. 1988). Bone sclerosis is rare. Complications such as pathologic fracture and osteonecrosis of the femoral or humeral heads also may be seen.

Chloroma, also known as granulocytic sarcoma, is a focal usually extramedullary (rarely intramedullary) tumor mass composed of myeloid elements. Its name reflects the greenish hue of the tumor that results from copper ions in the myeloperoxidase proteins. Chloromas are most commonly associated with AML in children, although they also are observed in the adult population as well as in other varieties of leukemias (Fig. 7). Sometimes these tumors arise in the absence of known disease. In such instances, chloromas are typically followed within months by the onset of acute leukemia. Bone, as well as soft tissue, the orbits, lymph nodes, and skin may be involved. Osseous lytic lesions are commonly seen in the skull, spine, ribs, and long bones (Woodard et al. 1999). Spinal epidural chloroma is not common, but a review of 32 cases has been reported (Seok et al. 2010). Twenty-three cases involved lumbosacral levels, 16 cases were in the thoracic region, and 5 cases involved cervical levels. There was often more than one level of involvement. Areas of involvement were; the spinal canal, along nerve roots, within nerve roots, and prevertebral soft tissues.

Plasma cell leukemia is a leukemic form of myeloma, with malignant plasma cells found in the peripheral circulation. The radiographic appearance is that of typical multiple myeloma. It has the worst prognosis of all forms of myeloma. It is included in the chapter dedicated to myeloma found elsewhere in this book.

2.5 Findings in MRI

The basic MRI evaluation of skeletal involvement from leukemia, as well as from lymphoma to be described following this section, includes T1-weighted and fat saturated T2-weighted or inversion recovery sequences in multiple planes. Inversion recovery sequences are often superior to fat-saturated T2-weighted sequences especially for large fields of

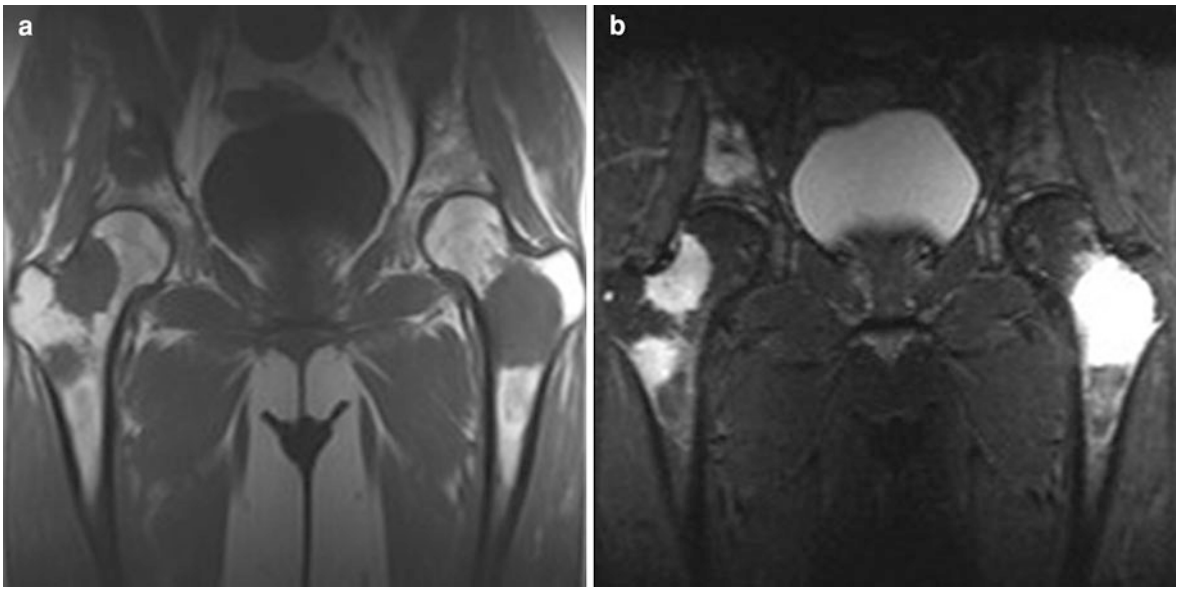

Fig. 7 A 23-year-old woman with AML who presented with new pain 2 years after chemotherapy and bone marrow transplant. Matched coronal pelvic MR images with **a** T1-weighting and **b** inversion recovery, show multiple focal areas of bone marrow replacement in both proximal femurs and the right acetabulum proven to be chloromas

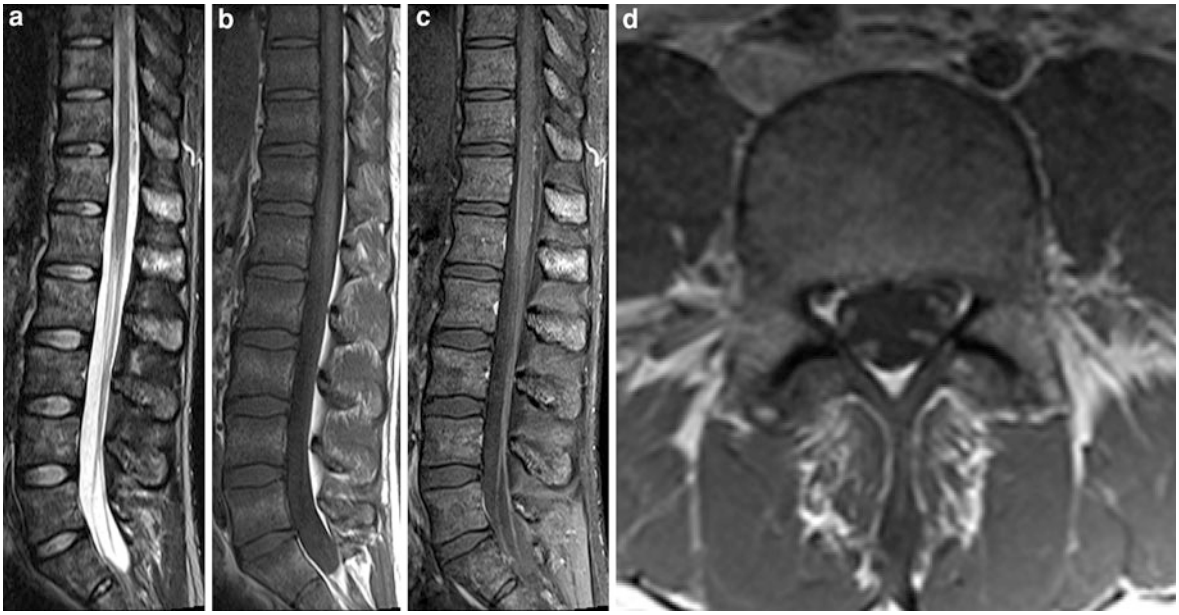

Fig. 8 A 28-year-old man with ALL. Sagittal **a** T2-weighted, **b** T1-weighted, and **c** T1-weighted post-contrast fat-suppressed MRI sequences demonstrate diffusely abnormal, mildly heterogeneous marrow signal. Abnormal T1 hypointense signal is noted within the marrow, particularly near the vertebral body endplates. Abnormal leptomeningeal enhancement is also noted along the conus medullaris and the nerve roots of the cauda equina on post-contrast imaging

view (as often done for spine imaging), with metal artifact, and in other instances where there is magnetic field inhomogeneity.

Intravenous gadolinium-based contrast is not needed routinely, and has shown mixed results in the past. One more recent paper (Zha et al. 2010)

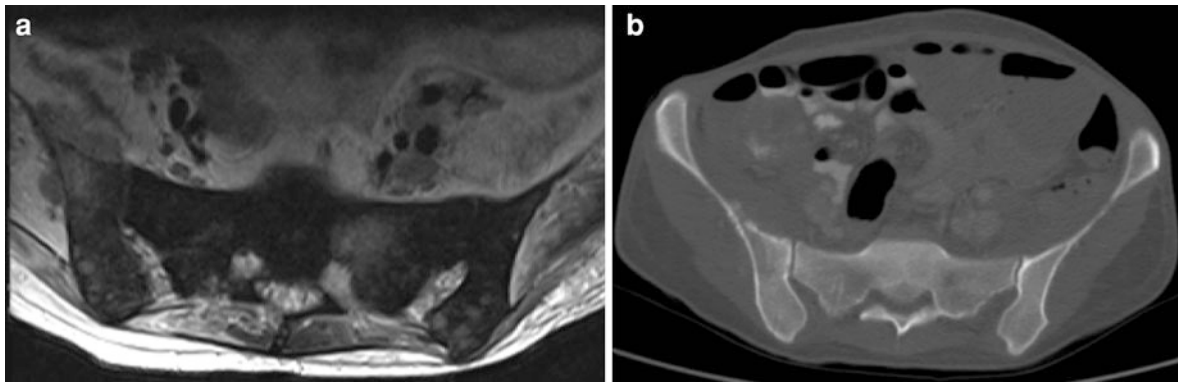

Fig. 9 A 27-year-old woman with CML. **a** Axial T2-weighted MR and **b** axial CT image demonstrate a large lesion centered in the right iliac crest that demonstrates extra-osseous extension and a soft tissue component. Extra-osseous extension is better demonstrated with MR. Mild cortical breakthrough and periosteal reaction is seen on the corresponding CT image

however, indicated a role for dynamic contrast enhancement in detecting diffuse marrow infiltration and in assessment of histological grade. Diffusion weighted imaging and chemical shift imaging also can be used in certain circumstances.

Despite the nonspecific nature of many findings of leukemia, MR imaging offers a superior evaluation of the bone marrow compared to other diagnostic imaging modalities (Fig. 8, 9). Leukemic marrow involvement is typically diffuse and is seen as lower T1 signal than adjacent skeletal muscle with accompanying high T2 signal (Moulopoulos and Dimopoulos 1997). This appearance is nonspecific and similar or identical to other marrow replacement processes chiefly myeloma, lymphoma, and metastatic disease. Focal abnormalities may be present especially in acute myelogenous leukemia (Bohndorf et al. 1990).

MR imaging is currently the modality of choice for the evaluation of the vertebral bone marrow. It is also useful in the assessment of local spinal complications. Vertebral compression fractures are common and may be secondary to leukemic infiltration or osteoporosis as corticosteroid therapy is a mainstay of chemotherapy regimens (Strauss et al. 2001). Several features on MRI can help distinguish benign and malignant causes of vertebral collapse. A benign acute osteoporotic fracture is suggested; when posterior retropulsion of a bone fragment is present, when normal T1 fat signal intensity of the vertebral body is preserved, or when a horizontal fracture plane is seen on T1- and T2-weighted sequences (Jung et al. 2003). A pathologic cause of fracture is suggested when the posterior cortex is convex towards the spinal canal or when an epidural mass is present. Direct soft tissue extension from a pathologically involved vertebra can easily be characterized using standard MRI techniques. These descriptive features can be augmented with findings from in-phase/opposed phase imaging sequences to differentiate benign and malignant conditions, as reported in a study of 49 cases (Erly et al. 2006).

2.5.1 Evaluation of Relapse/Response to Therapy

Because of the high sensitivity of MRI for bone marrow abnormalities, some studies report that MR imaging may provide an option for monitoring response to therapy (Fig. 10, 11) and subsequent surveillance. Quantitative chemical shift MR imaging has shown promise in staging leukemic patients. This technique takes advantage of the differential bone marrow signal contribution from marrow fat and water. In one study, signal derived from water, presumably from pathologic leukemic cells, and associated edema, sequentially decreased in the bone marrow of patients who responded to therapy, whereas a low marrow fat fraction persisted in non-responding patients (Gerard et al. 1992). Another group of researchers showed that changes in bulk T1 signal may be able to predict response to therapy in CLL patients (Lecouvet et al. 1997). One recent study reports that dynamic contrast enhancement characteristics may provide an indication of outcome and survival in patients who are in complete remission from acute myeloid leukemia (Chen et al. 2011).

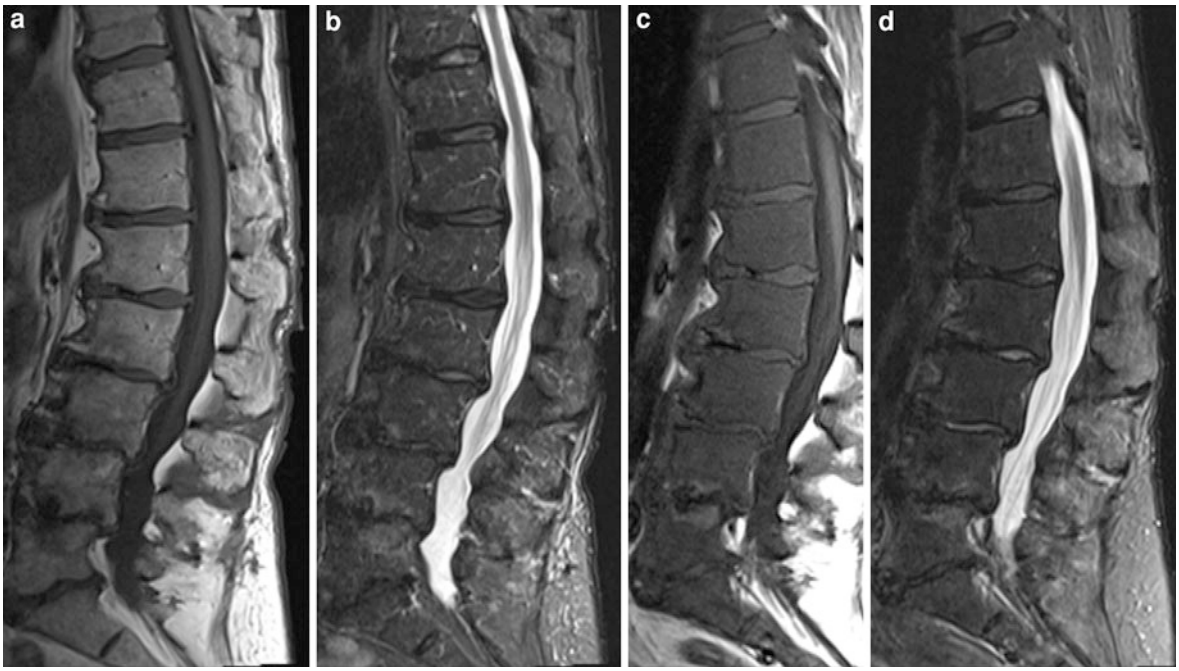

Fig. 10 A 70-year-old woman with AML. **a** Sagittal T1-weighted and **b** STIR MR images of the lumbar spine 2 months after initial diagnosis demonstrate extensive degenerative changes but relatively unremarkable marrow signal. Follow-up imaging performed 10 months later, following chemotherapy and relapse of disease, demonstrates diffusely abnormal **c** T1 and **d** STIR signal abnormality related to relapse of leukemia

2.5.2 Differential Diagnosis

A potential pitfall of MRI evaluation of marrow infiltration can be encountered with imaging of the pediatric population. Because many of the leukemias affect children, signal changes on T1-weighted and T2-weighted sequences as a result of leukemic infiltration sometimes can be difficult to distinguish from the normal signal seen with red marrow reconversion (Fig. 12) or with residual hematopoietic marrow (Moore et al. 1986; Babyn et al. 1998). Similarly, effects of hematopoietic growth factors (specifically G-CSF and GM-CSF) can mimic bone marrow signal changes seen with marrow infiltration processes (Fletcher et al. 1993).

3 Lymphoma

3.1 Epidemiology and Clinical Background

The lymphomas make up a heterogeneous group of disorders arising from lymphoid cell origins. They are broadly categorized as Hodgkin's lymphoma (HL) and other lymphoid cell tumors collectively termed non-Hodgkin's lymphoma (NHL). HL is distinctly characterized histologically by the presence of multinucleated Reed Sternberg cells. NHL is a more diverse group and a more malignant group of lymphoid tumors. Some of its subtypes include diffuse large B-Cell lymphoma, follicular lymphoma, anaplastic large cell lymphoma, lymphoblastic lymphoma, and Burkitt's lymphoma. The incidence of NHL is more than seven times greater than that of HL (Howlader et al. 2010). The recently updated WHO classification attempts to further categorize these diseases based on the cell type of origin (B, T, or NK cells) and by the phenotypic, molecular, and/or cytogenetic characteristics (Swerdlow et al. 2008).

Regardless of type, the hallmark of lymphoma is proliferation of clonal lymphoid cells typically resulting in massive enlargement of lymph nodes and secondary lymphoid tissues. Less commonly, extra nodal tissues may become involved, affecting the gastrointestinal tract, head and neck (Waldeyer's ring), orbits, central nervous system, lung, skin, and sometimes bone. Commonly observed clinical

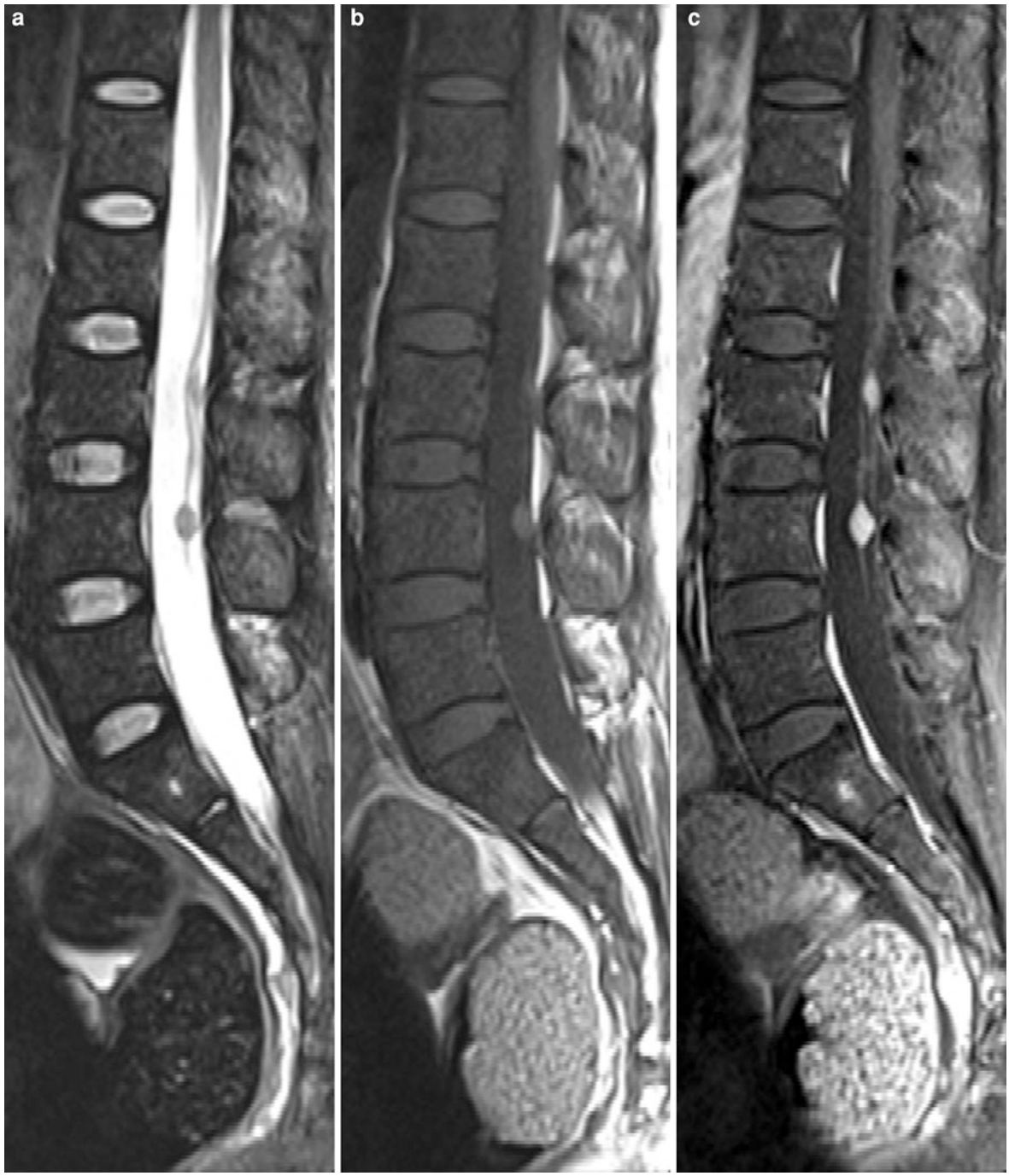

Fig. 11 A 49-year-old male with CML. **a** Sagittal STIR, **b** T1-weighted and **c** T1-weighted post-contrast fat-suppressed MR images of the lumbar spine demonstrate extensive abnormal decreased marrow signal intensity on all sequences and multiple enhancing nodules along the nerve roots of the cauda equina, thought to reflect leukemic deposits. Extra-osseous extension of tumor and multiple soft tissue masses were also seen

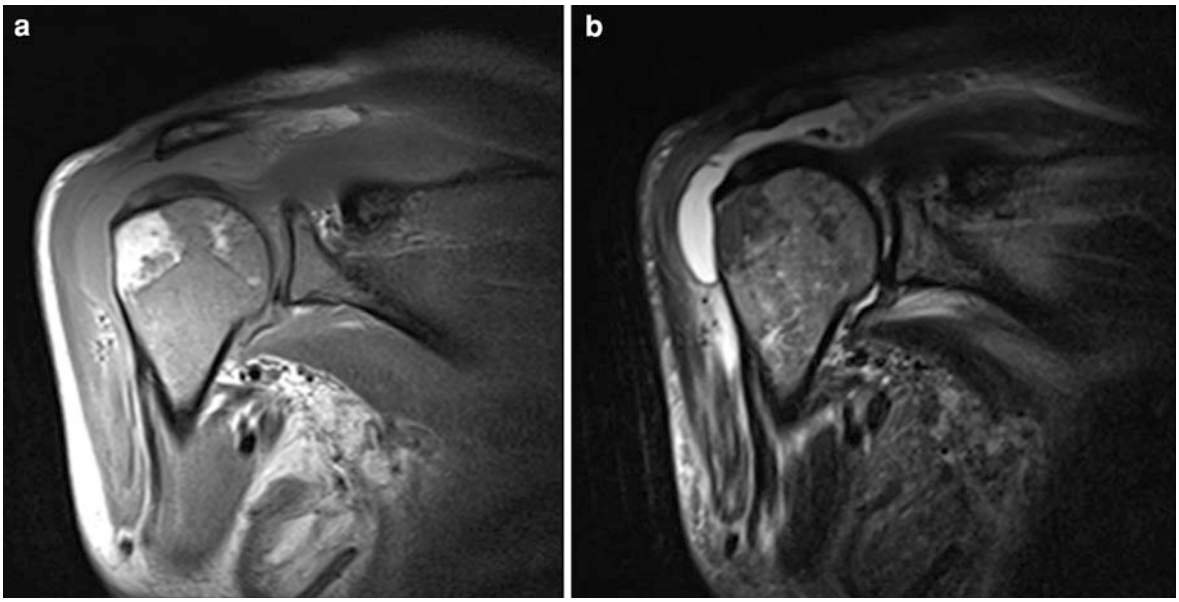

Fig. 12 A 48-year-old woman with AML and pain after a fall. **a** Oblique coronal T1 and matched **b** oblique coronal STIR images of the shoulder show signal change within the proximal humeral metaphysis spreading into the adjacent humeral head epiphysis typical of red marrow reconversion. T1 signal intensity is not lower than adjacent muscle and STIR signal intensity is not bright. Note marked distension of the subacromial bursa due to the acute injury

findings of lymphoma are lymphadenopathy, mediastinal and abdominal masses, and hepatosplenomegaly. Vague constitutional symptoms that include fever, night sweats, and weight loss comprise the B symptoms and carry a worse prognosis than for those patients who do not exhibit these symptoms (Lister et al. 1989). Additional clinical manifestations vary based on the malignancy subtype and the precise distribution of tumor involvement.

The skeleton, most commonly becomes involved secondary to venous hematogenous spread of malignant lymphocytes when seeding and proliferation occurs in the favorable nutrient rich environment of the bone marrow. Direct invasion from adjacent lymphoid tissue is another avenue by which the osseous structures may become involved. The marrow replacement process is more common within the NHL spectrum of tumors and carries a poorer prognosis (Parker et al. 1980).

Alternatively, lymphoid malignancies can arise as a primary process within bone. Solitary primary osseous involvement of a lymphoreticular nature, with or without regional nodal involvement and, importantly, with no evidence of systemic disease for a subsequent 6-month period, defines the distinct entity of primary lymphoma of bone (PLB) (Ostrowski et al. 1986; Baar et al. 1994). The presence of enlarged regional lymph nodes, at the time of diagnosis of the primary osseous lesion, is a point of debate for some investigators. Nevertheless, this disease is one of the rarest of the primary bone malignancies, accounting for approximately 5% of all malignant primary bone tumors. Its peak incidence is in the fourth through sixth decades of life, with slight male predominance. It is rarely seen in patients younger than 10 years of age. These neoplasms are almost always (>90%) a non-Hodgkin's type lymphoma, with diffuse large B-cell lymphoma accounting for most cases. Only about 6% of all PLB cases are due to Hodgkin's lymphoma, as was reported in one of the largest review series (237 cases) published to date (Mulligan et al. 1999).

Certain rheumatologic conditions may be associated with the lymphomas. These include; systemic lupus erythematosus, rheumatoid arthritis, ataxia telangiectasia, relapsing polychondritis, and the nephritic syndrome. Secondary gout and hypertrophic osteoarthropathy also have been shown to be associated with lymphoma.

3.2 Hodgkin's Lymphoma

Hodgkin's lymphoma is a lymphocytic tumor characterized by the presence of multinucleated giant cells that are known as Reed Sternberg cells. It is thought that mutations in tumor suppressor genes do not allow these Reed Sternberg cells to properly undergo apoptosis. Consequently, there is a continual accumulation of these nonfunctioning cells that are not fully differentiated, eventually manifesting as the disease (Skinnider and Mak 2002). HL has bimodal peaks in the adolescent population and also in the sixth decade of life. The skeletal abnormalities seen in HL are more common in adults than in children. Bone involvement may develop by hematogenous tumor dissemination (metastatic disease) or via direct invasion from adjacent lymph nodes. Hematogenous metastatic spread is associated with a poor prognosis (Parker et al. 1980). Direct invasion is most commonly seen in the sternum, ribs, and vertebrae (Appell et al. 1981).

3.2.1 Findings in Radiographs and CT

The radiographic appearance of HL is variable and the osseous lymphomatous lesions can be lytic, sclerotic, or mixed lytic-sclerotic. As with non-Hodgkin's lymphoma, osteolytic lesions are poorly defined but periostitis is more common with HL. In addition, hypertrophic osteoarthropathy also may be present. Local mass effect from enlarging lymph nodes may lead to scalloping of the adjacent bone, if direct invasion has not taken place. Hodgkin's lymphoma, along with osteoblastic metastatic disease, metabolic conditions, and Paget's disease, is the differential diagnosis for an "ivory vertebra."

3.3 Burkitt's Lymphoma

Burkitt's lymphoma is a subtype of NHL which affects children most frequently. There is a strong association with Epstein Barr virus (EBV). In tropical Africa, osseous destruction of the facial bones is characteristic (Burkitt 1958). It most commonly involves the maxilla and to a lesser degree the mandible, often resulting in severe deformity. The femur and tibia, especially around the knee joint, are affected less frequently, but involvement at those sites can be just as debilitating. Soft tissue masses are commonly multiple. They are extensions of intraosseous tumor through the compromised cortex. Soft tissue masses from the facial bones can extend into the mouth or into the paranasal sinuses (Fowles et al. 1983).

3.4 Non-Hodgkin's Lymphoma

Non-Hodgkin's lymphoma is the heterogeneous collection of lymphoid neoplasms that are not classified as Hodgkin's lymphoma. The median age at diagnosis is the sixth decade of life for most subtypes, although Burkitt's lymphoma and lymphoblastic lymphoma (an entity on a spectrum with ALL) tend to occur in younger populations. While the cause of Non-Hodgkin's lymphoma remains uncertain, there is growing evidence that immune-regulation dysfunction, with resulting clonal expansion of dedifferentiated immature cells, contributes to malignant transformation into non-Hodgkin's lymphoma (Guillerman et al. 2011; Cairo et al. 2005). This hypothesis stems partly from observations that there is a well-known increased incidence of lymphoma in patients who are immunosuppressed due to HIV infection. In addition, those patients who have undergone solid organ or bone marrow transplantation and are iatrogenically immunosuppressed are also at risk of developing post transplant lymphoproliferative diseases (Gottschalk et al. 2005). Other studies show a link between Epstein Barr virus and the pathogenesis of lymphoproliferative diseases (Saha and Robertson 2011).

3.4.1 Findings in Radiographs and CT

The prevalence of skeletal findings in disseminated non-Hodgkin's lymphoma is estimated to be 10–20% in adults and 20–30% in children. These changes are typically observed after the initial presentation. The axial skeleton is more commonly involved with multifocal disease in the spine, pelvis, skull, ribs, and facial bones. The typical radiographic appearance is moth-eaten or permeative osteolytic destruction of the skeleton often involving multiple bones. Endosteal scalloping and cortical destruction are associated with adjacent soft tissue extension. Periosteal reaction and osteosclerosis may be present, although these are findings more commonly seen with Hodgkin's lymphoma.

In comparison, primary lymphoma of bone involves a solitary appendicular skeletal site more frequently than an axial skeletal site. The distal femur representing the most commonly involved site (25%) in a review of 237 cases (Mulligan et al. 1999) but other long bones such as the proximal tibia and humerus can be affected as well. The skull, vertebra, and the pelvis are other common sites of involvement. Insidious symptoms like intermittent bone pain and swelling are common clinical presentations. The radiographic appearance of PLB typically shows a solitary permeative or moth-eaten pattern of bone destruction. In long bones, the destruction is usually centered at the metadiaphyseal junction. Highly aggressive patterns of periosteal reaction are common and soft tissue masses are frequently associated. A sequestrum is also a common finding seen in up to 15% of cases (Mulligan and Kransdorf 1993) as are pathologic fractures which may lead to the initial presentation. A multifocal form of PLB is reported, that typically involves the skull, distal femur, proximal tibia, and spine (Melamed et al. 1997).

3.4.2 Prognosis

While PLB is rare, it is important to distinguish it from other disorders in the differential diagnosis (Ewing's sarcoma and neuroblastoma in the young, and myeloma, metastasis, and infection in the older population) as the prognosis and treatment is drastically different compared with the other primary bone malignancies and infectious processes. In one recent report the 5-year survival, for ten patients with PLB, following treatment was 100% (Kirsch et al. 2006).

3.5 Findings in MRI and PET/CT

Bone marrow evaluation MRI techniques for lymphoma are similar to the techniques discussed earlier in the leukemia section. Also, much of the discussion of MRI findings in leukemia also applies to lymphoma. There are subtle differences between these two disease processes, however. Much like leukemia, lymphomatous infiltration of the bone marrow can be focal (Fig. 13) or diffuse (Fig. 14) and is typically low in T1 signal compared to adjacent skeletal muscle (Moulopoulos and Dimopoulos 1997). Interestingly, the corresponding T2 signal, however, can be inhomogeneous with the marrow signal hypointense, isointense, or hyperintense compared to the adjacent skeletal muscle (Stiglbauer et al. 1992; White et al. 1998; Hermann et al. 1997). In one of these studies, histological analysis, of the bone lesions demonstrating low T2 signal, revealed a high content of fibrous tissue, which could explain the signal behavior on MRI (Stiglbauer et al. 1992).

MR imaging offers an obvious advantage for assessing the soft tissue surrounding bone compared to conventional radiography or CT. Lymphomatous infiltration of the musculature can represent primary soft tissue involvement, or more commonly, direct extension from adjacent intraosseous tumor mass or adjacent lymph nodes. The involved muscle typically shows isointense or slightly hyperintense signal intensity compared to normal muscle on T1-weighted sequences and hyperintense signal intensity compared to normal muscle on T2-weighted sequences (Chun et al. 2010). The MR (or less commonly seen CT) triad of extensive intramedullary disease, with intact cortical bone, and surrounding soft tissue mass (Fig. 15) is characteristic of the small, round cell tumor group that includes the lymphomas and Ewing's family of sarcomas (Mulligan et al. 1999). Frequently, when skeletal muscle is the primary site of disease, adjacent fat is infiltrated and multiple muscle compartments, and a long segment of a limb, may be involved (Lee et al. 1997; Chew et al. 1999). The differential diagnosis for skeletal muscle lymphoma includes; myositis, infarction, denervation changes, and sarcoidosis. MRI also can be useful in localizing and analyzing the extent of extraosseous disease (Fig. 16) in lymphoma (Li et al. 1992). Finally, involvement extending across joints is another distinct feature which can be detected more easily using MR imaging (Mulligan et al. 1999).

18F-fluoro-deoxyglucose positron emission tomography (FDG-PET) has largely replaced 67 Ga scintigraphy for functional imaging of lymphoma. Due to the nature of functional imaging, PET uniquely enjoys the ability to distinguish between viable tumor and necrotic or fibrotic tissue in residual masses that are often present following treatment. PET has also been shown to be superior, to CT alone, for assessing normal size lymph nodes and extra nodal disease sites, including the bone marrow (Paes et al. 2010). Currently, FDG-PET provides the best whole body scanning technique for staging, as well

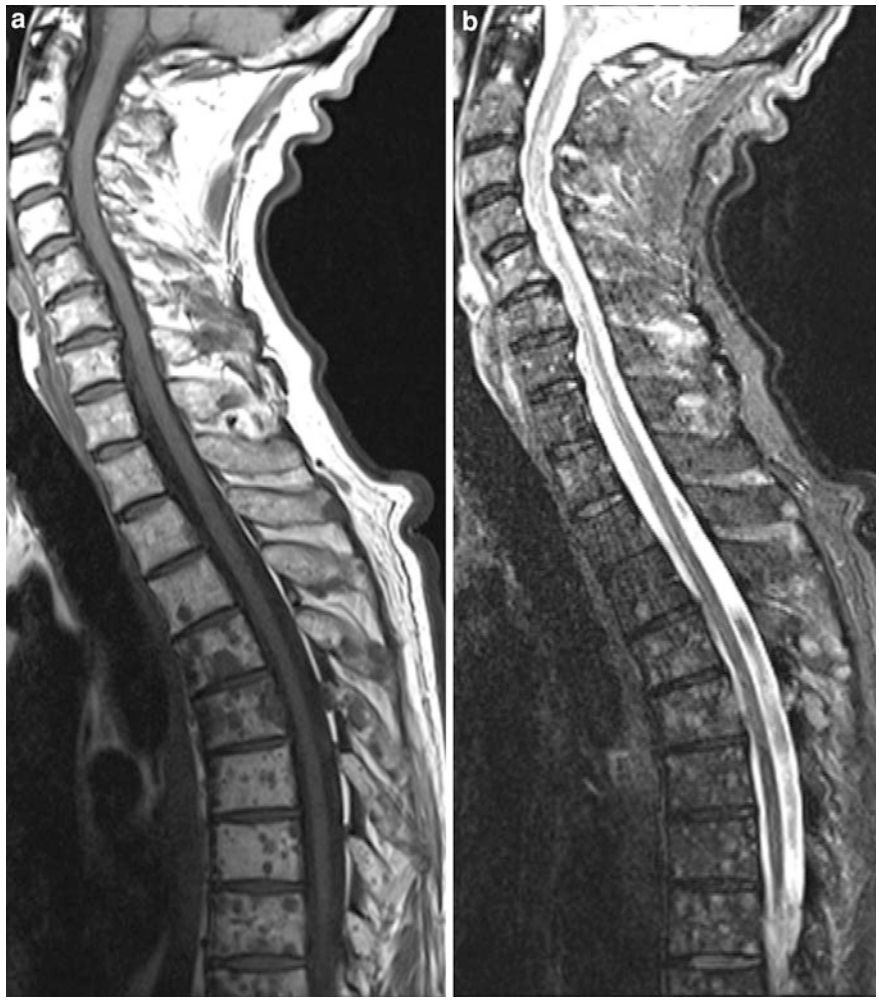

Fig. 13 A 55-year-old man with Non-Hodgkins lymphoma. **a** Sagittal T1-weighted and **b** STIR MR sequences through the cervical and upper thoracic spine demonstrate innumerable scattered focal areas of abnormal marrow signal

as comprehensively and accurately assessing response to therapy, for Hodgkin's lymphoma and diffuse large B-cell type non-Hodgkin's lymphoma (Juweid et al. 2007). A recent meta-analysis showed the pooled sensitivity and specificity of FDG-PET for detection of residual disease, after completion of first-line therapy in HL, was 84 and 90%, respectively. Those parameters for diffuse large B-cell lymphoma were 72 and 100%, respectively (Zijlstra et al. 2006). When combined with CT, the co registered PET/CT images provide the highest sensitivity and specificity for detecting disease (Fig. 17) and correlating site of abnormal hypermetabolic activity to a specific anatomic structure (Hutchings et al. 2006).

4 Chronic Myeloproliferative Disorders

4.1 Epidemiology and Clinical Background

The chronic myeloproliferative disorders include three entities such as; osteomyelofibrosis/sclerosis (OMF/OMS), polycythemia vera, and essential thrombocythemia. These are monoclonal diseases of the myeloid stem cells with an autonomous proliferation of one or more hematopoietic cell lines. In the initial stages all three cell lines can be increased.

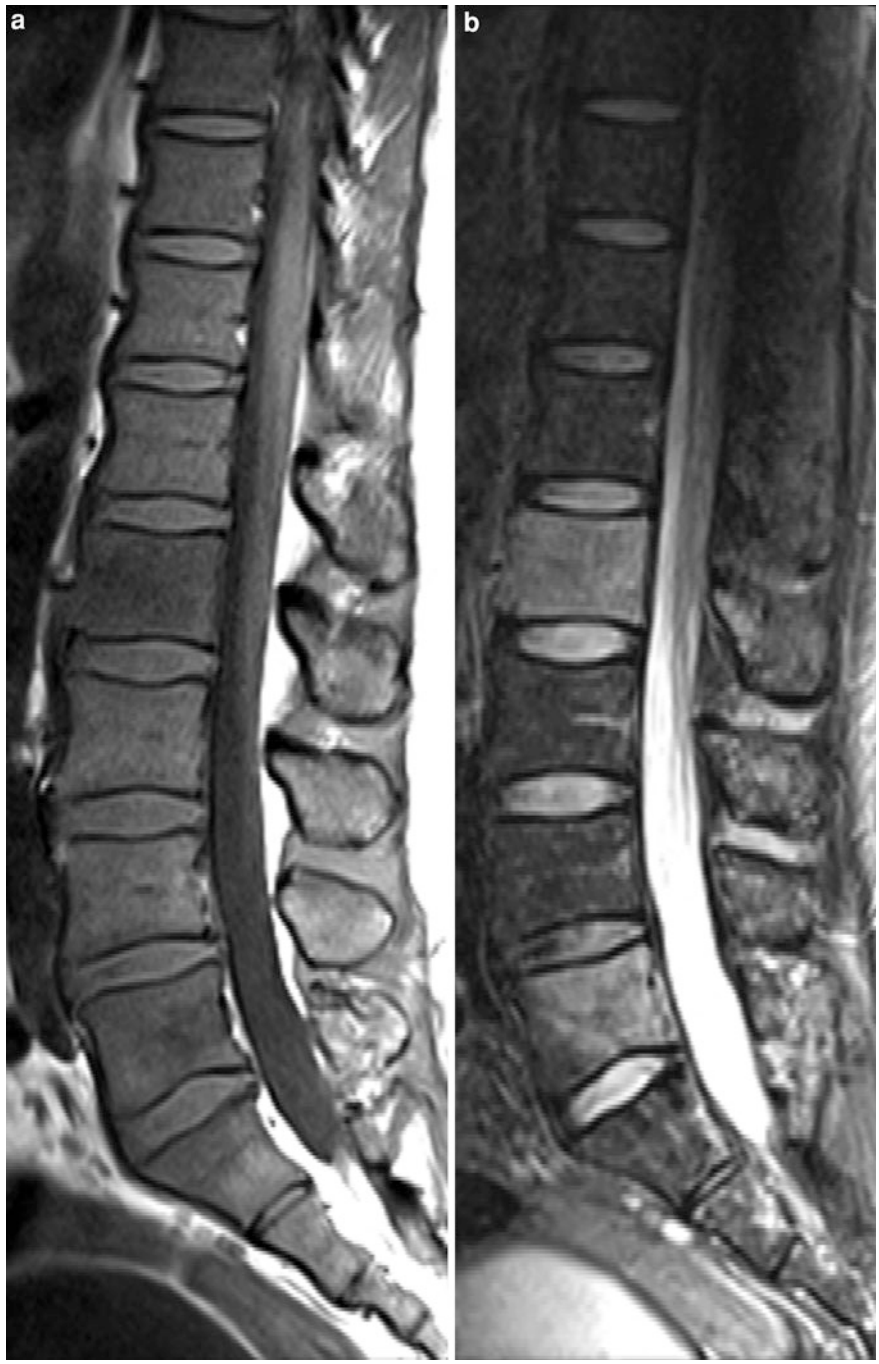

Fig. 14 A 48-year-old male with B cell lymphoma. **a** Sagittal T1-weighted and **b** STIR images of the lumbar spine demonstrate abnormal T1 hypointensity and STIR hyperintensity in the L2 and L5 vertebral bodies. Diagnosis was confirmed by biopsy of the L2 vertebral body

4.2 OMF/OMS

OMF/OMS is a disease of older adults with a peak incidence in the sixth and seventh decades of life. OMF/OMS can be either a primary or a secondary condition, in association with other malignant bone marrow disorders, such as leukemia and lymphoma, which are discussed in other sections of this chapter, or in association with multiple myeloma, which is discussed elsewhere in this book. In the early stages of OMF/OMS, the histological picture is characterized by hyperplastic marrow with an increase of all

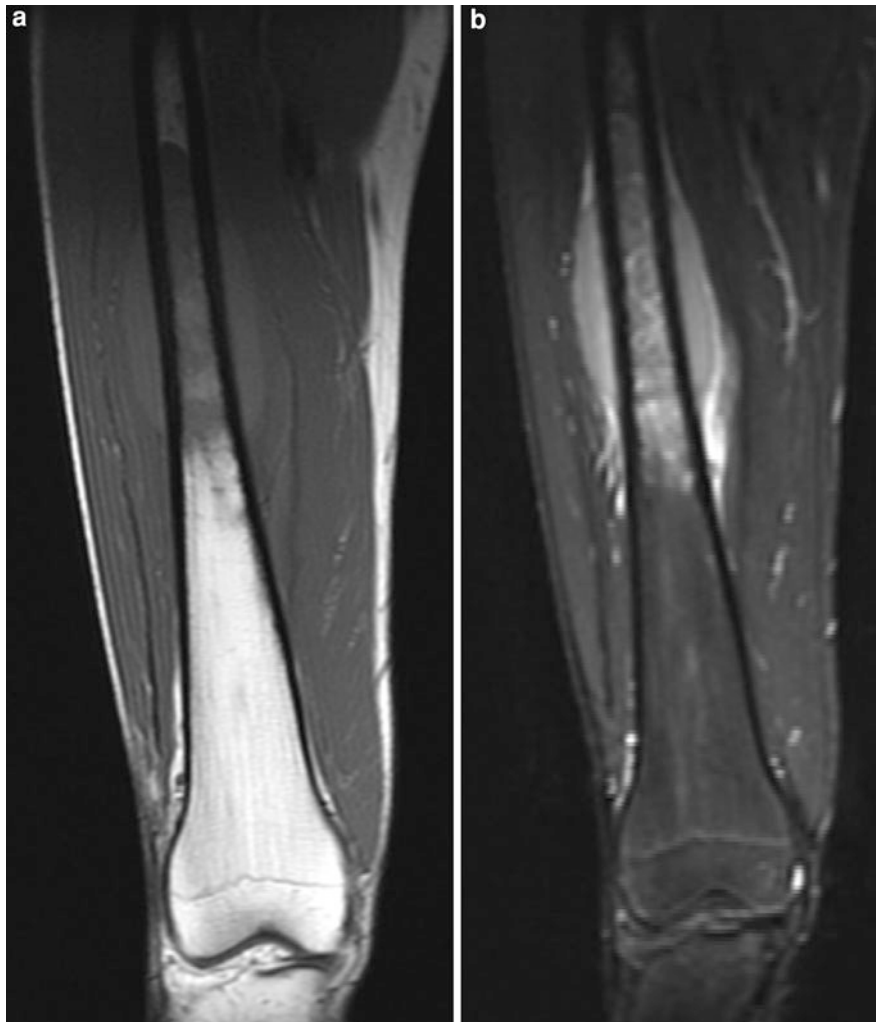

Fig. 15 A 19-year-old male with B cell lymphoma who presented with right hip pain. Coronal **a** T1-weighted and **b** STIR MR images through the proximal femur demonstrate a large infiltrative lesion within the medullary cavity, with an associated extra-osseous soft tissue component but no pronounced cortical destruction

three cell lines, and clusters of large dysplastic megakaryocytes. The normal amount of intramedullary fat is reduced. This picture is followed by subsequent marrow fibrosis, sclerosis and a hypocellular stage. Intramedullary fat is also reduced in this stage. Typically, extramedullary hematopoiesis, with e.g. paravertebral soft tissue masses, and hepatosplenomegaly is found in patients at the most advanced stages of the disease. Clinical symptoms are often nonspecific, but may include fatigue, weakness, and weight loss. Examination of a peripheral blood smear demonstrates a normocytic anemia.

4.2.1 Findings in Radiographs and CT

A homogeneous osteosclerosis of the skeleton, especially the axial skeleton, can be found in 30–70% of patients (Fig. 18). The osteosclerotic areas usually involve those bones with active red marrow. In the long bones, endosteal sclerosis can lead to cortical thickening. In the spine, the sclerotic changes are typically homogeneous but can be limited to cortical accentuation of only the endplates, resulting in the so-called "sandwich vertebra" appearance. Diffuse osteoporosis is the second in frequency radiographic finding in myelofibrosis, while the coexistence of osteosclerosis and osteoporosis also may occur. Osteolytic lesions are uncommon and when present often mixed with osteosclerosis. In the literature small lytic areas within the cortex of the bones also have been described. These are attributed to excess development of connective tissue that, by compression, produces atrophy and destruction of the osseous tissue (Meszaros and Sinsson 1961). A case report of a patient with myelofibrosis in the context of

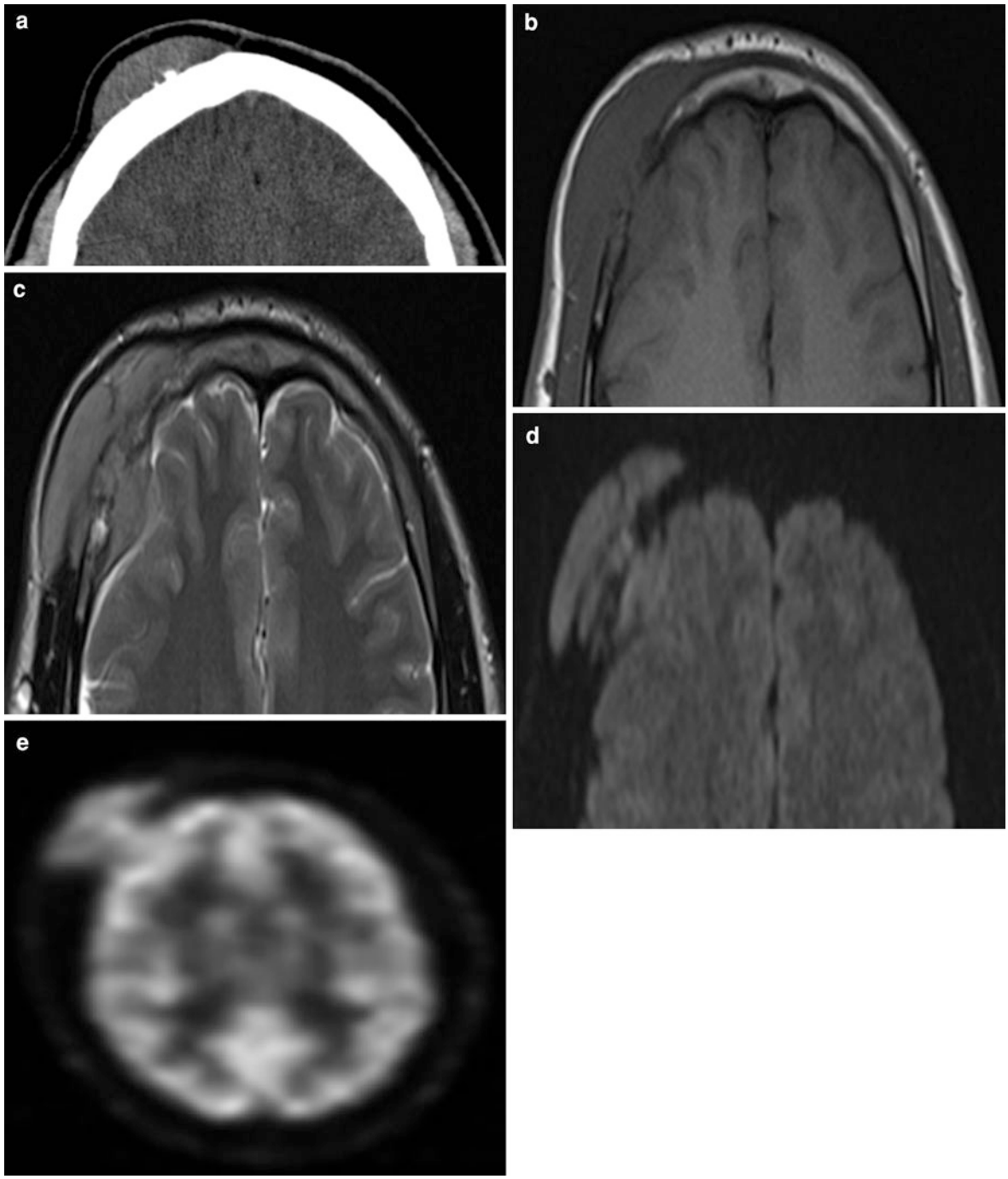

Fig. 16 A 17-year-old male with history of B cell lymphoma, testicular primary, who presents 10 years after initial diagnosis with right frontal mass. **a** Non-contrast CT demonstrates a soft tissue mass along the right frontal scalp with associated periosteal reaction that suggests osseous involvement. On MRI, the bone lesion is **b** T1 hypointense, **c** T2 isointense and shows **d** restricted diffusion. There is extension into the intracranial compartment as well as the overlying soft tissues. **e** FDG-PET image demonstrates corresponding hypermetabolism. This mass was biopsy-proven disease recurrence

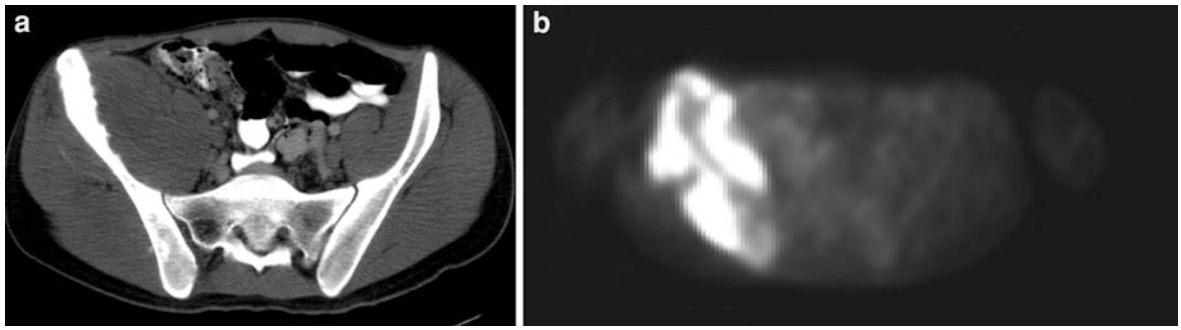

Fig. 17 **a** CT of the pelvis demonstrates a large soft tissue mass on either side of the right iliac wing, with associated periosteal reaction but no pronounced cortical destruction. **b** FDG-PET image demonstrates marked hypermetabolism corresponding to the right iliac lesion, which is centered in the bone. Additional sites were also involved by disease proven to represent B cell lymphoma

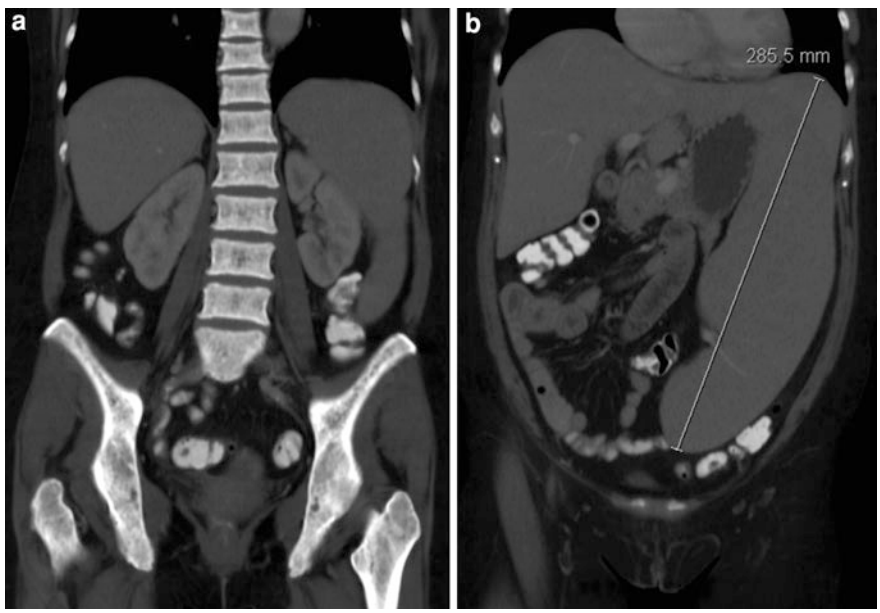

Fig. 18 A 57-year-old woman with myelofibrosis. Coronal reformatted CT images show **a** diffuse osteosclerosis and **b** grossly enlarged spleen

polycthemia vera described multiple large lytic areas of bone destruction (Sideris et al. 2006). A polyarthritis simulating rheumatoid arthritis also has been described. Hemarthrosis can be the initial manifestation of the disease. Impaired platelet production and function, due to the marrow fibrosis, presumably contributes to bleeding disorders. Gout occurs in 5–20% of patients, as an additional complication, and a gouty arthritis attack, may predate the diagnosis of OMF/OMS. The differential diagnosis includes; osteopetrosis, diffuse osteoblastic metastatic disease, mastocytosis, and renal osteodystrophy (Baur-Melnyk and Reiser 2008).

4.2.2 Findings in MRI

MRI findings include diffuse marrow changes (Fig. 19) that are dependent on the stage of disease (Guermazi et al. 1999). Signal intensity typically is markedly reduced on T1-weighted and T2-weighted sequences due to the increase in marrow cells and reduction in fat cells in the early stages, or due to extensive marrow fibrosis in the late stages. Small residual areas of fatty marrow can be interspersed in the background of the abnormal marrow. If gadolinium-based intravenous contrast agents are administered, marked enhancement in the bone marrow will be seen in the majority of patients due to; increase in the number of capillaries,

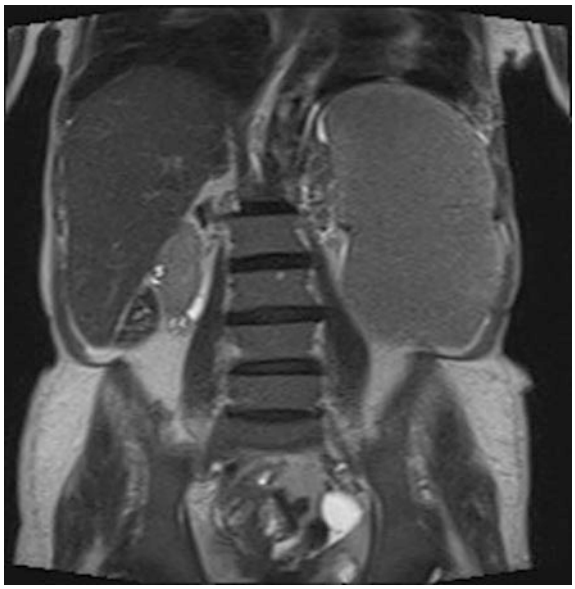

Fig. 19 An 86-year-old woman with myelofibrosis. Coronal MR image **a** shows splenomegaly with homogeneous signal intensity. Note diffuse homogeneous signal intensity of the visualized vertebral bodies

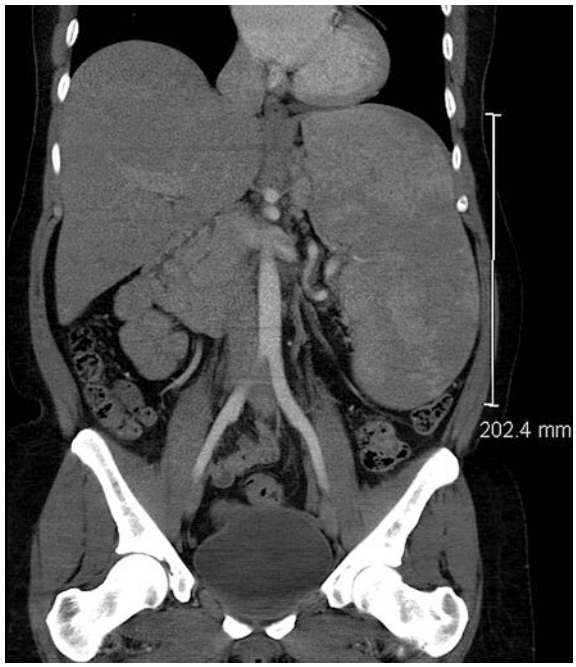

Fig. 20 A 46-year-old woman with polycythemia vera who had left upper quadrant pain after a motor vehicle accident. Coronal reformatted CT image shows enlarged heterogeneous spleen but no evidence of acute injury

widened sinusoids, and increased permeability of the vessels (Amano et al. 1997). Areas of bone marrow ischemia can cause non enhancing regions to occur (Vande Berg et al. 1993).

4.2.3 Differential Diagnosis

The differential diagnosis for OMF/OMS includes; myeloma and leukemia in the early stages of OMF/OMS, and hemosiderosis and diffuse osteoblastic metastatic disease in the late stages of OMF/OMS.

4.3 Polycythemia Vera (PV)

4.3.1 Polycythemia vera (PV): Epidemiology and Clinical Background

PV is one of the less common malignant myeloproliferative disorders with a yearly prevalence of about 0.7–1/100.000/year. The exact cause is not known, but there is recent evidence for a genetic abnormality identified as JAK2 (James et al. 2005; Mustjoki et al. 2009). PV's most prominent feature is increased red blood cell mass due to a clonal hematopoietic stem cell abnormality. Myelofibrosis might occur together with PV, rarely in the early phase but more often in the late stage of disease. There is also an increase in white blood cells and platelets. Adults in the fifth to seventh decades of life make up the majority of cases. Men and women are equally affected. Symptoms and signs are related to the hematopoietic cell line proliferations and include; thrombosis (that may result in Budd Chiari syndrome and/or pulmonary embolism) bleeding, and splenomegaly. The diagnosis is based on examination of the peripheral blood smear and bone marrow aspirate, as well as quantitative assessment of the total red blood cell volume (Streiff et al. 2002).

4.3.2 Imaging Findings

Extensive imaging of the patient usually is not needed. Confirmation of suspected splenomegaly may be done with ultrasound or CT (Fig. 20). Radiographs often show no abnormality. Diffuse osteopenia has been described in the bones that harbor active marrow. Secondary myelofibrosis may occur in the disease process. MRI and PET/CT findings are similar to other myeloproliferative disorders as discussed previously in this chapter (van Ufford et al. 2011; Basu et al. 2007).

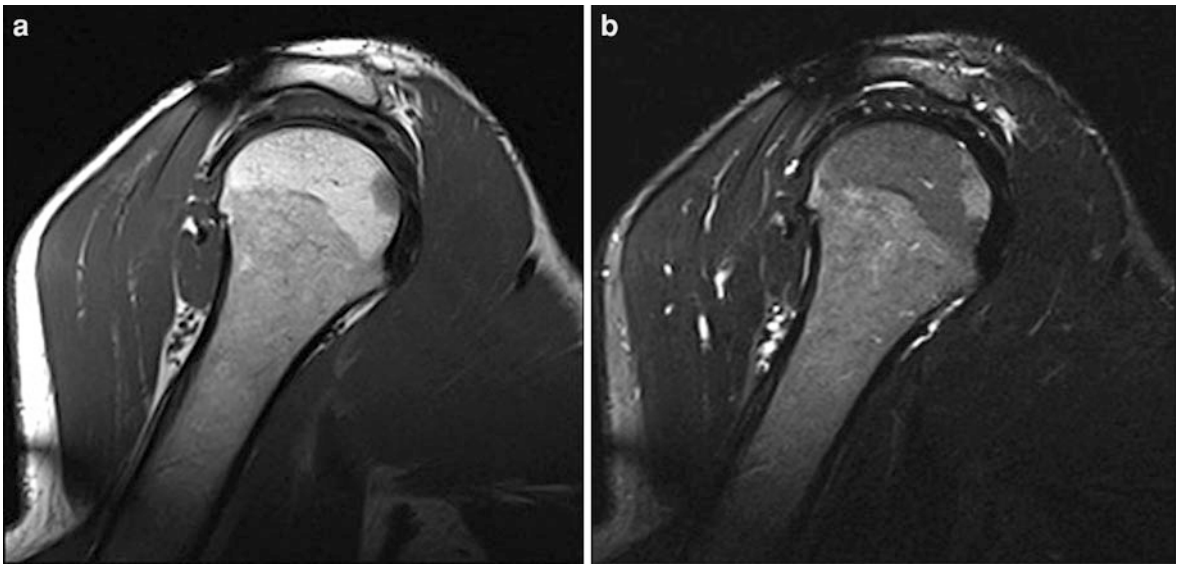

Fig. 21 A 40-year-old man with polycythemia vera who had shoulder pain. Matched oblique sagittal MR images **a** T1-weighted and **b** STIR show diffuse homogeneous marrow throughout the proximal humeral shaft and one small focal area of marrow reconversion within the epiphysis

In a study by Kaplan et al. in 1992 MRI was performed in 14 patients with biopsy-proved polycythemia vera ($n = 4$) or myelofibrosis ($n = 10$) in order to determine whether MR imaging findings can be correlated with the clinicopathologic diagnosis and established clinical parameters of severity [serum lactate dehydrogenase (LDH) and cholesterol levels] and chronicity (spleen size). Evaluation of marrow in the proximal femurs showed that patients could be categorized into three distinct groups based on anatomic patterns of normal fatty and abnormal low-signal-intensity (non-fatty) marrow in the femoral capital epiphysis and greater trochanter. The apophyses (greater trochanter) were more resitstant to reconversion than the epiphyses (femoral head). Patients with involvement in both the epiphysis and greater trochanter had significantly higher clinical activity of disease than patients with fatty marrow in at least the greater trochanter. Splenic volume was significantly greater in the myelofibrosis group than in the polycythemia vera group (Kaplan et al.1992).

Patients with PV typically show diffuse abnormality in active marrow sites on MRI (Fig. 21) or PET/CT. In addition to PET agents, other scintigraphic agents including monoclonal antigranulocyte antibodies labeled with 99m Tc may be useful (Agool et al. 2011).

4.3.3 Therapy/Prognosis

Treatment, in the past, consisted simply of repeated phlebotomy as needed. The newest treatment available, is drug therapy with JAK1/JAK2 inhibitor class agents. Without treatment, median survival is only on the order of 2–3 years. With treatment, survival of 10–20 years can be achieved. Rarely, there can be complications related to the development of granulocytic sarcoma or AML (Abdulkarim 2009).

4.3.4 Differential Diagnosis

The differential diagnosis includes entities such as; essential thrombocytosis, CML, agnogenic myeloid metaplasia, and conditions that result in secondary polycythemia.

4.4 Essential Thrombocythemia (ET): Epidemiology and Clinical Background

Like polycythemia vera, ET is another of the chronic myeloproliferative disorders. Its distinct feature is overproduction of platelets (>600,000/μL) due to abnormal sustained megakaryocyte proliferation (Kwon et al. 2009). The cause of this condition is not

yet known, although a JAK2 V617F mutation is reported in up to 50% of patients (Spanoudakis et al. 2008). Approximately 6000 new cases are reported each year in the United States (Mesa et al. 1999). Two age groups are affected; young women comprise one group, and older adults (male = female) in the other group. Symptoms and signs are related to the platelet overproduction, with thrombosis and hemorrhage most common. Splenomegaly is present in 40–50% of patients and hepatomegaly is seen in 20%. The diagnosis is made after examination of the peripheral blood smear and bone marrow aspirate.

4.4.1 Imaging Findings

Extensive imaging of the patient usually is not needed. Confirmation of suspected organomegaly may be done with ultrasound or CT. MRI and PET/CT findings are similar to other myeloproliferative disorders as discussed elsewhere in this chapter.

4.4.2 Treatment/Prognosis

Treatment with low dose aspirin is directed to avoid thrombotic complications. The primary disease process in the marrow is treated with agents such as hydroxyurea and interferon (Harrison et al. 2005). Prognosis is good, with 10-year survival rates in 60–80% of cases. Transformation to other processes such as AML, PV, or agnogenic myeloid metaplasia can occur but is unusual (Cervantes et al. 1991).

4.4.3 Differential Diagnosis

The differential diagnosis includes many of the other chronic myeloproliferative disorders including agnogenic myeloid metaplasia, CML, PV, myelodysplastic syndrome, and other conditions that might cause secondary thrombocytosis. Molecular studies such as polymerase chain reaction (PCR) or Southern (genomic) blotting may be used as sensitive means of excluding chronic myelogenous leukemia.

References

Abdulkarim K, Girodon F, Johansson P et al (2009) AML transformation in 56 patients with Ph-MPD in two well defined populations. Eur J Haematol 82:106–111

Agool A, Glaudemans AW, Boersma HH et al (2011) Radionuclide imaging of bone marrow disorders. Eur J Nucl Med Mol Imaging 38:166–178

Amano Y, Onda M, Amano M, Kumazaki T (1997) Magnetic resonance imaging of myelofibrosis. Clin Imaging 21: 264–268

Appell RG, Oppermann HC, Brandeis WE (1981) Skeletal lesions in Hodgkin's disease. Review of literature and case reports. Pediatr Radiol 11:61–65

Appell RG, Bühler T, Willich E (1985) Absence of prognostic significance of skeletal involvement in acute lymphocytic leukemia and non-Hodgkin lymphoma in children. Pediatr Radiol 15:245–248

Baar J, Burkes R, Bell R et al (1994) Primary non-Hodgkin's lymphoma of bone. A clinicopathologic study. Cancer 73:1194–1199

Babyn P, Ranson M, McCarville M (1998) Normal bone marrow: signal characteristics and fatty conversion. Magn Reson Imaging Clin North Am 6:473–495

Basu S, Houseni M, Bural G et al (2007) Magnetic resonance imaging based bone marrow segmentation for quantitative calculation of pure red marrow metabolism using 2-deoxy-2-[F-18]fluoro-D-glucose-positron emission tomography: a novel application with significant implications for combined structure-function approach. Mol Imaging Biol 9:361–365

Baur-Melnyk A, Reiser M (2008) Oncohaematologic disorders affecting the skeleton in the elderly. Radiol Clin North Am 46:785–798

Bennett JM, Catovsky D, Daniel MT et al (1976) Proposals for the classification of the acute leukaemias. French–American–British (FAB) co-operative group. Br J Haematol 33:451–458

Bennett JM, Catovsky D, Daniel MT et al (1989) Proposals for the classification of chronic (mature) B and T lymphoid leukaemias. French–American–British (FAB) cooperative group. J Clin Pathol 42:567–584

Benz G, Brandeis WE, Willich E (1976) Radiological aspects of leukaemia in childhood: an analysis of 89 children. Pediatr Radiol 4:201–213

Bernard EJ, Nicholls WD, Howman-Giles RB et al (1998) Patterns of abnormality on bone scans in acute childhood leukemia. J Nucl Med 39:1983–1986

Bohndorf K, Benz-Bohm G, Gross-Fengels W et al (1990) MRI of the knee region in leukemic children. Part I. Initial pattern in patients with untreated disease. Pediatr Radiol 20:179–183

Burkitt D (1958) A sarcoma involving the jaws in African children. Br J Surg 46:218–223

Cairo MS, Raetz E, Lim MS et al (2005) Childhood and adolescent non-Hodgkin lymphoma: new insights in biology and critical challenges for the future. Pediatr Blood Cancer 45:753–769

Cervantes F, Tassies D, Salgado C et al (1991) Acute transformation in nonleukemic chronic myeloproliferative disorders: actuarial probability and main characteristics in a series of 218 patients. Acta Haematol 85:124–127

Chen BB, Hsu CY, Yu CW (2011) Dynamic contrast-enhanced MR imaging measurement of vertebral bone marrow perfusion may be indicator of outcome of acute myeloid leukemia patients in remission. Radiology 258:821–831

Chew FS, Schellingerhout D, Keel SB (1999) Primary lymphoma of skeletal muscle. Am J Roentgenol 172:1370

Chun CW, Jee WH, Park HJ et al (2010) MRI features of skeletal muscle lymphoma. Am J Roentgenol 195:1355–1360

Cohn SL, Morgan ER, Mallette LE (1987) The spectrum of metabolic bone disease in lymphoblastic leukemia. Cancer 59:346–350

Costello PB, Brecher ML, Starr JI et al (1983) A prospective analysis of the frequency, course, and possible prognostic significance of the joint manifestations of childhood leukemia. J Rheumatol 10:753–757

Erly W, Oh E, Outwater E (2006) The utility of in-phase/opposed-phase imaging in differentiating malignancy from acute benign compression fractures of the spine. Am J Neuroradiol 27:1183–1188

Evans TI, Nercessian BM, Sanders KM (1994) Leukemic arthritis. Semin Arthritis Rheum 24:48–56

Fletcher BD, Wall JE, Hanna SL (1993) Effect of hematopoietic growth factors on MR images of bone marrow in children undergoing chemotherapy. Radiology 189: 745–751

Fowles JV, Olweny CL, Katongole-Mbidde E et al (1983) Burkitt's lymphoma in the appendicular skeleton. J Bone Joint Surg Br 65:464–471

Gambacorti-Passerini C, Antolini L, Mahon FX et al (2011) Multicenter independent assessment of outcomes in chronic myeloid leukemia patients treated with imatinib. J Natl Cancer Inst 103:553–561

Gerard EL, Ferry JA, Amrein PC et al (1992) Compositional changes in vertebral bone marrow during treatment for acute leukemia: assessment with quantitative chemical shift imaging. Radiology 183:39–46

Glatt W, Weinstein A (1969) Acropachy in lymphatic leukemia. Radiology 92:125–126

Gottschalk S, Rooney CM, Heslop HE (2005) Post-transplant lymphoproliferative disorders. Annu Rev Med 56:29–44

Greaves M (2005) In utero origins of childhood leukaemia. Early Hum Dev 81:123–129

Guermazi A, de Kerviler E, Cazals-Hatem D, Zagdanski AM, Frija J (1999) Imaging findings in patients with myelofibrosis. Eur Radiol 9:1366–1375

Guillerman RP, Voss SD, Parker BR (2011) Leukemia and lymphoma. Radiol Clin North Am 49:767–797

Hann IM, Gupta S, Palmer MK et al (1979) The prognostic significance of radiological and symptomatic bone involvement in childhood acute lymphoblastic leukaemia. Med Pediatr Oncol 6:51–55

Harrison CN, Campbell PJ, Buck G et al (2005) Hydroxyurea compared with anagrelide in high-risk essential thrombocythemia. N Engl J Med 353:33–45

Hehlmann R, Hochhaus A, Baccarani M et al (2007) Chronic myeloid leukaemia. Lancet 370:342–350

Heinrich SD, Gallagher D, Warrior R et al (1994) The prognostic significance of the skeletal manifestations of acute lymphoblastic leukemia of childhood. J Pediatr Orthop 14:105–111

Hermann G, Klein MJ, Abdelwahab IF et al (1997) MRI appearance of primary non-Hodgkin's lymphoma of bone. Skeletal Radiol 26:629–632

Herold CJ, Wittich GR, Schwarzinger I et al (1998) Skeletal involvement in hairy cell leukemia. Skeletal Radiol 17:171–175

Higashida T, Kawasaki T, Sakata K et al (2007) Acute lymphocytic leukemia recurring in the spinal epidural space. Neurol Med Chir 47:375–378

Howlader N, Noone AM, Krapcho M et al. (2008) SEER Cancer Statistics Review, 1975–2008, National Cancer Institute. Bethesda, MD http://seer.cancer.gov/csr/1975_2008/, based on November 2010 SEER data submission, posted to the SEER web site, 2011

Hutchings M, Loft A, Hansen M et al (2006) Position emission tomography with or without computed tomography in the primary staging of Hodgkin's lymphoma. Haematologica 91:482–489

James C, Ugo V, Le Couedic JP et al (2005) A unique clonal JAK2 mutation leading to constitutive signalling causes polycythaemia vera. Nature 434:1144–1148

Jung HS, Jee WH, McCauley TR et al (2003) Discrimination of metastatic from acute osteoporotic compression spinal fractures with MR imaging. Radiographics 23:179–187

Juweid ME, Stroobants S, Hoekstra OS et al (2007) Use of positron emission tomography for response assessment of lymphoma: consensus of the Imaging Subcommittee of International Harmonization Project in Lymphoma. J Clin Oncol 25:571–578

Kaplan KR, Mitchell DG, Steiner RM et al (1992) Polycythemia vera and myelofibrosis: correlation of MR Imaging, clinical and laboratory findings. Radiology 183: 329–334

Kirsch J, Ilaslan H, Bauer TW et al (2006) The incidence of imaging findings, and the distribution of skeletal lymphoma in a consecutive patient population seen over 5 years. Skeletal Radiol 35:590–594

Kwon M, Osorio S, Muñoz C et al (2009) Essential thrombocythemia in patients with platelet counts below 600 × 10(9)/L: applicability of the 2008 World Health Organization diagnostic criteria revision proposal. Am J Hematol 84:452–454

Lecouvet FE, Vande Berg BC, Michaux L et al (1997) Early chronic lymphocytic leukemia: prognostic value of quantitative bone marrow MR imaging findings and correlation with hematologic variables. Radiology 204:813–818

Lee VS, Martinez S, Coleman RE (1997) Primary muscle lymphoma: clinical and imaging findings. Radiology 203:237–244

Li MH, Holtås S, Larsson EM (1992) MR imaging of spinal lymphoma. Acta Radiol 33:338–342

Lister TA, Crowther D, Sutcliffe SB et al (1989) Report of a committee convened to discuss the evaluation and staging of patients with Hodgkin's disease: Cotswolds meeting. J ClinOncol 7:1630–1636

Manson D, Martin RF, Cockshott WP (1989) Metaphyseal impaction fractures in acute lymphoblastic leukemia. Skeletal Radiol 17:561–564

Masera G, Carnelli V, Ferrari M et al (1977) Prognostic significance of radiological bone involvement in childhood acute lymphoblastic leukaemia. Arch Dis Child 52:530–533

Melamed JW, Martinez S, Hoffman CJ (1997) Imaging of primary multifocal osseous lymphoma. Skeletal Radiol 26:35–41

Melhem RE, Saber TJ (1980) Erosion of the medial cortex of the proximal humerus. A sign of leukemia on the chest radiograph. Radiology 137:77–79

Mesa RA, Silverstein MN, Jacobsen SJ et al (1999) Population-based incidence and survival figures in essential thrombocythemia and agnogenic myeloid metaplasia: an Olmsted County Study, 1976–1995. Am J Hematol 61:10–15

Meszaros WT, Sinsson M (1961) Myelofibrosis. Radiology 11:958–967

Moore SG, Gooding CA, Brasch RC et al (1986) Bone marrow in children with acute lymphocytic leukemia: MR relaxation times. Radiology 160:237–240

Moulopoulos LA, Dimopoulos MA (1997) Magnetic resonance imaging of the bone marrow in hematologic malignancies. Blood 90:2127–2147

Mulligan M, Kransdorf M (1993) Sequestra in primary lymphoma of bone: prevalence and radiologic features. Am J Roentgenol 160:1245–1248

Mulligan ME, McRae GA, Murphey MD (1999) Imaging features of primary lymphoma of bone. Am J Roentgenol 173:1691–1697

Mustjoki S, Borze I, Lasho TL et al (2009) JAK2V617F mutation and spontaneous megakaryocytic or erythroid colony formation in patients with essential thrombocythaemia (ET) or polycythaemia vera (PV). Leuk Res 33:54–59

Nixon GW, Gwinn JL (1973) The roentgen manifestations of leukemia in infancy. Radiology 107:603–609

Nowell PC, Hungerford DA (1960) Chromosome studies on normal and leukemic human leukocytes. J Natl Cancer Inst 25:85–109

O'Hara AE (1967) Roentgenographic osseous manifestations of the anemias and the leukemias. Clin Orthop Relat Res 52:63–82

Ostrowski ML, Unni KK, Banks PM et al (1986) Malignant lymphoma of bone. Cancer 58:2646–2655

Paes FM, Kalkanis DG, Sideras PA et al (2010) FDG PET/CT of extranodal involvement in non-Hodgkin lymphoma and Hodgkin disease. Radiographics 30:269–291

Parker BR, Marglin S, Castellino RA (1980) Skeletal manifestations of leukemia, Hodgkin disease, and non-Hodgkin lymphoma. Semin Roentgenol 15:302–315

Pui CH, Robison LL, Look AT (2008) Acute lymphoblastic leukaemia. Lancet 371:1030–1043

Resnick D, Haghighi P (2002) Lymphoproliferative and Myeloproliferative disorders. In: Resnick D (ed) Diagnosis of bone and joint disorders, 4th edn. Saunders, Philadelphia

Révész T, Kardos G, Kajtár P et al (1985) The prognostic significance of bone and joint manifestations in childhood leukemia. J Rheumatol 12:647–648

Ribeiro RC, Pui CH, Schell MJ (1988) Vertebral compression fracture as a presenting feature of acute lymphoblastic leukemia in children. Cancer 61:589–592

Rosenfield NS, McIntosh S (1977) Prospective analysis of bone changes in treated childhood leukemia. Radiology 123:413–415

Saha A, Robertson ES (2011) Epstein-Barr virus-associated B-cell lymphomas: pathogenesis and clinical outcomes. Clin Cancer Res 17:3056–3063

Schrek R, Donnelly WJ (1966) "Hairy" cells in blood in lymphoreticular neoplastic disease and "flagellated" cells of normal lymph nodes. Blood 27:199–211

Seok J, Park J, Kim S et al (2010) Granulocytic sarcoma of the spine: MRI and clinical review. Am J Roentgenol 194:485–489

Sideris P et al (2006) Unusual radiological findings in a case of myelofibrosis secondary to polycythemia vera. Ann Hematol 85:555–556

Sinigaglia R, Gigante C, Bisinella G et al (2008) Musculoskeletal manifestations in pediatric acute leukemia. J Pediatr Orthop 28:20–28

Skinnider BF, Mak TW (2002) The role of cytokines in classical Hodgkin lymphoma. Blood 99:4283–4297

Smith MA, Ries LA, Gurney J, Get al (1999) Cancer incidence and survival among children and adolescents. United States SEER Program 1975–1995. National Cancer Institute, Leukemia, Bethesda

Spanoudakis E, Margaritis D, Kotsianidis I et al (2008) Long-term bone marrow cultures (LTBMC) from essential thrombocythemia (ET) patients with or without JAK2617 V>F mutation. Leuk Res 32:1593–1596

Spilberg I, Meyer GJ (1972) The arthritis of leukemia. Arthritis Rheum 15:630–635

Stiglbauer R, Augustin I, Kramer J et al (1992) MRI in the diagnosis of primary lymphoma of bone: correlation with histopathology. J Comput Assist Tomogr 16:248–253

Strauss AJ, Su JT, Dalton VM (2001) Bony morbidity in children treated for acute lymphoblastic leukemia. J Clin Oncol 19:3066–3072

Streiff MB, Smith B, Spivak JL (2002) The diagnosis and management of polycythemia vera in the era since the Polycythemia Vera Study Group: a survey of American Society of Hematology members' practice patterns. Blood 99:1144–1149

Swerdlow SH, Campo E, Harris NL et al (2008) WHO classification of tumours of haematopoieticand lymphoid tissues, 4th edn. International Agency for Research on Cancer, Lyon

Van Slyck, EJ (1972) The bony changes in malignant hematologic disease. Orthop Clin North Am 3:733–734

van Ufford HM, Kwee TC, Beek FJ et al (2011) Newly diagnosed lymphoma: initial results with whole-body T1-weighted, STIR, and diffusion-weighted MRI compared with 18F-FDG PET/CT. AJR Am J Roentgenol 196:662–669

Vande Berg B, Malghem J, Labaisse A, Michaux L, Maldague B (1993) Apparent focal bone marrow ischemia in patients with marrow disorders: MR studies. J Comput Assist Tomogr 17:792–797

White LM, Schweitzer ME, Khalili K et al (1998) MR imaging of primary lymphoma of bone: variability of T2-weighted signal intensity. AJR Am J Roentgenol 170:1243–1247

Wilson JKV (1959) The bone lesions of childhood leukemia. Radiology 72:672–681

Woodard WL 3rd, Kneisl JS, Lipford EH (1999) Isolated granulocytic sarcoma of the humerus. Orthopedics 22:773–775

Yeoh EJ, Ross ME, Shurtleff SA et al (2002) Classification, subtype discovery, and prediction of outcome in pediatric acute lymphoblastic leukemia by gene expression profiling. Cancer Cell 1:133–143

Zha Y, Li M, Yang J (2010) Dynamic contrast enhanced magnetic resonance imaging of diffuse spinal bone marrow infiltration in patients with hematological malignancies. Korean J Radiol 11:187–194

Zijlstra JM, Lindauer-van der Werf G, Hoekstra OS et al (2006) 18F-fluoro-deoxyglucose positron emission tomography for post-treatment evaluation of malignant lymphoma: a systematic review. Haematologica 91:522–529

MRI of Bone Metastases

Gerwin Paul Schmidt and Andrea Baur-Melnyk

Contents

Abstract

The skeletal system is a frequent target of metastatic spread from various primary tumors such as carcinoma of the breast, lung and prostate cancer. Therefore, it is highly important to accurately assess skeletal metastases in order to facilitate adequate therapy and predict patients' prognosis. However, only pronounced destruction of bone with loss of mineral content exceeding 50% is readily visible in radiographic examinations. Computed tomography (CT) is definitely more sensitive than radiography and it is the imaging modality of choice to evaluate the extent of destruction of trabecular and cortical bone and to assess stability and fracture risk. Magnetic resonance imaging (MRI), on the other hand, allows visualization of bone marrow structure, such as hematopoietic— and fat cell components. Moreover, tumor infiltration into the spinal canal and paravertebral soft tissues is clearly depicted. The combination of unenhanced T1-weighted-spin echo- and turbo-STIR-sequences has shown to be most useful for the detection of bone marrow abnormalities and is able to discriminate benign from malignant bone marrow changes. Compared with other imaging modalities like radiography, CT or bone scintigraphy, it is the most sensitive technique for the detection of bone marrow pathologies, even if trabecular bone is not destroyed. Recently, multichannel whole-body MRI (WB-MRI) scanners have been introduced and allow for head-to-toe assessment of the whole skeletal system without compromises in image quality compared with dedicated examinations of limited anatomical

G. P. Schmidt (✉) · A. Baur-Melnyk
Department of Clinical Radiology,
University Hospitals Munich/Grosshadern, LMU,
Marchioninistr. 15, 81377, Munich, Germany
e-mail: gerwin.schmidt@med.uni-muenchen.de

A. Baur-Melnyk (ed.), *Magnetic Resonance Imaging of the Bone Marrow*, Medical Radiology. Diagnostic Imaging,
DOI: 10.1007/174_2011_495, © Springer-Verlag Berlin Heidelberg 2013

areas. Accordingly, WB-MRI has become a useful and sensitive alternative to standard whole-body imaging procedures such as skeletal scintigraphy or whole-body CT.

1 Introduction

The bone marrow is a frequent target of neoplastic and hematologic disease and therefore the early detection of bone metastases has an important impact on patient management and may contribute to prevent complications such as pathological fractures. In clinical practice, most commonly multi-modality algorithms are used in case of suspected metastatic bone disease, including conventional X-ray, bone marrow or skeletal scintigraphy, computed tomography (CT) or positron emission tomography (PET). These examinations are performed in order to evaluate the presence and type of bone lesions, to assess their extent and localization and eventually guide potential biopsy. All these modalities have different performances in terms of sensitivity and specificity. Yet, MRI is an imaging technique that allows a direct visualization of bone marrow components with high spatial resolution. The unique soft-tissue contrast of MRI provides a precise assessment of bone marrow infiltration and tumor spread into surrounding tissue at high sensitivity, even in the absence of pronounced osteolytic or metabolic changes. Recently, the advent of multi-receiver channel scanner with more flexible coil systems has made whole-body MRI (WB-MRI) clinically feasible and is introduced as an integrative, highly sensitive method for the detection of metastatic disease to the bone marrow.

2 Clinical Background

2.1 Frequency, Subtypes and Anatomical Distribution

The skeletal system constitutes the third most common location of metastatic manifestations after the liver and the lung. The primary tumors with the highest incidence of skeletal metastases are prostate cancer in men and breast cancer in women, followed by thyroid-, renal- and lung carcinomas. These tumors account for approximately 80% of metastatic bone disease. Approximately 70% of patients who die from prostate- or breast cancer have evidence of skeletal involvement at autopsy (Rubens 1998). Clinically, bone metastases are the most common cause of pain from cancer, which results from either mechanical or chemical stimulation of pain receptors in the periosteum and endosteum. Furthermore, spread of tumor from bone to surrounding neurological structures, such as the spinal cord or nerve roots may cause neurological disability. Compression of the spinal cord or cauda equina in patients with metastatic disease of the spine is a medical emergency necessitating prompt diagnosis and treatment. Pathological fracture is a major complication of metastatic bone disease, causing severe pain and often prolonged disability. Fractures of long bones have the most serious consequences and occur in approximately 10% of patients with bone metastases.

Based on morphological criteria in radiography, CT and MRI, skeletal metastases are classified as osteolytic (approximately 50%), osteoblastic (35%) and mixed type (15%). Bone metastases from colon-, kidney- and lung cancer usually have an osteolytic appearance radiologically and predisposing these lesions to complications, such as pathological fracture. Patients suffering from prostate- and breast cancer more frequently show the osteoblastic type of lesions, while the mixed appearance often is observed in thyroid cancer.

The predominantly hematogenous spread of bone metastases explains its frequent distribution in active hematopoetic bone marrow, especially in the axial skeleton. However, it has been reported that up to 40% of bone metastases may occur in the appendicular skeleton, underlining the importance of whole-body anatomic coverage (Krishnamurthy et al. 1977).

2.2 Diagnostic Imaging Algorithms for Bone Metastases

In patients with local symptoms or pain and in absence of trauma history, radiographs are usually performed as the initial approach for the verification of osteolytic changes indicating possible malignancy (Fig. 1). The fact that only distinct focal osteolytic changes with loss of 30–50% mineral density are discernible on plain film explains its low sensitivity in

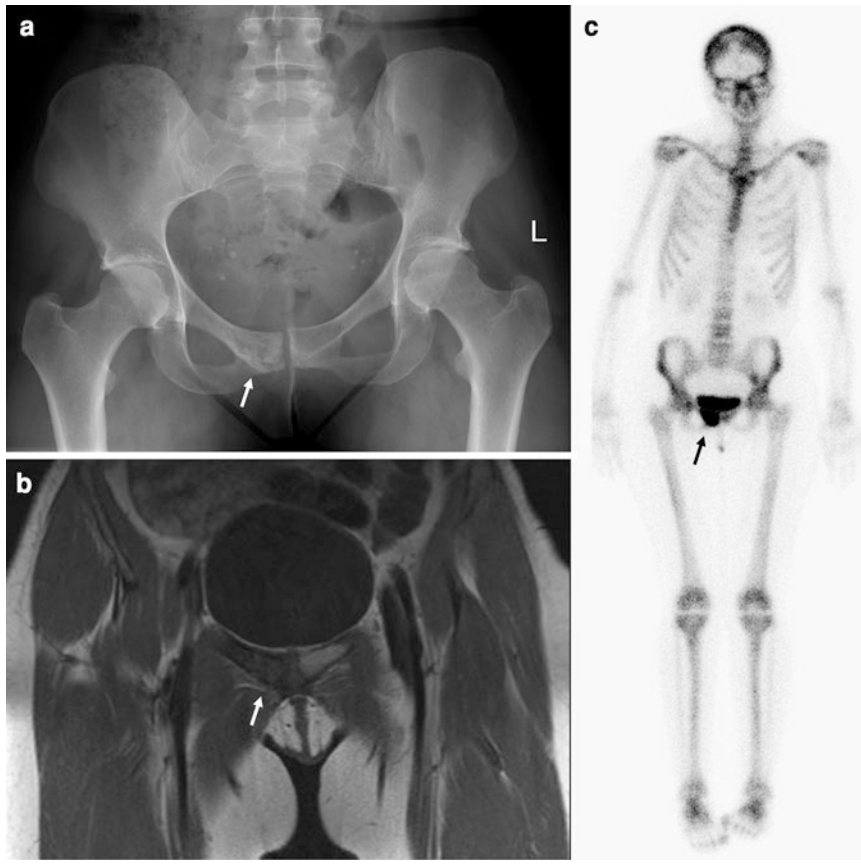

Fig. 1 29-year-old patient with breast cancer and pain in the right pubic region. **a** X-ray shows an osteolysis with pathologic fracture of the right pubic bone (*arrow*); **b** MRI scan depicts T1w-hypointense bone marrow infiltration compared to normal hyperintense bone marrow signal in the left pubic bone (*arrow*); **c** corresponding ^{99m}Tc-bone scan reveals a focal pathologic tracer increase in the described area

the detection of metastases compared with magnetic resonance imaging (MRI), multislice computed tomography (MS-CT) or bone scintigraphy (Edelstyn et al. 1967; Fochem and Ogris 1976; Baur-Melnyk and Reiser 2004; Roberts et al. 1976; Fig. 2). Experimental studies in the spine showed that in cancellous bone 50–75% of the bony thickness in the beam axis of the vertebral body must be destroyed until it can be seen on lateral radiographs. The detection rate was even less accurate on a-p radiographs (Edelstyn et al. 1967). It has been reported that conventional radiographs show no evidence of pathology in 40–63% of cases where bone scans depict a pathological tracer accumulation indicating malignancy (Roberts et al. 1976). Chassang et al. proposed low-dose-CT for the evaluation of the spine affected by myeloma, bone metastases and fractures secondary to osteoporosis with a superior sensitivity compared with conventional radiographic studies (Chassang et al. 2007). Lecouvet et al. compared the performance of MRI and radiography to detect focal osteolytic bone lesions and showed a clear superiority of MRI in specific anatomical areas such as the spine (76 vs. 42% detected lesions) and pelvis (75 vs. 46% detected lesions) (Lecouvet et al. 1999).

In asymptomatic patients, Technetium^{99m} (^{99m}Tc)-phosphonate-based scintigraphy has long been the standard method for systemic bone marrow screening, especially in the search for bone metastases with osteoblastic activity. In a recent meta-analysis on the detection of bone metastases from breast cancer, the patient-based sensitivity of bone scintigraphy has been described as moderate with 78%, at a specificity of 87%, respectively (Shie et al. 2008). An increase in specificity has been reported through the implementation of bone marrow scintigraphy techniques using ^{99m}Tc-monoclonal antigranulocyte antibodies as a complement to standard bone scintigraphy with a reported specificity of up to 90%, in patients with equivocal bone scan results (Prior et al. 2003). Results of another study suggest that bone scintigraphy may not necessarily be required when CT staging with bone

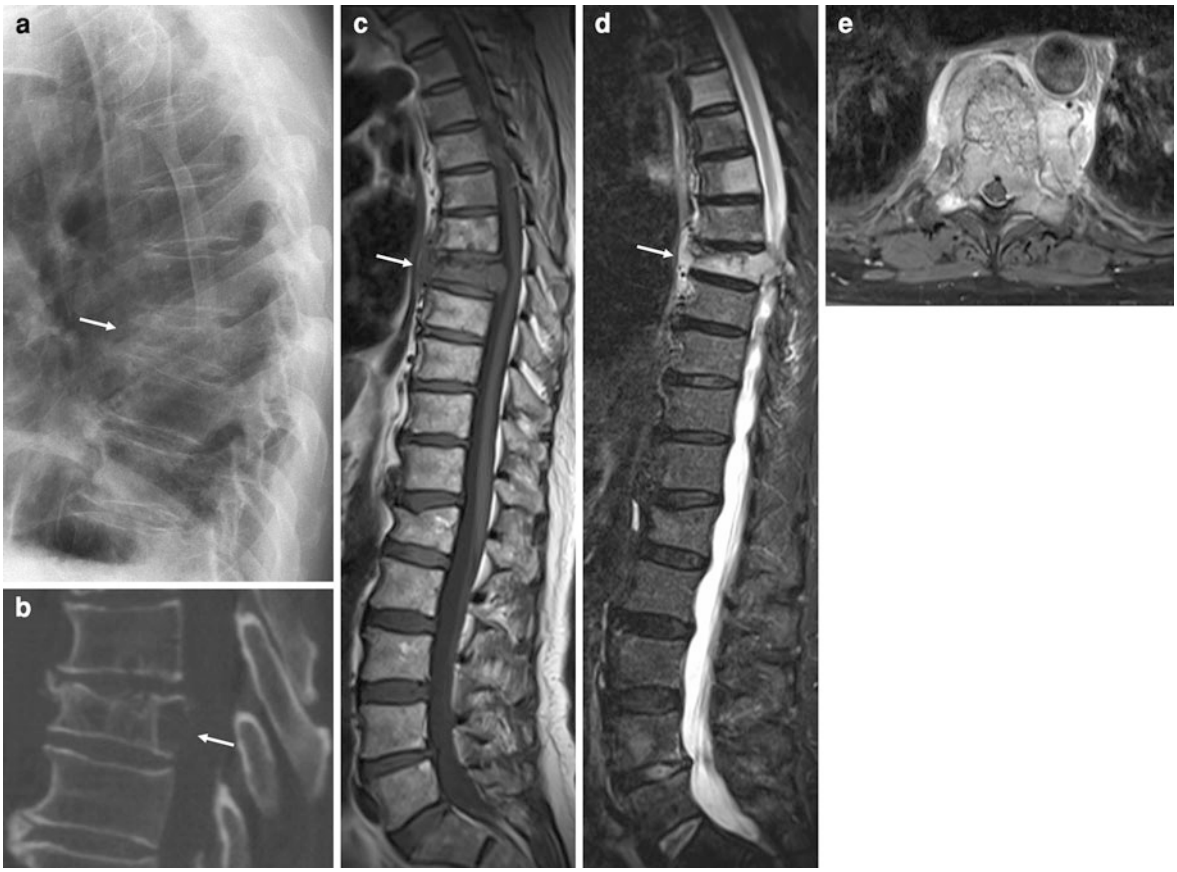

Fig. 2 77-year-old patient with cancer of unknown primary and new bone pain in the thoracic spine. **a** X-ray shows a compression fracture in Th8. No vertebral osteolyses are discernible, diagnostic value is further impaired by overlaying anatomic structures; **b** CT scan depicts an osteolysis with >50% destruction of the posterior border, which led to vertebral instability; **c**, **d** MRI shows T1w-hypointense and STIR-hyperintense bone metastases with posterior bulging (*arrows*). Further metastases are delineated in adjacent vertebrae not depicted in conventional imaging; **e** T1w fat saturated axial MRI delineates a large paravertebral tumor component with infiltration of the posterior body elements and into the spinal canal with incipient encasement of the spinal cord

kernel reconstruction has previously been performed. In a patient-based analysis, MS-CT revealed skeletal metastases in 43 of 44 patients, whereas scintigraphy was false-positive in 11 patients without metastatic disease (Bristow et al. 2008). Nevertheless, bone scintigraphy still remains a favored imaging modality for the evaluation of skeletal metastases, owing mainly to its cost effectiveness and wide availability.

MS-CT is frequently used in oncological imaging and allows for a rapid bone marrow assessment within a CT staging examination using the bone window setting. With the introduction of multislice CT, especially 16-row scanners, a very thin collimation of ~0.7 mm became possible. Therefore small details and especially the trabecular network can be visualized. An important advance has been the introduction of automated tube current dose modulation systems, which have reduced exposure of the patient to ionizing radiation by 10–30% for whole-body scans without substantially sacrificing image quality (Mulkens et al. 2005). Finally, MS-CT for interventional purposes is an established guiding tool for high-precision biopsies performed either as a minimal invasive method or biopsy punch.

For the detection of bone destructions, MS-CT is far more sensitive than radiography and unique in its

ability to evaluate the extent of osseous destructions and to assess cortical bone stability and fracture risk (Fig. 2; Poitout et al. 1991). For this purpose, Taneichi et al. established guidelines to estimate probability of vertebral collapse, depending on the anatomic level of metastatic infiltration within the spine (see Table 1; Taneichi et al. 1997). There are major differences between the thoracic (Th 1-10) and thoracolumbar vertebral bodies (Th 11-L5) since the rib cage serves as a stabilizer of the thoracic vertebral column. Four factors are decisive: percentage of osteolysis in the vertebral body, presence of involvement of the pedicles, posterior elements and costovertebral joint involvement at thoracic level. A vertebral body is at risk of fracture in the thoracic spine if more than 50% of the vertebral body is missing or if more than 25% osseous destruction of the vertebral body is combined with a destruction of the costovertebral joint. In the lumbar spine a vertebral body is at risk of fracture if more than 35% of the body is destroyed or if a more than 20% destruction of the body is combined with involvement of the posterior elements/pedicles (Table 1). This assessment has a crucial impact on therapy management to decide between systemic chemotherapy, local irradiation and prophylactic stabilization. Furthermore, MS-CT allows the detection of osteoblastic bone marrow changes as well as mixed patterns with osteosclerosis and destruction. In cases with diffuse bone marrow infiltration, inhomogeneous osteoporosis may be detected. Especially the use of ultrathin collimation (0.5 mm) provides excellent image quality for the neck and peripheral skeleton. Krahe et al. compared conventional radiographs and CT examinations of 112 patients with primary and secondary bone tumors of the spine. Of 268 affected vertebrae identified on CT, 88% were identified by radiographs when the vertebral body was infiltrated, but only 66% when other parts of the vertebrae were affected. Of intraspinal and paravertebral tumor extension, only 23 and 33%, respectively, were correctly diagnosed by plain radiography (Krahe et al. 1989). Yet, in an own study on the spine comparing 64-MS-CT with MRI in 41 patients with vertebral metastases, it has been shown that although MS-CT provides excellent image quality and a high spatial resolution in the assessment of vertebral bony structures, metastatic lesions without significant bone destruction may be missed (Buhmann Kirchhoff et al. 2009). Overall, the diagnostic accuracy of MRI proved to be significantly superior to MS-CT for the detection of osseous metastases. Of 201 vertebral bodies defined as metastatically affected, MS-CT detected 133/201 lesions and MRI 198/201 lesions. Sensitivity was significantly lower for MS-CT (66.2%) than for MRI (98.5%), specificity was not significantly different for both methods (MS-CT: 99.3%; MRI: 98.9%). The diagnostic accuracy resulted in 88.8% for MS-CT and 98.7% for MRI.

Table 1 Assessment of fracture risk in the spine (Taneichi et al. 1997)

Fracture risk assessment in vertebral bodies
>50% destruction of thoracic (Th1-10) v.b.
>25% destruction of thoracic v.b. + costovertebral destruction
>35% destruction of thoracolumbar (Th11-L5) v.b.
>20% destruction of thoracolumbar (Th11-L5) + infiltration of pedicle/post. elements

3 MRI of Bone Metastases

3.1 Sequences and Signal Characteristics

For MRI bone screening, the combination of unenhanced T1-weighted turbo spin echo (TSE) and turbo-STIR-sequences proved to be highly sensitive to discriminate benign from malignant marrow disorders (Walker et al. 2000). Normal fatty marrow shows a homogeneous hyperintense signal compared to adjacent muscle tissue in T1-weighted sequences. Tumor spread is identified by replacement of normal fat containing marrow, resulting in a hypointense focal bone marrow signal. Fat-suppressed sequences, such as short tau inversion recovery (STIR), depict neoplastic lesions by virtue of the hyperintense signal due to increased content of water within the tumor cells (Fig. 3). However, osteoblastic metastases may be depicted in STIR-sequences with variable signal intensities ranging from hypointense in dense sclerotic lesions to hyperintense when more cellular components are present (Figs. 4, 5; Vanel et al. 1998). After Gadolinium-administration vital bone metastases usually show contrast media uptake which can have a “ring-like” appearance. In metastases deriving

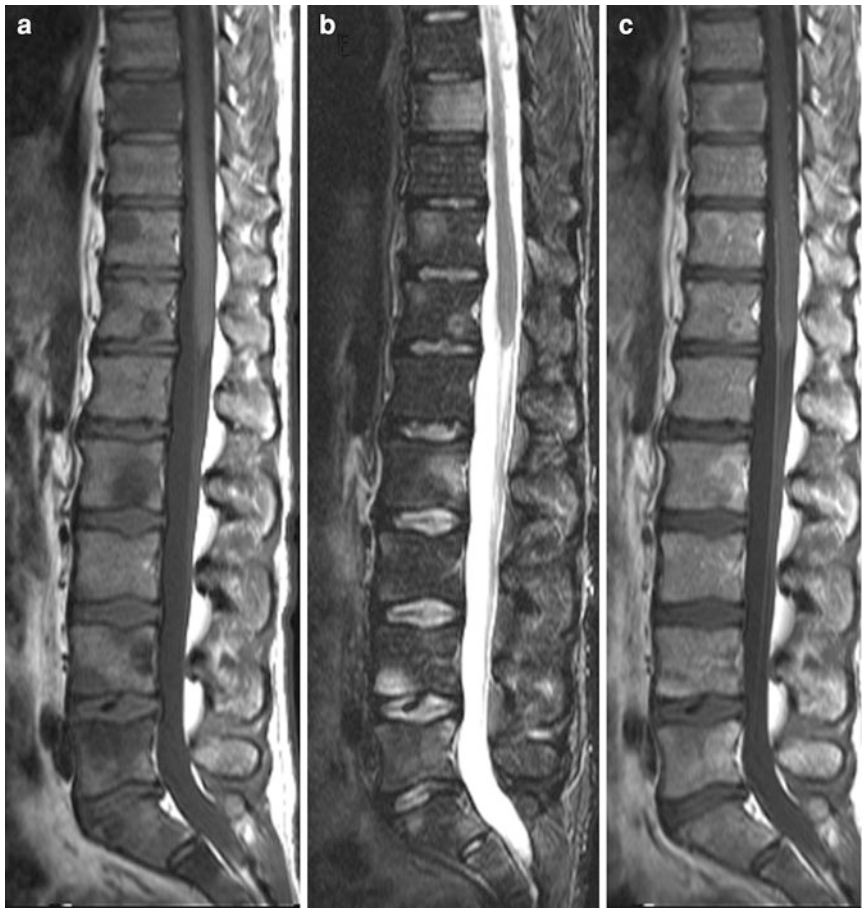

Fig. 3 57-year-old patient with bronchial carcinoma and osteolytic metastases. **a**, **b** T1w-TSE sequence indicates multifocal hypointense lesions in the lower thoracic- and lumbar spine which appear hyperintense in STIR imaging; **c** after contrast administration the lesions show a peripheral "ring-like" enhancement

from squamous cell carcinoma a central necrotic area may be discernible (Fig. 6).

The unique soft-tissue contrast of MRI allows a precise assessment of tumor spread within the bone marrow and even diffuse infiltration of the bone marrow with neoplastic cells, not associated with focal bone destructions or formation of new bone, is detected. In case of diffuse bone marrow infiltration, signal alterations may be more subtle, ranging from hardly visible homogeneous signal alterations in mild diffuse infiltration patterns to a pronounced hypointense decrease of bone marrow signal in T1-weighted TSE sequences and a consecutive increase in STIR (Fig. 7). In this case, a so-called "bright disc sign" maybe visible in T1-weighted imaging due to a relative contrast reversal of hyperintense appearing intervertebral discs on the background of pathologic hypointense packed bone marrow, representing almost total replacement by malignant cells (Castillo et al. 1990).

Depending on the site of suspected bone metastasis (e.g. in case of suspected infiltration into surrounding tissue like the spinal canal) additional sequences including T2-weighted contrast and contrast-enhanced fat saturated proton density (PD) sequences in primarily axial orientation may be useful to further ameliorate lesion delineation. In some cases specific techniques, such as dynamic studies of signal enhancement after gadolinium injection, may be performed for more accurate differentiation of metastases from benign bone marrow changes, such as hyperplastic bone marrow formation. In the presence of early diffuse bone marrow infiltration patterns, which may be present, for example, in multiple myeloma or lymphoma, the use of contrast-enhanced sequences with the calculation of percentage signal increase may be advised. Baur et al. described an increased sensitivity compared to unenhanced studies for early diffuse infiltration patterns in multiple myeloma, setting a cutoff of more than 40% signal

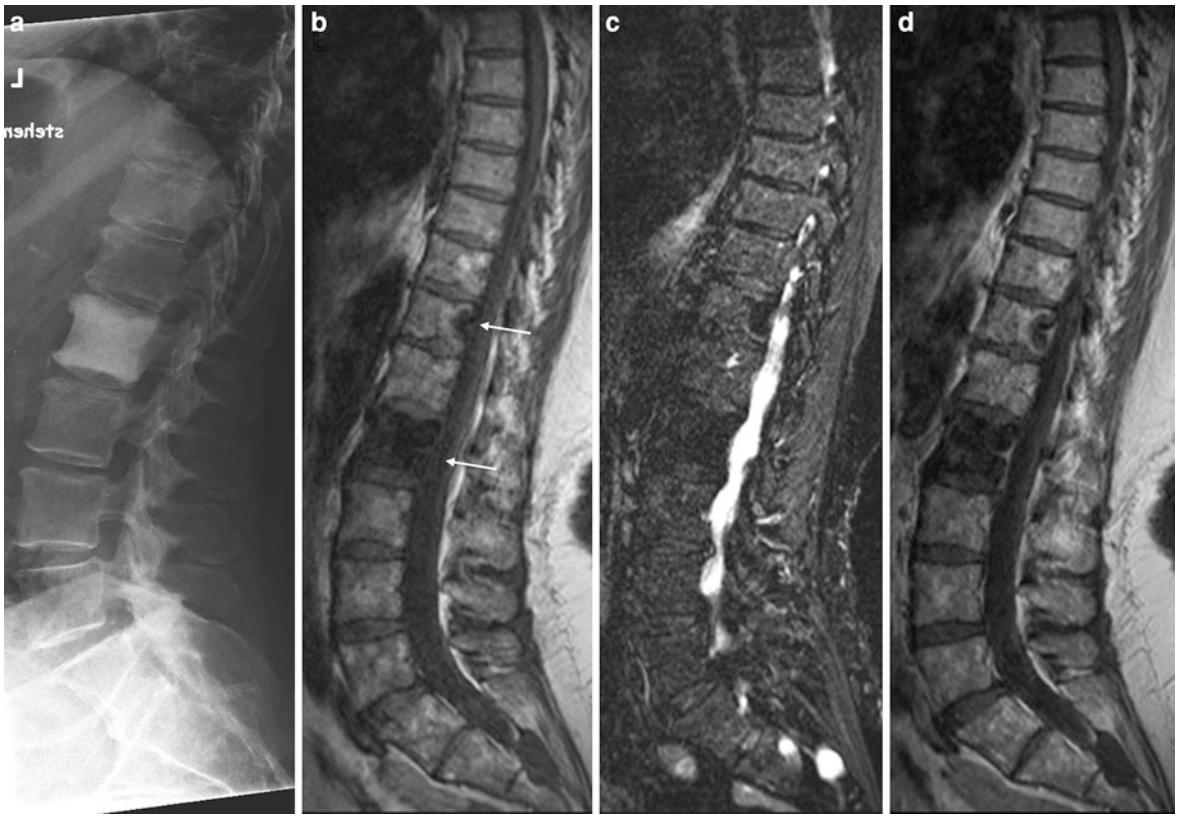

Fig. 4 71-year-old patient with purely osteoblastic metastases. **a** Conventional imaging indicates a large osteosclerotic lesion in L1, the lower thoracic spine is only partly assessable due to overlying diaphragm. T1w-TSE sequence (**b**) depicts 2 hypointense lesions in Th12 and L1 which also appear hypointense in STIR imaging (**c**). After contrast administration (**d**) the lesions show no enhancement due to the sclerotic nature of the metastases

increase after gadolinium administration as a strong indicator for malignancy (Baur et al. 1997).

3.2 WB-MRI for the Detection Bone Metastases

3.2.1 Technical Advances and Imaging Approaches

Because of its lack of ionizing radiation, high spatial resolution for bone marrow components, and excellent contrast of adjacent soft-tissue structures (e.g., the spinal canal), MRI in principle is an ideal candidate for whole-body imaging of the bone marrow. However, for a long time the main focus of MRI has been on the dedicated assessment of specific organ systems and pathologies within a defined anatomical region. Initially, whole-body MRI (WB-MRI) was performed with a sequential scanning approach, which implied at least one patient repositioning process and a time-consuming rearrangement of the coil setup. Therefore, a total examination time well beyond 1 h had to be taken into account, limiting clinical feasibility and patient acceptance. First improvements in hardware consisted of a rolling platform system mounted on top of a conventional scanner table, which for the first time allowed for large FOV scanning without restrictions along the *z*-axis. With the use of this platform, the patient was moved manually in between the body coil fixed in the center of the bore and the integrated spine coil. Lauenstein et al. applied this system for the detection of bone metastases in 26 patients, using coronal scans at five different body levels with T1-weighted gradient-recalled echo (GRE), half-Fourier acquisition single-shot turbo spin echo, and short tau inversion recovery (STIR) sequences (Lauenstein et al. 2002). A high correlation was found between WB-MRI and

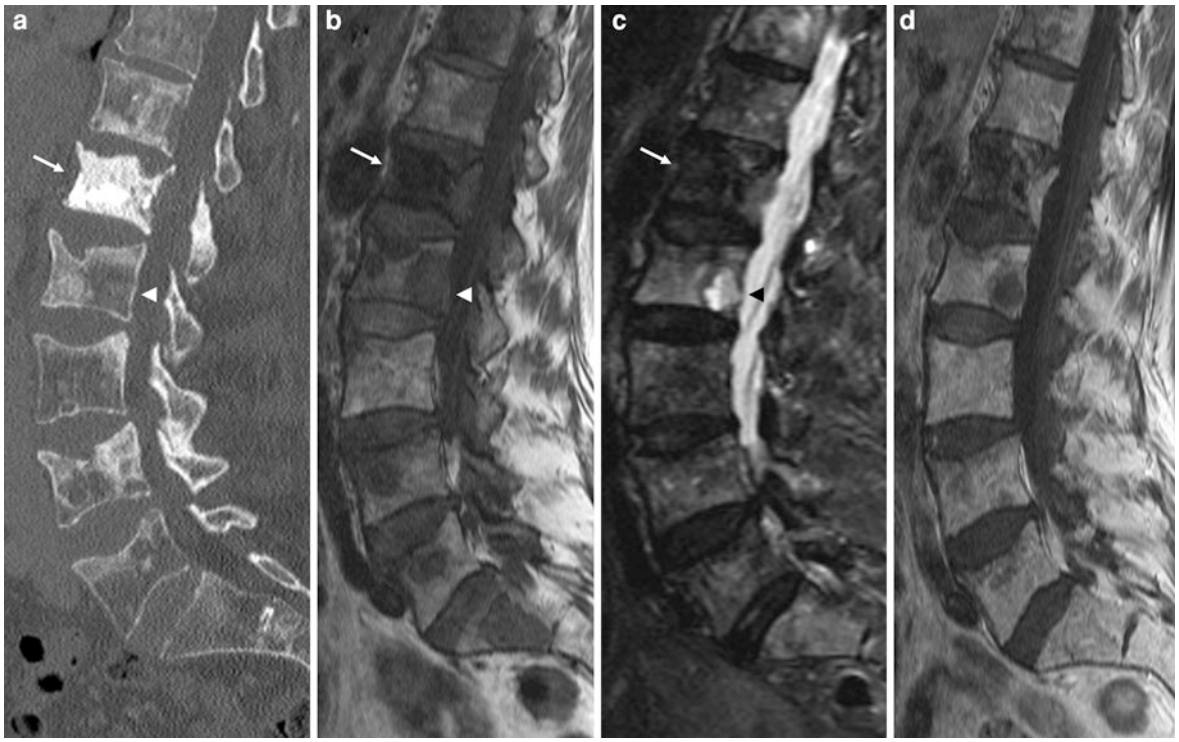

Fig. 5 68-year-old patient with mixed osteolytic and osteoblastic metastases from breast cancer. **a** MS-CT shows the extent of mixed lytic and sclerotic (*arrow*) infiltration pattern; **b** T1w-TSE sequence; **b**, **c** MRI depicts lesions with strong hypointense signal in both T1w-TSE and STIR (osteoblastic) next to lesions with typical osteolytic signal behavior (*arrowheads*). Especially the lytic lesions show a strong contrast uptake (**d**)

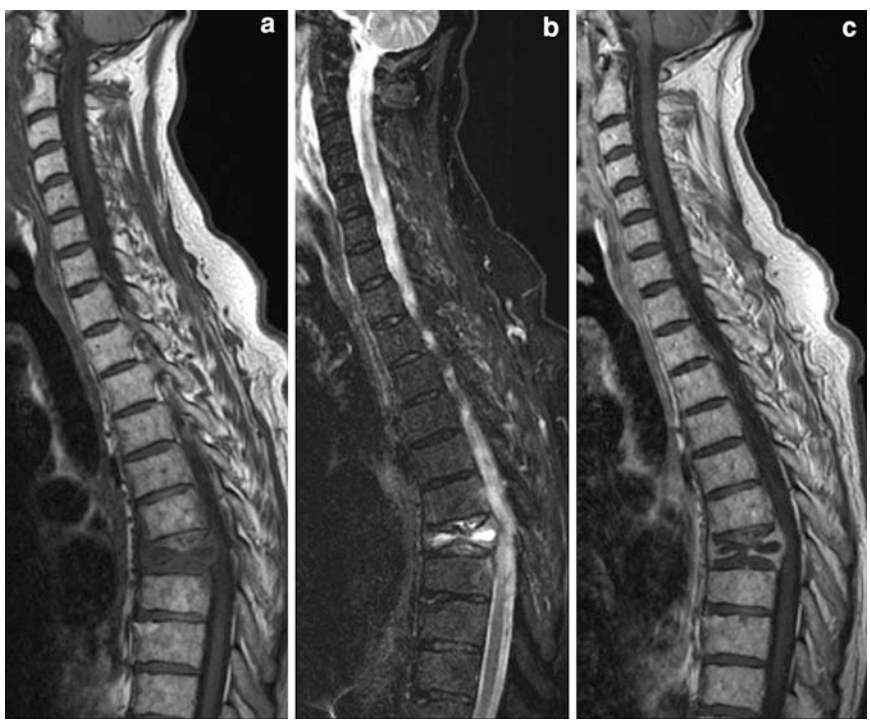

Fig. 6 64-year-old patient with squamous cell cancer of the larynx. **a** The T1-w-TSE sequence shows a compression fracture of Th8 provoked by a necrotic bone metastasis; **b** STIR imaging delineates the hyperintense centrally necrotic part of the lesion; **c** after Gadolinium administration enhancement is observed in the peripheral solid parts of the lesion. This pattern is fairly typical for squamous cell tumors since they often become necrotic centrally due to their fast growth

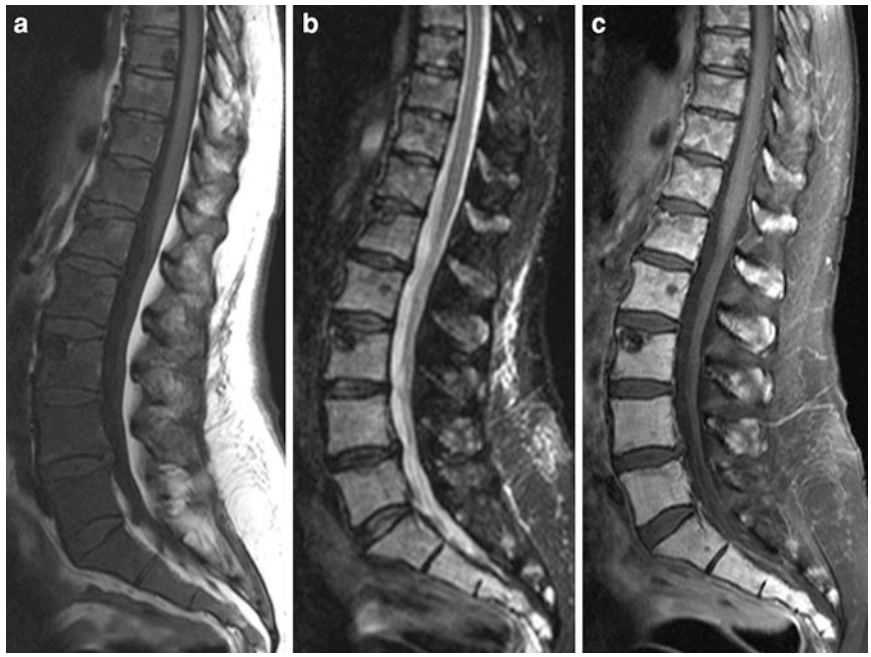

Fig. 7 60-year-old patient with breast cancer and diffuse metastastic infiltration of the bone marrow. **a**, **b** T1w-TSE sequence shows homogenously decreased signal of fatty marrow with corresponding hyperintense aspect in STIR indicating high grade infiltration by tumor cells; **c** after Gadolinium administration a significant, pathologic uptake of contrast agent is visible. Also, scattered focal osteosclerotic lesions in Th9, L2 and L3 with persistent hypointense signal are discerned

bone scintigraphy: 53 of 60 regions affected in bone scintigraphy were also identified in MRI and additional lesions were detected in the spine, femur and pelvis. Yet, despite these promising initial results for whole-body tumor screening within reduced scan times, a significant compromise in spatial resolution had to be taken into account because of the use of the body coil in the head/neck region or in peripheral body parts. With the introduction of multi-receiver channel MR systems, using multiple phased-array coil elements covering the whole body like a matrix, imaging of the total skeletal system without compromises in spatial resolution has become possible. Especially the combination of free table movement with parallel imaging acquisition (PAT) techniques has resulted in significantly shorter room time. This allows the integration of otherwise time-consuming, but indispensable sequence types for whole-body bone marrow imaging, like STIR-sequences.

Recently, approved clinical WB-MRI scanners with a field strength of 3 Tesla have become commercially available, equipped with the same technique of multiple phased-array coils and receiver channels. This has opened the way to migrate multi-organ and whole-body applications to higher field strength. The gain of signal-to-noise ratio (SNR) can be used to reduce the overall scan time, especially for the acquisition of T2-weighted- and STIR-sequences at a constant image resolution. Alternatively, image resolution can further be increased to potentially gain higher sensitivity. The higher SNR allows recording of large highly resolved isotropic 3D data sets within short acquisition times, which can further ameliorate diagnosis of bone pathologies in complex anatomical structures, such as the pelvis, rib cage or spinal pedicles. Three-dimensional TSE sequences with high sampling efficiency [spatial and chemical-shift encoded excitation (SPACE)] have recently been developed with T1-weighted-, STIR- and T2-weighted contrast. STIR-SPACE imaging of the whole spine, for example, is possible within 10 min scan time at a resolution of $0.8 \times 0.8 \times 2.0$ mm.

Finally, a promising new application in near future will be real-time WB-MRI during continuous table movement. Feasibility of 3D whole-body continuous data acquisition, especially for large FOV imaging in short-bore systems, has already been reported (Brauck et al. 2008; Weckbach et al. 2010). Brauck et al. have introduced this technique as a new potential strategy for WB-MRI screening of metastases, using real-time T2-weighted/T1-weighted steady-state free precession sequences pre- and post-contrast with a reported detection rate of 13 of 14 bone metastases in 11 examined patients (Brauck et al. 2008).

Table 2 Whole-body MRI protocol at 1.5 T for total bone marrow assessment without use of contrast agent

Localisation	WB-MRI protocol at 1.5 Tesla			
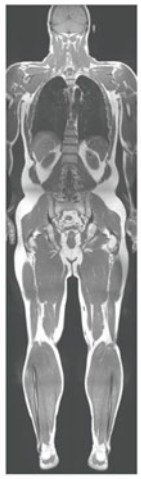	STIR cor *Head/neck*	T1 cor *Head/neck*		
	STIR cor *Thorax/Abdomen*	T1 cor *Thorax/Abdomen*	T1 sag *Upper spine*	STIR sag *Upper spine*
	STIR cor *Pelvis*	T1 cor *Pelvis*	T1 sag *Lower spine*	STIR sag *Lower spine*
	STIR cor *Femurs*	T1 cor *Femurs*		
	STIR cor *Thighs*	T1 cor *Thighs*		
	0 min → 45 min			

In-plane resolution is 1.3 × 1.1 mm for T1w TSE- and 1.8 × 1.3 mm for STIR imaging

3.2.2 Whole-Body MRI Examination Protocol

The proposed imaging protocol at 1.5 T for high-resolution T1-weighted TSE- and STIR-imaging from head to toe, combined with dedicated imaging of the complete spine, results in a total scan time of 42 min (1.3 × 1.1 and 1.8 × 1.3 mm in-plane resolution; Table 2). The protocol has proven a high diagnostic accuracy for the detection of skeletal metastases without administration of contrast agent (Fig. 8). On a 3 T scanner the increased SNR may be used to further reduce imaging time. In a preclinical step of platform migration, our group analyzed image quality criteria and artefacts between 1.5 and 3 T for the proposed whole-body bone marrow protocol on 15 healthy volunteers using identical sequence and resolution parameters. Results showed a comparably good performance on both scanners with only slightly increased artefacts at 3 T, yet without restraining influence on image quality, at a further reduced total scan time of 31 min (Schmidt et al. 2007a).

Some authors propose whole-body diffusion MRI (WB-DWI) as an adjunct sequence for screening of bone metastases and have reported its efficacy, especially to detect multifocal metastastatic spread (Gutzeit et al. 2009).

3.2.3 Special MR Imaging Techniques

Diffusion-weighted magnetic resonance imaging (DWI) is a technique that allows non-invasive characterization of biologic tissues based on measurements of the random microscopic motion of water protons (Brownian motion). The degree of water motion has been found to be proportional to the degree of signal attenuation. DWI has revealed great potential in the evaluation of patients with musculoskeletal malignancy, as it supplies both quantitative and qualitative information. The basic biological premise for the use of DWI is that malignant tissues are more cellular and have higher water content than benign/normal tissues; both these features will result in higher signal intensity of malignant disease on high b-value images with a corresponding low apparent diffusion coefficient (ADC).

DWI has been extensively evaluated for its role in the assessment of vertebral compression fractures, especially to distinguish between metastatic pathologic and benign osteoporotic fracture. Although morphologic aspects, such as paravertebral soft-tissue masses, total vertebral body signal changes and infiltration of the posterior elements are recognized signs indicating malignancy, differentiation to atypical manifestations

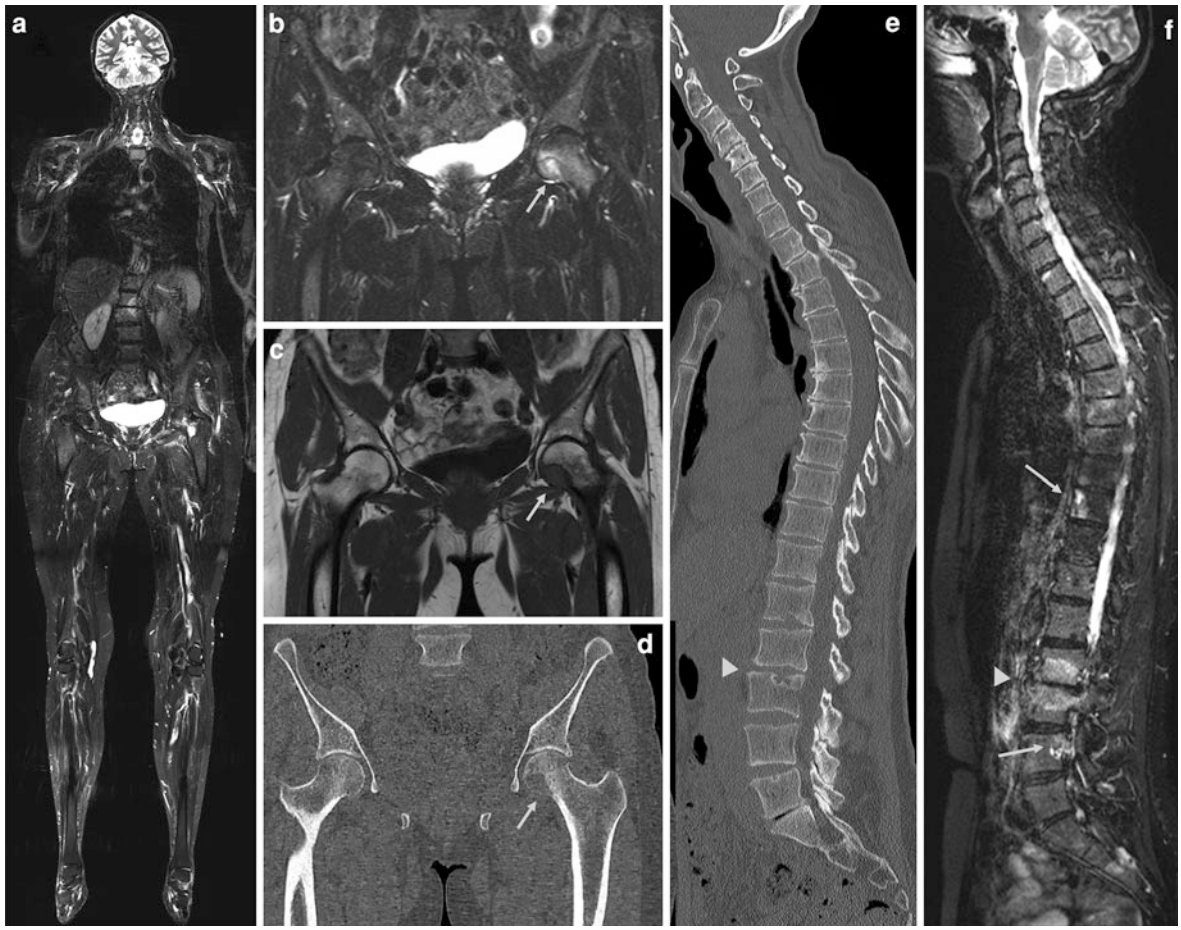

Fig. 8 61-year-old patient with breast cancer. **a**, **b** WB-STIR imaging indicates a hyperintense focal lesion in the left femoral neck (*arrow*); **c** the lesion shows corresponding hypointense bone marrow signal in the T1-weighted TSE and is consistent with a large osteolysis, confirmed by the CT scan (**d**); **e** additional CT of the spine shows signs of pronounced degeneration with osteochondrosis (*arrowhead*), yet, no further osteolysis are visible; **f** however, STIR imaging of the spine shows more metastases (*arrows*) adjacent to activated osteochondrosis (*arrowhead*)

of osteoporotic compression fractures can often remain challenging. In this setting, DWI is a very helpful adjunct to morphological criteria alone (Baur et al. 2001).

Three-dimensional diffusion-weighted whole-body imaging with background body signal suppression (DWIBS) has been introduced as a method for the detection of metastatic deposits (Takahara et al. 2004). From these DWI datasets, it is possible to produce 3D-maximum intensity projection displays by inverting the attenuation similar to those obtained by skeletal scintigraphy. Gutzeit et al. compared the diagnostic accuracy of DWIBS with whole-body skeletal scintigraphy for the differentiation of skeletal bone lesions in patients suffering from breast- or prostate carcinoma. Interestingly, DWIBS showed diagnostic advantages especially in multifocal metastases (>10 lesions per patient), indicating the additional benefit from DWIBS of enhanced display of metastatic lesions (Gutzeit et al. 2009; Fig. 9).

A further development of the technique has been fused data sets of morphologic MR images, e.g. T2w-TSE, with DWI data. However, initial studies report no added value compared to side-by-side image interpretation (Fischer et al. 2011).

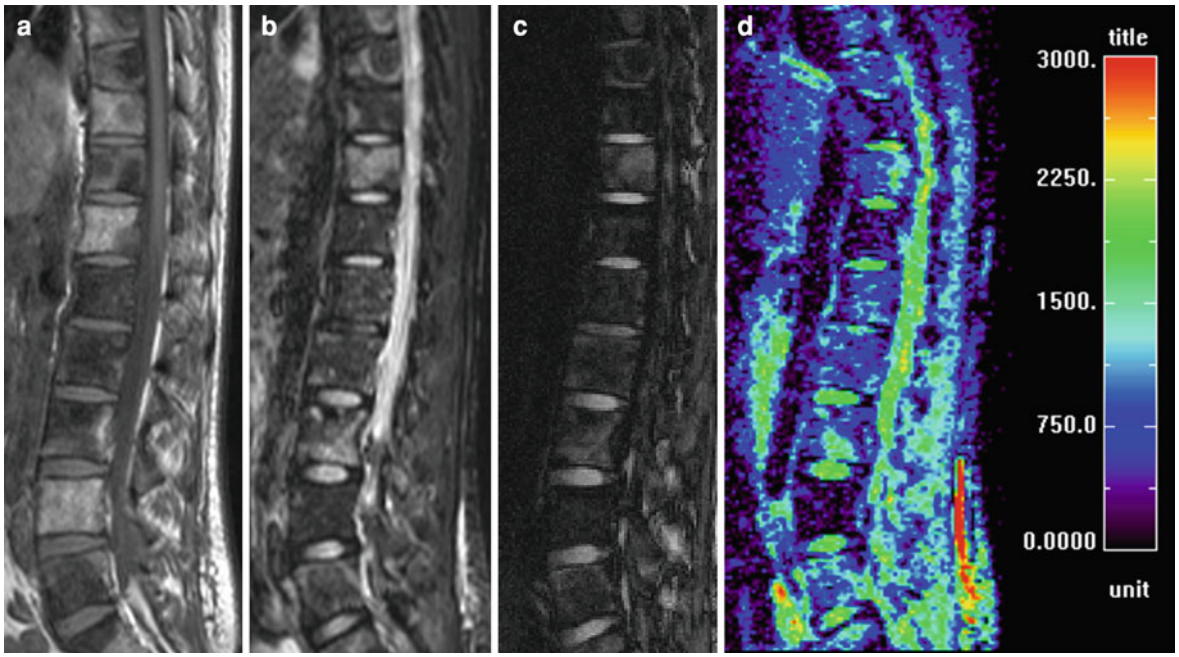

Fig. 9 Diffusion weighted imaging (DWI) of a patient with multifocal bone metastases. **a**, **b** T1w-TSE and STIR imaging shows multifocal bone metastases in the thoracolumbar spine; **c** DWI with a b-value of 800 shows marked signal increase within the lesions indicating restricted diffusion with corresponding moderate ADC values (**d**)

3.3 Diagnostic Performance of MRI Compared to Other Imaging Modalities

In many institutions ^{99m}Tc-phosphonate-based bone scanning is performed as the method of initial bone marrow screening. However, scintigraphy provides only limited spatial resolution and at an early stage of disease lesions may remain invisible in the absence of an osteoblastic response. Furthermore, misinterpretation of tracer uptake in healing fractures or degenerative disease may lead to false-positive findings. The diagnostic performance of MRI compared with bone scintigraphy has been examined in various studies and higher specificity and sensitivity in the early detection of skeletal metastases has been reported (Eustace et al. 1997; Steinborn et al. 1999; Engelhard et al. 2004; Daldrup-Link et al. 2001). Steinborn et al. compared combined T1-weighted and STIR WB-MRI with bone scintigraphy using the sequential scanning approach in a lesion-by-lesion analysis (Brauck et al. 2008). WB-MRI reliably detected more confirmed skeletal metastases (91%) than bone scintigraphy (85%). The authors described potential diagnostic limitations for WB-MRI occuring in the thoracic cage, especially when coronal imaging orientation is used, a problem that is further increased by motion artefacts. These problems might be overcome when using fast TSE sequences for thoracic imaging in combination with axial slice orientation.

In contrast to MRI, PET using [18F]-fluorodeoxyglucose (FDG) provides functional information by tracing increased FDG uptake directly into the tumor cells. Recent studies indicate that whole-body FDG-PET increases specificity of bone screening compared with bone scintigraphy, although there is conflicting evidence whether there is a significant gain in sensitivity (Fogelman et al. 2005). Still, FDG is a tracer that is not tumor-specific and may also accumulate in the presence of inflammation and thus lead to false-positive findings. Also, FDG is not suitable for several tumor entities due to poor tracer uptake, e.g., prostate cancer, myxoid tumors of the gastrointestinal tract, low-grade sarcomas or renal cell carcinomas (Reske and Kotzerke 2001). A clear technical disadvantage of PET, similar to scintigraphy, used to be its poor anatomical resolution, which often made the exact localization of a lesion difficult. Fused PET-CT scanners combine the functional data of PET with the detailed anatomical information of MS-CT scanners

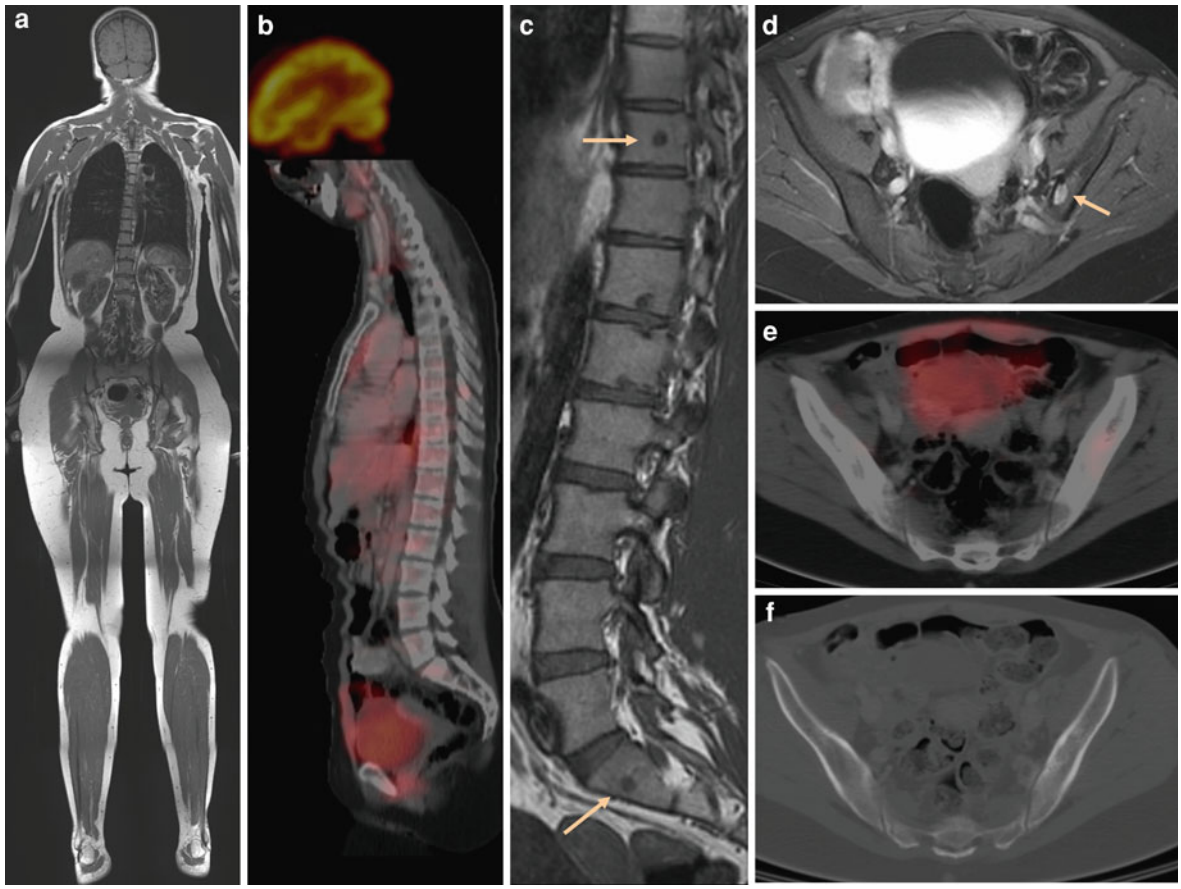

Fig. 10 **a** WB-MRI with TSE sequence of a 29-year-old patient with breast cancer; **b** sagittal reconstruction of the spine from the PET-CT scan shows physiological body uptake of FDG; **c** yet, T1-w TSE sequence of the lower spine reveals multifocal, small bone metastases (*arrows*); **d** another metastasis is detected in the left iliac bone (*arrow*); **e** corresponding PET-CT image did not indicate pathologic tracer uptake and hardly visible bone changes in bone window setting

in a single examination and have further improved diagnostic accuracy. Various authors have reported a significant decrease in ambiguous lesions and an improvement in the specificity of PET-CT for the detection of malignant disease compared to PET alone (Metser et al. 2004; Even-Sapir et al. 2004). Only a few study groups have directly compared the performance of MRI with FDG-PET-CT for the detection of skeletal metastases (Antoch et al. 2004; Schmidt et al. 2007b). Antoch et al. analyzed the accuracy of both modalities in 98 patients for TNM-based tumor staging. Both imaging procedures revealed a similiar diagnostic sensitivity for the detection of distant metastases (WB-MRI 93%, PET-CT 94%). Regarding bone metastases, the sensitivity was significantly higher when using WB-MRI (85%) compared to PET-CT (62%) (Antoch et al. 2004). In a lesion-by-lesion analysis performed by our group comparing T1-weighted TSE/STIR WB-MRI and FDG-PET-CT for the detection of skeletal metastases, 102 malignant and 25 benign bone lesions were described in 30 patients, confirmed by histological examination or follow-up. WB-MRI showed a significantly higher diagnostic accuracy than PET-CT (91 vs. 78%, respectively). WB-MRI especially showed a superior sensitivity (94%), because more lesions <5 mm were depicted (cutoff size, 2 mm), compared with PET-CT (78%; cutoff size, 5 mm, Fig. 10). Lesions less than double the size of the spatial resolution of the PET scanner can lead to false-negative results. Yet, latest generation PET-CT scanners have been equipped with high-definition PET systems, increasing PET resolution up to 2–3 mm, thus potentially ameliorating sensitivity for

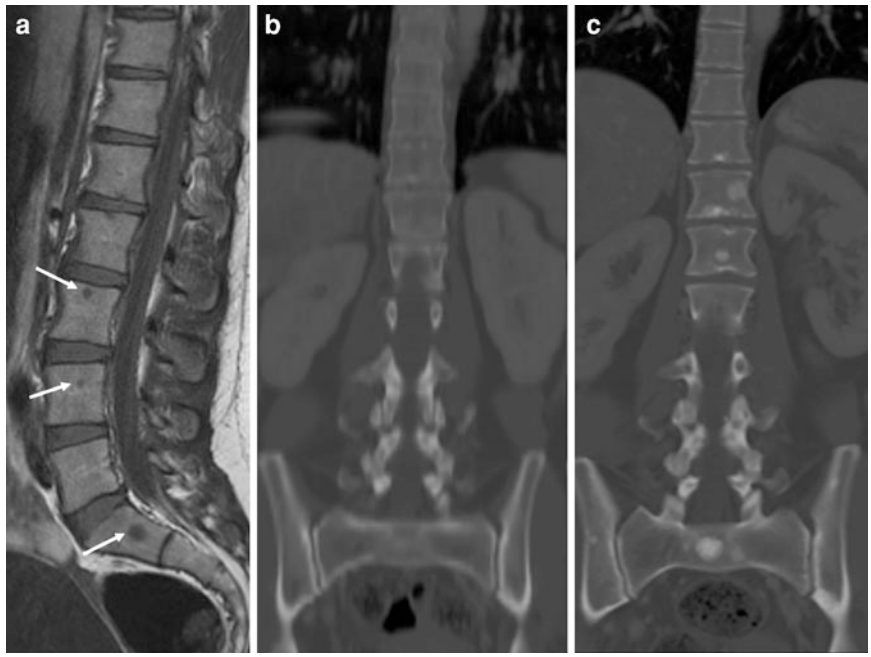

Fig. 11 Diagnostic follow up Of the same patient described in Fig. 9. Initial MRI revealed several metastases in the spine and sacral bone, but there were no visible lesions in MS-CT (**b**). In the follow-up CT after 4 months (**c**) the lesions underwent sclerotic transformation under chemotherapy and were primarily—without the knowledge of initial MRI before therapy—falsely estimated as "tumor progress" (development of new sclerotic mets)

small-sized malignant bone lesions. Additionally, WB-MRI revealed 10 additional bone metastases in 5 patients due to the larger field of view (Schmidt et al. 2007b). However, in the described study, specificity was higher for PET-CT (80 vs. 76% for WB-MRI). In this regard the metabolic information of PET plays the most important role in discriminating between malignant and benign lesions (e.g., atypical hemangioma). On the other hand, at least in breast cancer, different patterns of FDG uptake have been reported in osteoblastic, osteolytic or mixed lesions, indicating that sclerotic lesions may be less FDG-avid (Cook et al. 1998). The additional morphologic information of PET/CT compared with PET alone is certainly of great value to increase diagnostic sensitivity. Also, significant improvement in diagnostic accuracy has been reported when 18F-fluoride is used for PET or PET-CT for the assessment of malignant skeletal disease. ^{18}F-fluoride is a tracer that, similar to ^{99m}Tc-diphosphonate, specifically adsorbs onto bone surfaces with a predilection for sites of active bone formation (Even-Sapir et al. 2004).

An important pitfall that has to be considered when diagnosing supposed osteoblastic metastases is sclerotic transformation of primarily osteolytic metastases as a response to therapy, commonly observed e.g. in breast cancer metastases. This phenomenom can potentially be misdiagnosed as new osteoblastic bone metastases when small osteolyses originally were hardly detectable on MS-CT and negative in scintigraphy. Therefore, this setting of therapy response should not be false-diagnosed as tumor progress (Fig. 11).

3.4 Follow-Up of Bone Metastases

An important indication in bone imaging is lesion monitoring after chemotherapy or radiation therapy. It has to be taken in account that in MRI necrotic bone metastases may remain virtually unchanged in morphology or signal characteristics, which may make evaluation of therapeutic response difficult. Compared to viable tumors, the contrast enhancement may be less pronounced and less fast in tumors that have responded to a particular therapy. On the other hand, reduction in tumor size may be delayed and is no sensitive sign in assessment of response.

DWI has been proposed by several authors as a tool to assess response of bone metastases to therapy. Changes in tissue diffusivity depicted by DWI can differentiate between viable tumor and necrotic tissue during active treatment. A recent study evaluating DWI monitoring of radiation treatment response of vertebral metastases showed convincing changes from pre-therapy b-value hyperintensity to hypointensity following therapy (Byun et al. 2002). This study

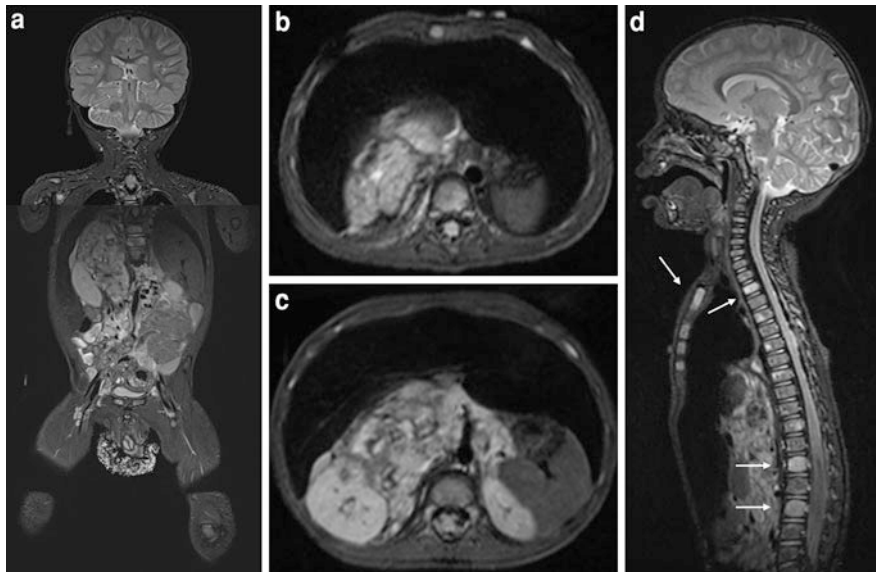

Fig. 12 5-year-old boy with Neuroblastoma. **a** Whole-body-STIR imaging depicts a large tumor mass extending from the right thorax into the upper abdomen; **b**, **c** axial slices shows paravertebral tumor extension and encasement of upper abdominal vessels; **d** sagittal imaging reveals multifocal bone metastases affecting the thoracic spine and sternum (*arrows*)

compared DWI with conventional T1-w and T2-w SE follow-up images of spinal metastases. Morphologic imaging revealed no significant interval changes, indicating that they are of limited use in monitoring treatment response. However, in patients with clinical improvement, the corresponding b-values in DWI showed demonstrable conversion to hypointensity on subsequent follow-up at the end of therapy, consistent with increased water molecular diffusion due to cellular membrane loss from tumor apoptosis. In contrast, patients with no clinical improvement demonstrated persistent bone marrow b-value hyperintensity suggestive of persistent tumor hypercellularity causing restriction of water diffusion.

In the long-term in general the decrease in the signal intensity of bony infiltrations is later accompanied by decreasing ADC values in the setting of successful therapy. Tumor necrosis, bone sclerosis, secondary myelofibrosis and reappearance of yellow marrow assist in long-term reduction of signal intensity on high b-value images and in ADC values of successfully treated lesions.

3.5 Bone Metastases in the Pediatric Patient

Especially in young patients whole-body MR examinations are especially useful, on one hand to quickly assess systemic manifestations of malignant disease to evaluate therapeutic options and on the other hand to avoid excessive radiation exposure in potential multiple follow-up examinations. Furthermore, multi-modal staging examinations which each may require individual sedation, can potentially be avoided. The overall smaller patient size allows image acquisition with less examination steps, thus further reducing total scan time. Various authors have reported the efficacy of WB-MRI for the detection of multifocal metastases in pediatric tumors that frequently metastasize to the bone, such as neuroblastoma, Ewing-sarcoma or osteosarcoma (Daldrup-Link et al. 2001; Goo 2010; Kumar et al. 2008; Fig. 12). Kumar et al. reported in a recent study on small-cell tumors in 26 children and adolescents (mainly Ewing's sarcoma, rhabdomyosarcoma and neuroblastoma) a sensitivity of 30% for standard skeletal scintigraphy and 98% for WB-MRI, while specificity of both methods was equally high (99%). Additionally, a higher sensitivity of WB-MRI compared to PET/CT was observed (98 vs. 90%). In an earlier study, Daldrup-Link et al. analyzed WB-MRI, scintigraphy and PET for the detection of bone metastases in 39 children and young adults with a comparable tumor cohort and observed a higher sensitivity of 82% for WB-MRI compared with 71% for scintigraphy, with increasing difference in medium-sized lesions between 1 and 5 cm (Daldrup-Link et al. 2001). Interstingly, advantages of PET over WB-MRI were

observed (90 vs. 82%). In some cases diagnostic problems in MRI may arise in young patients, where the differentiation of highly cellular hematopoietic marrow and neoplasia can be difficult, and therefore knowledge of age-dependent conversion patterns is required.

3.6 Differential Diagnoses

Imaging assessment of bone metastases is facilitated in the presence of a known primary, pathologic tracer uptake in nuclear medical imaging studies and radiologic findings endorsing diagnosis of malignancy. However, a wide range of focal and diffuse bone marrow alterations of malignant and benign cause, including metabolic and hematologic disorders, may mimick skeletal metastases. A frequent differential diagnosis for focal or multifocal osteolytic lesions is systemic hematological malignancies such as multiple myeloma and lymphoma. A classic benign finding is atypical hemangioma which in many cases can be reliably diagnosed by its classic feature of central trabeculation in MS-CT. Benign bone marrow edema always should be included in the differential as it may show similar hypointense signal patterns in T1-w and hyperintense signal in STIR images. Yet, tumor infiltration often demonstrates stronger, more defined hypointensity on T1-w TSE images compared to bone marrow changes caused by edema. This can be explained by the fact that in edema usually a certain amount of fat cells remains in place.

In the presence of an osteosclerotic focus, benign osteoma or sclerotic bony islands should be considered in the differential. Malignant causes of sclerotic lesions are primary osteoblastic bone tumors and lymphoma. In mixed osteolytic-osteoblastic types malignant lymphoma is the main differential. Again, MS-CT may aid in differentiation.

Finally, in the presence of diffuse bone marrow changes of the osteolytic type an important differential of malignant cause is multiple myeloma. However, benign conditions, such as stimulated hematopoesis in the course of chemotherapy or in chronic bone marrow disorders may mimick appearance of diffuse malignant bone marrow infiltration and hamper diagnosis accurate diagnosis. Furthermore, the diagnostic differentiation to benign senile osteoporosis can be complicated. In case of a diffuse osteosclerotic pattern hematologic disorders such as ostemyelofibrosis (OMF) need to be considered. Table 3 gives an overview of differential diagnoses to bone metastases.

Table 3 Main differential diagnoses of metastatic manifestations in bone marrow

Bone metastases: differential diagnoses
Focal osteoblastic metastases
Multiple myeloma
Lymphoma
Primary osteolytic bone tumors
Atypical hemangioma
Acute Schmorl's nodes
Sarcoidosis
Brown tumor
Histiocytosis
Focal osteoblastic metastases
Lymphoma
Primary osteoblastic bone tumors
Osteoma
CRMO/SAPHO
Haematopoetic islands
Sarcoidosis
Benign notochordial tumor (BNCT)
Diffuse malignant osteoporosis
Senile osteoporosis
Multiple Myeloma
Lymphoma
Mastocytosis
Stimulated hematopoesis
Diffuse osteosclerotic metastases
OMF/OMS
Sarcoidosis
Mastocytosis
osteopetrosis

References

Antoch G, Saoudi N, Kuehl H et al (2004) Accuracy of whole-body dual-modality fluorine-18-2-fluoro-2-deoxy-D-glucose positron emission tomography and computed tomography (FDG-PET/CT) for tumor staging in solid tumors: comparison with CT and PET. J Clin Oncol 22:4357–4368

Baur A, Staebler A, Bartl R, Lamerz R, Scheidler J, Reiser MF (1997) MRI gadolinium enhancement of bone marrow:

age-related changes in normals and diffuse neoplastic infiltration. Skelet Radiol 26:414–418

Baur A, Huber A, Ertl-Wagner B, Dürr R, Zysk S, Arbogast S et al (2001) Diagnostic value of increased diffusion weighting of a steady-state free precession sequence for differentiating acute benign osteoporotic fractures from pathologic vertebral compression fractures. Am J Neuroradiol 22(2):366–372

Baur-Melnyk A, Reiser M (2004) Staging of multiple myeloma with MRI: comparison to MSCT and conventional radiography (in German). Radiologe 44(9):874–881

Brauck K, Zenge MO, Vogt FM et al (2008) Feasibility of whole-body MR with T2- and T1-weighted real-time steady-state free precession sequences during continuous table movement to depict metastases. Radiology 246(3):910–916

Bristow AR, Agrawal A, Evans AJ et al (2008) Can computerised tomography replace bone scintigraphy in detecting bone metastases from breast cancer? a prospective study. Breast 17(1):98–103

Buhmann Kirchhoff S, Becker C, Duerr HR, Reiser M, Baur-Melnyk A (2009) Detection of osseous metastases of the spine: comparison of high resolution multi-detector-CT with MRI. Eur J Radiol 69(3):567–573

Byun WM, Shin SO, Chang Y, Lee SJ, Finsterbusch J, Frahm J (2002) Diffusion-weighted MR imaging of metastatic disease of the spine: assessment of response to therapy. Am J Neuroradiol 23(6):906–912

Castillo M, Malko JA, Hoffman JC (1990) The bright intervertebral disk: an indirect sign of abnormal spinal bone marrow on T1-weighted MR images. Am J Neuroradiol 11: 23–26

Chassang M, Grimaud A, Cucchi JM et al (2007) Can low-dose computed tomographic scan of the spine replace conventional radiography? an evaluation based on imaging myelomas, bone metastases and fractures from osteoporosis. Clin Imaging 31(4):225–227

Cook GJ, Houston S, Rubens R et al (1998) Detection of bone metastases in breast cancer by 18-FDG-PET: differing metabolic activity in osteoblastic and osteolytic lesions. J Clin Oncol 16:3375–3379

Daldrup-Link HE, Franzius C, Link TM et al (2001) Whole-body MR imaging for detection of bone metastases in children and young adults: comparison with skeletal scintigraphy and FDG PET. Am J Roentgenol 177:229–236

Edelstyn GA, Gillespie PJ, Grebbel FS (1967) The radiological demonstration of osseous metastases: experimental observations. Clin Radiol 18:158–162

Engelhard K, Hollenbach HP, Wohlfahrt K, Von Imhoff E, Fellner FA (2004) Comparison of whole-body MRI with automated moving table technique and bone scintigraphy for screening for bone metastases in patients with breast cancer. Eur Radiol 14:99–105

Eustace S, Tello R, DeCarvalho V et al (1997) A comparison of whole-body turbo STIR MR imaging and planar ^{99m}TC-methylene diphosphonate scintigraphy in the examination of patients with suspected skeletal metastases. Am J Roentgenol 169:1655–1661

Even-Sapir E, Metser U, Flusser G, Zuriel L, Kollender Y, Lerman H (2004) Assessment of malignant skeletal disease: initial experience with 18F-fluoride PET/CT and comparison between 18F-fluoride PET and 18F-fluoride PET/CT. J Nucl Med 45:272–278

Fischer MA, Nanz D, Hany T, Reiner CS, Stolzmann P, Donati OF et al (2011) Diagnostic accuracy of whole-body MRI/DWI image fusion for detection of malignant tumours: a comparison with PET/CT. Eur Radiol 21(2):246–255

Fochem K, Ogris E (1976) Early recognition of bone metastases (comparative study between bone scintigraphy and X-ray examination [in German]. Acta Med Austriaca 3(5):170–176

Fogelman I, Cook G, Israel O, Van der Wall H (2005) Positron emission tomography and bone metastases. Sem NuclMed 35:135–142

Goo HW (2010) Whole-body MRI of neuroblastoma. Eur J Radiol 75(3):306–314

Gutzeit A, Doert A, Froehlich JM, Eckhardt BP, Meili A, Scherr P (2009) Comparison of diffusion-weighted whole body MRI and skeletal scintigraphy for the detection of bone metastases in patients with prostate or breast carcinoma. Skeletal Radiol 39:333–343

Krahe T, Nicolas V, Ring S, Warmuth-Metz M, Koster O (1989) Diagnostic evaluation of full X-ray pictures and computed tomography of bone tumors of the spine (in German). Rofo 150(1):13–19

Krishnamurthy GT, Tubis M, Hiss J, Blahd WH (1977) Distribution pattern of metastatic bone disease: a need for total body skeletal image. JAMA 237(23):2504–2506

Kumar J, Seith A, Kumar A, Sharma R et al (2008) Whole-body MR imaging with the use of parallel imaging for the detection of skeletal metastases in pediatric patients with small-cell neoplasms: comparison with skeletal scintigraphy and FDG-PET-CT. Pediatr Radiol 38:953–962

Lauenstein T, Freudenberg L, Goehde S et al (2002) Whole body MRI using a rolling table platform for the detection of bone metastases. Eur Radiol 12:2091–2099

Lecouvet FE, Malghem J, Michaux L, Maldague B, Ferrant A, Michaux JL et al (1999) Skeletal survey in advanced multiple myeloma: radiographic versus MR imaging survey. Br J Haematol 106(1):35–39

Metser U, Lerman H, Blank A, Lievshitz G, Bokstein F, Even-Sapir E (2004) Malignant involvement of the spine: assessment by 18FDGPET-CT. J Nucl Med 45:279–284

Mulkens TH, Bellinck P, Baeyaert M et al (2005) Use of an automatic exposure control mechanism for dose optimization in multi-detector row CT examinations: clinical evaluation. Radiology 237(1):213–223

Poitout D, Gaujoux G, Lempidakis M et al (1991) X-ray computed tomography or MRI in the assessment of bone tumor extension (in French). Chirurgie 117(5–6):488–490

Prior JO, Barghouth G, Delaloye JF, Leyvraz S, Bischof Delaloye A (2003) The value of bone marrow scintigraphy using ^{99m}Tc monoclonal antigranulocyte antibodies in complement to bone scintigraphy in detecting bone metastases from primary breast cancer. Nucl Med Commun 24(1):29–36

Reske SN, Kotzerke J (2001) FDG-PET for clinical use: results of the 3rd German interdisciplinary consensus conference. Eur J Nucl Med 28:1707–1723

Roberts JG, Gravelle IH, Baum M, Bligh AS, Leach KG, Hughes LE (1976) Evaluation of radiography and isotopic scintigraphy for detecting skeletal metastases in breast cancer. Lancet 1(7953):237–239

Rubens RD (1998) Bone metastases: the clinical problem. Eur J Cancer 34:210–213

Schmidt GP, Wintersperger B, Graser A, Baur-Melnyk A, Reiser MF, Schoenberg SO (2007) High-resolution whole-body magnetic resonance imaging applications at 1.5 and 3 Tesla: a comparative study. Invest Radiol 42(6):449–459

Schmidt GP, Schoenberg SO, Schmid R et al (2007b) Screening for bone metastases: whole-body MRI using a 32-channel system versus dual-modality PET-CT. Eur Radiol 17(4): 939–949

Shie P, Cardarelli R, Brandon D, Erdman W, Abdulrahim N (2008) Meta-analysis: comparison of F-18 fluorodeoxyglucosepositron emission tomography and bone scintigraphy in the detection of bone metastases in patients with breast cancer. Clin Nucl Med 33(2):97–101

Steinborn M, Heuck AF, Tiling R, Bruegel M, Gauger L, Reiser MF (1999) Whole body bone marrow MRI in patients with metastatic disease to the skeletal system. J Comput Assist Tomogr 23:123–129

Takahara T, Imay Y, Yamashita T et al (2004) Diffusion weighted whole body imaging with background body signal suppression (DWIBS): technical improvement using free breathing, STIR and high resolution 3D display. Radiat Med 22:275Y282

Taneichi H, Kaneda K, Takeda N, Abumi K, Satoh S (1997) Risk factors and probability of vertebral body collapse in metastases of the thoracic and lumbar spine. Spine (Phila Pa 1976) 22(3):239–245

Vanel D, Bittoun J, Tardivon A (1998) MRI of bone metastases. Eur Radiol 8:1345–1351

Walker R, Kessar P, Blanchard R et al (2000) Turbo STIR magnetic resonance imaging as a whole-body screening tool for metastases in patients with breast carcinoma: preliminary clinical experience. J Magn Reson Imaging 11:343–350

Weckbach S, Michaely HJ, Stemmer A, Schoenberg SO, Dinter DJ (2010) Comparison of a new whole-body continuous-table-movement protocol versus a standard whole-body MR protocol for the assessment of multiple myeloma. Eur Radiol 20(12):2907–2916

Multiple Myeloma

Andrea Baur-Melnyk and Melvin D'Anastasi

Contents

A. Baur-Melnyk (✉) · M. D'Anastasi
Institut für Klinische Radiologie,
Klinikum der Universität München-Großhadern,
Marchioninistraße 15, 81377, München, Germany
e-mail: Andrea.Baur@med.uni-muenchen.de

Abstract

Multiple myeloma is a malignant bone marrow neoplasia in which a monoclonal strain of atypical plasma cells proliferates and typically secretes paraproteins. It typically affects the elderly population with a peak incidence in the eighth decade. The atypical plasma cells are distributed in the bone marrow either focally or in a diffuse manner and may result in bone destruction, but may also occur in soft tissue. Bone marrow aspirates or bone marrow biopsies are essential for the diagnosis. Due to various therapeutic options and the large variability in survival, the sensitive detection of myeloma involvement of the skeleton is mandatory to enable accurate disease staging. Various imaging methods are employed in assessing the disease burden in multiple myeloma. The following chapter reviews the findings in multiple myeloma in conventional radiography, computed tomography (CT), positron-emission tomography (PET)/CT, and magnetic resonance imaging (MRI) and compares the various methods. Whole-body MRI is superior to the skeletal survey and whole-body multidetector CT (MDCT). On the other hand, MDCT is the method of choice for displaying osteolytic lesions and determining fracture risk. PET-CT has a high sensitivity and specificity in detecting myeloma involvement and has been shown to be more sensitive than other modalities for detecting extramedullary sites of disease.

A. Baur-Melnyk (ed.), *Magnetic Resonance Imaging of the Bone Marrow*, Medical Radiology. Diagnostic Imaging,
DOI: 10.1007/174_2011_443, © Springer-Verlag Berlin Heidelberg 2013

The increased sensitivity of these imaging techniques has led to further refinement of the classic Durie and Salmon staging system. We review the role of the various imaging methods in the staging, assessment of prognosis, and evaluation of relapse/response to therapy in multiple myeloma. Knowledge of the use and limitations of the various imaging modalities, imaging findings, staging, and treatment-related changes is essential for the accurate assessment of the disease burden in multiple myeloma by the radiologist.

1 Epidemiology and Clinical Background

Multiple myeloma accounts for about 10% of all haematological malignancies. The incidence of multiple myeloma in Europe is 4.5–6.0/100,000/year with a median age at diagnosis of between 63 and 70 years; the mortality is 4.1/100,000/year (Harousseau and Dreyling 2010). The disease has a higher incidence in men and in the black population.

Multiple myeloma represents a clonal B-lymphocyte neoplasm of terminally differentiated plasma cells. The cause of multiple myeloma remains still unclear. A higher risk was recognized after high or long-term radiation exposure, in animal farm workers, exposure to diverse chemical dust or gas and long-term exposure to electromagnetic waves (especially radar workers (Durie 2001)).

Clinical presentation is mostly uncharacteristic. It includes weakness, nausea and weight loss. In some cases the disease is diagnosed by chance in a laboratory screening due to increased ESR and anaemia. Further laboratory diagnostic work-up includes immune electrophoresis and urine examination for Bence Jones protein content. The monoclonal strain of atypical plasma cells in the bone marrow typically secretes paraproteins, consisting of two heavy and two light chains. According to the heavy chains, the type of myeloma is characterized by IgG (60%), IgA (25%) or rarely IgD and IgE. The myeloma cells also express light chains of lambda or kappa type. The paraproteins are detected in serum electrophoresis by a high peak in the alpha or gamma region. In Bence Jones myeloma (20%) only light chains are secreted, which can be detected in urine electrophoresis. In non-secretory myeloma (rare) no paraproteins are produced.

The myeloma cells displace normal haematopoiesis in the bone marrow, resulting in anaemia, leukopenia and thrombocytopenia. Renal insufficiency and hypercalcemia are signs of progressive disease. Osteolytic lesions can cause localized bone pain. Vertebral fractures with cord compression can cause neurological impairment.

For the diagnosis "multiple myeloma" three criteria have to be fulfilled: $\geq$10% atypical plasma cells in the bone marrow and/or the presence of biopsy-proven plasmacytoma, monoclonal paraprotein present in the serum and/or urine and myeloma related organ dysfunction (hypercalcemia, renal insufficiency, anaemia, lytic bone lesions) (Durie et al. 2003).

2 Genetic Classification and Genetic Prognostic Factors

Several subtypes of the disease have been identified at the genetic and molecular level, which have been associated with unique clinico-pathological features and different outcomes.

Overall, the disease may be classified into two major categories; hyperdiploid MM (h-MM) (with numerous chromosomal trisomies and a low prevalence of IgH translocations) and non-hyperdiploid MM (nh-MM) (hypodiploid, pseudodiploid and near tetraploid MM, and highly enriched for IgH translocations). The three main IgH translocations in myeloma are the t(11;14)(q13;q32), t(4;14)(p16;q32) and t(14;16)(q32;q23). Several genetic progression factors have been identified including deletions of chromosomes 13 and 17 and abnormalities of chromosome 1. Patients with h-MM tend to have a better outcome, to be older patients with a slight male preponderance and to have a higher incidence of multiple myeloma bone disease. In 2009 the International Myeloma Working Group proposed a new molecular cytogenetic classification with classification into further subcategories (Fonseca et al. 2009).

The guidelines of the International Myeloma Workshop Consensus Panel (2011) recommend the inclusion of standard metaphase cytogenetics and fluorescent in situ hybridisation (FISH) in the initial assessment of a patient with high suspicion of

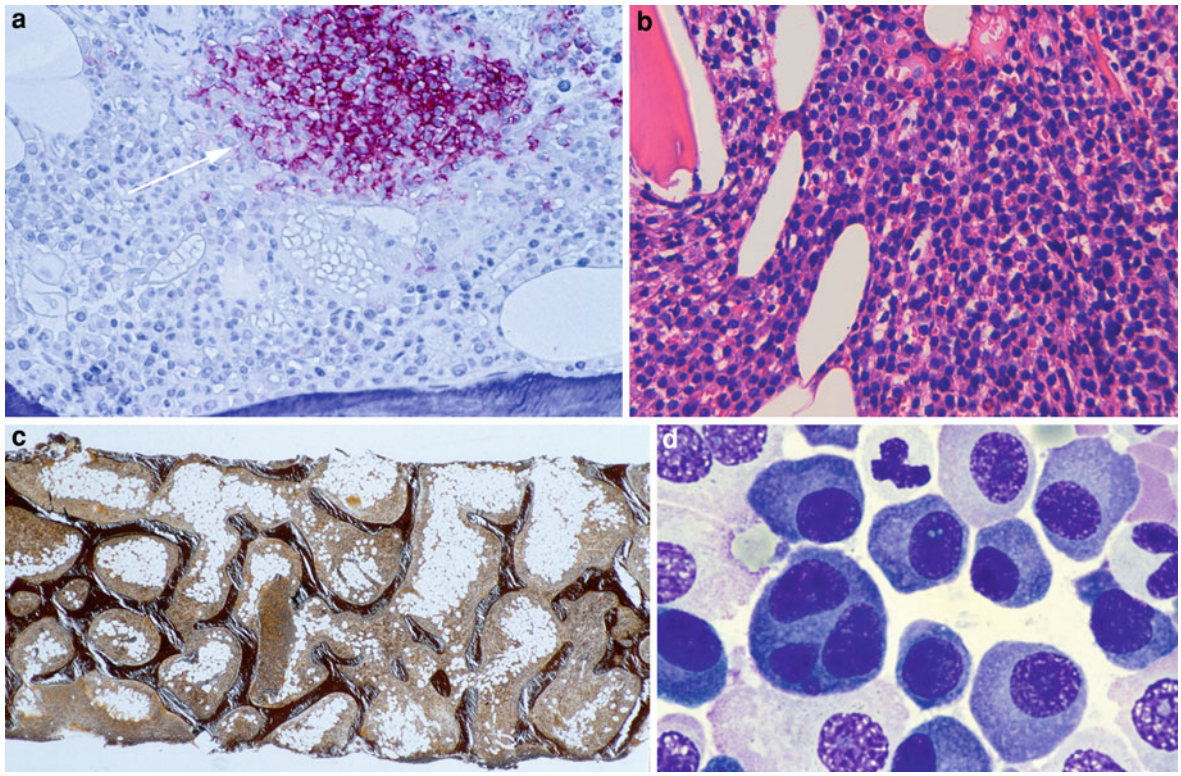

Fig. 1 Bone marrow biopsies and aspirate from the iliac crest in patients with multiple myeloma **a** (immunohistology, ×100) showing strictly nodular infiltration of plasma cells in the bone marrow (arrow), (*Courtesy Prof. R Bartl*, *Munich*). **b** (H&E, ×250) showing a diffuse infiltration of myeloma cells (*Courtesy*: *Dr. C. Weiler*, *Munich*) **c** (Gomori, ×20) showing a salt and pepper infiltration pattern with central areas of fat cells surrounded by myeloma cells in the paratrabecular region (*Courtesy*: *Prof. R. Bartl*, *Munich*) **d** (Giemsa, ×1000) showing atypical plasma cells with variations in cell size and nuclear size and shape with marked nucleoli and multinuclearity (*Courtesy*: *Prof. R. Bartl*, *Munich*)

multiple myeloma as these may provide useful prognostic information (Dimopoulos et al. 2011).

3 Histology

Bone marrow biopsy or bone marrow aspirate is essential for the diagnosis of multiple myeloma (Malpas 1998) (Fig. 1). Multiple myeloma is a disease of terminally differentiated B-lymphocytes. Different cell types, according to the stage of dedifferentiation, have been described (Marschalko type, small cell type, cleaved type, polymorphous type, synchronous type, blastic types) (Bartl 1988). At an initial stage it may be difficult to distinguish multiple myeloma from reactive plasmacytosis. An increase of the nuclear-cytoplasmic ratio and an atypical nuclear configuration are helpful signs for malignancy. The distribution of plasma cells in the marrow is also important. In reactive plasmacytosis the plasma cells are distributed along vessels whereas in multiple myeloma they are interstitially or focally distributed. In many institutions bone marrow biopsies are favoured over bone marrow aspirates due to the methodological problems of aspirates. In addition, in bone marrow biopsies quantification of bone marrow plasmacytosis is more reliable (Terpstra et al. 1992). Hematopoiesis is reduced through direct displacement by myeloma cells and indirect displacement via hematopoiesis-inhibiting cytokines. In early stages bone marrow fat can be increased, in more advanced disease fatty components in the marrow as well as hematopoiesis are displaced. Osteoclast-activating factors in combination with osteoblast-inhibiting factors lead to osteoporosis and osteolytic destructions.

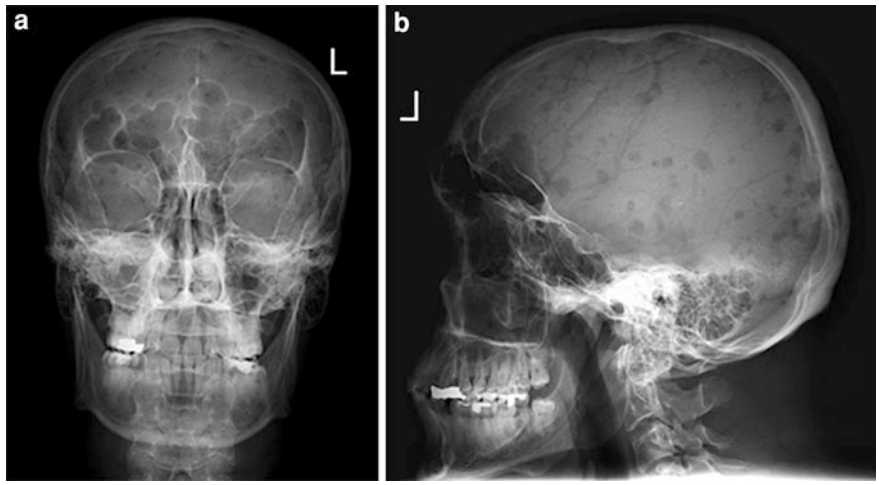

Fig. 2 A 39-year-old male with multiple myeloma. A.P. (**a**) and lateral (**b**) radiographs of the skull showing multiple punched-out lesions

4 Findings in Radiographs and Computed Tomography (CT)

4.1 Radiographs

The standard imaging technique in patients with multiple myeloma is the skeletal survey including radiographs in two planes of the skull, the spine, the upper arms, the pelvis, the rib cage and the upper legs. These skeletal regions represent the normal distribution of active red marrow in adults. Predilection sites are the axial skeleton (spine and pelvis) but also the ribs, the shoulder region, the skull and the proximal femora. The appearance of multiple myeloma in X-rays is of either focal circumscribed "punched-out" osteolytic lesions or diffuse inhomogeneous osteoporosis, especially in the spine (Carson et al. 1955; Heiser and Schwartzman 1952; Meszaros 1974) (Figs. 14a, 16a). In the skull multiple lytic lesions of similar size are found (Fig. 2). In the long bones lytic lesions are usually centrally located. With increase in size they lead to endosteal scalloping of the cortex (Figs. 3, 4). Sometimes large osteolytic lesions penetrate the cortex and demonstrate a soft-tissue component. They can lead to an expansion of bone with a soap bubble appearance. Affection of the ribs is usually present as lytic lesions or an inhomogeneous appearance of the spongiosa in combination with a circumscribed expansion of the bone. The differentiation of multiple myeloma from metastatic skeletal disease is not possible without the knowledge of laboratory parameters.

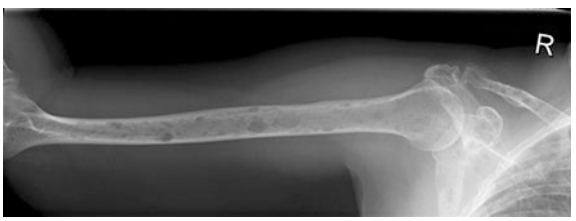

Fig. 3 A 66-year-old female with multiple myeloma. Lateral X-ray of the right humerus and shoulder showing multiple osteolytic lesions of the humerus with mild cortical scalloping. Osteolytic lesions of the clavicle and scapula as well as rib fractures are also visible

Rarely sclerotic lesions or lytic lesions with a sclerotic rim have been reported (Grover and Dhar 2000). Primary diffuse sclerosis of the skeleton in multiple myeloma accounts for less than 3% of cases. This appears more often after therapy, although rare. Differential diagnoses in these cases include osteoblastic metastases, myelofibrosis, lymphoma, renal osteodystrophy and mastocytosis (Grover and Dhar 2000; Hall and Gore 1988).

Diffuse osteoporosis due to myeloma infiltration is difficult to distinguish from postmenopausal or senile osteoporosis. This is also true for vertebral fractures. Both osteoporotic fractures as well as neoplastic fractures are common in this patient group. In addition, the combination of the age of the patients and cortisone therapy favours osteopenia. In such cases MRI can help in the differential diagnosis.

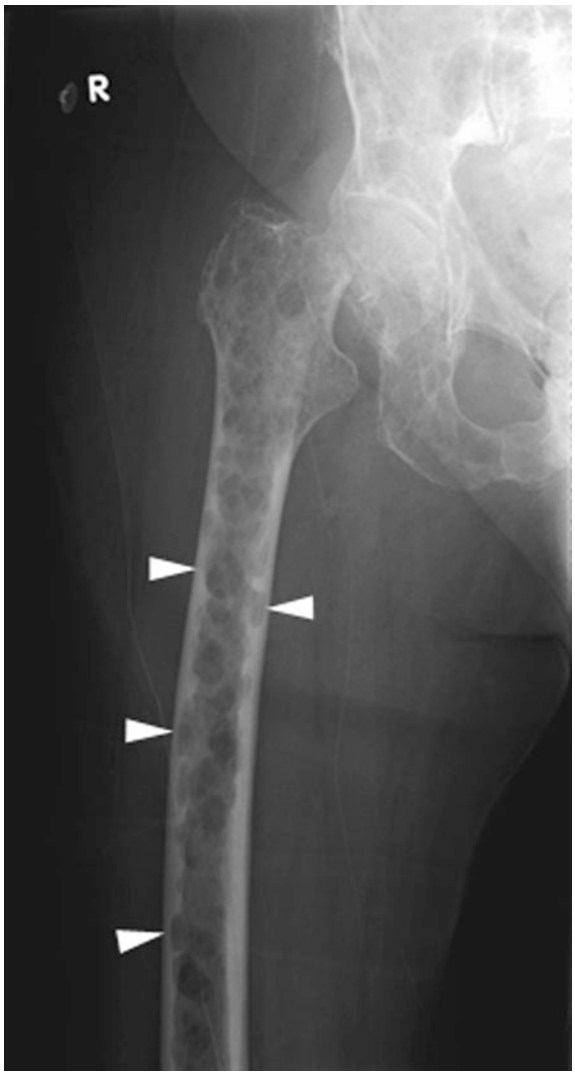

Fig. 4 A 79-year-old female with IgG multiple myeloma. A.p. view of the right femur showing multiple osteolytic lesions with a pathological fracture of the femoral neck. There is extensive scalloping (*arrowheads*) of the femoral cortex. Also seen are diffuse osteolytic lesions of the right hemipelvis

4.2 Computed Tomography-CT

Multidetector-CT is the method of choice for evaluation of the presence of osteolytic lesions or fracture risk. Whole-body MDCT is now often used instead of the radiographic skeletal survey, since the sensitivity is higher and examination time is reduced to 1–2 min with MDCT-scanners. At least a 16-row scanner is necessary. Primarily the tumour infiltrates the bone marrow. Complex biochemical mechanisms and the secretion of osteoclast activating factors lead to bony destructions. Osteolytic lesions in multiple myeloma are usually well circumscribed and have a small zone of transition (Figs. 5, 6, 7). They usually show attenuation values of soft-tissue density (~40–80 Hounsfield units (HU)). Osteolytic lesions are primarily situated within the trabecular bone. In case of enlargement of the focally growing tumour they can lead to cortical destructions and large soft-tissue masses (Fig. 12). In the skull the lytic lesions are punched-out lesions, which are situated within the tabula externa and interna (Figs. 2, 8). In the diaphyses of the long tubular bones, where only sparse trabecular bone is present, early lytic lesions may be missed when reading the images solely in bone window. Circumscribed soft-tissue alterations within the normal fatty marrow (negative HUs) are highly suspicious of myeloma lesions. Comparison to the other side may be helpful in evaluating marrow involvement (Fig. 9). Cortical scalloping in the long bones may be visible on axial or reformatted coronal or sagittal planes. Rib lesions are often overlooked since the ribs are small structures and signs of involvement may be subtle. Focal enlargement of the rib with soft-tissue density within the lesion accounts for myeloma involvement (Fig. 7). The cortex may be normal or thinned. If the tumour continues to grow a pathological fracture will result. Careful examination with scrolling back and forth at every rib level is necessary to avoid overlooking lesions. The shoulder girdle with its complex structures (acromion, coracoid process etc.) is another predilection site.

In cases with diffuse bone marrow infiltration inhomogeneous osteoporosis can be detected with MDCT. However, like in the radiographic skeletal survey, this is often hard to distinguish from senile or post-menopausal osteoporosis.

Extraosseous Manifestations

Extraosseous manifestations of multiple myeloma may occur and can affect virtually any organ. The imaging findings are non-specific and can mimic other disorders. Common imaging features include soft-tissue masses with homogenous attenuation on CT (Fig. 10), absence of necrosis or calcification, low T2 signal on MRI due to high cellularity, and FDG-uptake on FDG-PET (Hall et al. 2010).

In a recent study by Varettoni et al. involving an analysis of 1003 multiple myeloma patients, 13% of

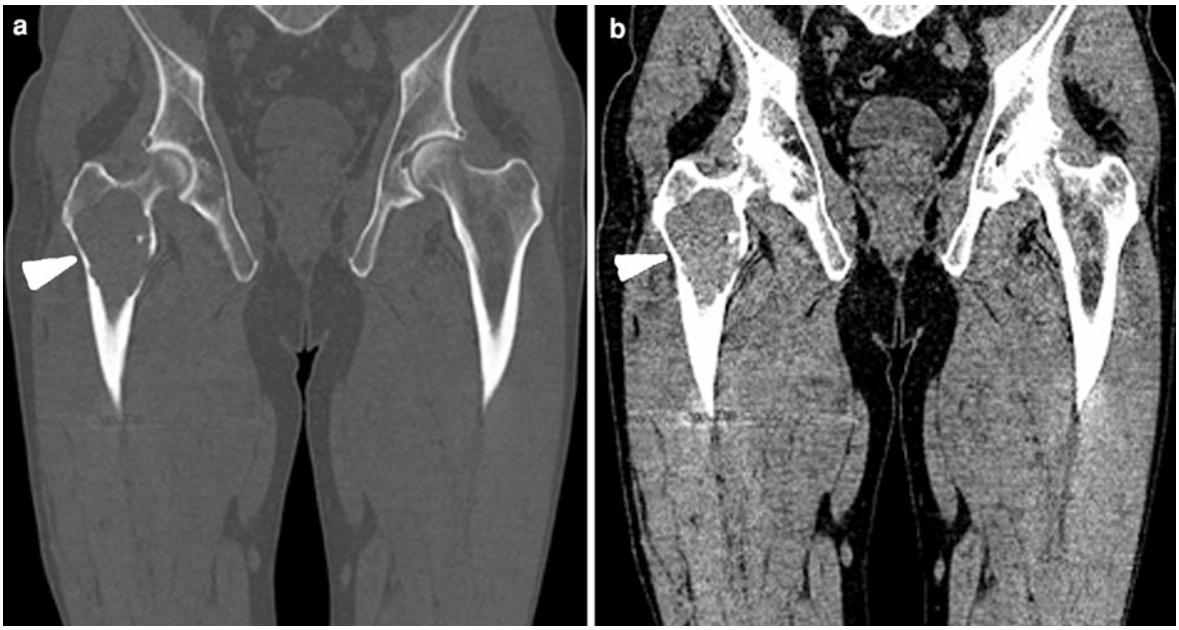

Fig. 5 A 72-year-old male with multiple myeloma. Coronal CT images of the lower pelvis and proximal femora in (**a**) bone window and (**b**) soft-tissue window, showing a large osteolytic lesion of the right proximal femur (*arrowheads*) with significant cortical thinning and a break in the continuity of the cortex medially. The lesion has soft-tissue equivalent attenuation values

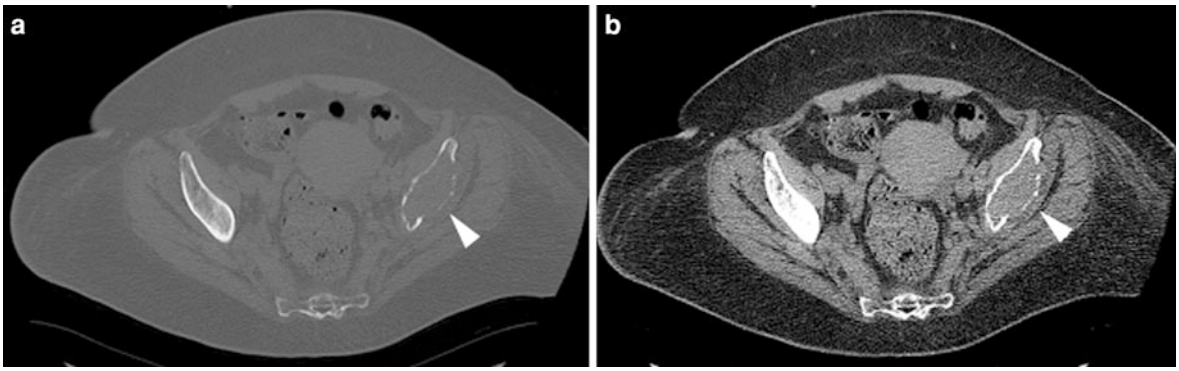

Fig. 6 Large osteolytic lesion of the left iliac bone shown in bone window (**a**) and in soft tissue window (**b**) with cortical thinning and destruction of the lateral cortex

patients were found to have extramedullary disease. In 85% of cases soft tissues surrounding the axial skeleton were involved. Plasmacytomas of lymph nodes, liver, kidney, airways, skin and breast accounted for 15% of cases. Extramedullary disease was associated with shorter overall and progression-free survival (Varettoni et al. 2010). Because of its prognostic significance, the presence of extraosseous myeloma has been integrated in the Durie and Salmon PLUS Staging System (Table 2) (Durie 2006).

5 Findings in Scintigraphy and PET-CT

5.1 Scintigraphy

Multiple myeloma is a neoplasm which primarily produces osteolytic lesions. Detection of bony involvement with Technetium 99-m bone scanning relies on an osteoblastic response of the skeletal

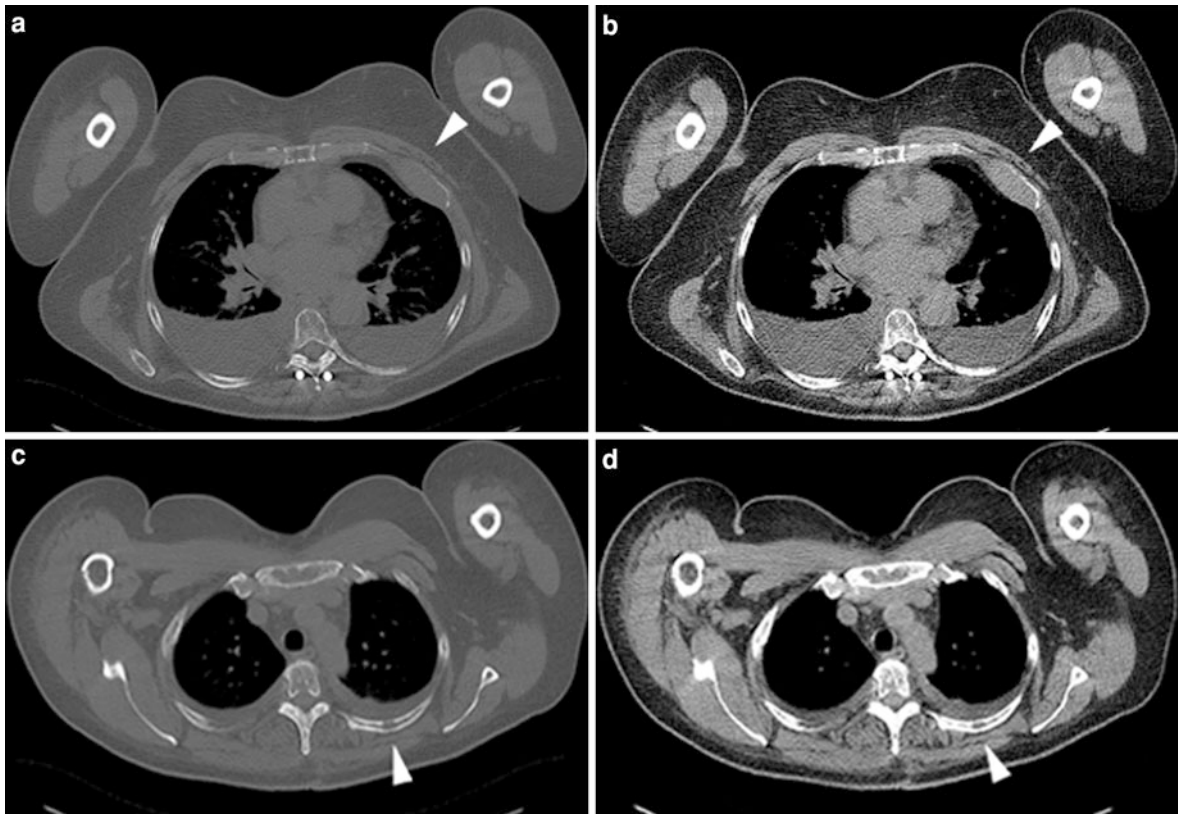

Fig. 7 Osteolytic lesions of the ribs in a 48-year-old female patient with multiple myeloma. (**a**) axial CT image in bone window and in soft-tissue window (**b**) showing a large osteolytic expansile lesion of the ventral 4th left rib. Also shown are osteolytic lesions of the sternum and the 7th vertebral body. (**c**) axial CT image in bone window of the same patient showing a small osteolytic lesion of the right dorsal 4th rib with focal expansion. Also shown are osteolytic lesions of the 4th thoracic vertebra and sternum

system. This results in an under appreciation of the extent of the disease and is not recommended for the diagnostic work-up in patients with multiple myeloma (Scutellari et al. 1985; Woolfenden et al. 1980).

5.2 PET/CT

Efforts have been made towards direct imaging of tumour cells with FDG-PET. Active lesions at FDG PET/CT show FDG-uptake which is greater than the background level (Schirrmeister et al. 2002; Durie et al. 2002; Bredella et al. 2005) (Figs. 11, 12). Schirrmeister et al. (2002) examined 28 patients with multiple myeloma and 15 patients with solitary plasmacytoma of bone. Focally increased tracer uptake was observed in 38 out of 41 known osteolytic bone lesions. A total of 71 further bone lesions were detected which were negative on X-rays. As a result of FDG-PET imaging clinical management was influenced in five patients. FDG-PET proved to be superior to X-ray diagnostics and contributed to staging. In a study by Durie and coworkers, 16 previously untreated patients with multiple myeloma had positive FDG scans, either focally or diffuse. Four of them had negative X-rays and in further four patients extramedullary disease was detected (Durie et al. 2002). In a study of Bredella et al. (2005) including 13 patients, the sensitivity of FDG-PET in detecting myeloma involvement was 85% and specificity was 92%. PET/CT studies have also been shown to be more sensitive than other imaging modalities for localising extramedullary sites of disease (Dimopoulos et al. 2009). In another study by Schirrmeister and colleagues, 33% of patients with extramedullary

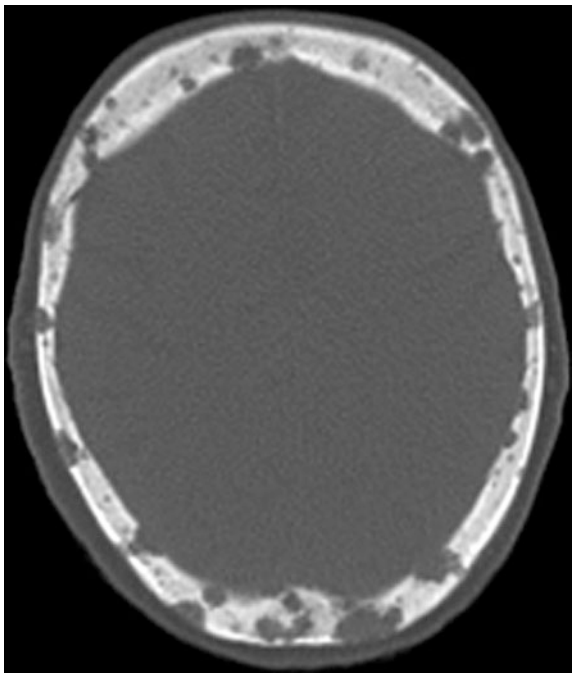

Fig. 8 A 79-year-old female with IgG MM. Axial CT image of the skull in bone window shows multiple punched-out lesions

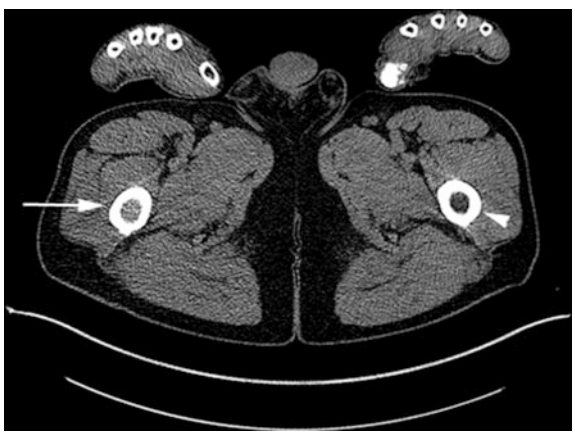

Fig. 9 A 72-year-old male with multiple myeloma. Axial CT image showing the proximal femora in soft-tissue window. There is bone marrow infiltration in the right proximal femur (*arrow*) with positive attenuation values, as opposed to the left femoral marrow (*arrowhead*) with negative attenuation values

plasmacytoma had additional disease sites discovered with PET imaging that led to management changes in 27% of the patients (Schirrmeister et al. 2003). In a

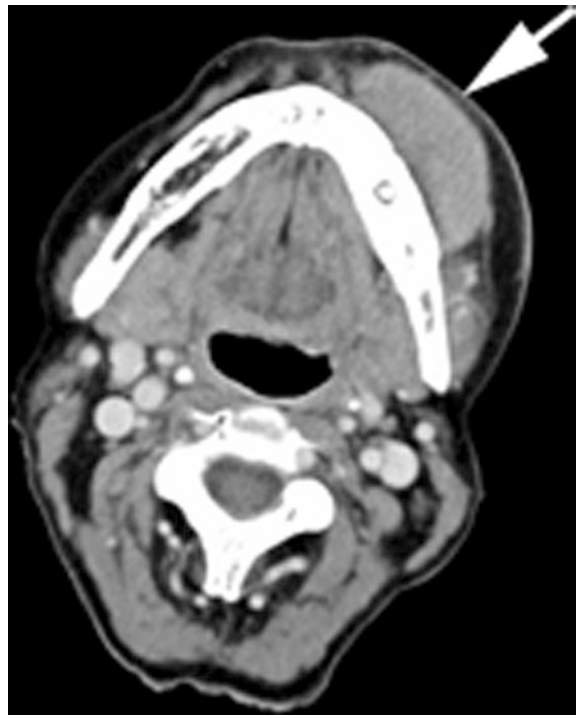

Fig. 10 Extraosseous manifestation in a 69-year-old female with known multiple myeloma. The patient presented with an enlarging soft-tissue mass in the left cheek and left facial nerve palsy. Contrast-enhanced CT image in soft-tissue window shows a soft tissue mass with homogeneous contrast-enhancement anterior to the left mandible (*arrow*)

further recent study involving patients with presumed solitary plasmacytoma of bone, PET-CT allowed the detection of other unsuspected sites of involvement, upstaging the extent of disease (Nanni et al. 2008).

PET/CT is reliable for most bone lesions with a minimum diameter of 1 cm using a standard SUV cut-off of 2.5 to indicate the presence of disease (Dimopoulos et al. 2009). For lesions smaller than 5 mm in diameter it has been suggested that any amount of FDG uptake should be considered positive, regardless of SUV. Lesions between 5 and 10 mm are considered indeterminate if the SUV is less than 2.5 (Dimopoulos et al. 2009).

6 Findings in MRI

Multiple myeloma is a primary disease of the bone marrow. Therefore it affects primarily the bone marrow and secondly the bone itself in terms of osseous

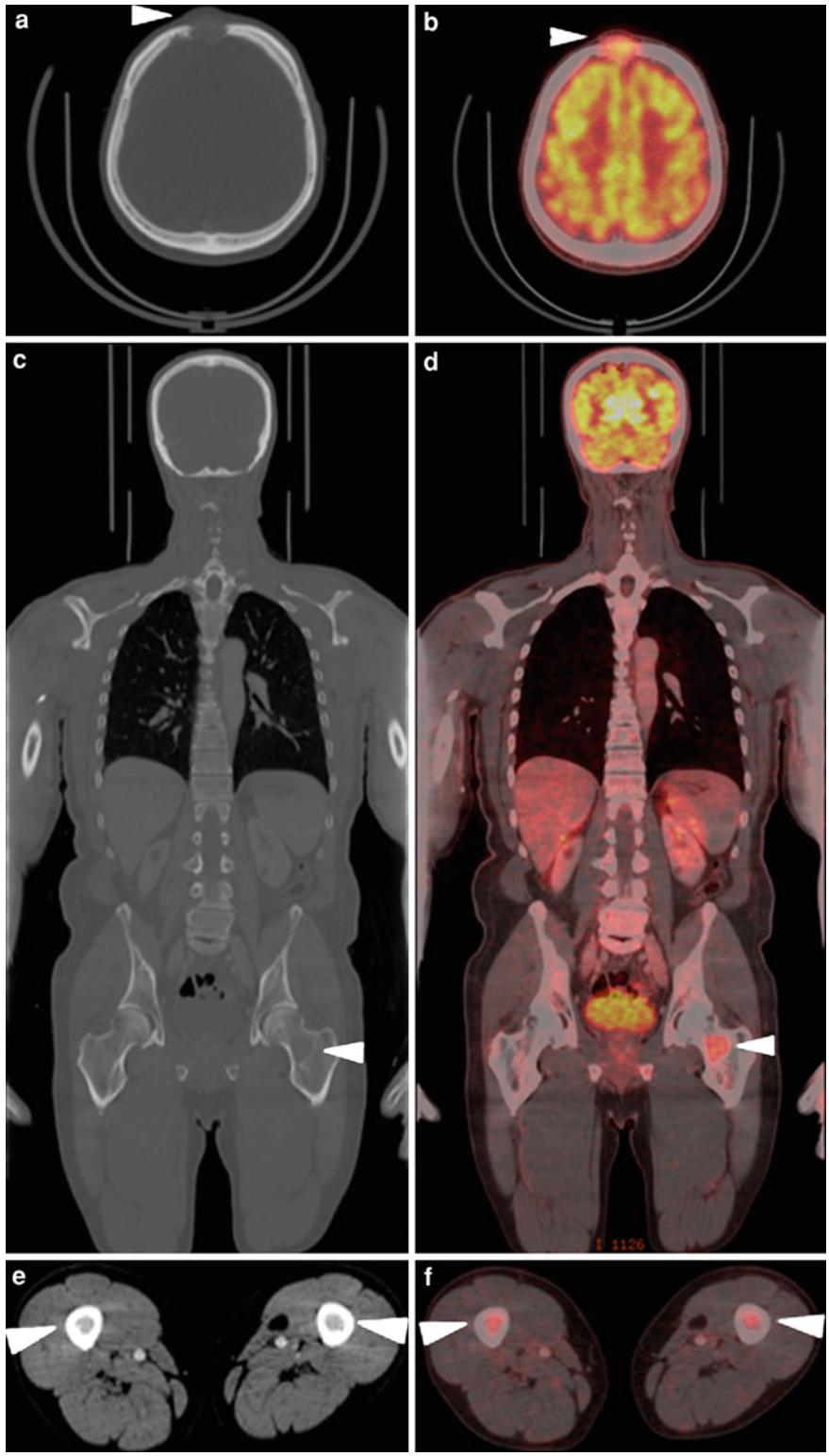

Fig. 11 A 68-year-old male with multiple myeloma with IgA-lambda paraproteinaemia. (**a**, **c**, **e**) CT images in bone-window showing (**a**) an osteolytic lesion of the frontal bone of the skull (*arrowhead*), (**c**) an osteolytic lesion in the left femoral neck (*arrowhead*), (**e**) infiltration of the femoral bone marrow on both sides (*arrowheads*) (with positive soft-tissue equivalent attenuation values). (**b**, **d**, **f**) Fused FDG/PET-CT images showing increased FDG-uptake at the sites of involvement (*arrowheads*)

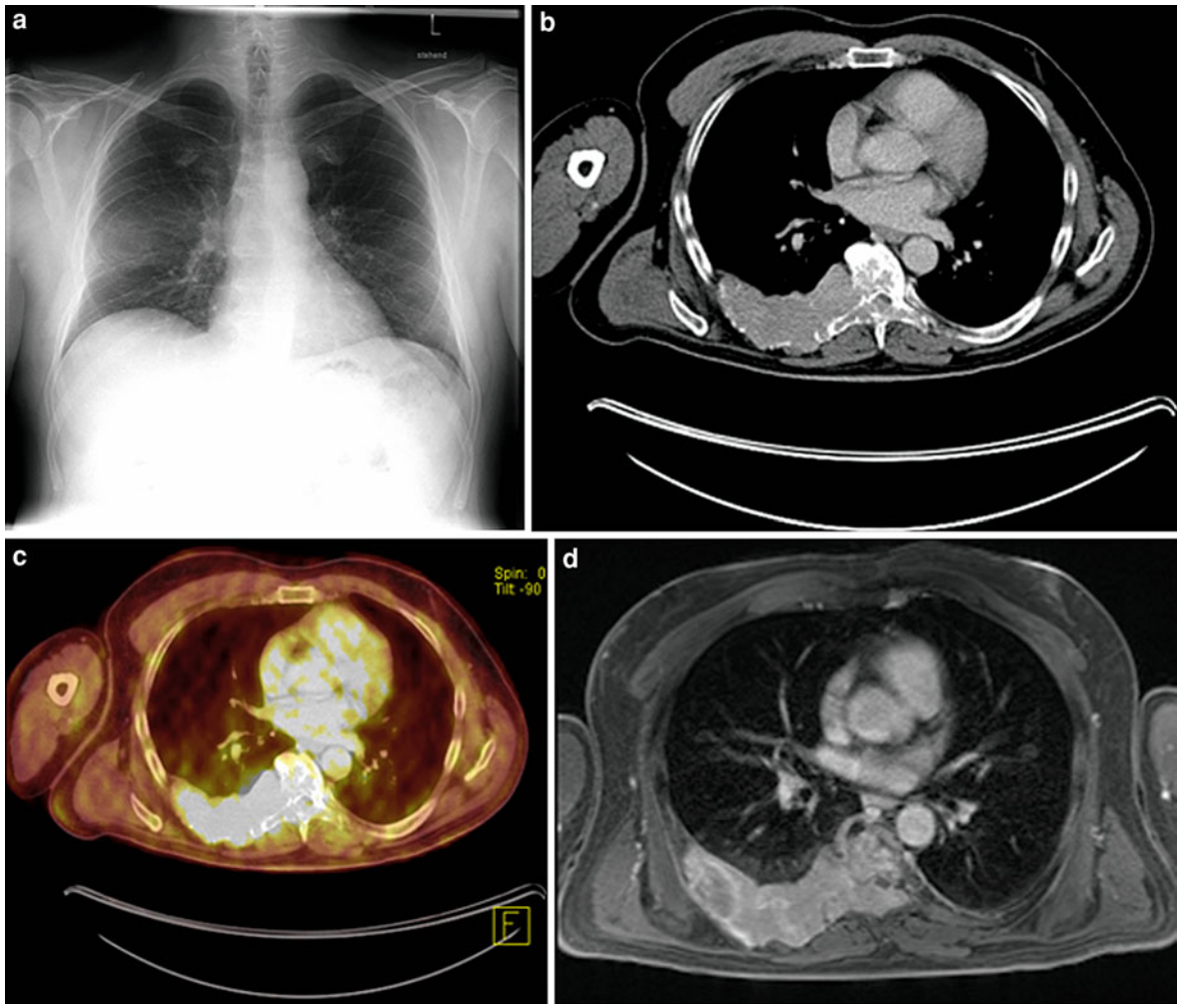

Fig. 12 A 56-year-old male with IgA Kappa Multiple Myeloma. **a** P.A. chest X-ray showing an opacity in the right middle lung field with destruction of the 7th rib. **b** Contrast-enhanced axial CT image of the chest (soft-tissue window) showing a large right paravertebral soft tissue mass at level of T6 and T7 with infiltration of the vertebral bodies and destruction of the 7th rib as well as infiltration of the spinal canal. **c** Fused axial FDG-PET/CT image showing markedly increased FDG-uptake by the paravertebral mass. **d** Axial contrast-enhanced T1 VIBE image showing the paravertebral soft tissue mass, infiltration of T7 as well as infiltration of the spinal canal

destructions. With radiography and CT the bone is visualized. With MRI, the primary site of involvement, the bone marrow is displayed (Fig. 13).

In patients with multiple myeloma five different infiltration patterns can be described in MRI (Baur et al. 1996).

First, in 28% of the patients a *normal looking bone marrow signal* is found in all sequences with high signal on T1-weighted and intermediate signal intensity on T2-weighted spin-echo images as well as low signal in fat-saturated sequences, such as STIR. In histology this corresponds to a slight interstitial plasma cell infiltration (<20 Vol% in bone marrow biopsy). Normal bone marrow signal in MRI do not exclude the diagnosis of multiple myeloma (Algra et al. 1991; Carlson et al. 1995; Avrahami et al. 1993; Fruehwald et al. 1988). However, those patients are eligible to a "watch and wait" strategy.

Second, *focal myeloma infiltration* can be found in about 30% of cases (Fig. 14). Circumscribed areas of high signal intensity can be identified on gradient echo and fat saturated sequences, such as STIR

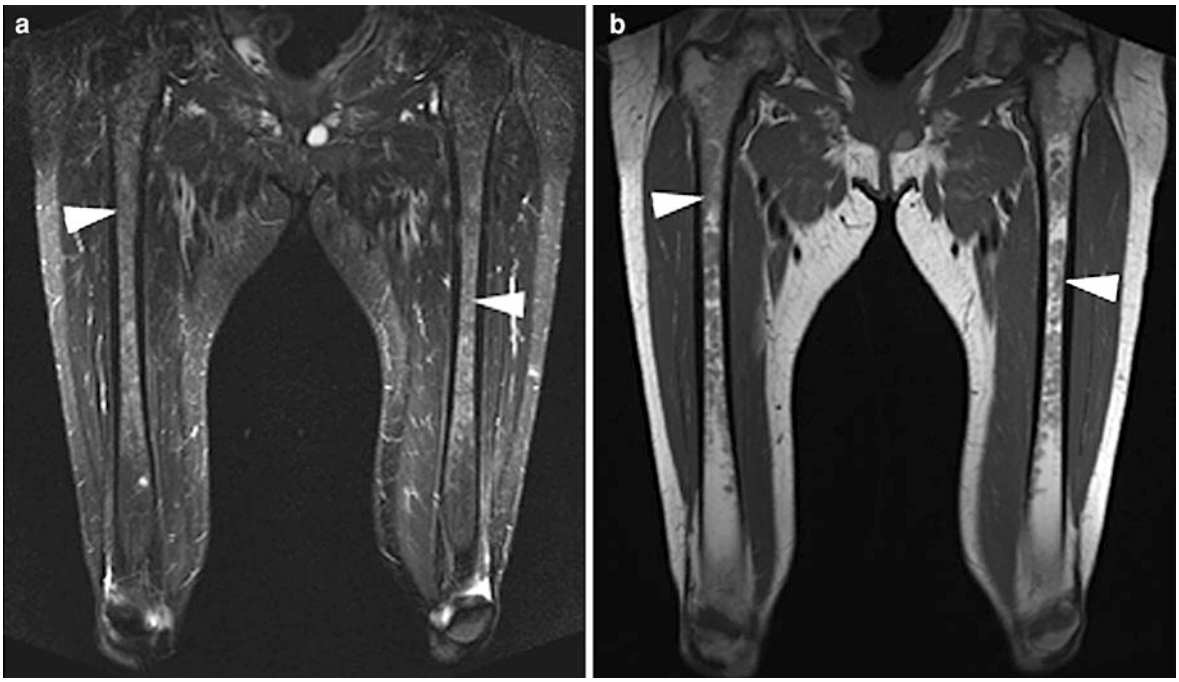

Fig. 13 A 63-year-old female with IgG Kappa MM. Coronal STIR **a** image shows diffusely increased signal intensity of the femoral bone marrow on both sides. Coronal T1-w SE image **b** shows corresponding areas of diffusely decreased signal intensity

images. These correspond to areas of low signal intensity on unenhanced T1-weighted SE images. In a few cases isointense signal is found on T1-weighted SE images (Rahmouni et al. 1993a). Due to the high signal intensity of normal fat-containing marrow on T2-weighted Turbo spin echo sequences there is mostly no contrast to the focal infiltrates by myeloma, which are also hyperintense (Dohner et al. 1989). Focal myeloma infiltrations were depicted with highest sensitivity when using fat-suppressed pulse sequences (Avrahami et al. 1993; Rahmouni et al. 1993a; Baur et al. 1998). Two principal methods exist: a frequency-selective fat-saturation such as a STIR or sequences with spectral fat-saturation. In our investigations STIR sequences compared favourably with spectral fat saturation because of a homogeneous fat-saturation in large fields of views (250 × 500 mm). Some authors employed chemical shift imaging by using opposed phased gradient echo sequences. By means of opposed phasing of fat-, and respectively water-bound protons in normal bone marrow, multiple myeloma infiltrations are displayed as areas with high signal intensity (Algra et al. 1991; Avrahami et al. 1993; Stabler et al. 1996; Daffner et al. 1986). A greater sensitivity was found for contrast-enhanced, shifted-phase gradient echo sequences in comparison to unenhanced images in one study (Hosten et al. 1992).

Third, *diffuse bone marrow infiltration* is characterized by a homogeneous decrease of signal on T1-weighted SE images and increased signal intensity on fat-suppressed images (Fig. 15). In cases of high-grade diffuse involvement (>50 Vol% in bone marrow biopsy) the signal intensity is nearly equal to the signal intensity of the intervertebral disc or muscle on T1-weighted SE images due to the increase of water and decrease of fatty components (Fig. 15). In cases of intermediate grade of involvement in biopsy (20–50 Vol%) the signal reduction is only moderate and often hard to diagnose (Baur et al. 1997). In those cases intravenous injection of gadolinium-chelates is recommended to verify diffuse involvement. Based on the results of a control cohort the corresponding enhancement of normal bone marrow showed great variations between 3 and 40%, mean 17%, age >40 years). However, if the percentage increase of signal exceeds the limit of 40%, this can be considered as pathologic (Baur et al. 2004).

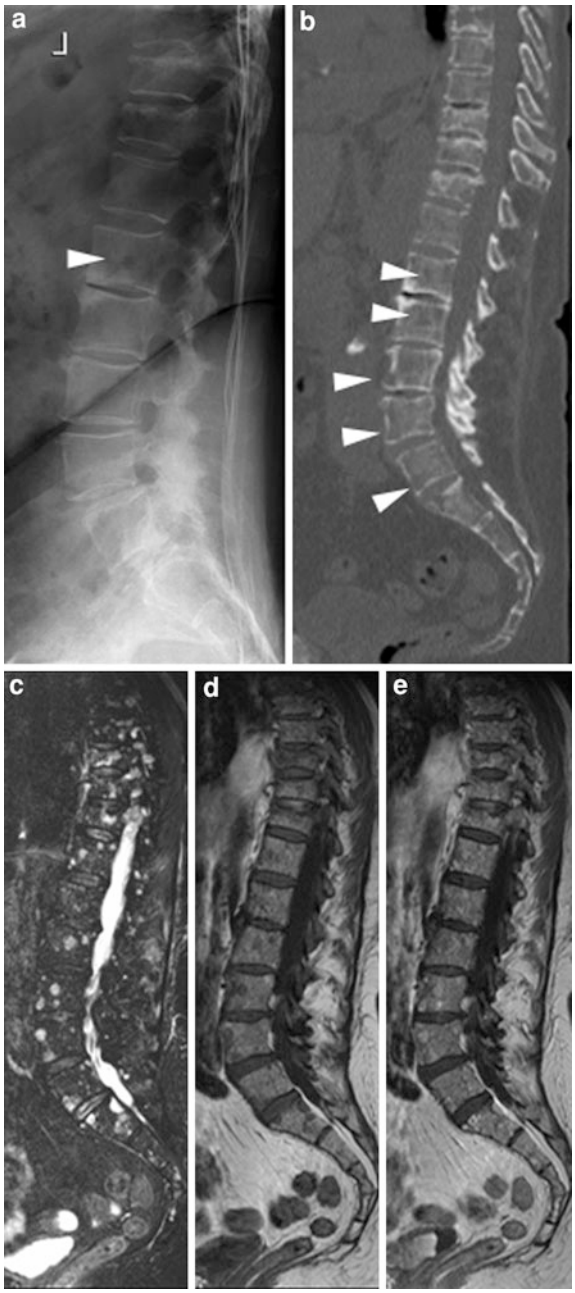

Fig. 14 High-grade focal infiltration pattern in a 66-year-old female with multiple myeloma. **a** Lateral radiograph of the lower thoracic and lumbar spine showing fractures of the superior end-plates of T10 and T11 and a sharply demarcated osteolytic lesion of L1. **b** Sagittal CT image of the lower thoracic and lumbar spine in bone window showing more osteolytic lesions (*arrowheads* point to some of the lesions). **c** Sagittal STIR image showing multiple well-demarcated hyperintense focal lesions. **d** Sagittal non-contrast T1-w SE image correspondingly showing these areas as low signal intensity. **e** Sagittal contrast-enhanced T1-w SE image showing contrast-uptake of the focal lesions

Fourth, a *combined focal and diffuse infiltration* pattern can be found in about 11% of patients. On T1-weighted SE images the bone marrow signal intensity is diffusely decreased with additional foci interspersed (Fig. 16). Those foci are often better demarcated on fat saturated or gradient echo images.

Fifth, in about 3% of cases a so-called "*salt-and-pepper*"-pattern can be found (Baur et al. 1996; Stabler et al. 1996). On T1-weighted SE images, but also on gradient echo and T2-weighted SE sequences, the bone marrow presents a very inhomogeneous patchy pattern. However, no hyperintense areas are demarcated in fat saturated sequences (Fig. 17). In histology this corresponds to bone marrow with circumscribed fat islands beside normal bone marrow with a minor infiltration of plasma cells (<20 Vol%). In the early stage of multiple myeloma this special pattern is thought to be initiated by a hematopoiesis-inhibiting factor. Enhancement of bone marrow does not exceed 40%. These patients usually have stage I disease and do not require therapy!

Focal or diffuse signal alterations are not specific for myeloma. They may be found in various other conditions too. Differential diagnoses for focal lesions include metastases, lymphoma, atypical hemangiomas and hematopoietic islands. Differential diagnoses for diffuse disease includes metastases, lymphoma, leukaemia, myelodysplastic syndrome, chronic myeloproliferative diseases and stimulated bone marrow (Vogler and Murphy 1988; Nobauer and Uffmann 2005).

7 Comparison of Methods

7.1 X-ray Versus MRI

Several studies demonstrated that X-rays often yield false negative results, especially in the spine and pelvis where anatomical regions are complex and overlain by ribs or bowel, respectively.

In an own study, 55% of the focal and 59% of the diffuse infiltrations were not detected by conventional X-rays (Baur et al. 1996). In studies of Fruehwald et al. (1988) and Ludwig et al. (1987) only 27 and 10% of focal involvement, respectively, were verified in conventional X-rays on the basis of form and structural changes. Tertti et al. (1995) compared MRI of the lumbar spine with conventional X-rays.

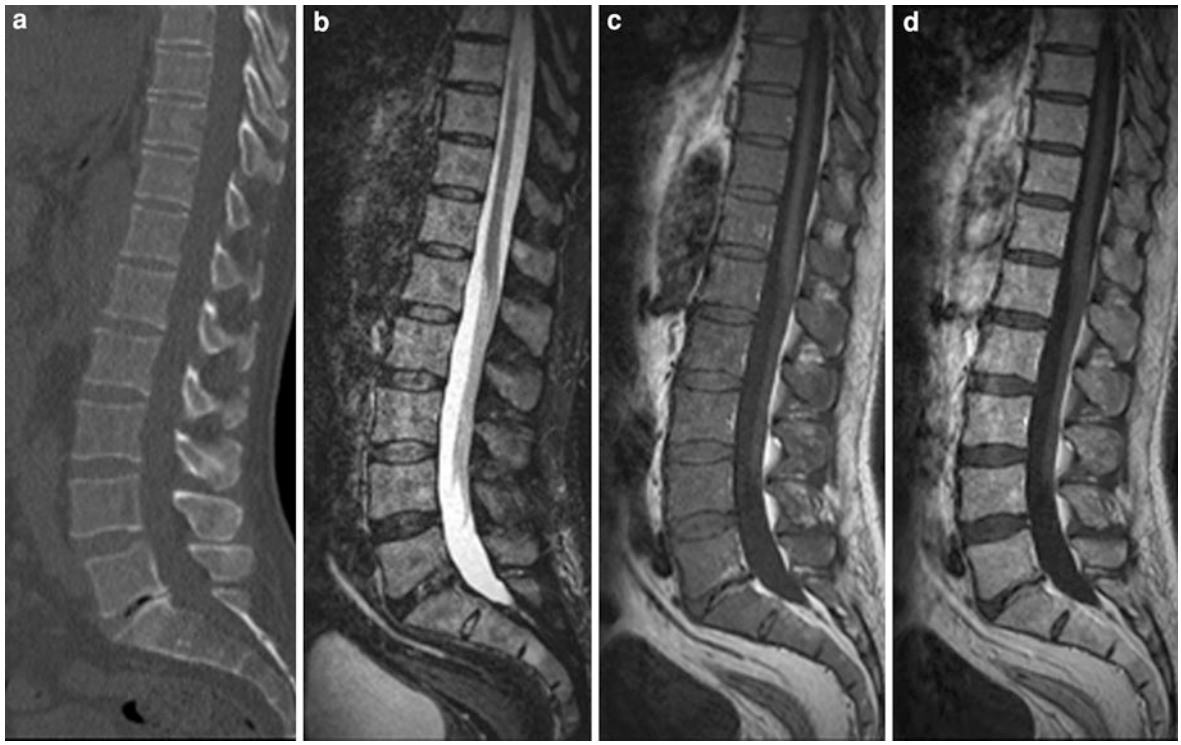

Fig. 15 High-grade diffuse infiltration of the spine in a 61-year-old male with multiple myeloma. **a** Sagittal CT image showing no osseous destruction. **b** Sagittal STIR image shows a high-grade diffusely increased signal intensity of the vertebral bone marrow. **c** Non-contrast sagittal T1-w SE image shows a diffusely reduced signal intensity of the vertebral bone marrow, approximately equivalent to that of the intervertebral discs. **d** Post-contrast sagittal T1-w SE image shows a diffuse high-grade contrast-enhancement of the vertebral bone marrow (ca. 100%). There are no focal lesions visible

In 13 out of 41 patients "false-negative" findings in conventional X-ray were reported. They came to the conclusion that in case of spine X-rays without pathological findings an MRI examination should be performed for definite exclusion of myeloma lesions. Other authors demonstrated that even in asymptomatic patients infiltrations can be found by the use of MRI, despite unremarkable X-rays (Mariette et al. 1999; Van de Berg et al. 1996; Dimopoulos et al. 1993; Moulopoulos et al. 1995). In these studies, in 29–50% of asymptomatic patients a diffuse or focal tumour infiltration was already present in MRI.

Lecouvet et al. (1999) examined 80 patients with stage III disease (Durie&Salmon) and found 34% false negative results in X-rays of the spine and 29% false negative results in X-rays of the pelvis compared to MRI. On the other hand, if the conventional X-ray would have been replaced with MRI scans of the spine and pelvis only, in 10% of patients the stage of disease would have been underestimated. A total of 8 out of 80 patients showed lesions only in peripheral long bones, at the ribs or at the skull. Walker et al. demonstrated a higher sensitivity of MRI compared to the skeletal survey in detecting focal lesions. MRI- but not MBS-defined focal lesions independently affected survival. They therefore recommended that in addition to the skeletal survey, MRI should be used routinely for staging, prognosis and response assessment in myeloma (Walker et al. 2007).

More recent studies comparing whole-body MRI to the radiographic skeletal survey have similarly demonstrated a greater sensitivity and specificity of whole-body MRI in lesion detection (Ghanem et al. 2006; Dinter et al. 2009). In the study by Dinter et al. in 19 out of 60 patients, tumour stage was upgraded (using Durie and Salmon Plus) due to the findings of WB-MRI. In 10 out of these 19 patients the WB-MRI result led to a decision to initiate further therapy (Dinter et al. 2009).

Conventional and whole-body MRI techniques in multiple myeloma are well established. Various

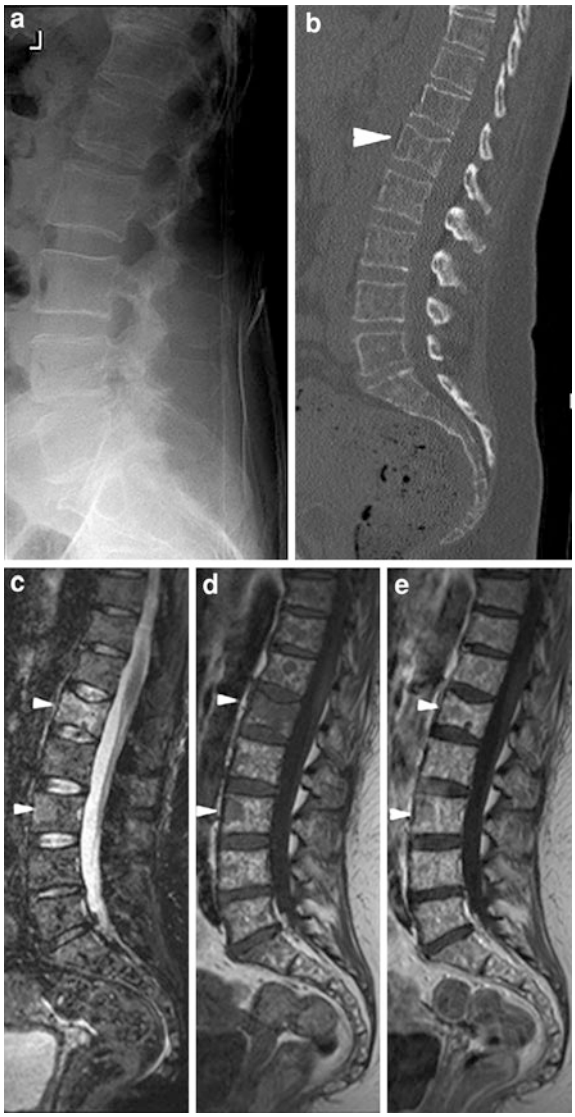

Fig. 16 Combined focal and intermediate diffuse infiltration of the spine in a 48-year-old female patient with multiple myeloma. **a** Lateral radiograph of the lumbar spine showing diffuse inhomogeneous osteoporosis. **b** Sagittal CT image of the lower thoracic and lumbar spine in bone window showing diffuse infiltration of the spine with a partial collapse of the superior endplate of L1 (*arrowhead*). **c** Sagittal STIR image. **d** Sagittal non-contrast T1-w SE image. **e** Sagittal contrast-enhanced T1-w SE image. The MR images show intermediate diffuse marrow infiltration as well as several focal lesions, the largest lesions being at L1 and L3 (*arrowheads*). Post-contrast there is enhancement of the focal lesions as well as diffuse enhancement of the vertebral bone marrow

MRI protocols are described in the literature, from standard unenhanced T1-weighted, T2-weighted and STIR imaging to contrast-enhanced T1-weighted fat-saturated imaging, to screening MR imaging with only T1-weighted and STIR imaging of the bone marrow (Hanrahan et al. 2010). Due to the possibility of using receiver-coil elements, such as total imaging matrix (TIM, Siemens systems) and parallel imaging, scan time and the time-consuming repositioning of patients is reduced. Thus, a complete display of the whole bone marrow within approximately 35 min can be obtained.

Continuous table movement (CTM) has been recently introduced as a promising new concept in MR imaging (Zenge et al. 2009; Kruger et al. 2005; Zenge et al. 2005). It enables seamless real-time WB-MR imaging by permitting continuous table movement during data acquisition (Weckbach et al. 2010). Weckbach and colleagues compared a WB-CTM protocol with a standard unenhanced WB-MR protocol in 18 patients with multiple myeloma. Overall image quality was found to be comparable. Artefacts were rated as mild but non-disturbing in 50% of patients, whereas in the other 50% of patients artefacts were classified as disturbing for the CTM protocol and non-disturbing for the standard protocol. Organ assessability was better using the CTM protocol. Depiction of bone marrow and soft tissue lesions was identical without a staging shift. Vertebral fractures were observed in two patients using the standard protocol. These were not detected by the CTM protocol. Mean protocol time was 6:38 min with the CTM protocol and 24:32 min with the standard WB-MRI protocol. CTM is therefore a promising new technique, significantly shortening scanning time and allowing a higher patient throughput. However, as the authors point out, as long as vertebral fractures are not detectable, the protocol cannot currently be safely used for clinical routine without the acquisition of additional sagittal sequences for the spine (Weckbach et al. 2010).

7.2 CT Versus X-rays

Two studies compared the detection rate of myeloma manifestations of radiographs versus CT. In a study of Schreiman et al. (1985) 32 patients with multiple myeloma were examined with a single row CT. Twelve patients showed osseous affections in both modalities. CT, however, usually demonstrated a more extensive involvement. In 6/13 patients only CT detected myeloma involvement despite normal

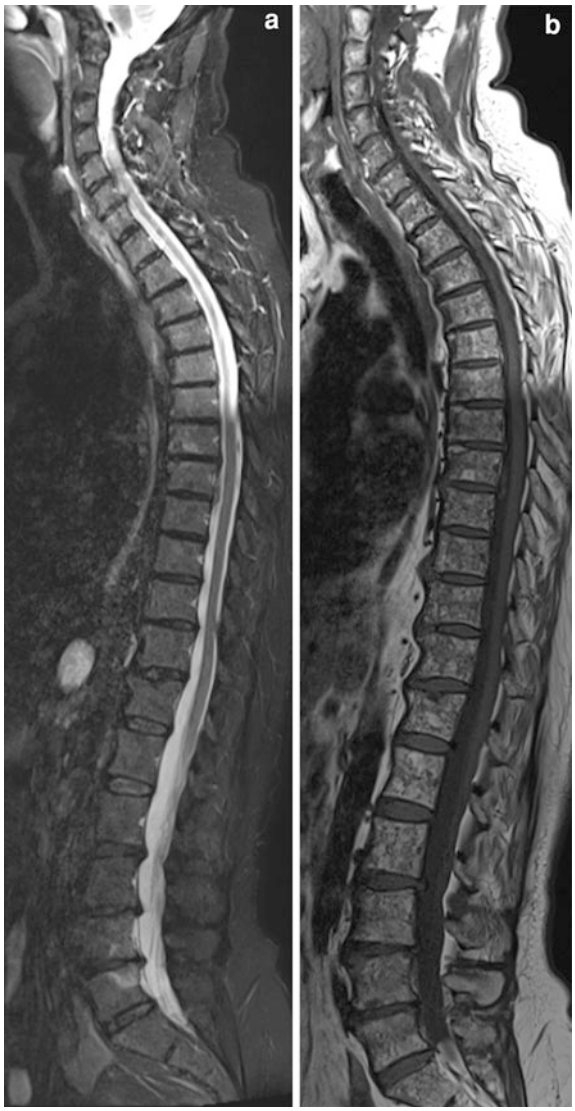

Fig. 17 "Salt and pepper" pattern in a 66-year-old female patient with multiple myeloma. **a** sagittal STIR image of the spine shows no focal hyperintensities. **b** sagittal non-contrast T1-w image of the spine shows an inhomogenous patchy pattern of the bone marrow. This is explained by the fact that focal fat islands are mixed within normal bone marrow with only low grade diffuse infiltration of bone marrow. Due to the strong hyperintensities of the fat islands the normal marrow seems to be pathologically low in signal. These patients usually have stage I disease and do not require any therapy. This pattern is often misdiagnosed as diffuse or multifocal small herd infiltration. Please also see histology in Figure 1c

radiographs. In another study using a 4-row MDCT scanner in 18 patients with multiple myeloma MDCT was also superior to radiography (Mahnken et al. 2002). In MDCT 24 lesions were additionally found when compared to radiography. The authors concluded that CT is more sensitive in the detection of myeloma involvement than radiography. Gleeson et al. recently assessed the feasibility of whole-body low-dose computed tomography (WBLDCT) in the diagnosis and staging of multiple myeloma and compared it to the skeletal survey, using bone marrow biopsy and whole-body MRI as a gold standard. In an analysis of 39 patients, WBLDCT detected more myelomatous lesions than the plain radiographic skeletal survey in 28 of 39 cases. This led to restaging in 25 instances (20 upstaged, 5 downstaged) (Gleeson et al. 2009).

7.3 MSCT Versus MRI

Three studies have compared MRI and MSCT in patients with multiple myeloma. Results of an own study, enrolling 41 patients, proved that WB-MRI is significantly more sensitive than WB-MSCT. Patients were examined on a 1.5 Tesla MRI scanner (Siemens Magnetom Symphony) using a whole-body-protocol and on a 16-row or 64-row MSCT scanner (Siemens Sensation-16) using a 0.75 mm collimation. On MRI, 15 patients showed no involvement. In 26 patients, 975 regions were affected: 21 patients were stage I, two were stage II, and 18 were stage III. On MDCT, 19 patients showed no involvement. In 22 patients, 462 regions were affected. According to MDCT, 25 patients were stage I, 7 were stage II, and 9 were stage III. In 21 patients with involvement detected on both methods, MRI showed more extensive disease than MDCT. WB-MRI was shown to be statistically superior to WB-MDCT in the detection of myeloma lesions. False negative results in MSCT could be explained by the fact that in MRI bone marrow replacement can be displayed before any osteolytic changes occur in the bone. False positive results in MDCT were due to inhomogeneous osteoporosis. Eleven patients were understaged with MDCT compared with MRI (Baur-Melnyk et al. 2008). Similar results could be achieved by Gleeson et al. (2009) who compared 23 patients with WBMDCT and WBMRI (Gleeson et al. 2009).

In the study of Mahnken et al. (2002) 18 patients with stage III multiple myeloma underwent a 4-MSCT-exam as well as an MRI examination of the spine and pelvis. A total number of 325 vertebral

bodies were evaluated. Of them, 226 showed coinciding findings in terms of normal findings or in terms of affection. In MSCT 231 vertebral bodies were classified as "affected", whereas 224 vertebral bodies were considered to be involved by myeloma in MRI. Thus, in MSCT, seven vertebrae showed affection which were normal on MRI. On the other hand, five vertebral bodies in MRI yielded a pathological signal while the MSCT findings were considered to be normal. These "false-negative" findings in MSCT might be due to early bone marrow infiltration without any signs of osseous destruction. The "false-negative" MRI-findings on the other hand might be attributed to response to treatment. No information about previous therapy was given in this study. According to other studies, following a successful therapy and/or stem cell transplantation bone marrow infiltrations can disappear whereas osteolytic lesions persist (Rahmouni et al. 1993a; Moulopoulos et al. 1994). The relatively high sensitivity of MSCT in this study might be attributed to the fact that all patients were of advanced disease (stage III).

7.4 Whole-Body Versus Spinal MR-Imaging

In a recent study, Bäuerle et al. examined whether standard MR imaging of the axial skeleton (spine and sacral bone) is sufficient for evaluation of patients with multiple myeloma or monoclonal gammopathy of undetermined significance (MGUS) or if whole-body MR imaging is necessary. A total of 100 patients with MM or MGUS were examined with WB-MRI and with MRI of the axial skeleton. Thirty-nine patients had lesions in the axial skeleton and 37 had lesions in the extra-axial skeleton. Nine patients in the latter group had no axial lesions and 13 patients had lesions that violated the cortical bone with a consequent increase in fracture risk. Due to their extra-axial location lesions in these patients could only be diagnosed by whole-body MRI. No single or combination of clinical factors allowed the authors to identify patients with an increased probability of having extra-axial lesions. The authors demonstrated the importance of whole-body MR imaging in the initial work-up of patients with MGUS or MM, as almost one half of all observed lesions would have been missed by using spinal MR imaging only and clinical parameters could not exclude the presence of extra-axial lesions (Bäuerle et al. 2009).

7.5 Whole-Body MRI Versus PET-CT

In a recent study by Shortt et al. involving 24 patients with bone marrow biopsy-proven multiple myeloma, the results of bone marrow biopsy performed within 7 days of FDG PET-CT and whole-body MRI were compared with disease activity on the two modalities. PET had a sensitivity of 59% and a specificity of 75% for findings of active disease, whereas whole-body MRI had a higher sensitivity and specificity of 68 and 83%, respectively. When used in combination and with concordant findings they were found to have a specificity and a positive predictive value of 100%. The authors suggested that this feature might be of value in assessing the effectiveness of aggressive and expensive treatment regimens (Shortt et al. 2009).

8 Prognosis

The time of survival in patients with multiple myeloma can significantly vary between courses of a few months to more than 10 years, the so-called "smoldering myeloma" (Kyle 1983). These various course characteristics, which are associated with different therapeutic options indicate the need for strong prognostic parameters. Different laboratory parameters showed a significant association with time to progression and survival, respectively. These include: elevated levels of β-2-microglobulin, decreased levels of serum albumin, deletion of chromosome 13 (Bataille et al. 1986).

Due to the possibility of detecting tumour infiltrations earlier with MRI than with the skeletal survey, the value of MRI with respect to patients' prognosis was analysed in patients defined as stage I disease according to the staging system of Durie and Salmon. In a study of Mariette et al. (1999) 55 patients were examined. In 17 of these 55 patients with negative X-rays, diffuse ($n = 3$) or focal ($n = 14$) infiltrations were found in MRI and proved to be associated with a significantly worse prognosis compared to patients with a normal bone marrow in MRI. During a follow-up of an average of 25 months, 8 of 17 patients with pathological MRI findings

versus only 2 out of 38 patients with normal MRI showed progression of the disease. In patient groups of 24 and 38 patients respectively examined, by van de Berg et al. (1996) and Moulopoulos et al. (1995) suffering from multiple myeloma stage I, patients with pathological MRI findings proved to exhibit a significantly earlier progression of disease compared to patients with normal MRI findings. The patients with pathological MRI findings required earlier treatment. Dimopoulos et al. examined 23 patients in stage I disease and found 7/23 patients with definite myeloma infiltrates in MRI despite normal X-rays. A disease progression was noted after an average of 11 months in patients with infiltrates versus 44 months without evidence of involvement in MRI (Dimopoulos et al. 1993). Kusomoto et al. reported about 61 patients in different stages of the disease with similar results. Patients showing pathological MRI scans presented a 5-year survival rate of 30% while patients with normal MRI had a 5-year survival rate of 80% (Kusomoto et al. 1997).

MRI helped to define and to differentiate patients with intermediate risk from those with a high risk for disease progression (Weber et al. 1997). In the study of Weber et al. a multivariate analysis found paraproteins >3/dl, a type Ig-A plasmacytoma and uric-excretion of Bence Jones proteins >50 mg/d to have the greatest influence on the prognosis as independent variables. According to the findings mentioned above, 101 patients with multiple myeloma were split into three different groups of risk (1 = low risk; 2 = intermediate; 3 = high risk). Patients included in the intermediate risk group with abnormal MRI findings had a significantly earlier progress of disease (median 21 months) compared to patients with normal MRI findings (median 57 months).

In an own study on 77 patients with newly diagnosed multiple myeloma we could show for the first time that MRI of the spine provided a significant prognostic tool not only concerning the time to progression but also concerning the survival of patients (Baur et al. 2002a). A total of 25/77 patients would have been understaged according to the established staging system of Durie and Salmon, which includes only X-ray as imaging tool. MRI staging represented an independent prognostic parameter and the inclusion of MRI in the staging system of Durie and Salmon improved the discrimination of the three risk groups (low-intermediate-high). Concerning the infiltration patterns a significantly longer survival time was found in patients with normal looking bone marrow and also in patients presenting a salt and pepper pattern. Patients with diffuse or focal infiltrates did not differ significantly in survival time. The extent of infiltration was much more important.

As mentioned previously, Walker et al. performed a study in which both baseline skeletal surveys and MRI were available in 611 patients uniformly treated with a tandem autologous transplantation-based protocol. These were evaluated to determine their respective merits for disease staging, response assessment and outcome prediction. MRI was more sensitive than the skeletal survey in the detection of focal lesions. MRI but not skeletal survey-defined focal lesions independently affected survival. MRI-focal lesions correlated with low albumin and elevated levels of C-reactive protein, LDH and creatinine. Resolution of MRI-focal lesions, occurring in 60% of cases was associated with superior survival (Walker et al. 2007).

Hillengass et al. performed WB-MRI in 149 patients with asymptomatic multiple myeloma. The presence of focal lesions and a number of greater than one focal lesions were the strongest adverse prognostic factors for progression into symptomatic multiple myeloma in a multivariate analysis. A diffuse infiltration pattern in MRI, a monoclonal protein of 40 g/L or greater, and a plasma cell infiltration in bone marrow of 20% or greater were other adverse prognostic factors for progression-free survival in univariate analysis. The authors recommended the use of whole-body MRI for risk stratification of patients with asymptomatic multiple myeloma (Hillengass et al. 2010).

In a recent study by Ailawadhi et al. involving 170 patients the extent of bone marrow involvement was evaluated by MRI. Clinical and laboratory parameters were assessed in patients with active MM and correlations between variables were assessed statistically. There was a significant association between the degree of bone marrow involvement on MRI and Durie and Salmon Stage, ISS stage, the presence of lytic bone disease and mean β-2 microglobulin levels. Among the patients with previously untreated MM, there was a significant association between BM-MRI stage and overall survival (Ailawadhi et al. 2010).

Bartel et al. (2009) evaluated the metastatic bone survey, MRI and FDG-PET/CTs in 239 newly diagnosed MM patients, subsequently treated with the

Total Therapy three regimen. They demonstrated that several imaging parameters related to tumour burden, such as focal lesion number assessed by MRI and PET, intensity of tumour metabolism (SUV-FL) and metastatic spread (extramedullary disease) all affect survival outcomes. FDG suppression on PET/CT post-therapy was reported to have independent predictive value. The presence of >3 focal lesions (FL) with increased FDG uptake was more highly associated with inferior overall and event-free survival after induction therapy than the metastatic bone survey or whole-body MRI. FDG-suppression in focal lesions (SUV-FL) before first transplantation was identified as an independent favourable prognostic variable (Bartel et al. 2009).

9 Staging

Controversies exist on which imaging modality should be used in patients with multiple myeloma on a routine basis. The radiographic skeletal survey has been shown to partly result in false negative findings in many studies, therefore in many institutions whole-body MRI or whole-body MDCT is currently performed at primary diagnosis and for follow-up examinations. MSCT is more widely available and image interpretation is easier than in MRI. On the other hand MRI is much more sensitive for evaluating early bone marrow involvement.

The latest guidelines for the standard investigative work-up in suspected multiple myeloma from the International Myeloma Workshop Consensus Panel (2011) (Dimopoulos et al. 2011) still recommend the skeletal survey as the standard method for imaging screening at diagnosis, as it is readily available at modest cost, allows large areas to be assessed and may detect long bone lesions at risk of impending fracture. An MRI of the spine and pelvis is deemed as mandatory in:

(i) all patients with a presumed diagnosis of solitary plasmacytoma,
(ii) In symptomatic patients for a detailed evaluation of a painful area of the skeleton to look for a soft tissue mass arising from a bone lesion,
(iii) for the investigation of patients with a suspicion of cord compression.

The Consensus Panel also recommends considering an MRI in the following situations:

(i) smoldering (asymptomatic myeloma) as it can detect occult lesions and, if positive, can predict for more rapid progression to symptomatic myeloma,
(ii) in symptomatic myeloma due to:
  (a) possibility of visualisation of unsuspected focal lesions and soft tissue plasmacytomas involving the spine and pelvis
  (b) prognostic significance of patterns of MRI abnormality (i.e. diffuse pattern or a high number of focal lesions).

Worldwide different staging systems have been created by various groups. The most widely accepted staging system is that of Durie and Salmon created in 1975 (Table 1) (Durie and Salmon 1975). Apart from the content of haemoglobin, the paraprotein component, the calcium-value, the Bence-Jones-protein-uric excretion and the findings of conventional X-rays are included. However, if available, the use of whole-body MRI is strongly recommended for more precise evaluation of the bulk of disease (Durie et al. 2003). In the Durie and Salmon PLUS staging system (Durie 2006) the amount of focal lesions and the extent of diffuse infiltration has to be determined. The cut-off value for stage II versus I is >5 lesions or moderate diffuse infiltration. The cut-off value for stage III versus stage II are 20 focal lesions or severe diffuse infiltration (Table 2).

In a recent study, Fechtner et al. investigated the concordance of the Durie–Salmon staging system with the Durie–Salmon PLUS staging system in monoclonal plasma cell disease. Lesions in 403 untreated patients with MGUS, solitary plasmacytoma, amyloid light-chain amyloidosis and MM were first staged on the basis of the classic Durie–Salmon staging system, which included conventional radiography. After examination with WBMRI lesions in these patients were in addition staged by using the Durie–Salmon PLUS staging system. The two staging systems were concordant in only 45% of all examined patients with monoclonal plasma cell disease. In 14% of patients a higher staging level, and in 41% of patients a lower staging level was found with the Durie–Salmon PLUS staging system when compared with the Durie–Salmon staging system. The authors concluded that indication for therapy in patients with multiple myeloma should not solely be based on MR imaging findings but in conjunction with clinical findings and laboratory results (Fechtner et al. 2010). Since the cut-off

Table 1 Durie and Salmon staging system

Criteria	Myeloma cell mass (myeloma cells in billons/m^2)[a]
Stage I (low cell mass)	600 billion
All of the following:	
1. Haemoglobin value >10 g/dl	
2. Serum calcium value normal ≤ 12 mg/dl	
3. Bone X-ray, normal bone structure (scale 0), or solitary plasmacytoma only.	
4. Low M-component production rates:	
a. IgG value <5.0 g/dl	
b. IgA value <3.0 g/dl	
c. Urine light chain M-component on electrophoresis <4 g/24 h	
Stage II (intermediate cell mass)	600 to 1,200 billion
Fitting neither Stage I nor Stage III	
Stage III (high cell mass)	>1,200 billion
One or more of the following:	
1. Haemoglobin value <8.5 g/dl	
2. Serum calcium value >12 mg/dl	
3. Advanced lytic bone lesions (scale 3)	
4. High M-component production rates:	
a. IgG value >7 g/100 ml	
b. IgA value >5 g/100 ml	
c. Urine light chain M-component on electrophoresis >12 g/24 h	
Subclassification (either A or B):	
A: relatively normal renal function (serum creatinine value) <2.0 mg/dl	
B: abnormal renal function (serum creatinine value) ≥ 2.0 mg/dl	
Examples: Stage IA (low cell mass with normal renal function)	
Stage IIIB (high cell mass with abnormal renal function)	

[a] Myeloma cells in whole body
Source adapted from Kyle 1983

values for focal lesions are different in the Durie and Salmon and the Durie and Salmon PLUS staging system it is not astonishing that these are discordant. One problem is that the cut-off values were not clearly defined in the Durie and Salmon staging system of 1975 (Table 1) for stage II versus stage III. In the Durie and Salmon PLUS staging system for focal lesions definite cut off values (e.g. >20 for stage III) were given. However, those cut-off values have never been determined statistically in a survival analysis by the authors. Due to other MR studies with large patient cohorts and survival analysis and the "old" Durie and Salmon staging system the cut-off values for focal lesions should be lower (Hillengass et al. 2010). A cut-off of 7 or 10 lesions would be a good discriminator for stage II versus stage III. This has been shown in the survival analysis of Walker et al. (2007) and Baur et al. (2002a). According to the literature, for discrimination between stage I versus stage II a cutoff value of >1 focal lesion or moderate diffuse disease would be appropriate (Baur 2002a; Hillengass 2010).

For staging purposes in the radiologic report the following points have to be addressed:

- X-rays/CT: Osteolytic lesions (number, localisations, fracture risk), vertebral fractures (osteoporotic/neoplastic)
- MRI: Infiltration pattern (focal, diffuse, combined focal and diffuse, salt + pepper). Pathologic fractures, spinal cord compression.

Table 2 Durie and Salmon PLUS staging system

Classification	New imaging MRI and/or FDG PET
MGUS	All negative
Stage IA* (Smoldering or indolent)	Can have single Plasmacytoma and/or limited disease on imaging
Multiple Myeloma	
Stages IB*, IIA/B*, IIIA/B*	
Stage I B*	<5 Focal lesions; mild diffuse disease
Stage II A/B*	5–20 Focal lesions; moderate diffuse disease
Stage III A/B*	>20 Focal lesions; severe diffuse disease
* A:	
• Serum creatinine <2.0 mg/dl	
• No extramedullary disease (EMD)	
* B:	
• Serum creatinine >2.0 mg/dl	
• Extramedullary disease (EMD)	

Source Durie et al. (2003)

- MRI: Localisations + extent of infiltration: Focal: number of lesions, count up to 20; Grade I-III Durie and Salmon PLUS: grade I: <5, grade II: 5–20, grade III: >20); diffuse infiltration (grade I: no/mild infiltration, grade II: moderate infiltration, grade III: strong infiltration.)
- Presence of soft tissue components, extraosseous lesions

10 Subtypes of Plasma Cell Disease

10.1 MGUS

Primary differential diagnoses in case of elevated laboratory paraprotein are monoclonal gammopathy of unknown significance (MGUS) and smoldering myeloma. *Monoclonal gammopathy of uncertain significance* (*MGUS*) is a common cause of a laboratory discovered elevated paraprotein. The paraprotein level is typically low. It is usually an incidental finding. The incidence in patients >70 years of age is about 3%. Several laboratory parameters have to be fulfilled to diagnose MGUS. Follow-up examinations, which confirm stable disease, are necessary to qualify for MGUS rather than for myeloma. No osteolyses should be present. Whole-body MRI is always negative in MGUS and can be used as a tool to underline the diagnosis (Table 3). MGUS can evolve to manifest multiple myeloma, chronic lymphatic leukemia, lymphoma, Waldenströms macroglobulinemia or amyloidosis. Van de Berg et al. performed MR imaging in 35 patients with clinically suspected MGUS in MRI. In seven patients abnormalities were found typical for myeloma. Of the patients without lesions in MRI none required therapy after a follow-up of 30 months. Conversely 4/7 patients with lesions in MRI required therapy within the following 5 years (Vande Berg et al. 1997). This shows that laboratory parameters alone are not sufficient for the diagnosis of MGUS. In the new guidelines for diagnosis and staging (Dimopoulos et al. 2009), whole-body MRI has to be negative in patients with MGUS, otherwise the diagnosis must be changed to overt myeloma.

10.2 Smoldering Myeloma

Smoldering myeloma is an intermediate category between MGUS and multiple myeloma, as now defined, is stage IA in the Durie and Salmon staging system (Table 4). Such patients can have mild degrees of myeloma-related organ dysfunction,

Table 3 MGUS: monoclonal gammopathy of undetermined significance

Diagnostic criteria: all 3 required
1. Serum Monoclonal protein and/or urine monoclonal protein level low*
2. Monoclonal bone marrow plasma cells <10%
3. Normal serum calcium, haemoglobin level and serum creatinine.
• No bone lesions on full skeletal X-ray survey and/or other imaging if performed.
• No clinical or laboratory features of amyloidosis or light chain deposition disease.
*Low is defined as:
• Serum IgG <3.5 g/dl
• Serum IgA <2.0 g/dl
• Urine monoclonal kappa or lambda <1.0 g/24 h

Source Durie et al. (2003)

Table 4 Smoldering or indolent myeloma

Diagnostic criteria
1. Serum M-protein ≥3 g/dL
and/or
2. ≥10% bone marrow plasma cells with no evidence of end-organ damage hypercalcemia, renal insufficiency, anaemia or bone lesions
3. Not meeting criteria for MGUS, multiple myeloma, or solitary plasmacytoma of bone

Source adapted from Blade et al. (2010)

Table 5 Solitary plasmacytoma of bone

Diagnostic criteria: all 3 required
1. Biopsy proven monoclonal plasmacytoma of bone in a single site only. X-rays and MRI and/or FDG-PET imaging must be negative outside the primary site. The primary lesion may be associated with a low* serum and/or urine M-component.
2. The bone marrow contains <10% monoclonal plasma cells.
3. No other myeloma related organ dysfunction.
*Low is defined as:
• Serum IgG <3.5 g/dl
• Serum IgA <2.0 g/dl
• Urine monoclonal kappa or lambda <1.0 g/24 h

Source Durie et al. (2003)

e.g. slight anaemia. The bone marrow contains between 10 and 30 Vol% plasma cells. The patients are eligible for supportive care measures such as erythropoietin and bisphosphonates. Abnormalities on MRI or FDG-PET imaging indicate an increased risk of early disease progression (Durie et al. 2003; Blade et al. 2010).

10.3 Solitary Plasmacytoma

Solitary bone plasmacytoma affects less than 5% of patients with plasma cell myeloma (Dimopoulos et al. 2000). Diagnostic criteria for solitary plasmacytoma of bone varied over the years (Table 5). Routine bone marrow biopsy usually is normal and there should be no organ dysfunction. X-rays typically show a singular lytic lesion with a narrow zone of transition. It may be also expansile in nature with a soft-tissue component. It may affect any bone but has a preference for the axial skeleton in particular the vertebrae (Dimopoulos et al. 2000). For therapy planning (surgery and or radiation) CT or MRI are required to display osseous destructions and the soft-tissue component. In the spine, the soft-tissue component may cause spinal cord or nerve root compression. A small, if any, M-protein component usually decreases after local radiation therapy. Several studies report that screening of patients with solitary plasmacytoma of bone with MRI revealed additional lesions (Moulopoulos et al. 1993). Moulopoulos et al. (1993) showed that MRI of the thoracic and lumbosacral spine showed additional foci of marrow replacement in 4 out of 12 patients with solitary plasmacytoma. In a study by Schirrmeister et al. 15 patients with known solitary plasmacytoma underwent FDG-PET. Twenty further plasmacytoma lesions, which were negative on standard imaging methods, were detected in four patients (27%), leading to a change in therapy (Schirrmeister et al. 2003). Some authors postulate that solitary plasmacytoma of bone is only a precursor for multiple myeloma or only one lesion is detected despite several others, since X-rays are often false negative. Thus, whole-body MRI is strongly

recommended, since therapeutic regimens are different for solitary plasmacytoma and multiple myeloma.

11 Therapy of Multiple Myeloma

Due to the complexity and great variability in the aggressiveness of the disease the management of patients with myeloma needs an interdisciplinary approach. At an initial stage without any lesions patients can be followed according to a "watch and wait" consensus, because in this stage chemotherapy was found not to result in a prolonged time of survival (Riccardi et al. 2000). The treatment with bisphosphonates resulted in a reduced incidence of fractures and an increased quality of life (Jantunen and Laakso 1996; Kyle 2000). The use of high-dose chemotherapy followed by autologous or a combined autologous and allogenic stem cell transplantation in patients with stage II and III disease (Durie and Salmon) has resulted in a significantly longer survival time compared to the classic Alexanian scheme with melphalan and prednisone (Desikan et al. 2000; Barlogie et al. 2001). In patients ineligible for high-dose chemotherapy with stem-cell support, oral combination of melphalan and prednisone has been the standard of treatment, but should now be replaced by combinations with novel agents. Randomised studies have shown that the combination of melphalan-prednisone with thalidomide is superior to melphalan-prednisone. Bortezomib in combination with melphalan-prednisone also achieved significantly higher survival rates and a complete remission rate comparable to that achieved with high-dose therapy plus stem cell transplantation. Melphalan-prednisone plus either thalidomide or bortezomib are therefore the new standards in Europe. Lenalidomide combined with low-dose dexamethasone also yields improved response and overall survival rates, and is well tolerated even in patients >65 years of age (Harousseau and Dreyling 2010). In advanced stages therapy of complications (e.g. renal insufficiency, anaemia) and pain with medication and radiation are important for treatment.

Unstable pathologic fractures at the extremities and the spine are usually stabilized operatively with compound osteosynthesis or endoprosthesis. These methods usually allow an early mobilisation of the patients.

Percutaneous vertebroplasty is one of the most promising new interventional procedures for relieving or reducing painful vertebra, with the injection of surgical polymethylmethacrylate or cement into vertebral bodies (Fig. 18). This image-guided technique, originally used to treat vertebral hemangioma, has recently been used to treat metastases, osteoporotic compression fractures and large osteolytic lesions (Guglielmi et al. 2005). Patients with multiple myeloma are the main patient group for percutaneous vertebroplasty since they often suffer from osteoporotic fractures as well as from osteolytic lesions.

Indications for percutaneous vertebroplasty are patients with acute and subacute osteoporotic fractures, not eligible for surgery, that show no pain relief despite conservative treatment. Healed fractures without bone marrow edema at MRI are usually not an indication for percutaneous vertebroplasty, since pain in those patients, mostly derives from other causes, such as muscle tension, osteochondrosis etc. About 30% of osteoporotic fractures show an intravertebral cleft, filled with fluid or gas indicating motion between the opposing surfaces of the vertebral fracture cleft (Baur et al. 2002b). Placing cement into the cleft can reduce pain significantly presumably from immobilizing those two fracture segments (Peh et al. 2003). Patient selection is of utmost importance. Physical examination including neurological examination should be performed in any patient to localise his pain. It should be ruled out that there is no discrepancy between the fracture site and the level of pain.

Other indications are osteolytic lesions that are not eligible for surgery and that are either extremely painful (require high doses of analgetic drugs) or that are at risk for fracture. The final treatment approach should be the result of a consensus agreement between clinician, spinal surgeon and the radiologist performing the percutaneous vertebroplasty. Large tumour infiltrations can be pretreated by radiofrequency ablation before filling in the cement. Post-vertebroplasty radiation is usually performed. Contraindications are a marked defect in the posterior part of the vertebral body and soft tissue masses in the epidural space due to the risk of cement extrusion into the spinal canal resulting in spinal cord compression.

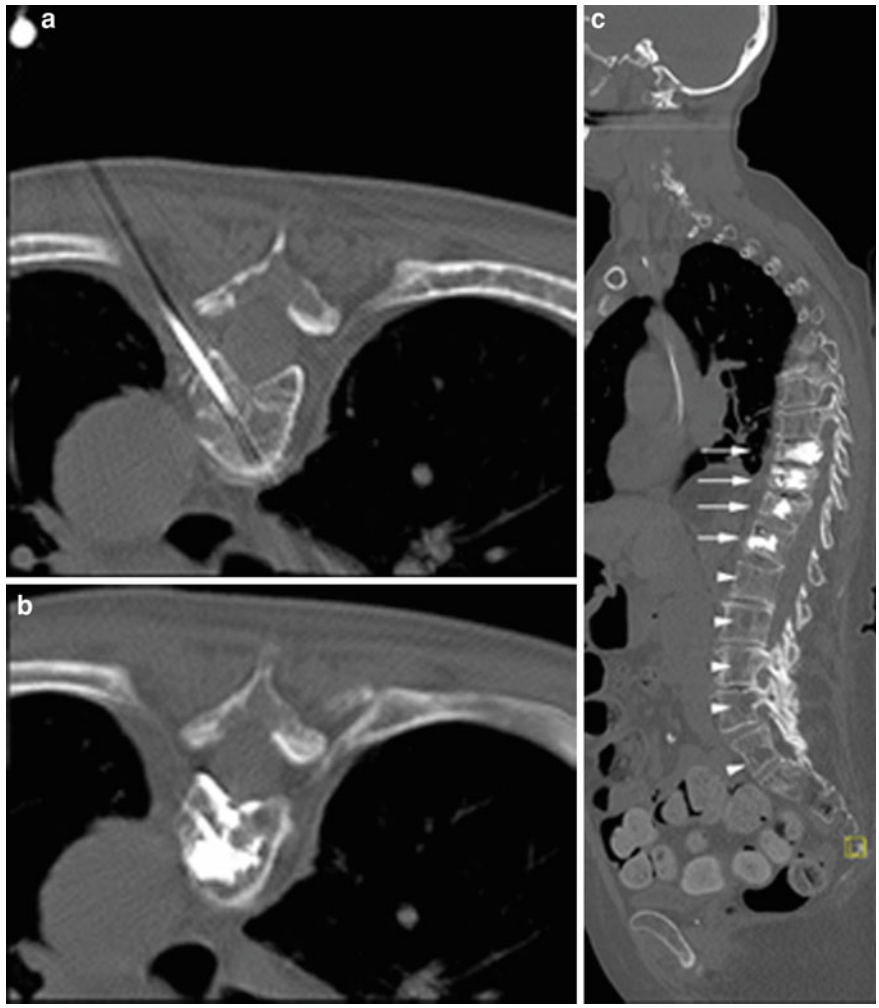

Fig. 18 Vertebroplasty in a 66-year-old female with multiple myeloma. **a**, **b** Axial CT images in bone window showing CT-guided injection of poly-methylmethacrylate in the T5 vertebral body. **c** sagittal CT image of the spine in bone window showing cement following vertebroplasty at the levels of T9–T12 (*arrows*). Arrowheads denote focal osteolytic lesions in the lumbar vertebral bodies

12 Evaluation of Relapse/Response to Therapy

The International Myeloma Working Group has developed response criteria for multiple myeloma which are being widely accepted as the current standards for diagnosis and staging (Durie et al. 2006). The major response categories include complete response (CR), partial response (PR), stable disease (SD), progressive disease (PD) and relapse from CR.

- *Complete response* (*CR*) requires negative immunofixation on the serum and urine and disappearance of any soft tissue plasmacytomas with less than 5% plasma cells in the bone marrow (Durie et al. 2006).
- *Partial response* (*PR*) requires a ≥50% reduction of serum M-protein and reduction in 24-h urinary M-protein by ≥90% or to <200 mg per 24 h. If the serum and urine M-protein are unmeasurable, a ≥50% decrease in the difference between involved and uninvolved free light chain levels is required in place of the M-protein criteria. If serum and urine M-protein are unmeasurable, and serum free light assay is also unmeasurable, a ≥50% reduction in plasma cells is required in place of M-protein, provided baseline bone marrow plasma cell percentage was ≥30%. Additionally, if present at baseline, a ≥50% reduction in the size of soft tissue plasmacytomas is also required (Durie et al. 2006). The development of new vertebral compression fractures does not exclude a response.

- *Stable disease* (*SD*) is not recommended for use as an indicator of response; stability of disease is best described by providing the time to progression estimates. However it is defined as not meeting criteria for CR, PR or progressive disease (Durie et al. 2006).

  The above categories also require no known evidence of progressive or new bone lesions if radiographic studies were performed. Radiographic studies are not required to satisfy these response requirements.
- *Progressive disease* (*PD*) requires any one or more of the following:

  Increase of ≥25% from baseline in:
  - Serum M-component and/or (absolute increase must be ≥0.5 g/dl)
  - Urine M-component and/or (absolute increase must be ≥200 mg/24 h)
  - Only in patients without measurable serum and urine M-protein levels: the difference between involved and uninvolved free light-chain (FLC) levels. The absolute increase must be >10 mg/dl.
  - Bone marrow plasma cell percentage: the absolute percentage must be ≥10%.
  - Definite development of new bone lesions or soft tissue plasmacytomas or definite increase in size of existing bone lesions or soft tissue plasmacytomas.
  - Development of hypercalcemia that can be attributed solely to the plasma cell proliferative disorder (Durie et al. 2006).

    The development of new vertebral compression fractures does not automatically imply progressive disease.
- *Clinical relapse* (for use in clinical practice) requires one or more of:
  - Development of new soft tissue plasmacytomas or bone lesions.
  - Definite increase in size of existing plasmacytomas or bone lesions. A definite increase is defined as a 50% (and at least 1 cm) increase as measured serially by the sum of the products of the cross-diameters of the measurable lesions.
  - Hypercalcemia.
  - Decrease in haemoglobin of ≥2 mg/dl or more.
  - Rise in serum creatinine by 2mg/dl or more (Durie et al. 2006).

The judgement of increasing/decreasing soft-tissue plasmacytoma or increasing/decreasing size or number of lesions, in most cases, can only be assessed reliably by cross-sectional imaging, such as CT or MRI. Only a few studies have focussed on bone marrow signal changes in patients with multiple myeloma with respect to therapy.

Moulopoulos et al. (1994) examined 20 patients before and after chemotherapy including high-dosed cortisone application. Patients with clinically evaluated complete remission showed either a normalization of bone marrow signal in MRI or an absent or peripheral enhancement of the lesions. However, these changes were not detected in all patients with clinical response to therapy. Homogeneous enhancement was still persistent in 5 of 18 focal lesions. Patients with partial response to therapy showed an overall decrease of bone marrow alterations with an increase in signal on T1-w SE images due to an increase of fat cells. In those patients focal and diffuse pathological contrast media uptake was still present. Despite clinical remission, new compression fractures occurred in the spine of ten patients while the bone marrow MRI signal was normalised. Thus, those vertebral fractures were assumed to emerge from progressive osteoporosis, which is regularly observed in multiple myeloma due to the combination of senile and cortisone-induced osteoporosis.

Rahmouni et al. observed similar therapy effects (13 patients treated with combination of chemotherapy and irradiation to spinal lesions; five patients received only chemotherapy). Before treatment all lesions had high signal intensity on T2-w SE images. All except one were hypointense on unenhanced T1-w SE. All nodules enhanced on turbo-FLASH images obtained in the arterial phase after contrast injection with persistence of contrast on delayed contrast-enhanced T1-w SE images. In 13 of 18 patients the correlation between MR pattern and clinical response to treatment was good. MR showed a lower signal on T2-w images and lack of enhancement or rim enhancement). However, in five patients discrepancies were found between clinical and MRI findings (Rahmouni et al. 1993b).

Carlson et al. calculated a tumour mass index at the time point of primary diagnosis and after the application of Alexanian I scheme of chemotherapy. The tumour mass index (TMI) was calculated by estimating the total myeloma mass visualised at MR imaging. The tumour mass index showed correlation with the extent of ß-2-microglobulin (Carlson et al. 1995). Patients offering a low tumour mass index at

primary diagnosis (before therapy) showed a longer survival time. Therapy response assessment by MR imaging (measurement of TMI) and by clinical response criteria provided similar results, indicating that the two methods measure changes in tumour mass in a similar way. The calculation of the described tumour mass index was only used in cases of focal infiltration. In patients with a diffuse infiltration form, who responded to therapy, the infiltrates showed a conversion of diffusely infiltrated marrow to more fatty marrow from peripheral to central body areas whereas focal lesions persisted. Conversely, focal infiltration forms at the time of disease progression, changed into diffuse infiltrates mainly affecting the spine and the pelvis (Carlson et al. 1995).

Lecouvet et al. assessed the prognostic value of MR imaging before and after treatment of the bone marrow with myeloablative therapy and bone marrow transplantation as well as the prognostic value of an index reflecting changes on MR images obtained before and after treatment. Pre- and post-contrast T1-w images and T2*-w images of the spine and pelvis were obtained 1 month before and 1 month after marrow transplantation in 25 patients with Durie–Salmon stage III myeloma. Pre and posttreatment MR imaging patterns of marrow involvement (normal, focal, diffuse), number of focal lesions, and a "marrow evolution index" (0–8 on the basis of comparison of the [number (0-decrease in number of lesions, 1-no change, 2-increase), size (0-decrease, 1-no change, 2-increase), contrast-enhancement (lesions showing diffuse contrast enhancement compared to number of lesions showing no enhancement or rim-enhancement 0-decreased, 1-remained stable, 2-increased] and of the surrounding bone marrow background on pre and posttreatment MR images (0-change from diffuse alteration to normal appearance, 1-stable, 2-change from normal to diffuse alteration) were determined. Hematologic and MR imaging parameters were correlated with the quality of response to treatment (complete versus partial remission) and with relapse-free and overall survival. Response quality did not differ among categories of patients determined on the basis of MR images. Individual MR imaging parameters (lesion size, number, and contrast enhancement, and changes in the MR imaging appearance of the marrow background) showed no correlation with response duration and survival. Patients with a low marrow evolution index had significantly longer relapse-free ($p < 10^{-3}$) and overall survival ($p = 0.005$) than patients with a high index. Thus the using a bone marrow evolution index rather than individual parameters may help predict response duration and survival (Lecouvet et al. 2001).

Horger et al. assessed whole-body low-dose MDCT scans from 131 consecutive myeloma patients with or without therapy (total of 439 examinations). The number and size of osteolytic lesions and the number, size and density of focal or diffuse medullary and extramedullary lesions were analysed. Those results and the results at follow-up were correlated to current laboratory tests for myeloma. Validation was achieved by the combined reading of both hematologic and radiologic parameters at follow-up. Association between diagnostic modalities was assessed by using European Group for Bone and Marrow Transplantation response criteria, Hematologic parameters proved correct in 84% of all exams, whereas whole-body low-dose multi-detector CT resulted in correct assessment in 94% of all examinations. A total of 21% of examinations produced discrepant findings. In 75% of these, WBLD-MDCT proved correct, as determined at further follow-up. The combination of WBLD-MDCT with conventional laboratory-based follow-up resulted in significantly greater diagnostic accuracy compared with laboratory testing alone. The authors concluded that WBLD-MDCT represents a reliable imaging-based method for the direct monitoring of the course of patients with myeloma under specific therapy, and it showed good concordance with established histologic parameters (Horger et al. 2007).

In a recent study, Lin et al. compared bone marrow changes at whole-body dynamic contrast-enhanced MR imaging with clinical response in 30 patients who underwent whole-body dynamic contrast-enhanced MR imaging before treatment, after induction chemotherapy and after autologous stem cell transplantation. Maximal percentages of bone marrow (BME_{max}) and focal lesion (FLE_{max}) enhancement were assessed at each MR imaging examination. Clinical responses were determined on the basis of international uniform response criteria. Posttreatment changes in BME_{max} and FLE_{max} were compared with clinical response to therapy. After induction chemotherapy, mean BME_{max} differed significantly between good and poor responders

(94.3% vs 138.4%, respectively). Excluding results from six exams with focal lesions in which a poor clinical response was classified but BME_{max} had normalised, a posttreatment BME_{max} of more than 96.8% had 100% sensitivity and 76.9% specificity for the identification of poor responders. Mean FLE_{max} after induction chemotherapy did not differ between good and poor responders. Mean timing (i.e. the number of post-contrast dynamic acquisitions where FLE_{max} was observed) was significantly delayed in good responders compared with poor responders. The authors concluded that with quantitative analysis of BME_{max} and the timing of FLE_{max} whole-body dynamic contrast-enhanced MR imaging can be used to assess treatment response assessment in patients with multiple myeloma (Lin et al. 2010). However, these preliminary studies have to be proved in further studies. In addition it is a rather time-consuming method.

Results in several studies indicate that F18-FDG PET may be a promising tool in monitoring relapse or response to therapy. In a study of Durie and coworkers FDG PET identified high-risk myeloma. Negative PET scans reliably predicted stable MGUS. Sixteen previously untreated patients with multiple myeloma had positive FDG scans, either focally or diffuse. The development of new FDG positive sites in the skeleton after therapy indicated relapse and poor prognosis (Durie et al. 2002). As part of a study of Bredella et al. on the use of FDG-PET in assessing multiple myeloma, three patients underwent serial MRI, CT, radiographs and FDG PET scans to assess response to chemotherapy and bone marrow transplant (Bredella et al. 2005). All patients showed persistent abnormal bone marrow signal on MRI, and abnormal lytic lesions on CT and radiographs, suspicious for residual tumour. Subsequent FDG PET demonstrated decline in metabolic activity in two patients, which was concordant with clinical improvement. In one patient, a new focus of abnormal uptake was detected on follow-up scan in an area distant to the original tumour, consistent with recurrent disease.

As mentioned above FDG suppression on PET/CT post-therapy was reported to have independent predictive value. The presence of >3 focal lesions (FL) with increased FDG uptake was more highly associated with inferior overall and event-free survival after induction therapy than the metastatic bone survey or whole-body MRI (Bartel et al. 2009). FDG-suppression in focal lesions (SUV-FL) before first transplantation was identified as an independent favourable prognostic variable. This has been the largest study to date analysing the role of PET/CT in predicting outcome after treatment, involving 239 newly diagnosed MM patients (Bartel et al. 2009).

In a recent study involving 37 patients, Elliott et al. compared the predictive values of PET/CT, concurrent laboratory testing, and their combination in prediction of 12-month progression, as determined by current International Myeloma Working Group criteria. PET/CT and labs (serum chemistry, ß2-microglobulin, immunofixation, bone marrow biopsy, serum free light chain) were reviewed, and date of relapse/progression was determined by IMWG criteria. Sensitivity of PET/CT for predicting relapse/progression was lower than that of labs but PET/CT was more specific. When labs and PET/CT data were combined, a positive result for either one of both tests was 89% sensitive, and a positive result for both tests was 100% specific for predicting 12-month progression of disease. The authors conclude that combining PET/CT with laboratory data improves the accuracy of prediction of relapse/progression within 12 months compared with each test alone. They therefore recommended integration of PET/CT into myeloma follow-up (Elliott et al. 2011).

13 Differential Diagnosis

Differential diagnosis includes metastases from other primaries usually presenting as focal lesions. Diffuse disease can be mimicked by chronic myeloproliferative diseases, such as polycythemia vera and chronic myeloid leukemia and other leukemias. There is no signal pattern in MRI that is specific for multiple myeloma. Either of these pathologies can mimic myeloma with focal or diffuse disease. However, an elevated monoclonal paraprotein is a quick and important diagnostic clue for the diagnosis of myeloma. The exact diagnosis has to be determined via biopsy of a lesion.

References

Ailawadhi S, Abdelhalim AN, Derby L, Mashtare TL, Miller KC, Wilding GE, Alberico RA, Gottlieb R, Klippenstein DL, Lee K, Chanan-Khan AA (2010) Extent of disease burden determined with magnetic resonance imaging of the bone marrow is predictive of survival outcome in patients with multiple myeloma. Cancer 116(1):84–92. doi:10.1002/cncr.24704

Algra PR, Bloem JL, Tissing H, Falke TH, Arndt JW, Verboom LJ (1991) Detection of vertebral metastases: comparison between MR imaging and bone scintigraphy. Radiographics 11(2): 219–232

Avrahami E, Tadmor R, Kaplinsky N (1993) The role of T2-weighted gradient echo in MRI demonstration of spinal multiple myeloma. Spine 18(13):1812–1815

Barlogie B, Desikan R, Eddlemon P, Spencer T, Zeldis J, Munshi N, Badros A, Zangari M, Anaissie E, Epstein J, Shaughnessy J, Ayers D, Spoon D, Tricot G (2001) Extended survival in advanced and refractory multiple myeloma after single-agent thalidomide: identification of prognostic factors in a phase 2 study of 169 patients. Blood 98(2):492–494

Bartel TB, Haessler J, Brown TL, Shaughnessy JD Jr, van Rhee F, Anaissie E, Alpe T, Angtuaco E, Walker R, Epstein J, Crowley J, Barlogie B (2009) F18-fluorodeoxyglucose positron emission tomography in the context of other imaging techniques and prognostic factors in multiple myeloma. Blood 114(10):2068–2076. doi:10.1182/blood-2009-03-213280

Bartl R (1988) Histologic classification and staging of multiple myeloma. Hematol Oncol 6(2):107–113

Bataille R, Durie BG, Grenier J, Sany J (1986) Prognostic factors and staging in multiple myeloma: a reappraisal. J Clin Oncol 4(1):80–87

Bäuerle T, Hillengass J, Fechtner K, Zechmann CM, Grenacher L, Moehler TM, Christiane H, Wagner-Gund B, Neben K, Kauczor HU, Goldschmidt H, Delorme S (2009) Multiple myeloma and monoclonal gammopathy of undetermined significance: importance of whole-body versus spinal MR imaging. Radiology 252(2):477–485. doi:10.1148/radiol.2522081756

Baur A, Stabler A, Bartl R, Lamerz R, Reiser M (1996) Infiltration patterns of plasmacytomas in magnetic resonance tomography. Rofo 164(6):457–463. doi:10.1055/s-2007-1015689

Baur A, Stabler A, Bartl R, Lamerz R, Scheidler J, Reiser M (1997) MRI gadolinium enhancement of bone marrow: age-related changes in normals and in diffuse neoplastic infiltration. Skeletal Radiol 26(7):414–418

Baur A, Stabler A, Steinborn M, Schnarkowski P, Pistitsch C, Lamerz R, Bartl R, Reiser M (1998) Magnetic resonance tomography in plasmacytoma: ranking of various sequences in diffuse and focal infiltration patterns. Rofo 168(4): 323–329. doi:10.1055/s-2007-1015137

Baur A, Stabler A, Nagel D, Lamerz R, Bartl R, Hiller E, Wendtner C, Bachner F, Reiser M (2002a) Magnetic resonance imaging as a supplement for the clinical staging system of Durie and Salmon? Cancer 95(6):1334–1345. doi:10.1002/cncr.10818

Baur A, Stabler A, Arbogast S, Duerr HR, Bartl R, Reiser M (2002b) Acute osteoporotic and neoplastic vertebral compression fractures: fluid sign at MR imaging. Radiology 225(3): 730–735

Baur A, Bartl R, Pellengahr C, Baltin V, Reiser M (2004) Neovascularization of bone marrow in patients with diffuse multiple myeloma: a correlative study of magnetic resonance imaging and histopathologic findings. Cancer 101(11):2599–2604. doi:10.1002/cncr.20697

Baur-Melnyk A, Buhmann S, Becker C, Schoenberg SO, Lang N, Bartl R, Reiser MF (2008) Whole-body MRI versus whole-body MDCT for staging of multiple myeloma. Am J Roentgenol 190(4):1097–1104. doi:10.2214/AJR.07.2635

Blade J, Dimopoulos M, Rosinol L, Rajkumar SV, Kyle RA (2010) Smoldering (asymptomatic) multiple myeloma: current diagnostic criteria, new predictors of outcome, and follow-up recommendations. J Clin Oncol 28(4):690–697. doi:10.1200/JCO.2009.22.2257

Bredella MA, Steinbach L, Caputo G, Segall G, Hawkins R (2005) Value of FDG PET in the assessment of patients with multiple myeloma. Am J Roentgenol 184(4):1199–1204

Carlson K, Astrom G, Nyman R, Ahlstrom H, Simonsson B (1995) MR imaging of multiple myeloma in tumour mass measurement at diagnosis and during treatment. Acta Radiol 36(1):9–14

Carson CP, Ackerman LV, Maltby JD (1955) Plasma cell myeloma; a clinical, pathologic and roentgenologic review of 90 cases. Am J Clin Pathol 25(8):849–888

Daffner RH, Lupetin AR, Dash N, Deeb ZL, Sefczek RJ, Schapiro RL (1986) MRI in the detection of malignant infiltration of bone marrow. Am J Roentgenol 146(2):353–358

Desikan R, Barlogie B, Sawyer J, Ayers D, Tricot G, Badros A, Zangari M, Munshi NC, Anaissie E, Spoon D, Siegel D, Jagannath S, Vesole D, Epstein J, Shaughnessy J, Fassas A, Lim S, Roberson P, Crowley J (2000) Results of high-dose therapy for 1000 patients with multiple myeloma: durable complete remissions and superior survival in the absence of chromosome 13 abnormalities. Blood 95(12):4008–4010

Dimopoulos MA, Moulopoulos A, Smith T, Delasalle KB, Alexanian R (1993) Risk of disease progression in asymptomatic multiple myeloma. Am J Med 94(1):57–61

Dimopoulos MA, Moulopoulos LA, Maniatis A, Alexanian R (2000) Solitary plasmacytoma of bone and asymptomatic multiple myeloma. Blood 96(6):2037–2044

Dimopoulos M, Terpos E, Comenzo RL, Tosi P, Beksac M, Sezer O, Siegel D, Lokhorst H, Kumar S, Rajkumar SV, Niesvizky R, Moulopoulos LA, Durie BG (2009) International myeloma working group consensus statement and guidelines regarding the current role of imaging techniques in the diagnosis and monitoring of multiple Myeloma. Leukemia 23(9):1545–1556. doi:10.1038/leu.2009.89

Dimopoulos M, Kyle R, Fermand JP, Rajkumar SV, San Miguel J, Chanan-Khan A, Ludwig H, Joshua D, Mehta J, Gertz M, Avet-Loiseau H, Beksac M, Anderson KC, Moreau P, Singhal S, Goldschmidt H, Boccadoro M, Kumar S, Giralt S, Munshi NC, Jagannath S (2011) Consensus recommendations for standard investigative workup: report of the International myeloma workshop consensus panel 3. Blood 117(18):4701–4705. doi:10.1182/blood-2010-10-299529

Dinter DJ, Neff WK, Klaus J, Bohm C, Hastka J, Weiss C, Schoenberg SO, Metzgeroth G (2009) Comparison of whole-body MR imaging and conventional X-ray examination in patients with multiple myeloma and implications for therapy. Ann Hematol 88(5):457–464. doi:10.1007/s00277-008-0621-6

Dohner H, Guckel F, Knauf W, Semmler W, van Kaick G, Ho AD, Hunstein W (1989) Magnetic resonance imaging of bone marrow in lympho proliferative disorders: correlation with bone marrow biopsy. British J Haematol 73(1):12–17

Durie BG (2001) The epidemiology of multiple myeloma. Seminars in Hematol 38(2 Suppl. 3):1–5

Durie BG (2006) The role of anatomic and functional staging in myeloma: description of Durie/Salmon plus staging system. Eur J Cancer 42(11):1539–1543. doi:10.1016/j.ejca.2005.11.037

Durie BG, Salmon SE (1975) A clinical staging system for multiple myeloma. Correlation of measured myeloma cell mass with presenting clinical features, response to treatment, and survival. Cancer 36(3):842–854

Durie BG, Waxman AD, D'Agnolo A, Williams CM (2002) Whole-body (18)F-FDG PET identifies high-risk myeloma. J Nucl Med 43(11):1457–1463

Durie BG, Kyle RA, Belch A, Bensinger W, Blade J, Boccadoro M, Child JA, Comenzo R, Djulbegovic B, Fantl D, Gahrton G, Harousseau JL, Hungria V, Joshua D, Ludwig H, Mehta J, Morales AR, Morgan G, Nouel A, Oken M, Powles R, Roodman D, San Miguel J, Shimizu K, Singhal S, Sirohi B, Sonneveld P, Tricot G, Van Ness B (2003) Myeloma management guidelines: a consensus report from the scientific advisors of the international myeloma fundation. Hematol J 4(6):379–398. doi:10.1038/sj.thj.6200312

Durie BG, Harousseau JL, Miguel JS, Blade J, Barlogie B, Anderson K, Gertz M, Dimopoulos M, Westin J, Sonneveld P, Ludwig H, Gahrton G, Beksac M, Crowley J, Belch A, Boccadaro M, Cavo M, Turesson I, Joshua D, Vesole D, Kyle R, Alexanian R, Tricot G, Attal M, Merlini G, Powles R, Richardson P, Shimizu K, Tosi P, Morgan G, Rajkumar SV (2006) International uniform response criteria for multiple myeloma. Leukemia 20(9):1467–1473. doi:10.1038/sj.leu.2404284

Elliott BM, Peti S, Osman K, Scigliano E, Lee D, Isola L, Kostakoglu L (2011) Combining FDG-PET/CT with laboratory data yields superior results for prediction of relapse in multiple myeloma. Eur J Haematol 86(4):289–298. doi:10.1111/j.1600-0609.2010.01575.x

Fechtner K, Hillengass J, Delorme S, Heiss C, Neben K, Goldschmidt H, Kauczor HU, Weber MA (2010) Staging monoclonal plasma cell disease: comparison of the Durie–Salmon and the Durie–Salmon PLUS staging systems. Radiology 257(1):195–204. doi:10.1148/radiol.10091809

Fonseca R, Bergsagel PL, Drach J, Shaughnessy J, Gutierrez N, Stewart AK, Morgan G, Van Ness B, Chesi M, Minvielle S, Neri A, Barlogie B, Kuehl WM, Liebisch P, Davies F, Chen-Kiang S, Durie BG, Carrasco R, Sezer O, Reiman T, Pilarski L, Avet-Loiseau H (2009) International myeloma working group molecular classification of multiple myeloma: spotlight review. Leukemia 23(12):2210–2221. doi:10.1038/leu.2009.174

Fruehwald FX, Tscholakoff D, Schwaighofer B, Wicke L, Neuhold A, Ludwig H, Hajek PC (1988) Magnetic resonance imaging of the lower vertebral column in patients with multiple myeloma. Invest Radiol 23(3):193–199

Ghanem N, Lohrmann C, Engelhardt M, Pache G, Uhl M, Saueressig U, Kotter E, Langer M (2006) Whole-body MRI in the detection of bone marrow infiltration in patients with plasma cell neoplasms in comparison to the radiological skeletal survey. Eur Radiol 16(5):1005–1014. doi:10.1007/s00330-005-0055-7

Gleeson TG, Moriarty J, Shortt CP, Gleeson JP, Fitzpatrick P, Byrne B, McHugh J, O'Connell M, O' Gorman P, Eustace SJ (2009) Accuracy of whole-body low-dose multidetector CT (WBLDCT) versus skeletal survey in the detection of myelomatous lesions, and correlation of disease distribution with whole-body MRI (WBMRI). Skeletal Radiol 38(3):225–236. doi:10.1007/s00256-008-0607-4

Grover SB, Dhar A (2000) Imaging spectrum in sclerotic myelomas: an experience of three cases. Eur Radiol 10(11):1828–1831

Guglielmi G, Andreula C, Muto M, Gilula LA (2005) Percutaneous vertebroplasty: indications, contraindications, technique, and complications. Acta Radiol 46(3):256–268

Hall FM, Gore SM (1988) Osteosclerotic myeloma variants. Skeletal Radiol 17(2):101–105

Hall MN, Jagannathan JP, Ramaiya NH, Shinagare AB, Van den Abbeele AD (2010) Imaging of extraosseous myeloma: CT, PET/CT, and MRI features. Am J Roentgenol 195(5):1057–1065. doi:10.2214/AJR.10.4384

Hanrahan CJ, Christensen CR, Crim JR (2010) Current concepts in the evaluation of multiple myeloma with MR imaging and FDG PET/CT. Radiographics 30(1):127–142. doi:10.1148/rg.301095066

Harousseau JL, Dreyling M (2010) Multiple myeloma: ESMO clinical practice guidelines for diagnosis, treatment and follow-up. Ann Oncol 21(Suppl)5:v155–v157. doi:10.1093/annonc/mdq178

Heiser S, Schwartzman JJ (1952) Variations in the roentgen appearance of the skeletal system in myeloma. Radiology 58(2):178–191

Hillengass J, Fechtner K, Weber MA, Bäuerle T, Ayyaz S, Heiss C, Hielscher T, Moehler TM, Egerer G, Neben K, Ho AD, Kauczor HU, Delorme S, Goldschmidt H (2010) Prognostic significance of focal lesions in whole-body magnetic resonance imaging in patients with asymptomatic multiple myeloma. J Clin Oncol 28(9):1606–1610. doi:10.1200/JCO.2009.25.5356

Horger M, Kanz L, Denecke B, Vonthein R, Pereira P, Claussen CD, Driessen C (2007) The benefit of using whole-body, low-dose, nonenhanced, multidetector computed tomography for follow-up and therapy response monitoring in patients with multiple myeloma. Cancer 109(8):1617–1626. doi:10.1002/cncr.22572

Hosten N, Schorner W, Neumann K, Sander B, Oertel J, Kirsch A, Schubeus P, Cordes M, Felix R, Huhn D (1992) Magnetic resonance tomographic screening studies of the bone marrow with gradient-echo sequences. II. Gadolinium-DTPA-supported studies of plasmocytoma patients. Rofo 157(1):53–58. doi:10.1055/s-2008-1032965

Jantunen E, Laakso M (1996) Bisphosphonates in multiple myeloma: current status; future perspectives. British J Haematol 93(3):501–506

Kruger DG, Riederer SJ, Polzin JA, Madhuranthakam AJ, Hu HH, Glockner JF (2005) Dual-velocity continuously moving table acquisition for contrast-enhanced peripheral magnetic resonance angiography. Magn Reson Med Official J Soc Magn Reson Med/Soc Magn Reson Med 53(1):110–117. doi:10.1002/mrm.20324

Kusumoto S, Jinnai I, Itoh K, Kawai N, Sakata T, Matsuda A, Tominaga K, Murohashi I, Bessho M, Harashima K, Heshiki A (1997) Magnetic resonance imaging patterns in patients with multiple myeloma. British J Haematol 99(3):649–655

Kyle RA (1983) Long-term survival in multiple myeloma. N Engl J Med 308(6):314–316. doi:10.1056/NEJM198302103080604

Kyle RA (2000) The role of bisphosphonates in multiple myeloma. Ann Intern Med 132(9):734–736

Lecouvet FE, Malghem J, Michaux L, Maldague B, Ferrant A, Michaux JL, Vande Berg BC (1999) Skeletal survey in advanced multiple myeloma: radiographic versus MR imaging survey. British J Haematol 106(1):35–39

Lecouvet FE, Dechambre S, Malghem J, Ferrant A, Vande Berg BC, Maldague B (2001) Bone marrow transplantation in patients with multiple myeloma: prognostic significance of MR imaging. Am J Roentgenol 176(1):91–96

Lin C, Luciani A, Belhadj K, Deux JF, Kuhnowski F, Maatouk M, Beaussart P, Cuenod CA, Haioun C, Rahmouni A (2010) Multiple myeloma treatment response assessment with whole-body dynamic contrast-enhanced MR imaging. Radiology 254(2):521–531. doi:10.1148/radiol.09090629

Ludwig H, Fruhwald F, Tscholakoff D, Rasoul S, Neuhold A, Fritz E (1987) Magnetic resonance imaging of the spine in multiple myeloma. Lancet 2(8555):364–366

Mahnken AH, Wildberger JE, Gehbauer G, Schmitz-Rode T, Blaum M, Fabry U, Gunther RW (2002) Multidetector CT of the spine in multiple myeloma: comparison with MR imaging and radiography. Am J Roentgenol 178(6): 1429–1436

Malpas JS (1998) In: Malpas JS et al (eds) Myeloma: biology and management, 2nd edn. Oxford University Press, U S A. ISBN:10: 0192628828

Mariette X, Zagdanski AM, Guermazi A, Bergot C, Arnould A, Frija J, Brouet JC, Fermand JP (1999) Prognostic value of vertebral lesions detected by magnetic resonance imaging in patients with stage I multiple myeloma. British J Haematol 104(4):723–729

Meszaros WT (1974) The many facets of multiple myeloma. Semin Roentgenol 9(3):219–228

Moulopoulos LA, Dimopoulos MA, Weber D, Fuller L, Libshitz HI, Alexanian R (1993) Magnetic resonance imaging in the staging of solitary plasmacytoma of bone. J Clin Oncol 11(7):1311–1315

Moulopoulos LA, Dimopoulos MA, Alexanian R, Leeds NE, Libshitz HI (1994) Multiple myeloma: MR patterns of response to treatment. Radiology 193(2):441–446

Moulopoulos LA, Dimopoulos MA, Smith TL, Weber DM, Delasalle KB, Libshitz HI, Alexanian R (1995) Prognostic significance of magnetic resonance imaging in patients with asymptomatic multiple myeloma. J Clin Oncol 13(1): 251–256

Nanni C, Rubello D, Zamagni E, Castellucci P, Ambrosini V, Montini G, Cavo M, Lodi F, Pettinato C, Grassetto G, Franchi R, Gross MD, Fanti S (2008) 18F-FDG PET/CT in myeloma with presumed solitary plasmocytoma of bone. In Vivo 22(4):513–517

Nobauer I, Uffmann M (2005) Differential diagnosis of focal and diffuse neoplastic diseases of bone marrow in MRI. Eur J Radiol 55(1):2–32. doi:10.1016/j.ejrad.2005.01.015

Peh WC, Gelbart MS, Gilula LA, Peck DD (2003) Percutaneous vertebroplasty: treatment of painful vertebral compression fractures with intraosseous vacuum phenomena. Am J Roentgenol 180(5):1411–1417

Rahmouni A, Divine M, Mathieu D, Golli M, Dao TH, Jazaerli N, Anglade MC, Reyes F, Vasile N (1993a) Detection of multiple myeloma involving the spine: efficacy of fat-suppression and contrast-enhanced MR imaging. Am J Roentgenol 160(5):1049–1052

Rahmouni A, Divine M, Mathieu D, Golli M, Haioun C, Dao T, Anglade MC, Reyes F, Vasile N (1993b) MR appearance of multiple myeloma of the spine before and after treatment. Am J Roentgenol 160(5):1053–1057

Riccardi A, Mora O, Tinelli C, Valentini D, Brugnatelli S, Spanedda R, De Paoli A, Barbarano L, Di Stasi M, Giordano M, Delfini C, Nicoletti G, Bergonzi C, Rinaldi E, Piccinini L, Ascari E (2000) Long-term survival of stage I multiple myeloma given chemotherapy just after diagnosis or at progression of the disease: a multicentre randomized study. Cooperative Group of Study and Treatment of Multiple Myeloma. Br J Cancer 82(7):1254–1260. doi:10.1054/bjoc.1999.1087

Schirrmeister H, Bommer M, Buck AK, Muller S, Messer P, Bunjes D, Dohner H, Bergmann L, Reske SN (2002) Initial results in the assessment of multiple myeloma using 18F-FDG PET. Eur J Nucl Med Mol Imaging 29(3): 361–366

Schirrmeister H, Buck AK, Bergmann L, Reske SN, Bommer M (2003) Positron emission tomography (PET) for staging of solitary plasmacytoma. Cancer Biother Radiopharm 18(5): 841–845. doi:10.1089/108497803770418382

Schreiman JS, McLeod RA, Kyle RA, Beabout JW (1985) Multiple myeloma: evaluation by CT. Radiology 154(2): 483–486

Scutellari PN, Spanedda R, Feggi LM, Cervi PM (1985) The value and limitations of total body scan in the diagnosis of multiple myeloma: a comparison with conventional skeletal radiography. Haematologica 70(2):136–142

Shortt CP, Gleeson TG, Breen KA, McHugh J, O'Connell MJ, O'Gorman PJ, Eustace SJ (2009) Whole-Body MRI versus PET in assessment of multiple myeloma disease activity. Am J Roentgenol 192(4):980–986. doi:10.2214/AJR.08.1633

Stabler A, Baur A, Bartl R, Munker R, Lamerz R, Reiser MF (1996) Contrast enhancement and quantitative signal analysis in MR imaging of multiple myeloma: assessment of focal and diffuse growth patterns in marrow correlated with biopsies and survival rates. Am J Roentgenol 167(4): 1029–1036

Terpstra WE, Lokhorst HM, Blomjous F, Meuwissen OJ, Dekker AW (1992) Comparison of plasma cell infiltration in bone marrow biopsies and aspirates in patients with multiple myeloma. British J Haematol 82(1):46–49

Tertti R, Alanen A, Remes K (1995) The value of magnetic resonance imaging in screening myeloma lesions of the lumbar spine. British J Haematol 91(3):658–660

Van de Berg BC, Lecouvet FE, Michaux L, Labaisse M, Malghem J, Jamart J, Maldague BE, Ferrant A, Michaux JL (1996) Stage I multiple myeloma: value of MR imaging of the bone marrow in the determination of prognosis. Radiology 201(1):243–246

Vande Berg BC, Michaux L, Lecouvet FE, Labaisse M, Malghem J, Jamart J, Maldague BE, Ferrant A, Michaux JL (1997) Nonmyelomatous monoclonal gammopathy: correlation

of bone marrow MR images with laboratory findings and spontaneous clinical outcome. Radiology 202(1): 247–251

Varettoni M, Corso A, Pica G, Mangiacavalli S, Pascutto C, Lazzarino M (2010) Incidence, presenting features and outcome of extramedullary disease in multiple myeloma: a longitudinal study on 1003 consecutive patients. Ann Oncol 21(2):325–330. doi:10.1093/annonc/mdp329

Vogler JB III, Murphy WA (1988) Bone marrow imaging. Radiology 168(3):679–693

Walker R, Barlogie B, Haessler J, Tricot G, Anaissie E, Shaughnessy JD Jr, Epstein J, van Hemert R, Erdem E, Hoering A, Crowley J, Ferris E, Hollmig K, van Rhee F, Zangari M, Pineda-Roman M, Mohiuddin A, Yaccoby S, Sawyer J, Angtuaco EJ (2007) Magnetic resonance imaging in multiple myeloma: diagnostic and clinical implications. J Clin Oncol 25(9):1121–1128. doi:10.1200/JCO.2006.08.5803

Weber DM, Dimopoulos MA, Moulopoulos LA, Delasalle KB, Smith T, Alexanian R (1997) Prognostic features of asymptomatic multiple myeloma. British J Haematol 97(4):810–814

Weckbach S, Michaely HJ, Stemmer A, Schoenberg SO, Dinter DJ (2010) Comparison of a new whole-body continuous-table-movement protocol versus a standard whole-body MR protocol for the assessment of multiple myeloma. Eur Radiol 20(12):2907–2916. doi:10.1007/s00330-010-1865-9

Woolfenden JM, Pitt MJ, Durie BG, Moon TE (1980) Comparison of bone scintigraphy and radiography in multiple myeloma. Radiology 134(3):723–728

Zenge MO, Ladd ME, Vogt FM, Brauck K, Barkhausen J, Quick HH (2005) Whole-body magnetic resonance imaging featuring moving table continuous data acquisition with high-precision position feedback. Magn Reson Med Off J Soc Magn Reson Med/Soc Magn Reson Med 54(3):707–711. doi:10.1002/mrm.20598

Zenge MO, Ladd ME, Quick HH (2009) Novel reconstruction method for three-dimensional axial continuously moving table whole-body magnetic resonance imaging featuring auto calibrated parallel imaging GRAPPA. Magn Reson Med Off J Soc Magn Reson Med/Soc Magn Reson Med 61(4):867–873. doi:10.1002/mrm.21859

MRI For Response Assessment In Oncologic Bone Marrow Lesions

F. Lecouvet, P. Omoumi, A. Larbi, B. Tombal, N. Michoux, B. Vande Berg, M. Lonneux, and J. Malghem

Contents

Abstract

Imaging has multiple roles in oncology. Besides lesion detection and characterization, disease staging, the quantification of the tumor load and the evaluation of response to therapy are of critical importance for the patient and for the clinician, both in primary and metastatic cancers. The assessment of the response to treatment of bone lesions has been considered difficult or impossible even for most prestigious cancer authorities, compared to lesions involving soft tissues or other organs like the lungs or liver, for which response evaluation criteria exist. This is mainly due to the lack of sensitivity, specificity and measurement capabilities of imaging techniques that have been available for years for the assessment of bone lesions, i.e. bone scintigraphy (BS), radiographs and X-ray computed tomography (CT). This chapter first summarizes the possibilities and limitations of the aforementioned techniques. It illustrates the capabilities of "modern" imaging modalities, i.e. positron emission tomography (PET) and most importantly magnetic resonance imaging (MRI). Practical morphologic as well as functional observations that can be made using MRI at primary diagnosis are emphasized as well as the evaluation of response of bone marrow lesions to treatment. Technical advances in MRI, which further refine the capabilities of this modality for early evaluation of the response, including dynamic contrast-enhanced (DCE) imaging and diffusion-weighted imaging (DWI), are also covered.

F. Lecouvet (✉) · P. Omoumi · A. Larbi · N. Michoux · B. Vande Berg · M. Lonneux · J. Malghem
Department of Radiology,
Cliniques Universitaires Saint-Luc,
UCL Université de Louvain,
Hippocrate Avenue, 10/2942,
1200 Brussels, Belgium
e-mail: lecouvet@yahoo.fr

B. Tombal
Department of Urology,
Cliniques Universitaires Saint-Luc,
UCL Université de Louvain,
Hippocrate Avenue, 10/2942,
1200 Brussels, Belgium

A. Baur-Melnyk (ed.), *Magnetic Resonance Imaging of the Bone Marrow*, Medical Radiology. Diagnostic Imaging,
DOI: 10.1007/174_2011_492, © Springer-Verlag Berlin Heidelberg 2013

1 Clinical Background

The assessment of the therapeutic response of neoplastic conditions is of critical importance in the daily practice of oncology and in clinical trials. Both the clinician and the researcher want to know whether their patient's lesions respond to therapy, either to adapt the patient's treatment or to evaluate the benefit of new treatments. Besides clinical and biological tumoral markers, imaging is a fundamental actor in this evaluation of tumor response. Morphologic and functional imaging plays a key role in many cancers for the evaluation of the response to treatment of primary lesions and metastases, using quantitative measurement tools (RECIST, WHO criteria), validated for soft tissue lesions, mainly involving lung, liver, brain, lymph nodes and other organs (Therasse et al. 2000; Eisenhauer et al. 2009). In contrast, there is a critical need for validated monitoring tools in hematologic diseases involving the skeleton and in "osteophilic" cancers (which show a specific tropism for bone in their dissemination). In the absence of monitoring tools for bone disease, the clinician can only rely on "skeletal related events" (SRE) to monitor the disease, which presents well-known limits (Scher et al. 2011). Moreover, the clinician needs endpoints, i.e. prognostic parameters that provide information on the further evolution of the patient and of the disease, for example in terms of complications, progression free survival and overall survival. Among these endpoints, treatment response has been repeatedly demonstrated to be an important determinant of survival, which critically lacks in patients with predominant or exclusive involvement of bones (Sonpavde et al. 2011). Hence, the advent of valuable tools for the evaluation of bone marrow involvement and of the response to therapy generates wide interest among oncologists and hematologists.

2 Available Imaging Techniques: Overview

The historical difficulty of bone assessment results from the characteristics of imaging techniques used until now. Conventional radiography, BS and CT rely on the activation of bone cells—osteoblasts and osteoclasts—to detect changes in bone trabeculae caused by neoplastic lesions. This explains their lack of sensitivity at the early stages of the disease. Other limitations of these techniques are the lack of measurement capabilities, a poor sensitivity to treatment induced changes, and confusing findings such as the "flare phenomenon", that can be misinterpreted as a false progression of the disease.

PET and MRI have proven to be able to detect the neoplastic colonization of bone before the activation of bone cells. PET relies on the affinity of tumor cells for some radiopharmaceuticals and has the great advantage to propose a one step "whole body—all organ" staging. MRI offers excellent sensitivity for the detection of neoplastic cells within the bone marrow using basic anatomic sequences. Most useful sequences are T1-weighted FSE sequences, due to their high sensitivity in detecting fatty marrow replacement by neoplastic colonization, with a high contrast between the low signal intensity of the lesions and the high signal intensity of the surrounding marrow. These sequences are often completed by a fluid-sensitive sequence. The performance of MRI, and its superiority over BS and conventional radio graphy in terms of lesion detection, has been widely demonstrated in metastases from solid cancers and in hematologic malignancies (Daldrup-Link et al. 2001; Eustace et al. 1997; Ghanem et al. 2006; Nakanishi et al. 2005; Yang et al. 2011). Recent advances in hardware and software have lead to the development of sequences that can cover the whole body (WBMRI). The advent of DWI and DCE sequences further boosts this ability to detect and monitor bone lesions, even in anatomic areas of the skeleton that are more difficult to evaluate using conventional sequences (ribs, peripheral bones…), and to monitor their response to therapy (Ghanem et al. 2005; Schmidt et al. 2007).

3 Bone Scintigraphy and Single Photon Emission Computed Tomography

Based on its wide availability, limited cost, and sensitivities and specificities that have been considered acceptable for several decades, BS has been and still remains commonly used for the detection of bone lesions in "osteophilic" cancers (breast, prostate, thyroid, kidney…). The technique is based on the use

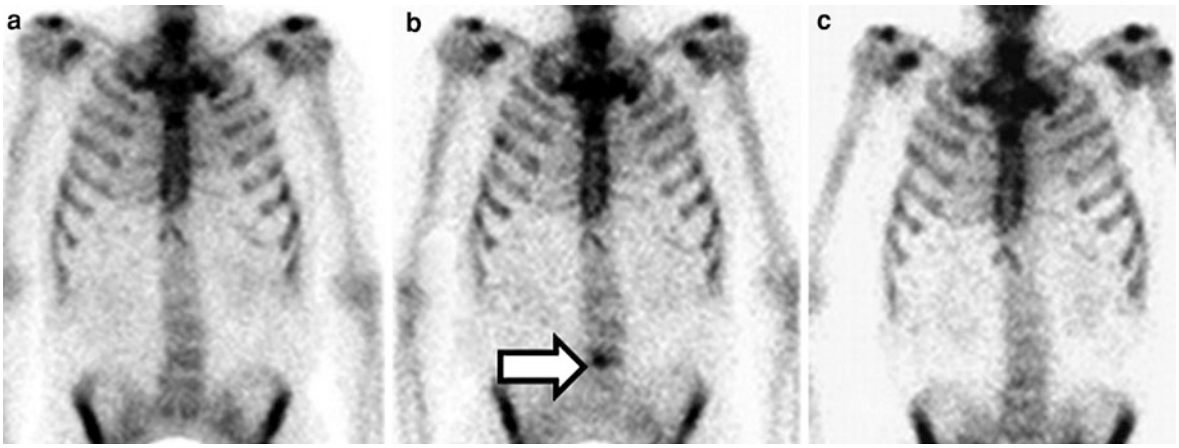

Fig. 1 Illustration of the "flare phenomenon" on consecutive Tc99 m bone scans (BS) in a patient with breast cancer. **a** Initial staging does not reveal any significant uptake. **b** Three-month follow-up BS reveals appearance of a focal uptake (*arrow*), suggesting the appearance of a metastasis. **c** Six-month follow-up BS shows disappearance of this focal abnormality; this observation, and the continuous decrease in seric markers, confirm the "flare phenomenon" observed at three-month follow-up (osteoblastic response within a previously occult BS lesion)

of a tracer (diphosphonate-bound 99 m-Technetium) showing an affinity for osteoblasts. This explains a limited sensitivity, especially in (predominantly) osteolytic bone lesions. Modern imaging techniques (PET and MRI) reveal the presence of lesions in a significant proportion of patients with negative BS, with critical impact on the therapeutic decisions (Avrahami et al. 1989; Balliu et al. 2010; Gosfield et al. 1993). Curative therapy may indeed only be considered if no metastasis is present; if metastases are present, systemic treatment is required.

Since BS is a marker of osteoblastic activity, its specificity is also limited, with frequent uptake in benign conditions such as degenerative joint diseases, benign fractures or Paget disease. This often raises the need for second line examinations to clarify BS findings, most often radiographs, which may leave the radiologist with a residual doubt, leading to the discussion of third line imaging modalities (CT or MRI) when radiographs do not provide neither a typical benign nor a frank malignant explanation to the abnormal uptake seen on the BS (discrepancy between negative BS and positive radiographs). This multistep approach raises evident questions of costs, time, irradiation and convenience for the patient (Lecouvet et al. 2007).

In terms of response assessment, BS is even more insufficient, not only due to its lack of sensitivity and specificity, but most importantly due to its lack of spatial resolution and measurement capabilities, and delay for detecting significant changes or even disease resolution, compared to other clinical parameters of response or progression (Condon et al. 1981; Scher 2003).

Moreover, BS findings after treatment may be falsely positive for disease progression. The "flare phenomenon" is characterized by the appearance of new abnormalities or enlargement of previous pathologic foci, due to an osteoblastic response, i.e. new bone formation within pre-existing, and sometimes occult lesions, which respond to therapy and are wrongly considered as new or progressive lesions (Ciray et al. 2000; Venkitaraman et al. 2009). The correct identification of this transient phenomenon is only made a posteriori on the follow-up BS that shows fading of the falsely progressive lesions, often more than 6 months after treatment response (Pollen et al. 1984) (Fig. 1). This phenomenon is not uncommon, with reported frequencies of 6–25% in patients with prostate cancer metastases, and in 33% of patients with treated breast metastases (Messiou et al. 2009).

Single-photon emission computed tomography (SPECT), now most commonly combined with CT technology, improves the anatomic resolution and reduces the number of equivocal and false positive findings compared to BS. However, SPECT remains limited in terms of sensitivity and provides significant irradiation (Even-Sapir et al. 2006; Savelli et al. 2001). Its role in lesion follow-up under treatment also remains to be evaluated.

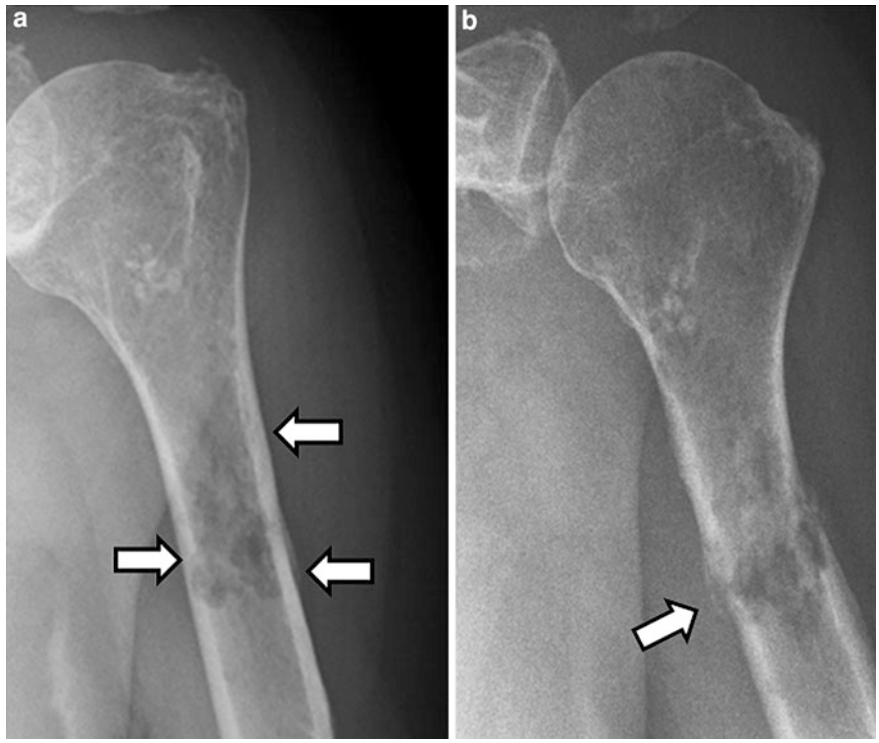

Fig. 2 Radiographic diagnosis of a pathologic fracture. **a** Radiograph of the left humerus obtained because of scintigraphic uptake shows lytic lesion (*arrows*) within the diaphysis typical for a metastasis. **b** Two weeks later, radiograph performed in the emergency room because of acute spontaneous pain reveals pathologic fracture (*arrow*)

4 Radiography

Radiography remains the first line tool for investigating painful skeletal areas and for the positive diagnosis of pathologic fractures once they have occurred, in patients with or without known cancer or bone involvement (Fig. 2). There is no role for radiographs in the setting of a systematic screening for neoplastic bone lesions, except for multiple myeloma (MM) (cf. infra). They have indeed a low sensitivity, especially for the detection of lytic lesions within the trabecular bone, which require 30–75% bone loss before being detectable (Vinholes et al. 1996).

In metastatic disease, their main role is the clarification of a nonspecific or equivocal BS finding, the evaluation of the either osteolytic or osteoblastic "behavior" of a lesion and the evaluation of the fracture risk associated with lesions detected by BS, PET or MRI.

The observation of radiographic signs of therapeutic response of bone lesions—peripheral sclerosis, lesion filling and condensation—is often delayed by several months, ambiguous or absent despite clinical improvement, which explains that there is no place for X-rays in the systematic evaluation of response (Coombes et al. 1983; Galasko 1995; Hamaoka et al. 2004; Libshitz and Hortobagyi 1981).

In multiple myeloma (MM), radiographs are still used in most centers for the staging (Durie and Salmon), while its replacement by MRI is commonly advocated for an earlier detection of lesions associated with (a risk of evolution to) an advanced stage of disease (Durie 2006; Lecouvet et al. 1999). This radiographic survey has a limited value for disease follow-up, as the comparison with MRI clearly demonstrates the frequent persisting visibility of lytic areas on radiographs despite evident signs of response based on the bone marrow signal changes at MRI (Baur-Melnyk et al. 2005; Moulopoulos et al. 1994).

5 Computed Tomography

As this technique is irradiating, CT exploration is generally targeted to a definite portion of the body and is not used as a tool for systematic bone screening in cancer. This might be reconsidered over the years due to the advent of multidetector CT (MDCT)-based whole body capabilities and consistent efforts to reduce the radiation doses necessary to achieve

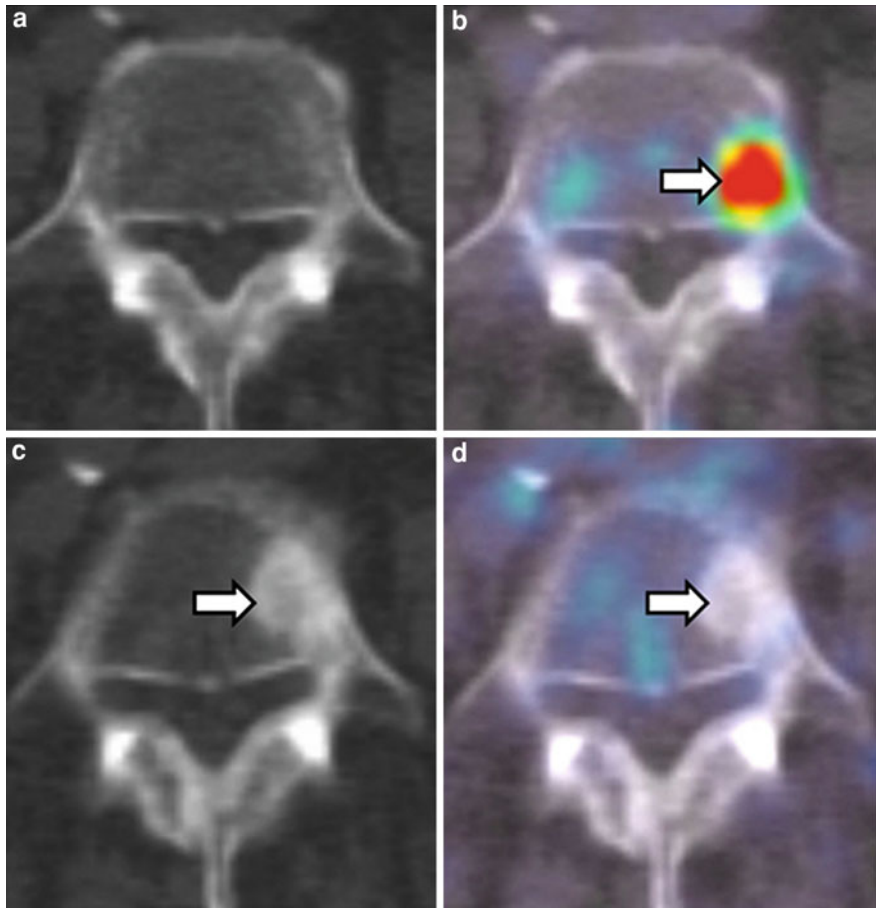

Fig. 3 18FDG-PET/CT correlation at diagnosis (**a**, **b**) and after treatment (**c**, **d**) in a patient with breast cancer. (**a**, **b**) At diagnosis, CT does not show any abnormality within this lumbar vertebra despite evident left-sided focus of FDG uptake, typical for a metastasis (*arrow* in **b**). (**c**, **d**) After three cycles of chemotherapy, an osteoblastic focus is evident on the CT (*arrow* in c), which could be mistaken as a new sclerotic metastasis on the basis of the CT; PET shows disappearance of the FDG uptake, indicating responsive lesion (*arrow* in **d**)

sufficient diagnostic information (Hamaoka et al. 2004; Groves et al. 2006; Horger et al. 2005).

The sensitivity of CT for a systematic detection of bone metastases is poorly known. It is more sensitive than radiographs for lesion detection and provides information on the adjacent soft tissues (Bauerle and Semmler 2009). Comparison with MRI and PET shows a lower sensitivity of CT compared to these techniques (Yang et al. 2011; Sundaram and McGuire 1988). Moreover, as for radiographs and BS, CT can be falsely positive in the evaluation of response to therapy, due to the appearance of osteosclerotic areas in relation to the response to treatment within osteolytic or previously undetected lesions. This is frequently illustrated by the correlation of CT and PET findings before and after therapy of bone metastases (Fig. 3).

For these reasons, CT is not used as a primary tool for bone lesions monitoring. However, the technique is available in a significant proportion of cancer patients, as thoraco-abdomino-pelvic examinations are often repeated for visceral lesion detection and follow-up. These examinations provide a "free access" to bones, especially the spine and pelvis. This bone study can then be optimized by the use of adequate acquisition and reconstruction parameters (windows, kernels, slice thickness…). On these examinations, an increase in size of an osteolytic lesion, appearance of osteolysis in a previously sclerotic lesion and increase in the soft tissue extension of a bone lesion can be regarded as reliable signs of disease progression. Any other observation (lack of change, appearance of sclerosis, appearance of a new sclerotic areas…) should be considered more cautiously and should not be taken into account for valuable response evaluation (Figs. 3, 4) (Hamaoka et al. 2004).

In multiple myeloma, comparison of whole body CT (WBCT) to WBMRI for lesion screening has shown that WBCT was less sensitive to detect the bone involvement by the disease (Baur-Melnyk et al. 2008).

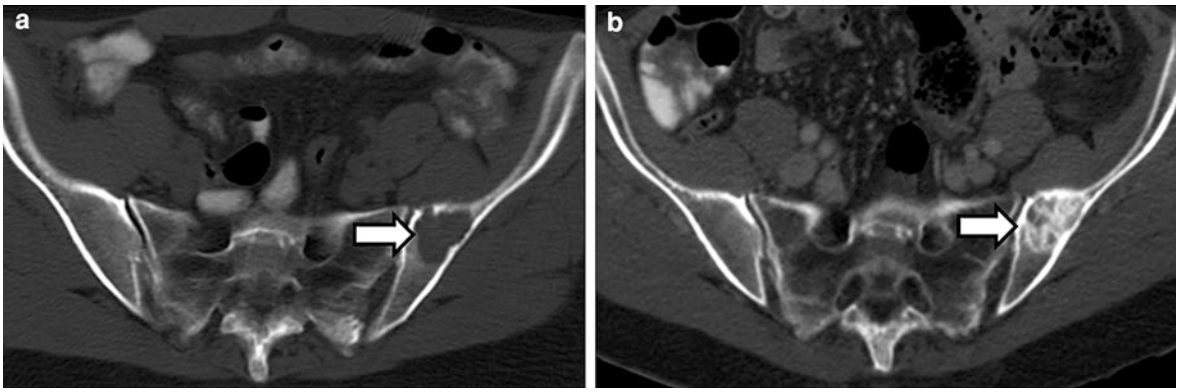

Fig. 4 CT follow-up of osteolytic metastasis. **a** Initial CT reveals lytic lesion within the posterior left iliac crest. **b** Follow-up after chemotherapy shows sclerosis of this lesion suggestive of response to the treatment

6 Positron Emission Tomography and PET-CT

PET provides metabolic—functional—information on the uptake of positron-emitting tracers by tissues. It enables a "whole body—all organ" screening. The combination of PET with CT and more recently with MRI on hybrid scanners combines the functional information provided by PET to the improved anatomic localization offered by CT (Hamaoka et al. 2004; Antoch et al. 2003). Under treatment, both PET and CT provide original and complementary information on the evolution of lesions: decrease in metabolic activity and increase in CT attenuation due to osteoblastic reaction are observed in responding lesions (Fig. 4) (Yang et al. 2011; Tateishi et al. 2008).

The most commonly used PET radiopharmaceutical, 18F-fluorodeoxyglucose (18FDG), is a non-specific tracer analog of glucose. It provides information on glucose metabolism and transport associated with several tumors, but also with some benign conditions. It enters the neoplastic cells by a membrane protein and is trapped within the cell once phosphorylated into FDG-6-phosphate. The technique allows qualitative whole body screening, showing often the primary lesion and its metastases to various organs (Fig. 5). Quantitative analysis is also obtained through the measurements of standardized uptake values (SUV), which reflect the tissue activity within a region of interest corrected for the injected activity and for the patients' body weight. Assessment of response is based on the follow-up of these qualitative and quantitative analyses.

18FDG-PET has proven to be a technique of choice for whole organ staging and follow-up of several cancers, especially lung, breast, head and neck neoplasms, melanoma, lymphoma (Tateishi et al. 2008; De Giorgi et al. 2010). However, the translation of PET to the daily practice of oncology as a tool of response assessment requires several precisions: the definition of cut-off quantitative changes for defining response/progression, time intervals for follow-up, and the optimal indications of CT as adjunct in PET-CT (dose, contrast…) (Shankar et al. 2006; Young et al. 1999; Suzuki et al. 2008).

FDG is a nonuniversal tracer. Several cancers and secondary lesions, especially prostate, neuroendocrine or some bronchial cancers, and osteoclerotic meta stases, show little affinity for this marker compared to other cancers and osteolytic lesions (Yang et al. 2011; Young et al. 1999; Shreve et al. 1996). Other tracers have been developed to target cancers with poor affinity for FDG, on the basis of other metabolic pathways. Their availability in clinical practice is less evident due to more difficult synthesis and shorter half-life. Among these, 11C/18F-choline and 11C-acetate raise much interest, especially in prostate cancer. Choline is transported into cells and trapped as a constituent of the membrane phospholipids. 18F-choline and 11C-choline have respective advantages and limitations. 18F-choline is excreted in the urine, which interferes with pelvic imaging. 11C-choline is better suited for pelvic imaging but interferes with upper abdomen imaging due to

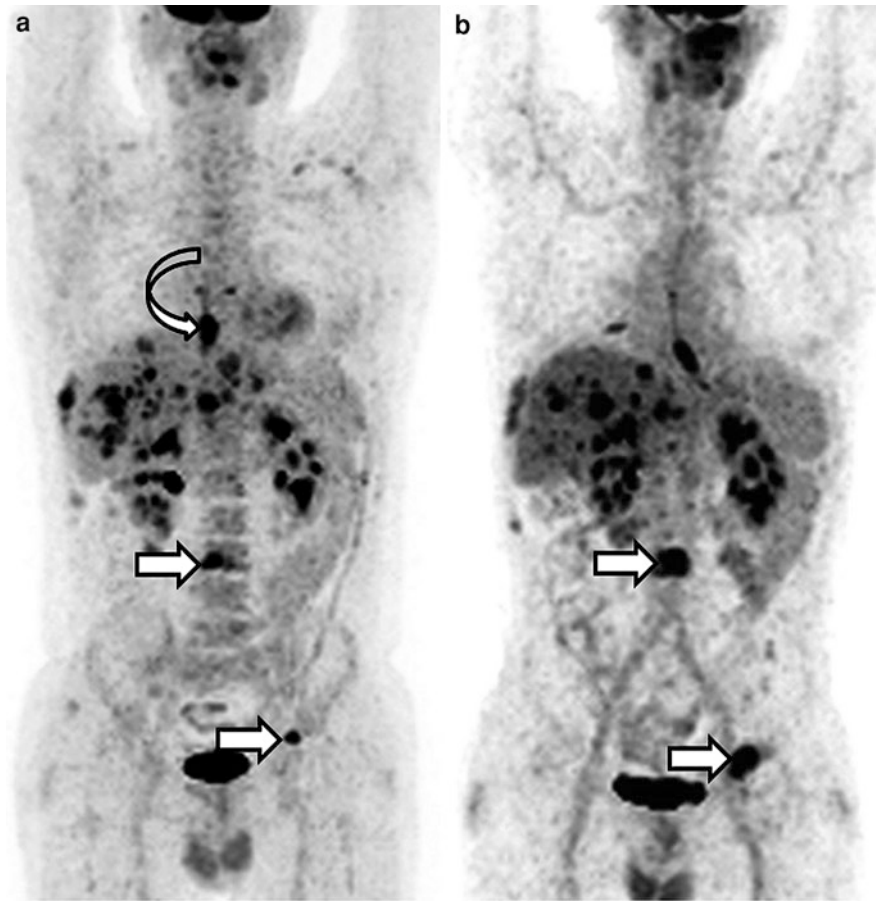

Fig. 5 FDG PET, staging and follow-up, in a patient with cancer of the oeso-gastric junction. **a** The technique not only shows the primary tumor (*curved arrow*), but also enables all organs screening: liver mets are evident, and bone mets are present in a right rib, in a lower lumbar vertebra and in the left iliac bone (*arrows*). **b** Six-month follow-up PET shows evident increase in size of the lumbar and iliac lesions, with heterogeneous behavior of the liver lesions

accumulation in the liver, kidneys, pancreas and spleen; moreover, its very short half-life limits its use to sites with cyclotrons (Langsteger et al. 2006). 11C-acetate also shows marked uptake in prostate cancer and has been shown to be more sensitive to detect prostate cancer than 18FDG PET; but there is limited information on bone metastases (Oyama et al. 2002). Another interesting tracer is 18F-fluoride, taken up by bone metastases in relation with their osteoblastic activity, incorporated as fluoroapatite at the bone surface where the turnover is the greatest, leading to conspicuous distinction between metastases and adjacent normal bone. The images resemble those obtained at BS, but with higher quality and higher spatial resolution, and the technique appears superior to BS for detecting both osteoblastic and osteolytic bone metastases (Even-Sapir et al. 2006).

Finally, additional radiopharmaceuticals are developed, targeting specific tumor receptors, especially in hormonal receptor-positive breast cancer and in neuroendocrine cancers.

7 Magnetic Resonance Imaging

Radiographs, BS and CT only detect neoplastic lesions to bone at a relatively late stage, weeks or months after the appearance of tumor cells within the bone marrow, since they rely on the activation of bone cells—osteoblasts and osteclasts—to become able to detect the tumor. MRI is sensitive to early changes in bone marrow that precede this osteoclastic/osteoblastic response of the bone matrix to tumor

infiltration, before bone trabeculae or cortices are affected by the disease (Vande Berg et al. 1998a, b).

The availability of the technique, its repeatability, the lack of irradiation and its ability to provide (almost) whole body evaluation contribute to promote MRI as a first line tool for the detection and characterization of many tumoral lesions involving the skeleton, and from there for the staging of cancers and evaluation of their response to treatment. Besides conventional anatomic sequences, advances in perfusion and diffusion imaging further refine the assessment of tumoral lesions during the (early) phases of therapy, providing the clinician with tools to evaluate the efficacy of treatments targeting bone lesions (Messiou et al. 2009).

7.1 Sequences

MRI contrast relies on the differences in T1 and T2 relaxation times between neoplastic lesions and their normal marrow environment. Metastatic infiltration of the bone marrow leads to a lengthened T1 relaxation time and signal loss, which contrasts with the surrounding high signal related to the fat content of the bone marrow (Vande Berg et al. 1998a).

T1-weighted images are the basis of bone marrow screening, due to their exquisite sensitivity to the alteration of the balance between fat and nonfat components of the bone marrow and to their universality, i.e. transposability for acquisition and reading from one center to the other, from one magnet to the other and, in the setting of assessment of treatment response, from one examination to the other. While these T1-weighted images are often sufficient for lesion detection and follow-up under treatment, especially in patients with poor (fatty) surrounding bone marrow in relation with age or treatment, most centers acquire additional T2 or T2-equivalent images (T2-weighted fat-suppressed or short tau inversion recovery (STIR) sequences) as part of the routine marrow screening and follow-up. Post-injection images and quantitative evaluation of marrow enhancement after contrast injection are only obtained when the distinction is not evident on conventional sequences between diffuse neoplastic infiltration and benign hyperplasia of the bone marrow or for the optimal definition of the extra osseous spread of tumors, for example within the spinal canal (Vande Berg et al. 2005; Baur et al. 1997). This injection of contrast material is also indicated when meningeal carcinomatosis is suspected.

7.2 Target Anatomic Areas

As hematologic cancers and metastases have a preferential tropism for red marrow containing skeletal areas, MRI studies will "focus" on these areas, for both lesion detection and follow-up. Screening of the whole spine in the sagittal plane and pelvis in the coronal plane covers about 90% of these skeletal areas and is considered sufficient by many authors, offering reproducibility, rapidity, with no or very little loss in diagnostic performance compared to whole body studies, since the vast majority of patients presenting lesions in the peripheral skeleton also present lesions within the central skeleton (Lecouvet et al. 2010; Russell et al. 1966). Of note, an MRI study limited to the spine appears insufficient, at least in multiple myeloma, for the marrow screening (Bauerle and Semmler 2009). However, whole body protocols with their increasing availability on MR magnets, with the improvement in their image resolution and shortening of acquisition time, along with the development whole body DWI (WBDWI) and "all organ" capabilities (cf. infra), are now being employed at many institutions (Schmidt et al. 2009; Moynagh et al. 2010).

7.3 Target Cancers

Screening of the skeleton for neoplastic lesions and evaluation of their response to therapy has major importance in "osteophilic" cancers (i.e. prostate, breast, kidney, thyroid, lung…) and in hematologic disorders involving bones (i.e. multiple myeloma and lymphoma).

As bone tumors have been considered "non measurable" for years, the use of MRI for the assessment of lesion response in patients who were previously treated "blinded" or based on the limited value of "skeletal related events", offers new perspectives and generates wide interest in many malignancies, especially in prostate and breast cancers, lymphoma and myeloma (Dreicer 1997).

For several of these cancers, other tools, especially 18FDG-PET scan as already mentioned, offer reliable

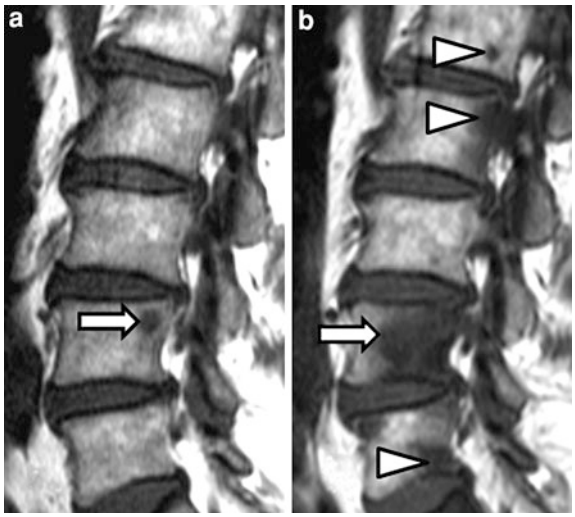

Fig. 6 Progressive metastatic disease at MRI: increase in the number and size of marrow lesions in a man with prostate cancer. **a** Sagittal T1-weighted MR image of the lumbar spine shows an isolated focus of low signal intensity within L4, corresponding to a metastasis (*arrow*). **b** Despite initiation of systemic therapy, 3-month follow-up MR image shows increase in the L4 lesion (*arrow*), and multiple new lesions (*arrowheads*), indicating disease progression

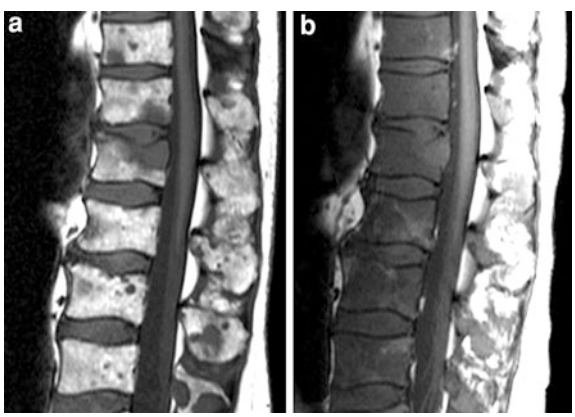

Fig. 7 Progressive metastatic disease: evolution from multifocal marrow lesions to diffuse neoplastic marrow infiltration in a man with prostate cancer. **a** Sagittal T1-weighted MR image of the lumbar spine shows multiple foci of low signal intensity within the vertebral bodies and posterior elements, corresponding to metastases. **b** Despite initiation of systemic therapy, 3-month follow-up MR image shows severe diffuse decrease of the marrow signal indicating progression of the neoplastic infiltration of the bone marrow

all organ screening and response evaluation. This technique is very efficient in lung cancer and lymphoma, for example. The comparison between PET

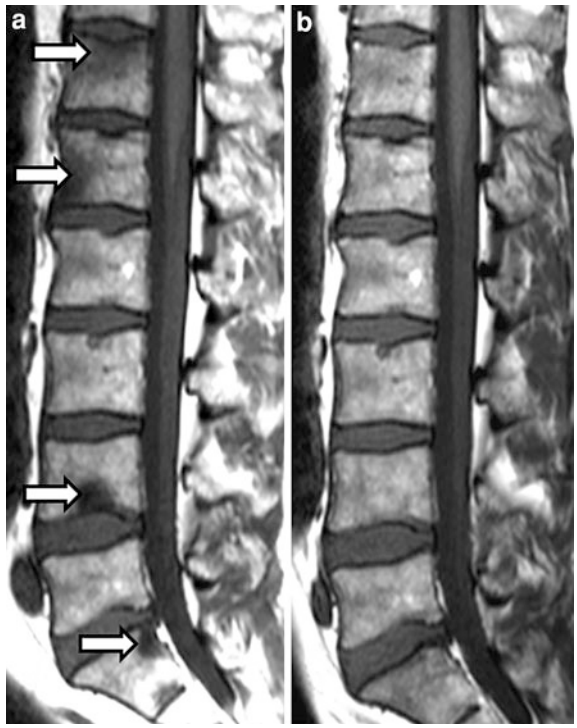

Fig. 8 Complete response: evolution from multifocal marrow lesions to normal marrow appearance in a woman with breast cancer. **a** Initial sagittal T1-weighted MR image of the lumbar spine shows multiple foci of low signal intensity, corresponding to metastases (*arrows*). **b** After 3-month systemic therapy, follow-up image shows complete disappearance of the lesions and return to normal homogeneous high signal intensity of the bone marrow

and WBMRI in terms of diagnostic performance, and also in terms of costs, has to be assessed (Ghanem et al. 2005; Antoch et al. 2003; Schmidt et al. 2007).

7.4 Qualitative (Morphologic) Analysis of Bone Marrow Involvement and of Tumor Response

The patterns of marrow involvement in metastatic disease to bone and in hematologic malignancies have been widely described (Vande Berg et al. 1998a, b). Contrasting with the homogeneous relatively high signal intensity of the normal bone marrow on T1-weighted images and its low signal on STIR or PD fat saturated images, the neoplastic involvement of the marrow will present either a focal appearance (low/intermediate to high signal intensity foci on T1/STIR or PD-fs images) or a diffuse appearance (diffuse low/

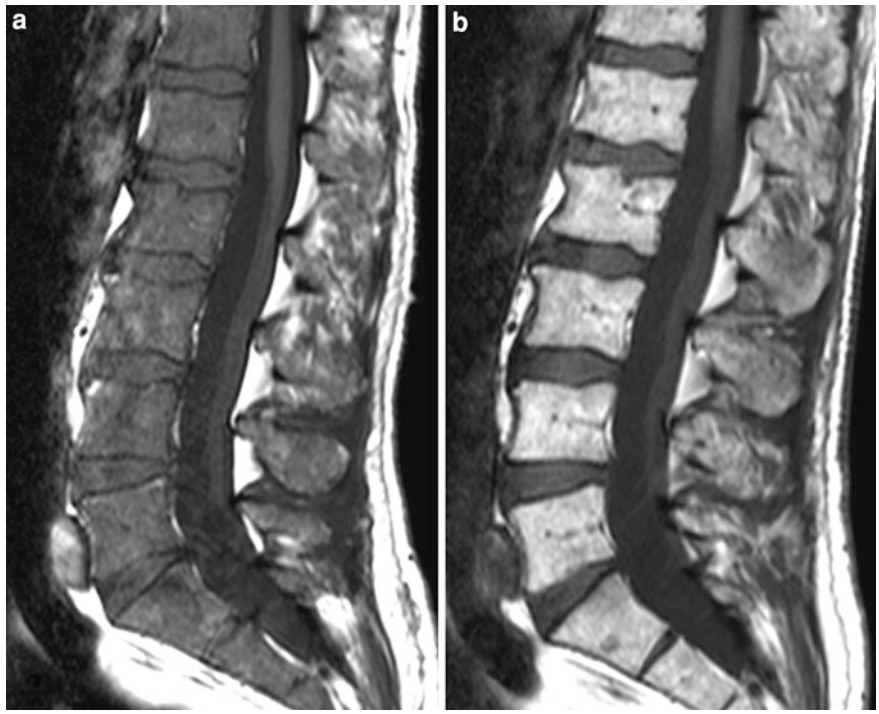

Fig. 9 Complete MRI response: evolution from diffuse marrow infiltration to return to normal marrow appearance in a man with myeloma. **a** Initial sagittal T1-weighted MR image of the lumbar spine shows diffuse decrease of the marrow signal, identical to that of disks, indicating diffuse neoplastic infiltration. **b** After 6-month systemic therapy, follow-up MR image shows complete return to homogeneous high signal intensity of the bone marrow (complete remission was confirmed by bone marrow biopsy and seric tests)

intermediate to high signal intensity of the marrow, which becomes lower than disk or muscle signal intensity on T1-weighted images). Besides these focal and diffuse patterns, a less common "salt and pepper" pattern, characterized by multiple tiny foci of abnormal marrow signal, is reported, especially in hematologic malignancies (Baur-Melnyk et al. 2008; Vande Berg et al. 1998a).

The follow-up of patients with neoplastic bone involvement after treatment may show evolutions in these patterns. Some of these changes are with no ambiguity indicative either of disease progression or on the contrary of response to treatment. Evolution from a normal bone marrow appearance to a focal metastatic pattern or to diffuse marrow signal alteration, increase in the number and/or size of metastatic foci, evolution from focal to diffuse neoplastic infiltration will be indicative of progressive disease (Fig. 6, 7). Disappearance of focal lesions, decrease in their number and/or size and return from focal or diffuse marrow alterations to a normal marrow appearance are indicative of response to treatment (Fig. 8, 9). The complete disappearance of lesions may indicate "imaging" remission, which does not necessarily correlate with complete remission at the microscopic level.

Perfect stability in size and appearance of the marrow abnormalities after treatment should be interpreted cautiously: residual lesions may represent responsive, controlled, but still active disease or on the contrary, "cured" disease with persistence of "scar" tissue. Whether contrast material injection, study of perfusion or diffusion parameters will help or not in this difficult differential diagnosis remains uncertain. Some lesions showing evident decrease in their contrast enhancement after treatment have shown residual viable tumor cells at histology (Lecouvet et al. 1998a).

Relapse is characterized by the reappearance of one or several new lesions in a bone marrow that had shown previous return to normal appearance after therapy; sometimes it may also take the appearance of progression of a lesion that had previously shown size regression under treatment or was stabilized by this treatment.

A pitfall may be encountered when marrow stimulating factors are used in association with chemotherapy. This treatment may indeed lead to diffuse alteration of the bone marrow signal, with decrease of its signal intensity on T1-weighted images, due to marrow hyperplasia, which may be confusing for progression to diffuse neoplastic infiltration (Vande Berg et al. 2005; Ryan et al. 1995) (Fig. 10). The study

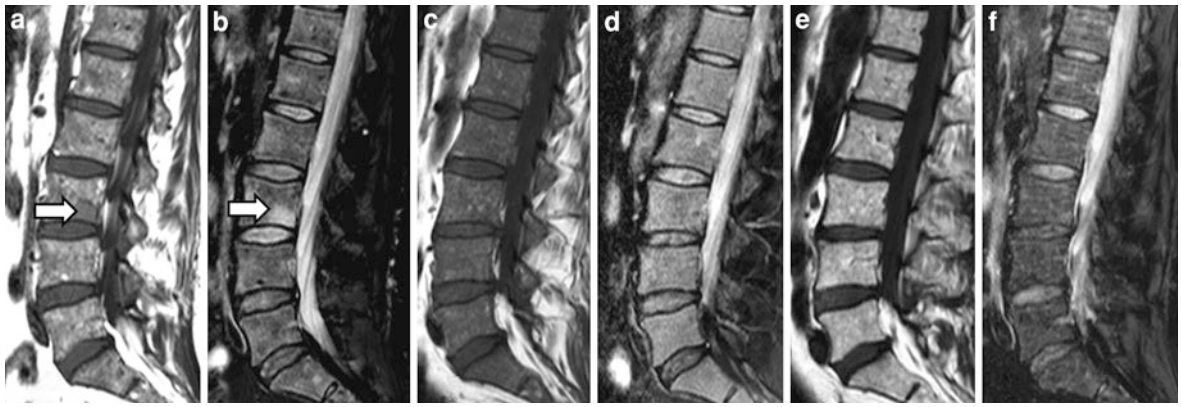

Fig. 10 False progression to diffuse marrow infiltration due to the use of hematopoietic growth factors in a treated multiple myeloma patient. **a**, **b** Pre-treatment T1- (**a**) and PD fat saturated (**b**) sagittal MRI of the lumbar spine show heterogeneous marrow signal with focus of marrow replacement in L3 (*arrow* in a and b). (**c**, **d**) After myeloablative treatment and intensive use of growth factors for stem cell mobilization before marrow transplantation, follow-up MR images show diffuse decrease of the marrow signal which becomes close to that of disks on T1 images of the spine (**c**) and discrete signal increase on PD fat saturated images (**d**). Contemporary bone marrow biopsy performed within the iliac crest revealed diffuse benign marrow hyperplasia. (**e**, **f**) Two-month follow-up MRI shows return to a normal homogeneous appearance of the bone marrow on all sequences

of marrow enhancement after contrast material injection and perfusion parameters enable the distinction between these conditions, as benign hyperplasia shows only limited enhancement compared to diffuse neoplastic infiltration (Baur et al. 1997).

Of note, metastatic cancer to bone may be a heterogeneous disease, with sometimes variable behavior among lesions under treatment, some of them showing obvious signs of response, while others show progression, suggesting appearance of resistance to treatment in some metastatic foci (Fig. 11). This observation underlines the need for extensive skeletal surveys, to avoid wrong conclusions (for instance, response) made on the basis of the follow-up of a limited number of lesions; this could advocate the use of WBMRI for lesion follow-up in multifocal skeletal involvement.

7.5 Particular Morphologic Aspects of Lesion Response

The response of focal marrow lesions to therapy may be characterized, along with their reduction in size, by the appearance of a peripheral halo of fatty marrow, with characteristic high signal intensity on T1-weighted images (Fig. 12). This "fatty halo sign" is indicative of lesion response and parallels the observation of the appearance of fat within "responsive" or "healing" nonneoplastic conditions such as benign vertebral compression fractures, spondylodiscitis or degenerative disk disease. In these conditions, the transition from "edema-like" marrow infiltration to "fat-like" signal also indicates stabilization or healing.

Contrasting with this "fatty" halo, a "cellular" halo, may be observed at the periphery of neoplastic lesions, consisting in a faint border with a low signal on T1 and high signal intensity on STIR/PD-fs images, which is interpreted as indicative of an "active" or "aggressive" tumoral lesion (Hwang and Panicek 2007). The disappearance of this halo at the periphery of treated lesions might be an early indicator of response.

Lesion response sometimes does not take the appearance of shrinking, but rather of progressive fading of the marrow signal abnormalities and return to normal marrow signal intensity within the lesions; whether this evolution is more typical for some types of treatments (cystostatic) remains to be established.

7.6 Ancillary Indicators of Response/ Progression

The occurrence of a pathologic fracture, due to focal bone weakening by a neoplastic lesion, and progression or appearance of soft tissue extension (for example

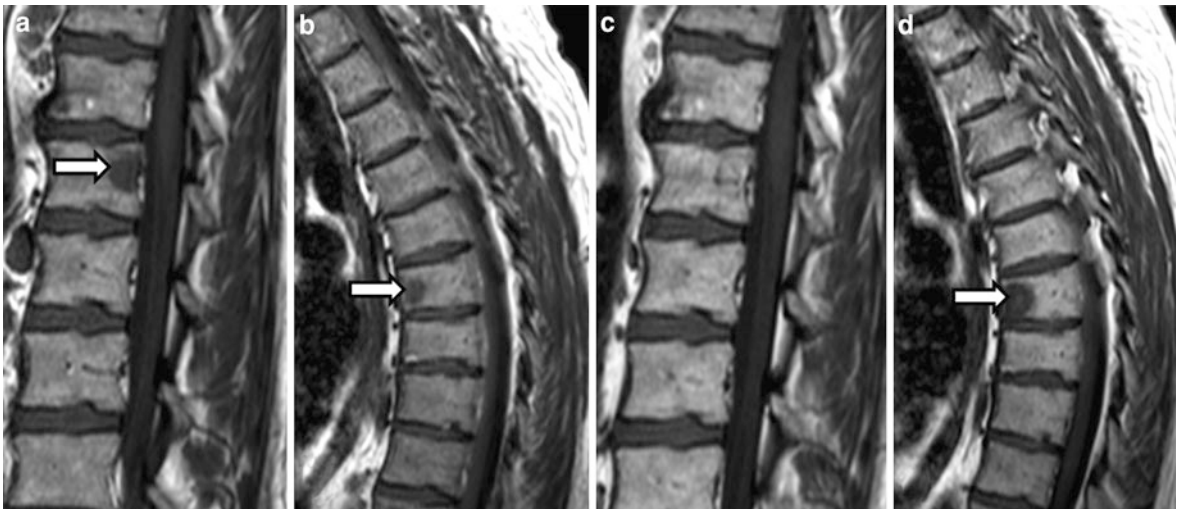

Fig. 11 Illustration of the potential asynchronic evolution of bone metastases. **a**, **b** Lumbar (**a**) and thoracic (**b**) sagittal T1-weighted MR images show two low signal intensity lesions corresponding to metastases (*arrows*). (**c**, **d**) After 3 months of systemic therapy, the lumbar lesion shows complete disappearance, whereas the thoracic lesion shows evident increase in size (*arrow* in **d**)

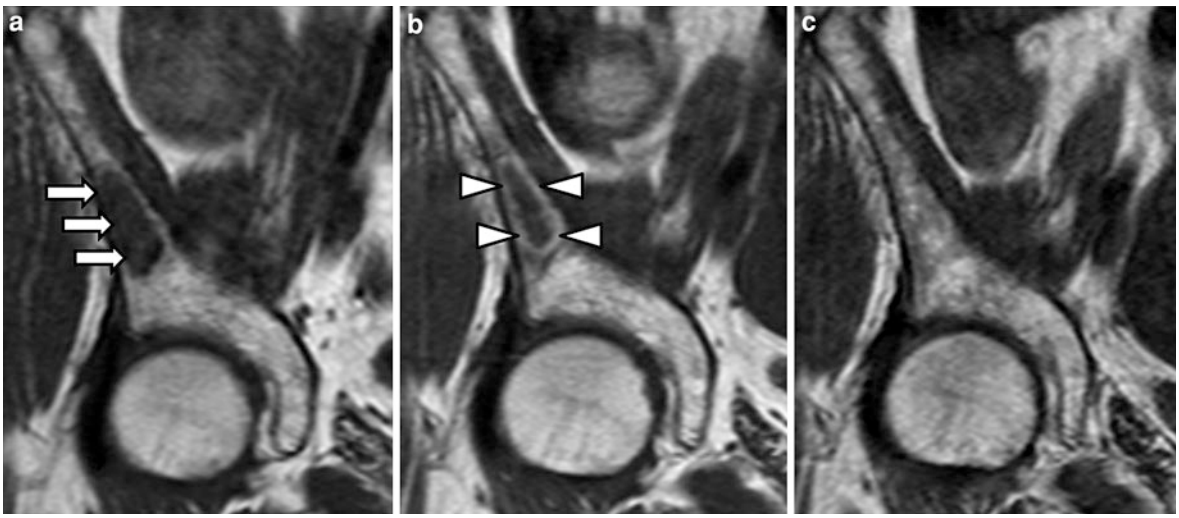

Fig. 12 Follow-up of neoplastic lesion during treatment: appearance of a peripheral fatty halo in a responding lesion. (**a**) Initial coronal T1-weighted MR image of the pelvis shows low signal intensity lesion within right iliac bone typical for a metastasis (*arrows*). (**b**) After 3-month systemic therapy, follow-up image shows the appearance of peripheral halo of high signal intensity, corresponding to fat surrounding the "shrinking" lesion (*arrowheads*). (**c**) Two-year follow-up shows complete disappearance of the lesion, with reappearance of normal marrow within the lesion

epidural) from a marrow lesion, are obvious signs of disease progression. Of note, benign osteoporotic fractures may occur during the course of the disease, which could be regarded as signs of disease progression on the basis of clinical records or conventional radiographs, but for which MRI shows the benign origin, sometimes contrasting with concurrent signs of response in neoplastic lesions. This discordance illustrates how "skeletal related events" are sometimes falsely indicative of progressive disease (Fig. 13).

The importance of the evaluation of soft tissue extension from bone lesions must be emphasized, especially in the spine environment. The presence of paraspinal or epidural infiltration may justify careful

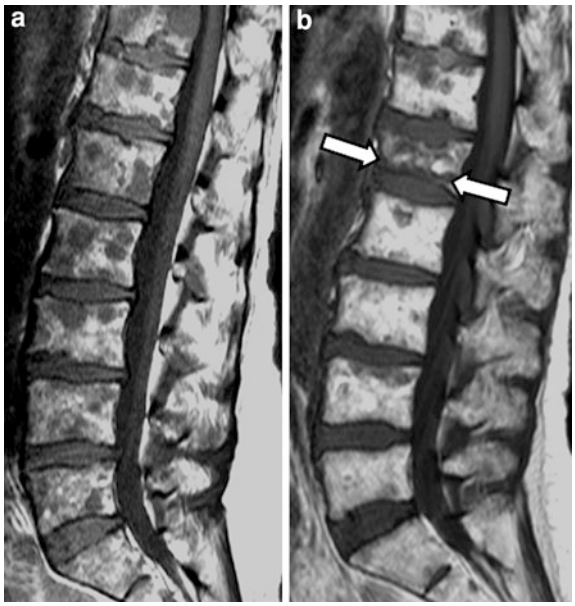

Fig. 13 "Discordance" between MRI and clinical evaluation of response: appearance of a new vertebral fracture despite evident signs of response in a patient with metastatic breast cancer. **a** Initial sagittal T1-weighted MR image of the lumbar spine shows multiple foci of low signal intensity, corresponding to metastases. **b** After 3-month systemic therapy, follow-up image shows frank decrease in the size and number of neoplastic lesions, with increase in the marrow signal intensity. A new benign (osteoporotic) vertebral fracture is observed in L1 (*arrows* in b). This new "skeletal event" would represent evolutive disease in the absence of MRI monitoring

MR imaging follow-up if threatening or impinging on the spinal cord or nerve roots (Figs. 14, 15). Progression or appearance of soft tissue extension should be regarded as a sign of disease progression, sometimes more evident than changes observed within the originating bone lesions. Failure to regress under therapy may prompt the indication of surgical decompression of epidural extension (Fig. 14). In myeloma and lymphoma, the response of this tumoral extension to systemic or regional (radiation) therapy is often spectacular.

7.7 Quantitative Criteria

Several approaches are proposed to quantify the efficacy of treatment on bone lesions, inspired by tools used to evaluate the response to treatment using imaging in primary or secondary soft tissue tumors. These tools are mainly based on the follow-up of lesion size, and they use several response categories (progressive disease, complete response, partial response, stable disease) (RECIST). The evaluation of tumor burden provided by these various measurement tools and its follow-up during therapy show promising correlation with other imaging (soft tissue metastasis quantification) indices of tumor response to therapy and with the clinical and follow-up evaluation of treatment response in breast, prostate and other cancers (Brown et al. 1998; Ciray et al. 2001; Tombal et al. 2005). This offers the perspective to increase the number of patients (i.e. those with bone metastatic disease) in whom response to usual isolated treatments or to new drugs may be evaluated.

7.8 Diffusion-Weighted Imaging

The use of morphologic and size criteria for the assessment of the response of neoplastic lesions to therapy is facing limitations, for bone marrow MRI like for other techniques and other organs, mainly due to the difficult interpretation of lesion persistence after therapy and to the advent of new drugs with new effects, i.e., cytostatic therapies, which are known to have no, limited or delayed impact on lesion size despite histologic efficacy (Padhani and Koh 2011).

Without going into details of underlying physics and principles, DWI provides a measure of the mobility of water molecules in tissues (Bammer 2003). Though permanent, this motion (induced by the thermal agitation of the molecules) is restricted by several physiological barriers. Tissues with a higher cellularity, hence with higher proportions of membranes, intracellular organelles or restricted free extracellular space, demonstrate impeded water diffusibility compared to normal surrounding tissues, explaining the ability of DWI to detect tumoral conditions with increased cellular density.

DWI provides both morphologic (qualitative) as well as functional (quantitative) information on tumoral lesions. Reconstructed MIP or MPR images of DWI, covering the whole body or limited to the central skeleton, show tumoral foci with a high signal intensity on high b-value images, providing easy "at a glance" qualitative evaluation of the tumor burden and driving the attention to areas of difficult analysis on anatomic sequences. Comparison of DWI to skeletal scintigraphy or to PET (choline) for bone metastases detection in osteophilic cancers shows equivalent or superior

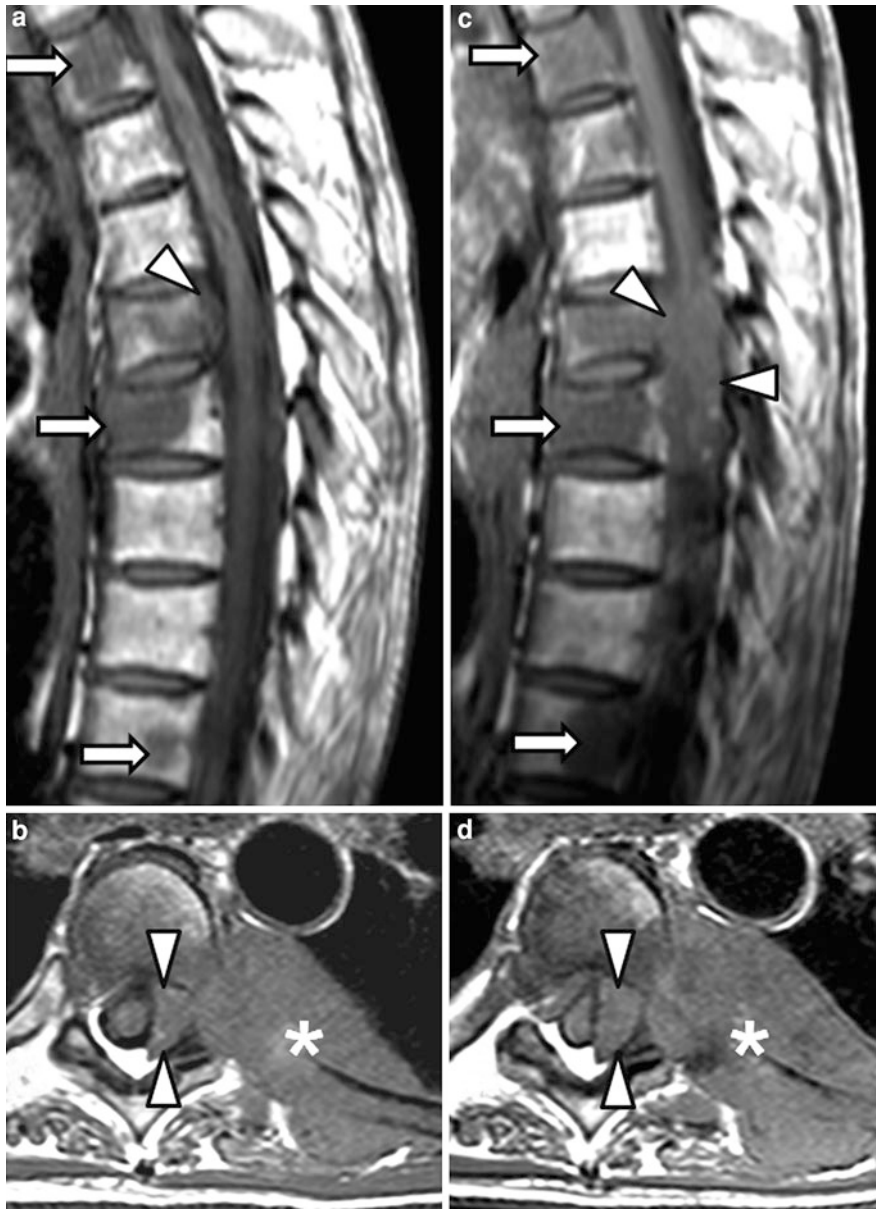

Fig. 14 Progression of bone and soft tissue extension in metastases from colon cancer: use of MRI to evaluate the response. **a**, **b** Initial sagittal (**a**) and transverse (**b**) T1-weighted MR images of the thoracic spine show multiple foci of low signal intensity, corresponding to metastases (*arrows* in **a**). Evident epidural extension is seen (*arrowheads* in **a** and **b**). Rib involvement with soft tissue extension is evident (*). (**c**, **d**) After 3 weeks of systemic therapy, corresponding follow-up images show increase in size of the bone metastases (*arrows* in **c**) and evident increase of the epidural extension and mass effect on the spinal cord (*arrowheads* in **c** and **d**) (indication of surgical decompression). Rib involvement with soft tissue extension also shows evident progression (*)

diagnostic value of DWI-MRI (Luboldt et al. 2008; Lecouvet et al. 2009; Gutzeit et al. 2010). The technique also shows great promises for response assessment. DWI is able to detect changes in water diffusion that occur after therapy as a result of changes in cellular density and loss of membrane integrity (Charles-Edwards and deSouza 2006; Padhani 2011). The impeded water mobility observed in tumoral tissue will decrease or disappear in relation with the loss of cellular integrity in response to treatment, for example due to the occurrence of necrosis (Charles-Edwards and deSouza 2006; Khoo et al. 2011; Koh et al. 2007). Comparison of two consecutive examinations obtained in a treated patient provides a rapid and generally non ambiguous evaluation of the disease response or progression under therapy (Fig. 16). Quantitative assessment is provided by the measurement of an apparent diffusion coefficient (ADC, units 10^{-3} mm^2/s) calculated from the diffusional signal attenuation following the application of motion sensitizing gradients. Generally, a decrease in ADC values due to the presence of a tumoral focus parallels the observation of a bright signal on high

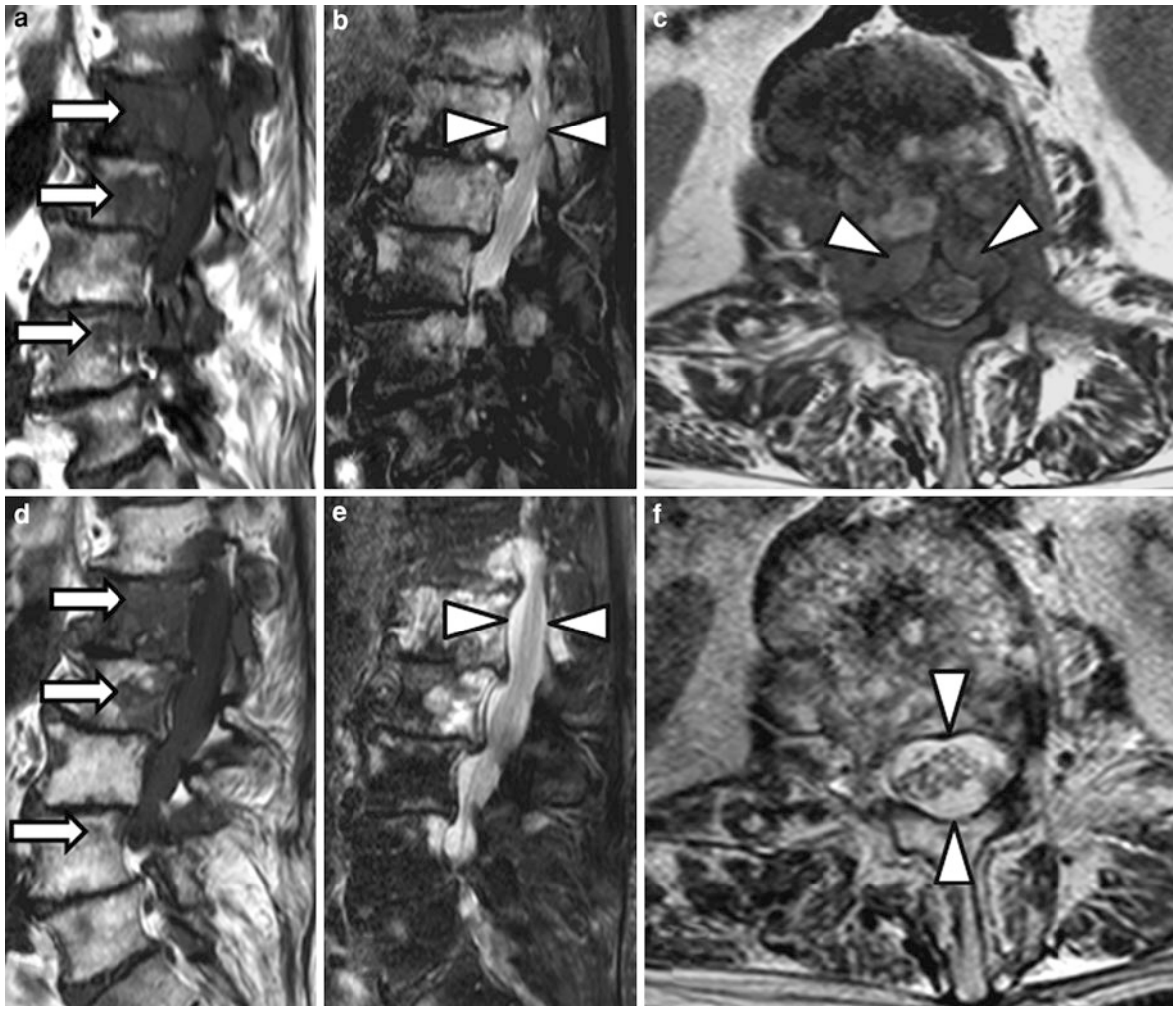

Fig. 15 Demonstration of response of soft tissue extension: lymphoma with multiple bone lesions and epidural extension: use of MRI to monitor the early response of epidural soft tissue extension (absence of response would lead to indication of surgical decompression). (**a**, **b**, **c**) Initial sagittal T1 and PD fat saturated (**b**) MR images of the lumbar spine show multiple foci of low signal intensity, corresponding to metastases (*arrows* in **a**). Evident epidural extension is seen, impinging on the cauda equina (*arrowheads* in **b**). Transverse T2-weighted MR image shows the retropulsion of the posterior longitudinal ligament by this soft tissue extension (*arrowheads* in **c**). (**d**, **e**, **f**) After 2-weeks of radiation and systemic therapy, corresponding follow-up T1 image shows decrease in size of the bone lesions (*arrows* in **d**) and increase in the marrow signal in relation to irradiation; T2-weighted MR images show complete disappearance of the epidural extension and mass effect on the nerve roots (*arrowheads* in **e** and **f**)

b-values DW images, in relation to the increased cellularity and increased water content in the tumor. Follow-up of treated lesions show concurrent decrease of lesion signal on high b-values MR images and increase in ADC values (Byun et al. 2002). This decrease in ADC values in tumors compared to surrounding tissues can be monitored over time after chemotherapy (Byun et al. 2002). DWI has been shown able to detect ADC increase within prostate cancer metastases treated with antiandrogen therapy as early as one month after treatment initiation (Gutzeit et al. 2010; Koh et al. 2007; Reischauer et al. 2010). The effectiveness of ADC monitoring to predict the response of bone metastases to therapy is however controversial (Messiou et al. 2011). The interpretation of changes in ADC values is indeed complex, mainly due to tumor and response heterogeneity. Post-treatment necrosis may sometimes be characterized by the

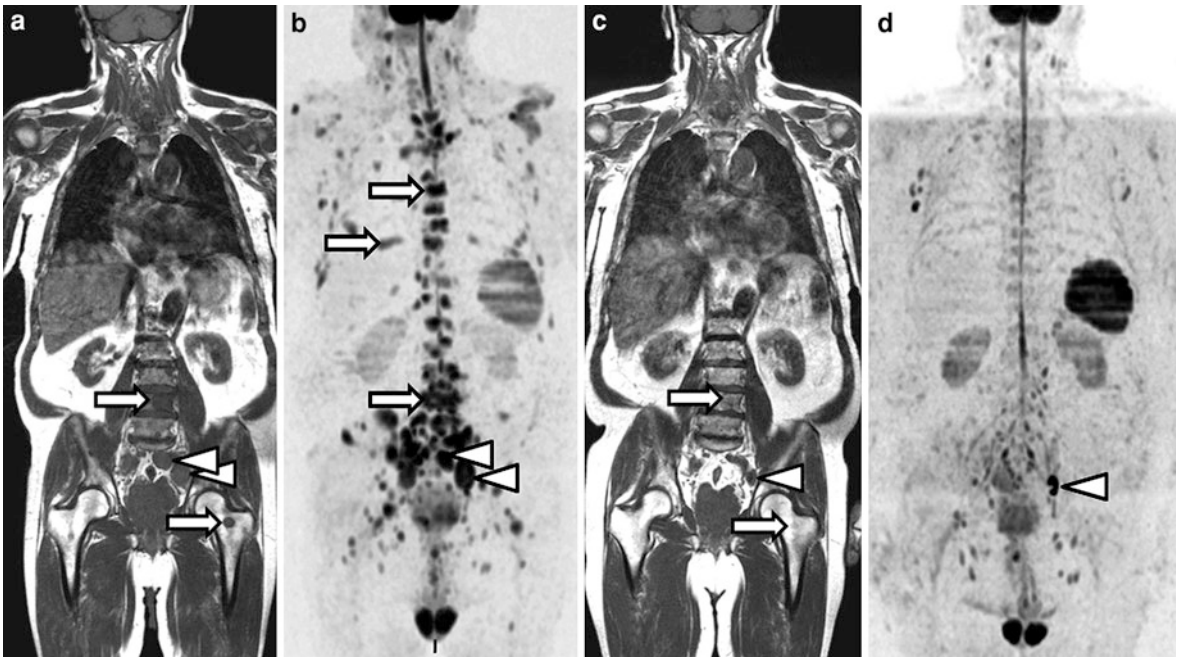

Fig. 16 Follow-up of metastatic prostate cancer during treatment using whole-body MRI: disappearance of bone and lymph node lesions. (**a**, **b**) Initial coronal T1- and diffusion-weighted MR images of the whole body show lesions typical for bone metastases (*arrows*) and concurrent pelvic lymph nodes (*arrowheads*). (**c**, **d**) After 3-month hormonotherapy, follow-up images show the disappearance of bone lesions (*arrows*) and only one small size residual lymph node (*arrowhead*)

observation of persisting high signal foci on DWI images, but with increased ADC values due to loss of membranes; this is called the "T2 shine through effect". Other pitfalls in the visual analysis of high b-values DW images exist and must be known. Since DWI not only reflects cellular load but also water content of tissues, benign conditions such as degenerative joint diseases, fractures, post-radiation changes or benign tumors (angiomas) may present a high signal intensity on DWI images. The technique may also present false negative findings, mainly in very sclerotic or calcified metastases. These pitfalls underline the need for a systematic correlation of DW images with the morphologic appearance of the lesions on conventional MR sequences among which T1-weighted images are most likely the more helpful (Lecouvet et al. 2009; Koh et al. 2007; Komori et al. 2007). Newer analysis methods (called ADC parametric response map or functional diffusion map) take into account spatial information and tumor heterogeneity. They are based on careful voxel-by-voxel follow-up of treatment induced changes and evaluation of the proportion of tumor tissue in which significant changes occur (Reischauer et al. 2010). These approaches seem to be able to detect very early changes – increase in ADC – after treatment initiation (Lee et al. 2007).

Finally, one must remember that the relationship between the ADC and the actual diffusion of water molecules in the tissues of interest is highly complex and influenced by DWI sequence parameterization. Though single-shot echo planar imaging (SS-EPI) is the most common technique of acquisition, multi-shot EPI (MS-EPI), single-shot fast spin echo (SS-FSE) or steady state free precession (SSFP) can also used in DWI (Khoo et al. 2011). Diffusion can be hypothesized isotropic or anisotropic, thus modifying the orientation and the number of diffusions gradients to be used. The diffusional signal decay can be modeled using a mono-exponential (most often), multi-exponential or stretched-type function. The interval and number of b-values used impact ADC measurements as well as the delineation of the tumor from normal or necrotic tissues. Theoretically, high b-values are required to cancel the blood flow contribution (i.e. perfusion) to the water molecules mobility, in order to study the true diffusional motion. These issues are the subject of many studies.

7.9 Dynamic Contrast-Enhanced MRI

DCE—or perfusion—MRI provides information on tumor perfusion and permeability of vessels. This technique has been proven useful for the early monitoring of the response to various anticancer treatments, especially those targeting tumoral angiogenesis (Montemurro et al. 2004; Bauerle et al. 2010).

Perfusion uses repeated imaging (i.e. a dynamic sequence) to track the entrance of a diffusible tracer into a tissue over time. When the dynamic sequence is T2*-weighted, perfusion is based on susceptibility contrast (DSC-MRI). DSC-MRI is mainly used in brain imaging where tracer extravasation is expected to be limited due to the blood brain barrier. When the sequence is T1-weighted, a contrast-enhanced imaging (DCE-MRI) is achieved. DCE-MRI is the standard method used in cancers outside the brain and in the particular setting of bone marrow cancers, where tracer extravasation is important due to a rupture (or a hyperpermeability) of the endothelial barrier.

The principle of the technique may be summarized as follows. Shortly after its injection, the tracer begins to circulate through the body and diffuses over time into the extravascular extracellular space, inducing changes in the signal intensity. These signal changes over time are studied in the tissues of interest, either qualitatively (study of enhancement patterns), semi-quantitatively (study of the maximum up-slope, area under the curve, time to peak or wash-out slope…) or quantitatively (study of physiological parameters such as blood flow, blood volume, interstitial volume or permeability-surface area product derived from a kinetic model fitted to the curve). Quantitative models provide parameters independent from the MR acquisition and interesting simplified physiological information reflecting the actual mechanisms of transport in tissues.

The usefulness of DCE-MRI in normal and pathological vertebral bone marrow, in various benign and malignant musculoskeletal lesions and its prognostic potential in multiple myeloma has been demonstrated (Hawighorst et al. 1999; Biffar et al. 2010; Hillengass et al. 2007). The evaluation of DCE-MRI in early clinical trials has shown that the technique provides useful information on tumor biology and response to treatment (O'Connor et al. 2007).

DCE-MRI presents certain practical, as well as theoretical, limitations. The first limitation of DCE-MRI remains the need for an intravenous injection of a paramagnetic contrast agent. Since quantitative DCE-MRI relies on signal intensity conversion into a measure of tracer concentration, the relationships between concentration and relaxation time T1 on one hand, and between T1 and signal intensity on the other hand, have to be accurately determined. It is known that inter-compartmental water exchange kinetics and B1 field inhomogeneities have a critical influence on the determination of these relationships (Yankeelov et al. 2003; Buckley et al. 2008; Parker et al. 2001). Moreover, for the determination of quantitative parameters, an arterial input function (AIF) (providing the knowledge of tracer concentration in the blood plasma) needs to be measured, which is more difficult to achieve in the coronal or sagittal planes, due to partial volume and inflow effects. As a result, analysis of a complete anatomic vertebra is often semi-quantitative (Hillengass et al. 2007). Alternative methods eliminating the need for a direct AIF measurement, such as the reference region model, are investigated (Yankeelov et al. 2003). As high temporal resolution is privileged for kinetic modeling, DCE images present limited spatial resolution, SNR and anatomic coverage (Kershaw and Cheng 2010). The estimation of the tumor perfusion and permeability may differ according to the kinetic model. Although the extended Tofts model is commonly used (because of its simple implementation), more sophisticated models can be discussed (Tofts et al. 1999; St Lawrence et al. 1998; Donaldson et al. 2010)

8 Multiple Myeloma

The radiographic skeletal survey is still performed as a key point in disease staging, as the detection of lytic lesions directly leads to categorization of the disease as advanced and requiring treatment (Durie and Salmon 1975). Since MRI is superior to radiography for the detection of bone marrow infiltration by plasma cells, an alternative "Durie and Salmon +"

staging system has been proposed, integrating the results of MRI (Durie 2006).

Bone marrow presents the same alterations at MRI as those described in other malignancies; a normal bone marrow appearance, focal lesions, diffuse infiltration or more discrete "salt and pepper" changes may be observed (Lecouvet et al.1998b). The definitive role of MRI for staging the disease remains, however, controversial. Axial skeleton or WBMRI is recommended in patients with myeloma who present with normal conventional radiographs and should be performed as part of staging in all patients with a solitary plasmacytoma of bone (Hillengass et al. 2010; Moulopoulos et al. 1993). In these settings, the observation of marrow lesions is correlated with a higher risk of disease progression and participates to the indication of systemic therapy.

MRI has been evaluated for the assessment of the response of MM to systemic treatment. The morphologic changes indicative of response include reduction in focal lesion size, return from a focal or diffuse pattern of neoplastic marrow involvement to a normal bone marrow appearance, decrease in diffuse marrow enhancement, and in focal lesion enhancement after contrast injection, with sometimes a residual peripheral enhancement halo (Moulopoulos et al. 1994). The lack of enhancement within a treated lesion should be considered carefully, as residual viable myeloma cells may be observed in this setting (Baur-Melnyk et al. 2005; Lecouvet et al. 1998a; Lecouvet et al. 2001). The complete disappearance of focal lesions with return to a completely normal marrow signal may be a very slow process (Hanrahan et al. 2010).

The role of imaging in patient follow-up and response assessment in MM remains controversial. Since lytic lesions show no or very delayed healing, the radiographic skeletal survey has no role in monitoring the response to treatment (Smith et al. 2006). Post-treatment monitoring with MRI is not currently systematic in MM, but several indications are established. MRI is the modality of choice in patients with focal symptoms, especially if a spinal complication is suspected, in non secretory myeloma to assess the treatment response, in cases suspect for relapse especially after high dose cytotoxic therapy and bone marrow transplantation, or after treatment of plasmocytoma. In this situation, MRI will substantiate a suspicion of relapse, and localize a target lesion that is then often biopsied using CT guidance to confirm this relapse.

Both DCE-MRI and DWI are proposed as potential tools for the early evaluation of treatment response in patients with MM. Early decrease in enhancement and increase in ADC values have shown positive correlation with response of the disease (Horger et al. 2011; Li et al. 2010). Although PET-CT can provide complementary information to MRI, its use in staging and follow-up of MM requires further evaluation before considering its role in clinical practice (Terpos et al. 2011).

9 Lymphoma

PET and, better, PET-CT, are the imaging methods of choice for "whole body—all organ" staging and for the evaluation of disease response after treatment, at least in Hodgkin lymphomas (HL) and aggressive non Hodgkin lymphomas (NHL), especially diffuse large B-cell NHL (DLBCL) (Juweid et al. 2007). In these indications, PET-CT outperforms anatomic imaging modalities. The value of PET relies on its ability to distinguish between viable tumor and necrosis or fibrosis in residual masses often present after treatment in patients without any other clinical or biochemical evidence of disease.

At morphologic analysis, evident increased (multi) focal bone marrow uptake is considered positive for lymphoma. Diffusely increased bone marrow uptake, after treatment, should be interpreted more cautiously, as it may be due to post-therapy marrow hyperplasia, spontaneous or "iatrogenic" (use of marrow stimulating factors), which may be confusing for diffuse lymphomatous marrow involvement (Messiou et al. 2009; Chhabra et al. 2006; Sugawara et al. 1998). However, a negative PET in the bone marrow does not completely rule out bone marrow involvement. Bone marrow biopsy, therefore, remains the standard procedure for assessment of bone marrow, although the use of MRI and of PET-MRI will probably raise interest in this setting (Messiou et al. 2009).

Besides this established value of PET-CT, WBMRI and WBDWI are emerging as an alternative diagnostic method for the staging of lymphomas,

and for the evaluation of their response to therapy, with reliable results (Abdulqadhr et al. 2011; Wu et al. 2011; Gu et al. 2011; Kwee et al. 2010; Vermoolen et al. 2011). An important advantage of MRI is the absence of irradiation, which is particularly interesting in a disease that involves young patients and requires repeated imaging follow-up.

References

Abdulqadhr G, Molin D, Astrom G, Suurkula M, Johansson L, Hagberg H, Ahlstrom H (2011) Whole-body diffusion-weighted imaging compared with FDG-PET/CT in staging of lymphoma patients. Acta Radiol 52:173–180. doi:10.1258/ar.2010.100246

Antoch G, Vogt FM, Freudenberg LS, Nazaradeh F, Goehde SC, Barkhausen J, Dahmen G, Bockisch A, Debatin JF, Ruehm SG (2003) Whole-body dual-modality PET/CT and whole-body MRI for tumor staging in oncology. JAMA 290:3199–3206

Avrahami E, Tadmor R, Dally O, Hadar H (1989) Early MR demonstration of spinal metastases in patients with normal radiographs and CT and radionuclide bone scans. J Comput Assist Tomogr 13:598–602

Balliu E, Boada M, Pelaez I, Vilanova JC, Barcelo-Vidal C, Rubio A, Galofre P, Castro A, Pedraza S (2010) Comparative study of whole-body MRI and bone scintigraphy for the detection of bone metastases. Clin Radiol 65:989–996

Bammer R (2003) Basic principles of diffusion-weighted imaging. Eur J Radiol 45:169–184

Bauerle T, Semmler W (2009) Imaging response to systemic therapy for bone metastases. Eur Radiol 19:2495–2507. doi:10.1007/s00330-009-1443-1

Bauerle T, Merz M, Komljenovic D, Zwick S, Semmler W (2010) Drug-induced vessel remodeling in bone metastases as assessed by dynamic contrast enhanced magnetic resonance imaging and vessel size imaging: a longitudinal in vivo study. Clini Cancer Res 16:3215–3225. doi:10.1158/1078-0432.CCR-09-2932

Baur A, Stabler A, Bartl R, Lamerz R, Scheidler J, Reiser M (1997) MRI gadolinium enhancement of bone marrow: age-related changes in normals and in diffuse neoplastic infiltration. Skeletal Radiol 26:414–418

Baur-Melnyk A, Buhmann S, Durr HR, Reiser M (2005) Role of MRI for the diagnosis and prognosis of multiple myeloma. Eur J Radiol 55:56–63. doi:10.1016/j.ejrad.2005.01.017

Baur-Melnyk A, Buhmann S, Becker C, Schoenberg SO, Lang N, Bartl R, Reiser MF (2008) Whole-body MRI versus whole-body MDCT for staging of multiple myeloma. Am J Roentgenol 190:1097–1104. doi:10.2214/AJR.07.2635

Biffar A, Sourbron S, Schmidt G, Ingrisch M, Dietrich O, Reiser MF, Baur-Melnyk A (2010) Measurement of perfusion and permeability from dynamic contrast-enhanced MRI in normal and pathological vertebral bone marrow. Magn Reson Med 64:115–124. doi:10.1002/mrm.22415

Brown AL, Middleton G, MacVicar AD, Husband JE (1998) T1-weighted magnetic resonance imaging in breast cancer vertebral metastases: changes on treatment and correlation with response to therapy. Clin Radiol 53:493–501

Buckley DL, LE Kershaw, Stanisz GJ (2008) Cellular-interstitial water exchange and its effect on the determination of contrast agent concentration in vivo: dynamic contrast-enhanced MRI of human internal obturator muscle. Magn Reson Med 60:1011–1019. doi:10.1002/mrm.21748

Byun WM, Shin SO, Chang Y, Lee SJ, Finsterbusch J, Frahm J (2002) Diffusion-weighted MR imaging of metastatic disease of the spine: assessment of response to therapy. Am J Neuroradiol 23:906–912

Charles-Edwards EM, deSouza NM (2006) Diffusion-weighted magnetic resonance imaging and its application to cancer. Cancer Imaging 6:135–143. doi:10.1102/1470-7330.2006.0021

Chhabra A, Batra K, Makler PT, Makler PT, Jr (2006) Obscured bone metastases after administration of hematopoietic factor on FDG-PET. Clin Nucl Med 31:328–330. doi:10.1097/01.rlu.0000218575.91735.5f

Ciray I, Astrom G, Andreasson I, Edekling T, Hansen J, Bergh J, Ahlstrom H (2000) Evaluation of new sclerotic bone metastases in breast cancer patients during treatment. Acta Radiol 41:178–182

Ciray I, Lindman H, Astrom KG, Bergh J, Ahlstrom KH (2001) Early response of breast cancer bone metastases to chemotherapy evaluated with MR imaging. Acta Radiol 42:198–206

Condon BR, Buchanan R, Garvie NW, Ackery DM, Fleming J, Taylor D, Hawkes D, Goddard BA (1981) Assessment of progression of secondary bone lesions following cancer of the breast or prostate using serial radionuclide imaging. Br J Radiol 54:18–23

Coombes RC, Dady P, Parsons C, McCready VR, Ford HT, Gazet JC, Powles TJ (1983) Assessment of response of bone metastases to systemic treatment in patients with breast cancer. Cancer 52:610–614

Daldrup-Link HE, Franzius C, Link TM, Laukamp D, Sciuk J, Jurgens H, Schober O, Rummeny EJ (2001) Whole-body MR imaging for detection of bone metastases in children and young adults: comparison with skeletal scintigraphy and FDG PET. Am J Roentgenol 177:229–236

De Giorgi U, Mego M, Rohren EM, Liu P, Handy BC, Reuben JM, Macapinlac HA, Hortobagyi GN, Cristofanilli M, Ueno NT (2010) 18F-FDG PET/CT findings and circulating tumor cell counts in the monitoring of systemic therapies for bone metastases from breast cancer. J Nucl Med 51:1213–1218. doi:10.2967/jnumed.110.076455

Donaldson SB, West CM, Davidson SE, Carrington BM, Hutchison G, Jones AP, Sourbron SP, and Buckley DL. (2010) A comparison of tracer kinetic models for T1-weighted dynamic contrast-enhanced MRI: application in carcinoma of the cervix. Magn Reson Med. 63:691-700. 10.1002/mrm.22217

Dreicer R (1997) Metastatic prostate cancer: assessment of response to systemic therapy. Semin Urol Oncol 15:28–32

Durie BG (2006) The role of anatomic and functional staging in myeloma: description of Durie/Salmon plus staging system. Eur J Cancer 42:1539–1543. doi:10.1016/j.ejca.2005.11.037

Durie BG, Salmon SE (1975) A clinical staging system for multiple myeloma Correlation of measured myeloma cell mass with presenting clinical features, response to treatment, and survival. Cancer 36:842–854

Eisenhauer EA, Therasse P, Bogaerts J, Schwartz LH, Sargent D, Ford R, Dancey J, Arbuck S, Gwyther S, Mooney M, Rubinstein L, Shankar L, Dodd L, Kaplan R, Lacombe D, Verweij J (2009) New response evaluation criteria in solid tumours: revised RECIST guideline (version 1.1). Eur J Cancer 45:228–247

Eustace S, Tello R, DeCarvalho V, Carey J, Wroblicka JT, Melhem ER, Yucel EK (1997) A comparison of whole-body turboSTIR MR imaging and planar 99mTc-methylene diphosphonate scintigraphy in the examination of patients with suspected skeletal metastases. Am J Roentgenol 169: 1655–1661

Even-Sapir E, Metser U, Mishani E, Lievshitz G, Lerman H, Leibovitch I (2006) The Detection of Bone Metastases in Patients with High-Risk Prostate Cancer: 99mTc-MDP Planar Bone Scintigraphy, Single- and Multi-Field-of-View SPECT, 18F-Fluoride PET, and 18F-Fluoride PET/CT. J Nucl Med 47:287–297

Galasko CS (1995) Diagnosis of skeletal metastases and assessment of response to treatment. Clin Orthop Relat Res:64–75

Ghanem N, Uhl M, Brink I, Schafer O, Kelly T, Moser E, Langer M (2005) Diagnostic value of MRI in comparison to scintigraphy, PET, MS-CT and PET/CT for the detection of metastases of bone. Eur J Radiol 55:41–55

Ghanem N, Altehoefer C, Kelly T, Lohrmann C, Winterer J, Schafer O, Bley TA, Moser E, Langer M (2006) Whole-body MRI in comparison to skeletal scintigraphy in detection of skeletal metastases in patients with solid tumors. In Vivo 20:173–182

Gosfield E 3rd, Alavi A, Kneeland B (1993) Comparison of radionuclide bone scans and magnetic resonance imaging in detecting spinal metastases. J Nucl Med 34:2191–2198

Groves AM, Beadsmoore CJ, Cheow HK, Balan KK, Courtney HM, Kaptoge S, Win T, Harish S, Bearcroft PW, Dixon AK (2006) Can 16-detector multislice CT exclude skeletal lesions during tumour staging? Implications for the cancer patient. Eur Radiol 16:1066–1073

Gu J, Khong PL, Wang S, Chan Q, Law W, Zhang J (2011) Quantitative assessment of diffusion-weighted MR imaging in patients with primary rectal cancer: correlation with FDG-PET/CT. Mol Imaging Biol. 13:1020–1028. doi: 10.1007/s11307-010-0433-7

Gutzeit A, Doert A, Froehlich JM, Eckhardt BP, Meili A, Scherr P, Schmid DT, Graf N, von Weymarn CA, Willemse EM, Binkert CA (2010) Comparison of diffusion-weighted whole body MRI and skeletal scintigraphy for the detection of bone metastases in patients with prostate or breast carcinoma. Skeletal Radiol 39:333–343

Hamaoka T, Madewell JE, Podoloff DA, Hortobagyi GN, Ueno NT (2004) Bone imaging in metastatic breast cancer. J Clin Oncol 22:2942–2953

Hanrahan CJ, Christensen CR, Crim JR (2010) Current concepts in the evaluation of multiple myeloma with MR imaging and FDG PET/CT. Radiographics 30:127–142. doi: 10.1148/rg.301095066

Hawighorst H, Libicher M, Knopp MV, Moehler T, Kauffmann GW, Kaick G (1999) Evaluation of angiogenesis and perfusion of bone marrow lesions: role of semiquantitative and quantitative dynamic MRI. J magn reson imaging 10: 286–294

Hillengass J, Wasser K, Delorme S, Kiessling F, Zechmann C, Benner A, Kauczor HU, Ho AD, Ho AD, Ho AD, Goldschmidt H, Moehler TM (2007) Lumbar bone marrow microcirculation measurements from dynamic contrast-enhanced magnetic resonance imaging is a predictor of event-free survival in progressive multiple myeloma. Clin Cancer Res 13:475–481. doi:10.1158/1078-0432.CCR-06-0061

Hillengass J, Fechtner K, Weber MA, Bauerle T, Ayyaz S, Heiss C, Hielscher T, Moehler TM, Egerer G, Neben K, Ho AD, Kauczor HU, Delorme S, Goldschmidt H (2010) Prognostic significance of focal lesions in whole-body magnetic resonance imaging in patients with asymptomatic multiple myeloma. J Clin Oncol 28:1606–1610. doi: 10.1200/JCO.2009.25.5356

Horger M, Claussen CD, Bross-Bach U, Vonthein R, Trabold T, Heuschmid M, Pfannenberg C (2005) Whole-body low-dose multidetector row-CT in the diagnosis of multiple myeloma: an alternative to conventional radiography. Eur J Radiol 54:289–297. doi:10.1016/j.ejrad.2004.04.015

Horger M, Weisel K, Horger W, Mroue A, Fenchel M, Lichy M (2011) Whole-body diffusion-weighted MRI with apparent diffusion coefficient mapping for early response monitoring in multiple myeloma: preliminary results. Am J Roentgenol 196:W790–W795. doi:10.2214/AJR.10.5979

Hwang S, Panicek DM (2007) Magnetic resonance imaging of bone marrow in oncology, Part 2. Skeletal Radiol 36: 1017–1027. doi:10.1007/s00256-007-0308-4

Juweid ME, Stroobants S, Hoekstra OS, Mottaghy FM, Dietlein M, Guermazi A, Wiseman GA, Kostakoglu L, Scheidhauer K, Buck A, Naumann R, Spaepen K, Hicks RJ, Weber WA, Reske SN, Schwaiger M, Schwartz LH, Zijlstra JM, Siegel BA, Cheson BD (2007) Use of positron emission tomography for response assessment of lymphoma: consensus of the Imaging Subcommittee of International Harmonization Project in Lymphoma. J Clin Oncol 25:571–578. doi:10.1200/JCO.2006.08.2305

Kershaw LE, Cheng HL (2010) Temporal resolution and SNR requirements for accurate DCE-MRI data analysis using the AATH model. Magn Reson Med 64:1772–1780. doi: 10.1002/mrm.22573

Khoo MM, Tyler PA, Saifuddin A, Padhani AR (2011) Diffusion-weighted imaging (DWI) in musculoskeletal MRI: a critical review. Skeletal Radiol 40:665–681. doi: 10.1007/s00256-011-1106-6

Koh DM, Takahara T, Imai Y, Collins DJ (2007) Practical aspects of assessing tumors using clinical diffusion-weighted imaging in the body. Magn Reson Med Sci. 6:211–224

Komori T, Narabayashi I, Matsumura K, Matsuki M, Akagi H, Ogura Y, Aga F, Adachi I (2007) 2-[Fluorine-18]-fluoro-2-deoxy-D-glucose positron emission tomography/computed tomography versus whole-body diffusion-weighted MRI for detection of malignant lesions: initial experience. Ann Nucl Med 21:209–215

Kwee TC, Fijnheer R, Ludwig I, van Quarles Ufford HM, Uiterwaal CS, Bierings MB, Takahara T, Nievelstein RA (2010) Whole-body magnetic resonance imaging, including diffusion-weighted imaging, for diagnosing bone marrow involvement in malignant lymphoma. Br J Haematol 149:628–630. doi:10.1111/j.1365-2141.2010.08093.x

Langsteger W, Heinisch M, Fogelman I (2006) The role of fluorodeoxyglucose, 18F-dihydroxyphenylalanine, 18F-choline, and 18F-fluoride in bone imaging with emphasis on prostate and breast. Semin Nucl Med 36:73. doi:10.1053/j.semnuclmed.2005.09.002

Lecouvet FE, De Nayer P, Garbar C, Noel H, Malghem J, Maldague BE, Vande_Berg BC (1998a) Treated plasma cell lesions of bone with MRI signs of response to treatment: unexpected pathological findings. Skeletal Radiol 27:692–695

Lecouvet FE, Vande Berg BC, Michaux L, Malghem J, Maldague BE, Jamart J, Ferrant A, Michaux JL (1998b) Stage III multiple myeloma: clinical and prognostic value of spinal bone marrow MR imaging. Radiology 209:653–660

Lecouvet FE, Malghem J, Michaux L, Maldague B, Ferrant A, Michaux JL, Vande Berg BC (1999) Skeletal survey in advanced multiple myeloma: radiographic versus MR imaging survey. Br J Haematol 106:35–39

Lecouvet FE, Dechambre S, Malghem J, Ferrant A, Vande Berg BC, Maldague B (2001) Bone marrow transplantation in patients with multiple myeloma: prognostic significance of MR imaging. Am J Roentgenol 176:91–96

Lecouvet FE, Geukens D, Stainier A, Jamar F, Jamart J, d'Othee BJ, Therasse P, Berg BV, Tombal B (2007) Magnetic resonance imaging of the axial skeleton for detecting bone metastases in patients with high-risk prostate cancer: Diagnostic and cost-effectiveness and comparison with current detection strategies. J Clin Oncol 25:3281–3287

Lecouvet FE, VandeBerg BC, Malghem J, Omoumi P, Simoni P (2009) Diffusion-weighted MR imaging: adjunct or alternative to T1-weighted MR imaging for prostate carcinoma bone metastases? Radiology 252:624. doi:10.1148/radiol.2522090263

Lecouvet FE, Simon M, Tombal B, Jamart J, Vande Berg BC, Simoni P (2010) Whole-body MRI (WB-MRI) versus axial skeleton MRI (AS-MRI) to detect and measure bone metastases in prostate cancer (PCa). Eur Radiol. 10.1007/s00330-010-1879-3

Lee KC, Sud S, Meyer CR, Moffat BA, Chenevert TL, Rehemtulla A, Pienta KJ, Ross BD (2007) An imaging biomarker of early treatment response in prostate cancer that has metastasized to the bone. Cancer Res 67:3524–3528. doi:10.1158/0008-5472.CAN-06-4236

Li WF, Hou SX, Yu B, Li MM, Ferec C, Chen JM (2010) Genetics of osteoporosis: accelerating pace in gene identification and validation. Hum Genet 127:249–285. doi:10.1007/s00439-009-0773-z

Libshitz HI, Hortobagyi GN (1981) Radiographic evaluation of therapeutic response in bony metastases of breast cancer. Skeletal Radiol 7:159–165

Luboldt W, Kufer R, Blumstein N, Toussaint TL, Kluge A, Seemann MD, Luboldt HJ (2008) Prostate carcinoma: diffusion-weighted imaging as potential alternative to conventional MR and 11C-choline PET/CT for detection of bone metastases. Radiology 249:1017–1025

Messiou C, Cook G, deSouza NM (2009) Imaging metastatic bone disease from carcinoma of the prostate. Br J Cancer 101:1225–1232. doi:10.1038/sj.bjc.6605334

Messiou C, Collins DJ, Giles S, de Bono JS, Bianchini D, de Souza NM (2011) Assessing response in bone metastases in prostate cancer with diffusion weighted MRI. Eur Radiol 21:2169–2177. doi:10.1007/s00330-011-2173-8

Montemurro F, Russo F, Martincich L, Cirillo S, Gatti M, Aglietta M, Regge D (2004) Dynamic contrast enhanced magnetic resonance imaging in monitoring bone metastases in breast cancer patients receiving bisphosphonates and endocrine therapy. Acta Radiol 45:71–74

Moulopoulos LA, Dimopoulos MA, Weber D, Fuller L, Libshitz HI, Alexanian R (1993) Magnetic resonance imaging in the staging of solitary plasmacytoma of bone. J Clin Oncol 11:1311–1315

Moulopoulos LA, Dimopoulos MA, Alexanian R, Leeds NE, Libshitz HI (1994) Multiple myeloma: MR patterns of response to treatment. Radiology 193:441–446

Moynagh MR, Colleran GC, Tavernaraki K, Eustace SJ, Kavanagh EC (2010) Whole-body magnetic resonance imaging: assessment of skeletal metastases. Semin Musculoskelet Radiol 14:22–36. doi:10.1055/s-0030-1248703

Nakanishi K, Kobayashi M, Takahashi S, Nakata S, Kyakuno M, Nakaguchi K, Nakamura H (2005) Whole body MRI for detecting metastatic bone tumor: comparison with bone scintigrams. Magn Reson Med Sci. 4:11–17

O'Connor JP, Jackson A, Parker GJ, Jayson GC (2007) DCE-MRI biomarkers in the clinical evaluation of antiangiogenic and vascular disrupting agents. Br J Cancer 96:189–195. doi:10.1038/sj.bjc.6603515

Oyama N, Akino H, Kanamaru H, Suzuki Y, Muramoto S, Yonekura Y, Sadato N, Yamamoto K, Okada K (2002) 11C-acetate PET imaging of prostate cancer. J Nucl Med 43:181–186

Padhani AR (2011) Diffusion magnetic resonance imaging in cancer patient management. Semin Radiat Onco 21:119–140. doi:10.1016/j.semradonc.2010.10.004

Padhani AR, Koh DM (2011) Diffusion MR imaging for monitoring of treatment response. Magn Reson Imaging Clin N Am 19:181–209. doi:10.1016/j.mric.2010.10.004

Parker GJ, Barker GJ, Tofts PS (2001) Accurate multislice gradient echo T(1) measurement in the presence of non-ideal RF pulse shape and RF field nonuniformity. Magn Reson Med 45:838–845

Pollen JJ, Witztum KF, Ashburn WL (1984) The flare phenomenon on radionuclide bone scan in metastatic prostate cancer. Am J Roentgenol 142:773–776

Reischauer C, Froehlich JM, Koh DM, Padevit C, John H, Binkert CA, Boesiger P, Gutzeit A (2010) Bone metastases from prostate cancer: assessing treatment response by using diffusion-weighted imaging and functional diffusion maps–initial observations. Radiology 257:523–531. doi:10.1148/radiol.10092469

Russell WJ, Yoshinagah Antoku S, Mizuno M (1966) Active bone marrow distribution in the adult. Br J Radiol 39:735–739

Ryan SP, Weinberger E, White KS, Shaw DW, Patterson K, Nazar-Stewart V, Miser J (1995) MR imaging of bone marrow in children with osteosarcoma: effect of granulocyte colony-stimulating factor. Am J Roentgenol 165:915–920

Savelli G, Maffioli L, Maccauro M, De Deckere E, Bombardieri E (2001) Bone scintigraphy and the added value of SPECT (single photon emission tomography) in detecting skeletal lesions. Qua J Nuclear Med 45:27–37

Scher HI (2003) Prostate carcinoma: defining therapeutic objectives and improving overall outcomes. Cancer 97: 758–771. doi:10.1002/cncr.11151

Scher HI, Morris MJ, Basch E, Heller G (2011) End points and outcomes in castration-resistant prostate cancer: from clinical trials to clinical practice. J Clin Oncol 29:3695–3704. doi:10.1200/JCO.2011.35.8648

Schmidt GP, Schoenberg SO, Schmid R, Stahl R, Tiling R, Becker CR, Reiser MF, Baur-Melnyk A (2007) Screening for bone metastases: whole-body MRI using a 32-channel system versus dual-modality PET-CT. Eur Radiol 17: 939–949

Schmidt GP, Reiser MF, Baur-Melnyk A (2009) Whole-body MRI for the staging and follow-up of patients with metastasis. Eur J Radiol 70:393–400. doi:10.1016/j.ejrad.2009.03.045

Shankar LK, Hoffman JM, Bacharach S, Graham MM, Karp J, Lammertsma AA, Larson S, Mankoff DA, Siegel BA, Van den Abbeele A, Yap J, Sullivan D (2006) Consensus recommendations for the use of 18F-FDG PET as an indicator of therapeutic response in patients in National Cancer Institute Trials. J Nucl Med 47:1059–1066

Shreve PD, Grossman HB, Gross MD, Wahl RL (1996) Metastatic prostate cancer: initial findings of PET with 2-deoxy-2-[F-18] fluoro-D-glucose. Radiology 199:751–756

Smith A, Wisloff F, Samson D (2006) Guidelines on the diagnosis and management of multiple myeloma 2005. Br J Haematol 132:410–451. doi:10.1111/j.1365-2141.2005.05867.x

Sonpavde G, Pond GR, Berry WR, de Wit R, Eisenberger MA, Tannock IF, Armstrong AJ (2011) The association between radiographic response and overall survival in men with metastatic castration-resistant prostate cancer receiving chemotherapy. Cancer 117:3963–3971. doi:10.1002/cncr.25982

St Lawrence K, Lee TY, Henkelman M (1998) Spatial localization combining projection presaturation with a two-dimensional excitation pulse. Magn Reson Med 40: 944–947

Sugawara Y, Fisher SJ, Zasadny KR, Kison PV, Baker LH, Wahl RL (1998) Preclinical and clinical studies of bone marrow uptake of fluorine-1-fluorodeoxyglucose with or without granulocyte colony-stimulating factor during chemotherapy. J Clin Oncol 16:173–180

Sundaram M, McGuire MH (1988) Computed tomography or magnetic resonance for evaluating the solitary tumor or tumor-like lesion of bone? Skeletal Radiol 17:393–401

Suzuki H, Hasegawa Y, Terada A, Ogawa T, Hyodo I, Suzuki M, Nakashima T, Tamaki T, and Nishio M. (2008) Limitations of FDG-PET and FDG-PET with computed tomography for detecting synchronous cancer in pharyngeal cancer. Arch Otolaryngol Head Neck Surg 134:1191–1195. 10.1001/archotol.134.11.1191

Tateishi U, Gamez C, Dawood S, Yeung HW, Cristofanilli M, Macapinlac HA (2008) Bone metastases in patients with metastatic breast cancer: morphologic and metabolic monitoring of response to systemic therapy with integrated PET/CT. Radiology 247:189–196. doi:10.1148/radiol.2471070567

Terpos E, Moulopoulos LA, Dimopoulos MA (2011) Advances in imaging and the management of myeloma bone disease. J Clin Oncol 29:1907–1915. doi:10.1200/JCO.2010.32.5449

Therasse P, Arbuck SG, Eisenhauer EA, Wanders J, Kaplan RS, Rubinstein L, Verweij J, Van Glabbeke M, van Oosterom AT, Christian MC, Gwyther SG (2000) New guidelines to evaluate the response to treatment in solid tumors. European Organization for Research and Treatment of Cancer, National Cancer Institute of the United States, National Cancer Institute of Canada. J Natl Cancer Inst 92:205–216

Tofts PS, Brix G, Buckley DL, Evelhoch JL, Henderson E, Knopp MV, Larsson HB, Lee TY, Mayr NA, Parker GJ, Port RE, Taylor J, Weisskoff RM (1999) Estimating kinetic parameters from dynamic contrast-enhanced T(1)-weighted MRI of a diffusable tracer: standardized quantities and symbols. J mag reson imaging 10:223–232

Tombal B, Rezazadeh A, Therasse P, Van Cangh PJ, Vande Berg B, Lecouvet FE (2005) Magnetic resonance imaging of the axial skeleton enables objective measurement of tumor response on prostate cancer bone metastases. Prostate 65:178–187

Vande Berg BC, Lecouvet FE, Michaux L, Ferrant A, Maldague B, Malghem J (1998a) Magnetic resonance imaging of the bone marrow in hematological malignancies. Eur Radiol 8:1335–1344

Vande Berg BC, Malghem J, Lecouvet FE, Maldague B (1998b) Classification and detection of bone marrow lesions with magnetic resonance imaging. Skeletal Radiol 27: 529–545

Vande Berg BC, Lecouvet FE, Galant C, Maldague BE, Malghem J (2005) Normal variants and frequent marrow alterations that simulate bone marrow lesions at MR imaging. Radiol Clin North Am 43:761–770. doi:10.1016/j.rcl.2005.01.007

Venkitaraman R, Cook GJ, Dearnaley DP, Parker CC, Khoo V, Eeles R, Huddart RA, Horwich A, Sohaib SA (2009) Whole-body magnetic resonance imaging in the detection of skeletal metastases in patients with prostate cancer. J Med Imaging Radiat Oncol 53:241–247. doi:10.1111/j.1754-9485.2009.02070.x

Vermoolen MA, Kersten MJ, Fijnheer R, van Leeuwen MS, Kwee TC, Nievelstein RA (2011) Magnetic resonance imaging of malignant lymphoma. Expert Rev Hematol 4:161–171. doi:10.1586/ehm.11.17

Vinholes J, Coleman R, Eastell R (1996) Effects of bone metastases on bone metabolism: implications for diagnosis, imaging and assessment of response to cancer treatment. Cancer Treat Rev 22:289–331

Wu X, Kellokumpu-Lehtinen PL, Pertovaara H, Korkola P, Soimakallio S, Eskola H, Dastidar P (2011) Diffusion-weighted MRI in early chemotherapy response evaluation of patients with diffuse large B-cell lymphoma—a pilot study: comparison with 2-deoxy-2-fluoro-D-glucose-positron emission tomography/computed tomography. NMR Biomed 10.1002/nbm.1689

Yang HL, Liu T, Wang XM, Xu Y, Deng SM (2011). Diagnosis of bone metastases: a meta-analysis comparing (18)FDG PET, CT, MRI and bone scintigraphy. Eur Radiol 10.1007/s00330-011-2221-4

Yankeelov TE, Rooney WD, Li X, Springer CS, Jr (2003) Variation of the relaxographic "shutter-speed" for transcytolemmal water exchange affects the CR bolus-tracking curve shape. Magn Reson Med 50:1151–1169. doi: 10.1002/mrm.10624

Young H, Baum R, Cremerius U, Herholz K, Hoekstra O, Lammertsma AA, Pruim J, Price P (1999) Measurement of clinical and subclinical tumour response using [18F]-fluorodeoxyglucose and positron emission tomography: review and 1999 EORTC recommendations. European Organization for Research and Treatment of Cancer (EORTC) PET Study Group. Eur J Cancer 35: 1773–1782

Differentiation of Benign and Malignant Vertebral Compression Fractures

Andrea Baur-Melnyk and Tobias Geith

Contents

Abstract

The differentiation between acute benign osteoporotic and malignant vertebral fractures is sometimes challenging, since they both occur without adequate trauma and are common in the elderly population. Conventional X-ray is the first imaging method to depict vertebral fractures, however it lacks specificity. CT allows better delineation of osseous destruction in neoplastic fractures, however it is not always possible to define the exact cause of the fracture. MRI is more specific as well as more sensitive in detecting especially discrete osteoporotic fractures. In most cases the combination of morphological signs in CT and MRI allows the determination of a benign or malignant cause of the vertebral fracture. However, there remain uncertain cases with contradictory imaging features. In the following chapter, we discuss the morphological signs which help in the differentiation between acute benign and neoplastic vertebral fractures. We describe the latest techniques such as diffusion-weighted, chemical-shift, and perfusion MRI as well as nuclear-medical techniques.

1 Epidemiology and Clinical Background

Vertebral compression fractures occurring without adequate trauma are a common clinical problem. The most common cause of benign vertebral compression fractures is osteoporosis. The European Vertebral Osteoporosis Study (EVOS) examined radiographs of 15,570 males and females aged 50–79 years in 19

A. Baur-Melnyk (✉) · T. Geith
Institut für Klinische Radiologie,
Klinikum der Universität Munchen-Großhadern,
Marchioninistraße 15, 81377 Munich, Germany
e-mail: Andrea.Baur@med.uni-muenchen.de

A. Baur-Melnyk (ed.), *Magnetic Resonance Imaging of the Bone Marrow*, Medical Radiology. Diagnostic Imaging,
DOI: 10.1007/174_2011_493, © Springer-Verlag Berlin Heidelberg 2013

European countries and showed a prevalence of osteoporotic vertebral fractures ranging from 6 to 21%, with a prevalence of 15.1% in men (mean age 64.0 years) and 17.2% in women (mean age 65.5 years) (O'Neill et al. 1996). Since many vertebral fractures escape clinical diagnosis, and because back pain is a common complaint in the elderly, it is difficult to establish a reliable epidemiology. Menopause, advanced age, and a maternal history of fractures are associated with lower bone density, which leads to an increased risk of osteoporotic fractures (Melton 1997). The yearly incidence of vertebral fracture in women rises from 0.6% at an age between 55 and 57 years to 2.3% at an age between 75 and 79 years (van der Klift et al. 2004). Estrogen deficiency is the most important factor in the pathogenesis of vertebral osteoporosis, with environmental or genetic factors also appearing to be contributory factors (O'Neill et al. 1996).

Metastatic lesions are the most common tumors of the spine (95–98%). The spine is the third most frequent place of metastatic deposits, following the lung and the liver. Forty percent of cancer patients have spinal metastases, 10–20% of them are symptomatic (Harrington 1986; White et al. 2006). The metastatic seeding occurs mainly through the arterial blood supply, a retrograde spread through the Batson plexus is also possible (Batson 1940).

In a study on 600 cases of spinal metastases, the most frequent primary cancers were cancers of the prostate and the reproductive system (21%), the lung (19%), and sarcoma (9%) in men, and breast cancer (53%), uterus cancer (9%) and hematological malignancies (5%) in women (Constans et al. 1983). Multiple myeloma or solitary plasmocytoma and lymphoma are also common (Cuenod et al. 1996).

About 70% of symptomatic lesions are found in the thoracic region of the spine, particularly at the level of T4–T7. Twenty percent are found in the lumbar region and 10% are found in the cervical spine. More than 50% of patients with spinal metastasis have several levels of involvement. About 10–38% of patients have involvement of several noncontiguous segments.

One-third of cancer patients also have osteoporotic fractures without malignant infiltration (Fornasier and Czitrom 1978). A correct diagnosis is crucial for appropriate clinical staging, treatment, and prognostic determination, if a new vertebral fracture appears in these patients (Jung et al. 2003).

2 Conventional Imaging Techniques in the Differentiation of Benign Versus Malignant Vertebral Fractures

2.1 Plain Film Radiographs

Conventional radiographs of the spine are the standard technique in assessing vertebral fractures. The age of a fracture is difficult to be determined on plain film radiographs. An increased density due to impaction of trabeculae adjacent to the endplate and cortical disruption are signs of more recent, acute fractures. Subacute fractures show callus formation along the endplate. Osteoporotic fractures may only show minimal increase in density, because the overall bone density is already low. MRI is more sensitive, showing bone marrow edema in acute and subacute fractures (Link et al. 2005).

Vertebral compression fractures are classified as crush, wedge (loss of anterior vertebral body height with relative preservation of posterior body height), and end-plate fractures. Wedge-type fractures may lead to increased segmental kyphosis (Wasnich 1996).

Genant et al. (1993) evaluated vertebral fractures in plain film radiographs and semi-quantitatively characterized vertebral bodies as follows (Fig. 1):

- Grade 0 shows no fracture without reduction in vertebral height.
- Grade 1 describes a mild fracture with a reduction in vertebral height of 20–25%, compared with adjacent normal vertebrae.
- Grade 2 shows a moderate fracture with a reduction in height of 25–40%.
- Grade 3 represents a severe fracture with a reduction in height of more than 40%.

The discrimination of an osteoporotic from a malignant vertebral body fracture is limited in plain film radiographs.

Signs of osteoporotic vertebral fractures are the typical localization in the middle thoracic and the upper lumbar spine, a typical "fish-mouth" or "wedge-shaped" vertebra, further vertebral compression fractures, an intravertebral vacuum phenomenon and band-like sclerosis adjacent to the vertebral endplates. A concave posterior border is more likely a sign of an osteoporotic fracture, especially if there is some retropulsion of osseous

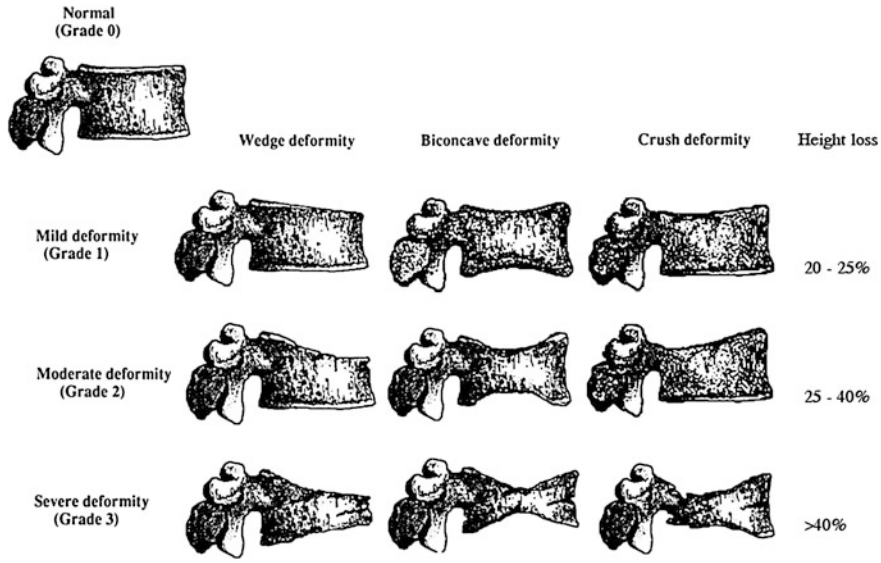

Fig. 1 Spinal fracture index according to Genant et al. (1993)

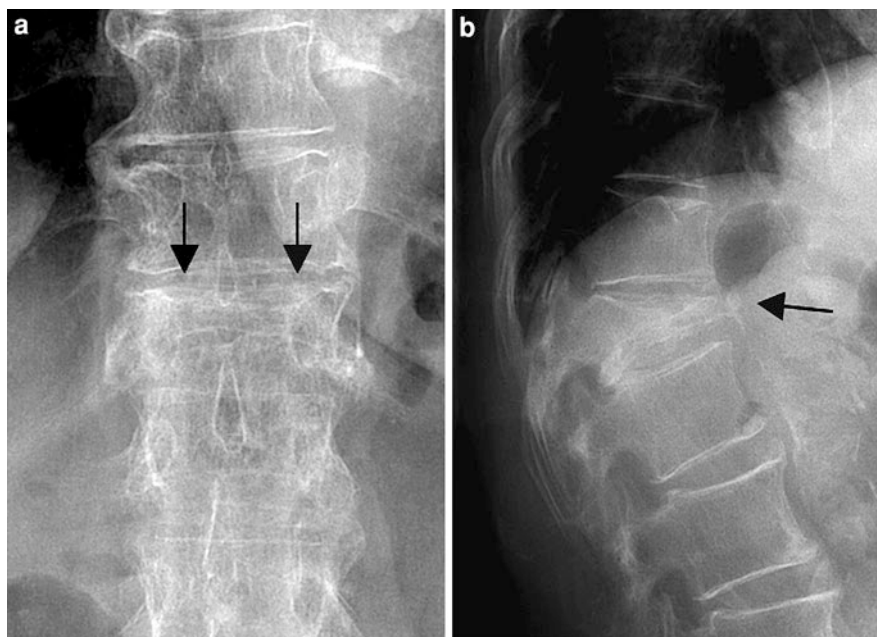

Fig. 2 65-year-old patient with a typical osteoporotic fracture of Th 12. **a** A.p. radiograph showing a symmetric infraction, since the whole vertebral body is weakened; **b** lateral radiograph showing a severe wedge deformity (Genant Grade 3)

fragments into the spinal canal. Osteoporotic fractures usually show a more symmetric infraction of the endplates without osteolyses, since the whole vertebral body is weakened (Laredo et al. 1995; Link et al. 2005). Figure 2 shows the a.p. and lateral radiographs of a typical osteoporotic vertebral fracture.

Signs of malignancy are an inhomogeneous osseous structure with osteolyses and sclerotic areas as a sign of metastatic affection, a convex posterior border, involvement of the pedicles (vanished "eyes of the vertebra"; Fig. 3a), fractures of the posterior part of the vertebral body, a paraspinal soft tissue mass, and localization above Th 7. An asymmetric height loss in antero-posterior (a.-p.)-projection is also a sign of malignancy, since an osteolysis is often asymmetrically located at one side of the vertebra (Sartoris et al. 1986; Link et al. 2005). Figure 3 shows the a.p. and lateral radiographs of a typical malignant vertebral fracture.

Table 1 gives an overview of the X-ray and CT features of benign and malignant vertebral fractures.

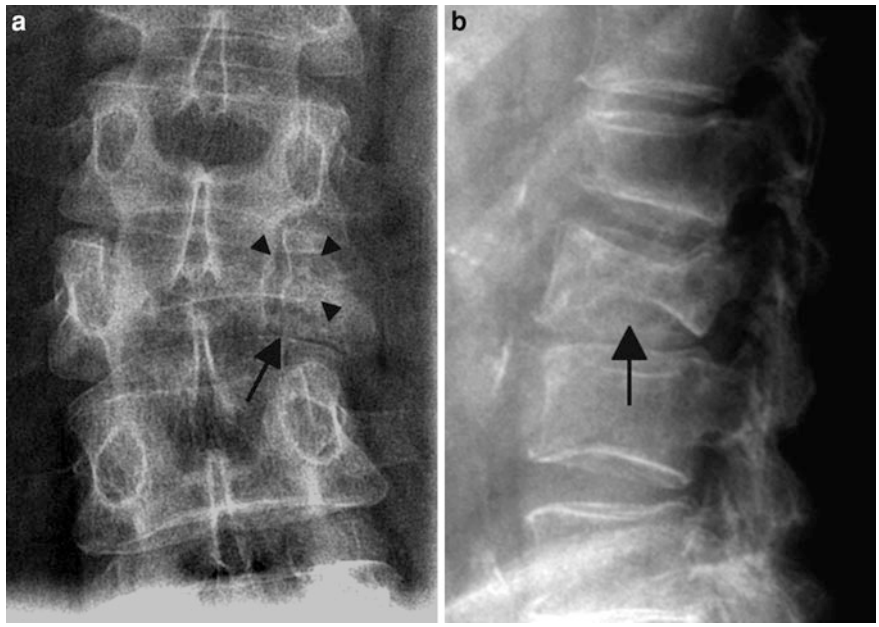

Fig. 3 55-year-old patient with a typical malignant fracture of L2. **a** A.p. radiograph showing an asymmetric infraction (*arrow*) and involvement of the left pedicle (vanished "eye of the vertebra") (*arrowheads*); **b** lateral radiograph showing an angling of the end-plate (arrow)

Sartoris et al. (1986) examined the radiographic patterns of 99 autopsy specimens with vertebral body collapse and endplate deformity of the thoracolumbar spine and found that angling of endplates was highly predictive of a malignant cause, whereas concavity was more suggestive of a benign disease. Focal versus diffuse involvement, the position of the apex of collapse, the condition of adjacent disks, and level of involvement within the spine appeared to be less important differentiation features.

However it must be stated, that in most cases a reliable distinction between acute benign and malignant vertebral compression fractures is not possible with plain film radiographs only.

2.2 Computed Tomography

In comparison with plain film radiographs, CT as a cross sectional method has a higher sensitivity and specificity. It is well-suited to assess the stability of an osteolytic lesion or fracture since it directly visualizes the osseous structures and demonstrates fracture lines in detail, but is less sensitive than MRI in depicting bone marrow and soft tissue pathology.

Sagittal and coronal reformations are fundamental for the differentiation between benign and malignant vertebral compression fractures. Early studies showed a weaker diagnostic accuracy of some morphologic CT signs (Laredo et al. 1995), presumably because they used only axial CT images with relatively thick slices (5 mm), whereas newer studies (Kubota et al. 2005) used axial images as well as sagittal and coronal multiplanar reconstructions with a thinner slice thickness of 0.7–1 mm, and therefore had a more detailed view of the fractures.

Osteoporotic fractures

Laredo et al. (1995) evaluated the CT findings in 34 benign and 32 malignant cases of nontraumatic acute vertebral collapse. *Cortical fractures without associated cortical destruction* (called "*puzzle sign*") were an almost constant finding in osteoporotic fractures and rather specific, since they were only seen in 9% of the malignant fractures. Another study by Kubota et al. (2005) revealed an accuracy up to 98.7% (sensitivity 97.8%, specificity 100%) for fractures of the anterolateral and/or posterior cortex without any cortical destruction of the vertebral body as a very reliable sign of a benign fracture.

Retropulsed bone fragments (Fig. 8a) of the superior or posterior corner of the vertebral body are very specific for an osteoporotic fracture (specificity up to 97%), and must be distinguished from a diffuse bulging of the posterior cortex, which is a rather common finding in malignant vertebral collapse (Laredo et al. 1995).

Table 1 *X-ray* and *CT features* of benign and malignant vertebral fractures

Benign osteoporotic fracture	Malignant fracture
Localization in middle thoracic and upper lumbar spine below Th 7	Localization above Th 7
Concave posterior border—retropulsion of bony fragments	Convex posterior border (bulging)
Intravertebral vacuum	No intravertebral vacuum—soft tissue density
Symmetric infraction (in a.p. view), wedge-shaped or fish-like vertebra	Asymmetric infraction (in a.p. view), Involvement of the pedicles (vanished "eyes of the vertebra")
Homogeneous osseous structure	Inhomogeneous osseous structure with osteolyses and sclerotic areas
Band-like sclerosis adjacent to vertebral cover plate	Fractures of the posterior part of the vertebra

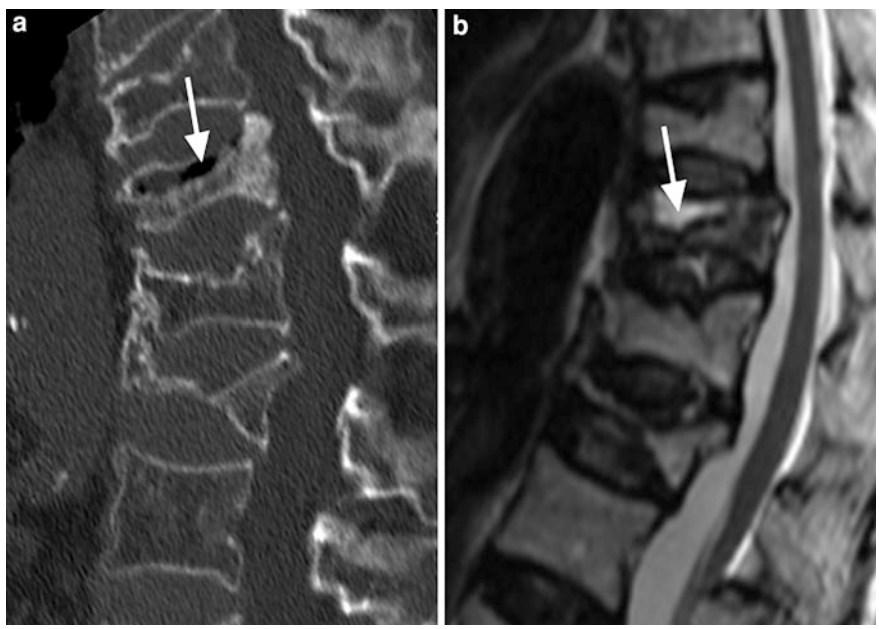

Fig. 4 72-year-old patient with an osteoporotic fracture. **a** Sagittal CT in bone window showing the intravertebral vacuum (*arrow*); **b** corresponding T2-w MRI showing the "fluid sign" with a fluid-like hyperintense signal intensity (*arrow*) in the fractured vertebral body. The intravertebral vacuum and the intravertebral fluid are typical signs for the benign cause of the fracture

Fracture lines within the vertebral body are, although non-specific, a suggestive finding of an osteoporotic fracture, as well as defined margins of the fracture lines which are suggestive of a benign origin (Laredo et al. 1995).

Noninfectious gas collections in preformed or artificial areas of the vertebral body, where normally no gas accumulations are found, are called *vacuum phenomena*. They can be observed in various joints without having pathological relevance and are often seen in degenerative intervertebral discs. Patients with osteoporosis have a low vascularization and a high fat content of the vertebral bone marrow. The exact mechanism of the intravertebral vacuum cleft (Fig. 4) is still controversial. It is assumed that the formation of gas in the vertebral body is a reaction to the negative pressure, which arises when the initially compressed trabecular bone is partially distracted due to movement forces (Stäbler et al. 1999). There is possibly some form of pseudarthrosis following osteonecrosis (Hasegawa et al. 1998). The intravertebral vacuum cleft may be a stable phenomenon (Lafforgue et al. 1997) or can be replaced by fluid on MRI after supine positioning of the patient (Fig. 4) (Malghem et al. 1993; Linn et al. 2009).

Several studies on osteoporotic and malignant vertebral fractures found the intravertebral vacuum phenomenon only in cases of osteoporotic fractures (Golimbu et al. 1986; Laredo et al. 1995; Kubota et al. 2005). Exceptions are fractures in patients with plasmacytoma, where intravertebral vacuum has also been detected (Resnick et al. 1981; Kumpan et al. 1986;

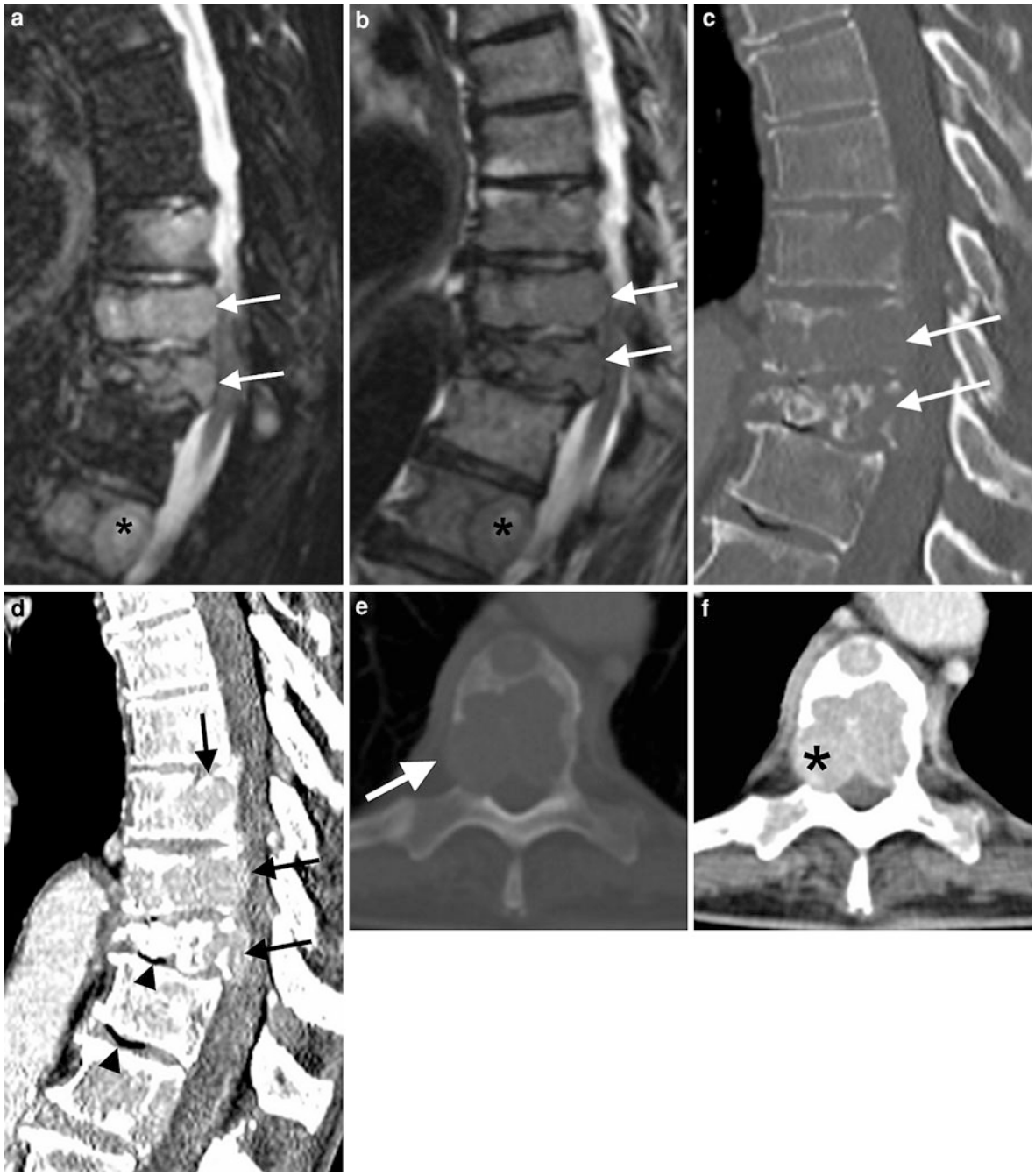

Fig. 5 67-year-old patient with breast cancer and typical metastatic fractures of Th 9–11 and metastasis in L1. **a** STIR image showing the posterior cortical bulging with narrowing of the spinal canal (*arrows*). Further metastasis in the non-fractured L1 (*asterisk*); **b** corresponding T2-w image; **c** sagittal CT in bone window showing cortical destruction and destruction of the cancellous bone; **d** corresponding CT in soft-tissue window showing the cortical destruction and a soft-tissue mass (*arrows*). Intradiscal (not intravertebral!) vacuum (*arrowheads*) due to osteochondrosis; **e** axial CT of Th 10 in bone window showing a cortical destruction (*arrow*); **f** corresponding axial CT in soft-tissue window showing the soft-tissue mass that causes cortical destruction (*asterisk*)

Gagnerie et al. 1987). Other extremely rare cases of intravertebral gas are infections with gas-producing bacteria (Bhalla and Reinus 1998).

As shown by Stäbler et al. (1999), there is a clear connection between the amount of reduction of the bone marrow density (BMD) and the occurrence of intraosseous vacuum phenomenon. The vacuum phenomenon is indicative of osteoporotic fractures due to its high specificity (up to 100%) if plasmacytoma is excluded (Kubota et al. 2005).

Some authors described a *thin paraspinal soft tissue mass* surrounding the whole vertebral body, which could be detected in some osteoporotic vertebral body fractures. Laredo et al. (1995) described it in 41% of the osteoporotic fractures, and in 12% of the malignant fractures. It is usually less than 5–10 mm thick and shows an equal thickness all around the vertebral body, or a slight predominance around the anterior aspect of the vertebra. This paraspinal soft tissue mass may either represent a traumatic paravertebral hematoma, a post-fracture reparative process or an expression of bone marrow out of the vertebral body due to the compression forces (Laredo et al. 1995; Kubota et al. 2005), and must be differentiated from thick and focal soft tissue masses due to malignant infiltration.

Malignant fractures

The *destruction* (i.e. osteolysis) *of the anterolateral and/or posterior cortex* of the vertebral body is an extremely reliable sign of malignancy (up to 100% accuracy for destruction of the posterior cortex) (Fig. 5). It is one of most frequent CT findings in malignant compression fractures and suggests, that the destruction of the vertebral cortex is the most common trigger of vertebral body collapse in cases of malignancy (Kubota et al. 2005). CT better differentiates cortical bone comminution and burst fragments from cortical destruction than plain film radiographs, where all these findings appear as bone destruction (Sattari et al. 2008).

Laredo et al. (1995) reported in their study, that destruction of cortical bone was less common in myelomatous compression fractures than in metastatic ones. An advanced destruction of cancellous bone with relative preservation of cortical bone was considered to be a characteristic CT sign of myelomatous fractures.

Since many metastases present as soft tissue masses, destroying the vertebral structure (Moulopoulos et al. 1999), an *epidural mass* is highly specific (sensitivity 66.7%, specificity 97–100%, accuracy 85.9%) of malignant vertebral fractures (Laredo et al. 1995; Kubota et al. 2005). It usually has a convex or bilobated appearance and has to be carefully differentiated from a flatly shaped epidural soft tissue mass, sometimes appearing in osteoporotic fractures, that most likely represents epidural veins, that are displaced by the extruded bone marrow from the vertebral collapse (Sattari et al. 2008).

Metastatic paraspinal soft tissue masses in malignant fractures are typically *focal* and often involve only one part of the periphery of the vertebral body (Fig. 5). This sign is highly specific (specificity 100%) and has a sensitivity of 54.5% and an accuracy of 80.8% (Kubota et al. 2005). They are usually more than 10 mm thick and must be differentiated from the thin paraspinal masses surrounding the entire vertebral body, which are observed in osteoporotic fractures, and probably equal pressed out bone marrow or hematoma (Laredo et al. 1995).

The *destruction of a pedicle* (Fig. 5) is a highly specific finding of a malignant vertebral fracture. Metastases are frequently detected in the posterior aspects of the vertebral bodies, expanding into the posterior vertebral structures (Lecouvet et al. 1997), which can be explained by the particular blood support of the vertebral bodies (Batson 1940). Laredo et al. (1995) showed a specificity of 100% for destruction of the pedicles. The study by Kubota et al. (2005) reported similar values (sensitivity 51.5%, specificity 100%, accuracy 79.5%).

The *destruction of the cancellous bone* of the vertebral body (Fig. 5) was demonstrated as a reliable sign of malignancy (up to 97.4% accuracy) (Kubota et al. 2005). Another study by Laredo et al. (1995) showed a weak specificity (70%) for malignancy, since they observed some degree of destruction in 29% of the osteoporotic fractures, which was discussed as part of the healing response to the fracture. Probably Laredo et al. (1995) may have misinterpreted fracture lines as a destruction of cancellous bone, since they used only axial images and relatively thick slices (5 mm).

Other rather specific but not very sensitive signs of malignancy in the study by Kubota et al. (2005) are the destruction of the endplate (sensitivity 33.3%, specificity 100%, accuracy 71.8%), and a diffuse paraspinal soft tissue mass >5 mm (sensitivity 51.5%, specificity 100%, accuracy 85.9%).

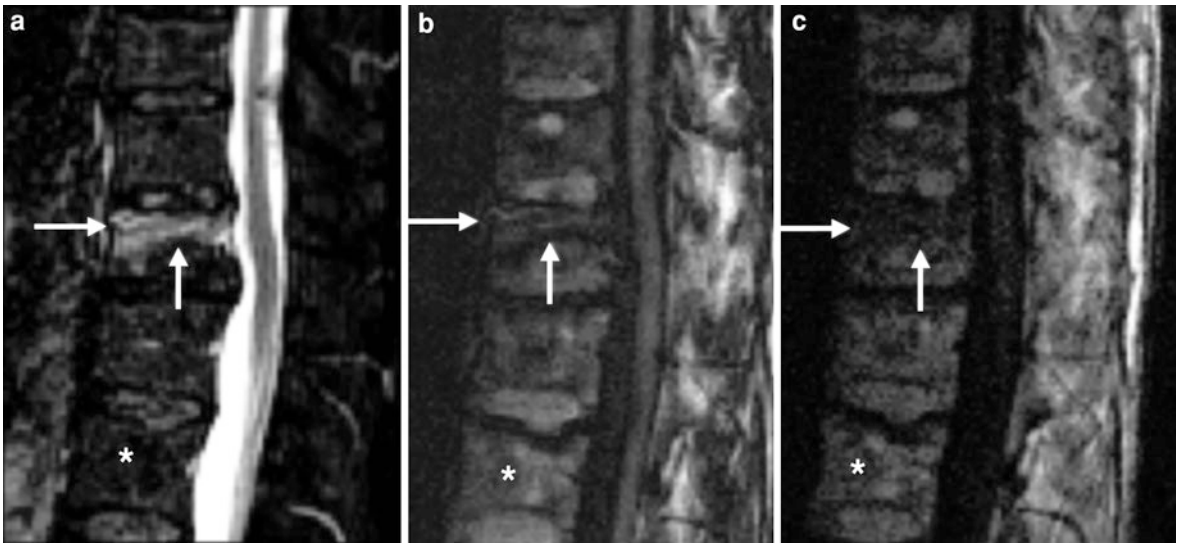

Fig. 6 75-year-old patient with a typical osteoporotic fracture and diffusion-weighted SSFP (PSIF). Sagittal STIR image (**a**) showing a strong edema (*arrows*) within the fractured L1 vertebral body. Diffusion-weighted SSFP with delta = 3 ms (**b**) showing mildly hypointense signal intensity within the edema (*arrows*) in comparison with normal vertebral marrow (*asterisk*). PSIF with delta = 6 ms (**c**) showing stronger hypointensity with higher diffusion weighting (*arrows*)

Table 1 gives an overview of the X-ray and CT features of benign and malignant vertebral fractures.

Less useful findings in differentiating benign and malignant vertebral fractures

Sclerosis, marked comminution of the cancellous bone, Schmorl's nodes and fracture of a pedicle had little or no value in the differentiation of benign from malignant vertebral fractures in the study by Laredo et al. (Laredo et al. 1995).

2.3 Magnetic Resonance Imaging

MRI is the method of choice to visualize bone marrow, while osseous structures are not well depicted due to their low proton density. Chronic benign vertebral fractures can be easily detected due to an absence of abnormal signal intensity on STIR and T1w images in the compressed vertebra (An et al. 1995; Jung et al. 2003). The distinction between metastatic and acute osteoporotic vertebral fractures on the basis of MR imaging findings has a sensitivity of 85–100%, a specificity of 79–100%, and an accuracy of 86–95%, depending on the patient population (Frager et al. 1988; An et al. 1995; Shih et al. 1999; Jung et al. 2003).

Osteoporotic fractures

In osteoporotic compression fractures the *vertebral body* appears *hypointense on T1-w images* and *hyperintense on fat saturated sequences such as STIR* (Yuh et al. 1989; Baker et al. 1990; Cuenod et al. 1996; Leeds et al. 2000). *T2-w images* show a *normal or heterogeneously to homogenously abnormal signal*, which may be *related to the age* of the fracture (Yuh et al. 1989). Areas corresponding to the *fracture line* or *trabecular impaction* can be seen on *T2-w images as linear regions with low signal* (Uetani et al. 2004). The acute signal abnormalities are *mostly incomplete or band-like* (Yuh et al. 1989; Baker et al. 1990; Cuenod et al. 1996; Baur et al. 1998, 2002b) (Fig. 6a) and appear well-defined in about 71% and ill-defined in about 29% of the cases (Shih et al. 1999). Figure 7 shows a typical acute and typical old osteoporotic fracture.

Contrast-enhanced T1-w images show a complete or partial equalization of the signal intensity in comparison with normal, not fractured vertebrae, termed "*return to normal signal intensity*" (Cuenod et al. 1996). Acute cases of osteoporotic collapse may show an intense contrast-enhancement (Cuenod et al. 1996). Subacute or chronic benign fractures show a slight enhancement that can either be homogenous or heterogeneous with

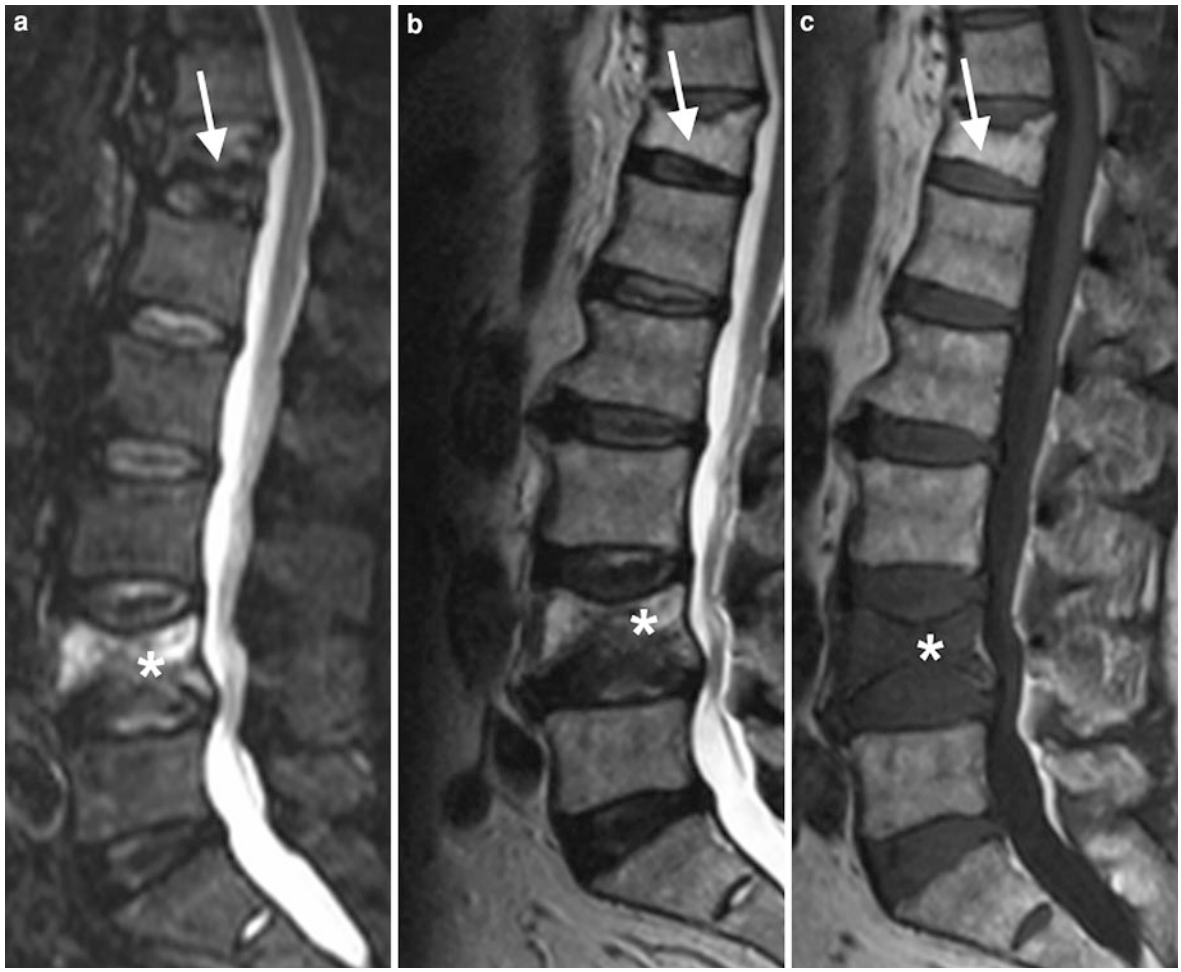

Fig. 7 66-year-old patient with a typical acute osteoporotic fracture in L4 (*asterisk*) and a typical old osteoporotic fracture in Th 12 (*arrow*). **a** STIR image showing a high signal intensity in the acute fracture in L4 and an isointense signal intensity in the old fracture in Th 12. The acute fracture (*asterisk*) shows a high signal intensity area in the T2-w image (**b**) and a low signal intensity in the T1-w image without fat-saturation (**c**) due to edema. The healed fracture (*arrow*) shows a high signal intensity in the T2-w (**b**) and in the T1-w image without fat-saturation (**c**) due to fatty replacement

greater enhancement in the posterior vertebral body, which might be due to blood stasis as a result of fracture (Shih et al. 1999). Accordingly, contrast-enhancement in the vertebral body is no reliable sign to distinguish benign and malignant vertebral fractures until edema has been absorbed.

On T1-w images most benign fractures show some amount of normal fatty marrow that is opposite to the fractured endplate. The *band-like hypointense region adjacent to the preserved marrow* is considered specific for osteoporotic collapse (An et al. 1995; Cuenod et al. 1996; Moulopoulos et al. 1996). Fibrotic replacement of bone and marrow after a fracture can cause temporary hypointensity on T1-w images and might be mistaken for malignancy (Vaccaro et al. 1999). Nineteen percent of cases of benign collapse show focal areas of signal abnormality in other adjacent vertebrae that often corresponds to benign fracture lines, bone impaction or Schmorl's nodes, but cannot always be differentiated from metastasis with T1-w imaging alone (Cuenod et al. 1996). Osteoporotic fractures without remaining fatty marrow and a resulting complete vertebral body involvement can easily be confused with malignant fractures (Fig. 10) (Moulopoulos et al. 1996; Baur et al. 1998). Histology in osteoporotic vertebral compression fractures shows

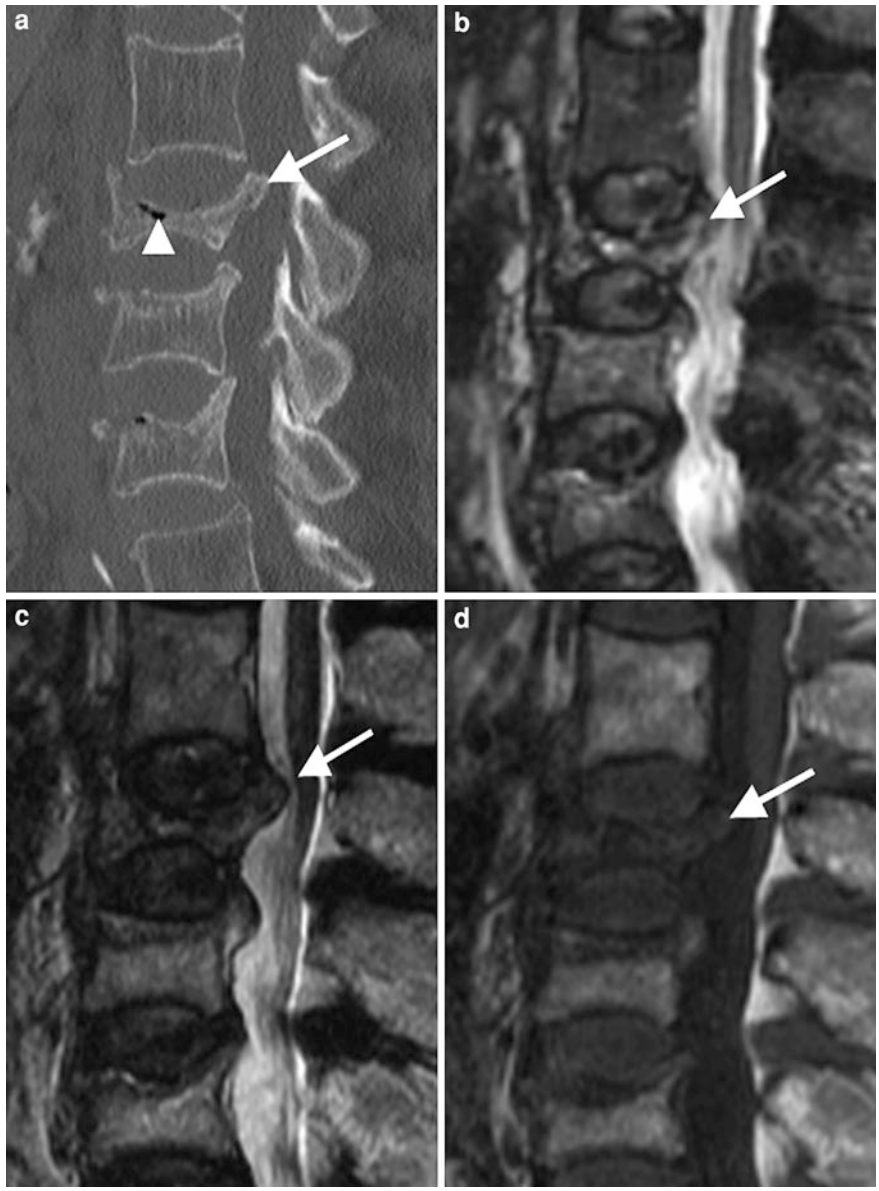

Fig. 8 75-year-old patient with an acute osteoporotic fracture of L2. Sagittal CT (**a**) showing a retropulsion of a bony fragment into the spinal canal (*arrow*). Also the both caudal vertebral bodies are fractured. There is also a small vacuum sign adjacent to the fractured vertebral cover plate (*arrowhead*). Corresponding sagittal STIR (**b**), T2-w (**c**) and T1-w (**d**) images

bone marrow edema, fibrosis, increased trabecular turnover, and hemorrhage.

The size of the altered signal remains unchanged in the initial 2–4 months and then gradually reverts to normal. The time to complete restoration of the normal marrow signal intensity is variable (3–6 months) (Yuh et al. 1989; Cuenod et al. 1996), but usually does not exceed 12 months. Healed fractures usually show again hyperintense signal on T1-w SE and hypointense signal on fat suppressed images, such as STIR, and do not enhance with contrast (Fig. 7). Often the fat signal is even higher than in the neighboring vertebral bodies due to a higher amount of fat cells within the healed vertebral body.

The *retropulsion of a posterior or posterosuperior bone fragment* of the vertebral body into the spinal canal (Fig. 8) is highly specific of an osteoporotic fracture (specificity 89–100%), but an intermediate to low sensitivity (16–60%) has been reported (Tan et al. 1991; Cuenod et al. 1996; Jung et al. 2003). One study (Tan et al. 1991) showed this finding only in osteoporotic fractures. Another study found retropulsion of bony fragments in both osteoporotic and malignant vertebral fractures, but significantly

associated with osteoporotic fractures (Jung et al. 2003). Usually the retropulsed fragment does not lead to a significant spinal stenosis (Cuenod et al. 1996).

Multiple compression fractures are a rather weak sign of osteoporotic fractures, since they are also typical in multiple myeloma. In a study on 55 acute osteoporotic and 27 malignant vertebral compression fractures, Jung et al. (2003) found a significant correlation of multiple compression fractures with non-malignancy. However this is not a reliable sign. In patients with myeloma a mixture of signs may be present. Myeloma patients may show the typical focal soft-tissue lesion within a vertebral body, leading to a fracture due to osteolysis. On the other hand, some patients have diffuse disease, leading to diffuse osteoporosis and thus multiple vertebral fractures. Under these circumstances the amount of tumor cells may be limited. Therefore the fractures do not show the typical signs of a pathologic fracture (Lecouvet et al. 1997). In addition to that, myeloma patients are usually elderly subjects with preexisting osteoporosis which can by itself lead to osseous weakening and therefore to an osteoporotic fracture. Rupp et al. (1995) performed a study on 18 malignant and 16 osteoporotic vertebral compression fractures including patients with multiple myeloma, and did not find any significant difference between osteoporotic and malignant vertebral compression fractures.

The *fluid sign* is defined as a focal, linear, or triangular area of strong ("fluid-like") hyperintensity on STIR images on a background of diffuse hyperintensity in the vertebral body because of acute collapse (Fig. 4). The signal intensity of the fluid sign has to be equivalent to that of cerebrospinal fluid. In a former study (Baur et al. 2002b), we showed, that the fluid sign is significantly associated with osteoporotic vertebral fractures, while rarely seen in malignant fractures. Osteoporotic fractures show a significant correlation of the fluid sign with the severity of the fracture. The fluid sign corresponded to osteonecrosis, edema, and fibrosis in histological examination.

Malignant fractures

Spin-echo T1-w images mostly show a *complete replacement of normal bone marrow* with *diffuse hypointense signal in the whole vertebral body* (Cuenod et al. 1996). *Spin-echo T2-w images* show an *isointense to hyperintense signal* with a homogeneous (Baker et al. 1990) or heterogeneous (Cuenod et al. 1996) pattern. After intravenous administration of *gadolinium-containing contrast agent*, the signal is *hyperintense on T1-w fat suppressed images* compared to surrounding normal marrow (Leeds et al. 2000) with mostly heterogeneous enhancement due to uneven blood supply or tumor necrosis (Shih et al. 1999). However, up to 33% of the cases show incomplete marrow replacement with small areas of preserved fatty marrow. Usually the marrow replacement in malignant fractures is circumscribed and focal, whereas in osteoporotic fractures it is band-like or diffuse (Yuh et al. 1989; Cuenod et al. 1996). Figure 9 shows a malignant vertebral fracture due to breast cancer.

The signal changes of malignant fractures commonly progress or persist and do not show a return to normal signal, because tumor persists without restoration of normal fatty bone marrow.

Most malignant compression fractures do not only show *involvement* of the bone marrow of the vertebral body, but also of the *pedicles and the neural arch*. Involvement of the pedicles has a sensitivity of 80%, a specificity of 94%, a positive predictive value of 86% and a negative predictive value of 91% for a malignant fracture (Cuenod et al. 1996). In the cases with pedicle involvement, there is a complete affection in 75% and an incomplete affection in 25% (Moulopoulos et al. 1996). About 55% of the cases with pedicle involvement show an expansion of the pedicles (Shih et al. 1999). However abnormal signal intensity in pedicles can also be observed on contrast-enhanced T1-w images with fat suppression or on STIR images due to extension of the edema into the pedicle in up to 9% of the cases in osteoporotic fractures (Kaplan et al. 1987; Yuh et al. 1989; Jung et al. 2003). Additional CT can help excluding a fracture of the pedicles that may be responsible for the signal changes. Ishiyama et al. (Ishiyama et al. 2010) found frequent pedicle involvement in the early phase of osteoporotic compression fractures and suggested, that the diagnosis of a malignant fracture should not be assumed when pedicle involvement is the only present sign (Fig. 10).

Epidural soft-tissue masses are, if present, a highly specific sign for malignant vertebral collapse (Fig. 9e), especially when it is an encasing epidural mass (Tan et al. 1991; Jung et al. 2003). The tumor tissue spreads out of the vertebral body and grows into the spinal canal. The specificity of this sign for a malignant vertebral fracture is up to 100%, and its sensitivity is 80% (Cuenod et al. 1996).

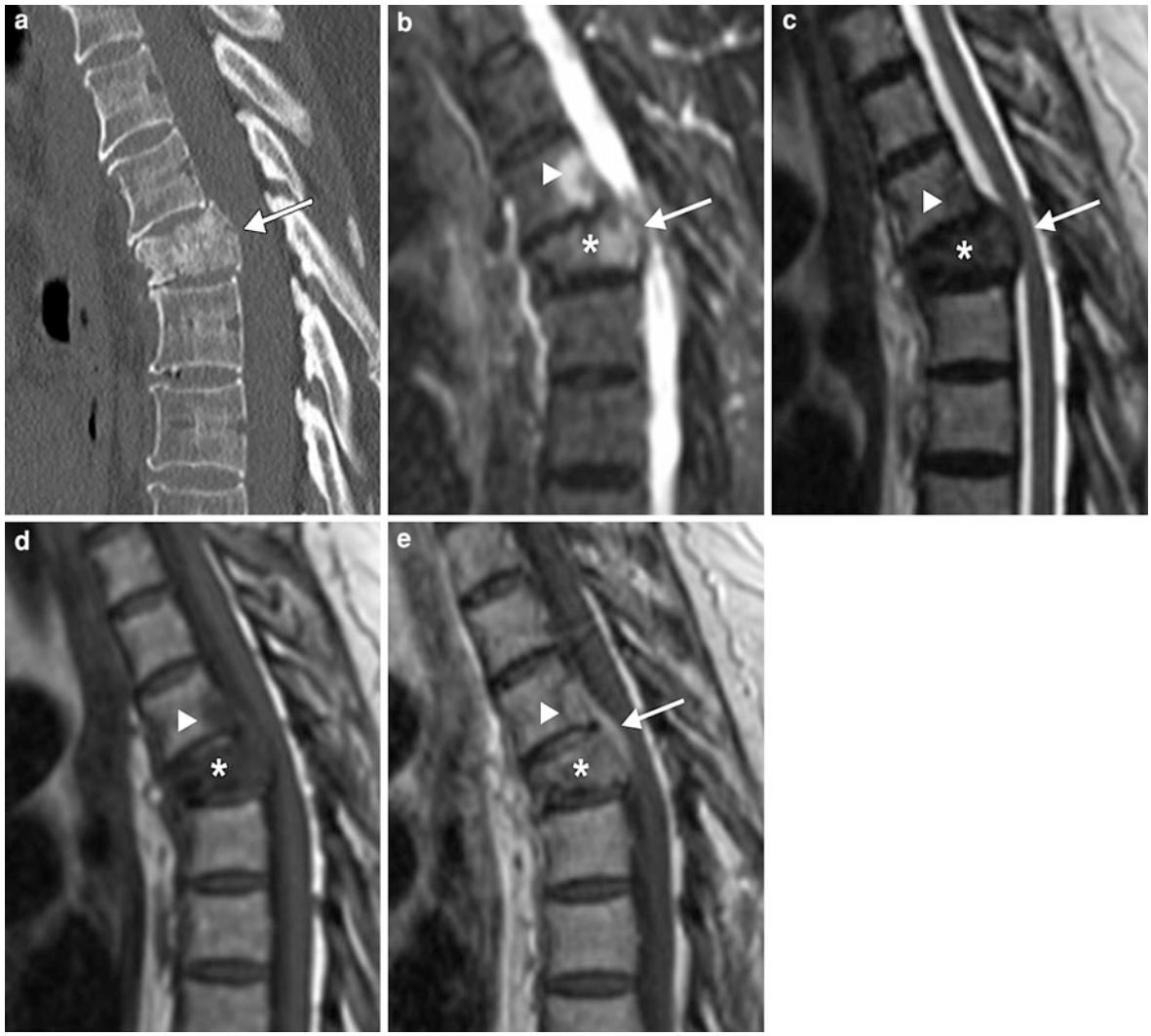

Fig. 9 64-year-old patient with a typical malignant fracture of Th 3 due to breast cancer. **a** CT in bone window showing a mainly sclerotic metastasis in the fractured vertebra and a posterior bulging (*arrow*); **b** sagittal STIR image showing a hyperintense signal in the whole fractured vertebral body (*asterisk*), a posterior bulging (*arrow*) and another metastasis (*arrowhead*) in an adjacent vertebral body; **c** corresponding T2-w image showing hypointense signal in the whole fractured vertebral body due to the mainly sclerotic nature of the metastases (*asterisk*). The spinal canal is narrowed (*arrow*). Sagittal T1-w images before (**d**) and after (**e**) i.v. administration of Gadolinium-containing contrast agent showing enhancement in the fractured vertebral body (*asterisk*) and the further metastasis in Th 2 (*arrowhead*). Please also note the contrast enhancing epidural tumor mass (*arrow*) in (**e**)

Focal paraspinal masses caused by tumor growth are, if present, typical for metastatic compression fractures and have a sensitivity of 41%, a specificity of 93% and an accuracy of 75% (Jung et al. 2003).

In malignant compression fractures, the underlying tumor leads to an expansion of the vertebral body which results in a *convex bulge involving the whole posterior cortex* (Fig. 9). This sign has a sensitivity of 70–74%, a specificity of 80–94%, a positive predictive value of 84%, a negative predictive value of 87% and an accuracy of up to 78% (Cuenod et al. 1996; Jung et al. 2003). However, it is also seen in 2–19% of osteoporotic fractures, probably caused by bone marrow pushed out during the collapse (Rupp et al. 1995; Cuenod et al. 1996; Moulopoulos et al. 1996).

Table 2 *MRI features* of benign and malignant vertebral fractures

Benign osteoporotic fracture	Malignant fracture
Spared normal bone marrow, incomplete or band-like signal changes	Complete replacement of normal vertebral bone marrow, diffuse hyperintense signal on STIR
Isointensity after Gd on T1w images ("*return to normal signal intensity*")	High/inhomogenous SI after Gd on T1w images
No involvement of the pedicles and the neural arch	Involvement of the pedicles and the neural arch
Intravertebral "*fluid sign*"	No intravertebral "*fluid sign*"
No or only thin surrounding paraspinal mass	Epidural soft tissue mass—focal paraspinal mass
Retropulsion of posterior bone fragment into spinal canal	Bulging of posterior cortex
Other (old) osteoporotic fractures	Other spinal metastases

Frequently well-demarcated round signal abnormalities in the marrow of other than the collapsed vertebrae can be found, indicating *other spinal metastases* (Fig. 5) (Cuenod et al. 1996; Jung et al. 2003).

Table 2 gives an overview of the MRI features of benign and malignant vertebral fractures.

The described morphological features may help in the differentiation of benign and malignant fractures in most of the cases, but especially in acute (Tan et al. 1991) and subacute (Frager et al. 1988) fractures, unequivocal results can lead to a wrong diagnosis. Correlation with other imaging techniques like CT, follow-up imaging or, in selected cases, bioptic samples may help in making the correct diagnosis. CT provides information on the osseous structures, that cannot reliably be depicted by MRI, and often shows destruction of the cortical bone, cancellous bone, and pedicle in malignant fractures, as mentioned before (Laredo et al. 1995).

Since vertebral fractures due to multiple myeloma often have the appearance of benign osteoporotic fractures on MRI (Lecouvet et al. 1997), they should be taken in consideration in cases of non-traumatic, benign-appearing vertebral compression fracture (Uetani et al. 2004).

New MR imaging techniques of bone marrow like diffusion-weighted imaging (DWI), perfusion imaging and chemical-shift imaging, as well as PET-CT techniques can provide additional information, which may help in differentiating acute benign and malignant vertebral fractures in cases where morphological CT and MRI signs are insufficient in the determination of fracture etiology. These emerging techniques are discussed in the following chapters.

3 Advanced Techniques for the Differentiation of Benign and Malignant Vertebral Fractures

3.1 Diffusion-Weighted Imaging

Conventional MRI is very sensitive but not always specific in the differentiation of acute osteoporotic and malignant vertebral fractures. Several studies suggested that diffusion-weighted MR imaging (DW-MRI) could be useful to distinguish between benign and malignant vertebral compression fractures (Baur et al. 1998; Park et al. 2004; Thurnher and Bammer 2006; Oztekin et al. 2009).

There are two ways to assess vertebral fractures with DWI-MRI. On one hand, the signal intensity of diseased vertebrae can be compared with normal appearing vertebrae and can be qualitatively characterized as hypo-, iso- or hyper-intense. On the other hand, quantitative imaging uses the apparent diffusion coefficient (ADC) that is calculated using two or more images with different diffusion weightings (b-values). These ADC values can be used to characterize the lesions quantitatively.

Acute osteoporotic fractures show an increased diffusion with low signal intensity on diffusion-weighted scans and high values on ADC maps, which is explained by the disruption of the trabecular structure and bone marrow edema in the diseased vertebrae.

Malignant fractures tend to be associated with restricted diffusion, i.e. high signal intensity on diffusion-weighted scans and lower values on ADC maps. In spinal tumors with vertebral body compression

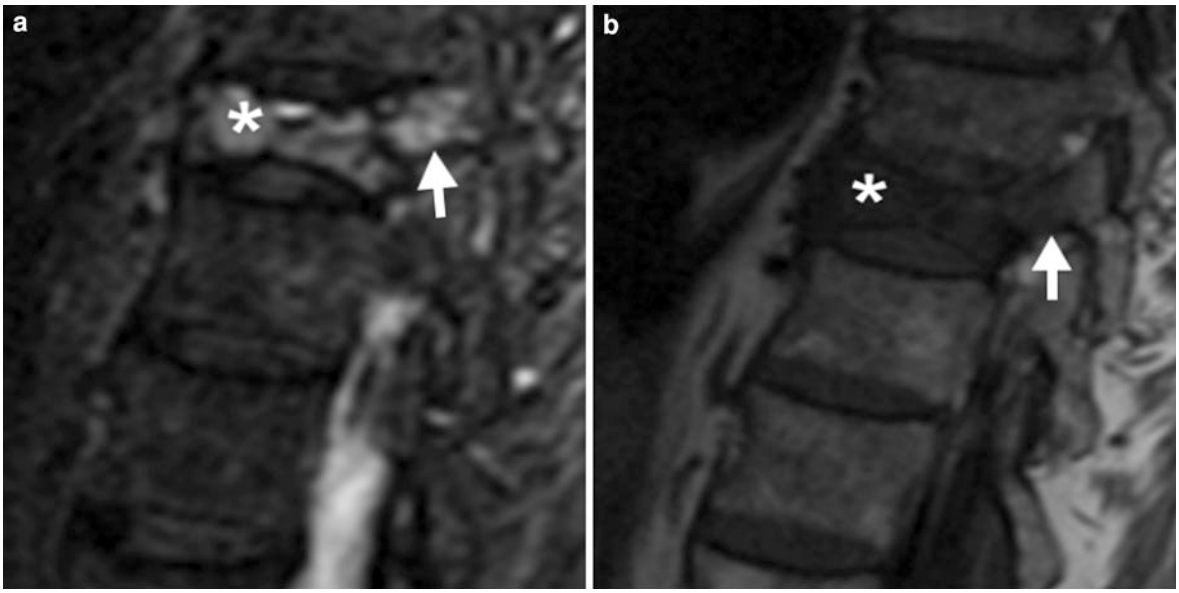

Fig. 10 68-year-old patient with a typical osteoporotic fracture of L2. The sagittal STIR image (**a**) shows a high signal intensity in the pedicle (*arrow*). The sagittal T1-w image (**b**) shows a low signal intensity in the pedicle (*arrow*). Signal changes in the whole vertebral body (*asterisk*) plus involvement of the pedicles are usually signs of malignancy, but can also be observed in osteoporotic fractures due to extension of edema or fracture in the pedicles

fractures, increased tumor cell packing leads to a smaller and more restricted extracellular space, resulting in increased signal from restricted water protons, as has been observed in lytic metastases (Baur et al. 2003).

The reverse fast imaging with steady-state free-precession (PSIF) sequence is a diffusion-weighted steady-state free-precession (SSFP) sequence, where only a single (monopolar) diffusion gradient is inserted into each repetition time (TR). The exact quantification of ADC is not possible with this sequence, due to the influence of many different parameters (Dietrich et al. 2009). In a first study (Baur et al. 1998), we evaluated the usefulness of the PSIF sequence in the differentiation of 22 acute benign and 39 acute malignant vertebral body fractures, and showed that all benign vertebral compression fractures were iso- or hypo-intense, while malignant fractures were hyper-intense in comparison with normal adjacent vertebral bodies. In another own study (Baur et al. 2002a), we examined a larger group of patients, where hyperintensity as a sign of malignancy in a vertebral fracture on PSIF provided a sensitivity of 100%, a specificity of 93%, a positive predictive value of 91% and a negative predictive value of 100%. The PSIF sequence is relatively fast and insensitive to bulk motion. Using a diffusion-weighted SSFP sequence, the differences between benign and malignant vertebral body fractures are clearer than when using alternative pulse sequences like single-shot EPI, single-shot TSE, or conventional spin-echo or stimulated-echo sequences (Dietrich et al. 2009). Figures 6 and 11 show an osteoporotic and a malignant vertebral fracture on STIR and diffusion-weighted SSFP sequences (PSIF).

Hypointense vertebral metastases in diffusion-weighted SSFP (Castillo et al. 2000) may be explained by former treatment with radiotherapy or sclerosis with lower water content (Dietrich et al. 2009). Sclerotic vertebral metastases of prostate cancer show less signal than metastases of other tumors (Hacklander et al. 2006). In a meta-analysis of eight studies, it could be shown, that lesions classified as "hypointense" or "hypointense and isointense" were significantly more likely to be benign (Karchevsky et al. 2008).

Using PSIF with a diffusion-pulse length of 3 ms provides the best differentiation of benign and malignant fractures. In unclear cases, an additional diffusion-pulse with a length of 6 ms can be applied, where osteoporotic fractures become hypointense, while malignant fractures remain hyperintense (Baur et al. 2001, 2002a). Because the contrast to

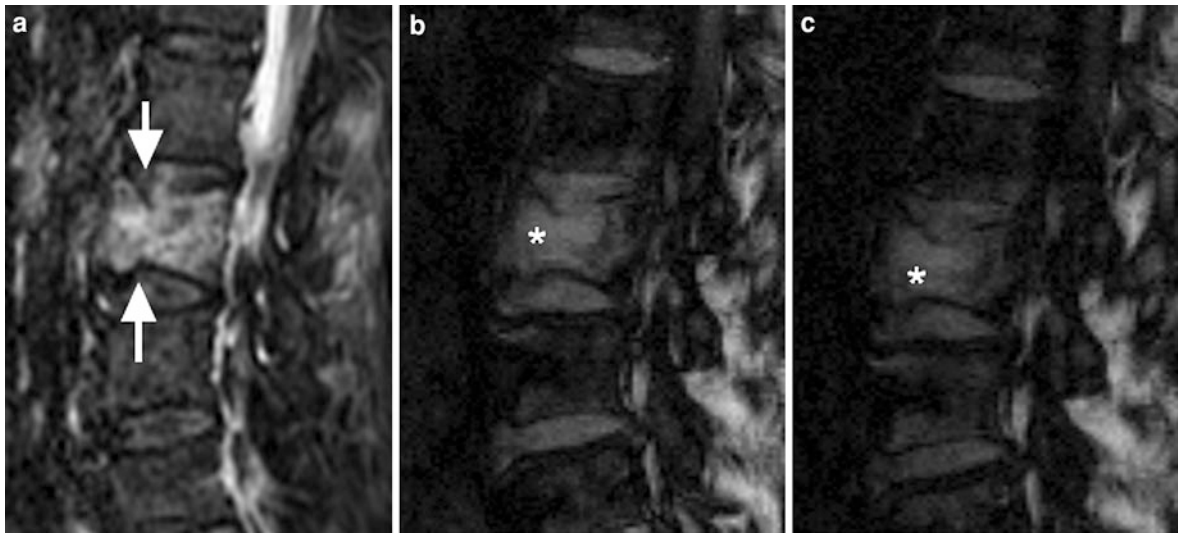

Fig. 11 71-year-old patient with a malignant fracture of L3 due to metastasis of adenocarcinoma and diffusion-weighted SSFP (PSIF). Sagittal STIR image (**a**) showing edema in the whole vertebral body and end plate fractures. Diffusion-weighted SSFP with delta = 3 ms (**b**) and delta = 6 ms (**c**) showing a hyperintense signal intensity in the edema (*asterisk*) in comparison with normal vertebral marrow

normal bone marrow is used, patients with known hematologic disorders like osteomyelofibrosis or leukemia should not be evaluated with a PSIF sequence (Baur et al. 2002a).

Figures 6 and 11 show a typical osteoporotic and a typical malignant vertebral fracture on STIR and diffusion-weighted SSFP sequences (PSIF).

Another imaging technique, echo-planar imaging (EPI), decreases acquisition time, but general problems of this technique are a limited spatial resolution, sensitivity to eddy currents and local susceptibility gradients, as well as chemical-shift (Le Bihan 1998). Oztekin et al. (2009) used diffusion-weighted EPI with a b-value of 300 s/mm^2 and examined patients with osteoporotic and traumatic vertebral fractures and vertebral tumor infiltration. A hyperintense signal was highly sensitive and specific for metastatic tumor infiltration (93% sensitivity, 90% specificity). Sclerotic metastases were found to be hypointense.

Tang et al. (2007) examined the influence of the b-value in the differentiation of benign and malignant vertebral compression fractures using EPI with spectral presaturation and inversion recovery (SPIR) and b-values of 0–800 s/mm^2. They found that b-values around 300 s/mm^2 provided the best differentiation between benign and malignant fractures. All malignant fractures were hyperintense, while most benign fractures were isointense and a few slightly hyperintense at this b-value.

Park et al. (2004) used a diffusion-weighted single-shot fast spin-echo sequence with a b-value of 500 s/mm^2. In this study, all benign fractures had low signal intensities on diffusion-weighted images. Malignant vertebral tumors showed a heterogeneous signal behavior with hypointensity in 58%, intermediate signal intensity in 25%, and hyperintensity in 6%. With a high or intermediate signal intensity indicating malignancy, the study found a high specificity of 95% but a low sensitivity of 42%. The authors concluded that the differences in the malignant lesions were due to patient selection bias and different degrees of T2 shine through effect.

The differences in the signal behavior in the studies mentioned above may be explained by the different diffusion weightings, the different sequence types and sequence parameters. At low b-values <150 s/mm^2, the diffusion effect can be overestimated due to the contribution of perfusion and T2 shine through effect (Chan et al. 2002; Herneth et al. 2005), while high b-values >600 s/mm^2 may lead to an underestimation due to signal intensities comparable with the noise level (Dietrich et al. 2009).

Several studies applied quantitative DWI to normal and pathological vertebral bone marrow. Although the results showed a certain variability, the majority of the studies revealed typical ADC ranges associated with normal and pathological bone marrow. Normal bone

marrow shows ADCs of 0.2–0.5 × 10^{-3} mm^2/s. Metastases or malignant fractures range from ~0.7 to 1.0 × 10^{-3} mm^2/s, osteoporotic or traumatic fractures show ADCs of ~1.0–2.0 × 10^{-3} mm^2/s (Dietrich et al. 2009). Studies always showed a remarkable overlap, which limited the value of quantitative DWI in differentiating between benign and malignant fractures. Figures 12 and 13 show the ADC maps of a malignant and an osteoporotic fracture.

The calculation of ADC values eliminates the influence of the T2 weighting and depicts the cellular barriers in the tissue, but low signal-to-noise-ratio in diffusion-weighted fast spin-echo sequences is a major source of error, that leads to an overlap and diminishes accuracy (Zhou et al. 2002). The most important influence is the application of fat saturation, which is required for single-shot EPI but is optional in combination with SE or FSE techniques. Because the ADC of vertebral fat is close to zero, the ADCs of normal bone are systematically decreased, when fat saturation is not applied (Dietrich et al. 2009).

Using a fast spin-echo diffusion-pulse sequence with b-values of 0–250 s/mm^2, Zhou et al. (2002) showed, that metastatic vertebral fractures show ADC values of 1.9 × 10^{-4} mm^2/s ± 0.3 × 10^{-4} mm^2/s and benign fractures show ADC values of 3.2 × 10^{-4} mm^2/s ± 0.5 × 10^{-4} mm^2/s with significant differences between both groups, but with a substantial overlap. Lesions were better separated on the basis of ADC values than on conventional T1-w, T2-w, contrast-enhanced T1-w or qualitative diffusion-weighted images. Sensitivity, specificity, and accuracy were not reported.

Biffar et al. (2010a) examined 24 osteoporotic vertebral fractures and 20 malignant vertebral fractures and showed, that DW-ssTSE (b-values 100, 250, 400, 600 s/mm^2) could significantly discriminate between both entities showing a sensitivity of 65% and specificity of 88% at an ADC of 1.49 × 10^{-3} mm^2/s as a cutoff-value. DW-EPI showed no statistical differences due to an underestimated signal attenuation and gross geometrical image distortions caused by susceptibility heterogeneities.

Chan et al. (2002) examined 25 acute osteoporotic fractures in 18 patients, 18 acute malignant fractures in 12 patients and 6 acute fractures due to tuberculosis in 2 patients, with a diffusion-weighted EPI sequence at 1.5 T. ADC values were calculated, using b-values of 200, 500, 800, and 1,000 s/mm^2. The quantitative evaluation showed mean ADC values of 0.82 × 10^{-3} mm^2/s for malignant fractures, and 1.92 × 10^{-3} mm^2/s for osteoporotic fractures, revealing a significant difference between these two entities ($p < 0.001$). Fractures due to tuberculosis (mean ADC 0.98 × 10^{-3} mm^2/s) were
not significantly different from malignant fractures. Additionally, the signal intensities of the collapsed vertebral bodies were qualitatively assessed at a b-value of 1,000 s/mm^2, where all benign acute vertebral fractures were hypointense. The malignant fractures were hyperintense, except sclerotic metastases, which were hypointense and showed ADC values close to zero.

In a meta-analysis Karchevsky et al. (2008) reviewed 4 studies assessing the ADC values of benign and malignant vertebral fractures and showed, that mean ADC values in benign fractures were significantly higher than malignant fractures with a standardized mean difference (SMD) of 2, 8 and a 95% confidence interval for the SMD of 2.1 to 3.5. Mean ADCs of pathologic fractures and malignant lesions were in the range from 0.19 to 0.853 × 10^{-3} mm^2/s, benign fractures showed ADCs from 0.32 to 1.94 × 10^{-3} mm^2/s.

The ADC value shows significant differences between benign and malignant vertebral fractures, but all studies showed a remarkable overlap limiting its specificity. Although the ADC value itself should be independent from sequence type and sequence parameters, the measured values are influenced by sequence specific artifacts, range of used b-values, application of fat saturation, noise, and perfusion effects. DWI of bone marrow requires considerably more robust imaging techniques than typical MRI of the brain. Being still a technique undergoing active research, DWI of the bone marrow provides a unique imaging method, which can help in the differentiation of benign and malignant vertebral fractures.

3.2 In-Phase/Opposed-Phase (Chemical-Shift) Imaging

In-phase (IP)/opposed-phase (OP) imaging (also known as chemical-shift imaging) uses the different precession frequencies of water and fat protons due to the differences in their molecular environment. Water and fat protons are in-phase with one another at a TE of 4.6 ms, and 180° opposed at a TE of 2.3 ms at

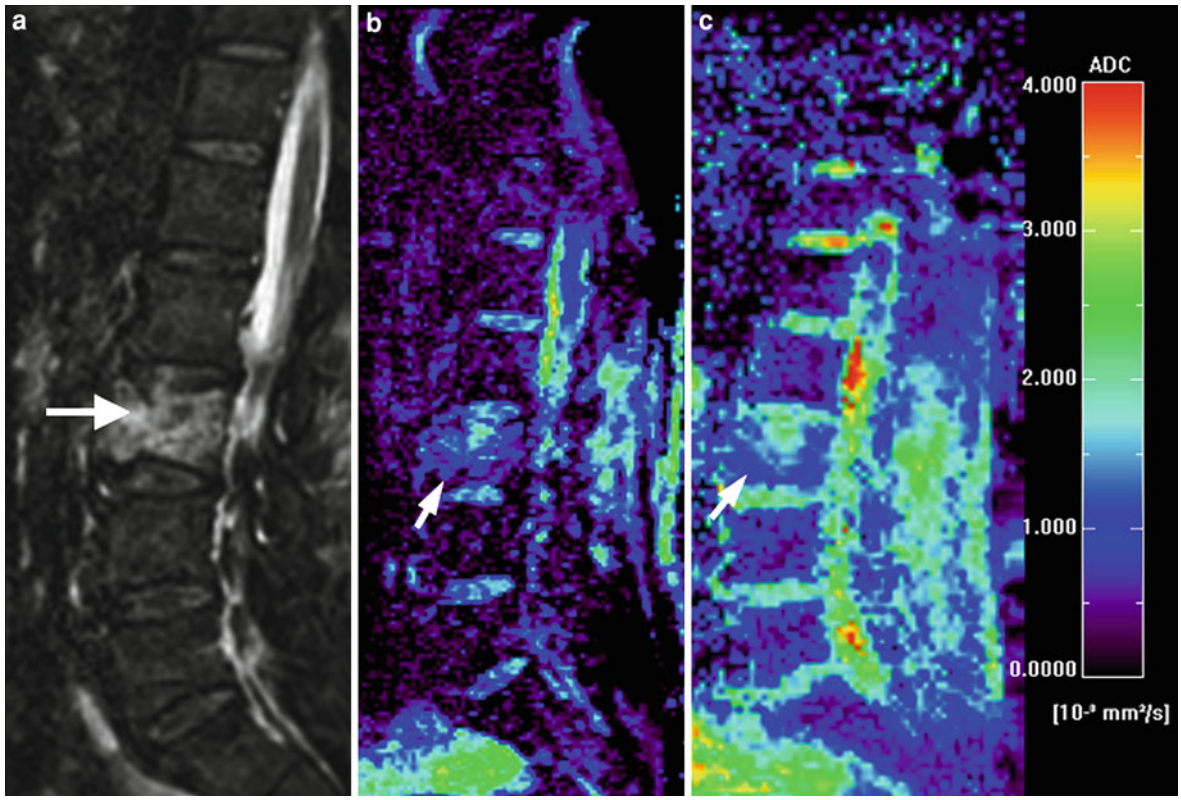

Fig. 12 71-year-old patient with a malignant fracture of L3 due to metastasis of adenocarcinoma and DWI. Sagittal STIR image (**a**) showing hyperintense signal in the whole diseased vertebral body. ADC maps calculated from DW-EPI (**b**) and DW-HASTE (**c**) images showing average ADC values of 0.9×10^{-4} mm^2/s (DW-EPI) and 1.38×10^{-4} mm^2/s (DW-HASTE) (*arrows*)

1.5 T. When there are both fat and water protons in a given voxel, there will be some signal intensity loss on images that are obtained, when the protons are in their opposed-phase, without a refocusing pulse. More signal intensity loss occurs when the volume of fat and water is roughly equal (Erly et al. 2006). The percentage decrease of the bone marrow signal intensity on opposed-phase images compared with in-phase images (Zajick et al. 2005) or the relative signal intensity ratio (signal intensity$_{OP}$/signal intensity$_{IP}$) (Eito et al. 2004; Erly et al. 2006) can be calculated for quantitative measurement.

Normal vertebral bone marrow has fat and water components. In adults, the vertebrae, sternum, and ribs contain hematopoietic red marrow, which has about 40% fat content while yellow marrow contains 80% fat (Eastell 2007). Malignant neoplasms tend to replace the fatty marrow components and therefore cause a lack of suppression on the opposed-phase images. Benign vertebral fractures usually show no marrow displacement, which results in low signal intensity on the opposed-phase images (Baker et al. 1990; Eito et al. 2004; Zajick et al. 2005; Erly et al. 2006). Figures 14 and 15 show the IP and OP images and the calculated ratios of an osteoporotic and a malignant vertebral fracture.

If vertebral bodies are highly deformed and compressed, containing almost no water or fat, they may show weak signal intensity in OP and IP images, resulting in a high signal intensity ratio mimicking malignancy. Therefore, signal intensity ratios may be high because the decreased signal intensity is related to decay resulting from the use of TEs of 2.3 to 4.6 ms. T1-w images can be used to show a signal loss due to severe compression (Eito et al. 2004). One study noticed the return of a malignant lesion to a benign signal intensity ratio after treatment with X-ray therapy, whereas the standard spin-echo

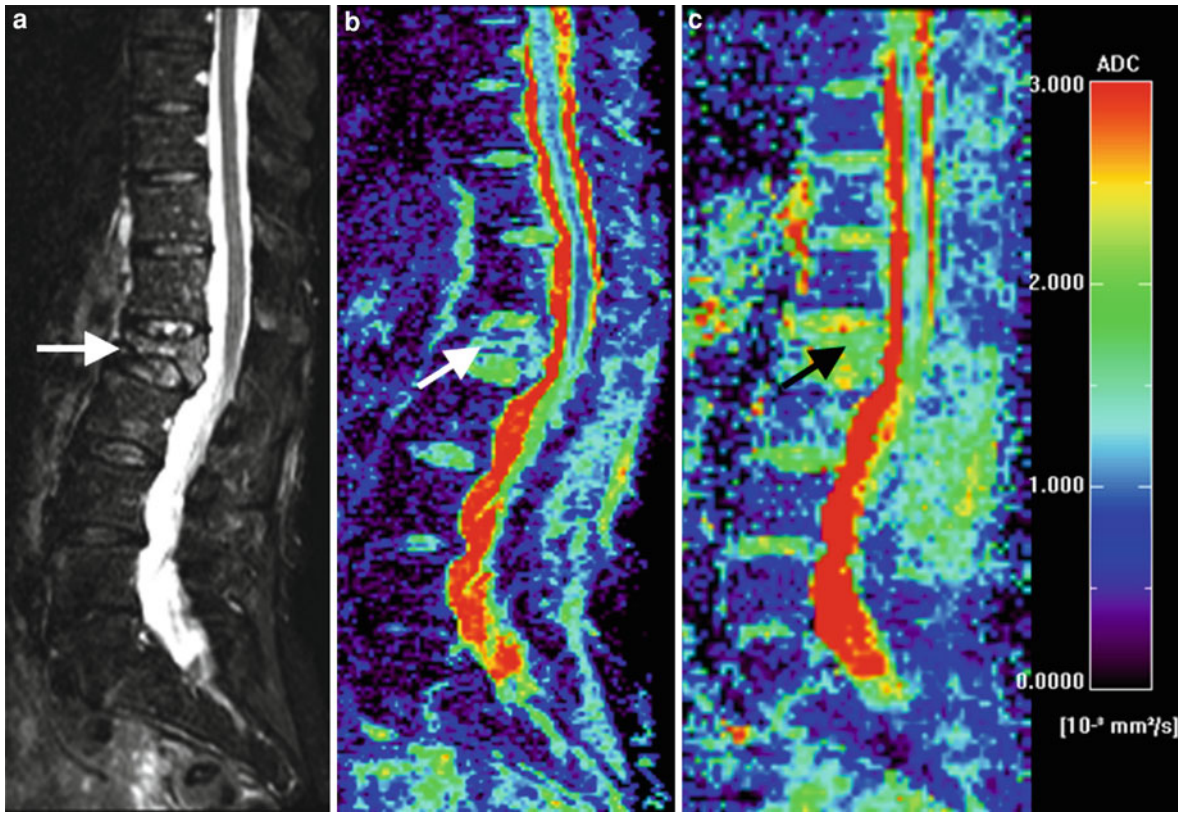

Fig. 13 70-year-old patient with an osteoporotic fracture of L2 and DWI. Sagittal STIR image (**a**) showing hyperintense signal in the whole fractured vertebral body. ADC maps calculated from DW-EPI (**b**) and DW-HASTE (**c**) images showing higher (compared with malignant fractures) average ADC values of 1.25×10^{-4} mm^2/s (DW-EPI) and 1.73×10^{-4} mm^2/s (DW-HASTE) (*arrows*)

sequences remained abnormal, suggesting that in-phase/opposed-phase imaging might be an early marker for response to treatment of osseous metastatic disease, but studies on this are still lacking (Erly et al. 2006).

Eito et al. (2004) showed, that at 1.5 T normal non-fractured vertebrae have mean signal intensity ratios of 0.46 ± 0.14 (SD), whereas non-neoplastic fractured vertebrae (mean 0.63 ± 0.21 SD) and malignant compression-fractured vertebrae (mean 1.02 ± 0.11 SD) have higher signal intensity ratios (i.e. the signal drop from in-phase to opposed-phase is highest in normal vertebrae, whereas non-malignant fractures and malignant fractures show less signal drop or even increased signal intensity on opposed-phase images). All three groups showed significant differences between each other.

Erly et al. (2006) compared 29 benign compression fractures and 20 malignant lesions at 1.5 T, and showed a significant difference of the mean signal intensity rates of benign vertebral compression fractures (0.58 ± 0.02 SD) and malignant vertebral compression fractures (0.98 ± 0.095 SD). Performing ROC-analysis, a signal intensity ratio of >0.8 indicating malignancy showed best discrimination of benign and malignant vertebral fractures with a sensitivity of 95% and a specificity of 89%.

Zajick et al. (2005) examined normal vertebral bone marrow, benign lesions, and metastases. They found a decrease in signal intensity for all normal vertebrae (mean 58.5%) and for benign lesions (endplate degeneration mean 52.2%, Schmorl's nodes mean 58.0%, hemangiomas mean 49.4%, benign fractures 49.3%) on opposed-phase images. Metastases showed either a minimal decrease or an increase of signal intensity (mean 2.8% decrease). Although the results showed overlaps between the different groups, the authors suggested a decrease in signal

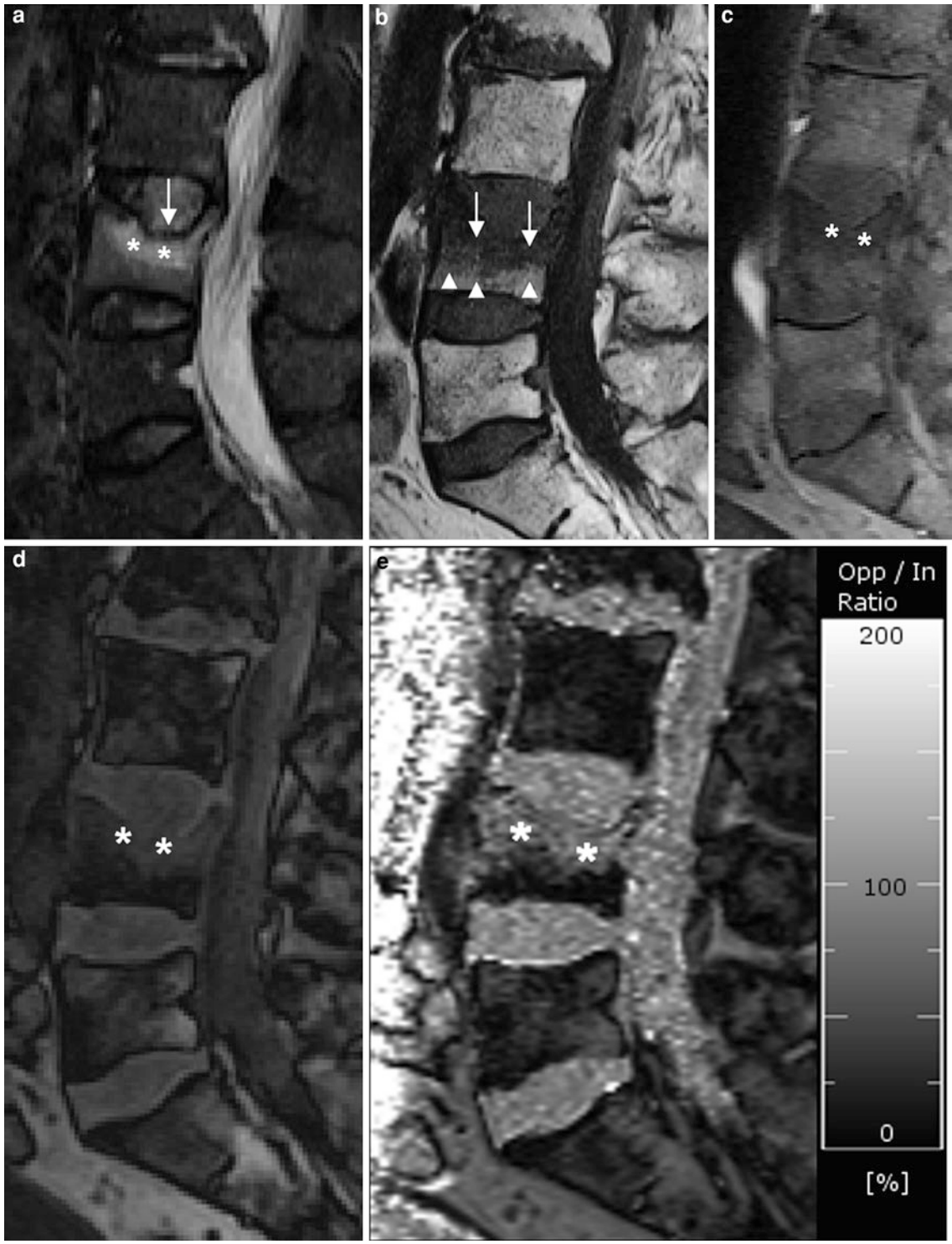

Fig. 14 67-year-old patient with an osteoporotic fracture of L4 and chemical-shift imaging. STIR image (**a**) showing a band-like edema (*asterisks*) adjacent to the impressed upper vertebral end-plate (*arrow*). T1-w image (**b**) showing the hypointense signal of the edema (*arrows*) and the preserved fatty marrow adjacent to the opposite cover plate (*arrowheads*). Corresponding in-phase (**c**) and opposed-phase (**d**) images showing a signal drop on the opposed-phase image. A map showing the calculated opposed-phase/in-phase ratio (**e**) exhibits a signal drop of 39% corresponding to an opposed-phase/in-phase ratio of 61% in the edema (*asterisks*). Normal fatty marrow shows a greater signal drop due to the almost equal amount of fat and water bound protons in normal marrow

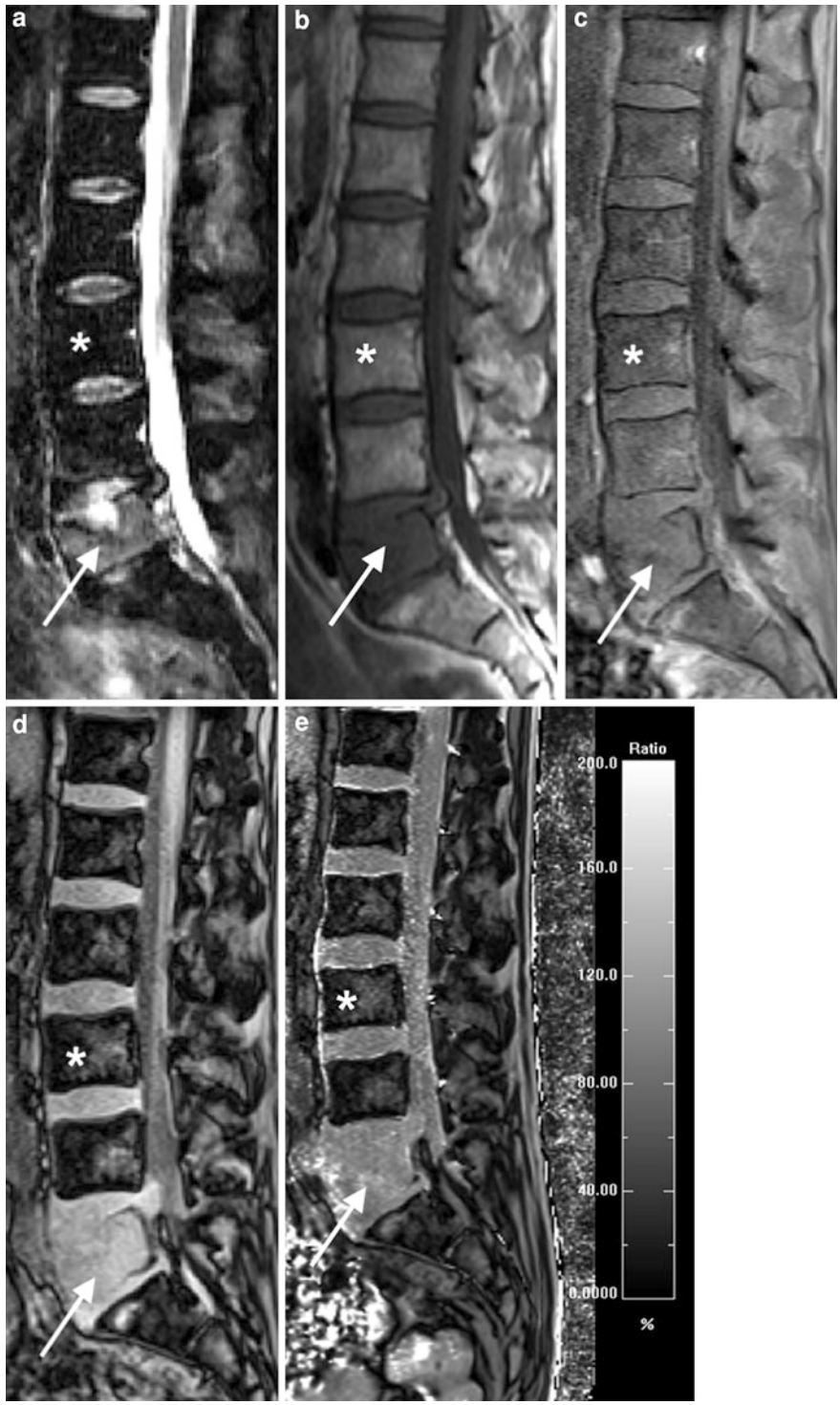

Fig. 15 60-year-old patient with a malignant fracture of L3 due to metastasis of hypopharyngeal carcinoma. Sagittal STIR image (**a**) showing hyperintense signal in the whole diseased vertebral body (*arrow*). T1-w image (**b**) showing hypointense signal (*arrow*). Corresponding in-phase (**c**) and opposed-phase (**d**) images showing a slight signal drop on the opposed-phase image (*arrow*), while normal vertebral bodies (*asterisk*) show a great signal drop. A map showing the calculated opposed-phase/in-phase ratio (**e**) exhibits a signal drop of 9% corresponding to an opposed-phase/in-phase ratio of 91% in the edema pattern (*arrow*). Normal fatty marrow (*asterisk*) shows a greater signal drop due to the almost equal amount of fat and water bound protons in normal marrow

intensity of more than 20% on opposed-phase images compared with in-phase images to be a reliable cut-off threshold for benign vertebral bone marrow abnormalities, while malignant vertebral bone marrow lesions show less than 20% decrease in signal intensity.

Ragab et al. (2009) examined patients with osteoporotic and neoplastic vertebral fractures and showed a different proportional change (percentage decrease) of marrow signal intensity in OP compared with IP of 58.51 ± 9.38 for osteoporotic and 13.55 ± 11.63 for neoplastic lesions. A decrease in SI >35% as a cut-off value showed a sensitivity of 95% and a specificity of 100% with a positive predictive value of 100% and a negative predictive value of 95.2%.

Thus in-phase/opposed-phase imaging is a reliable additional tool for the differentiation of benign and malignant vertebral collapse. However, if strong edema and reduced fat content are present, the signal intensities can also be high on opposed-phase images in osteoporotic fractures. Care should be taken to acquire the same sequence type with the appropriate sequence parameters, since a slight shift e.g. in TE and flip-angle can cause a significant shift in contrast.

3.3 Dynamic Contrast-Enhanced MRI

Dynamic contrast-enhanced (DCE)-MRI does not focus on morphological features but uses measurements of the signal changes of intravenously administered contrast agents over time to measure hemodynamic parameters, using ultra-fast imaging methods. Gadolinium-containing contrast agents show similar pharmacokinetics to that of iodinized contrast agents and produce an increase of signal intensity (SI) in T1-w images by reducing T1 relaxation time (Brasch et al. 1984).

The distribution of yellow and red bone marrow strongly influences marrow perfusion. Yellow marrow mainly consists of fat cells and a sparse network of capillaries, venules, and thin-walled veins (Vogler and Murphy 1988). It shows only minor and gradual increase of SI after administration of contrast agents (Erlemann et al. 1988). Red bone marrow includes a rich and arborized vascular network. On contrast-enhanced images, the signal enhancement is rarely obvious on T1-w images without fat suppression since fatty marrow has a high intrinsic SI, which hides the enhancement. It can be detected by careful SI measurements (Vande Berg et al. 1998).

Studies showed, that bone marrow perfusion decreases with age (Baur et al. 1997; Chen et al. 2001; Montazel et al. 2003; Griffith et al. 2005), an increasing fat content corresponds to a decrease of marrow perfusion (Bluemke et al. 1995; Montazel et al. 2003; Griffith et al. 2005), and perfusion is higher in the upper compared to the lower lumbar spine (Savvopoulou et al. 2008).

For the correct interpretation of a perfusion analysis, it is useful to know the distribution pattern between the water and fat component in the assessed vertebral bone marrow. Otherwise, an increase/decrease of the fat component might be falsely interpreted as a decrease/increase of perfusion due to a pathologic cause (Biffar et al. 2010c, d).

Initial studies assessing the value of DCE-MRI in the discrimination of benign and malignant vertebral fractures semi-quantitatively examined the perfusion of bone marrow using descriptive parameters like the peak contrast-enhancement percentage, enhancement slope, and time-intensity-curve (TIC) patterns based on operator-defined regions of interest (ROIs) (Chen et al. 2002; Tokuda et al. 2005).

The observed TICs can be classified into five groups:

A: nearly flat TIC,

B: slow inclination curve,

C: rapidly rising slope (wash-in) during early phase, followed by a plateau after the peak enhancement is achieved,

D: rapidly rising slope (wash-in) during the initial short period like in type C, followed by a wash-out phase,

E: initially rapidly rising slope followed by a second slow-rising phase.

If the difference in maximal enhancement and SI at the endpoint is greater than 20% of baseline SI, a type C curve is defined as either type D or type E, depending on the wash-in or wash-out of contrast (Chen et al. 2002; Tokuda et al. 2005).

Chen et al. (2002) examined 42 patients with acute compression fractures ($n = 12$), chronic compression fractures ($n = 21$), and metastatic vertebral lesions with ($n = 6$) or without ($n = 32$) compression fracture. A type D curve was highly predictive (positive predictive value 100%) for a metastatic lesion with or without fracture, since the packed viable tumor cells are thought to lead to an early wash-out because of scarcity of matrix. But since the type D curve was found in only one-third (18 out of 38) of malignant lesions, the sensitivity for diagnosing malignant vertebral lesions was not regarded to be sufficiently high.

A type E curve was predictive for benign acute or chronic compression fractures (positive predictive value 85.7%), because an increase in vascularity, infiltration of inflammatory cells, vasodilatation, and exudation of plasma is thought to result in extravasation of more contrast agent into the extracapillary space without balanced venous wash-out. But since only 6 out of 33 (18.2%) of the vertebral compression fractures showed a type E curve, its sensitivity for diagnosing benign vertebral compression fractures is also low. There were no significant differences for peak enhancement percentage and enhancement slope with overlapping areas between benign and malignant lesions.

Another study performed by Tokuda et al. (2005) found some contradictory results with TIC patterns not being able to distinguish between benign and malignant lesions. They examined patients with osteoporotic compression fractures ($n = 8$) with ages of the fractures ranging from 27 to 45 days, benign vertebral lesions (giant cell tumor, avascular necrosis, tuberculous spondylitis, Schmorl's nodes, vertebral hemangioma) without compression fractures ($n = 11$), and metastatic vertebral lesions with ($n = 8$) and without ($n = 21$) compression fractures. Type E curves were not only seen in benign fractures, but also observed in metastatic vertebral lesions without compression fracture. Type D lesions were also nonspecific. In this study, peak enhancement, steepest slope, and slope were significantly higher in pathologic compression fractures, than in osteoporotic fractures. The authors hypothesize that this difference might be because of the time delay (27–45 days) from fracture to imaging: if osteoporotic fractures are examined in the early phase of healing during the inflammatory phase (like those of Chen et al. 2002), an increase in vascularity might show higher peak enhancement, steepest slope, and slope, comparable with those of pathologic compression fractures. But unfortunately, this study does not provide information about the exact sensitivities and specificities of the examined parameters, and the study subgroup population was small.

Since studies based on semi-quantitative parameters revealed discrepant results and depend on well-known limitations, like a dependence on examination parameters like the injection protocol and an unclear interpretation in terms of hemodynamic parameters (Biffar et al. 2010c, d), another approach quantitatively analyzes the dynamic contrast-enhanced data and directly assesses the perfusion and endothelial permeability using high temporal resolution T1w-MRI.

Therefore, the tissue concentration–time curve is derived from the signal–time curve assuming a linear relationship between the concentration of the tracer and T1 and a known functional dependence between the signal intensity and T1. In a second step, the perfusion- and/or permeability parameters are determined with tracer-kinetic analysis, which provides a relation between the hemodynamic parameters and the measured TICs (Jaquez 1985; Tofts et al. 1999; Brix et al. 2004). The quantitative analysis requires the additional measurement of an arterial input function (AIF) in the feeding artery to correct variations of the tissue concentration, which are not directly related to the hemodynamic state of the tissue itself (injection rate, bolus shape, etc.) (Biffar et al. 2010b). The AIF can be obtained using a circular ROI in the aortic lumen, and can be calculated as the relative signal enhancement divided by (1−hematocrit) to derive the plasma concentrations (Biffar et al. 2010c, d). Most studies used an arbitrary hematocrit value of 0.45, since exact values for individual patients were not always available (Biffar et al. 2010c, d, 2011).

The current standard model in tracer-kinetic analysis of DCE-MRI produces a parameter K^{trans} that represents a mixture of perfusion and permeability (Tofts et al. 1999). Using a two-compartment model (Brix et al. 2004) or a distributed parameter model (Buckley et al. 2004), perfusion and permeability can be fully separated. Four independent perfusion parameters can be derived, characterizing the degree of vascularity and capillary perfusion, plasma flow (PF), plasma volume (PV), extraction flow (EF), and the interstitial volume.

Initial examinations evaluated the potential of the quantitative assessment of DCE-MRI in osteoporotic fractures. Biffar et al. (2010c, d) showed in 20 patients with acute osteoporotic compression fractures that perfusion is strongly increased compared to normal appearing bone marrow. In the same study, quantitative DW-MRI (ADC values) was compared with the perfusion parameters. IV and ADC value positively correlated, confirming the assumption that ADC is essentially determined by the diffusion of water in the extracellular space, and that intracellular water has a weaker contribution. The negative correlation of PV

and ADC may be explained firstly by the fact that the perfusion effects have been eliminated by the choice of the *b-values*, and secondly by the fact that an increase of the PV leads to a decrease of the IV. In normal appearing bone marrow, the interstitial compartment is most likely bigger than the intravascular compartment, because the TIC did not reproduce the AIF. The shape of the TIC suggested that normal appearing bone marrow corresponds to the intermediate regime of contrast agent exchange between both compartments.

Other studies showed, that quantitative DCE-MRI can successfully be used to differentiate between normal and diseased vertebral bone marrow (Biffar et al. 2010c, d, 2011). The use of tracer-kinetic models might be useful in the differentiation of benign and malignant vertebral fractures, studies on this purpose are still ongoing.

3.4 FDG-PET/PET-CT

Fluorodeoxyglucose positron emission tomography (FDG-PET) visualizes the increased glucose metabolism that occurs in malignant and inflammatory lesions, and has been used extensively to differentiate malignant tumors from benign lesions in many organ systems (Strauss and Conti 1991; Hoh et al. 1997). While tumor cells typically accumulate FDG, osteoporotic fractures are not expected to accumulate a high amount of FDG, which may allow differentiation between benign and malignant compression fractures (Bredella et al. 2008). False-positive results can occur in patients who have been treated with bone marrow stimulating agents. One to two months after treatment, FDG-uptake is expected to return to normal (Bredella et al. 2008). Osteomyelitis and discitis can show an increased uptake, mimicking malignancy (Guhlmann et al. 1998a, b; Schmitz et al. 2002). Chronic fractures have also been reported to show a high FDG accumulation due to infiltration with macrophages and granulation tissue (Palmer et al. 1995; Guhlmann et al. 1998a, b).

For this reason, the patient's clinical history should be actively sought when interpreting positive findings, especially in cases with diffuse osseous uptake, mimicking a diffuse osseous process (Bredella et al. 2008). In PET-CT, the CT portion improves the exact fracture localization and provides additional information on fracture morphology (Metser et al. 2004; Bredella et al. 2008).

Kato et al. (2003) examined 10 patients with acute benign vertebral fractures, 9 patients with acute malignant, and one patient with both acute benign and malignant vertebral compression fractures. FDG-PET showed significant differences ($p = 0.0006$) between benign and malignant vertebral compression fractures with a mean SUV of 1.36 ± 0.49 (SD) in the benign, and 4.46 ± 2.12 (SD) in the malignant group. No significant correlation was noted between the histologic type of primary malignant tumor and FDG accumulation of the metastatic lesion. At a cut-off value of SUV 2.0, a sensitivity of 80%, a specificity of 88.9%, and an accuracy of 85.7% could be shown.

Bredella et al. (2008) retrospectively evaluated the use of FDG-PET and FDG-PET-CT in differentiating benign from malignant compression fractures. The neoplastic fractures were due to different underlying malignancies, e.g. leukemia, ovarian cancer, or esophageal cancer. There were 21 patients with 29 benign, and 12 patients with 14 malignant compression fractures. Only 5 of the benign fractures were acute, based on clinical history and imaging characteristics on additionally evaluated MRI scans. The age of the other fractures was not listed in the study.

Malignant fractures demonstrated intense radiotracer uptake and a mean standardized uptake value (SUV) of 3.99 ± 1.52, while benign compression fractures showed only mildly increased or no increased uptake of FDG-PET and a mean SUV of 1.94 ± 0.97, leading to significant differences for the standardized uptake values (SUV) for benign and malignant fractures. Acute and chronic benign fractures could not be differentiated. FDG-PET showed a sensitivity of 86%, a specificity of 83%, a positive predictive value of 84%, a negative predictive value of 71% and an accuracy of 92% (Bredella et al. 2008). In this study some of the false-positive results were found in patients that had been treated with marrow-stimulating agents resulting in an increased FDG-PET uptake (Bredella et al. 2008), what was consistent with the effects described in previous studies (Aoki et al. 2003). Therefore in interpreting positive findings, possible treatment with marrow-stimulating agents should be verified. In contrast to bone scintigraphy, where there is an increased uptake

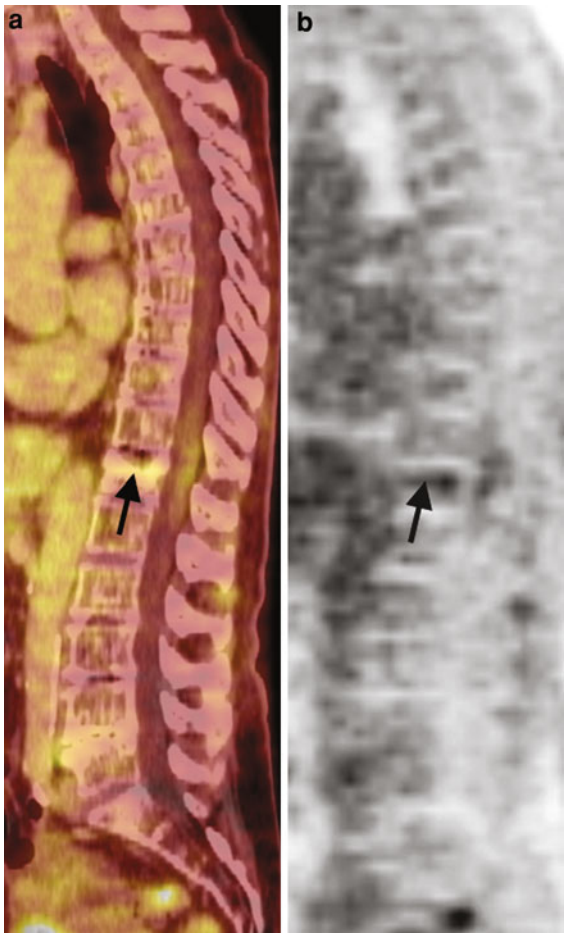

Fig. 16 62-year-old patient with a fracture of Th 12 due to osteoporosis. Sagittal FDG-PET-CT fusion image (**a**) showing a fracture of the upper vertebral cover plate of Th 12 with an adjacent band-like increased uptake (SUV 1.2), that is also depicted in the PET image (**b**)

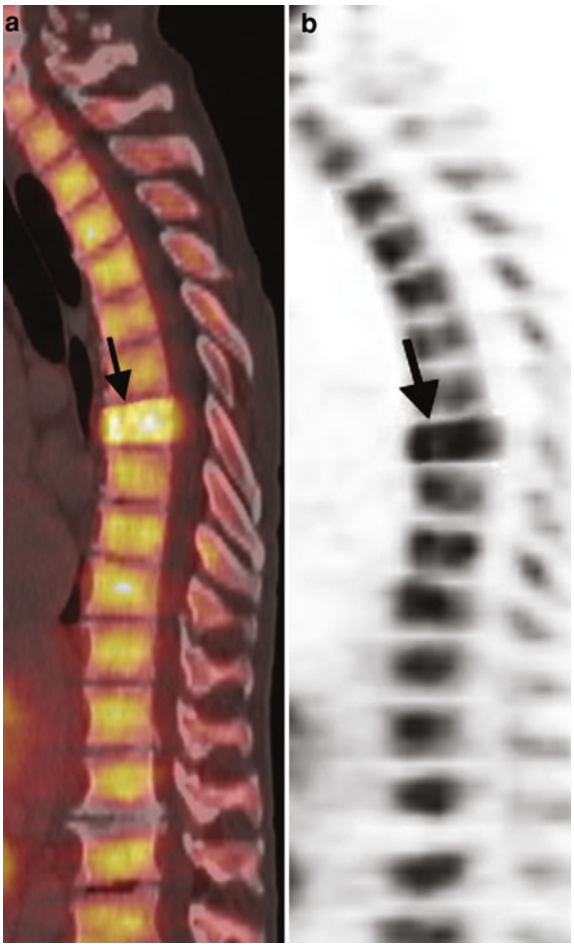

Fig. 17 67-year-old patient with a malignant fracture due to metastasis of a neuroendocrinal tumor. Sagittal Ga^{68}-DOTA-TATE PET-CT fusion image (**a**) showing a heavily increased tracer uptake in a wedge-shaped vertebral fracture (*arrow*). There is also an increased uptake in the other non-fractured vertebral bodies due to metastases, as can also be seen in the PET image (**b**)

for many months (Masala et al. 2005), in FDG-PET there is only a mild to moderately increased uptake in acute benign fractures, while chronic benign fractures show no or only mildly increased uptake (Bredella et al. 2008).

Figures 16 and 17 show PET-CT images of an osteoporotic and a malignant vertebral fracture.

FDG-PET is recommended not as a screening test, but rather as an additional imaging modality in problem cases, with the possibility to evaluate the entire skeletal system in search for metastatic disease. Patients with contraindications to MRI (pacemakers, claustrophobia, severe pain) can profit from FDG-PET(-CT) (Bredella et al. 2008).

3.5 Scintigraphy/SPECT

Scintigraphy and single-photon emission computed tomography (SPECT) use the emission of radiation of radiopharmaceuticals, which aggregate in areas of high metabolism.

Bone Technetium-99 hydroxymethylene diphosphonate (Tc-99 HMDP) scintigraphy is an established screening method for skeletal metastases. Multiple increased uptakes are often considered as suspicious for malignancy, while a solitary increased uptake of the fractured vertebra is observed in most recent benign and malignant fractures (Taoka et al. 2001).

Acute vertebral compression fractures, degenerative, and inflammatory diseases show similar radionuclide dynamics of Tc-99 HMDP, which leads to a lack of sensitivity in differentiating benign from malignant vertebral compression fractures.

Tokuda et al. (2011) examined 53 malignant vertebral compression fractures in 51 patients, and 44 acute benign vertebral compression fractures in 40 patients to compare the diagnostic value of SPECT with Tc-99 HMDP and morphologic MRI features. The results showed, that the overall accuracy of MRI was significantly greater than that of the SPECT images for both observers in the study. In vertebral compression fractures with partial replacement of the fatty marrow, MRI performed significantly better in differentiating between the two entities. However, fractures with a complete replacement of fatty marrow did not show significant differences between the sensitivities (up to 87.1% for SPECT, up to 94.9% for MRI), specificities (up to 89.5% for SPECT, up to 89.5% for MRI) and accuracies (up to 91.4% for SPECT, up to 91.4% for MRI) of both techniques. Therefore the authors suggested, that SPECT represents a valid alternative to MR imaging for differentiating malignant from benign vertebral compression fractures in patients, which are not able to undergo MRI due to contraindications, like cardiac pacemakers. MRI should still be used for patients without contraindications.

Thariat et al. (2004) used Thallium-201 chloride (^{201}TI), which is a radionuclide with gamma-ray emission that is mainly used as a myocardial perfusion marker, for the differentiation of benign and malignant vertebral fractures that were not older than 3 months. Conventional bone scintigraphy and SPECT were performed. The authors showed a weak sensitivity (28.6%), which did not support its systematic use to distinguish benign from malignant recent vertebral fractures. SPECT showed unchanged results in comparison with conventional bone scintigraphy. But its high specificity (92.9% on early, and 100% on delayed images) may make ^{201}TI-scintigraphy or -SPECT a valuable tool to avoid any unnecessary invasive procedure, if performed prior to vertebral biopsy. In contrast to other studies that found a higher sensitivity in the evaluation of other soft tissues and peripheral bone tumors, the authors hypothesize that the soft tissues around the vertebrae might have attenuated the radionuclide gamma-rays in a much higher extent than expected, or that edema, necrosis, and an altered vascularization in vertebral fractures hamper the spread of ^{201}TI, which has been shown an accurate indicator of the viability, metabolic activity, and vascularization of tumors.

4 Therapy

Relieving pain and preserving mobility are the most important goals that may require short-term analgesic therapy in vertebral compression fractures. In cases of severe pain due to osteoporotic vertebral fracture hospitalization can be justified (Burge et al. 2002). Although there is a lack of randomized trials, analgesics, nonsteroidal anti-inflammatory drugs, and drugs relieving neuropathic pain are commonly used for the therapy of patients with acute osteoporotic vertebral fractures. Narcotics facilitate mobility and avoid a prolonged bed rest (Prather et al. 2007). Spinal orthoses can reduce pain and disability in the first weeks after a vertebral fracture (Pfeifer et al. 2004; Stadhouder et al. 2009). Therapeutic exercise programs may reduce pain and improve functional status, but the findings are not constant across studies (Dusdal et al. 2011). An adequate intake of vitamin D is recommended in patients with osteoporosis (Lips et al. 2010). Several pharmacotherapies, like bisphosphonates (MacLean et al. 2008), selective estrogen receptor modulators (MacLean et al. 2008; Silverman et al. 2008; Cummings et al. 2010), denosumab (Cummings et al. 2009), or strontium ranelate (Meunier et al. 2004) have shown efficacy in reducing the risk of vertebral fractures.

Therapeutic options for patients with pathological vertebral body fractures include medical therapy and surgical intervention. Non-steroidal anti-inflammatory drugs and steroids can be applied against bone pain, neuropathic drugs can be used for nerve root pain. Nonresponsive patients can be treated with radiotherapy, but mechanical instability is not corrected in these cases. Open surgical procedures are highly invasive and may offer an unfavorable risk/benefit ratio. Vertebroplasty and kyphoplasty are an favorable option in patients with malignant vertebral compression fractures that do not cause neurological deficits but compromise quality of live because of intractable pain (Tancioni et al. 2011).

Vertebroplasty and kyphoplasty are partly indicated for treatment of painful primary and secondary osteoporotic vertebral compression fractures refractory to conservative therapy (Kondo 2008), although in the last two years some studies questioned its usefulness (Buchbinder et al. 2009; Kallmes et al. 2009; Buchbinder and Kallmes 2010).

In percutaneous vertebroplasty (PVP) a cement substance with polymethylmethacrylate (PMMA) is injected into a collapsed vertebral body under fluoroscopic control resulting in structural stabilization (Kondo 2008). In kyphoplasty, prior to the injection of PMMA, an inflatable bone tamp is used to erect the collapsed vertebral body and minimize the kyphotic deformity (Lieberman et al. 2001). In osteoporotic fractures, the procedure is mostly done after 2–6 weeks of conservative treatment, but some practitioners favor an earlier intervention, because they believe that besides pain relief, the kyphotic deformity should be corrected, as it might increase the risk of future fractures due to an altered spinal load distribution (Gaitanis et al. 2005). Mechanical stabilization, which prevents further micro motion of the vertebral fracture and provides realignment of the anterior and posterior ligaments, as well as damage of local pain receptors due to the unreacted cytotoxic methacrylate monomer and the heat from the polymerization of PMMA, are discussed as possible mechanisms of pain relieve (Belkoff and Molloy 2003). More than 90% of patients show an immediate pain relief, and about 50% of the patients report decreased pain during the immediate postoperative period. Significant differences in the clinical outcome between vertebroplasty and kyphoplasty could not yet been shown, despite theoretical benefits of the correction of height and deformity (Gill et al. 2007). Both techniques exhibit relatively low complication rates from 1 to 3% in osteoporotic and up to 10% in tumor-related vertebral compression fractures. Possible complications are related to needle displacement, cement extravasation, infection, bleeding, or iatrogenic fractures (Kondo 2008).

If there are multiple compression fractures or chronic fractures, the correct vertebra can be identified by depicting the bone marrow in MRI. Tanigawa et al. (2006) showed, that patients with extensive bone marrow edema in the vertebral bodies that underwent vertebroplasty, showed a significantly greater clinical improvement than those without this pattern. This shows agreement with other studies that showed effectiveness in chronic fractures, but even better clinical outcomes in patients with acute compression fractures (Brown et al. 2004), because older vertebral compression fractures lose bone marrow edema pattern.

Voormolen et al. (2006) also found a more frequent decrease of pain in patients with observed BME, but also found that 71% of the patients without BME showed clinical improvement, so that the authors postulated that vertebroplasty should not be withheld based on absence of BME alone.

Two randomized, double-blind trials (Buchbinder et al. 2009; Kallmes et al. 2009) compared vertebroplasty with a sham procedure in patients with painful vertebral fractures, that had been identified within 12 months, and found no beneficial effects from vertebroplasty with respect to pain, quality of life, and functional disability. The mean duration of symptoms before the procedure was 12–13 weeks in one study (Buchbinder et al. 2009), and 16–20 weeks in the other (Kallmes et al. 2009). Analyses did not indicate that vertebroplasty was more beneficial than the sham procedure within the subgroup of patients with pain of shorter duration, although vertebroplasty and kyphoplasty have been proposed to be most effective for acute fracture pain.

Since new vertebral compression fractures often occur relatively soon after intervention in vertebral bodies adjacent to fractured vertebral bodies treated with vertebroplasty (Uppin et al. 2003), there is special interest in the possibility to predict new adjacent-level compression fractures to justify a prophylactic vertebroplasty there. Sugimoto et al. (2008) showed, that collapsed vertebral bodies adjacent to vertebral bodies treated with PVP show significantly higher ADCs than not collapsed vertebral bodies prior to PVP, indicating that DWI before PVP might be a predictor for new compression fractures following PVP.

Therefore, the treatment of acute vertebral collapse should be planned in an interdisciplinary team setting, taking into account conservative management as well as surgical treatment. Due to the contradictory results, vertebroplasty should only be performed in those cases where pain cannot be managed conservatively and bone marrow edema is still present.

References

An HS, Andreshak TG et al (1995) Can we distinguish between benign versus malignant compression fractures of the spine by magnetic resonance imaging? Spine (Phila Pa 1976) 20(16): 1776–1782

Aoki J, Endo K et al (2003) FDG-PET for evaluating musculoskeletal tumors: a review. J Orthop Sci 8(3):435–441

Baker LL, Goodman SB et al (1990) Benign versus pathologic compression fractures of vertebral bodies: assessment with conventional spin-echo, chemical-shift, and STIR MR imaging. Radiology 174(2):495–502

Batson OV (1940) The function of the vertebral veins and their role in the spread of metastases. Ann Surg 112(1):138–149

Baur A, Stabler A et al (1997) MRI gadolinium enhancement of bone marrow: age-related changes in normals and in diffuse neoplastic infiltration. Skelet Radiol 26(7):414–418

Baur A, Stabler A et al (1998) Diffusion-weighted MR imaging of bone marrow: differentiation of benign versus pathologic compression fractures. Radiology 207(2):349–356

Baur A, Huber A et al (2001) Diagnostic value of increased diffusion weighting of a steady-state free precession sequence for differentiating acute benign osteoporotic fractures from pathologic vertebral compression fractures. Am J Neuroradiol 22(2):366–372

Baur A, Huber A et al (2002a) Differentiation of benign osteoporotic and neoplastic vertebral compression fractures with a diffusion-weighted, steady-state free precession sequence. RoFo : Fortschritte auf dem Gebiete der Rontgenstrahlen und der Nuklearmedizin 174(1):70–75

Baur A, Stabler A et al (2002b) Acute osteoporotic and neoplastic vertebral compression fractures: fluid sign at MR imaging. Radiology 225(3):730–735

Baur A, Dietrich O et al (2003) Diffusion-weighted imaging of bone marrow: current status. Eur Radiol 13(7):1699–1708

Belkoff SM, Molloy S (2003) Temperature measurement during polymerization of polymethylmethacrylate cement used for vertebroplasty. Spine 28(14):1555–1559

Bhalla S, Reinus WR (1998) The linear intravertebral vacuum: a sign of benign vertebral collapse. Am J Roentgenol 170(6): 1563–1569

Biffar A, Baur-Melnyk A et al (2010a) Multiparameter MRI assessment of normal-appearing and diseased vertebral bone marrow. Eur Radiol 20:2679–2689

Biffar A, Dietrich O et al (2010b) Diffusion and perfusion imaging of bone marrow. Eur J Radiol 76:323–328

Biffar A, Sourbron S et al (2010c) Combined diffusion-weighted and dynamic contrast-enhanced imaging of patients with acute osteoporotic vertebral fractures. Eur J Radiol 76:298–303

Biffar A, Sourbron S et al (2010d) Measurement of perfusion and permeability from dynamic contrast-enhanced MRI in normal and pathological vertebral bone marrow. Magn Reson Med 64(1):115–124

Biffar A, Schmidt GP et al (2011) Quantitative analysis of vertebral bone marrow perfusion using dynamic contrast-enhanced MRI: initial results in osteoporotic patients with acute vertebral fracture. J Magn Reson Imaging 33(3):676–683

Bluemke DA, Petri M et al (1995) Femoral head perfusion and composition: MR imaging and spectroscopic evaluation of patients with systemic lupus erythematosus and at risk for avascular necrosis. Radiology 197(2):433–438

Brasch RC, Weinmann HJ et al (1984) Contrast-enhanced NMR imaging: animal studies using gadolinium-DTPA complex. Am J Roentgenol 142(3):625–630

Bredella MA, Essary B et al (2008) Use of FDG-PET in differentiating benign from malignant compression fractures. Skelet Radiol 37(5):405–413

Brix G, Kiessling F et al (2004) Microcirculation and microvasculature in breast tumors: pharmacokinetic analysis of dynamic MR image series. Magn Reson Med 52(2): 420–429

Brown DB, Gilula LA et al (2004) Treatment of chronic symptomatic vertebral compression fractures with percutaneous vertebroplasty. Am J Roentgenol 182(2):319–322

Buchbinder R, Kallmes DF (2010) Vertebroplasty: when randomized placebo-controlled trial results clash with common belief. Spine J (Official journal of the North American Spine Society) 10(3):241–243

Buchbinder R, Osborne RH et al (2009) A randomized trial of vertebroplasty for painful osteoporotic vertebral fractures. N Engl J Med 361(6):557–568

Buckley DL, Roberts C et al (2004) Prostate cancer: evaluation of vascular characteristics with dynamic contrast-enhanced T1-weighted MR imaging—initial experience. Radiology 233(3):709–715

Burge R, Puleo E et al (2002) Inpatient hospital and post-acute care for vertebral fractures in women. Value Health (Journal of the International Society for Pharmacoeconomics and Outcomes Research) 5(4):301–311

Castillo M, Arbelaez A et al (2000) Diffusion-weighted MR imaging offers no advantage over routine noncontrast MR imaging in the detection of vertebral metastases. Am J Neuroradiol 21(5):948–953

Chan JH, Peh WC et al (2002) Acute vertebral body compression fractures: discrimination between benign and malignant causes using apparent diffusion coefficients. Br J Radiol 75(891):207–214

Chen WT, Shih TT et al (2001) Vertebral bone marrow perfusion evaluated with dynamic contrast-enhanced MR imaging: significance of aging and sex. Radiology 220(1): 213–218

Chen WT, Shih TT et al (2002) Blood perfusion of vertebral lesions evaluated with gadolinium-enhanced dynamic MRI: in comparison with compression fracture and metastasis. J Magn Reson Imaging 15(3):308–314

Constans JP, de Divitiis E et al (1983) Spinal metastases with neurological manifestations: review of 600 cases. J Neurosurg 59(1):111–118

Cuenod CA, Laredo JD et al (1996) Acute vertebral collapse due to osteoporosis or malignancy: appearance on unenhanced and gadolinium-enhanced MR images. Radiology 199(2):541–549

Cummings SR, San Martin J et al (2009) Denosumab for prevention of fractures in postmenopausal women with osteoporosis. N Engl J Med 361(8):756–765

Cummings SR, Ensrud K et al (2010) Lasofoxifene in postmenopausal women with osteoporosis. N Engl J Med 362(8):686–696

Dietrich O, Biffar A et al (2009) Diffusion-weighted imaging of bone marrow. Semin Musculoskelet Radiol 13(2):134–144

Dusdal K, Grundmanis J et al (2011) Effects of therapeutic exercise for persons with osteoporotic vertebral fractures: a systematic review. Osteoporos Int (Journal established as result of cooperation between the European Foundation for Osteoporosis and the National Osteoporosis Foundation of the USA) 22(3):755–769

Eastell R (2007) Breast cancer and the risk of osteoporotic fracture: a paradox. J Clin Endocrinol Metab 92(1):42–43

Eito K, Waka S et al (2004) Vertebral neoplastic compression fractures: assessment by dual-phase chemical shift imaging. J Magn Reson Imaging 20(6):1020–1024

Erlemann R, Reiser M et al (1988) Time-dependent changes in signal intensity in neoplastic and inflammatory lesions of the musculoskeletal system following intravenous administration of Gd-DTPA. Der Radiologe 28(6):269–276

Erly WK, Oh ES et al (2006) The utility of in-phase/opposed-phase imaging in differentiating malignancy from acute benign compression fractures of the spine. Am J Neuroradiol 27(6):1183–1188

Fornasier VL, Czitrom AA (1978) Collapsed vertebrae: a review of 659 autopsies. Clin Orthop Relat Res 131:261–265

Frager D, Elkin C et al (1988) Subacute osteoporotic compression fracture: misleading magnetic resonance appearance. Skelet Radiol 17(2):123–126

Gagnerie F, Taillan B et al (1987) Intravertebral vacuum phenomenon in multiple myeloma. Clin Rheumatol 6(4): 597–599

Gaitanis IN, Carandang G et al (2005) Restoring geometric and loading alignment of the thoracic spine with a vertebral compression fracture: effects of balloon (bone tamp) inflation and spinal extension. Spine J 5(1):45–54

Genant HK, Wu CY et al (1993) Vertebral fracture assessment using a semiquantitative technique. J Bone Miner Res 8(9): 1137–1148

Gill JB, Kuper M et al (2007) Comparing pain reduction following kyphoplasty and vertebroplasty for osteoporotic vertebral compression fractures. Pain Physician 10(4):583–590

Golimbu C, Firooznia H et al (1986) The intravertebral vacuum sign. Spine (Phila Pa 1976) 11(10):1040–1043

Griffith JF, Yeung DK et al (2005) Vertebral bone mineral density, marrow perfusion, and fat content in healthy men and men with osteoporosis: dynamic contrast-enhanced MR imaging and MR spectroscopy. Radiology 236(3): 945–951

Guhlmann A, Brecht-Krauss D et al (1998a) Chronic osteomyelitis: detection with FDG PET and correlation with histopathologic findings. Radiology 206(3):749–754

Guhlmann A, Brecht-Krauss D et al (1998b) Fluorine-18-FDG PET and technetium-99 m antigranulocyte antibody scintigraphy in chronic osteomyelitis. J Nucl Med 39(12): 2145–2152

Hacklander T, Scharwachter C et al (2006) Value of diffusion-weighted imaging for diagnosing vertebral metastases due to prostate cancer in comparison to other primary tumors. RoFo: Fortschritte auf dem Gebiete der Rontgenstrahlen und der Nuklearmedizin 178(4):416–424

Harrington KD (1986) Metastatic disease of the spine. J Bone Joint Surg Am 68(7):1110–1115

Hasegawa K, Homma T et al (1998) Vertebral pseudarthrosis in the osteoporotic spine. Spine (Phila Pa 1976) 23(20): 2201–2206

Herneth AM, Friedrich K et al (2005) Diffusion weighted imaging of bone marrow pathologies. Eur J Radiol 55(1): 74–83

Hoh CK, Schiepers C et al (1997) PET in oncology: will it replace the other modalities? Semin Nucl Med 27(2): 94–106

Ishiyama M, Fuwa S et al (2010) Pedicle involvement on MR Imaging is common in osteoporotic compression fractures. Am J Neuroradiol 31(4):668–673

Jaquez JA (1985) Compartmental analysis in biology and medicine. The university of Michigan Press, Ann Arbor

Jung HS, Jee WH et al (2003) Discrimination of metastatic from acute osteoporotic compression spinal fractures with MR imaging. Radiographics 23(1):179–187

Kallmes DF, Comstock BA et al (2009) A randomized trial of vertebroplasty for osteoporotic spinal fractures. N Engl J Med 361(6):569–579

Kaplan PA, Orton DF et al (1987) Osteoporosis with vertebral compression fractures, retropulsed fragments, and neurologic compromise. Radiology 165(2):533–535

Karchevsky M, Babb JS et al (2008) Can diffusion-weighted imaging be used to differentiate benign from pathologic fractures? a meta-analysis. Skelet Radiol 37(9):791–795

Kato K, Aoki J et al (2003) Utility of FDG-PET in differential diagnosis of benign and malignant fractures in acute to subacute phase. Ann Nucl Med 17(1):41–46

Kondo KL (2008) Osteoporotic vertebral compression fractures and vertebral augmentation. Sem Intervent Radiol 25(4): 413–424

Kubota T, Yamada K et al (2005) High-resolution imaging of the spine using multidetector-row computed tomography: differentiation between benign and malignant vertebral compression fractures. J Comput Assist Tomogr 29(5):712–719

Kumpan W, Salomonowitz E et al (1986) The intravertebral vacuum phenomenon. Skelet Radiol 15(6):444–447

Lafforgue P, Chagnaud C et al (1997) The intravertebral vacuum phenomenon ("vertebral osteonecrosis"): migration of intradiscal gas in a fractured vertebral body. Spine (Phila Pa 1976) 22(16):1885–1891

Laredo JD, Lakhdari K et al (1995) Acute vertebral collapse: CT findings in benign and malignant nontraumatic cases. Radiology 194(1):41–48

Le Bihan DJ (1998) Differentiation of benign versus pathologic compression fractures with diffusion-weighted MR imaging: a closer step toward the "holy grail" of tissue characterization? Radiology 207(2):305–307

Lecouvet FE, Vande Berg BC et al (1997) Vertebral compression fractures in multiple myeloma: part I: distribution and appearance at MR imaging. Radiology 204(1):195–199

Leeds NE, Kumar AJ et al (2000) Magnetic resonance imaging of benign spinal lesions simulating metastasis: role of diffusion-weighted imaging. Top Magn Reson Imaging 11(4):224–234

Lieberman IH, Dudeney S et al (2001) Initial outcome and efficacy of "kyphoplasty" in the treatment of painful osteoporotic vertebral compression fractures. Spine 26(14):1631–1638

Link TM, Guglielmi G et al (2005) Radiologic assessment of osteoporotic vertebral fractures: diagnostic and prognostic implications. Eur Radiol 15(8):1521–1532

Linn J, Birkenmaier C et al (2009) The intravertebral cleft in acute osteoporotic fractures: fluid in magnetic resonance imaging-vacuum in computed tomography? Spine 34(2):E88–E93

Lips P, Bouillon R et al (2010) Reducing fracture risk with calcium and vitamin D. Clin Endocrinol 73(3):277–285
MacLean C, Newberry S et al (2008) Systematic review: comparative effectiveness of treatments to prevent fractures in men and women with low bone density or osteoporosis. Ann Intern Med 148(3):197–213
Malghem J, Maldague B et al (1993) Intravertebral vacuum cleft: changes in content after supine positioning. Radiology 187(2):483–487
Masala S, Schillaci O et al (2005) MRI and bone scan imaging in the preoperative evaluation of painful vertebral fractures treated with vertebroplasty and kyphoplasty. In Vivo 19(6):1055–1060
Melton LJ (1997) Epidemiology of spinal osteoporosis. Spine (Phila Pa 1976) 22(24 Suppl):2S–11S
Metser U, Lerman H et al (2004) Malignant involvement of the spine: assessment by 18F-FDG PET/CT. J Nucl Med 45(2): 279–284
Meunier PJ, Roux C et al (2004) The effects of strontium ranelate on the risk of vertebral fracture in women with postmenopausal osteoporosis. N Engl J Med 350(5):459–468
Montazel JL, Divine M et al (2003) Normal spinal bone marrow in adults: dynamic gadolinium-enhanced MR imaging. Radiology 229(3):703–709
Moulopoulos LA, Yoshimitsu K et al (1996) MR prediction of benign and malignant vertebral compression fractures. J Magn Reson Imaging 6(4):667–674
Moulopoulos LA, Dimopoulos MA et al (1999) Bone lesions with soft-tissue mass: magnetic resonance imaging diagnosis of lymphomatous involvement of the bone marrow versus multiple myeloma and bone metastases. Leuk Lymph 34(1–2):179–184
O'Neill TW, Felsenberg D et al (1996) The prevalence of vertebral deformity in European men and women: the European vertebral osteoporosis study. J Bone Miner Res (Official journal of the American Society for Bone and Mineral Research) 11(7):1010–1018
Oztekin O, Ozan E et al (2009) SSH-EPI diffusion-weighted MR imaging of the spine with low b values: is it useful in differentiating malignant metastatic tumor infiltration from benign fracture edema? Skelet Radiol 38(7):651–658
Palmer WE, Rosenthal DI et al (1995) Quantification of inflammation in the wrist with gadolinium-enhanced MR imaging and PET with 2-[F-18]-fluoro-2-deoxy-D-glucose. Radiology 196(3):647–655
Park SW, Lee JH et al (2004) Single shot fast spin echo diffusion-weighted MR imaging of the spine; is it useful in differentiating malignant metastatic tumor infiltration from benign fracture edema? Clin Imaging 28(2):102–108
Pfeifer M, Begerow B et al (2004) Effects of a new spinal orthosis on posture, trunk strength, and quality of life in women with postmenopausal osteoporosis: a randomized trial. Am J Phys Med Rehabil / Assoc Acad Physiatrists 83(3):177–186
Prather H, Watson JO et al (2007) Nonoperative management of osteoporotic vertebral compression fractures. Injury 38(Suppl 3):S40–S48
Ragab Y, Emad Y et al (2009) Differentiation of osteoporotic and neoplastic vertebral fractures by chemical shift in-phase and out-of phase MR imaging. Eur J Radiol 72(1):125–133
Resnick D, Niwayama G et al (1981) Spinal vacuum phenomena: anatomical study and review. Radiology 139(2):341–348
Rupp RE, Ebraheim NA et al (1995) Magnetic resonance imaging differentiation of compression spine fractures or vertebral lesions caused by osteoporosis or tumor. Spine (Phila Pa 1976) 20(23):2499–2503 discussion 2504
Sartoris DJ, Clopton P et al (1986) Vertebral-body collapse in focal and diffuse disease: patterns of pathologic processes. Radiology 160(2):479–483
Sattari A, Quillard A et al (2008) Benign nontraumatic osteolytic vertebral collapse simulating malignancy. Eur Radiol 18(3): 631–638
Savvopoulou V, Maris TG et al (2008) Differences in perfusion parameters between upper and lower lumbar vertebral segments with dynamic contrast-enhanced MRI (DCE MRI). Eur Radiol 18(9):1876–1883
Schmitz A, Risse JH et al (2002) FDG-PET findings of vertebral compression fractures in osteoporosis: preliminary results. Osteoporos Int 13(9):755–761
Shih TT, Huang KM et al (1999) Solitary vertebral collapse: distinction between benign and malignant causes using MR patterns. J Magn Reson Imaging 9(5):635–642
Silverman SL, Christiansen C et al (2008) Efficacy of bazedoxifene in reducing new vertebral fracture risk in postmenopausal women with osteoporosis: results from a 3-year, randomized, placebo-, and active-controlled clinical trial. J Bone Miner Res (Official journal of the American Society for Bone and Mineral Research) 23(12):1923–1934
Stäbler A, Schneider P et al (1999) Intravertebral vacuum phenomenon following fractures: CT study on frequency and etiology. J Comput Assist Tomogr 23(6):976–980
Stadhouder A, Buskens E et al (2009) Nonoperative treatment of thoracic and lumbar spine fractures: a prospective randomized study of different treatment options. J Orthop Trauma 23(8):588–594
Strauss LG, Conti PS (1991) The applications of PET in clinical oncology. J Nucl Med 32(4):623–648 discussion 649–650
Sugimoto T, Tanigawa N et al (2008) Diffusion-weighted imaging for predicting new compression fractures following percutaneous vertebroplasty. Acta Radiol 49(4):419–426
Tan SB, Kozak JA et al (1991) The limitations of magnetic resonance imaging in the diagnosis of pathologic vertebral fractures. Spine (Phila Pa 1976) 16(8):919–923
Tancioni F, Lorenzetti MA et al (2011) Percutaneous vertebral augmentation in metastatic disease: state of the art. J Support Oncol 9(1):4–10
Tang G, Liu Y et al (2007) Optimization of b value in diffusion-weighted MRI for the differential diagnosis of benign and malignant vertebral fractures. Skelet Radiol 36(11): 1035–1041
Tanigawa N, Komemushi A et al (2006) Percutaneous vertebroplasty: relationship between vertebral body bone marrow edema pattern on MR images and initial clinical response. Radiology 239(1):195–200
Taoka T, Mayr NA et al (2001) Factors influencing visualization of vertebral metastases on MR imaging versus bone scintigraphy. Am J Roentgenol 176(6):1525–1530
Thariat J, Toubeau M et al (2004) Sensitivity and specificity of thallium-201 scintigraphy for the diagnosis of malignant vertebral fractures. Eur J Radiol 51(3):274–278
Thurnher MM, Bammer R (2006) Diffusion-weighted magnetic resonance imaging of the spine and spinal cord. Semin Roentgenol 41(4):294–311

Tofts PS, Brix G et al (1999) Estimating kinetic parameters from dynamic contrast-enhanced T(1)-weighted MRI of a diffusable tracer: standardized quantities and symbols. J Mag Res Imaging 10(3):223–232

Tokuda O, Hayashi N et al (2005) Dynamic contrast-enhanced perfusion MR imaging of diseased vertebrae: analysis of three parameters and the distribution of the time-intensity curve patterns. Skelet Radiol 34(10):632–638

Tokuda O, Harada Y et al (2011) Malignant versus benign vertebral compression fractures: can we use bone SPECT as a substitute for MR imaging? Nucl Med Commun 32(3):192–198

Uetani M, Hashmi R et al (2004) Malignant and benign compression fractures: differentiation and diagnostic pitfalls on MRI. Clin Radiol 59(2):124–131

Uppin AA, Hirsch JA et al (2003) Occurrence of new vertebral body fracture after percutaneous vertebroplasty in patients with osteoporosis. Radiology 226(1):119–124

Vaccaro AR, Shah SH et al (1999) MRI description of vertebral osteomyelitis, neoplasm, and compression fracture. Orthopedics 22(1):67–73 quiz 74-65

van der Klift M, de Laet CE et al (2004) Risk factors for incident vertebral fractures in men and women: the Rotterdam study. J Bone Miner Res (Official journal of the American Society for Bone and Mineral Research) 19(7):1172–1180

Vande Berg BC, Malghem J et al (1998) Magnetic resonance imaging of the normal bone marrow. Skelet Radiol 27(9): 471–483

Vogler JB III, Murphy WA (1988) Bone marrow imaging. Radiology 168(3):679–693

Voormolen MH, van Rooij WJ et al (2006) Pain response in the first trimester after percutaneous vertebroplasty in patients with osteoporotic vertebral compression fractures with or without bone marrow edema. Am J Neuroradiol 27(7): 1579–1585

Wasnich RD (1996) Vertebral fracture epidemiology. Bone 18(3 Suppl):179S–183S

White AP, Kwon BK et al (2006) Metastatic disease of the spine. J Am Acad Orthop Surg 14(11):587–598

Yuh WT, Zachar CK et al (1989) Vertebral compression fractures: distinction between benign and malignant causes with MR imaging. Radiology 172(1):215–218

Zajick DC Jr, Morrison WB et al (2005) Benign and malignant processes: normal values and differentiation with chemical shift MR imaging in vertebral marrow. Radiology 237(2): 590–596

Zhou XJ, Leeds NE et al (2002) Characterization of benign and metastatic vertebral compression fractures with quantitative diffusion MR imaging. Am J Neuroradiol 23(1):165–170

Part III

Benign Processes Affecting the Bone Marrow

Diseases of the Reticuloendothelial System

Robert Hemke and Mario Maas

Contents

Abstract

This chapter will illustrate the strengths and weaknesses of various imaging techniques in patients with diseases involving the reticuloendothelial system, such as in Gaucher disease (GD), mastocytosis, and histiocytosis. The focus is primarily on Magnetic Resonance Imaging of bone and the bone marrow compartment, mainly focusing on GD. The emerging role of radiology in the management of GD patients, demands radiologists to be aware of specific features and the possibilities of radiology. This chapter will give an overview of up-to-date imaging techniques, -protocols, and -features, and reviews the current literature on skeletal involvement of diseases of the reticuloendothelial system.

1 Introduction

Magnetic Resonance Imaging (MRI) is the state-of-the-art imaging modality for the evaluation of the bone marrow compartment. Within the last two decades MRI is increasingly being used for the assessment and monitoring of skeletal involvement in diseases involving the reticuloendothelial system such as Gaucher disease (GD), mastocytosis, and histiocytosis.

In GD, assessing the skeletal involvement and response to treatment is important. The main goals of imaging bone and bone marrow in GD are to estimate the disease burden, to evaluate the presence of specific skeletal complications, and to monitor response to therapy. MRI is the most sensitive technique in assessing skeletal involvement in GD, as it is the up-to-date imaging modality for the evaluation of bone

R. Hemke · M. Maas (✉)
Department of Radiology, Academic Medical Center, University of Amsterdam, Meibergdreef 9, Amsterdam, The Netherlands
e-mail: m.maas@amc.uva.nl

A. Baur-Melnyk (ed.), *Magnetic Resonance Imaging of the Bone Marrow*, Medical Radiology. Diagnostic Imaging,
DOI: 10.1007/174_2012_717,

marrow. It is extremely sensitive in the evaluation of the skeletal pathologies found in GD including acute bone infarction, infection, trauma, marrow infiltration with Gaucher cells, and avascular necrosis. In order to quantitatively analyze bone marrow involvement and response to very expensive therapies in GD, quantitative chemical shift imaging was explored. As this technique is not widely available, numerous semi-quantitative scoring systems have been developed for the evaluation of bone marrow infiltration in adult Gaucher patients, including the Bone Marrow Burden (BMB) score. The BMB scoring method is considered to be the preferred scoring system as it includes measurements of both lumbar spine and femur, key anatomical sites of Gaucher cell infiltration, and has been validated against other methods and applied in multiple studies.

2 Morbus Gaucher

2.1 Epidemiology and Clinical Background

Gaucher disease (Gaucher 1882) is an inherited autosomal recessive metabolic defect due to a deficiency in the lysosomal enzyme β-glucocerebrosidase, which is unable to degrade its substrate glucocerebroside into ceramide and glucose. Although the enzyme deficiency exists in all cells in the body, accumulation of glucocerebroside within the lysosomes occurs mainly in macrophages, called Gaucher cells. This leads to accumulation of glucocerebroside in the body, predominantly in the liver, spleen, and bone marrow.

Gaucher disease is the most common lysosomal storage disease and is broadly subdivided into neuronopathic (types 2 and 3) and non-neuronopathic (type 1) phenotypes. GD type 1 is the most common variant (95 % of all cases) with an estimated prevalence of 1:75,000 births worldwide, but is more prevalent in individuals of Ashkenazi Jewish descent (Meikle et al. 1999; Poorthuis et al. 1999; Pinto et al. 2004; Guggenbuhl et al. 2008; Fuller et al. 2006).

The availability of enzyme replacement therapy in the 1990s made the management of GD more effective in terms of hepatosplenomegaly, cytopenia, and general wellbeing (Elstein et al. 1998; Hollak et al. 1995). However, the skeletal response to enzyme replacement therapy is considered slower and sometimes lacking (Grabowski et al. 1998; de Fost et al. 2008). Skeletal manifestations are the most painful and debilitating components of GD and have a negative impact on the patient's quality of life (Sims et al. 2008; Weinreb et al. 2007; Deegan et al. 2011). Therefore, assessing skeletal complications and their response to treatment is of great importance. The main goals of imaging bone and bone marrow in GD are to estimate the disease burden, to evaluate the presence of specific skeletal complications, and to track response to therapy. A variety of techniques has been used including plain radiography, CT, MRI, and radionuclide imaging tools.

2.2 Skeletal Involvement

The skeletal complications of GD type 1 are most painful and disabling with the long bones and vertebrae being most commonly affected (Charrow et al. 2004) Skeletal disease is a major complication in GD, afflicting 70–100 % of the patients (Poll et al. 2001; Pastores and Meere 2005). Three basic types of pathophysiological processes are deemed most important in these skeletal manifestations: (1). infarction of bone and bone marrow, (2). focal replacement of normal bone marrow by infiltration of Gaucher cells, and (3). osteopenia that can be focal or diffuse (Guggenbuhl et al. 2008; Rosenthal et al. 1986; Grabowski et al. 2004). All this concerns bone marrow infiltration, and therefore the evaluation of this compartment with a bone marrow evaluation technique is warranted. Since GD is a compartimental disease, the bone marrow compartment needs its own assessment. To stress this point: using assessment of organ size cannot adequately assess the bone marrow compartment (vom Dahl et al. 2006).

2.3 Magnetic Resonance Imaging

2.3.1 MRI

MRI is the prefered best technique in the assessment of skeletal involvement in GD, since it is the most sensitive imaging modality for the evaluation of bone marrow (Pastores and Meere 2005; Vogler and Murphy 1988). It is extremely sensitive in the evaluation of the skeletal pathologies found in GD including acute bone infarction, infection, trauma,

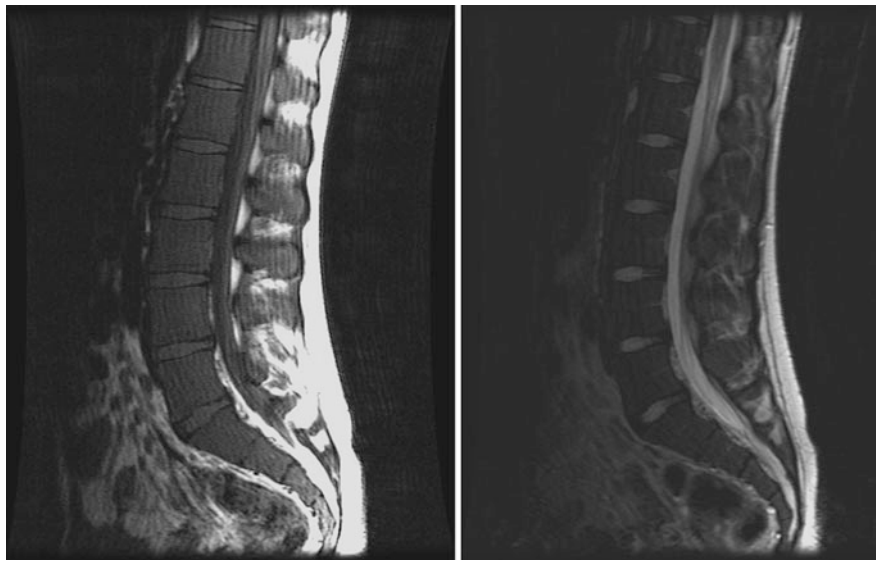

Fig. 1 Adult type I GD patient. Diffuse very low signal on T1 and T2 weighted images. Typical appearance of severe infiltration of axial marrow

marrow infiltration with Gaucher cells, and avascular necrosis (Rosenthal et al. 1986; Hermann et al. 1993; Farahati et al. 1996; Maas et al. 2002a, b).

In long bones of adults, the fatty yellow bone marrow is the predominant contributor to the hyperintense signal seen on T1-weighted images and an intermediate to hyperintense signal seen on T2- and T2*-weighted images (Vogler and Murphy 1988; Hermann et al. 1993; Farahati et al. 1996; Maas et al. 2002a, b; Dooms et al. 1985). On fat-saturated images, yellow bone marrow appears hypointense. As compared with normal yellow bone marrow, red cellular marrow can be seen as hypointense signal intensity on T1-weighted images and on fast spin-echo T2-weighted images hyperintense signal intensities can be seen for both fat and water (Vogler and Murphy 1988; Steiner et al. 1990).

A variety of MRI protocols, all of which include T1-weighted sequences, has been used for imaging bone marrow changes in GD (Poll et al. 2001; Terk et al. 2000). In GD, the normal bone marrow is replaced by Gaucher cells, in which a centrifugal spread, meaning that axial bone marrow is more often abnormally infiltrated than peripheral bone marrow, is recognized. Imaging protocols thus need to contain axial marrow as well as peripheral marrow compartment.

Concerning the MRI appearance, GD shows a typical signal intensity change, with drastically lowered signal intensity both on T1-, T2-, and T2*-weighted images (Rosenthal et al. 1986; Hermann et al. 1993; Terk et al. 2000) (Fig. 1).

This lowering of signal intensity can be mild, marked, or severe, in which the aspect of axial and peripheral marrow can be different. In some GD patients, structural bone damage is seen, preferably in the peripheral skeleton, with a hypointense signal on T1-weighted images and a mixed appearance of hypointense and hyperintense signal on T2-weighted images. These areas of low signal on T1-weighted images and high signal on T2-weighted images suggest an active bone complication, yet these areas remain unchanged for many years, and show no correlation with clinical complaints (Fig. 2). This is an important issue to address, since MR imaging protocols in MSK and Marrow radiology very often consists of fat-saturated T2-weighted or STIR sequences, in which these areas of high signal will be depicted instantly and interpreted as active disease/complication by the reading radiologist and intensification of treatment may erroneously be advised in the reading report.

Both homogeneous and heterogeneous patterns of involvement can be detected in GD (Hermann et al. 1993). For instance, the infiltration in the axial skeleton may show absence or persistence of fat in basivertebral vein region (Fig. 3). Bone marrow involvement progress from axial to peripheral and in long bones from proximal to distal, however, the epiphysis and apophysis remain relatively unaffected except in the most severe cases (Rosenthal et al. 1986, 1992; Hermann et al. 1993). Whole-body MRI is feasible as means of assessing the entire skeletal

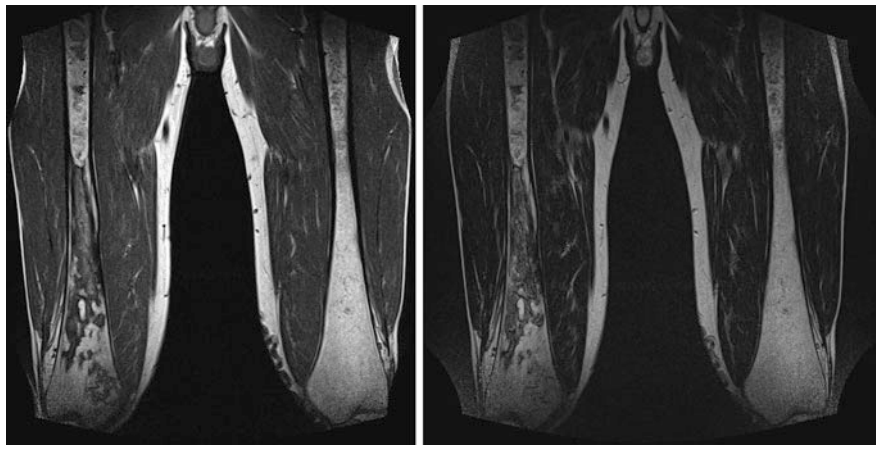

Fig. 2 T1 and T2 weighted images of an adult type I GD patient. Pathological features in both femurs are seen, most likely caused by earlier ischemic events. These features will not respond on therapy, are irreversible. BMB scoring is therefore limited

system and could be a valuable diagnostic and monitoring tool in the management of patients with type 1 GD (Poll et al. 2011), but the most practical approach for MRI of Gaucher bone disease is to evaluate the lumbar spine and/or the lower extremity with conventional T1- and T2-or T2*-weighted spin-echo sequences. However, a fat-suppressed sequence, for example STIR or fat-suppressed T2-/T2*-weighted images, might provide additional information regarding the evaluation of complications (Maas et al. 2002, 2003). In order to differentiate the described chronic abnormalities from an active or complicated bone marrow process such as acute bone crisis, occult fracture, infection, or bone infarction, close correlation with clinical status is absolutely mandatory.

Due to the complex situation of the bone marrow changes in GD, it is recommended that MRI studies take place at centers with experienced radiologists both in acquisition as well as interpretation (Rosenthal et al. 1986; Hermann et al. 1993; Roca et al. 2007).

Although conventional MRI evaluation is sensitive in the evaluation of the extent of disease in GD patients, a quantitative measurement tool is lacking. An objective quantification of bone marrow changes in GD is important in the assessment of disease status and response to therapy.

2.3.2 Quantitative Chemical Shift Imaging

Since very expensive enzyme supplementation therapy for the treatment of GD has become available, adequate monitoring of response to treatment is important in order to facilitate dose adjustments (Hollak et al. 1995; Barton et al. 1992; Rosenthal et al. 1995). In order to quantitatively analyze bone marrow involvement and response to therapy in GD, quantitative chemical shift imaging (QCSI) was explored by a modification of a technique introduced by Dixon (Dixon 1984; Johnson et al. 1992). The MR-signal for a normal MR image originates from two types of hydrogen nuclei: nuclei in water molecules and nuclei in fat molecules (Dixon 1984). These two types of nuclei have a slightly different precession frequency due to the so-called "chemical shift" effect. The Dixon method uses this difference in frequency to separate the signals from water and fat, which makes it possible to quantify the fat signal fraction, hence, the Dixon quantitative chemical shift imaging (Dixon QCSI) (Dixon 1984). This technique was evaluated as early as 1992 in differentiating various hematological bone marrow disorders (Rosen et al. 1988). QCSI was evaluated in healthy volunteers, patients with leukemia, or aplastic anemia on a 0.6 T magnet. It was shown that the fat fraction, measured by this QCSI technique, was the single best discriminator between the groups. The same research group explored the use of this technique to quantify longitudinal changes in bone marrow that occur during induction of chemotherapy in patients with acute leukemia (Gerard et al. 1992). Results were correlated with bone marrow biopsy results. QCSI data showed sequential increase in fat fractions among responding patients, consistent with biopsy-confirmed clinical remission. It was concluded that QCSI proved useful in assessing treatment response in acute leukemia during early bone marrow regeneration and later in ascertaining

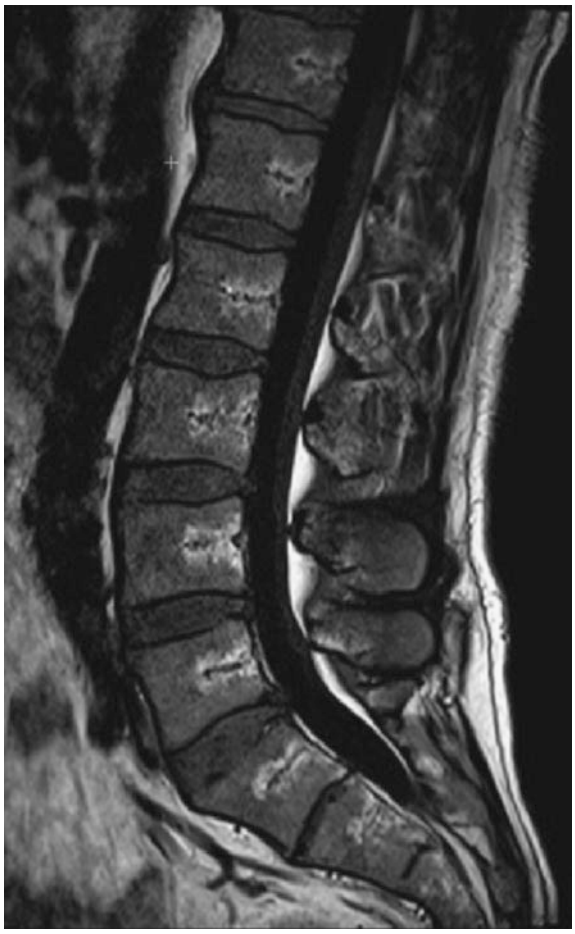

Fig. 3 Sagittal T1 weighted images of an adult type I GD patient. Mark the sparing of the fat surrounding the basivertebral veins in the vertebral bodies. Compare with Fig. 1

remission or relapse. Furthermore, an additional described benefit of QCSI was the ability to sample a large portion of marrow.

The same research group tested the QCSI technique in vertebral bone marrow patients with GD (Johnson et al. 1992). The measured fat fractions were correlated with quantitative analysis of marrow triglycerides and glucocerebrosides. An MR Spectroscopy performed in these surgical marrow specimens showed a single fat and water peak, thus validating the use of QCSI. Glucocerebroside concentrations were higher in bone marrow of GD patients and inversely correlated with triglyceride concentrations. It was concluded that QCSI is a sensitive, noninvasive technique for evaluating bone marrow infiltration in GD, showing great promise as a noninvasive method to monitor bone marrow response to treatment. In order to validate bone marrow response, quantitative lipid profiles of bone marrow specimens obtained from normal individuals and patients with Gaucher's disease were obtained and analyzed by QCSI (Miller et al. 1996). In normal marrow, triglycerides were by far the most abundant lipid (278 ± 70 mg/gm wet weight); the concentration of glucocerebroside in normal marrow was 0.061 ± 0.06 mg/gm wet weight. Gaucher marrow had dramatically lower triglyceride levels of 82 % (51 ± 53 mg/gm wet weight) and as expected marked elevation of glucocerebroside (7.1 ± 3.4 mg/gm wet weight) (Akkerman and Maas 1995). It was concluded that these data support a model of bone marrow alteration in GD in which triglyceride-rich adipocytes are progressively replaced by Gaucher cells, leading to an overall reduction in total lipid content. This phenomenon provides an explanation for the changes found in QCSI measurements in Gaucher patients (Miller et al. 1996).

In the Academic Medical Center in Amsterdam, this QCSI technique has been explored in greater detail (Akkerman and Maas 1995; Hollak et al. 2001; Maas et al. 2001). Important issues that were addressed were the reproducibility of the protocol and the normal mean fat fraction within a healthy adult population (Maas et al. 2001). The measured mean value in the lumbar spine in the healthy population was 0.37 (SD 0.08). The SD is due to repeating measurement, slice positioning and contour drawing were very small. It was concluded that that reproducibility was excellent.

The important use of this technique is the ability to detect response of the bone marrow compartment to enzyme replacement therapy. It is now a standard modality at the Academic Medical Center in Amsterdam for the assessment of BMB, and all patients receiving treatment are evaluated annually (Fig. 4). The limitations of QCSI are that the technology is not widely available, it does not use a standard MRI sequence (although the sequences are easy to implement), and a dedicated physicist and radiologist are needed to gain reliable results. Therefore, semi-quantitative scoring systems are developed on several sites (Poll et al. 2001; Rosenthal et al. 1986; Hermann et al. 1993; Terk et al. 2000; Maas et al. 2003; Cremin et al. 1990; Vlieger et al. 2002).

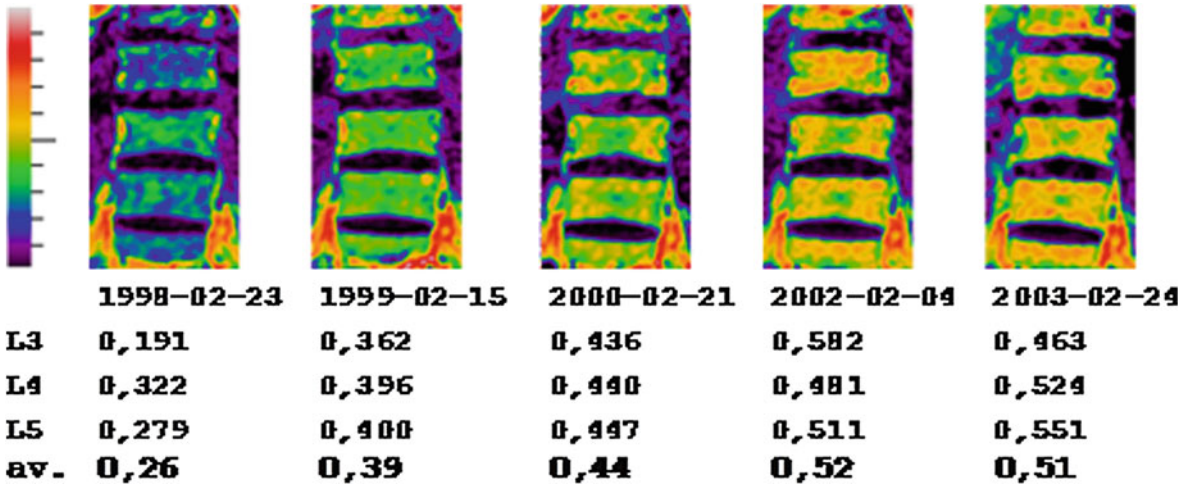

Fig. 4 Color coded display of the fat fraction measured annually in an adult type I GD patient

2.3.3 Semi-Quantitative MRI Methods

Numerous semi-quantitative scoring systems have been developed for the evaluation of bone marrow infiltration in adult Gaucher patients, including the Rosenthal scoring system, the Düsseldorf Gaucher score, the Terk classification, the vertebra disc ratio (VDR), and the BMB score (vom Dahl et al. 2006).

2.3.3.1 Rosenthal Scoring System

A semi-quantitative staging system was developed by Rosenthal et al. (1986, 1995), in which 11 sites of Gaucher cell infiltration in the lower extremities are scored in coronal view. These sites are numbered based on centrifugal disease spread, with the epiphysis and apophysis affected in more severe disease. The score is the highest numbered site at which MRI demonstrates involvement. This scoring system demonstrated improvement in bone marrow during enzyme replacement therapy, but was less sensitive than other measures that assess lumbar spine bone marrow (Rosenthal et al. 1995).

2.3.3.2 Düsseldorf Gaucher Score

The Düsseldorf 0–8 point scoring system is similar to the Rosenthal system but is based on eight anatomical sites in the lower extremities. Sites of altered marrow (based on MRI) are given a score and the highest numbered site of involvement is taken as a measure of disease severity. The Düsseldorf system identifies homogeneous and nonhomogeneous patterns of bone marrow infiltration (Poll et al. 2001).

2.3.3.3 Terk Classification

The Terk classification system consists of four groups based on the appearance of T1- and T2*-weighted MRI signals with or without avascular necrosis (eight classifications in total). A significant correlation has been demonstrated between bone marrow response (from the T1-weighted image) and reduction in the volume of the liver ($p < 0.005$) or spleen ($p < 0.005$) (Terk et al. 2000).

2.3.3.4 Vertebra Disc Ratio

The VDR measures pathological changes in the lumbar spine. It is defined as the ratio of the average T1-weighted MRI signal intensity of the L3 vertebra and a healthy L3/L4 disc (Vlieger et al. 2002). A normal VDR was measured as 1.90 ± 0.30; the VDR of an untreated Gaucher was 1.29 ± 0.31; and a long-term treated Gaucher patient was 1.70 ± 0.33. VDR measurements correlate with fat fraction as an internal control standard measured by QCSI—the most sensitive measure of marrow fat content. Currently, the VDR technique is not widely available. Different time of repetition and time of echo intervals could influence the appearance of signal intensities. Red marrow content could also interfere with signal intensities.

2.3.3.5 Spanish S-MRI Score

This method evaluates bone marrow infiltration with MRI using low field imaging. The new item of this method is the inclusion of the pelvic marrow next

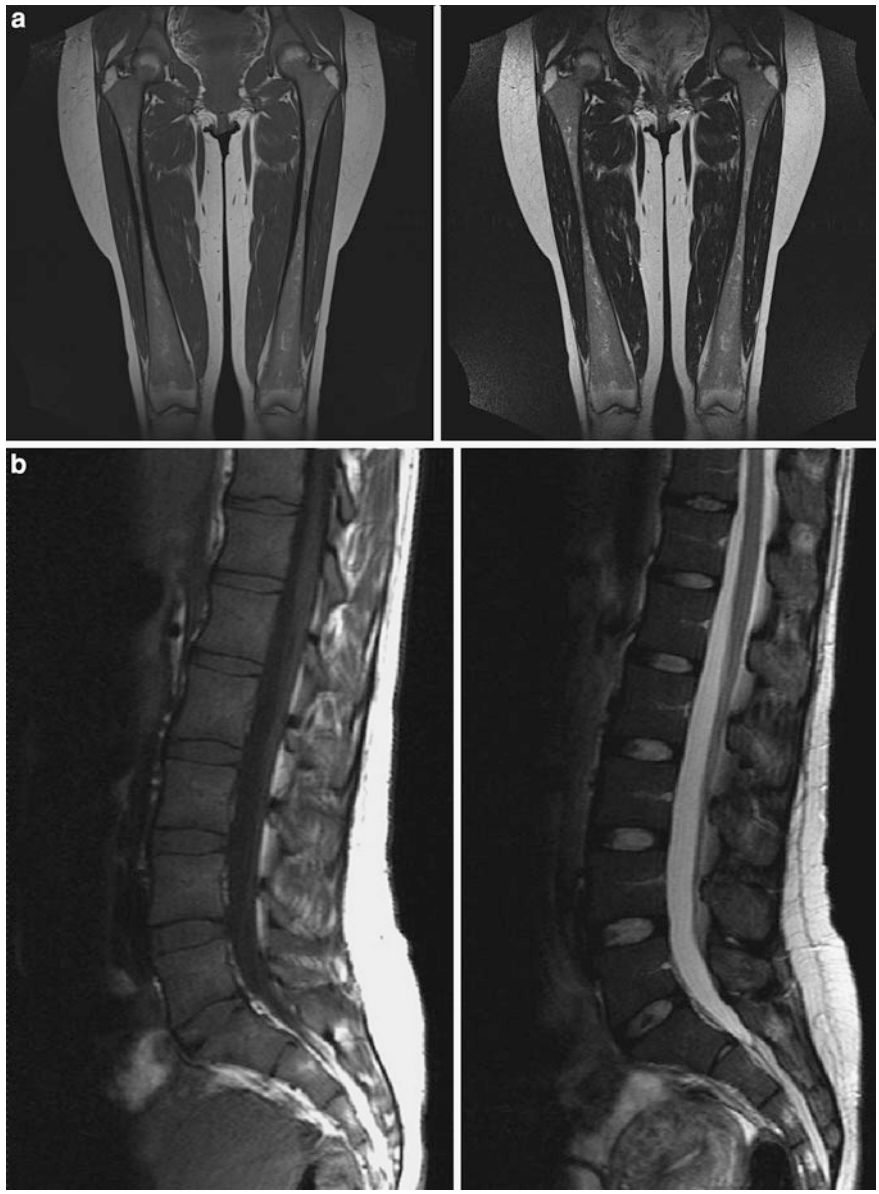

Fig. 5 **a** Coronal images of an adult type I GD patient. Mark the low signal intensity on both sequences in the diaphysis of both femurs. BMB score = 5 (hypointense on T1, hypointense on T2, located in diaphysis). **b** Sagittal T1 and T2 weighted images of the same adult type 1 GD patient. BMB = 6 (isointense on T1, hypointense on T2, diffuse, absence of fat in basivertebral vein region). Combined BMB = 11

to lumbar spine and femur MRI. In 46 patients (85.2 %), bone involvement was observed. A total of 39 (72.3 %) had their spine affected, 35 (64.8 %) pelvis, and 33 (61.2 %) femora. Correlation analysis between S-MRI and the later mentioned Bone Marrow Burden score (BMB) was ($r2 = 0.675$; $p = 0.0001$). This technique is used in 0.5 T MRI and in the Spanish population only. No comparison with other centers or populations is done. Also, no correlation with state-of-the-art QCSI has been done.

2.3.3.6 Bone Marrow Burden Score

This method, developed in the Academic Medical Center in Amsterdam, takes into account the progressive patterns of bone marrow infiltration in the lumbar spine (axial marrow) and the femur. A scoring system assigns up to 8 points for femoral involvement and 8 points for lumbar spine involvement to give a maximum score of 16 points. An example is shown in Fig. 5. This method has been tested for inter- and intra-observer variability (demonstrating high inter-observer reliability), correlates

Table 1 Evaluation of BMB in the Femora

A: *MR imaging signal intensity*		
Relaxation time	Signal intensity[a]	BMB score
T1	Slightly hyperintense or isointense	0
T1	Slightly hypointense	1
T1	Hypointense	2
T2	Hyperintense	2
T2	Slightly hyperintense	1
T2	Isointense	0
T2	Slightly hypointense	1
T2	Hypointense	2
T2	Mixed type	3
B: *Sites of involvement*		
Bone site involved		BMB score
Diaphysis		1
Proximal epiphysis/apophysis		2
Distal epiphysis		3

Note A higher BMB score signifies more severe bone marrow involvement
[a] Determined in relation to signal intensity of nondiseased intervertebral disk

Table 2 Evaluation of BMB in the lumbar spine

A: *MR imaging signal intensity*		
Relaxation time	Signal intensity[a]	BMB score
T1	Slightly hyperintense	0
T1	Isointense	1
T1	Slightly hypointense	2
T1	Hypointense	3
T2	Hyperintense	2
T2	Slightly hyperintense	1
T2	Isointense	0
T2	Slightly hypointense	1
T2	Hypointense	2
B: *Infiltration pattern*		
Pattern		BMB score
Patchy		1
Diffuse		2
Absence of fat in basivertebral vein region		1

Note A higher BMB score signifies more severe bone marrow involvement
[a] Determined in relation to signal intensity of nondiseased intervertebral disk

significantly with QCSI, and correlates with bone complications (Maas et al. 2003). The technique has the advantage that it provides a sensitive means of monitoring bone marrow changes in response to therapy. It can be carried out retrospectively and enables central reading of MRIs from various centers. Its use outside the Dutch patient group has been published in an American cohort as well as an

Australian cohort (Robertson et al. 2007; DeMayo et al. 2008). Both mentioned studies slightly modified BMB scoring system, to be used when STIR or fat-saturated T2 sequences are performed instead of plain T2 weighted sequences (Tables 1, 2).

According to the GD Working Group of international experts, the BMB scoring method is preferred over the other available scoring systems as it includes measurements of both lumbar spine and femur, key anatomical sites of Gaucher cell infiltration, and has been validated against other methods, and applied in multiple studies (Robertson et al. 2007). The most recent validated disease severity scoring system for adults with type 1 GD holds BMB score as the assessor of the marrow infiltration in GD (Maas et al. 2008; Weinreb et al. 2010).

The aforementioned successful quest for a noninvasive surrogate biomarker in GD is an example of real translational radiology. One might consider this a novel specialty of radiology, metabolic radiology (Maas et al. 2011).

2.4 Alternative Marrow Imaging in Gaucher Disease

2.4.1 Plain Radiography

Although MRI is the preferred imaging technique in the assessment of disease activity and response to therapy, in many centers worldwide it is not possible to have regular bone marrow evaluation with MRI. Therefore, it is often thought that conventional plain radiography is an acceptable alternative, being widely available and relatively inexpensive. Though, its sensitivity for defining the pattern of skeletal disease is only 30–40 % (Colbert 1972). Plain radiography is therefore not useful for diagnosing GD or monitoring the response of the skeleton to therapy (Rosenthal et al. 1986; Farahati et al. 1996; Maas et al. 2002; Terk et al. 2000; Rosenthal et al. 1992). A substantial Gaucher cell burden may be present without changes apparent on conventional radiographs. However, plain radiography could be used for detecting complications such as osteoarticular and medullar bone infarction, focal lytic lesions, endosteal scalloping, Erlenmeyer flask deformity, pathological fracture, subperiosteal hemorrhage, periostal new bone formation, and generalized osteopenia (Rosenthal et al. 1992; Lanir et al. 1986).

2.4.2 Computed Tomography

In patients with GD, the main use of helical CT is to measure spleen and liver volumes (Glass et al. 1987; Charrow et al. 1998). In general, there is no role for CT in assessing bone disease. Applications for CT are generally limited to unusual circumstances, such as when conventional radiographs leave doubt, MRI is unavailable or patients are not MRI-compatible, and sectional images are desired (Maas et al. 2002).

2.4.3 Dual Energy X-ray Absorptiometry

Osteopenia is a common finding in both pediatrics and adults with GD. It can be localized or diffused and is associated with an increased risk of pathological fractures (Weinreb et al. 2004; Wenstrup et al. 2002; Poll et al. 2002). Dual energy X-ray absorptiometry (DEXA) is widely used for the quantitative assessment of bone mineral density and it has also been shown to be useful in assessing generalized osteopenia in GD, although it is insensitive to local bone mineral density changes (Maas et al. 2002). Interpretation of DEXA data is confounded in patients with avascular necrosis of the hip, vertebral collapse, or sclerosis, due to high bone mineral density values (Mikosch et al. 2008).

2.4.4 Radionuclide Imaging

A number of radionuclide tracers have been used to measure bone marrow infiltration in GD (Mikosch et al. 2008). ^{99}Tcm-sulfur colloid is taken up by normal bone marrow. In GD, reduced visualization of the tracer or abnormal patterns of tracer uptake are seen, thereby indirectly indicating areas of pathological infiltration (Hermann et al. 1986). ^{99}Tcm-sestamibi has the advantage over ^{99}Tcm-sulfur colloid in its possibility to accumulate in areas of abnormal glycolipid deposition due to Gaucher cell infiltration and is therefore a direct measure of pathology (Mariani et al. 1996, 2003). A semiquantitative scoring system has been developed which correlates with the BMB score as measured on MRI (Maas et al. 2003; Weinreb et al. 2004; Wenstrup et al. 2002). Further, radionuclide scans with ^{99}Tcm methylene-diphosphonate show osteoblastic activity, which could potentially be useful for assessing bone turnover in GD. These nuclear techniques are very sensitive, but have a lower specificity, thereby, the main disadvantage is the poor

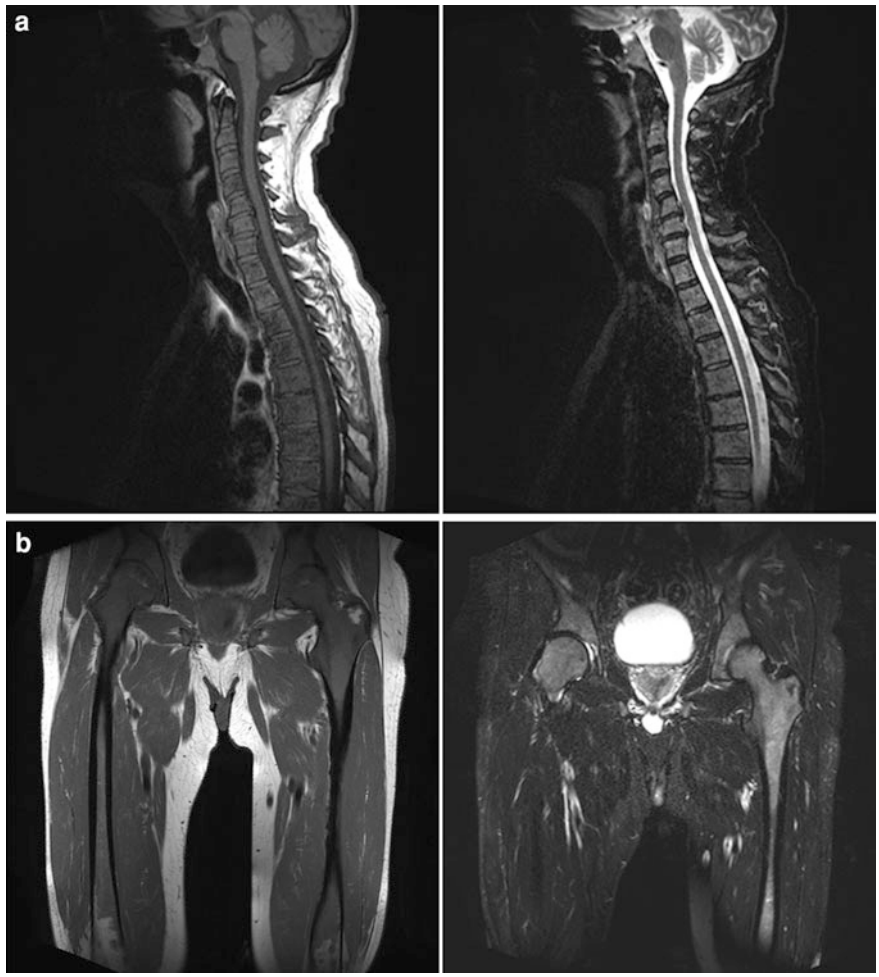

Fig. 6 **a**, **b** Diffuse infiltration of marrow in a mastocytosis patient. Mark the inhomogeneous pattern of infiltration. Courtesy A. Baur-Melnyk

spatial resolution compared with MRI and radiation dose (Rosenthal et al. 1992; Hermann et al. 1986). Therefore, MRI remains the most appropriate and recommended imaging modality for assessment of bone marrow infiltration (Weinreb et al. 2004; Wenstrup et al. 2002). Nonetheless, bone marrow scintigraphy can be useful, particularly in patients who are unable to undergo MRI. In addition, radionuclide imaging may help to distinguish between bone crisis and osteomyelitis in GD.

3 Mastocytosis

Mastocytosis is characterized by proliferation of mast cells that can infiltrate various tissues, such as skin (urticaria pigmentosa) and bone marrow.

Mastocytosis is classified in four different subtypes based on nonimaging parameters (Avila et al. 1998). Indolent Mastocytosis (IM) is most common, with the favorable prognosis. IM is subdivided into Ia (Urticaria Pigmentosa), with isolated skin involvement and Ib [Systemic mastocytosis (SM)], with skeletal pathologies. Mast cell proliferation in skeletal tissue is a well-known manifestation of SM, occurring in 79 % of patients (Roca et al. 1999). Category II is Mastocytosis with hematological disorder and III is aggressive mastocytosis with a poor prognosis. Category IV is mast cell leukemia.

In SM generally bone marrow infiltration is seen, and radiology can be helpful. Since there are nonspecific clinical signs, the diagnosis for the clinician might be challenging. Although the axial skeleton is usually involved in SM, this infiltration can be subclinical. Though, spinal infiltration can cause

specific back pain (Roca et al. 1999), also a more severe presentation can occur, such as a vertebral collapse. Whenever a pathological (non traumatic) fracture of a vertebra is seen, SM should be considered in the differential diagnosis (Arias et al. 2004; Stamm et al. 2008). Hence radiologists need to be aware of the general pattern of bone marrow involvement in SM, to consider its differential diagnosis. Earlier, radiological descriptions contained skeletal manifestations to be mostly osteosclerotic or a mixture of osteolytic and osteosclerotic lesions (Huang et al. 1987). Yet, also solely osteopenia is described to occur in mastocytosis (Grieser and Minne 1997). Thus, a vertebral collapse of an osteopenic skeleton should have SM in the radiological differential diagnosis.

The MRI features of SM are thus quite variable. There are reports that focal infiltration patterns of low signal on both T1 weighted and T2 weighted sequences are seen, resembling sclerotic metastatic disease (Metzgeroth et al. 2006). A more mosaic pattern of infiltration of the lumbar spine, with patchy intermediate signal on T1- and high signal on T2-weighted images is combined with areas of low-signal septation (both on T1- and T2-weighted sequences) has also been described (Haney et al. 1996). The low signal sclerotic septations are thought to be a response of new bone formation after trabecular destruction caused by the mast cell proliferation (Roca et al. 1999).

For scoring and reproducible assessment, three patterns of bone marrow infiltration are described in a study using a 1.5 T magnet: Normal, no infiltration (N), nonhomogeneous infiltration (NH), homogeneous infiltration (H) (Roca et al. 1999) (Fig. 6). Nonhomogeneous were subdivided into reticular pattern (considered less infiltration) (NHR), mottled pattern (more infiltration with somewhat normal marrow) (NHM), and diffuse pattern (nearly homogeneous) (NHD) (Roca et al. 1999). However, no clear correlation between histological proven amount of mast cell infiltration and MRI pattern is seen (Roca et al. 1999).

Another MR pattern is described (using 0.5 T field strength), in which abnormal marrow is either homogeneous or heterogeneous nonfatty infiltration (low signal intensity on T1-weighted images, high on fat-suppressed or STIR weighted images) or of intermediate infiltration (Avila et al. 1998). Also, in this second classification system, no correlation between MRI classification and clinical categorization is seen. Small sample size makes this difficult.

This is an important difference between SM and GD: in the latter, MRI classification and clinical correlation are established by various groups.

SM can also be differentiated from GD in clinical perspective, since bone crises have not been recognized in SM. This suggests that when infarcts or aseptic osteomyelitis are seen on MR, SM is an unlikely diagnosis and GD needs to be ruled out.

Whole-body MR imaging might be able to differentiate between aggressive SM and indolent SM. This is presented in a single center study, where the MR protocol enables evaluation of the pattern and extent of pathologic bone marrow signal in the spine and the extremities and includes other organ assessment on the presence of ascites, pathologic lymph nodes, hepatosplenomegaly, and focal organ lesions (Michaely et al. 2011).

4 Histiocytosis

Histiocytosis refers to a group of rare diseases which all share the presence of an excessive number of histiocytes. The term histiocytosis includes a number of different entities, including; Langerhans cell histiocytosis (LCH), juvenile xanthogranuloma, hemophagocytic lymphohistiocytosis, Niemann-Pick disease, sea-blue histiocytosis, acute monocytic leukemia, malignant histiocytosis, and Erdheim-Chester disease (ECD). In the following part, two of these—in which musculoskeletal imaging plays an important clinical role—will be discussed in more detail, namely LCH and ECD.

4.1 Langerhans Cell Histiocytosis

Langerhans cell histiocytosis refers to a spectrum of diseases characterized by idiopathic proliferation of histiocytes (Langerhans cells) causing local or systemic effects (Howarth et al. 1999). LCH can affect patients of any age, although it usually affects children between 1 and 15 years old, with a peak incidence in children between 5 and 10 years of age, and males being slightly more commonly affected than females (Broadbent et al. 1994).

The clinical symptoms of LCH depend on the site and extent of involvement. The disease may be

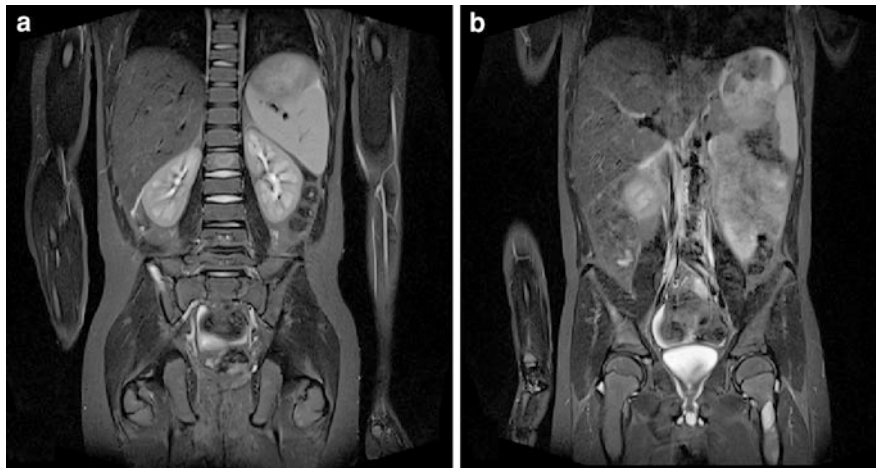

Fig. 7 Coronal STIR images of an 8-year-old boy with LCH, showing **a** diffuse ill-defined hyperintense signal intensity abnormalities in L1 and the right iliac bone, and **b** a sharply circumscribed lesion in the left femor with a high signal intensity

focal or systemic. The most common sites of involvement include the bone, lung, central nervous system, liver, thymus, skin, and lymph nodes. LCH, formerly known as histiocytosis X, encompasses three classic clinical syndromes that are considered to be clinical variations of the same disease: eosinophilic granuloma (localized benign form, isolated to bone and often monostotic), Hand–Schüller–Christian disease (classic triad of skull lesions, exophthalmos, and diabetes insipidus), and Letterer–Siwe disease (disseminated lesions involving multiple visceral organs) (Favara et al. 1997; Berry et al. 1986; Meyer et al. 1995; Azouz et al. 2005). The three entities are of unknown etiology, but appear to be histologically related. Up to 80 % of LCH lesions in children are of the eosinophilic granuloma type, and up to 90 % occur in bone (Azouz et al. 2005).

In LCH there is replacement of normal bone marrow by infiltration of Langerhans cells, eosinophils, neutrophils, and macrophages. Patients with osseous involvement present with pain, swelling, and soft tissue mass, but LCH may be underdiagnosed due to the presence of asymptomatic eosinophilic granuloma bony lesions. Lytic bone lesions in adults are often considered as more common diseases, such as fibrous dysplasia, multiple myeloma, or bone metastasis, rather than LCH. Although, differentiation of these diseases from skeletal LCH is important since different treatment is required compared with that of other bone tumors (Song et al. 2011). Therefore, accurate diagnosis is important to avoid inappropriate treatment or invasive procedures.

A variable radiographic appearance can be identified, though frequently the findings are of an ill-defined permeative pattern of bone destruction. On MRI, the lesion demonstrates a nonspecific signal pattern with extensive bone marrow edema and soft tissue reactions (Beltran et al. 1993; Davies et al. 1994; Monroc et al. 1994). A number of MRI characteristics can be observed. The most frequent MRI finding is a diffuse, ill-defined hypointense signal intensity of the bone marrow on T1-weighted images and hyper-intensity on T2-weighted images (Song et al. 2011; Beltran et al. 1993; Davies et al. 1994) (Fig. 7). Furthermore, endosteal scalloping and a periosteal reaction can often be seen (Song et al. 2011). The soft tissue reaction is usually ill-defined with hyperintensity on T2-weighted images, though a minority of cases may appear as focal or "mass like," displacing adjacent muscle groups (Beltran et al. 1993). Enhancement is usually evident in both the lesion and surrounding edema (Monroc et al. 1994). Later, lesions may appear sharply circumscribed, with a sclerotic appearance (James et al. 2008). A low signal rim on STIR sequences can be detected at the periphery of the lesion which has been suggested as an early indicator of healing (Davies et al. 1994). Furthermore, extensive bone marrow edema is thought to relate to the early phase of the disease with little or no edema being present in the late phase (James et al. 2008).

4.1.1 Whole-Body MRI

Fast SE STIR whole-body MRI allows the entire body to be imaged within a relatively short time. Therefore, this technique may be useful as a whole-body

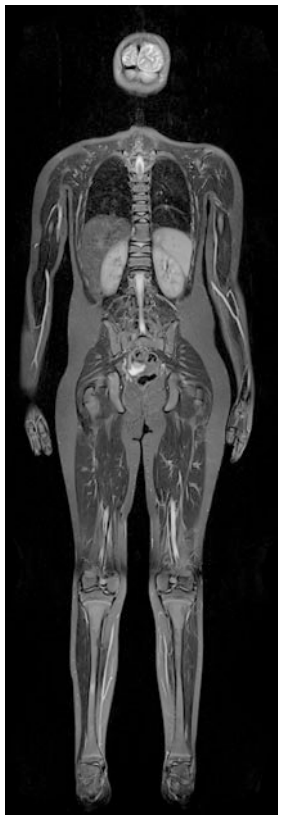

Fig. 8 Coronal STIR total-body MRI of a 10-year-old girl with LCH, showing a vertebral collapse of Th6 and a lesion with hyperintense signal intensity in the right tibia

screening tool in children (Fig. 8). Whole-body MRI using a STIR SE sequence proved to be more sensitive than bone scintigraphy in the detection of cortical bone and bone marrow metastasis, and it can, therefore, be used in the assessment of skeletal involvement of malignancies such as neuroblastoma, rhabdomyosarcoma, Ewing sarcoma, and other tumors that metastasize to bone (Eustace et al. 1997; Walker et al. 2000; Steinborn et al. 1999). In LCH, fast SE STIR whole-body MRI can be useful as a complementary imaging tool to detect otherwise unrecognized marrow involvement and has the potential for evaluation and determination of the extent of bone involvement (Kellenberger et al. 2004).

4.2 Erdheim-Chester Disease

In 1930, William Chester described the first two cases of "lipoid granulomatosis," later renamed ECD (Chester 1930). It is a rare non-LCH, with particular tropism for connective and adipose tissues. Typically, it affects adults of both sexes, with almost constant bone involvement and extraosseous involvement in 60 % of the patients (Breuil et al. 2002). The pattern of extraosseous involvement is highly variable and can be life threatening (Dion et al. 2006). ECD is associated with high mortality rates, and a 3 year survival rate of below 50 % (Braiteh et al. 2005). The most common extraosseous clinical manifestations are diabetes insipidus and painless bilateral exophthalmos. These two manifestations, together with bone pain, compose the classic ECD diagnostic triad (Veyssier-Belot et al. 1996). The diversity and the nonspecific clinical presentation of visceral involvement in ECD highlight the diagnostic value of skeletal radiologic findings.

Bone involvement in this disease is rather stereotyped and characterized at conventional radiography by symmetric bilateral osteosclerosis of the metaphyses and diaphyses of the long bones, sparing the axial skeleton, as well as the hands and feet (Dion et al. 2006; Veyssier-Belot et al. 1996). Appearances of ECD on MRI have been described. Findings on MRI include replacement of the normal fatty bone marrow signal intensity by markedly low signal intensities; hypo-intense compared with muscle and heterogeneous signal intensity on T1-weighted spin-echo images (Dion et al. 2006). Furthermore, replacement of the normal bone marrow can be seen as heterogeneous intermediate or high signal intensity on fat-suppressed T2-weighted images; isointense or hyperintense compared with muscle and with enhanced after gadolinium injection (Dion et al. 2006). On MRI, epiphyseal involvement can be seen as homogeneous or heterogeneous infiltrate, sparing the subchondral bone. In patients with a heterogeneous infiltration pattern, focal areas of fatty bone marrow often persist, particularly in the metaphyseal area (Dion et al. 2006). In some cases bone infarcts may occur, which look like well-defined lesions with irregular sclerotic rims of low signal intensity on both T1- and T2-weighted images (Dion et al. 2006). In the majority of the patients, periosteal reactions can be observed on MRI (Dion et al. 2006). Periostitis can be seen as a band of high signal intensity on T2-weighted images and gadolinium-enhanced fat-saturated spin-echo T1-weighted images along the outer margin of the cortex (Dion et al. 2006).

Erdheim-Chester disease may be confused with LCH, because it sometimes shares the same clinical

(diabetes insipidus and exophthalmos) or radiological findings. But, it also appears to have typical characteristics, since patients are older and have a worse prognosis than those with LCH.

References

Akkerman EM, Maas M (1995) A region-growing algorithm to simultaneously remove dephasing influences and separate fat and water in two-point Dixon imaging. Proceedings of the society for magnetic resonance in medicine and the European Society for Magnetic Resonance in Medicine and Biology, 1995

Arias M, Villalba C et al (2004) Acute spinal epidural hematoma and systemic mastocytosis. Spine 29(8):E161–E163

Avila NA, Ling A, Metcalfe DD, Worobec AS (1998) Mastocytosis: magnetic resonance imaging patterns of marrow disease. Skeletal Radiol 27(3):119–126

Azouz EM, Saigal G, Rodriguez MM, Podda A (2005) Langerhans' cell histiocytosis: pathology, imaging and treatment of skeletal involvement. Pediatr Radiol 35:103–115

Barton NW, Brady RO, Dambrosia JM et al (1992) Dose-dependent responses to macrophage-targeted glucocerebrosidase in a child with Gaucher disease. J Pediatr 120:277–280

Beltran J, Aparisi F, Bonmati LM, Rosenberg ZS, Present D, Steiner GC (1993) Eosinophilic granuloma: MRI manifestations. Skeletal Radiol 22:157–161

Berry DH, Gresik MV, Humphrey GB et al (1986) Natural history of histiocytosis X: a pediatric oncology group study. Med Pediatr Oncol 14:1–5

Braiteh F, Boxrud C, Esmaeli B, Kurzrock R (2005) Successful treatment of Erdheim-Chester disease, a non-Langerhans-cell histiocytosis, with interferon-alpha. Blood 106:2992–2994

Breuil V, Brocq O, Pellegrino C, Grimaud A, Euller-Ziegler L (2002) Erdheim-Chester disease: typical radiological bone features for a rare xanthogranulomatosis. Ann Rheum Dis 61:199–200

Broadbent V, Egeler RM, Nesbit ME Jr (1994) Langerhans cell histiocytosis—clinical and epidemiological aspects. Br J Cancer Suppl 23:S11–S16

Charrow J, Esplin JA, Gribble TJ et al (1998) Gaucher disease: recommendations on diagnosis, evaluation, and monitoring. Arch Intern Med 158:1754–1760

Charrow J, Andersson HC, Kaplan P et al (2004) Enzyme replacement therapy and monitoring for children with type 1 Gaucher disease: consensus recommendations. J Pediatr 144:112–120

Chester W (1930) Über Lipoidgranulomatose. Virchows Arch Pathol Anat Physiol 279:561–602

Colbert C (1972) The osseous system: an overview. Invest Radiol 7:223–239

Cremin BJ, Davey H, Goldblatt J (1990) Skeletal complications of type I Gaucher disease: the magnetic resonance features. Clin Radiol 41:244–247

Davies AM, Pikoulas C, Griffith J (1994) MRI of eosinophilic granuloma. Eur J Radiol 18:205–209

de Fost M, van Noesel CJ, Aerts JM, Maas M, Poll RG, Hollak CE (2008) Persistent bone disease in adult type 1 Gaucher disease despite increasing doses of enzyme replacement therapy. Haematologica 93:1119–1120

Deegan PB, Pavlova E, Tindall J et al (2011) Osseous manifestations of adult Gaucher disease in the era of enzyme replacement therapy. Medicine (Baltimore) 90:52–60

DeMayo RF, Haims AH, McRae MC, Yang R, Mistry PK (2008) Correlation of MRI-Based bone marrow burden score with genotype and spleen status in Gaucher's disease. AJR Am J Roentgenol 191(1):115–123

Dion E, Graef C, Miquel A et al (2006) Bone involvement in Erdheim-Chester disease: imaging findings including periostitis and partial epiphyseal involvement. Radiology 238:632–639

Dixon WT (1984) Simple proton spectroscopic imaging. Radiology 153:189–194

Dooms GC, Fisher MR, Hricak H, Richardson M, Crooks LE, Genant HK (1985) Bone marrow imaging: magnetic resonance studies related to age and sex. Radiology 155: 429–432

Elstein D, Abrahamov A, Hadas-Halpern I, Meyer A, Zimran A (1998) Low-dose low-frequency imiglucerase as a starting regimen of enzyme replacement therapy for patients with type I Gaucher disease. QJM 91:483–488

Eustace S, Tello R, DeCarvalho V et al (1997) A comparison of whole-body turboSTIR MR imaging and planar 99mTc-methylene diphosphonate scintigraphy in the examination of patients with suspected skeletal metastases. AJR Am J Roentgenol 169:1655–1661

Farahati J, Trenn G, John-Mikolajewski V et al (1996) Use of various diagnostic methods in a patient with Gaucher disease type I. Clin Nucl Med 21:619–625

Favara BE, Feller AC, Pauli M et al (1997) Contemporary classification of histiocytic disorders. The WHO committee on histiocytic/reticulum cell proliferations. Reclassification working group of the histiocyte society. Med Pediatr Oncol 29:157–166

Fuller M, Meikle PJ, Hopwood JJ (2006) Epidemiology of lysosomal storage diseases: an overview

Gaucher P (1882) De l'épithélioma primitif de la rate (hypertrophie idiopathique de la rate sans leucémie). Thèse Paris

Gerard EL, Ferry JA, Amrein PC et al (1992) Compositional changes in vertebral bone marrow during treatment for acute leukemia: assessment with quantitative chemical shift imaging. Radiology 183:39–46

Glass RB, Poznanski AK, Young S, Urban MA (1987) Gaucher disease of the liver: CT appearance. Pediatr Radiol 17: 417–418

Grabowski GA, Leslie N, Wenstrup R (1998) Enzyme therapy for Gaucher disease: the first 5 years. Blood Rev 12: 115–133

Grabowski GA, Andria G, Baldellou A et al (2004) Pediatric non-neuronopathic Gaucher disease: presentation, diagnosis and assessment. Consensus statements. Eur J Pediatr 163:58–66

Grieser T, Minne (1997) HW Systemic mastocytosis and skeletal lesions. Lancet 350:1103–1104

Guggenbuhl P, Grosbois B, Chales G (2008) Gaucher disease. Joint Bone Spine 75:116–124

Haney K, Russel W, Raila FA et al (1996) MRI characteristics of systemic mastocytosis of the lumbosacral spine. Skel Rad 25:171–173

Hermann G, Goldblatt J, Levy RN, Goldsmith SJ, Desnick RJ, Grabowski GA (1986) Gaucher's disease type 1: assessment of bone involvement by CT and scintigraphy. AJR Am J Roentgenol 147:943–948

Hermann G, Shapiro RS, Abdelwahab IF, Grabowski G (1993) MR imaging in adults with Gaucher disease type I: evaluation of marrow involvement and disease activity. Skeletal Radiol 22:247–251

Hollak CE, Aerts JM, Goudsmit R et al (1995) Individualised low-dose alglucerase therapy for type 1 Gaucher's disease. Lancet 345:1474–1478

Hollak CE, Maas M, Akkerman EM, Aerts H (2001) Dixon quantitative chemical shift imaging is a sensitive tool for the evaluation of bone marrow responses to individualized doses of enzyme supplementation therapy in type 1 Gaucher disease. Blood Cells Mol Dis 27:1005–1012

Howarth DM, Gilchrist GS, Mullan BP, Wiseman GA, Edmonson JH, Schomberg PJ (1999) Langerhans cell histiocytosis: diagnosis, natural history, management, and outcome. Cancer 85:2278–2290

Huang TY, Yam LT, Li CY (1987) Radiological features of systemic mast cell disease. Br J Radiol 60:765–770

James SL, Panicek DM, Davies AM (2008) Bone marrow oedema associated with benign and malignant bone tumours. Eur J Radiol 67:11–21

Johnson LA, Hoppel BE, Gerard EL et al (1992) Quantitative chemical shift imaging of vertebral bone marrow in patients with Gaucher disease. Radiology 182:451–455

Kellenberger CJ, Epelman M, Miller SF, Babyn PS (2004) Fast STIR whole-body MR imaging in children. Radiographics 24:1317–1330

Lanir A, Hadar H, Cohen I et al (1986) Gaucher disease: assessment with MR imaging. Radiology 161:239–244

Maas M, Akkerman EM, Venema HW, Stoker J, Den Heeten GJ (2001) Dixon quantitative chemical shift MRI for bone marrow evaluation in the lumbar spine: a reproducibility study in healthy volunteers. J Comput Assist Tomogr 25:691–697

Maas M, Poll LW, Terk MR (2002a) Imaging and quantifying skeletal involvement in Gaucher disease. Br J Radiol 75(Suppl 1):A13–A24

Maas M, Hollak CE, Akkerman EM, Aerts JM, Stoker J, Den Heeten GJ (2002b) Quantification of skeletal involvement in adults with type I Gaucher's disease: fat fraction measured by Dixon quantitative chemical shift imaging as a valid parameter. AJR Am J Roentgenol 179:961–965

Maas M, van Kuijk C, Stoker J et al (2003) Quantification of bone involvement in Gaucher disease: MR imaging bone marrow burden score as an alternative to Dixon quantitative chemical shift MR imaging–initial experience. Radiology 229:554–561

Maas M, Hangartner T, Mariani G et al (2008) Recommendations for the assessment and monitoring of skeletal manifestations in children with Gaucher disease. Skeletal Radiol 37:185–188

Maas M, Kuijper M, Akkerman EM (2011) From Gaucher's disease to metabolic radiology: translational radiological research and clinical practice. Semin Musculoskelet Radiol. 15(3):301–306

Mariani G, Molea N, La CL, Porciello G, Lazzeri E, Ferri C (1996) Scintigraphic findings on 99mTc-MDP, 99mTc-sestamibi and 99mTc-HMPAO images in Gaucher's disease. Eur J Nucl Med 23:466–470

Mariani G, Filocamo M, Giona F et al (2003) Severity of bone marrow involvement in patients with Gaucher's disease evaluated by scintigraphy with 99mTc-sestamibi. J Nucl Med 44:1253–1262

Meikle PJ, Hopwood JJ, Clague AE, Carey WF (1999) Prevalence of lysosomal storage disorders. JAMA 281:249–254

Metzgeroth G, Dinter D et al (2006) Systemic mastocytosis simulating osseous metastatic disease. British J Hematol 136:1

Meyer JS, Harty MP, Mahboubi S et al (1995) Langerhans cell histiocytosis: presentation and evolution of radiologic findings with clinical correlation. Radiographics 15: 1135–1146

Michaely HJ, Metzgeroth G, Haneder S, Riffel P, Schönberg SO, Reiter A (2011) Whole-body MR-imaging allows to differentiate indolent from aggressive systemic mastocytosis. ECR 2011 B052. RSNA 2011 SSC10-02

Mikosch P, Kohlfurst S, Gallowitsch HJ et al (2008) Is there a role for scintigraphic imaging of bone manifestations in Gaucher disease? A review of the literature. Nuklearmedizin 47:239–247

Miller SP, Zirzow GC, Doppelt SH, Brady RO, Barton NW (1996) Analysis of the lipids of normal and Gaucher bone marrow. J Lab Clin Med 127:353–358

Monroc M, le Ducou PH, Haddad S, Josset P, Montagne JP (1994) Soft tissue signal abnormality associated with eosinophilic granuloma. Correlation of MR imaging with pathologic findings. Pediatr Radiol 24:328–332

Pastores GM, Meere PA (2005) Musculoskeletal complications associated with lysosomal storage disorders: Gaucher disease and Hurler-Scheie syndrome (mucopolysaccharidosis type I). Curr Opin Rheumatol 17:70–78

Pinto R, Caseiro C, Lemos M et al (2004) Prevalence of lysosomal storage diseases in Portugal. Eur J Hum Genet 12:87–92

Poll LW, Koch JA, vom Dahl S et al (2001) Magnetic resonance imaging of bone marrow changes in Gaucher disease during enzyme replacement therapy: first German long-term results. Skeletal Radiol 30:496–503

Poll LW, Maas M, Terk MR et al (2002) Response of Gaucher bone disease to enzyme replacement therapy. Br J Radiol 75(Suppl 1):A25–A36

Poll LW, Cox ML, Godehardt E, Steinhof V, vom Dahl S (2011) Whole body MRI in type I Gaucher patients: evaluation of skeletal involvement. Blood Cells Mol Dis 46:53–59

Poorthuis BJ, Wevers RA, Kleijer WJ et al (1999) The frequency of lysosomal storage diseases in The Netherlands. Hum Genet 105:151–156

Robertson PL, Maas M, Goldblatt J (2007) Semiquantitative assessment of skeletal response to enzyme replacement therapy for Gaucher's disease using the bone marrow burden score. AJR Am J Roentgenol 188(6):1521–1528

Roca M, Mota J, Giraldo P, Garcia Erce JA (1999) Systemic mastocytosis: MRI of bone marrow involvement. Eur Rad 9:1094–1097

Roca M, Mota J, Alfonso P, Pocoví M, Giraldo P (2007) S-MRI score: a simple method for assessing bone marrow involvement in Gaucher disease. Eur J Radiol 62(1):132–137

Rosen BR, Fleming DM, Kushner DC et al (1988) Hematologic bone marrow disorders: quantitative chemical shift MR imaging. Radiology 169:799–804

Rosenthal DI, Scott JA, Barranger J et al (1986) Evaluation of Gaucher disease using magnetic resonance imaging. J Bone Joint Surg Am 68:802–808

Rosenthal DI, Barton NW, McKusick KA et al (1992) Quantitative imaging of Gaucher disease. Radiology 185:841–845

Rosenthal DI, Doppelt SH, Mankin HJ et al (1995) Enzyme replacement therapy for Gaucher disease: skeletal responses to macrophage-targeted glucocerebrosidase. Pediatrics 96:629–637

Sims KB, Pastores GM, Weinreb NJ et al (2008) Improvement of bone disease by imiglucerase (Cerezyme) therapy in patients with skeletal manifestations of type 1 Gaucher disease: results of a 48-month longitudinal cohort study. Clin Genet 73:430–440

Song YS, Lee IS, Yi JH, Cho KH, Kim DK, Song JW (2011) Radiologic findings of adult pelvis and appendicular skeletal Langerhans cell histiocytosis in nine patients. Skeletal Radiol 40:1421–1426

Stamm AC, Burbelko M, Rominger M (2008) Systemische Mastozytose-seltene Ursache einer pathologischen Wirbelkoerperfraktur. RoFo 180:155–156

Steinborn MM, Heuck AF, Tiling R, Bruegel M, Gauger L, Reiser MF (1999) Whole-body bone marrow MRI in patients with metastatic disease to the skeletal system. J Comput Assist Tomogr 23:123–129

Steiner RM, Mitchell DG, Rao VM et al (1990) Magnetic resonance imaging of bone marrow: diagnostic value in diffuse hematologic disorders. Magn Reson Q 6:17–34

Terk MR, Dardashti S, Liebman HA (2000) Bone marrow response in treated patients with Gaucher disease: evaluation by T1-weighted magnetic resonance images and correlation with reduction in liver and spleen volume. Skeletal Radiol 29:563–571

Veyssier-Belot C, Cacoub P, Caparros-Lefebvre D et al (1996) Erdheim-Chester disease: clinical and radiologic characteristics of 59 cases. Medicine (Baltimore) 75:157–169

Vlieger EJ, Maas M, Akkerman EM, Hollak CE, Den Heeten GJ (2002) Vertebra disc ratio as a parameter for bone marrow involvement and its application in Gaucher disease. J Comput Assist Tomogr 26:843–848

Vogler JB III, Murphy WA (1988) Bone marrow imaging. Radiology 168:679–693

vom Dahl S, Poll L, Di Roccio M et al (2006) Evidence-based recommendations for monitoring bone disease and the response to enzyme replacement therapy in Gaucher patients. Curr Med Res Opin 22:1045–1064

Walker R, Kessar P, Blanchard R et al (2000) Turbo STIR magnetic resonance imaging as a whole-body screening tool for metastases in patients with breast carcinoma: preliminary clinical experience. J Magn Reson Imaging 11:343–350

Weinreb NJ, Aggio MC, Andersson HC et al (2004) Gaucher disease type 1: revised recommendations on evaluations and monitoring for adult patients. Semin Hematol 41:15–22

Weinreb N, Barranger J, Packman S et al (2007) Imiglucerase (Cerezyme) improves quality of life in patients with skeletal manifestations of Gaucher disease. Clin Genet 71:576–588

Weinreb NJ, Cappellini MD, Cox TM, Giannini EH, Grabowski GA, Hwu WL, Mankin H, Martins AM, Sawyer C, vom Dahl S, Yeh MS, Zimran A (2010) A validated disease severity scoring system for adults with type 1 Gaucher disease. Genet Med 12(1):44–51

Wenstrup RJ, Roca-Espiau M, Weinreb NJ, Bembi B (2002) Skeletal aspects of Gaucher disease: a review. Br J Radiol 75(Suppl 1):A2–A12

Anemias and Bone Marrow Insufficiency

Iris-Melanie Noebauer-Huhmann
and Martin Uffmann

Contents

I.-M. Noebauer-Huhmann (✉)
Division of Neuroradiology and Musculoskeletal Radiology, Department of Radiology, Medical University of Vienna/Vienna General Hospital, Waerhringer Guertel 18-20, A-1090, Vienna, Austria
e-mail: iris.noebauer@meduniwien.ac.at

M. Uffmann
Landesklinikum Neunkirchen, Peischingerstrasse 19, 2620, Neunkirchen, Austria

Abstract

Anemia is the most common disorder of the blood, with a broad spectrum of underlying causes. The most important conditions and entities resulting in or representing anemia are discussed in this chapter. Detailed information is provided for hemoglobinopathies (as sickle cell anemia and thalassemia), for primary anemias and bone marrow insufficiency (aplastic anemia, and serous atrophy). Information on age-related anemias includes inherited anemias in the child, as well as acquired anemias in the elderly. For each entity, the etiology and clinical background, followed by mechanisms and histology, and imaging characteristics are provided. The clinical symptoms of anemia are relatively uniform. However, imaging characteristics as extramedullary hematopoiesis, or complications as osteonecrosis or osteomyelitis are more likely in some forms of anemia. Disease- and treatment-related bone marrow patterns are also discussed.

1 Introduction

Anemia is the most common disorder of the blood. For practical reasons, it has been defined as a decrease in one or more of the three major red blood cell (RBC) measurements below normal limits: hemoglobin concentration; hematocrit; or RBC count.

The different etiologies of anemia are classified according to two general approaches:

In the morphological approach, the size of the red blood cells (mean corpuscular volume (MCV)) is important for categorizing anemias. For instance, iron

A. Baur-Melnyk (ed.), *Magnetic Resonance Imaging of the Bone Marrow*, Medical Radiology. Diagnostic Imaging,
DOI: 10.1007/174_2012_726,

deficiency often results in erythrocytes smaller than normal (microcystic anemia). A further parameter for the morphological approach is the reticulocyte response (Tefferi 2003).

In the kinetic approach, three independent mechanisms responsible for the decrease in hemoglobin concentration are addressed: decreased or impaired RBC production; increased RBC destruction; and blood loss.

Examples of decreased RBC production include nutrient deficiencies (iron, vitamin B12, or folate), bone marrow disorders (e.g., tumor infiltration, aplastic anemia, RBC aplasia, myelodysplasia), bone marrow suppression (e.g., irradiation, chemotherapy, drugs), disorders of the endocrine system with low levels of hormones that stimulate RBC production (e.g., Erythropoietin (EPO), thyroid hormone, androgens), and congenital hypoplastic anemias with impaired RBC production (e.g., Fanconi anemia).

Increased RBC destruction is caused by inherited hemolytic anemias (e.g., hereditary spherocytosis, sickle cell disease, thalassemia major) and acquired hemolytic anemias (e.g., autoimmune hemolytic anemia, thrombotic thrombocytopenic purpura, hemolytic uremic syndrome, malaria).

Blood loss can be due to obvious bleeding (e.g., trauma, obvious gastrointestinal or gynecological bleeding), occult bleeding (low-volume bleeding or inconsistent bleeding of vascular malformations, ulcers, or carcinomas), or induced bleeding (in hemodialysis or due to excessive blood donations).

The most important conditions and entities resulting in or representing anemia are discussed in this chapter.

The clinical symptoms of anemia are relatively uniform despite the broad spectrum of underlying causes. The signs include a feeling of weakness, or fatigue, general malaise, and sometimes poor concentration. There may also be dyspnea on exertion present. In very severe anemia, the body may compensate for the lack of oxygen carrying capability of the blood by increasing cardiac output. The patient may have symptoms related to this, such as palpitations, angina (if preexisting heart disease is present), intermittent claudication of the legs, and symptoms of heart failure. The extent and severity of symptoms depend on the degree of anemia and the rate at which it has evolved, as well as the oxygen demands of the individual patient. In some patients, severe forms of anemia can be tolerated relatively well due to adaptive mechanisms, such as homeostatic forces adjusting to the reduced oxygen carrying capacity of the blood. In patients where anemia evolves quickly, the symptoms can be much more pronounced even when the degree of anemia is still moderate.

2 Hemoglobinopathies

2.1 Sickle Cell Anemia (Drepanocytosis)

2.1.1 Epidemiology and Clinical Background

Sickle cell disease belongs to the group of hemoglobinopathies, and clinically, to the hemolytic anemias. It is a common inherited erythrocyte disorder, which leads to anemia in homozygous patients (the heterozygous trait causes a milder clinical course in the carrier). It is characterized by an abnormality of the ß-globin chains (mainly Hb S, replacing Hb A), resulting in polymerization of the Hb S molecule when deoxygenated, and associated with a decreased flexibility of the Hb chains. Repeated oxygenation/deoxygenation leads to membrane damage and the formation of sickle-(or 'banana'-) shaped erythrocytes, which are destroyed early. In the newborn, 80 % of the Hb is HbF (fetal hemoglobin), which also protects the patient against sickle cell complications (Murphy 1994). Normally, HbF is reduced to 1 % at the age of 6 months, but may be elevated in sickle cell patients (Platt et al. 1991).

Patients with Hb S have a higher resistance to *Plasmodium falciparum* infections, leading to a higher incidence of the sickle cell trait in areas where malaria is endemic (Africa, the Middle East, Mediterranean countries, India, and countries with migration from those regions) (Aluoch 1997). The highest prevalence is observed in Africa, with up to 40 % of some African populations affected, and 8 % of African Americans carrying the gene for HbS. The manifest disease (HbSS), though, is only seen in 0.2 % of African Americans. The life expectancy is reduced by 25–30 years (Ejindu et al. 2007).

The bone is the most commonly involved site in sickle cell disease (SCD). Other organs affected include the skin, liver, spleen, kidneys, retina, and CNS.

Complications are typical in sickle cell disease.

They are mainly a result of three mechanisms: chronic hemolytic anemia (also resulting in jaundice); vaso-occlusive changes; and infection (Bahebeck et al. 2004).

The painful vaso-occlusive crisis is the most common acute complication. Vaso-occlusive crises occur in almost all patients (Platt et al. 1991; Bailey et al. 1992; Neonato et al. 2000), beginning mostly in late infancy, and recurring throughout life. The typical locations of vaso-occlusive crises are either the medullary cavity, resulting in bone marrow infarcts, or the epiphyses (Lonergan et al. 2001; Kim and Miller 2002), where tissue necrosis is termed avascular necrosis. Sickle cell disease is the most common cause of femoral head osteonecrosis in children (Styles and Vichinsky 1996), although the prevalence in children of epiphyseal avascular necrosis (AVN) (27 %) is lower than that in adults, presumably due to a protective effect by synovial nutrition (Adekile et al. 2001). In contrast to Legg-Calve-Perthes, an older age group is usually affected by AVN (Lonergan et al. 2001; Malizos et al. 2001). About half of the patients have experienced AVN by the age of 35 years (Styles and Vichinsky 1996). Chronic, painful avascular necrosis is seen in 41 % of adults (Ware et al. 1991), and 27 % of children (Adekile et al. 2001).

There is a predilection of painful vaso-occlusive crisis for the long bones (Keeley and Buchanan 1982). The occurrence of infarct in the femur has been described in 96 % of cases, in 48 % of cases in the humerus, in the small tubular bones of the hands and feet in 20–50 % of cases, and in the spine in 43–70 % of cases (Stoller et al. 2004; Rao et al. 1989). Typical sites of avascular necroses are the femoral heads, the heads of the humerus, the knee, and the small hand and feet joints (Jean-Baptiste and De Ceulaer 2000). In contrast to Legg-Calve-Perthes, the osteonecrosis in sickle cell anemia is bilateral in >50 % (Lonergan et al. 2001; Malizos et al. 2001). In general, SCD typically involves multiple joints. If the shoulder is affected, the hip is also involved in 74 % of these cases (Milner et al. 1991, 1993). The lesions tend to be larger (Malizos et al. 2001) and the distribution wider in SCD (in other entities, the size and distribution of the lesions are more related to mechanical stress).

Clinical manifestations include local intense pain (already seen in ischemia, before infarction), may lead to swelling (an example is swelling of the hands and feet in approximately 50 % of children with SCD (Stevens et al. 1981), tenderness, erythema, and may cause fever, and leukocytosis (Smith 1996). Patients with epiphyseal osteonecrosis typically suffer from motion restriction and pain in the joint involved. They also may experience joint effusions, resembling septic arthritis (Lonergan et al. 2001). Infarction as well as osteonecrosis may be found incidentally (Ware et al. 1991).

Medication with hydroxyurea, which increases Hb F, can reduce vaso-occlusive crises (Charache et al. 1995).

Infection is also common in SCD, with reported incidences of osteomyelitis of 12–18 %, and septic arthritis of 7 % (Bahebeck et al. 2004; Neonato et al. 2000).

The most commonly affected locations are the diaphyses of the femur, tibia, and humerus (Stark et al. 1991). In the non-SCD population, infections are more common in the metaphyses. Untreated osteomyelitis may extend into the joint, resulting in septic arthritis. Septic arthritis may also arise de novo. Facial bones and vertebrae may be involved.

Symptoms include pain, swelling, tenderness, moderate fever, and elevated inflammation markers, and therefore, are very similar to infarction. The process can also be indolent. Only in some cases erythema is observed. Abscess formation may be seen. Blood cultures are only positive in 50 % of cases, and should be performed immediately (Ejindu et al. 2007; Barrett-Connor 1971; Dirschl 1994).

The outcome of these complications is variable, ranging from restitution without sequelae, to chronic, progressive disability. For instance, femoral head impression is seen in 87 % of patients with hip osteonecrosis, if they remain untreated (Hernigou et al. 2003).

2.1.2 Mechanisms and Histology

2.1.2.1 Anemia

Anemia leads to increased hematopoiesis, resulting in reconversion or delayed conversion, and, in severe cases, in bone marrow expansion and extramedullary hematopoiesis. (Almeida and Roberts 2005); (Sidhu and Rich 1999). As a consequence of widening of the medullary spaces and thinning of the cortical bone, the incidence of insufficiency fractures is also increased (Bahebeck et al. 2002).

2.1.2.2 Complications

The erythrocyte sickling causes stasis and cell sequestration, which lead to ischemia and hypoxia, and finally, cell death in the perfused tissue. The process, in turn, worsens the sickling (Ejindu et al. 2007).

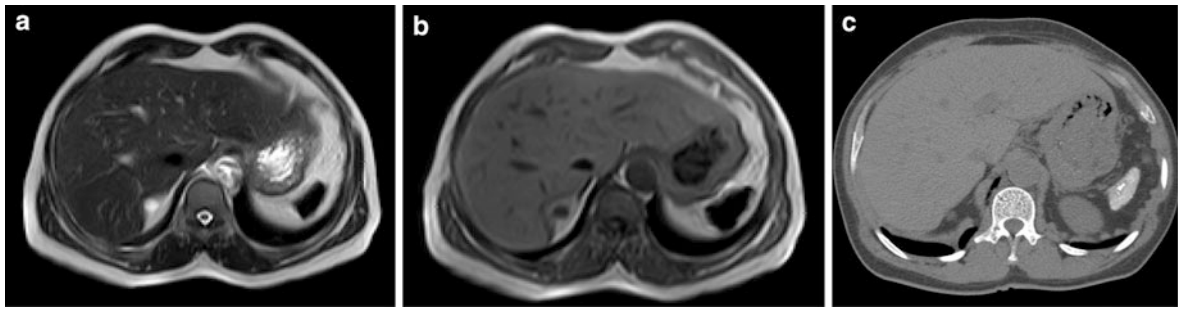

Fig. 1 A 54-year-old patient with sickle cell anemia, after multiple blood transfusions. Autosplenectomy, with small, hypointense spleen on T2w (**a**), and T1w (**b**) MRI of the abdomen. The CT (**c**) shows a hyperdense spleen with calcifications (courtesy of Prof. Dr. Franz Kainberger)

Bone infarction and osteonecrosis are described in detail in dedicated chapters.

The high incidence of the mostly hematogenous bone and joint infections has been postulated to be multifactorial. Locally, the congested cellular bone marrow with stasis and regional hypoxia, and the infarcted and necrotic bone provide a medium for bacterial growth. Systemically, the defense against infection is compromised by splenic damage (with autosplenectomy by vaso-occlusion, or hyposplensim with a small calcified spleen, (Fig. 1), and subsequent loss of bacterial filtration by the spleen, and by associated dysfunction (Almeida and Roberts 2005). The environment, especially an increased exposure to certain bacteria due to repeated hospitalizations, is also important (Resnick 2002).

In addition, sickling with mesenteric infarction leads to an increased bacteremia from the infarcted gastrointestinal tract (Anand and Glatt 1994). The most common causative organism in SCD bone infections is Salmonella species (in more than 50 % of the cases, *oral report A. Baur-Melnyk*), particularly nontypical serotypes such as *S. paratyphi B, S. enteritidis, S. typhimurium, and S. choleraesuis* (Piehl et al. 1993). *Staphylococcus aureus*, which is the leading cause of osteomyelitis in the normal population, is 2–5 times less common in SCD patients, but it is still the second most common pathogen (in approximately 10 %); others are Gram negative organisms and *M. tuberculosis* (Burnett et al. 1998; Atkins et al. 1997; Kooy et al. 1996). The frequent occurrence of enteric pathogens has been explained by possible microinfarctions of the gastrointestinal tract, which may lead to bacteremia (Overturf 1999).

Local spread from ulcers is another source for osseous infection, with skin commensals, such as *S. aureus* and anaerobic organisms (Burnett et al. 1998; Kooy et al. 1996).

Table 1 Osseous complications of sickle cell anemia

Acute osseous sequelae	Chronic osseous sequelae
Painful vaso-occlusive crisis	*Osteoporosis*
Vertebral collapse	Vertebral collapse
Insufficiency fractures	
Bone marrow necrosis	*Avascular necrosis*
Orbital bone infarction (→ compression)	
Acute chest syndrome	
Osteomyelitis	*Chronic arthritis*
Septic arthritis	Secondary osteoarthritis
Dental problems	Impaired growth

For osteomyelitis, please also see details in the dedicated chapter. An overview of the complications of sickle cell anemia is provided in table 1.

2.1.3 Imaging Characteristics

2.1.3.1 Anemia-Related Findings:

Projection radiographs show coarsened trabeculae, expanded medullary spaces, diffuse osteopenia, and cortical thinning (Brinker et al. 1998; Madani et al. 2007). The features tend to be less severe than in thalassemia major. The osteopenia may also be circumscribed, and appear as an osteolytic lesion, eventually necessitating further work-up to rule out tumorous origins.

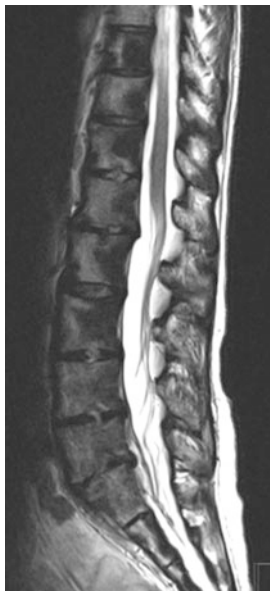

Fig. 2 Patient with sickle cell anemia, after multiple blood transfusions. T2w MRI of the spine, showing bone marrow inhomogeneity, with hypointense signal due to iron depositions, bone marrow infarcts, and central endplate impressions. Courtesy of Dr. Falk Miese

In children, widening of the diploic space, thinning of the outer and inner tables, and a "hair-on-end" appearance may be visible (Sebes and Diggs 1979). The latter is characterized by striations projecting from the outer aspect of the vault, caused by new bone formation with trabecular prominence. Involvement of the mandible with trabecular coarsening may be present, although involvement of the facial bones and the occipital bone is less common. Growth retardation, mainly due to marrow hyperplasia, may be observed.

MRI demonstrates an altered distribution of red and yellow bone marrow. Lack of the physiologic bone marrow conversion in the child leads to a persistence of red marrow in the appendicular skeleton. In the adult, hematopoietic marrow persists in the ankles, wrists, and metadiaphyses of the long bones (Resnick 2002). The typical features of reconversion may be seen (please also see dedicated chapter).

Extramedullary hematopoiesis is less common than in other hemolytic anemias, but may occur, mainly in the liver, but also in the spleen or thoracic soft tissues, adrenal glands, and skin. It can be assessed with CT or MRI. The masses have intermediate signal on T1w and T2w sequences. 99Tc-labeled sulfur colloid can identify hematopoiesis in the focal mass (Gilkeson et al. 1997).

In the spine, insufficiency fractures with end-plate compressions by the adjacent intervertebral discs lead to the characteristic "fish-mouth"-like biconcave deformity (Madani et al. 2007; Emodi and Okoye 2001; Williams 2004).

In patients who received multiple blood transfusions, the MRI may show iron deposition related bone marrow alterations (Fig. 2).

2.1.3.2 Imaging of Complications

Bone marrow infarcts:

Projection radiographs are initially negative in bone marrow infarcts (Madani et al. 2007). The infarct then manifests radiographically as an ill-defined osteolytic zone, which becomes more distinct over time, and subsequently shows typical serpiginous sclerotic zones at the border of the infarct.

In CT, those areas are therefore hypodense, with a blurred trabecular architecture. Serpiginous or festoon-like sclerotic rims of the lesion are typical long-term sequelae of bone marrow infarction. In the long bones, linear osteosclerotic lines may cause a "bone-in-bone" appearance (Lonergan et al. 2001). This feature is rarely seen in other forms of anemia.

Differential diagnoses include osteomyelitis, osteoblastic lesions, or Paget's disease. The differentiation can be difficult in cases with marked sclerosis (Sebes and Diggs 1979).

MRI is the most sensitive imaging method, and can demonstrate altered anatomy even a few days after the insult. Initially, fluid-sensitive MRI sequences show hyperintense signal (Resnick and Niwayama 1995), whereas these areas are hypointense on T1w, reflecting edema. Periostal and soft tissue alterations may be present, and lead to difficulties in the differential diagnosis versus infection (Frush et al. 1999). Chronic infarcts typically show central fat, surrounded by a serpiginous/festoon-like sclerotic demarcation zone, and a rim of high signal repair tissue. The end stage shows low signal intensity on all sequences due to fibrosis and sclerosis (Lonergan et al. 2001; Madani et al. 2007).

Other causes of bone marrow infarcts are therapy with cortisol, alcoholism with pancreatitis, collagenoses, and Gaucher disease.

Osteonecrosis: (Figs. 3, 4)

The imaging features are not different from osteonecroses in other clinical conditions and should be described according to the Association Research Circulation Osseous (ARCO) classification system

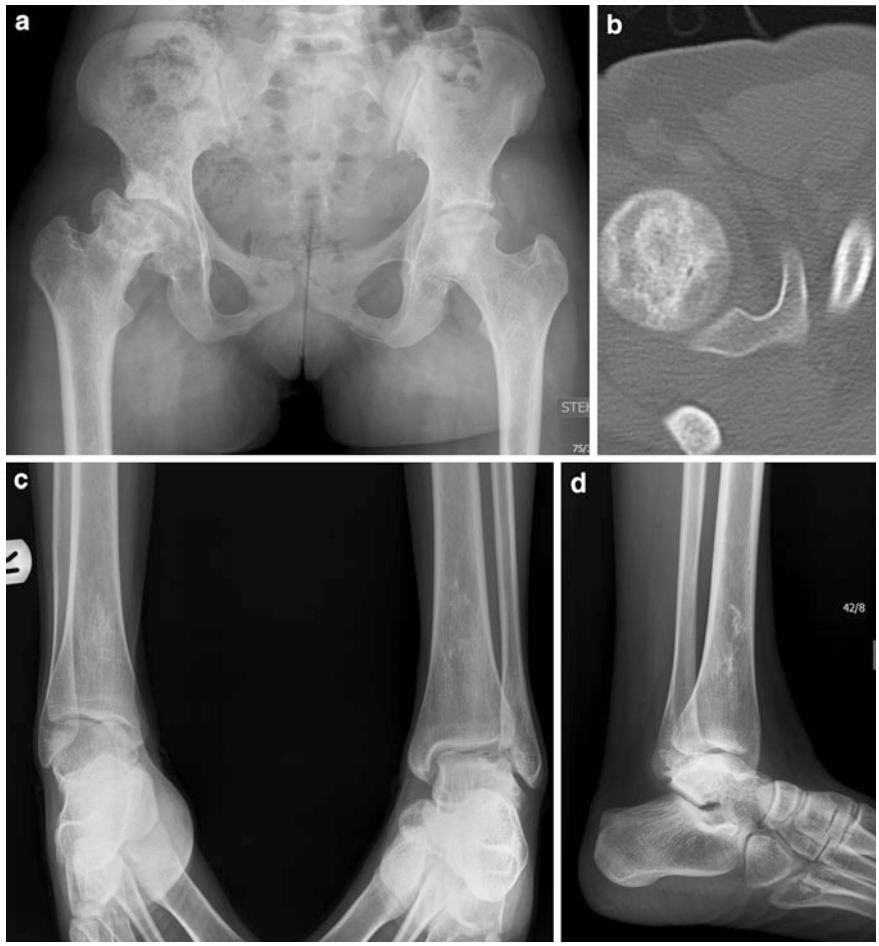

Fig. 3 A 19-year-old patient with sickle cell anemia. An AP projection radiograph of the hips (**a**) demonstrates femoral head necrosis of both hips, already fractured on the right side. In the same patient, a CT scan of the chest revealed avascular necrosis of the right shoulder (**b**, axial plane). Projection radiographs of the ankles (**c**, ap view, and **d**, lateral view of the left side) showed bilateral tibial distal metaphyseal bone marrow infarcts with a typical serpiginous sclerosis, and an osteochondral necrosis of the lateral aspect of the left talar dome (courtesy Doz. Dr. Milen Minkov, Doz. Dr. Helmut Prosch)

(Gardeniers 1993). Projection radiographs are also initially negative. In MRI, the initial diffuse changes are caused by ischemia, and represent edema. In the subacute phase, there might be some mottled attenuation of the epiphysis. The so-called "double-line-sign" represents granulation tissue surrounded by a sclerotic rim (Mitchell et al. 1987). Later, the epiphyseal contour is flattened. This flattening results in incongruency, and thus, predisposes to secondary osteoarthritis (Madani et al. 2007).

Special forms:

Vertebral bone infarcts have a pathognomonic appearance in 10 % of the patients. Marrow hyperplasia (Claster and Vichinsky 2003) (with ischemia of the central portion of the vertebral physis, and microvascular occlusion), with square-shaped end-plate impressions and subsequent overgrowth of the surrounding end-plate portions, may lead to typical "Lincoln log" or "H-shaped" collapsed vertebrae (Williams 2004) (Fig. 5) (Leong and Stark 1998). An overgrowth of the neighboring vertebral body, termed the "tower vertebra", can be observed in some patients (Kim and Miller 2002; Leong and Stark 1998; Marlow et al. 1998).

Dactylitis is seen in small children of less than 7 years of age, especially in 1- to 2-year olds (with red marrow in fingers and toes), and is the primary manifestation in small children between 6 months and 2 years of age in about 30–50 %. (Watson et al. 1963). Synonyms are "hand-foot-syndrome" or "aseptic dactylitis." Pain and fever are caused by infarction of the marrow, trabeculae, and inner parts of the cortex. Projection radiographs are initially negative. Within 10 days after the onset of symptoms, symmetrical subperiostal new bone formation may be seen (Weinberg and Currarino 1972). A combination of ill-defined osteolysis and periostitis may cause an aggressive appearance (Lonergan et al. 2001). The changes may show resolution, but the destructive changes may lead

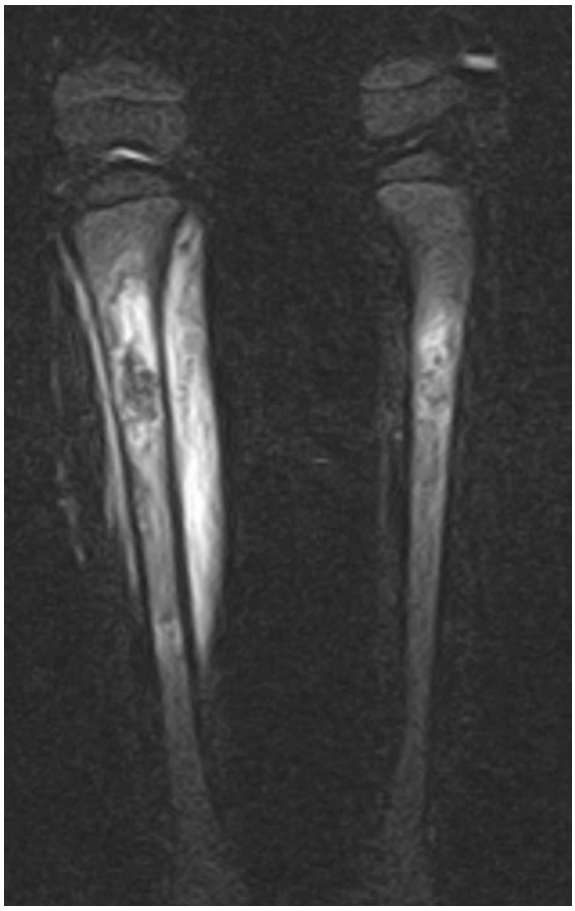

Fig. 4 Patient with sickle cell anemia. Coronal TIRM MRI shows bone marrow infarcts in the left tibia. Bone marrow signal alterations of the right tibia are visible, with extensive surrounding soft tissue edema, indicative of osteomyelitis (courtesy of Dr. Falk Miese)

to deformity, and also to digital shortening due to premature physeal fusion (Babhulkar et al. 1995). Differential diagnoses include tuberculous dactylitis, syphilis bone manifestations, leprosy, and fungal or pyogenic infection. Periostitis may also be seen in leukemia or infantile cortical hyperostosis.

Orbital bone infarction can lead to orbital compression syndrome because of periorbital swelling or subperiosteal (or intracranial) hematomas (Ganesh et al. 2001; Naran and Fontana 2001; Curran et al. 1997; Rebsamen et al. 1993).

Rib infarcts and pulmonary fat embolism can cause a painful acute chest syndrome (ACS) (Rucknagel 2001). However, the reasons for ACS, which is also defined by a newly diagnosed pulmonary consolidation, and may develop only after the admittance for pain crisis, are diverse and include pneumonias, in particular, which are more frequent in SCA. (Vichinsky et al. 1997).

Osteomyelitis:

Projection radiographs are usually negative for the first 8–10 days. Periostitis, and "osteopenia," as seen in projection radiography, are unspecific (Lonergan et al. 2001). CT may show abscesses and subperiosteal fluid collections, but they may also occur in infarcts (Stark et al. 1991; Frush et al. 1999).

Sonography is a widely available, portable, non-invasive modality without radiation exposure, and can be targeted interactively with the patient to the site of the greatest pain, and used for guidance of diagnostic or therapeutic intervention. However, it can only depict extraosseous pathology, especially subperiosteal fluid with periosteal elevation (sign:>4 mm), and soft tissue reactions (William et al. 2000; Rifai and Nyman 1997; Booz et al. 1999).

For radioisotope imaging, see chapter on osteomyelitis.

MRI with contrast agent administration is the imaging method of choice for the diagnosis, localization, and monitoring of therapy response (Lonergan et al. 2001). MRI depicts bone marrow edema and surrounding hyperemia (Bonnerot et al. 1994; Umans et al. 2000) as ill-defined signal hyperintensities on fluid-sensitive sequences, earlier than the changes become visible on projection radiographs. Contrast agent enhancement on T1w fat-saturated images has been found to be the most sensitive and specific sign of infection on MRI (Deely and Schweitzer 1997). Sequestrations within infected bone appear hypointense within hyperintense surrounding bone on fluid-sensitive, fat-saturated sequences. Those sequences also depict focal fluid collections, and the communication between extra- and intraosseous fluid collections through cortical defects (Fig. 6). Secondary fractures and subsequent healing may be monitored with projection radiography (Fig. 7).

Special forms:

De novo septic arthritis is seen less often than osteomyelitis, and mainly occurs together with vaso-occlusive disease (differential diagnosis, vaso-occlusive disease with reactive effusion (Jean-Baptiste and De Ceulaer 2000)). The symptoms are those of arthritis, including synovitis and effusion, soft tissue swelling, and, later, joint destruction, and "osteopenia." As a differential diagnosis to joint space

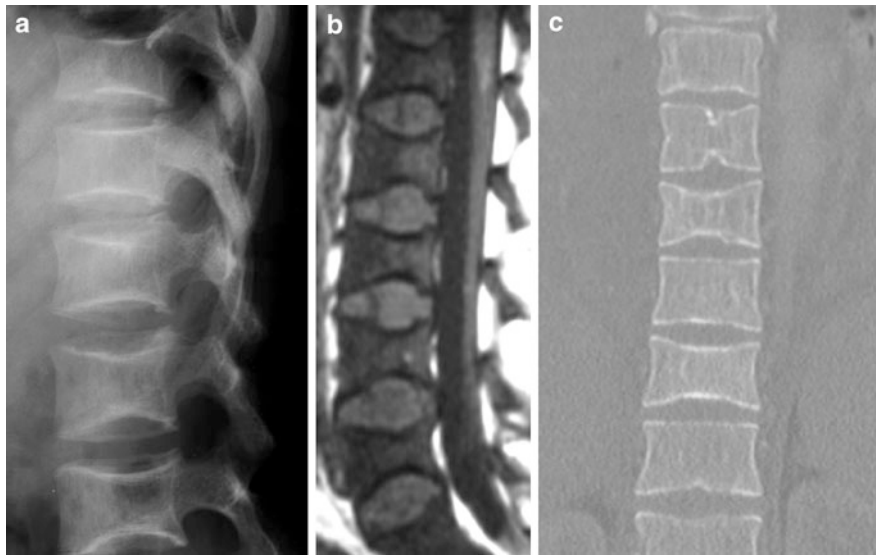

Fig. 5 Projection radiograph (**a**) and MRI (**b**) (courtesy of Prof. Dr. Bruno VandeBerg, and coronal reconstruction of a CT scan (**c**) (courtesy of Doz. Dr. Milen Minkov), in patients with sickle cell disease, showing typical "Lincoln log" or "H-shaped" collapsed vertebrae

narrowing, chondrolysis or chronic synovitis with plasmo-lymphocellulary infiltration of unknown origin may be considered. Sickle cell crises may also cause joint effusion (Schumacher et al. 1977).

Dental caries and pulpal necrosis (Laurence et al. 2002), as well as mandibular osteomyelitis (Adekeye and Cornah 1985) are other complications of SCD.

The differential diagnosis of infection versus infarction may be difficult (Fig. 5). In children, infarction has been found to be 50 times more common than osteomyelitis (Keeley and Buchanan 1982). Scintigraphy is a sensitive, but nonspecific method (Kim and Miller 2002; Amundsen et al. 1984; Skaggs et al. 2001). Decreased activity in the bone and bone marrow scan may be observed early, in the first few days, in contrast to the increased uptake seen in osteomyelitis (Chung et al. 1978). MRI should be performed if conventional management fails, or if osteomyelitis is suspected. Infarcts demonstrate a rim enhancement in the bone marrow, whereas osteomyelitis is more likely irregular, with geographic enhancement of the infected marrow (Umans et al. 2000). Cortical defects, with adjacent soft tissue involvement, as well as with adjacent fluid collections in the soft tissue, are typical of osteomyelitis (Ejindu et al. 2007). Gadolinium enhancement of the periosteum, the muscles, the fascia, and the fat may be seen in either entity, but this enhancement helps in monitoring therapy response to antibiotics (Almeida and Roberts 2005).

Delayed skeletal maturation (Barden et al. 2002) may be observed. Premature epiphyseal growth plate fusion leads to impaired growth (Collett-Solberg et al. 2002).

2.2 Thalassemia

2.2.1 Epidemiology and Clinical Background

Thalassemia is an inherited autosomal recessive disease (chromosome 11) with decreased or deficient formation of α or β-globin. The name is derived from the Greek word "θάλασσα," the sea.

β-Thalassemia is more common, with a homozygous form (β°), called thalassemia major, or Cooley′s anemia, and a heterozygous form (β^{+}), β-thalassemia intermedia or minor (Rund and Rachmilewitz 2005).

Carriers of the trait are protected from malaria infection to a certain degree. This survival advantage leads to perpetuation of the trait. Therefore, β-thalassemia is endemic in areas with malaria or in those with a past medical history of the disease. A high β-thalassemia gene prevalence of up to 15 % is found in the local population of the Mediterranean area, mainly around the Aegean sea, in Greece, on Mediterranean islands, in southern Italy, in Arab nations, and in Asia (Henderson et al. 2009; Kohne 2011). α-Thalassemia is found mainly in West African descendants (mainly in Africa and America), in Arab nations, and in South-East Asia (Weatherall et al. 2001).

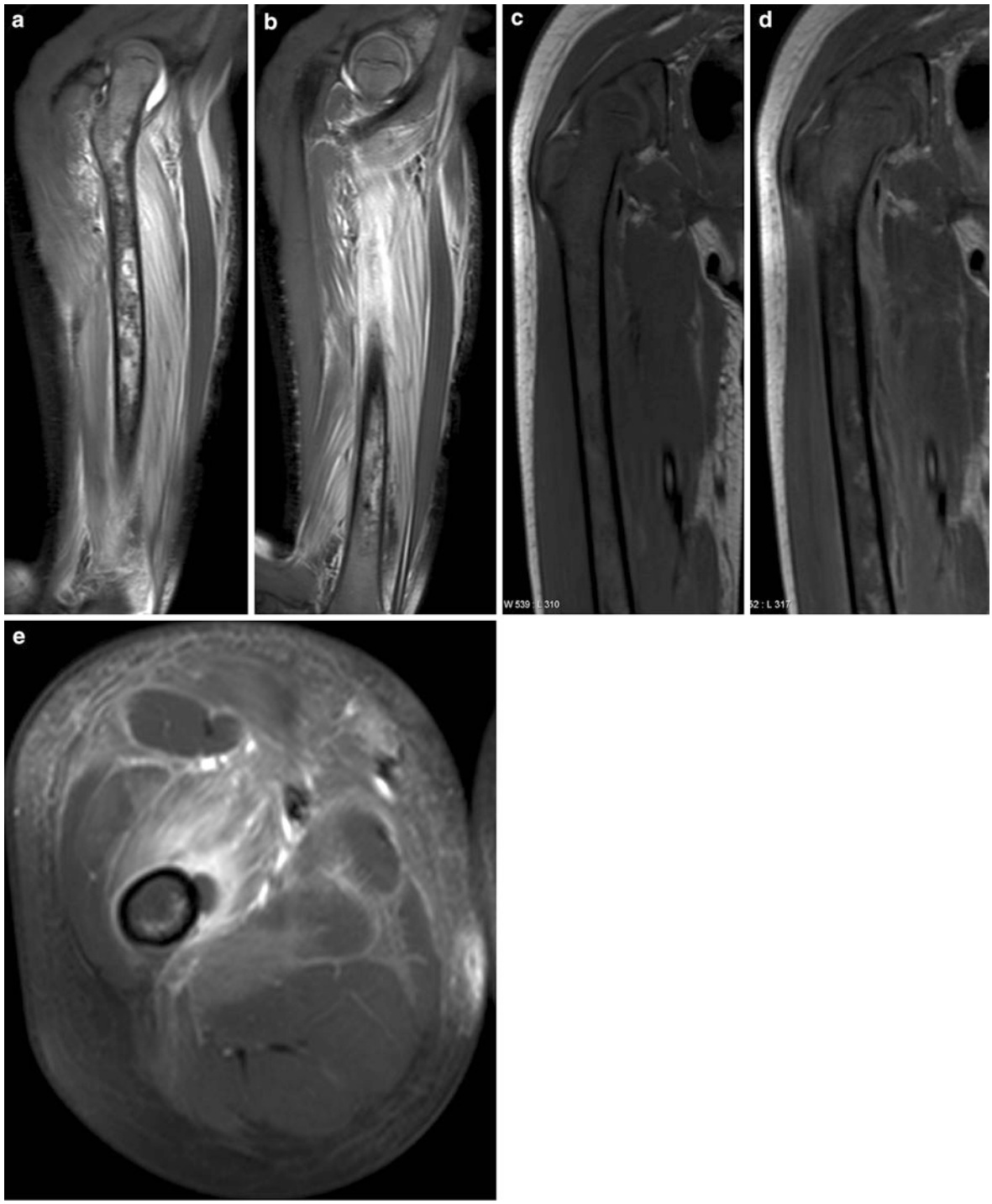

Fig. 6 Six-year-old patient with sickle cell anemia. The MRI of the right femur reveals bone marrow infarcts along the femoral shaft, with inhomogeneous signal alterations on the coronal proton density fat-saturated sequence (PDFS) (**a**, proximal, and **b**, distal), and the T1w sequence before (**c**) and after contrast agent injection (**d**). There is also some hip joint effusion (**a**). Surrounding soft tissue edema is also visible, involving the muscles and the fatty tissue, indicating additional osteomyelitis. This was confirmed by the axial fat-saturated T1w sequence after contrast agent injection (**e**), which demonstrates small abscesses along the femoral diaphysis (courtesy of Doz. Dr. Milen Minkov)

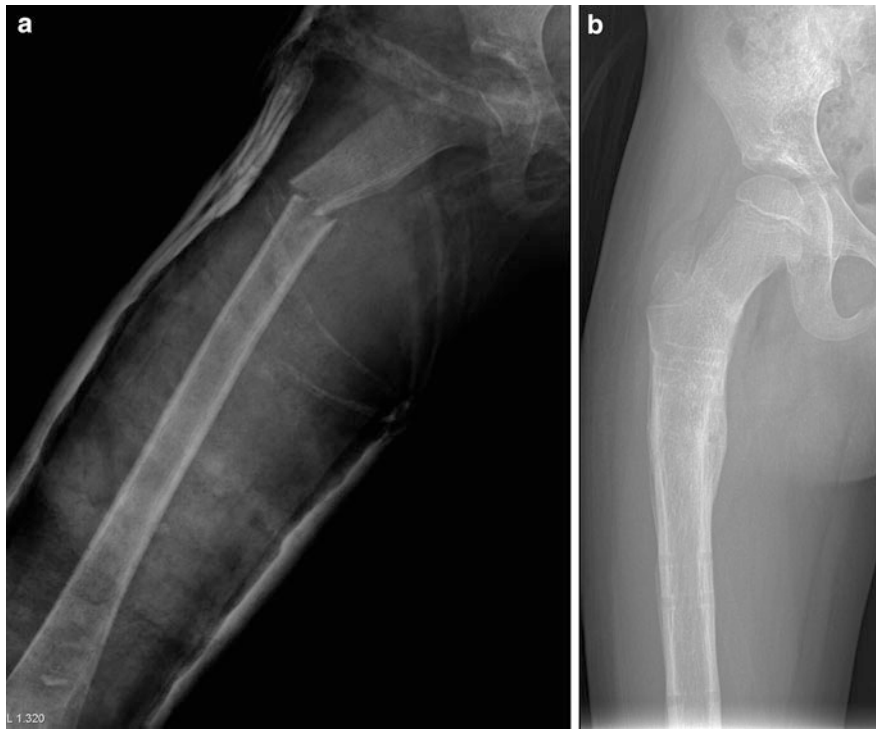

Fig. 7 The same patient as in Fig. 5, with sickle cell anemia, in whom an axial projection radiograph (**a**, in a cast) reveals a proximal fracture of the right femur. After external fixation, the follow-up AP projection demonstrated healing (**b**) (courtesy of Doz. Dr. Milen Minkov)

Clinical manifestations, treatment, and related changes

The ineffective erythropoiesis leads to anemia, hepatosplenomegaly, and extramedullary erythropoiesis with skeletal deformities.

α-Thalassemia patients show four different clinical patterns (Weatherall et al. 2001; Higgs and Weatherall 2009), which become apparent perinatally:

- α-thalassemia minima, mild hypochromia, with nearly normal Hb values
- α-thalassemia minor: The trait is either heterozygous α^0-thalassemia, (-/αα), or homozygous α^+-thalassemia, (-α/-α), with mild, microcytic hypochromic anemia
- HbH disease (compound heterozygous α+/α^0-thalassemia, with three inactive α-genes (-/-α) with moderate microcytic hypochromic anemia. These patients also show splenomegaly; infections and oxidants may lead to anemic crises; these patients may also experience gall stones, cardiac problems, ulcers of the lower leg, and folic acid deficiency (Kohne 2011). Usually, folic acid is regularly administered.
- Hb Bart's hydrops fetalis homozygous α^0-thalassemia (-/-). Severe intrauterine hemolytic anemia leads to hydrops, ascites, and intrauterine death if untreated (Kohne 2011). Treatment includes blood transfusions initiated in utero. If available, stem cell transplantation should be performed (Higgs and Weatherall 2009).

In patients with β-thalassemia, the clinical manifestations also depend on the genetic pattern.

- β-thalassemia minor (heterozygous β-thalassemia patients) suffer from mild, iron-refractory, microcytic hypochromic anemia, but do not require treatment (Kleihauer et al. 1996). An oral application of folic acid can be considered in more severe cases.
- untreated β-thalassemia intermedia, (mild homozygous or mixed heterozygous β-thalassemia) patients show moderately decreased hemoglobin levels of over 6 g/dL. They may show skeletal deformations and extramedullary hematopoiesis, whereas
- β-thalassemia major patients (severe homozygous or mixed heterozygous β-thalassemia) (Olivieri 1999) require regular blood transfusions to maintain a hemoglobin level above 9 g/dL (Rund and Rachmilewitz 2005).

The manifestation of β-thalassemia usually is seen from 3 to 6 months of age (Weatherall et al. 2001; Olivieri 1999; Kohne, Kleihauer 2010). The extent of the skeletal changes is dependent on the severity of the disease, with the most severe alterations, as observed in the homozygous form, starting in early childhood (even in 1-year-old toddlers). Untreated children die before the age of ten. Optimally treated patients have a projected life span of 50–60 years (Kohne 2011). International standards exist for the treatment of β-thalassemia major (Cario et al. 2010). Hematopoietic stem cell transplantation as a curative approach is the first-line treatment if a donor can be found (Storb et al. 2003). The other patients need supportive chronic blood transfusions with iron removal (Cario et al. 2010). In cases of hemosiderin-related organ damage, specific treatment is required (Gattermann 2009; Cario et al. 2007). If the levels drop beyond 8 g/dL, transfusions should be initiated, usually for 1–3 weeks, to maintain baseline Hb levels of 9–10.5 g/dL, and target Hb levels of 13–13.5 g/dL.

Patients who require chronic blood transfusions are in danger of accumulating toxic degradation products, the most important being iron overload. To prevent iron overload, iron chelation is achieved by the application of desferrioxamine (DFX) and deferiprone (Drakonaki et al. 2010; Kellenberger et al. 2004).

About one-third of the children with thalassemia major receive DFX (Chan et al. 2002; Miller et al. 1993), which should be initiated when the ferritin concentration repeatedly exceeds 1000 ng/mL (Cario H et al. 2010). It is usually applied as a subcutaneous infusion for 5–7 days per week. The patients must be monitored for reduced growth, bone damage, high frequency hearing loss, and retinal damage (Cario H et al. 2010). The dysplastic changes in transfused patients who started chelation therapy below the age of 3 years, and at higher dosage, are reportedly more severe, and more common (Resnick 2002).

A newer drug, deferasirox, seems to be a well-tolerated iron chelator in tablet form (in a dose of 20 mg/kg BW/day in β-thalassemia major (Gattermann 2009; Cario et al. 2007), which has yet to be tested in long-term studies. Side effects include kidney failure, agranulocytosis, and liver failure (Gattermann 2009; Cario et al. 2007).

In patients with splenomegaly and hypersplenism, leading to an increased need for transfusions, splenectomy is indicated.

Osteoporosis may occur in up to 90 % of patients with thalassemia, even under optimized transfusion and chelation protocols (Goni et al. 1995). Bisphosphonates are applied to treat the coexisting osteoporosis.

Therapy also includes transplantation of erythropoietic cells, and the administration of sex hormones.

2.2.2 Mechanisms and Histology

2.2.2.1 Anemia

The major form is characterized by a total lack of β-chains, whereas they are decreased in the minor form. Consecutively, excessively produced unnecessary α- chains (the construction of tetramers is not possible) adhere to the membrane of the red blood cells, damage it, and form toxic aggregates (Weatherall and Provan 2000).

The formation of abnormal hemoglobin molecules results in microcytic hypochromic anemia, hepatosplenomegaly, and extramedullary hematopoiesis, with subsequent skeletal deformities (Cooley and Witwer 1927; Tunaci et al. 1999).

2.2.2.2 Treatment-Related Changes

Multiple transfusions suppress the overactivity of the bone marrow, and thus, reduce ineffective erythropoiesis and bone marrow expansion. However, chronic transfusion therapy leads to increased hemolysis (Levin et al. 1995), resulting in accumulation of degradation products, especially iron overload. Iron deposition with hemosiderosis is seen in the bone marrow. Other organs include the liver, spleen, pancreas (the pancreas is especially affected after splenectomy), lymph nodes, kidney, heart, pituitary gland, and in some cases, also the breast.

In addition, hyperuricemia may occur (Tyler et al. 2006).

Growth retardation in transfused patients with iron overload is attributed to hypothalamic/pituitary system iron deposition, and is typically seen after the age of 11 years.

Prevention of iron overload can be performed by iron chelation with desferrioxamine (DFX) and deferiprone (Drakonaki et al. 2010; Kellenberger et al.

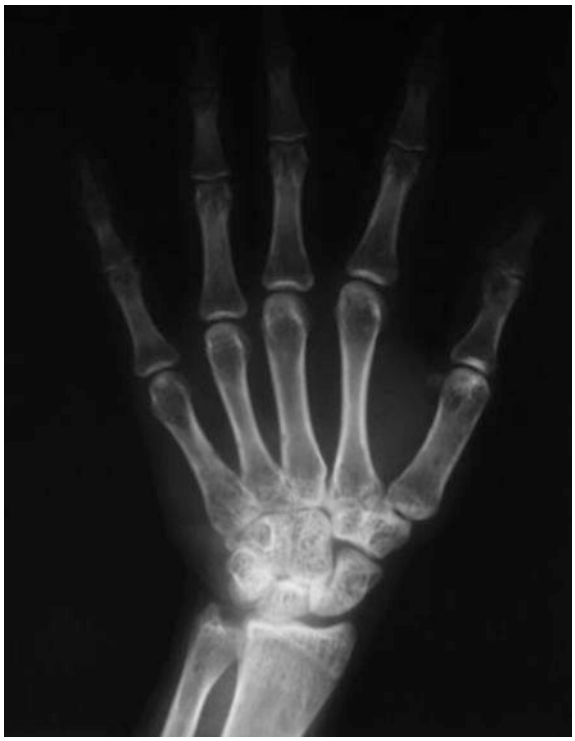

Fig. 8 Anteroposterior plain film of the hand of a patient with thalassemia, demonstrating coarse trabeculations due to bone marrow expansion (courtesy of Prof. Dr. Remide Arkun)

2004). However, those drugs may also cause toxic skeletal changes.

Desferrioxamine seems to inhibit osteoblastic activity and alter metaphyseal collagen synthesis (Chan et al. 2002), resulting in altered enchondral ossification and bone growth retardation. Dysplastic changes have been described in approximately one-third of these patients. About one-third of the children, in whom desferrioxamine therapy was initiated in early childhood, show growth retardation (Olivieri et al. 1992). If the optimized therapy was started after 5 years of age, but before 11 years, no significant height difference, compared to the mid-parental height, was observed (Bronspiegel-Weintrob et al. 1990).

Treatment-related toxicity has to be recognized, including visual and auditory neurotoxicity.

Bone marrow infarcts and epiphyseal osteonecrosis are observed less frequently.

2.2.3 Imaging Characteristics of Osseous Changes

2.2.3.1 Anemia-Related Findings

General features of bone structure and bone mineral density

Excessive expansion of the hematopoietic bone marrow leads to bone marrow trabecular coarsening and loss (Fig. 8), and to reabsorption of the cortex. The nutrient vessels and foramina may be enlarged. A generalized decrease in bone mineral density is observed in up to 90 % of the patients even though transfusion, chelation, sex hormone, and bisphosphonate therapy are optimized (Goni et al. 1995; Tunaci et al. 1999; Tyler et al. 2006). The osteopenia or osteoporosis is visible in projection radiographs, and can be quantified by the use of single-photon absorptiometry and dual-energy absorptiometry (DXA). A coarse "cobwebbing" trabecular pattern has been described (Tyler et al. 2006).

Typically, the spine, the skull, and the facial bones are involved, as well as the ribs and the metaphyses of the long bones (Tyler et al. 2006).

Typical site-specific features include:

The **skull** and the **facial bones**:

In the skull, increased hematopoiesis causes widening of the diploic space, with thinning of the outer table and thickening of the inner table (Resnick 2002) (Fig. 9). The process starts in the frontal region, and spares the occipital bone, which has a low bone marrow content. Together with early fusion of the occipital sutures, this leads to remodeling of the skull, i.e., the so-called "tower" skull (Martinoli et al. 2011). A characteristic, but rarely seen "hair-on-end" appearance (Fig. 10), occurs in the untreated child, resulting from spiculated periosteal calcification (Tunaci et al. 1999; Tyler et al. 2006; Reimann 1973).

The expansion of the facial bones inhibits the pneumatization of the perinasal sinuses (except for the ethmoidal cells, as the bony walls are low in red marrow (Fig. 11). The frontal, maxillary, and zygomatic "bossing" leads to lateral displacement of the orbits, and to maxillary protrusion with ventral displacement of the front teeth in up to 17 % of patients ("rodent" or "chipmunk" faces) (Tunaci et al. 1999; Abu Alhaija et al. 2002). This appearance is pathognomonic for thalassemia. The nasal bridge may be widened. If the growth center of the mandibular condyles is involved, the mandibular base length is reduced. In case of a thickened skull, fibrous dysplasia,

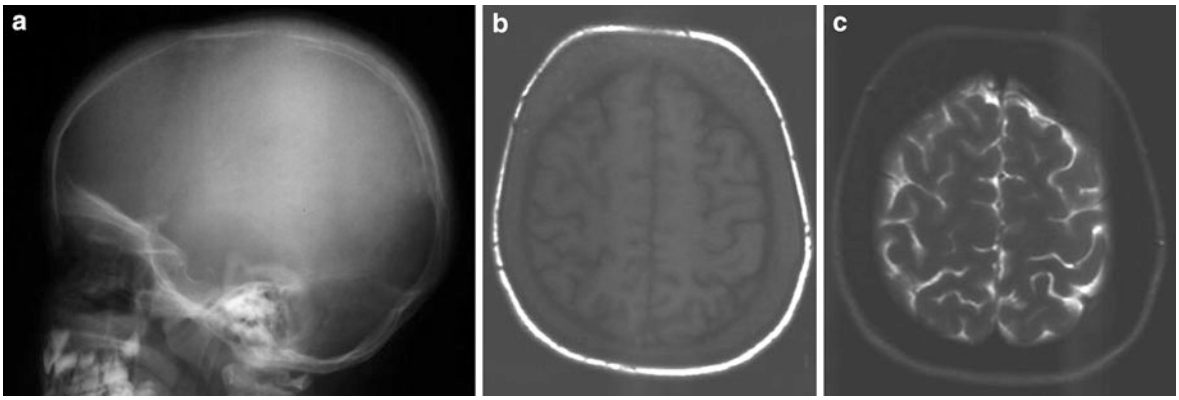

Fig. 9 Lateral projection radiograph (**a**) and MRI (**b**, **c**) exam of the cranium, in thalassemia showing increased density at the diploic space (**a**) and thickening and decreased signal intensity on both T1-weighted (**b**) and T2-weighted (**c**) axial images (courtesy of Prof. Dr. Remide Arkun)

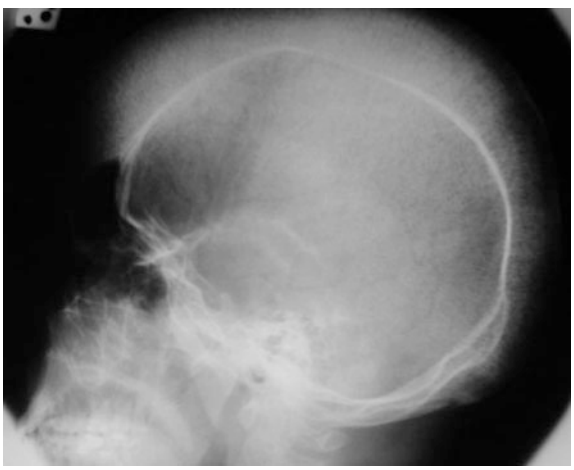

Fig. 10 Hair-standing-on-end appearance in an untreated thalassemic patient (courtesy of Prof. Dr. Remide Arkun)

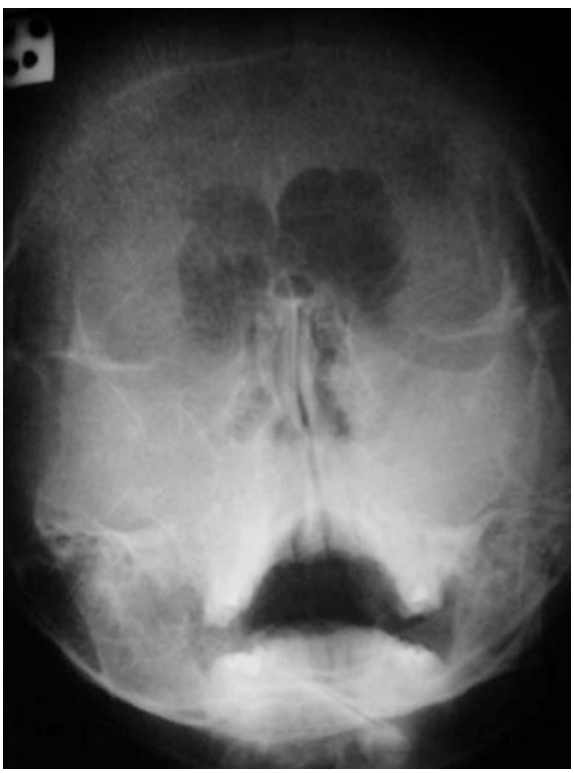

Fig. 11 Projection radiograph of the skull in an untreated thalassemic patient. Obliteration of maxillary sinuses due to bone marrow expansion (courtesy of Prof. Dr. Remide Arkun)

hypoparathyroidism, Paget's disease, or acromegaly should be considered as differential diagnoses.

Spine:

The medullary expansion first causes an increased height/width ratio. This phenomenon in untreated patients has been attributed to the opposing forces of weight bearing and marrow expansion. However, the subchondral bone thickness is decreased. As a consequence, the patients are prone to multisegmental osteoporotic end-plate compression fractures (Giardina et al. 1995). The vertebrae are usually biconcave or wedge-shaped, whereas H-shaped vertebra are, in contrast to sickle cell anemia, only rarely seen in thalassemia patients. On projection radiography, the displaced end-plate may appear as an additional line, with the so-called "bone-in-bone" sign (Tyler et al. 2006; Williams et al. 2004).

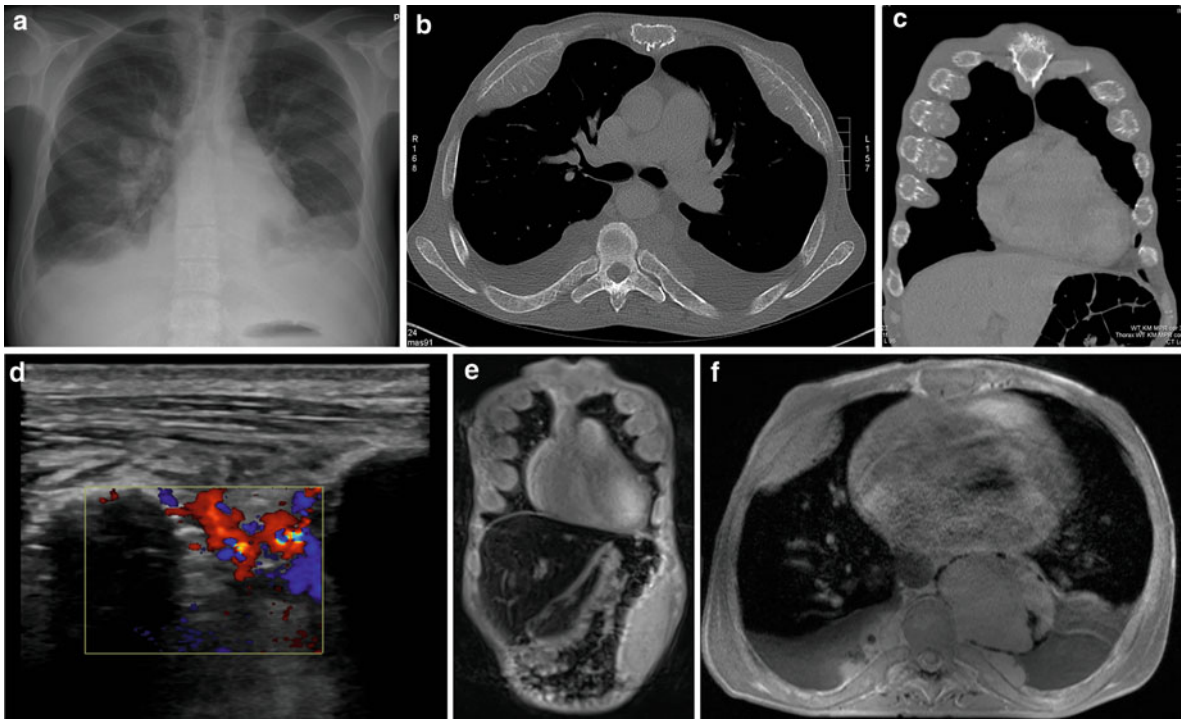

Fig. 12 A 41-year-old thalassemic patient, who reportedly had received few transfusions in his past medical history, without chelation therapy. The projection radiograph (**a**) of the thorax in the posterior-anterior projection shows extension of the ribs, especially at and near the costrochondral junctions. Extramedullary erythropoiesis was manifested as large paravertebral masses (courtesy of Dr. Helmut Prosch). The computed tomography scan of the same patient (**b**, axial, and **c**, coronal reconstruction) depicts widening of the bone, and spiculations due to excessive hematopoiesis (courtesy of Dr. Helmut Prosch). An ultrasound of the ribs (**d**) demonstrates extramedullary hematopoiesis with increased vascularization and blood flow (courtesy of Prof. Dr. Gerd Bodner). An MRI, with a coronal (**e**) and axial (**f**) T1w VIBE sequence shows the space-occupying extramedullary hematopoiesis; note the rim-like iron deposition around the largest of the masses

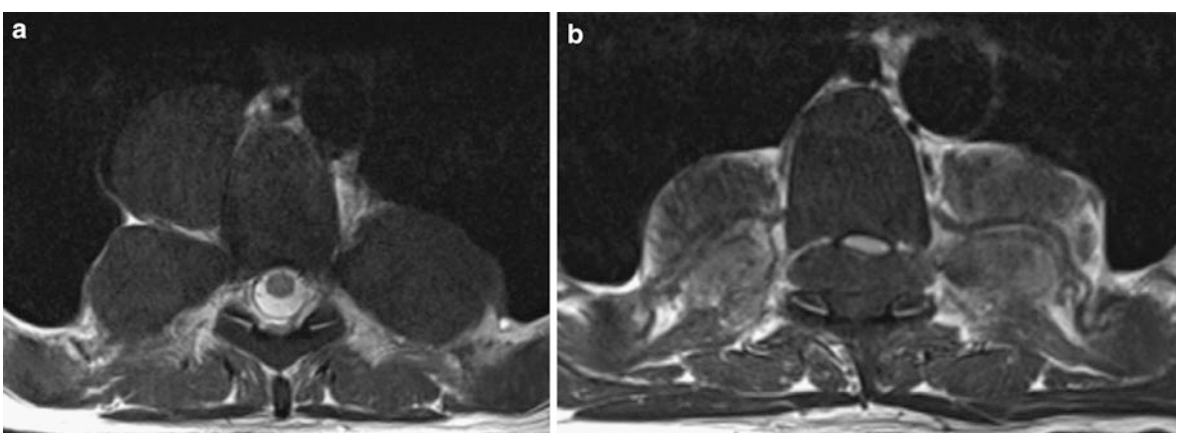

Fig. 13 A thalassemic patient with MR images of the thoracic spine. The axial T2w (**a**) and contrast-enhanced T1w (**b**) sequences reveal excessive paravertebral extramedullary hematopoiesis. Note the spinal stenosis with medullary compression in **b**, and the spiculation of the paravertebral masses (courtesy of Prof. Dr. Bruno VandeBerg)

Multisegmental fractures lead to axial deviations (Fig. 12) with scolioses and kyphoses (Fig. 17). The prevalence of scoliosis is associated with a low hematocrit, high ferritin levels, and long-standing DFX treatment, and has been reported to be 20 % for thalassemia patients in a Greek study (versus 6 % in the general population (Korovessis et al. 1996)).

MRI shows an increase of hematopoietic marrow with a red marrow predominance. Early degeneration of the intervertebral discs is seen, especially in the lumbar and lower thoracic segments.

Dorsal expansion of the hematopoietic marrow may cause spinal canal stenosis (Kalina and Hillstrom 1992) (Fig. 13). This most often occurs in the thoracic spine.

Ribs: (Figs. 12, 13)

The changes are most pronounced near the costovertebral joints (Tunaci et al. 1999; Lawson et al. 1981). The extension of the hematopoietic marrow beyond the original margin causes aggressive cortical destruction, with a complex periosteal reaction, such as spiculation. Spiculation is otherwise considered indicative of malignancy, as is often seen in osteosarcoma. On projection radiographs, the marrow extension may also lead to a "rib within-rib" appearance.

Long bones:

Extension of the hematopoietic marrow leads to a widening of all parts of the bone, causing a flask-like appearance in the epiphyses and metaphyses (in more severe cases), and loss of the diaphyseal concavity (Tyler et al. 2006). Those changes are most common in the humerus and femur. An involvement of the hands and feet is more common in children than in adults.

"Growth arrest lines" in the metaphyses of the proximal humerus and distal femur represent alternate growth arrest and recovery (Resnick 2002). In 10–15 % of the children with Cooley's anemia, premature growth plate fusion with growth arrest is seen as a sequel (Tyler et al. 2006). This is more common in the humerus than in the femur (Wonke 1998).

Premature physeal fusion has been described overall in 17 % of thalassemia patients (Currarino and Erlandson 1964). The resulting limb shortening can be uni- or bilateral. A large length discrepancy may necessitate surgery (Naselli et al. 1998).

Other bones:

Paradoxically, the iliac crest and other secondary ossification centers show delayed fusion.

Extramedullary hematopoiesis: Typically, multiple symmetrical paravertebral and presacral masses are observed (Figs. 13, 14). They appear round or ovoid and confluent (Gilkeson et al. 1997; Loh et al. 1996). The signal intensity is variable on T2-weighted sequences, intermediate T1-signal, with mild gadolinium enhancement.

Other manifestations include other organs with pluripotent stem cells. The liver, the spleen, the adrenal glands, and, in some cases, the breasts, are also involved.

99mTechnetium (Tc)-labeled sulfur colloid may help define the hematopoietic nature of extramedullary masses (Gilkeson et al. 1997; Tunaci et al. 1999).

Complications:

Insufficiency fractures occur in approximately one-third of untreated patients with thalassemia major. They often affect the femur, tibia and fibula, and may be multifocal, and recurrent.

2.2.3.2 Treatment-Related Findings and Related Complications:

Patients who receive multiple blood transfusions without iron overload prevention and high iron levels:

- show signal alterations in the hematopoietic bone marrow of the axial and the peripheral skeleton, due to iron deposition (Fig. 15). On MRI, this results in a signal decrease on T2w images (Argyropoulou et al. 2000), and T1w images (Levin et al. 1995) (Fig. 16), and, typically, increased susceptibility artifacts, especially on GRE sequences (Jelbert et al. 2009). In CT, areas of high attenuation can be depicted (Resnick 2002).
- show alterations of the synovia and the articular cartilage.
- may develop calcium pyrophosphate dihydrate crystal deposition disease (CPPD) with chondrocalcinosis and associated findings (Resnick 2002).
- may, less frequently, develop early degenerative osteoarthritis (Tyler et al. 2006), due to secondary hemochromatosis, especially in the larger joints (more than in primary hemochromatosis), and in the metacarpophalangeal joints. Features are loss of the joint space, osteophytes, subchondral cysts, and flattening and collapse of the subchondral bone, as well as sclerosis. An association with seronegative arthritis

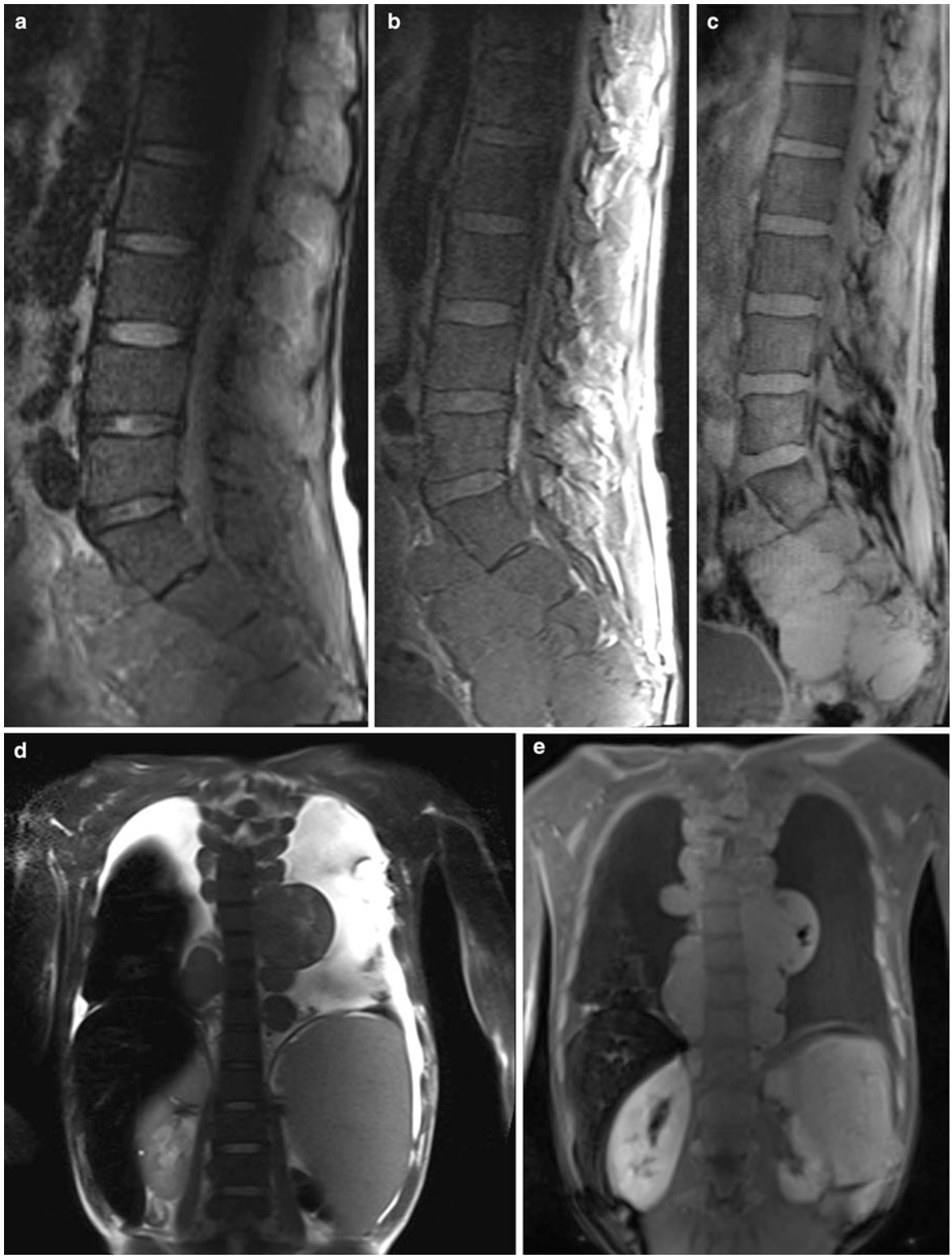
a
b
c
d
e

◀ **Fig. 14** Sagittal MRI of the lumbar spine and the sacrum in a patient with β-thalassemia major, with turbo inversion recovery magnitude (TIRM) (**a**), T1w (**b**), and GRE T1w opposed-phase (**c**) sequences, depicts excessive extramedullary hematopoietic masses in the presacral space. Signal alteration of the bone marrow is visible, with diffuse low signal intensity throughout the vertebral marrow as a sign of red marrow hyperplasia on T1w, leading to a bright disc sign. The bone marrow signal on the opposed-phase image is brighter, due to an imbalance between the fat/water content of the marrow. A coronal HASTE sequence (T2w, **d**) and VIBE (T1w 3D GRE, **e**) depict marked hepatosplenomegaly with signal intensity loss in the liver on T2 and on the T1w GRE sequence due to iron deposition in the liver in hemosiderosis. Note the splenomegaly due to extramedullary hematopoiesis and portal hypertension (courtesy of Dr. Helmut Prosch)

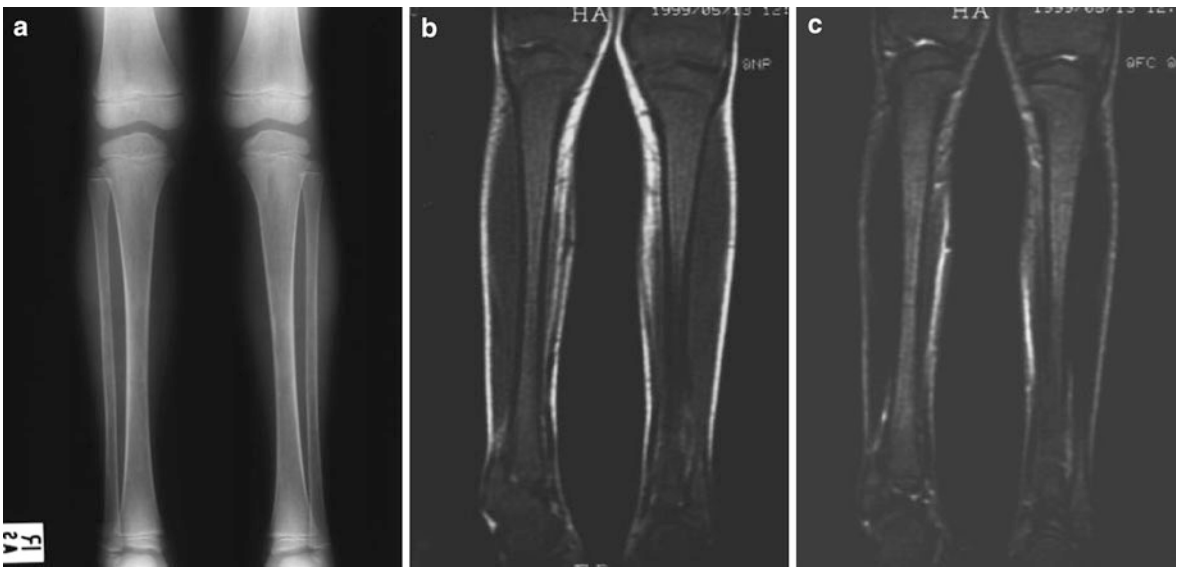

Fig. 15 A 14-year-old thalassemic patient, who received iron-chelation therapy, showed no abnormality on plain radiography of both lower legs (**a**). MRI showed decreased signal intensity on both T1-weighted and T2-weighted coronal images due to iron deposition in the bone marrow (**b**) (courtesy of Prof. Dr. Remide Arkun)

has been described. The joints including and distal to the knee and elbow are involved, with mild synovitis, effusions, joint space narrowing, and periarticular osteoporosis (Dorwart and Schumacher 1981).

- may develop hyperuricemia and show gout-related changes at typical (small joints of the hands and feet) and atypical sites (sacroiliac joint) (Tyler et al. 2006). As the gout is painful, and usually treated, the manifest disease is seen infrequently. Manifest radiographic changes (with precipitated urate crystals in a protein-rich mass in regions of low pH) often lead to asymmetric synovial, tendovaginal, and bursal crystal deposition, and, in chronic disease, to tophaceous gout in the soft tissue and bone. In MRI, the gout nodules are hyperintense on T2, and do not enhance, but show surrounding granulation tissue with intense contrast enhancement.
- have an increased risk of developing osteonecrosis (Fig. 17), infection, and growth disturbance.

Medication for preventing iron overload also causes osseous changes (Chan et al. 2002; Miller et al. 1993). Higher doses and earlier onset of iron chelation treatment lead to a higher incidence and more severe changes (Kellenberger et al. 2004; Diav-Citrin and Koren 1997). It is very important to recognize the sequelae of desferrioxamine (DFX) early, with subsequent dose reduction or a switch to deferiprone (Chan et al. 2000, 2002).

Desferrioxamine

- DFX typically affects the growth plates: children often develop dysplastic bone changes even under optimized therapy (Chan et al. 2002; Miller et al. 1993). Annual projection radiographs of the left hand have been recommended to assess dysplastic changes and to estimate the osseous age and potential growth retardation (Tyler et al. 2006).
- The long bones, especially the region around the knee and the distal ulna and radius, are affected most

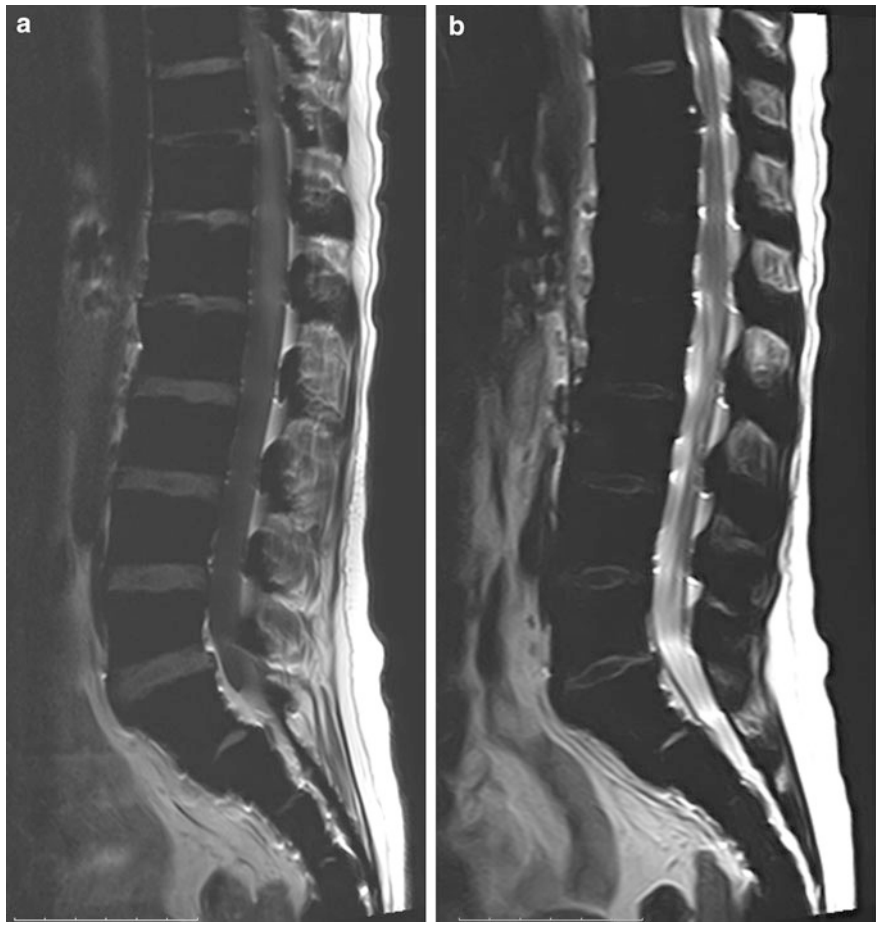

Fig. 16 MRI of the lumbar spine in a patient with thalassemia and multiple transfusions. Excessive iron deposition leds to extreme hypointensity on sagittal T1w (**a**) and T2w (**b**) sequences (courtesy of Dr. Falk Miese)

frequently (Orzincolo et al. 1988). Initially, a broad band-like zone of sclerosis is visible across the metaphysis, progresses toward the diaphysis, and may look flame-shaped (Tyler et al. 2006). More lucent areas might be visible within the sclerosis. Later, widened growth plates—especially at the periphery—and a blurred interface between the physis and metaphysis (resembling rickets) can be observed (Tyler et al. 2006). In MRI, the metaphyseal changes are hypointense on T1w sequences, and hyperintense on T2w (Drakonaki et al. 2010). The epiphyses are involved less frequently. Severe epiphyseal dysplasia may lead to genu valgum or varum, or cause slipped femoral heads, which necessitates surgery. Subchondral cystic defects and irregular sclerosis may also be observed.

- Premature growth plate fusion occurs only rarely in transfused and chelated patients (Goni et al. 1995). Growth retardation, however, is common, as a sequela of either the DFX therapy or of the thalassemia itself. Whereas the thalassemia-related growth retardation is known to occur mainly after the age of 11 years, one-third of the children in whom the DFX therapy was started before they had reached the age of 11 years showed impaired growth (Olivieri et al. 1992). Ninety percent of those patients had a body height below the 15th percentile.
- In the spine, platyspondyly is typical, with diffuse vertebral flattening and anteroposterior widening (De Sanctis et al. 1996). The changes are most common in the thoracic and lumbar sections, with anterior tapering of the upper thoracic spine (De Sanctis et al. 1996; Hartkamp et al. 1993) and a short trunk. Sclerosis of the costochondral junction may be visible.
- A low body weight (< 15th age percentile in 90 %) has also been observed (Chan et al. 2002).
- In patients with low iron levels, DFX also interferes with zinc, copper, and cobalt levels, further worsening the symptoms (a zinc deficiency is also associated

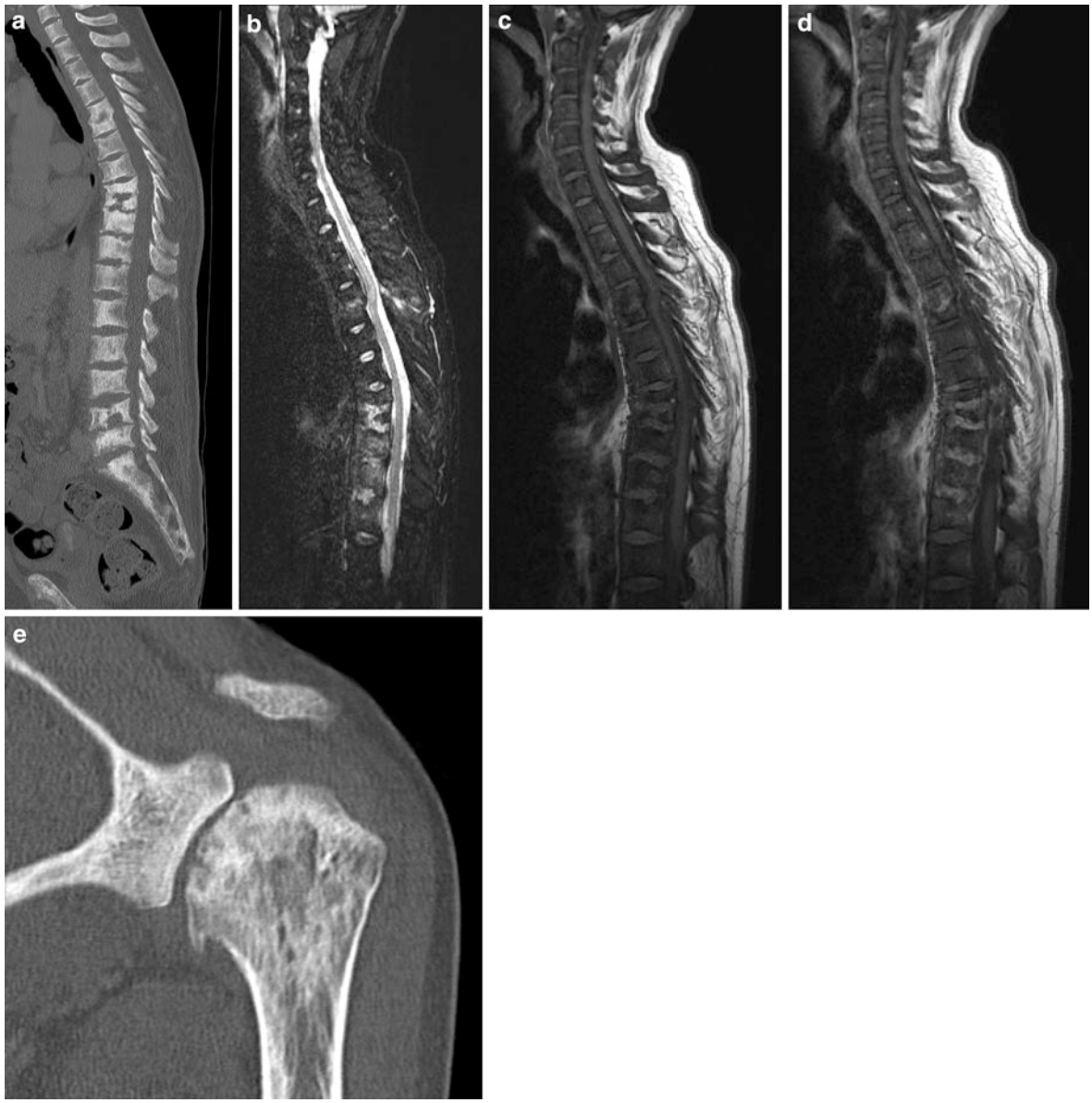

Fig. 17 A sagittal CT scan reconstruction of the vertebral spine (**a**) in a patient with thalassemia major shows inhomogeneous sclerosis in bone marrow infarcts, with subsequent multisegmental fractures. The corresponding MRI demonstrates edema around the more recent fractures in the STIR sequence (**a**), and inhomogeneous low signal on T1, due to sclerosis and iron deposition evident on the T1w sequence (**b**), with patchy contrast enhancement (**c**). Note the kyphosis and deviation of the dorsal alignment at level Th4/5, with incipient spinal stenosis and myelopathy, corresponding to the patient's neural symptoms. A coronal reconstruction of the left shoulder region in the same patient depicted avascular necrosis of the humeral head (**d**) (courtesy of Prof. Dr. Andrea Baur-Melnyk)

with delayed skeletal maturation and growth reduction) (Brill et al. 1991). Overdosage has to be avoided.

- Nonosseous alterations include auditory and visual impairment.

Deferiprone:

- Arthropathy has been described in up to 64 % of the patients receiving deferiprone (Kellenberger et al. 2004). The symptoms commonly begin within the first 8 months of treatment, are more severe in higher doses, and are reversible when the drug is stopped. (Kellenberger et al. 2004).

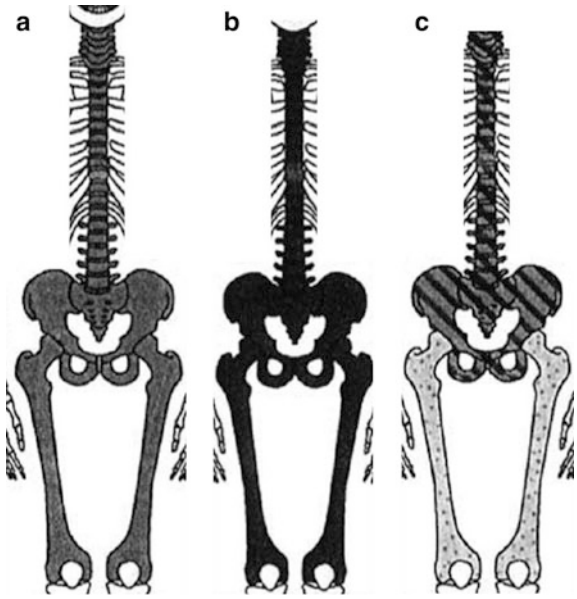

Fig. 18 Schematic drawing of bone marrow distribution and deposition in three groups of thalassemic patients: **a** untreated (neither transfused nor chelated); **b** hypertransfused but not chelated; and **c** hypertransfused and chelated

Typically, the knee region is involved, with cartilage and subchondral damage. In the earlier phase, the side effects are characterized by synovitis with iron deposition, joint effusion, swelling, and pain, (Fig. 17) which leads to flattening of all articular surfaces (femoral condyles, tibial plateau, and patella). After termination of the therapy, there is usually only minor improvement.

- An important nonosseous side effect is the development of agranulocytosis.
- The treatment regimen influences bone marrow distribution and iron deposition. Three different patterns have been observed in thalassemia patients. (Levin et al. 1995) (Fig. 18).

(a) Patients who never or rarely received transfusions do not show the physiologic age-dependent conversion pattern. They retain red marrow in the central and peripheral skeleton, extending to the distal femur.

(b) Unchelated patients with chronic transfusion therapy, and with elevated serum ferritin levels, develop iron deposition in both the central and the peripheral skeleton, especially in regions of red marrow. On MRI, the signal in T1w and T2w sequences is markedly reduced. There is only minor bone marrow extension. (Fig. 16).

(c) In patients with an optimized protocol of hypertransfusion and chelation, the iron chelation visible in MRI is mainly restricted to the axial skeleton.

Differential diagnosis of skeletal changes/Dysplasia: (Tyler et al. 2006):

- Rickets and thalassemia:

In these two disorders, there is splaying and fraying of the metaphyses, blurring of the metaphyseal margins, and widening of the growth plates. Due to weight bearing, the metaphyses might become cupped. There is decreased bone density, and the hypointense linear band of calcification (provisional) at the metaphyses on MRI is lost.

Rickets is characterized by a more symmetrical (central and peripheral) widening of the physes.

Chondrodysplasia:

Although rickets and thalassemia both show metaphyseal cupping, physeal widening is less pronounced. There is also epiphyseal flattening and fragmentation.

Scheuermann's disease:

In this disorder, there is anterior wedging of both vertebral bodies, leading to kyphosis.

However, there is typically no platyspondyly, and only a few vertebrae are involved, with onset at puberty.

2.3 Other Corpuscular Inherited Hemolytic Anemias

Other corpuscular inherited hemolytic anemias include hereditary spherocytosis and elliptocytosis. The structural red blood cell aberration also leads to early destruction in the spleen. Resulting marrow hyperplasia may lead to diploic widening, with thinning of the tabula externa. These forms of hemolytic anemias often manifest later, in the juvenile, and growth retardation is rare. Splenectomy may be performed, reducing the anemia and the skeletal sequelae.

3 Primary Anemias and Bone Marrow Insufficiency

3.1 Aplastic Anemias

3.1.1 Etiology and Clinical Background

Aplastic anemia is an uncommon disease. In the majority of patients (in about 50–70 % of cases), the pathogenesis cannot be determined, and those cases are termed idiopathic. Among the inherited forms, the

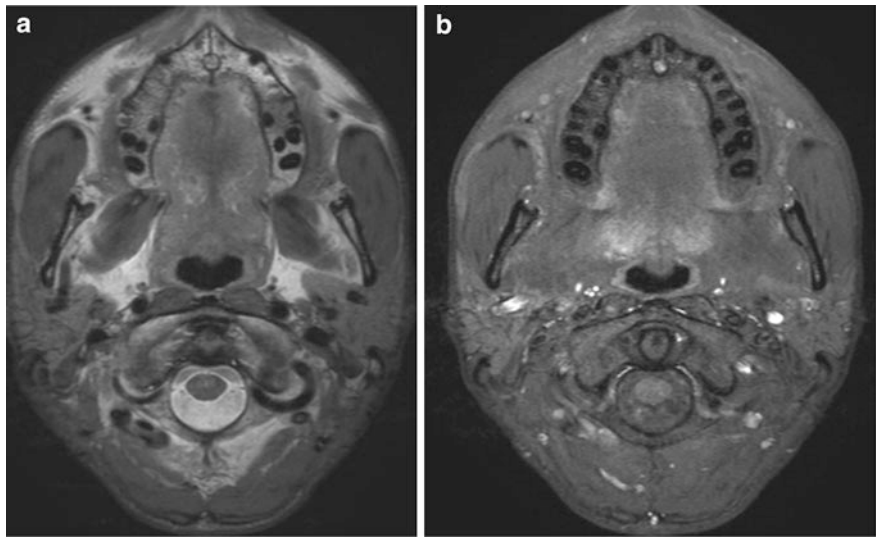

Fig. 19 MRI of the head. Axial TIRM (**a**) and T1 w (**b**) sequence show a water-like signal from the bone marrow. The subcutaneous fat is also consumed, with remaining loose vascular connective tissue

most common is the Fanconi anemia. Multiple conditions have been described as comprising a predisposition for the acquired forms (Young 1999). Aplastic anemia may occur in autoimmune disorders (Young 2000) (such as systemic lupus erythematosus (SLE) or rheumatoid arthritis), during pregnancy or in paroxysmal nocturnal hemoglobinuria (PNH), or develop in association with drugs such as chloramphenicol, chloroquine? D-penicillamine, estrogen; nonsteroidal antiphlogistics, such as indomethacine? and ibuprofen; anticonvulsive drugs, such as carbamazepin, phenytoin, and sulfonamide; or with toxins (e.g., gold, bismuth salts, arsenic, benzols). Aplastic anemia can also develop in patients with hepatitis (A, B, C), or other viral infections (parvovirus B19, herpes [EBV, CMV, HHV-6]) and HIV (Barrett et al. 2000; Hohloch et al. 2003).

3.1.2 Mechanisms and Histology

Aplastic anemia is characterized by decreased or absent hematopoietic precursors in the bone marrow due to a failure of the stem cells, resulting in pancytopenia in the peripheral blood.

Diagnosis is confirmed by bone marrow aspirate and trephine biopsy (Gupta et al. 2007). Histologically, the marrow consists mainly of stromal and fat cells and is hypocellular, with morphologically normal residual hematopoietic cells. No signs of fibrosis are present.

Treatment: Depending on the severity of the AA, supportive therapy must be administered. In case of a causative agent, that agent should be withdrawn. In autoimmune-mediated severe aplastic anemia, the treatment of choice in younger patients is bone marrow transplantation (BMT). In moderate AA, in or in older patients, or if no compatible donor can be found, immunosuppressive agents are administered. Immunosuppression is initiated with antithymocyte globulin (ATG), cyclosporine, or a combination of both (Marsh et al. 2003). Successful therapy leads to regrowth of active hematopoietic cells.

Without treatment, the chronic disease deteriorates gradually, and also leads to an increased risk of complications, such as infection or bleeding.

3.1.3 Imaging Findings

3.1.3.1 MRI

Aplastic anemia is characterized by an increase of fat, resulting in high signal on T1w sequences, and low signal in fluid-sensitive, fat-saturated images (as TIRM, T2w fat-saturated or PD fat-saturated sequences) (McKinstry et al. 1987; Amano and Kumazaki 1997).

In milder pancytopenia, a mottled bone marrow pattern at the time of diagnosis may be present (De Mola and Kurre 2009).

Treatment-related findings: As a sign of response to therapy, initially, patchy red marrow islands within the otherwise fatty bone marrow are apparent on MRI (Park et al. 2001). Later, the areas of hematopoietic marrow grow and may be confluent. The changes may also become diffuse. Like reconversion, the process is

likely first depicted in the axial skeleton, especially the vertebral spine (McKinstry et al. 1987; Kaplan et al. 1987). The extent of cellular marrow after bone marrow transplantation has been found to be higher than under immunosuppressive therapy (Park et al. 2001). The pattern during treatment, however, is unspecific (and therefore, cannot be safely differentiated from hematologic malignancy) (Gupta 2007).

Patients in long-term remission may retain a patchy bone marrow pattern (Hotta et al. 1990).

3.2 Serous Atrophy

3.2.1 Etiology and Clinical Background

Serous atrophy of the bone marrow is a condition that is seen in cachectic carcinoma patients, in anorexia nervosa, and in patients with (HIV) human immunodeficiency virus infection, as well as in emphysema, chronic renal failure, and in tumor patients with advanced carcinomas (Vande 1994; Eustace et al. 1994; Seaman et al. 1978; Smith and Spivak 1985; Amano and Kumazaki 1996; Amano et al. 1996).

In anorectic patients, hematologic alterations are found with an increased prevalence. The severity of anorexia is correlated with anemia and leukopenia.

3.3 Mechanism and Histology

Histology reveals fat atrophy and a marked increase in extracellular gelatinous material. Presumably, the blood supply of the marrow is also reduced (Amano and Kumazaki 1996). In those patients, the subcutaneous tissue is replaced by loose vascular connective tissue.

3.3.1 Imaging Findings

MRI depicts a water-like signal from the bone marrow, with low signal intensity on T1w images, and high signal intensity on fluid-sensitive sequences (also on fat-saturated sequences like the TIRM or PD FS) (Vande Berg et al. 1994; Eustace et al. 1994) (Fig. 19). This pattern is an unspecific one, also seen in reconversion or cell infiltration. The application of gadolinium-based contrast agent helps to differentiate serous atrophy from metastases or other forms of bone marrow infiltration. In contrast to those conditions, no contrast enhancement of the bone marrow is depicted in serous atrophy. The soft tissue behaves differently: the normal subcutaneous fatty tissue is consumed; the remaining loose vascular connective tissue enhances with contrast agent administration (Amano and Kumazaki 1996).

4 Inherited Anemias in Childhood

4.1 Epidemiology and Clinical Background

Inherited anemias are rare disorders. The underlying pathophysiological mechanism is a bone marrow failure that causes hypocellularity involving all or only the red blood cell lineage.

Inherited bone marrow failure syndromes are composed of a heterogeneous group of disorders, whose nomenclature and classification is very complex and still a matter of debate. These different entities represent the childhood manifestation of aplastic anemia, mostly occurring at 2–5 years of age (Alter 2003). In three of four children with inherited bone marrow failure, an identifiable cause can be found (Teo et al. 2008). The major inherited causes in children are Fanconi's anemia (incidence of 1 per 350000 births), congenital dyskeratosis, Shwachman-Diamond syndrome, and congenital amegakaryocytic thrombocytopenia (Kim and Miller 2002). These bone marrow disorders are usually associated with one or more somatic abnormalities, and do not necessarily demonstrate complete pancytopenia, particularly during the early phases of disease. They often present in childhood, but may not do so until adulthood in some cases. The clinical presentation is variable and includes symptoms and signs related to cytopenia in each of the three blood cell lineages (Dokal and Vulliamy 2010). Accordingly, the following symptoms may occur solely or in combination:

- Hemorrhagic manifestations caused by thrombocytopenia
- Fatigue and pallor secondary to progressive anemia
- Fever, bacterial infections, and mucosal ulcerations resulting from neutropenia

In the early stage, the blood count may be mildly abnormal. In children who present with persistent or progressive unexplained cytopenia, particularly with involvement of two or more cell lines and display short stature or other dysmorphic clinical signs, a further evaluation is mandatory.

4.2 Histology, Genetics, and Clinical Manifestation

The diagnosis is established by bone marrow aspiration and biopsy. Typical findings are a hypocellular bone marrow with a decrease in all hematopoietic elements. The marrow space is dominated by fat cells, lymphocytes, and marrow stroma. Often, dysplastic features may be present. However, malignant infiltrates are absent.

Inherited bone marrow failure syndromes are linked to specific genetic abnormalities.

Fanconi anemia is the most common form of inherited aplastic anemia (Alter 2003). It has an autosomal recessive trait and can also be X-linked recessive in small subsets. Multiple genes, spread widely throughout the genome, are responsible for Fanconi anemia, several of which are linked to tumor suppressor genes. Clinically, it is heterogeneous, with progressive development of bone marrow failure and cancer susceptibility (Dokal and Vulliamy 2010). The mean age of onset is 6-and-a-half years of age for boys and 8 years of age for girls (Alter 2003). The diagnosis may be delayed until adulthood, particularly for those patients for whom malignancy is the presenting clinical manifestation. The life expectancy is limited (Dokal and Vulliamy 2010). Fanconi's anemia is associated with developmental anomalies in a variety of organs. Skeletal abnormalities are encountered in 70 % of patients, half of which have radial ray abnormalities, more commonly affecting the thumb, with phalangeal hypoplasia and bifidity (Malizos et al. 2001; Alter 2003; Shimamura and Alter 2010). Other characteristic imaging findings include syndactyly, microdactyly, brachydactyly, pseudoepiphysis of the first metacarpal, growth retardation, hooked clavicles, Sprengel and Klippel-Feil deformities, and hip and spinal anomalies (Juhl et al. 1967; Minagi and Steinbach 1966).

Nonskeletal malformations include hypopigmented spots and café-au-lait spots, hypogonadism, and developmental delay (Shimamura and Alter 2010; Alter and Young 1994). Although short stature is a common abnormality, normal height does not rule out Fanconi anemia (Giampietro et al. 1997). Patients with Fanconi anemia are at high risk for the development of malignant diseases, particularly myelodysplastic syndromes, acute myelocytic leukemia, or squamous cell carcinomas (Kutler et al. 2003).

Dyskeratosis congenita is the second most common inherited bone marrow failure syndrome, characterized by a cancer predisposition and a variety of somatic manifestations. It has an X-linked recessive trait, an autosomal dominant trait, and can also be autosomal recessive in small subsets (Dokal 2000). Several genes are responsible for dyskeratosis congenita, and affect telomerase function (Walne et al. 2008). Clinical diagnosis is possible if the patient presents the triad of a reticulated hyperpigmented rash, nail dystrophy, and mucosal leukoplakia (Shimamura and Alter 2010). In the absence of these findings, the diagnosis may be missed or delayed. The mean age for the onset of bone marrow failure is 10 years of age, beginning with thrombocytopenia and anemia, followed by pancytopenia. Patients are at increased risk for developing a malignancy, particularly myelodysplastic syndrome, acute myelocytic leukemia, and squamous cell carcinomas. Malignancies occur mostly in the third and fourth decades of life (Dokal 1999; Alter et al. 2009).

Shwachman-Diamond Syndrome is another inherited bone marrow insufficiency, presenting in infancy with pancreatic dysfunction and skeletal abnormalities (Smith et al. 1996).

Amegakaryocytic thrombocytopenia presents in the newborn period with severe thrombocytopenia, subsequent bleeding into the skin, the mucous membranes, and the gastrointestinal tract (King et al. 2005), and progresses to severe aplastic anemia in early childhood (Young 1999; Alter 2003; King et al. 2005). In contrast to the other bone marrow failure syndromes, birth defects or developmental anomalies are not present.

4.3 Imaging Findings

The large majority of these conditions have not yet been investigated with imaging modalities (Martinoli et al. 2011). When studied, only scanty and often obsolete imaging reports are available, mainly describing ancillary findings, such as skeletal deformities or growth retardation (Cooley and Witwer 1927; Juhl et al. 1967; Minagi and Steinbach 1966). Knowledge of the normal age-dependent appearance is a prerequisite for the determination of aberrations, as delayed conversion might be the only imaging sign of anemia (Dooms et al. 1985; Cristy 1981).

5 Anemia in the Elderly

5.1 Epidemiology and Clinical Background

Anemia may be difficult to define in older adults. Normal values may be skewed toward anemic levels in an elderly population with a high incidence of chronic disease, malnutrition, or infection. There are additional underlying factors that contribute to the lowering of average hemoglobin levels in certain ethnic populations (e.g., heterozygote or homozygote carriers of thalassemia minima in African Americans (Beutler and West 2005)).

Anemia is common in the older adult population. The reported prevalence has a wide variability in the literature (between 2.9 and 51 % in males, and 3.3 and 41 % in females (Guralnik et al. 2004; Nissenson et al. 2003). The highest prevalence rates were found in nursing home residents and in hospitalized older adults, but anemia is also very prevalent in noninstitutionalized older adults (8–25 % (Patel 2008)).

While the anemia in the older adult is typically mild, it has been associated with substantial morbidity and mortality. Anemia has been found to be associated with decreased mobility (Penninx et al. 2003), muscle weakness (Penninx et al. 2004), falls (Penninx et al. 2005), and other related symptoms (depression, reduced quality of life (Thein et al. 2009)). Based on the available studies that have investigated anemia, it is still unclear whether increased morbidity or mortality is caused by the anemia itself or by the underlying diseases leading to anemia, or by comorbidities associated with anemia. It has been suggested that anemia, which potentially leads to generalized or local tissue hypoxia with a subsequent increase in cardiac output, could aggravate functional decline in the population of older adults. A strong association between anemia and mortality has been found in several studies (Chaves et al. 2004; den Elzen et al. 2009). This was true even in patients without obvious clinical disease (Izaks et al. 1999).

5.2 Etiology

The etiology of anemia in older adults was investigated in a case–control study (Price et al. 2010). The reasons for anemia were hematologic malignancies, including myelodisplastic syndrome (MDS) (22 %), iron deficiency (12 %), treatment for nonhematologic malignancies (11 %), inflammation (6 %), renal insufficiency (4 %), and other (10 %). In the majority of patients, the reason remained unexplained (35 %).

5.3 Imaging Findings

In the majority of patients, imaging findings are unspecific. CT and plain radiography provide only a very low sensitivity to alterations in the bone marrow. Imaging elderly anemic patients remains controversial. On the one hand, underlying hematologic malignancies have to be ruled out. On the other hand, MR cannot be generally recommended for the work-up in these patients for socioeconomic reasons. In addition, interpretation of the studies may be difficult. As in other fields of diagnostic radiology, it remains a challenge to differentiate between normal (successful aging) and abnormal findings.

References

Abu Alhaija ES, Hattab FN, al-Omari MA (2002) Cephalometric measurements and facial deformities in subjects with beta-thalassaemia major. Eur J Orthod 24:9–19

Adekeye EO, Cornah J (1985) Osteomyelitis of the jaws: a review of 141 cases. Br J Oral Maxillofac Surg 23:24–35

Adekile AD, Gupta R, Yacoub F, Sinan T, Al-Bloushi M, Haider MZ (2001) Avascular necrosis of the hip in children with sickle cell disease and high Hb F: magnetic resonance imaging findings and influence of alpha-thalassemia trait. Acta Haematol 105:27–31

Almeida A, Roberts I (2005) Bone involvement in sickle cell disease. Br J Haematol 129:482–490

Alter BP (2003) Inherited bone marrow failure syndromes. In: Nathan DG, Orkin SH, Ginsburg D, Look AT (eds) Nathan and Oski′s Hematology of infancy and childhood, Saunders, Philadelphia

Alter BP, Young AT (1994) Aplastic anemia:acquired and inherited. W.B. Saunders, Philadelphia

Alter BP, Giri N, Savage SA, Rosenberg PS (2009) Cancer in dyskeratosis congenita. Blood 113:6549–6557

Aluoch JR (1997) Higher resistance to Plasmodium falciparum infection in patients with homozygous sickle cell disease in western Kenya. Trop Med Int Health 2:568–571

Amano Y, Kumazaki T (1996) Case report: serous atrophy of bone marrow and subcutaneous tissue enhancement associated with recurrent rectal carcinoma: MR appearances. Comput Med Imaging Graph 20:183–185

Amano Y, Kumazaki T (1997) Proton MR imaging and spectroscopy evaluation of aplastic anemia: three bone marrow patterns. J Comput Assist Tomogr 21:286–292

Amano Y, Kumazaki T, Amano M (1996) MR images of bone marrow in aplastic anemia and correlation between MR findings and age. Nihon Igaku Hoshasen Gakkai Zasshi 56:546–549

Amundsen TR, Siegel MJ, Siegel BA (1984) Osteomyelitis and infarction in sickle cell hemoglobinopathies: differentiation by combined technetium and gallium scintigraphy. Radiology 153:807–812

Anand AJ, Glatt AE (1994) Salmonella osteomyelitis and arthritis in sickle cell disease. Semin Arthritis Rheum 24: 211–221

Argyropoulou MI, Metafratzi Z, Kiortsis DN, Bitsis S, Tsatsoulis A, Efremidis S (2000) T2 relaxation rate as an index of pituitary iron overload in patients with beta-thalassemia major. AJR Am J Roentgenol 175:1567–1569

Atkins BL, Price EH, Tillyer L, Novelli V, Evans J (1997) Salmonella osteomyelitis in sickle cell disease children in the east end of London. J Infect 34:133–138

Babhulkar SS, Pande K, Babhulkar S (1995) The hand-foot syndrome in sickle-cell haemoglobinopathy. J Bone Joint Surg Br 77:310–312

Bahebeck J, Ngowe M, Monny-lobe M, Sosso MA, Hoffmeyer P (2002) Fracture de stress du fémur dans la drépanocytose. Une complication rare.Rév Chir Orthop 88:816–818

Bahebeck J, Atangana R, Techa A, Monny-Lobe M, Sosso M, Hoffmeyer P (2004) Relative rates and features of musculoskeletal complications in adult sicklers. Acta Orthop Belg 70:107–111

Bailey K, Morris JS, Thomas P, Serjeant GR (1992) Fetal haemoglobin and early manifestations of homozygous sickle cell disease. Arch Dis Child 67:517–520

Barden EM, Kawchak DA, Ohene-Frempong K, Stallings VA, Zemel BS (2002) Body composition in children with sickle cell disease. Am J Clin Nutr 76:218–225

Barrett J, Sauntharajah Y, Molldrem J (2000) Myelodysplastic syndrome and aplastic anemia: distinct entities or diseases linked by a common pathophysiology? Semin Hematol 37:15–29

Barrett-Connor E (1971) Bacterial infection and sickle cell anemia. An analysis of 250 infections in 166 patients and a review of the literature. Medicine (Baltimore) 50:97–112

Beutler E, West C (2005) Hematologic differences between African-Americans and whites: the roles of iron deficiency and alpha-thalassemia on hemoglobin levels and mean corpuscular volume. Blood 106:740–745

Bonnerot V, Sebag G, de Montalembert M et al (1994) Gadolinium-DOTA enhanced MRI of painful osseous crises in children with sickle cell anemia. Pediatr Radiol 24:92–95

Booz MM, Hariharan V, Aradi AJ, Malki AA (1999) The value of ultrasound and aspiration in differentiating vaso-occlusive crisis and osteomyelitis in sickle cell disease patients. Clin Radiol 54:636–639

Brill PW, Winchester P, Giardina PJ, Cunningham-Rundles S (1991) Deferoxamine-induced bone dysplasia in patients with thalassemia major. AJR Am J Roentgenol 156: 561–565

Brinker MR, Thomas KA, Meyers SJ et al (1998) Bone mineral density of the lumbar spine and proximal femur is decreased in children with sickle cell anemia. Am J Orthop (Belle Mead NJ) 27:43–49

Bronspiegel-Weintrob N, Olivieri NF, Tyler B, Andrews DF, Freedman MH, Holland FJ (1990) Effect of age at the start of iron chelation therapy on gonadal function in beta-thalassemia major. N Engl J Med 323:713–719

Burnett MW, Bass JW, Cook BA (1998) Etiology of osteomyelitis complicating sickle cell disease. Pediatrics 101:296–297

Cario H, Kohne E (2010). Thalassämie. In: Bundesärztekammer (BÄK) KBK, Arbeitsgemeinschaft der Wissenschaftlichen Medizinischen Fachgesellschaften (AWMF) (ed) Leitlinie der Gesellschaft für Pädiatrische Onkologie und Hämatologie

Cario H, Janka-Schaub G, Janssen G, Jarisch A, Strauss G, Kohne E (2007) Recent developments in iron chelation therapy. Klin Padiatr 219:158–165

Chan YL, Li CK, Pang LM, Chik KW (2000) Desferrioxamine-induced long bone changes in thalassaemic patients—radiographic features, prevalence and relations with growth. Clin Radiol 55:610–614

Chan YL, Pang LM, Chik KW, Cheng JC, Li CK (2002) Patterns of bone diseases in transfusion-dependent homozygous thalassaemia major: predominance of osteoporosis and desferrioxamine-induced bone dysplasia. Pediatr Radiol 32:492–497

Charache S, Terrin ML, Moore RD et al (1995) Effect of hydroxyurea on the frequency of painful crises in sickle cell anemia. Investigators of the Multicenter Study of Hydroxyurea in Sickle Cell Anemia. N Engl J Med 332:1317–1322

Chaves PH, Xue QL, Guralnik JM, Ferrucci L, Volpato S, Fried LP (2004) What constitutes normal hemoglobin concentration in community-dwelling disabled older women? J Am Geriatr Soc 52:1811–1816

Chung SM, Alavi A, Russell MO (1978) Management of osteonecrosis in sickle-cell anemia and its genetic variants. Clin Orthop Relat Res 130:158–174

Claster S, Vichinsky EP (2003) Managing sickle cell disease. BMJ 327:1151–1155

Weatherall DJ, Clegg JB (2001) The thalassaemia syndromes, 4th ed Oxford Blackwell Science Ltd, Malden

Collett-Solberg PF, Ware RE, O'Hara SM (2002) Asymmetrical closure of epiphyses in a patient with sickle cell anemia. J Pediatr Endocrinol Metab 15:1207–1212

Cooley TB, Witwer ER (1927) Anemia in children with splenomegaly and peculiar changes in the bones. Am J Dis Child 34:347–363

Cristy M (1981) Active bone marrow distribution as a function of age in humans. Phys Med Biol 26:389–400

Curran EL, Fleming JC, Rice K, Wang WC (1997) Orbital compression syndrome in sickle cell disease. Ophthalmology 104:1610–1615

Currarino G, Erlandson ME (1964) Premature fusion of epiphyses in cooley's anemia. Radiology 83:656–664

De Mola RL, Kurre P (2009) MRI findings in aplastic anemia. Am J Hematol 84:754

De Sanctis V, Pinamonti A, Di Palma A et al (1996) Growth and development in thalassaemia major patients with severe bone lesions due to desferrioxamine. Eur J Pediatr 155: 368–372

Deely DM, Schweitzer ME (1997) MR imaging of bone marrow disorders. Radiol Clin North Am 35:193–212

den Elzen WP, Willems JM, Westendorp RG, de Craen AJ, Assendelft WJ, Gussekloo J (2009) Effect of anemia and comorbidity on functional status and mortality in old age: results from the Leiden 85-plus Study. CMAJ 181:151–157

Diav-Citrin O, Koren G (1997) Oral iron chelation with deferiprone. Pediatr Clin North Am 44:235–247
Dirschl DR (1994) Acute pyogenic osteomyelitis in children. Orthop Rev 23:305–312
Dokal I (1999) Dyskeratosis congenita: recent advances and future directions. J Pediatr Hematol Oncol 21:344–350
Dokal I (2000) Dyskeratosis congenita in all its forms. Br J Haematol 110:768–779
Dokal I, Vulliamy T (2010) Inherited bone marrow failure syndromes. Haematologica 95:1236–1240
Dooms GC, Fisher MR, Hricak H, Richardson M, Crooks LE, Genant HK (1985) Bone marrow imaging: magnetic resonance studies related to age and sex. Radiology 155:429–432
Dorwart BB, Schumacher HR (1981) Arthritis in beta thalassaemia trait: clinical and pathological features. Ann Rheum Dis 40:185–189
Drakonaki EE, Maris TG, Maragaki S, Klironomos V, Papadakis A, Karantanas AH (2010) Deferoxamine versus combined therapy for chelating liver, spleen and bone marrow iron in beta-thalassemic patients: a quantitative magnetic resonance imaging study. Hemoglobin 34:95–106
Ejindu VC, Hine AL, Mashayekhi M, Shorvon PJ, Misra RR (2007) Musculoskeletal manifestations of sickle cell disease. Radiographics 27:1005–1021
Emodi JI, Okoye IJ (2001) Vertebral bone collapse in sickle cell disease: a report of two cases. East Afr Med J 78:445–446
Eustace S, McGrath D, Albrecht M, Fogt F, Buff B, Longmaid HE (1994) Clival marrow changes in AIDS: findings at MR imaging. Radiology 193:623–627
Frush DP, Heyneman LE, Ware RE, Bissett GS 3rd (1999) MR features of soft-tissue abnormalities due to acute marrow infarction in five children with sickle cell disease. AJR Am J Roentgenol 173:989–993
Ganesh A, William RR, Mitra S et al (2001) Orbital involvement in sickle cell disease: a report of five cases and review literature. Eye (London) 15:774–780
Gardeniers JWM (1993) ARCO committee on terminology and staging. Report on the committee meeting at Santiago de Compostela, In, pp 79–82
Gattermann N (2009) The treatment of secondary hemochromatosis. Dtsch Arztebl Int 106:499–504
Giampietro PF, Verlander PC, Davis JG, Auerbach AD (1997) Diagnosis of Fanconi anemia in patients without congenital malformations: an international Fanconi Anemia Registry Study. Am J Med Genet 68:58–61
Giardina PJ, Schneider R, Lesser M, Simmons B, Rodriguez A, Gertner H (1995) Abnormal bone metabolism in thalassaemia. In: Ando S et al. (eds) Endocrine disorders in thalassemia. Berlin, Springer pp 39–46
Gilkeson RC, Basile V, Sands MJ, Hsu JT (1997) Chest case of the day. Extramedullary hematopoiesis (EMH). AJR Am J Roentgenol 169(267):270–273
Goni MH, Markussis V, Tolis G (1995) Bone mineral content by single and dual photon absorptiometry in thalassaemic patients. In: Ando S, Brancatti C (eds) Endocrine disorders in thalassaemic patient. Springer, Berlin
Gupta G, Robertson P, Szer J(2007) Focal lesions on magnetic resonance imaging in aplastic anaemia: multiple metastases or haemopoietic marrow. Australas Radiol 51 Spec No.: B110–114
Guralnik JM, Eisenstaedt RS, Ferrucci L, Klein HG, Woodman RC (2004) Prevalence of anemia in persons 65 years and older in the United States: evidence for a high rate of unexplained anemia. Blood 104:2263–2268
Hartkamp MJ, Babyn PS, Olivieri F (1993) Spinal deformities in deferoxamine-treated homozygous beta-thalassemia major patients. Pediatr Radiol 23:525–528
Henderson S, Timbs A, McCarthy J et al (2009) Incidence of haemoglobinopathies in various populations - the impact of immigration. Clin Biochem 42:1745–1756
Hernigou P, Bachir D, Galacteros F (2003) The natural history of symptomatic osteonecrosis in adults with sickle-cell disease. J Bone Joint Surg Am 85A:500–504
Higgs DR, Weatherall DJ (2009) The alpha thalassaemias. Cell Mol Life Sci 66:1154–1162
Hohloch K, Trumper L, Schroers R (2003) Aplastic anemia–diagnosis. Dtsch Med Wochenschr 128:1838–1840 quiz 1845–1836
Hotta T, Murate T, Inoue C et al (1990) Patchy haemopoiesis in long-term remission of idiopathic aplastic anaemia. Eur J Haematol 45:73–77
Izaks GJ, Westendorp RG, Knook DL (1999) The definition of anemia in older persons. JAMA 281:1714–1717
Jean-Baptiste G, De Ceulaer K (2000) Osteoarticular disorders of haematological origin. Baillieres Best Pract Res Clin Rheumatol 14:307–323
Jelbert A, Vaidya S, Fotiadis N (2009) Imaging and staging of haemophilic arthropathy. Clin Radiol 64:1119–1128
Juhl JH, Wesenberg RL, Gwinn JL (1967) Roentgenographic findings in Fanconi's anemia. Radiology 89:646–653
Kalina P, Hillstrom MM (1992) MR of extramedullary hematopoiesis causing cord compression in beta-thalassemia. AJNR Am J Neuroradiol 13:1407–1409
Kaplan PA, Asleson RJ, Klassen LW, Duggan MJ (1987) Bone marrow patterns in aplastic anemia: observations with 1.5-T MR imaging. Radiology 164:441–444
Keeley K, Buchanan GR (1982) Acute infarction of long bones in children with sickle cell anemia. J Pediatr 101:170–175
Kellenberger CJ, Schmugge M, Saurenmann T et al (2004) Radiographic and MRI features of deferiprone-related arthropathy of the knees in patients with beta-thalassemia. AJR Am J Roentgenol 183:989–994
Kim SK, Miller JH (2002) Natural history and distribution of bone and bone marrow infarction in sickle hemoglobinopathies. J Nucl Med 43:896–900
King S, Germeshausen M, Strauss G, Welte K, Ballmaier M (2005) Congenital amegakaryocytic thrombocytopenia: a retrospective clinical analysis of 20 patients. Br J Haematol 131:636–644
Kleihauer E, Kohne E, Kulozik AE (1996) Anomale Hämoglobine und Thalassämie-Syndrome Grundlagen und Klinik. Ecomed Verlagsgesellschaft, Landsberg
Kooy A, de Heide LJ, ten Tije AJ et al (1996) Vertebral bone destruction in sickle cell disease: infection, infarction or both. Neth J Med 48:227–231
Korovessis PG, Papanastasiou D, Tiniakou M, Beratis NG (1996) Prevalence of scoliosis in beta-thalassemia. J Spinal Disord 9:170–173
Kutler DI, Singh B, Satagopan J et al (2003) A 20-year perspective on the International Fanconi Anemia Registry (IFAR). Blood 101:1249–1256

Laurence B, Reid BC, Katz RV (2002) Sickle cell anemia and dental caries: a literature review and pilot study. Spec Care Dentist 22:70–74

Lawson JP, Ablow RC, Pearson HA (1981) The ribs in thalassemia. II. The pathogenesis of the changes. Radiology 140:673–679

Leong CS, Stark P (1998) Thoracic manifestations of sickle cell disease. J Thorac Imaging 13:128–134

Levin TL, Sheth SS, Ruzal-Shapiro C, Abramson S, Piomelli S, Berdon WE (1995) MRI marrow observations in thalassemia: the effects of the primary disease, transfusional therapy, and chelation. Pediatr Radiol 25:607–613

Loh CK, Alcorta C, McElhinney AJ (1996) Extramedullary hematopoiesis simulating posterior mediastinal tumors. Ann Thorac Surg 61:1003–1005

Lonergan GJ, Cline DB, Abbondanzo SL (2001) Sickle cell anemia. Radiographics 21:971–994

Madani G, Papadopoulou AM, Holloway B, Robins A, Davis J, Murray D (2007) The radiological manifestations of sickle cell disease. Clin Radiol 62:528–538

Malizos KN, Siafakas MS, Fotiadis DI, Karachalios TS, Soucacos PN (2001) An MRI-based semiautomated volumetric quantification of hip osteonecrosis. Skeletal Radiol 30:686–693

Marlow TJ, Brunson CY, Jackson S, Schabel SI (1998) "Tower vertebra": a new observation in sickle cell disease. Skeletal Radiol 27:195–198

Marsh JC, Ball SE, Darbyshire P et al (2003) Guidelines for the diagnosis and management of acquired aplastic anaemia. Br J Haematol 123:782–801

Martinoli C, Bacigalupo L, Forni GL, Balocco M, Garlaschi G, Tagliafico A (2011) Musculoskeletal manifestations of chronic anemias. Semin Musculoskelet Radiol 15:269–280

McKinstry CS, Steiner RE, Young AT, Jones L, Swirsky D, Aber V (1987) Bone marrow in leukemia and aplastic anemia: MR imaging before, during, and after treatment. Radiology 162:701–707

Miller TT, Caldwell G, Kaye JJ, Arkin S, Burke S, Brill PW (1993) MR imaging of deferoxamine-induced bone dysplasia in an 8-year-old female with thalassemia major. Pediatr Radiol 23:523–524

Milner PF, Kraus AP, Sebes JI et al (1991) Sickle cell disease as a cause of osteonecrosis of the femoral head. N Engl J Med 325:1476–1481

Milner PF, Kraus AP, Sebes JI et al (1993) Osteonecrosis of the humeral head in sickle cell disease. Clin Orthop Relat Res 289:136–143

Minagi H, Steinbach HL (1966) Roentgen appearance of anomalies associated with hypoplastic anemias of childhood: Fanconi's anemia and congenital hypoplastic anemia (erythrogenesis imperfecta). Am J Roentgenol Radium Ther Nucl Med 97:100–109

Mitchell DG, Rao VM, Dalinka MK et al (1987) Femoral head avascular necrosis: correlation of MR imaging, radiographic staging, radionuclide imaging, and clinical findings. Radiology 162:709–715

Murphy MF (1994) Disease of the blood. In: Clark M, Kumar P (eds) Clinical Medicine. Ballliere Tindall, London, pp 239–351

Naran AD, Fontana L (2001) Sickle cell disease with orbital infarction and epidural hematoma. Pediatr Radiol 31:257–259

Naselli A, Vignolo M, Di Battista E et al (1998) Long-term follow-up of skeletal dysplasia in thalassaemia major. J Pediatr Endocrinol Metab 11(Suppl 3):817–825

Neonato MG, Guilloud-Bataille M, Beauvais P et al (2000) Acute clinical events in 299 homozygous sickle cell patients living in France. French Study Group on Sickle Cell Disease. Eur J Haematol 65:155–164

Nissenson AR, Goodnough LT, Dubois RW (2003) Anemia: not just an innocent bystander? Arch Intern Med 163:1400–1404

Olivieri NF (1999) The beta-thalassemias. N Engl J Med 341: 99–109

Olivieri NF, Koren G, Harris J et al (1992) Growth failure and bony changes induced by deferoxamine. Am J Pediatr Hematol Oncol 14:48–56

Orzincolo C, Castaldi G, Bariani L, Franceschini F, Corcione S, Scutellari PN (1988) Circumscribed lytic lesions of the thalassaemic skull. Skeletal Radiol 17:344–347

Overturf GD (1999) Infections and immunizations of children with sickle cell disease. Adv Pediatr Infect Dis 14:191–218

Park JM, Jung HA, Kim DW, Lee JW, Kim CC, Hahn ST (2001) Magnetic resonance imaging of the bone marrow after bone marrow transplantation or immunosuppressive therapy in aplastic anemia. J Korean Med Sci 16:725–730

Patel KV (2008) Epidemiology of anemia in older adults. Semin Hematol 45:210–217

Penninx BW, Guralnik JM, Onder G, Ferrucci L, Wallace RB, Pahor M (2003) Anemia and decline in physical performance among older persons. Am J Med 115:104–110

Penninx BW, Pahor M, Cesari M et al (2004) Anemia is associated with disability and decreased physical performance and muscle strength in the elderly. J Am Geriatr Soc 52:719–724

Penninx BW, Pluijm SM, Lips P et al (2005) Late-life anemia is associated with increased risk of recurrent falls. J Am Geriatr Soc 53:2106–2111

Piehl FC, Davis RJ, Prugh SI (1993) Osteomyelitis in sickle cell disease. J Pediatr Orthop 13:225–227

Platt OS, Thorington BD, Brambilla DJ et al (1991) Pain in sickle cell disease. Rates and risk factors. N Engl J Med 325:11–16

Price EA, Mehra R, Holmes TH, Schrier SL (2010) Anemia in older persons: etiology and evaluation. Blood Cells Mol Dis 46:159–165

Rao VM, Mitchell DG, Rifkin MD et al (1989) Marrow infarction in sickle cell anemia: correlation with marrow type and distribution by MRI. Magn Reson Imaging 7:39–44

Rebsamen SL, Bilaniuk LT, Granet D et al (1993) Orbital wall infarction in sickle cell disease: MR evaluation. AJNR Am J Neuroradiol 14:777–779

Reimann F, Kuran S (1973) Cause, origin and nature of the "brush-like" symptom on the skull in severe blood disorders. VI. Studies on the alterations of the skeletal system in severe blood diseases. Virchows Arch A Pathol Pathol Anat 358:173–191

Resnick D (2002) Hemoglobinopathias and other andemias. In: Resnick D (ed) *Diagnosis of bone and joint disorders*. Saunders, Philadelphia, pp 2146–2187

Resnick D, Niwayama G (1995) Osteonecrosis: diagnostic techniques, specific situations, and complications. In: Resnick D (ed) *Diagnosis of bone and joint disorders*. Saunders, Philadelphia, pp 3495–3515

Rifai A, Nyman R (1997) Scintigraphy and ultrasonography in differentiating osteomyelitis from bone infarction in sickle cell disease. Acta Radiol 38:139–143
Rucknagel DL (2001) The role of rib infarcts in the acute chest syndrome of sickle cell diseases. Pediatr Pathol Mol Med 20:137–154
Rund D, Rachmilewitz E (2005) Beta-thalassemia. N Engl J Med 353:1135–1146
Schumacher HR, Dorwart BB, Bond J, Alavi A, Miller W (1977) Chronic synovitis with early cartilage destruction in sickle cell disease. Ann Rheum Dis 36:413–419
Seaman JP, Kjeldsberg CR, Linker A (1978) Gelatinous transformation of the bone marrow. Hum Pathol 9:685–692
Sebes JI, Diggs LW (1979) Radiographic changes of the skull in sickle cell anemia. AJR Am J Roentgenol 132:373–377
Shimamura A, Alter BP (2010) Pathophysiology and management of inherited bone marrow failure syndromes. Blood Rev 24:101–122
Sidhu PS, Rich PM (1999) Sonographic detection and characterization of musculoskeletal and subcutaneous tissue abnormalities in sickle cell disease. Br J Radiol 72:9–17
Skaggs DL, Kim SK, Greene NW, Harris D, Miller JH (2001) Differentiation between bone infarction and acute osteomyelitis in children with sickle-cell disease with use of sequential radionuclide bone-marrow and bone scans. J Bone Joint Surg Am 83-A:1810–1813
Smith JA (1996) Bone disorders in sickle cell disease. Hematol Oncol Clin North Am 10:1345–1356
Smith RR, Spivak JL (1985) Marrow cell necrosis in anorexia nervosa and involuntary starvation. Br J Haematol 60: 525–530
Smith OP, Hann IM, Chessells JM, Reeves BR, Milla P (1996) Haematological abnormalities in Shwachman-Diamond syndrome. Br J Haematol 94:279–284
Stark JE, Glasier CM, Blasier RD, Aronson J, Seibert JJ (1991) Osteomyelitis in children with sickle cell disease: early diagnosis with contrast-enhanced CT. Radiology 179:731–733
Stevens MC, Padwick M, Serjeant GR (1981) Observations on the natural history of dactylitis in homozygous sickle cell disease. Clin Pediatr (Phila) 20:311–317
Stoller DW Tirmann PFJ, Bredeller MA, Beltran S, Brandstetter RM III Blease SCP (2004) The Hip. In: Diagnostic imaging orthopedics. Salt Lake City, Amirsys pp 2–5
Storb RF, Lucarelli G, McSweeney PA, Childs RW (2003) Hematopoietic cell transplantation for benign hematological disorders and solid tumors. Hematology Am Soc Hematol Educ Program 1:372–397. doi: 10.1182/asheducation-2003.1.372
Styles LA, Vichinsky EP (1996) Core decompression in avascular necrosis of the hip in sickle-cell disease. Am J Hematol 52:103–107
Tefferi A (2003) Anemia in adults: a contemporary approach to diagnosis. Mayo Clin Proc 78:1274–1280
Teo JT, Klaassen R, Fernandez CV et al (2008) Clinical and genetic analysis of unclassifiable inherited bone marrow failure syndromes. Pediatrics 122:e139–e148
Thein M, Ershler WB, Artz AS et al (2009) Diminished quality of life and physical function in community-dwelling elderly with anemia. Medicine (Baltimore) 88:107–114
Tunaci M, Tunaci A, Engin G et al (1999) Imaging features of thalassemia. Eur Radiol 9:1804–1809
Tyler PA, Madani G, Chaudhuri R, Wilson LF, Dick EA (2006) The radiological appearances of thalassaemia. Clin Radiol 61:40–52
Umans H, Haramati N, Flusser G (2000) The diagnostic role of gadolinium enhanced MRI in distinguishing between acute medullary bone infarct and osteomyelitis. Magn Reson Imaging 18:255–262
Vande Berg BC, Malghem J, Devuyst O, Maldague BE, Lambert MJ (1994) Anorexia nervosa: correlation between MR appearance of bone marrow and severity of disease. Radiology 193:859–864
Vichinsky EP, Styles LA, Colangelo LH, Wright EC, Castro O, Nickerson B (1997) Acute chest syndrome in sickle cell disease: clinical presentation and course. Cooperative Study of Sickle Cell Disease. Blood 89:1787–1792
Walne AJ, Vulliamy T, Beswick R, Kirwan M, Dokal I (2008) TINF2 mutations result in very short telomeres: analysis of a large cohort of patients with dyskeratosis congenita and related bone marrow failure syndromes. Blood 112: 3594–3600
Ware HE, Brooks AP, Toye R, Berney SI (1991) Sickle cell disease and silent avascular necrosis of the hip. J Bone Joint Surg Br 73:947–949
Watson RJ, Burko H, Megas H, Robinson M (1963) The handfoot syndrome in sickle-cell disease in young children. Pediatrics 31:975–982
Weatherall DJ, Provan AB (2000) Red cells I: inherited anaemias. Lancet 355:1169–1175
Weinberg AG, Currarino G (1972) Sickle cell dactylitis: histopathologic observations. Am J Clin Pathol 58:518–523
William RR, Hussein SS, Jeans WD, Wali YA, Lamki ZA (2000) A prospective study of soft-tissue ultrasonography in sickle cell disease patients with suspected osteomyelitis. Clin Radiol 55:307–310
Williams VL (2004) Pathways of innovation: a history of the first effective treatment for sickle cell anemia. Perspect Biol Med 47:552–563
Williams HJ, Davies AM, Chapman S (2004) Bone within a bone. Clin Radiol 59:132–144
Wonke B (1998) Bone disease in beta-thalassaemia major. Br J Haematol 103:897–901
Kohne E (2011) Hemoglobinopathies: clinical manifestations, diagnosis, and treatment. Dtsch Arztebl Int 108:532–540
Kohne E, Kleihauer E (2010) Hemoglobinopathies: a longitudinal study over four decades. Dtsch Arztebl Int. 107:65–71
Young NS (1999) Acquired aplastic anemia. JAMA 282:271–278
Young NS (2000) Hematopoietic cell destruction by immune mechanisms in acquired aplastic anemia. Semin Hematol 37:3–14

Osteonecrosis and Bone Infarction

Anastasia Fotiadou and Apostolos Karantanas

Contents

Abstract

Bone ischemia is a relatively common condition, which may be idiopathic or secondary to a variety of clinical situations. Medullary infarction refers to dia-metaphyseal location whereas osteonecrosis to the epiphyseal and sub-articular involvement. In both situations, the lesions may be radiographically occult. Magnetic resonance imaging (MRI) is very sensitive in identifying and characterizing bone ischemia. Newer treatments on femoral head osteonecrosis require early diagnosis, accurate staging, and estimation of prognosis and assessment of treatment. This chapter reviews the current and evolving knowledge on the various faces of bone ischemia with emphasis on the role of MRI on the clinically most important forms of the disease.

1 Introduction

Ischemic bone lesions belong to a wide spectrum of clinical disorders and result from impaired perfusion. Secondary ischemia may result from injury/fracture, systemic corticosteroid administration, Cushing's disease, sickle cell anemia, thalassemia, hypercoagulation disorders, lipid storage diseases, autoimmune/collagen diseases, alcohol abuse, pancreatitis, radiation, dislipidemia, Gaucher's disease, smoking, hemodialysis, Caisson's disease and cytotoxic agents. When no predisposing cause exists, the ischemia is called idiopathic. The true prevalence of ischemic bone disease is unknown. About 10% of total hip replacements are thought to occur following joint degeneration related to femoral head osteonecrosis (FHON) (Steinberg et al. 1995).

A. Fotiadou
Department of Radiology, Hinchingbrooke Hospital, Huntingdon, Cambridgeshire, PE29 6NT, UK

A. Karantanas (✉)
Department of Medical Imaging, University Hospital, University of Crete, Heraklion, Greece
e-mail: akarantanas@gmail.com

A. Baur-Melnyk (ed.), *Magnetic Resonance Imaging of the Bone Marrow*, Medical Radiology. Diagnostic Imaging,
DOI: 10.1007/174_2011_496,

The clinical presentation is variable and ranges from incidental depiction of lesions at MR imaging (MRI) performed in a patient examined for irrelevant indication, to severe pain in bones and joints such as in cases with sickle cell crisis or articular surface collapse, respectively.

2 Bone Infarction

2.1 Background

The term "bone infarction" refers to osteonecrosis located within the metaphysis and diaphysis (Saini and Saifuddin 2004). The pathogenetic mechanism is considered to be arterial obstruction in the bone. This possibly explains why medullary bone infarctions are encountered mainly in fatty marrow and uncommonly in hematopoietic marrow, since the poor blood supply of yellow marrow, when compared with the rich one of red marrow, makes it more vulnerable. Soon after the onset of the necrotic process, reparative changes happen and a shell of reactive bone develops to surround the necrotic cavity. Quite infrequently, cystic degeneration or liquefaction may occur in this necrotic cavity. The bone cortex at this point becomes thinned, but the necrotic segment rarely expands into the adjacent soft tissue (Hermann et al. 2004).

Bone infarction predominantly occurs in patients with *sickle cell* disease. Vaso-occlusive crisis is a major disease manifestation in these patients (Saini and Saifuddin 2004). The organs most frequently affected are the bones, spleen, lungs, and the central nervous system, with microvascular occlusion, thromboses and subsequent infarction (Hermann et al. 2004). The most common cause of hospital admission however is acute bone pain, which in almost a third of all cases is caused by acute infarction (AI) and acute osteomyelitis (AO) (Saini and Saifuddin 2004; States 2001). The clinical features of both AI and AO are almost identical with pain, fever, swelling, redness and leukocytosis. Most patients receive treatment for both conditions with symptomatic pain relief and intravenous broad-spectrum antibiotics to prevent complications of a possible underlying osteomyelitis (Rao et al. 1986; Umans et al. 2000). Nonetheless, AI is about 50 times more frequent that AO.

Bone infarction is also encountered in patients with systemic lupus erythematosus, Gaucher's disease and diabetes mellitus. Patients with myeloproliferative disorders and renal transplantation are also considered to be at risk for osteonecrosis. The development of infarction in these patients may be a manifestation of the primary disease itself, or a complication of chemotherapy and corticosteroid therapy (Umans et al. 2000). Bone infarcts may also be seen in divers who work in pressurized atmospheres (Caisson disease) or may be idiopathic (Rao et al. 1986; Umans et al. 2000).

Clinically, medullary bone infarctions are usually asymptomatic and constitute an incidental finding in radiographs or bone scans performed for other reasons (Umans et al. 2000). There is no specific treatment available, apart from the above analyzed treatment for cases of sickle cell crisis.

2.2 Imaging Investigation

2.2.1 Radiography

Radiographs are not sensitive in detecting AI. In the early stage, focal lytic or sclerotic areas may be revealed. Other features include a moth-eaten appearance or mottled bone rarefaction. Mild reactive sclerosis can also be seen. In an old infarct, radiographs demonstrate calcifications within the necrotic segment and well-defined sclerotic margins surrounding it (Steiner et al. 1990). A lucent surrounding area and cortical thinning may be seen as well. Rarely the lesion might extend into the adjacent soft tissues through the thinned cortex, thus mimicking a malignant process (Norman and Steiner 1983; Mitchell et al. 1987). When the underlying abnormality is Gaucher's disease, osteopenia, medullary expansion, remodeling defects and the "Erlenmeyer flask deformity" might be visualized on radiographs (States 2001).

On radiographs, a medullary bone infarct might have to be differentiated from an enchondroma. The absence of endosteal scalloping, which is seen in larger enchondromas, and the typical sclerotic and serpiginous border that is associated with infarcts are the most reliable features.

2.2.2 Cross-Sectional Imaging

Computed tomography (CT) is more sensitive than MRI for detecting small amounts of calcification, and is useful in accurately demonstrating cortical involvement.

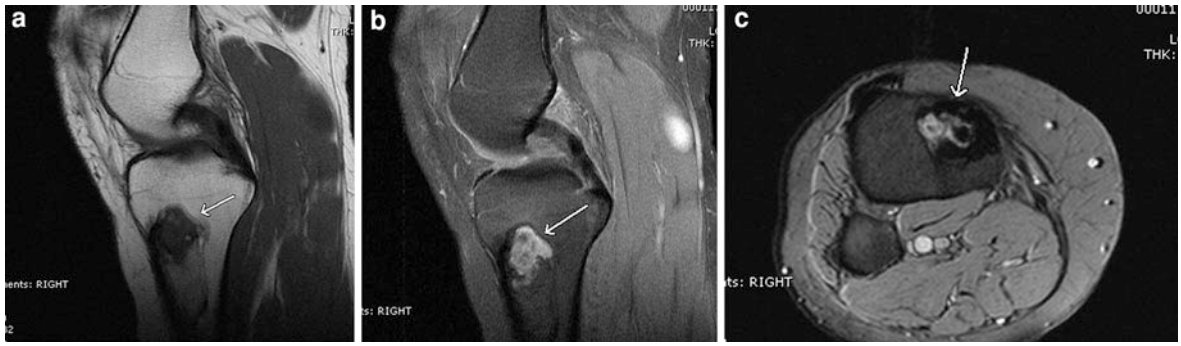

Fig. 1 A 32-year-old female patient who presented with a 7-month history of right lateral knee pain and posterior knee joint swelling. **a** The sagittal T1-w MR image shows well-demarcated intramedullary lesion in right tibia (*arrow*), compatible with a bone infarct. **b** The sagittal fat suppressed PD MR image demonstrates the high-signal intensity central part of the infarct and the low-signal intensity surrounding rim (*arrow*). **c** The axial T2*-w MR image shows that the infarct abuts the cortex of the tibia without associated cortical destruction or soft-tissue mass

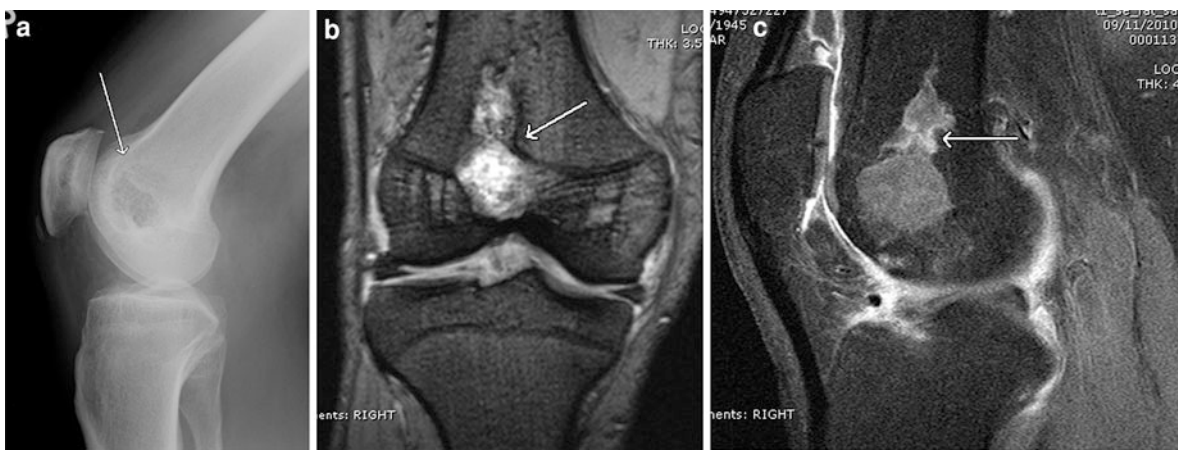

Fig. 2 A 65-year-old male patient who presented with increasing pain from right patello-femoral joint. **a** The lateral radiograph of the right knee shows a radiolucent lesion at the level of the intercondylar notch (*arrow*). **b** The coronal T2*-w MR image demonstrates a well delineated intramedullary lesion of high-signal intensity that is surrounded by a low-signal intensity rim (*arrow*) in the metaphyseal/epiphyseal region of the right femur, in keeping with an infarct. **c** The sagittal fat suppressed contrast-enhanced T1-w MR image shows some enhancement of the rim of the infarct (*arrow*). Also note the synovial enhancement

For the early detection of medullary bone infarction, MRI appears to be the most sensitive imaging investigation. During the acute phase, because of the presence of liquefactive necrosis, serum, plasma and inflammatory edema, a well-demarcated intramedullary lesion of high signal intensity (SI) on the fat suppressed (FS) PD/T2-w and STIR sequences is noted. This area returns low SI on T1-w images and is surrounded by a serpentine rim of low SI on all sequences. This rim seems to enhance post intravenous contrast material administration (Figs. 1, 2).

On non-FS T2-w images, the characteristic "*double line*" sign located at the interface between the viable and non-viable tissue is indicative of infarction. It consists of an inner rim of high SI, which corresponds to vascularized granulation tissue and/or chondroid metaplasia, and a surrounding outer low SI rim, corresponding to sclerotic bone (Saini and Saifuddin 2004). On T1-w images, this "*double line*" is shown as a single low-signal intensity linear area. Associated findings include increased SI on FS PD/T2-w MR images in the adjacent periosteum and surrounding soft

Table 1 Risk factors for osteonecrosis

Trauma
Corticosteroids
Alcohol abuse
Sickle cell anemia
Coagulopathies
Gaucher disease
Caisson disease
Radiation therapy
Chronic pancreatitis
Arterial disorders-intramedullary hemorrhage
Smoking

tissues. Ten to fourteen days following the initial insult, periosteal new bone formation can be detected.

During the chronic stage, a well-circumscribed area of uniformly low SI on all pulse sequences is shown. It reflects the replacement of the edematous tissue by calcification and dense fibrous tissue. The surrounding bone marrow returns serpiginous low signal due to perivascular fibrosis. Radial mottling of the signal might also be present (Umans et al. 2000).

2.2.3 Skeletal Scintigraphy

At skeletal scintigraphy (99mTc), an early infarct corresponds to an area of reduced uptake. This feature is helpful in the differentiation from malignancy and osteomyelitis. In later stages increased radiotracer uptake is noticed, which corresponds to the revascularization stage. In chronic lesions, decreased radiotracer uptake is again detected (Koren et al. 1984).

2.3 Differentiation of Acute Bone Infarcts from Acute Osteomyelitis

Imaging studies have been shown to have poor diagnostic accuracy in distinguishing between AI and AO. In cases of AI, as the reparative process completes and bone is reconstituted (which might take from months to up to a year), the high SI of AI lesions on pre-contrast FS T1-w MR images, resolves. However, on STIR and FS PD/T2-w images the abnormal marrow SI might persist due to marrow fibrosis and hypercellularity. On contrast-enhanced images, the acutely infarcted or sequestered bone marrow does not enhance. On the other hand, in patients with AO the abnormal bone shows marked contrast enhancement. Regarding the rim surrounding the medullary lesion, the pattern of enhancement is thin and linear in AI, as opposed to cases of AO where a thick irregular ring of enhancement is seen (Rao et al. 1986; Mitchell et al. 1987).

Differentiation of AI from AO can thus be based on the presence of a thin enhancing rim in AI and

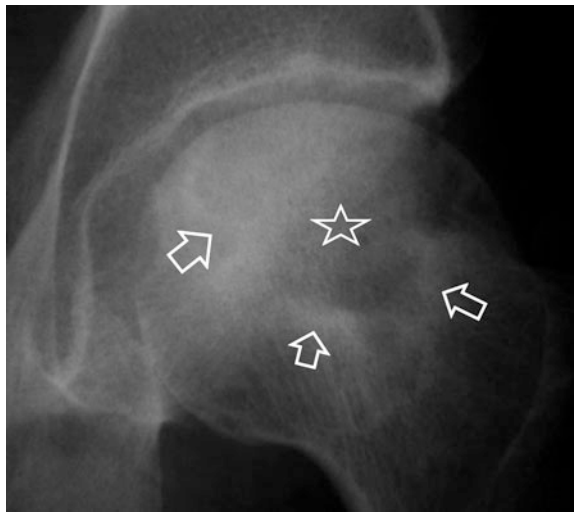

Fig. 3 The plain AP radiograph shows a lytic region (*asterisk*) surrounded by sclerosis (*arrows*) suggesting ARCO II stage lesion

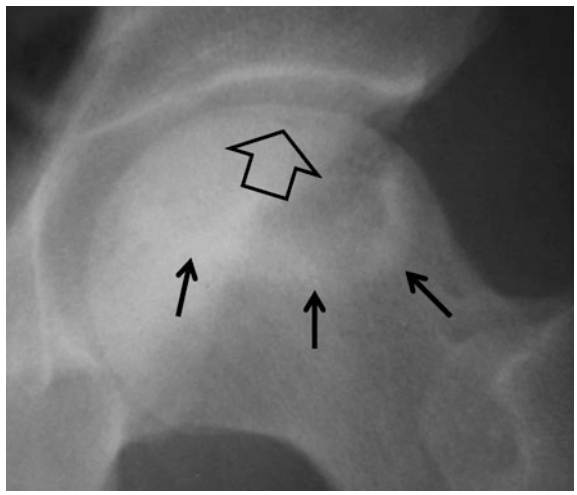

Fig. 4 The plain radiograph shows the osteonecrotic lesion (*black arrows*) and the subchondral fracture demonstrated with the "crescent" sign (*open arrow*)

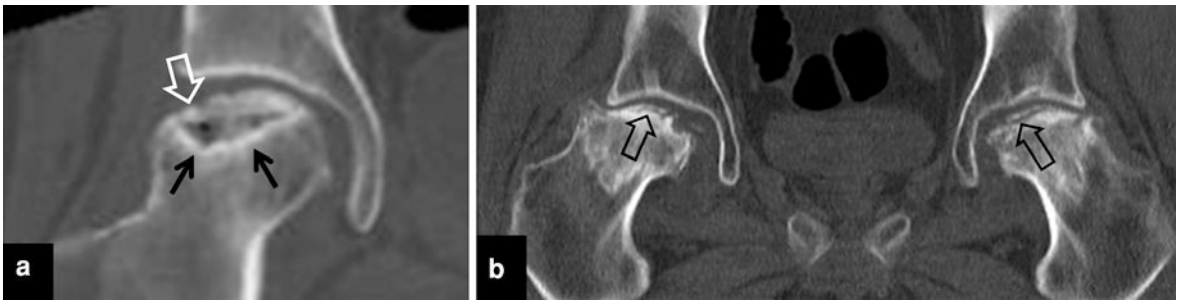

Fig. 5 Coronal MPR CT images in two patients with femoral head osteonecrosis. **a** The right hip joint shows the reactive sclerosis surrounding the necrotic area (*arrows*), a small quantity of air within the lesion and mild flattening of the femoral head (*open arrow*). **b** Both hip joints show advanced disease in this 23-year-old male patient with a history of steroid use and leukemia. There is subchondral fracture in both femoral heads (*open arrows*) as well as secondary osteoarthritis demonstrated with joint space narrowing

Table 2 ARCO's classification system

Stage	Radiological findings	Subclassification
I	Positive: MRI and/or bone scintigraphy negative/normal: radiograph/CT	[a]
II	Radiograph: sclerotic, cystic or osteoporotic changes of femoral head	[a]
III	Radiograph: subchondral fracture ("crescent sign")	[a]
IV	Radiograph: flattening of femoral head	[b]
V	Radiograph: flattening of femoral head and osteoarthritic changes	[b]

[a] *Location of femoral head necrosis:* (1) medial third, (2) median third, (3) lateral third. *Size of femoral head necrosis:* (A) <15%, (B) 15–30%, (C) >30%

[b] *Degree of femoral head collapse:* (A) <2 mm, (B) 2–4 mm, (C) >4 mm

patchy geographic enhancement of the marrow and/or a thick enhancing rim in AO (Umans et al. 2000). Nonetheless, these differences become apparent only days to weeks after the onset of acute bone pain and might therefore be considered of limited value.

It should be stressed that there is no consensus in the literature with regard to the use of contrast-enhanced MRI in the differentiation of AI from AO. Thus, contrast-enhanced MRI is only useful for the anatomical localization of lesions in order to guide biopsy or aspiration.

For the differentiation of AI from AO, in cases of acute sickle cell bone crisis, the unenhanced FS T1-w sequence is highly accurate. This has been attributed to the fact that the sequence nulls the high SI of fat in the bone marrow and subcutaneous tissues, thus highlighting the high SI of sequestered dense erythrocytes in the bone marrow, the subperiosteal spaces and the adjacent soft tissues. Therefore, these images could be used to differentiate between the high SI extraosseous hematoma or joint fluid in AI, and low SI reactive effusion or abscess in AO. In addition, the high SI of the adjacent soft-tissue component on pre-contrast FS T1-w images is very specific for AI, representing extravasated red blood cells or hematoma. The MRI protocol may be limited to STIR and unenhanced FS T1-w sequences, with contrast enhancement being optional for cases with positive STIR images and negative pre-contrast FS T1-w fat, to diagnose or exclude AO (Umans et al. 2000).

2.4 Sarcomas Associated With Bone Infarcts

In the literature, cases of malignant transformation of bone infarcts have been reported. Osteogenic sarcoma, fibrosarcoma, pleomorphic sarcoma, angiosarcoma and malignant fibrous histiocytoma might occasionally develop at the site of a bone infarct (Torres and Kyriakos 1992). The pathogenesis of dedifferentiation is still unclear. Mirra et al. (1977) suggested that these

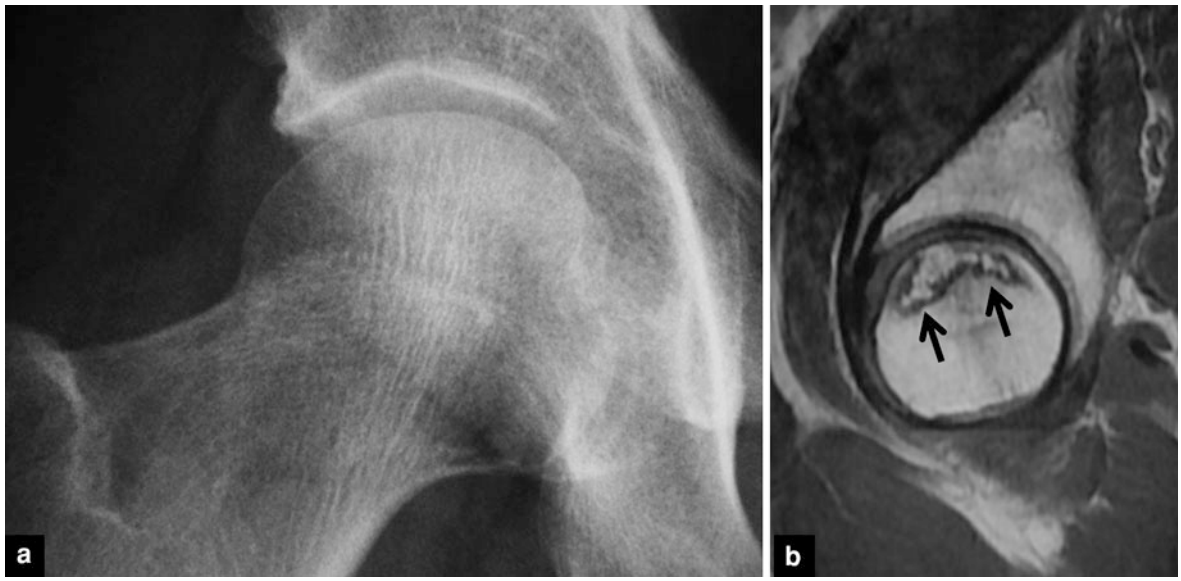

Fig. 6 A previously healthy asymptomatic 48-year-old male patient, without any predisposing factor for osteonecrosis. **a** The plain radiograph is unremarkable. **b** The sagittal T1-w MR image of the right femoral head shows the typical "band-like" sign of the osteonecrotic lesion (*black arrows*)

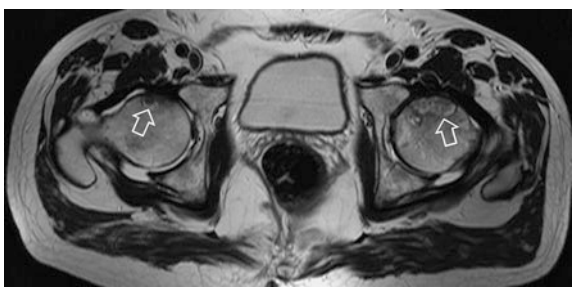

Fig. 7 The axial T2-w MR image shows bilateral femoral head osteonecrosis with the characteristic "double-line" sign (*arrows*). The lesion on the right side represents the so-called "minimal osteonecrosis or minimal avascular necrosis"

sarcomas are related to the cells involved in the chronic reparative process of a bone infarct. The mean age of patients with that type of sarcomas is 53.3 years and there is a male predominance. The survival rate has been reported to be poor. The femur is most commonly involved followed by the tibia, humerus and radius.

On radiographs there are no typical features that can differentiate sarcomas occurring in bone infarcts. A hint may be osseous destructions, lytic areas or cortical thinning or disruption. MRI demonstrates the extent of bone invasion and the associated soft-tissue mass of the tumor, and is therefore used for staging. Regardless of the degree of destruction and the size of the sarcoma, the bone infarct can usually be detected (Matsuno et al. 1996).

3 Osteonecrosis

3.1 Background

Osteonecrosis is the result of irreversible anoxia of the *subchondral bone*, resulting in death of osteocytes and compensatory osteoblastic activity at the adjacent viable bone (Saini and Saifuddin 2004). The death of bone cells due to decreased blood flow can lead to articular collapse and pain which in turn can lead to degenerative arthritis, most commonly of the hips and knees.

3.2 Osteonecrosis of the Femoral Head

FHON is also found in the literature with the synonyms *aseptic necrosis* and *avascular necrosis*. FHON is an increasingly common disease, affecting

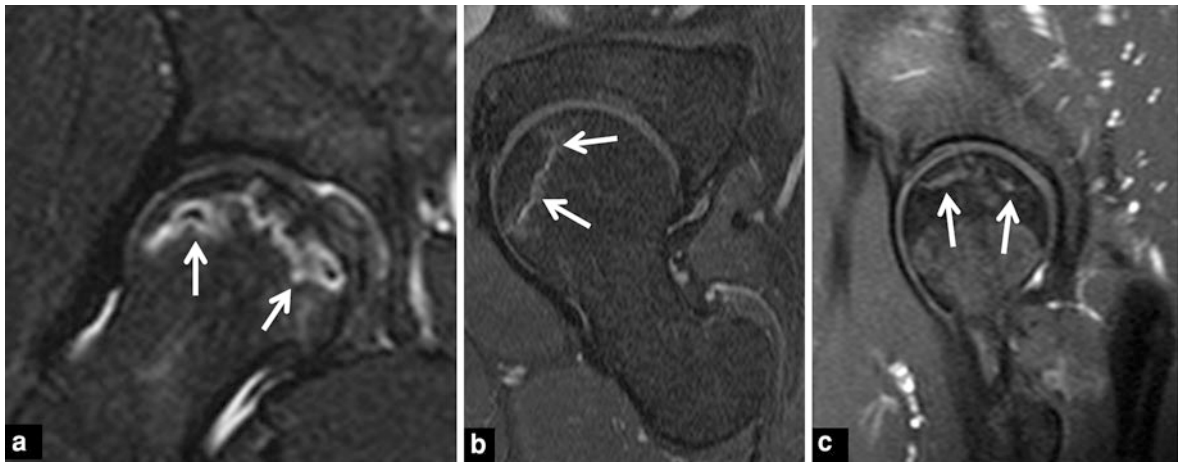

Fig. 8 The coronal fat suppressed T2-w (**a**), and the fat suppressed contrast-enhanced T1-w MR images in the axial oblique (**b**) and sagittal (**c**) planes, in three different patients with femoral head osteonecrosis, demonstrate the "bright band-like" sign (*arrows*). No bone marrow edema is depicted in these asymptomatic patients

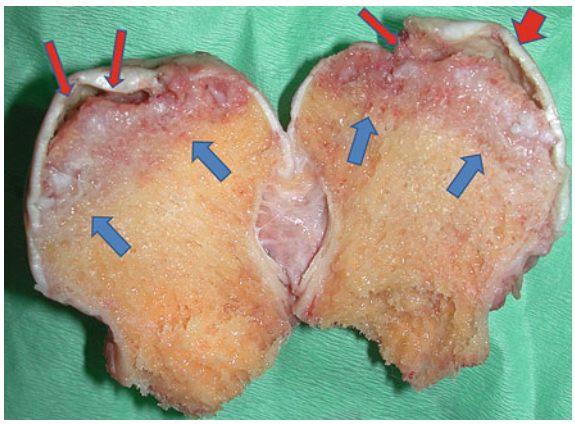

Fig. 9 The surgical specimen of the femoral head following total hip arthroplasty in a patient with advanced femoral head osteonecrosis, shows the necrotic areas (*blue arrows*) and the extensive subchondral fracture and delamination of the chondral plate (*red arrows*) (Courtesy Prof. K. Malizos)

up to 20,000 new patients per year in the USA (Steinberg et al. 1995). The ischemic insult may be associated with an apparent etiologic/risk factor (secondary FHON, Table 1) or may have no identified etiology (primary FHON) (Malizos et al. 2007a).

The disease affects mainly men at their 3d to 5th decades, is characterized by non-specific symptoms, and is initially unilateral with progression to bilateral femoral head involvement in up to 72% of patients (Assouline-Dayan et al. 2002). If left untreated, the disease will progress in 80% of cases and eventually require total hip arthroplasty (Mont and Hungerford 1995). The result of surgical treatment is determined largely by the stage of the disease when it is first depicted. As treatment at an early stage is directly associated with better prognosis, early diagnosis and accurate staging of FHON is crucial (Steinberg et al. 1984, 1995).

3.2.1 Imaging Investigation

Although in the past, scintigraphy and CT and more recently PET have been used for diagnosing FHON, currently the most important imaging methods consist of radiographs and MRI.

3.2.1.1 Radiographs

Radiographs are insensitive for detecting the early stages of FHON and bone ischemia in general. The earliest, still delayed in the disease course, findings include an osteosclerotic rim (calcified interface), circumscribing the lytic osteonecrosic area (Fig. 3). Later on, a "*crescent sign*" denotes progressive disease and corresponds to a subchondral fracture (Fig. 4). Both the subchondral fracture and the articular collapse which complicates it are better seen in the "frog-leg" view. The advanced disease is demonstrated with osteoarthritic changes in the hip joint. CT is able to demonstrate the sclerotic border surrounding the necrotic area as well as the subchondral fracture and currently is applied in

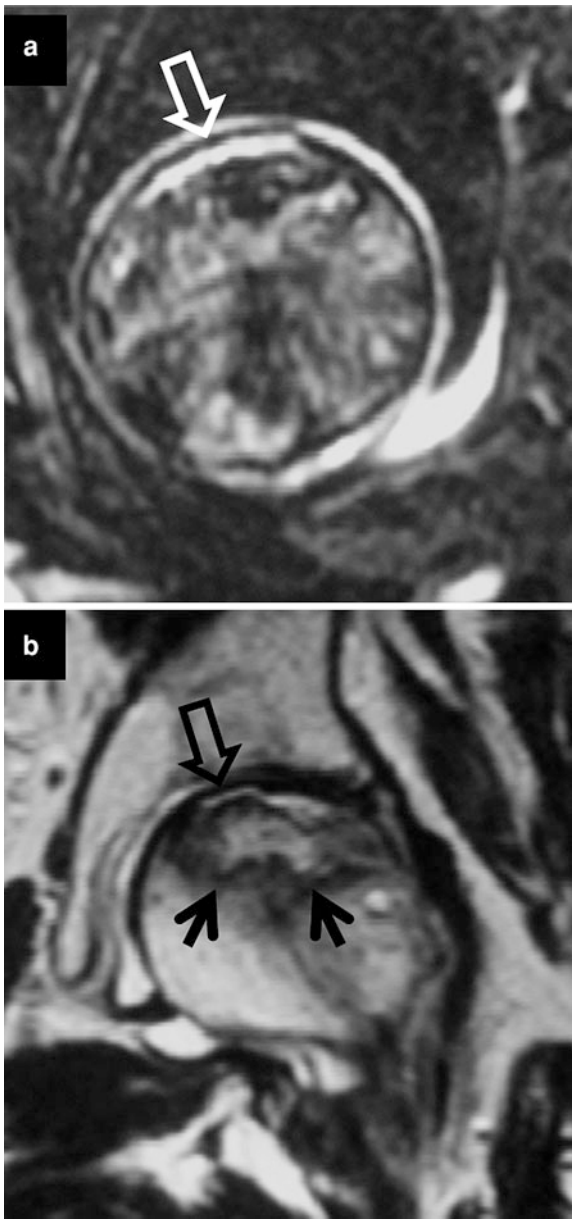

Fig. 10 A symptomatic patient with known femoral head avascular necrosis. **a** The sagittal STIR MR image shows diffuse bone marrow edema within the femoral head and a subchondral fracture demonstrated as a curvilinear high-signal intensity structure parallel to the cortex (*arrow*). **b** The coronal T2-w MR image shows the osteonecrotic area (*black arrows*) and the subchondral fracture (*open arrow*)

patients with contraindications to undergo MRI (Fig. 5). Although insensitive, plain radiographs remain the mainstay in most classification systems of FHON. In general, negative radiographs and

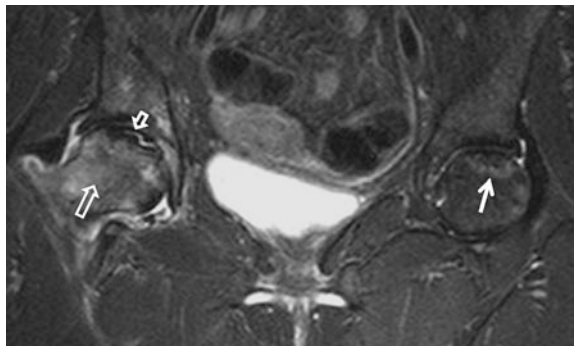

Fig. 11 A 50-year-old female patient with bilateral osteonecrosis and pain only on the right side. The coronal STIR MR image demonstrates the osteonecrotic lesions and in addition bone marrow edema on the right (*long open arrow*) and a subchondral fracture (*short arrow*). The necrotic lesion on the left side (*thin white arrow*) is not associated with bone marrow edema

positive scintigraphy and/or MRI represent stage I. In both most widely used classification systems, namely the *Steinberg's* and the *ARCO* (Table 2, Gardeniers 1993), the sclerosis and lysis belong to stage II whereas the "crescent" sign reflects a more advanced stage III. Joint preserving surgery is no longer considered as a treatment option after articular collapse. The secondary degenerative osteoarthritis is depicted on plain radiographs.

3.2.1.2 MR Imaging

MRI is highly sensitive in depicting early FHON and is the method of choice for accurate diagnosis and staging of the disease (Beltran et al. 1988; Genez et al. 1988; Coleman et al. 1988; Fordyce and Solomon 1993).

MR Imaging Protocol

A basic MRI examination protocol for suspected FHON includes coronal T1-w SE and STIR or FS PD/T2-w fast (turbo) SE sequences with large field of view. In case of femoral head marrow abnormalities, small field of view on either side with FS PD/T2-w and cartilage-specific sequences should be used and tailored to multiple planes, the axial oblique being more useful for the evaluation of the antero-superior surface. Contrast enhancement can be valuable for preoperative evaluation of the femoral head contour, monitoring a vascularized graft and early diagnosis of Legg-Calve-Perthes disease (Saini and Saifuddin 2004; Dillman and Hernandez 2009).

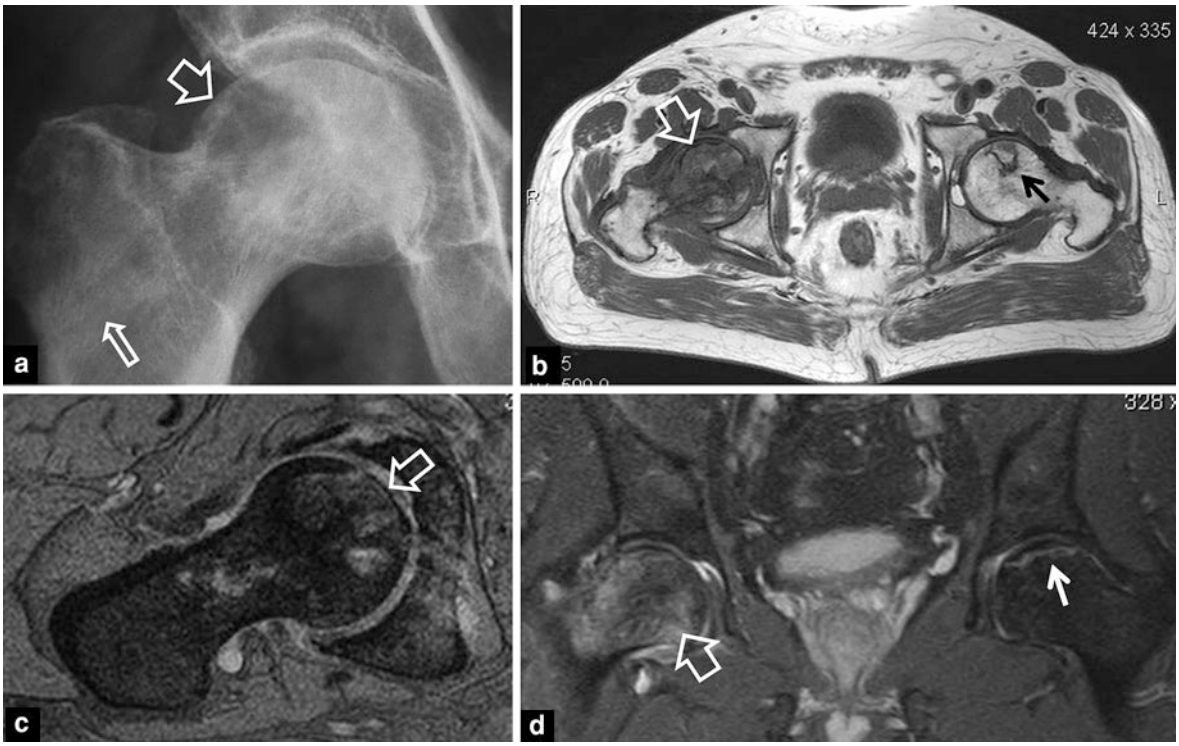

Fig. 12 A 59-year-old male patient with known bilateral osteonecrosis, symptomatic right hip joint and a history of recent core decompression of the right femoral head. **a** The plain radiograph shows the tunnel of the previous decompression (*thin arrow*) and a lytic area (*short arrow*) in the lateral aspect of the femoral head. **b** The axial T1-w MR image shows an osteonecrotic lesion on the left femoral head (*black arrow*) with the characteristic normal marrow signal within the lesion. On the right side, the low-signal intensity within the necrotic lesion (*open arrow*), corresponding to the lysis of the radiograph, suggests advanced disease. **c** The T2*-w MR image in the oblique axial plane shows mild flattening of the articular surface (*arrow*). **d** The fat suppressed PD MR image in the coronal plane shows the clinically silent lesion on the left (*thin arrow*), without any marrow edema and the extensive marrow edema (*open arrow*) on the right symptomatic side

Imaging Findings

The presence of a circumscribed subchondral "*band like*" lesion with low SI on T1-w sequences is considered the cornerstone of FHON (Fig. 6) (Mitchell et al. 1987). The *"double line"* sign seen on non-FS T2-w SE and turbo/fast SE images is virtually diagnostic of FHON. It occurs at the interface between viable and non-viable tissue and consists of an outer low SI rim (suggested to represent reactive sclerotic bone) and an inner high SI rim (considered to represent vascular granulation tissue and/or chondroid metaplasia) (Fig. 7). It was first described by Mitchell et al., who found this sign in 80% of FHON lesions (Mitchell et al. 1987). According to the SI of the region within the double line and based upon the chronological order of its appearance, Mitchell et al. proposed a classification system ranging from A (early stage, retaining normal fat SI) to D (advanced stage, low SI due to fibrous tissue and sclerosis). This system has not been used widely, as it did not correlate with radiographic staging and prognosis. The "double line" sign is considered to reflect a chemical shift artifact notified at the frequency encoding direction axis of the field (Sugimoto et al. 1992; Duda et al. 1993; Malizos et al. 2007a). Although the "double line" sign has the characteristics of an artifact, this does not alter its diagnostic significance. Nowadays, there is widespread use of T2-w fast (turbo) SE sequences with spectral fat saturation and thus, the "double line" sign is not seen but rather manifests as a "bright band-like" sign evident also on FS contrast-enhanced T1-w sequences (Fig. 8) (Malizos et al. 2007a).

Subchondral fractures in FHON typically occur as smooth and concave to articular surface low SI lines on T1-w MR images. On T2-w SE MR images, subchondral fractures may have a variable SI, as the

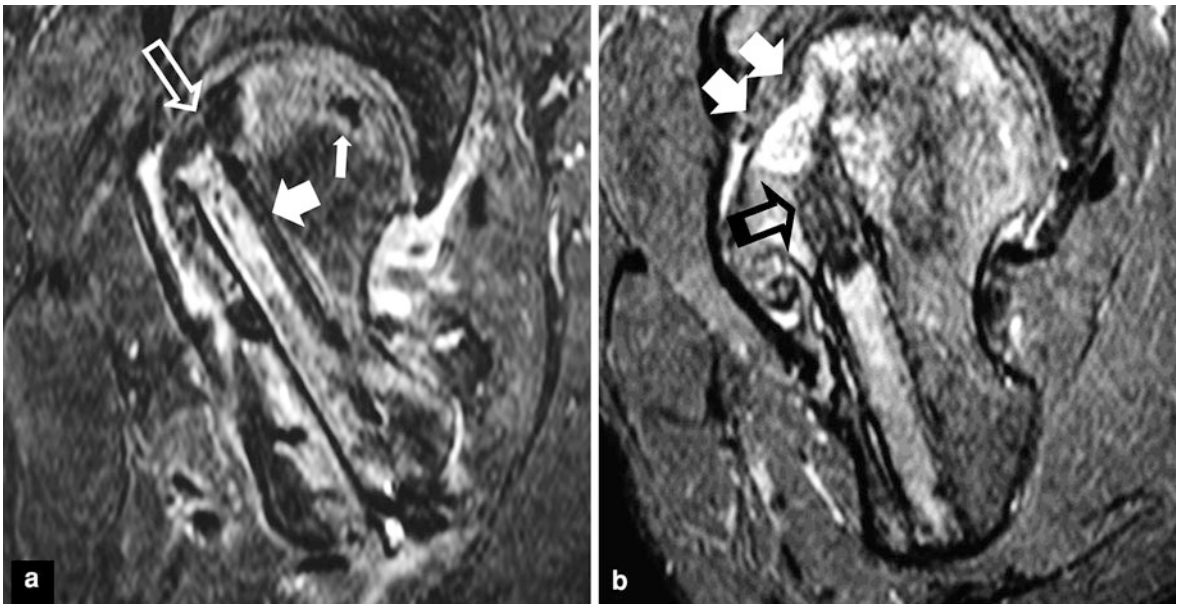

Fig. 13 A 23-year-old male smoker patient, treated with vascularized fibular graft. Oblique axial fat suppressed contrast-enhanced T1-w MR images. **a** The 2-w postoperative MR examination shows a mild flattening of the antero-superior articular surface (*long arrow*). The fibular graft shows normal enhancement (*short thick arrow*). The subchondral enhancement is the result of bone remodeling after grafting (*thin short arrow*). **b** The 16th-w postoperative MR examination shows failure of the graft with a low-signal osteonecrotic area (*black open arrow*) and increased bone marrow edema secondary to deteriorated articular collapse (*arrows*)

fracture may be filled by gas or fluid (Figs. 9, 10) (Stevens et al. 2003).

Joint effusion, probably secondary to synovitis, is seen in 58–72% of patients with FHON and is usually found in association with bone marrow edema (BME), more commonly (92%) in advanced disease (Huang et al. 2003).

MRI has been shown to be more sensitive than CT or scintigraphy for early detection of FHON in patients with normal radiographs (Stage I) (Fig. 6). The reported sensitivity of MRI for early diagnosis of FHON ranges between 88 and 100% (Coleman et al. 1988; Fordyce and Solomon 1993). In one study, MRI detected FHON in 25% of hips in the pre-radiological stage (stage I) (Beltran et al. 1987).

Staging

MRI is currently an integral part of several staging systems and has been used as a separate tool for lesion classification and lesion size quantification (Steinberg and Steinberg 2004). There are various grading and classification systems but no agreement yet on a single universal one. However, the most frequently used systems are those from University of Pennsylvania (Steinberg and Steinberg 2004) and the ARCO (Gardeniers 1993).

The most critical point in all the classification systems is the loss of spherical contour of the femoral head. Although MRI is used at the early pre-collapse stages, only radiographs are employed routinely for the evaluation of collapse. It has been shown that plain radiographs can miss important information in stages II and III, as they overestimate stage II, underestimate stage III lesions and are inaccurate in estimating the collapse size, which is an important parameter in therapeutic decisions (Zibis et al. 2007). Therefore it has been suggested that the wider use of MRI in any classification system could improve the accuracy and prognostic value by means of discriminating between early and advanced stages (Karantanas and Drakonaki 2011).

Bone Marrow Edema

BME may be seen in 30–50% of hips with FHON. It is located within the femoral head, neck and inter-trochanteric region and is probably a reaction to subchondral fracture and blockage of venous drainage (Koo et al. 1999; Kim et al. 2000; Iida et al. 2000; Huang et al. 2003). Distinction with transient

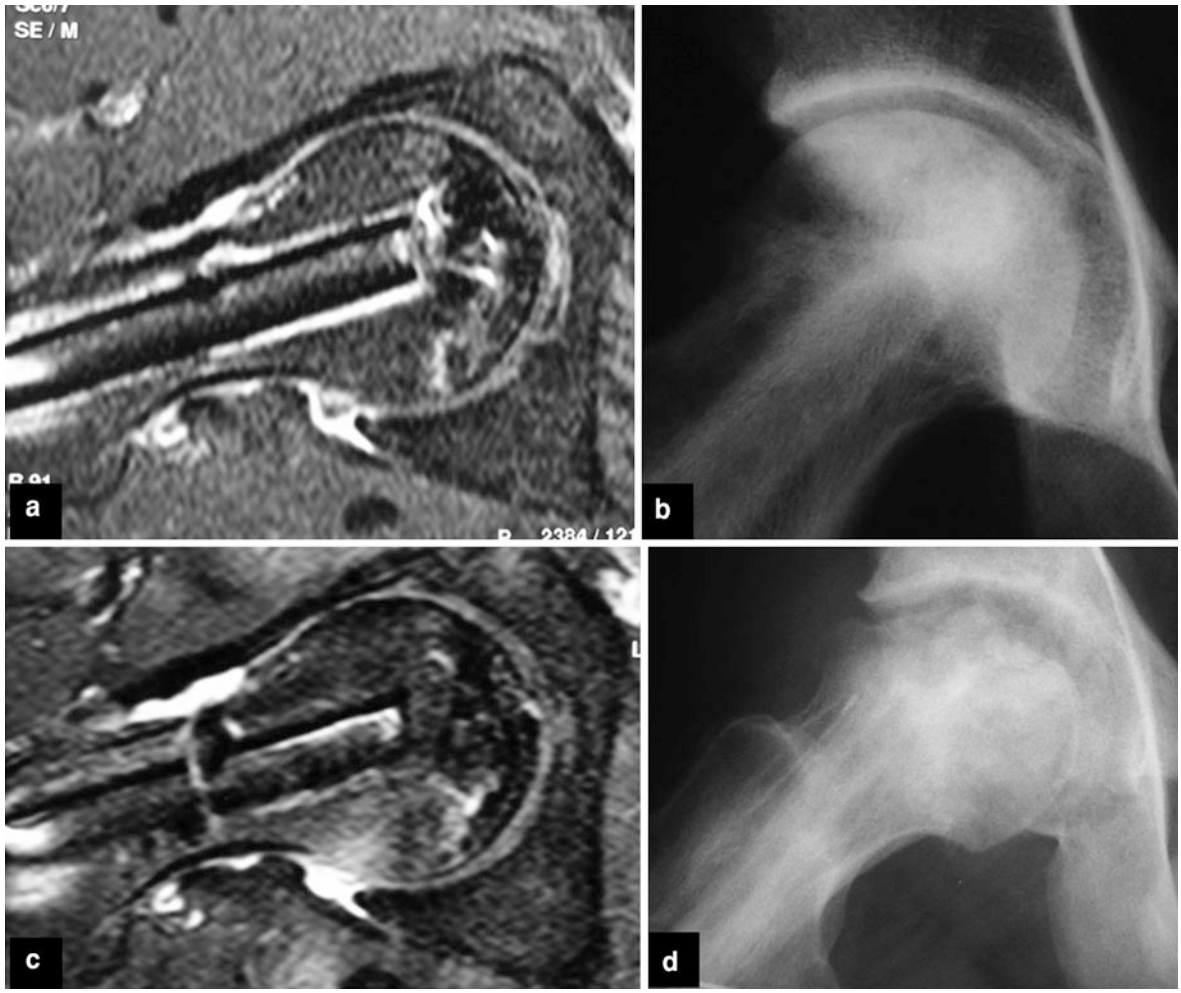

Fig. 14 A patient with symptomatic osteonecrosis of the right femoral head, treated with vascularized fibular graft. The 6-weeks postoperative oblique axial fat suppressed contrast-enhanced T1-w MR image (**a**) and the plain radiograph (**b**) show normal incorporation of the graft. The corresponding images 24 months postoperatively (**c**, **d**) show advanced disease with osteoarthritis, despite the normal appearance of the graft

osteoporosis of the hip is usually easy, if interpretation of images is based on findings in the subchondral area (Malizos et al. 2004; Karantanas and Drakonaki 2011). BME in patients with FHON has been controversial and initially it was considered to represent its early stage (Mitchell et al. 1987; Turner et al. 1989). It was later shown that BME is never found at the early stages before the appearance of the "band-like" sign, which is the initial change of FHON (Kubo et al. 1997; Kim et al. 2000; Fujioka et al. 2001). Further studies showed that BME develops after the onset or worsening of pain, which is typically identified in advanced (stage III) disease and it correlates with necrotic volume and articular collapse (Iida et al. 2000; Ito et al. 2006) (Fig. 11).

Regarding the effect of surgical treatment, it has been shown that the presence of BME is associated with failure of core decompression and progression to degenerative arthritis requiring total hip arthroplasty (Radke et al. 2004) (Fig. 12). In the postoperative setting, BME has been found after failure of vascularized bone grafting and femoral head collapse (Karantanas 2007) (Fig. 13). Thus, BME of the femoral head in the presence of discrete "band-like" subchondral lesions should be considered as a poor prognostic sign in the course of the disease.

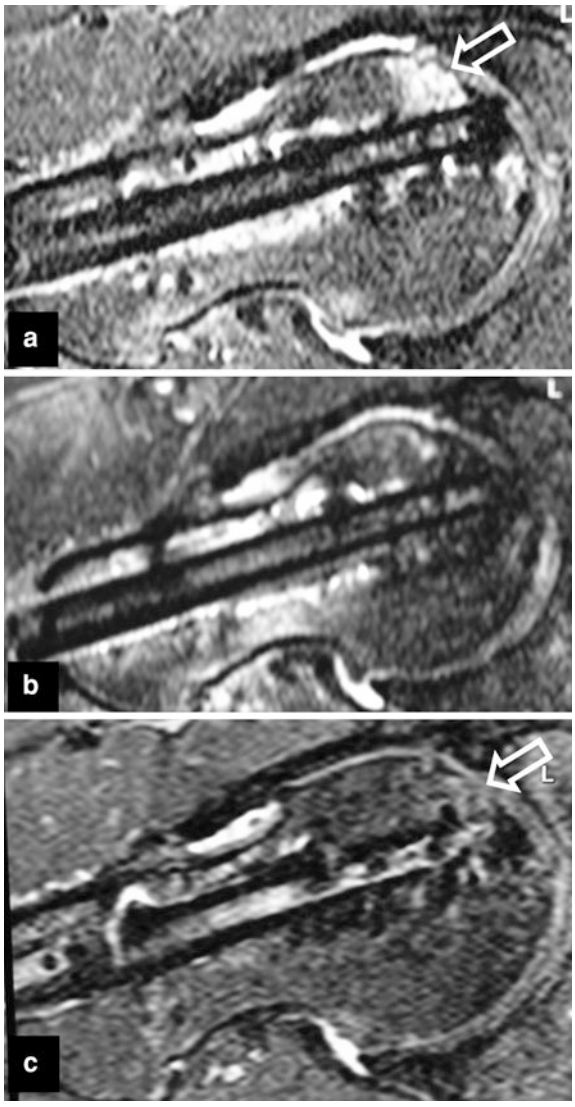

Fig. 15 A 33-year-old female patient treated with vascularized fibular graft. The oblique axial fat suppressed contrast-enhanced T1-w MR images show enhancement in the previous osteonecrotic lesion (*arrow* in **a**), 6 weeks after the operation. The corresponding images 6 months (**b**) and 1 year (**c**) after grafting show almost normal appearance of the bone marrow (*arrow* in **c**)

The Painful Hip Joint in FHON

Disabling pain may appear in various stages of FHON, even in the absence of articular collapse. Pain is rare in stages I and II and is commonly encountered in stage III of the disease. The cause of pain is not well understood and possible contributing factors include development of subchondral fracture, BME, large necrotic volume and joint effusion (Koo et al. 1999; Iida et al. 2000; Huang et al. 2003; Ito et al. 2006).

MRI may be extremely helpful in patients with predisposing factors for FHON and hip joint pain. It can accurately confirm or rule out FHON and in addition is able to investigate other causes of pain and disability.

Prognosis and MR Imaging

The lesion size and extent of femoral head involvement have been found to be the main factor in predicting outcome and determining treatment in FHON (Ohzono et al. 1992). The size of lesions on plain radiographs may be difficult to assess and might not correlate with the size on MRI. There are various methods of measuring the lesion size using MRI, varying from simple quantitative or visual methods to sophisticated ones requiring advanced software (Koo and Kim 1995; Kim et al. 1998; Steinberg et al. 1999; Malizos et al. 2001; Bassounas et al. 2007). The limited studies on the reproducibility and intraobserver variation of these methods have shown variable levels of consistency. The lesion location is also an important parameter in predicting femoral head collapse. It has been shown that lesions located posteroinferiorly or at the medial two thirds extending to acetabular ridge are more commonly associated with deterioration (Min et al. 2008).

Minimal FHON represents the presence of focal lesions which are localized eccentrically in relation to the weight-bearing area and extend to a limited portion of the femoral head (Saito et al. 1988; Theodorou et al. 2002). Minimal FHON does not lead to articular collapse (Fig. 7).

Monitoring

MRI may be of value for long-term assessment of lesion size and progress of the repair process. Studies have shown that small early lesions in stage I can undergo reduction in volume or even spontaneous resolution over the course of a few years (Kopecky et al. 1991; Zhao et al. 2010). MRI could also serve as a reliable technique for monitoring the outcome of vascularized bone grafting in FHON (Fig. 13, 14, 15). The absence of enhancement of the graft bone marrow in the postoperative follow up MRI and the deterioration of collapse suggest failure (Karantanas 2007; Karantanas and Drakonaki 2011).

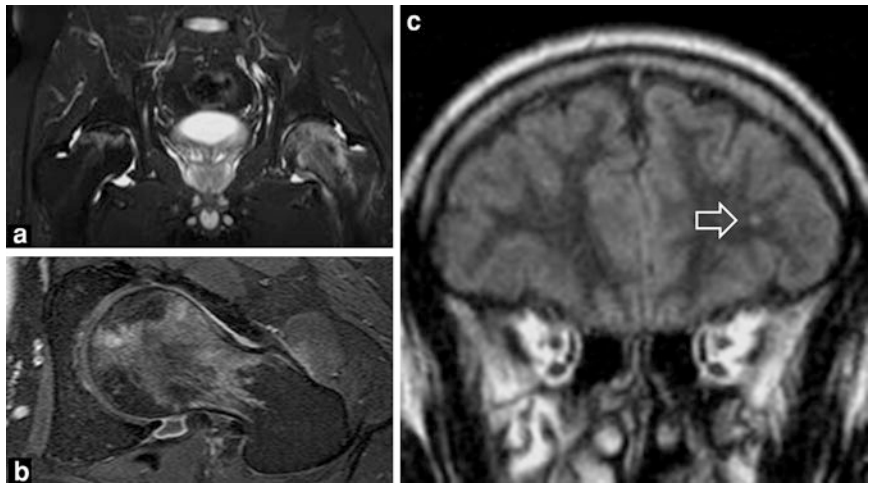

Fig. 16 A 30-year-old male patient with idiopathic osteonecrosis of both femoral heads. Only left side was symptomatic. The coronal fat suppressed PD (**a**) and oblique axial fat suppressed contrast-enhanced T1-w (**b**) MR images show the necrotic lesions and the bone marrow edema only on the left side. The coronal FLAIR MR image (**c**) shows a high-signal intensity area in the subcortical white matter (*arrow*)

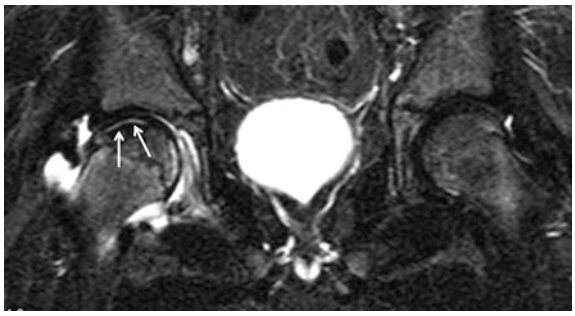

Fig. 17 A 9-year-old-girl with right LCP disease. The plain film was unremarkable (not shown). The coronal STIR MR image demonstrates right proximal femoral epiphyseal subchondral fluid signal, consistent with subchondral fracture due to necrotic phase LCP disease (*arrows*). There is also a right hip joint effusion

The development of multichannel whole body MRI has enabled bone marrow screening at high diagnostic accuracy (Schmidt et al. 2009). Screening for FHON might draw further attention as there is evidence that this disease is rather a multisystemic disorder not necessarily located exclusively in the skeleton. One study showed that cerebral white matter lesions are detected with high frequency (56.9%) in young adult patients with non-traumatic FHON of the femoral head compared to age and sex-matched controls (Hadjigeorgiou et al. 2004) (Fig. 16).

The differential diagnosis of FHON on imaging studies is limited since the typical on MR images signs suggest the correct diagnosis. Femoroacetabular impingement-cam type and bursitis could present with identical symptoms and signs but the MRI diagnosis is straightforward. In the presence of articular collapse, occasionally its difficult to discriminate advanced FHON from subchondral insufficiency fracture of the femoral head, degenerative osteoarthritis/rapidly progressive osteoarthritis, transient or systemic osteoporosis complicated with insufficiency fracture, metastatic lesion in patients with known malignancy and complicated low grade septic arthritis. The age, sex and clinical profile of the patients, narrow significantly the list of differentials.

3.2.2 Legg-Calvé-Perthes' Disease

Legg-Calvé-Perthes' (LCP) disease is a form of idiopathic osteonecrosis occurring in preadolescent children, mainly boys (peak age 5–6 years). Most cases are unilateral; when bilateral (10–15%), the lesions are usually asynchronous (Barker and Hall 1986). At the early stage, LCP remains occult on radiographs. MRI is a useful tool, for prompt diagnosis, accurate staging and detection of complications and assessment of prognosis (Dillman and Hernandez 2009). The MRI protocol for evaluation of a possible LCP should include both conventional and cartilage-specific sequences as well as more demanding techniques depending upon the individual patient (Lamer et al. 2002; Karantanas and Drakonaki 2011).

MRI is both sensitive and specific for the early detection of LCP disease. During the early avascular (necrotic) phase, which can present with normal radiographs, MRI reveals focal or diffuse low or intermediate SI on T1-w and high SI on STIR/FS PD/T2-w sequences in the epiphysis of the

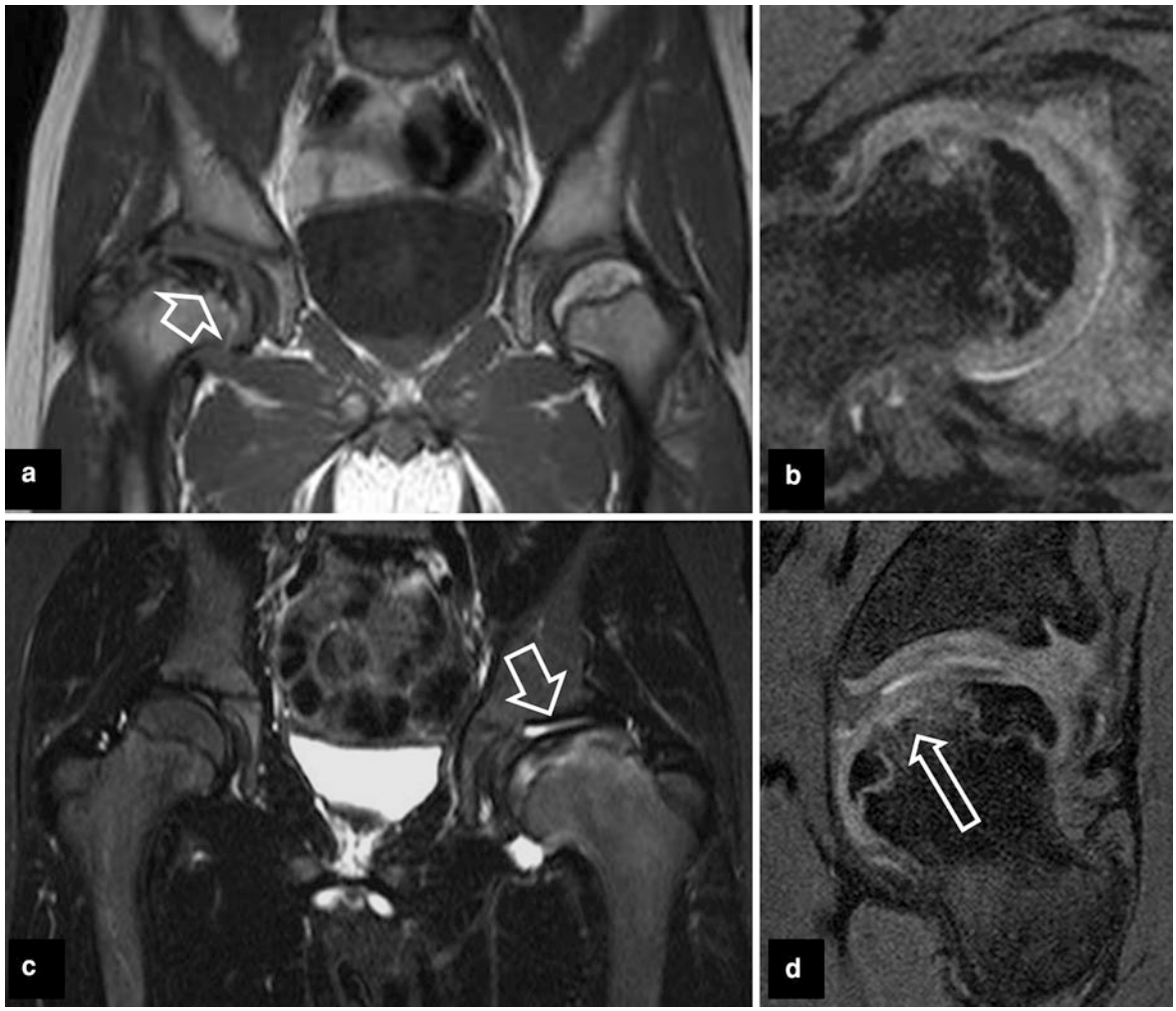

Fig. 18 LCP in two different patients. A 10-year-old boy with LCP on the right side. **a** The coronal T1-w MR image shows the low—compared to the left side—signal intensity and remodeling of the femoral head epiphysis (*arrow*). **b** The high resolution oblique axial gradient echo-water excitation T1-w MR image shows the intact femoral head articular cartilage. A 11-year-old-boy with left LCP disease. The coronal STIR MR image (**c**) shows the abnormal shape (flattening of the superior femoral head) and abnormal signal of the epiphyseal bone marrow on the left (*arrows*). **d** The oblique axial 3D-T1-w water excitation GRE MR image demonstrates the abnormality consisting of a bone bridge and disruption of the normal growth plate (*arrow*)

femoral head. The latter can also depict a curvilinear subchondral lesion in the antero-superior aspect of the femoral head ("*crescent*" sign or "*Caffey*" sign) representing a subchondral fracture (Fig. 17). Metaphyseal involvement is an important prognostic sign for the clinician since it interferes with the patient's normal growth. Metaphyseal involvement is demonstrated with increased signal within the epiphyseal plate and the metaphysis on FS T2-w sequences.

More advanced necrosis is demonstrated with epiphyseal low SI on all sequences, partial or complete non-enhancement 2 min after IV injection and joint effusion and synovitis (Dillman and Hernandez 2009) (Fig. 18). During the revascularization and reparative phases, revascularization areas typically show high SI on FS PD/T2-w and STIR MR images, delayed persistent contrast enhancement or hyperenhancement (Lamer et al. 2002). MRI can also depict various morphologic abnormalities including

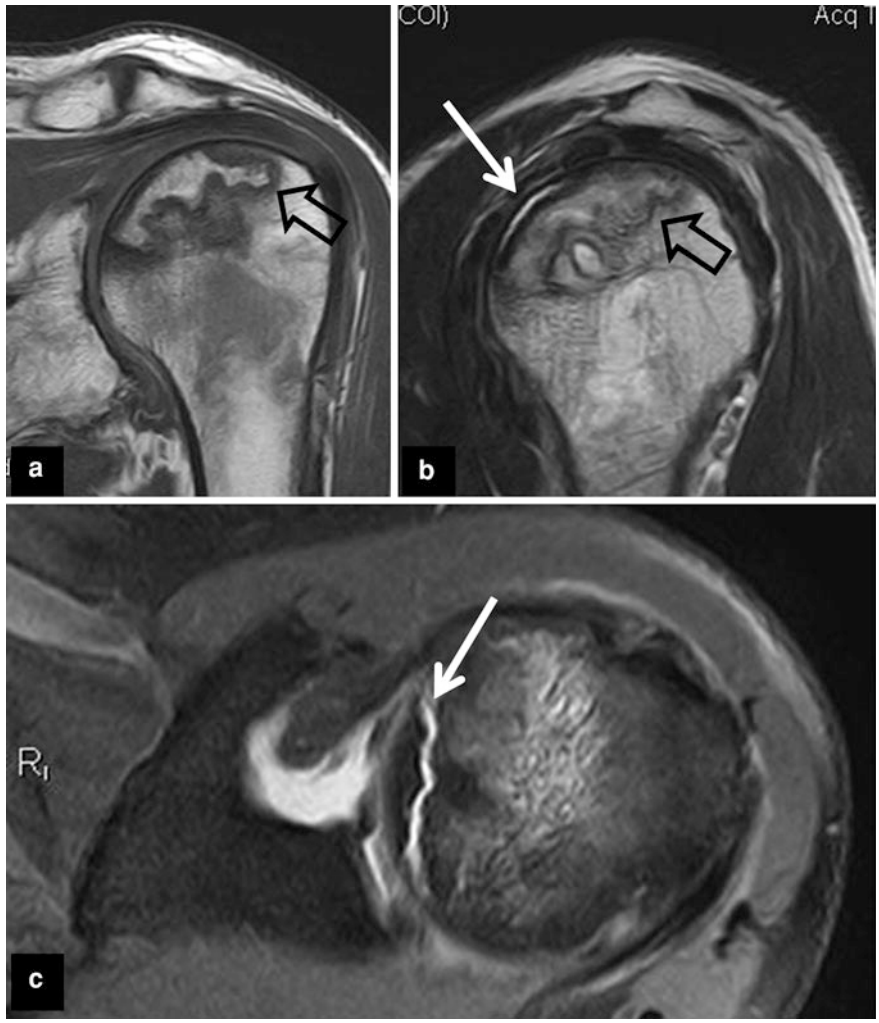

Fig. 19 A 66-year-old previously healthy male patient, with idiopathic osteonecrosis of the humeral head. **a** The oblique coronal T1-w MR image shows the typical "band-like" sign (*arrow*). **b** The oblique sagittal T2-w image shows the "double-line" sign (*open arrow*) and the "crescent" sign of the subchondral fracture (*thin white arrow*). **c** The fat suppressed axial T2-w MR image confirms the presence of the subchondral fracture in the medial aspect of the humeral head (*arrow*). The presence of bone marrow edema and joint effusion suggest advanced disease

flattening and fragmentation of the epiphysis and lateral subluxation of the femoral head (Fig. 18c) (Merlini et al. 2010).

3.3 Other Locations

3.3.1 Upper Limb

3.3.1.1 Humerus

The MRI findings in the humeral head are similar to the ones observed in FHON (Fig. 19). Due to the fact that the glenohumeral joint is not bearing significant weight, clinical and radiogical deterioration is quite delayed compared to weight-bearing joints.

3.3.1.2 Elbow

Panner's disease or *osteonecrosis of the capitellum* represents an osteochondrosis, most commonly seen in fast-ball pitchers and competitive gymnasts younger than 10 years. Osteochondritis dissecans of the capitellum typically occurs in adolescents and is associated with loose body formation. Panner's disease and osteochondritis dissecans likely represent a continuum of disordered endochondral ossification.

Panner's disease is a self limited disorder. As the findings in plain radiographs are subtle, this disorder is most probably underdiagnosed. It is widely accepted that Panner's disease is associated with repeated valgus stress on the elbow at the age when

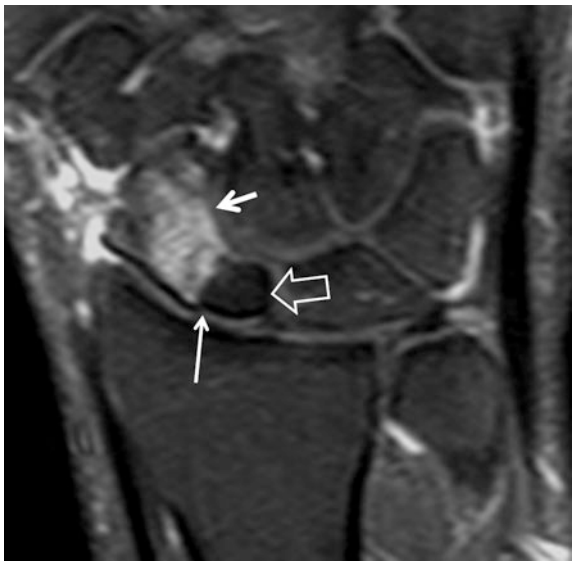

Fig. 20 The coronal fat suppressed contrast-enhanced T1-w MR image, in a 24-year-old patient with a known scaphoid fracture non-union, shows cortical disruption at the fracture site (*long thin arrow*), increased enhancement in the distal two thirds of the scaphoid bone (*short arrow*) and decreased perfusion (lower signal of the marrow as compared to the surrounding bones) of the proximal part (*open arrow*), in keeping with osteonecrosis. This was confirmed surgically by means of absence of any bleeding points

the capitellum has the most vulnerable blood supply. The MRI findings in Panner's disease are similar to those of LCP hip osteochondrosis.

3.3.1.3 Wrist and Hand

In acute *scaphoid* fractures as well as in established scaphoid *nonunion*, the proximal scaphoid fragment may undergo osteonecrosis, which is likely to happen in 30% in middle-third fractures and in up to 100% of proximal pole (Cooney et al. 1980). Ischemia following a fracture has an anatomical explanation as the vascular supply occurs from distal to proximal part and there is no interosseous anastomosis between the vascular territories of the dorsal and palmar branches. Newer surgical techniques, such as vascularized grafting, should be planned after a thorough preoperative imaging (Dailiana et al. 2004; Malizos et al. 2007b; Karantanas et al. 2007). Contrast-enhanced MRI is currently the best imaging method to evaluate the viability of the proximal pole in scaphoid nonunion (Schmitt et al. 2011a, b) (Fig. 20).

Preiser's Disease

Idiopathic osteonecrosis of the scaphoid is a rare condition which was first described by Preiser in 1910. Up to now, both the etiology and pathology are not entirely understood. The particularities in scaphoid perfusion play an important role in the development of Preiser's disease. Although a history of wrist trauma must be excluded for this diagnosis, routinely it is difficult to really exclude minor or repetitive injuries of the wrist (Schmitt et al. 2011a, b). MRI is able to assess the early stage of the disease by depicting BME. Later in the course, osteosclerosis is better depicted by CT. However, the viability of the bone marrow is better assessed with MRI (Karantanas et al. 2007) (Fig. 21). In the advanced stage of the disease, the proximal pole is becoming more sclerotic and progressively narrowed. The term "*nipple sign*" describes this reduced volume (Fig. 21). A pathologic fracture at the proximal scaphoid pole may also occur in the advanced stage (Schmitt et al. 2011a, b)

Kienbock's Disease or Lunatomalacia

Trauma or minus ulnar variant may result in osteonecrosis of the *lunate* bone, also known as *Kienbock's* disease. MRI is able to show BME which corresponds to the earliest phase of the disease, at which the plain radiographs are unremarkable. Later in the course of the disease, MRI is able to assess if there is still viability of the bone marrow when plain radiographs show osteosclerosis (Fig. 22). MRI is useful before the stages III (fracture of the lunate) and IV (progressive collapse and osteoarthritis) which are obvious on plain radiographs.

Other Locations

Osteonecrosis of the *metacarpal heads* may also occur and are associated with trauma and use of corticosteroids. Few reports exist in the literature (Sagar et al. 2010). Most commonly men are involved in the middle finger, followed by the index, ring and small fingers. This disorder has also been described as *Mauclaire's* disease when affecting juveniles. MRI imaging is indicated in high risk groups such as athletes and patients on steroids, when plain radiographs are normal.

Osteonecrosis of the *capitate* and the *hamate* bones usually affects their proximal pole. *Caffey's disease* represents a rare condition; osteonecrosis of all carpal bones (Schmitt et al. 1997).

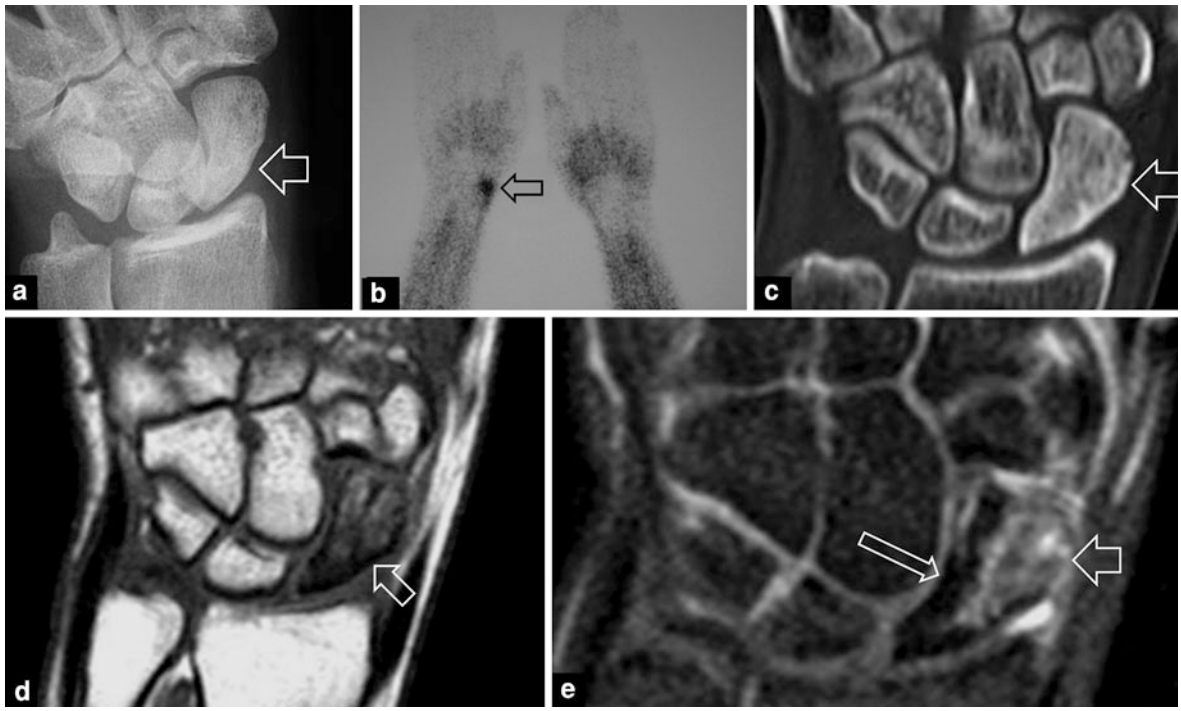

Fig. 21 A 25-year-old female patient with a 12-month wrist pain. Idiopathic osteonecrosis of the scaphoid bone or Preisser's disease (*arrows*) is demonstrated with increased osteosclerosis on plain radiographs (**a**), increased uptake on scintigram (**b**) and increased density on computed tomography (**c**). The coronal T1-w (**d**) and STIR (**e**) MR images show the signal alteration in the bone marrow of the scaphoid bone (*arrows*). The STIR image (**e**) is able to discriminate the viable marrow showing edema (*short arrow*) from the necrotic one which shows lower signal intensity that the normal one of the surrounding carpal bones (*long arrow*). The "nipple sign" represents the reduced volume of the bone in its proximal pole

Rare forms of osteonecrosis include the *Thiemann's* disease (involvement of the proximal base of the first phalanx at II and III fingers) and the trauma-related necrosis of the epiphyseal plates (Schmitt et al. 1997).

3.3.2 Lower Limb

3.3.2.1 Knee

The knee is the second most common site for osteonecrosis to occur and its involvement may coexist with the hip's (Fig. 23). The lesions are usually found in the lateral femoral and tibial condyles as well as in the medial femoral condyle. Multiple lesions may be seen as incidental findings. The imaging findings are similar to other locations. Long-standing osteonecrotic lesions may be complicated by subchondral fracture and articular surface collapse (Fig. 24).

Spontaneous Osteonecrosis

Spontaneous osteonecrosis (SONK) was first described by Ahlbäck in 1968 who thought that this is primary osteonecrotic process (Ahlbäck et al. 1968). SONK is clinically expressed with acute pain without trauma and most frequently is seen in women older than 60 years of age. These patients may have a systemic osteopenia and commonly present with a torn or degenerated meniscus. In addition, the duration of symptoms before imaging has a negative relation to prognosis (Karantanas et al. 2008). Currently, the term SONK is misleading as the disorder is believed to represent an insufficiency fracture with secondary osteonecrosis following the collapse. The terms currently used include the'*subchondral insufficiency fracture*' (Yamamoto and Bullough 2000; Kattapuram and Kattapuram 2008) and '*insufficient bone-related arthropathy of the knee*' (Karantanas et al. 2008). On MRI, a low SI subchondral

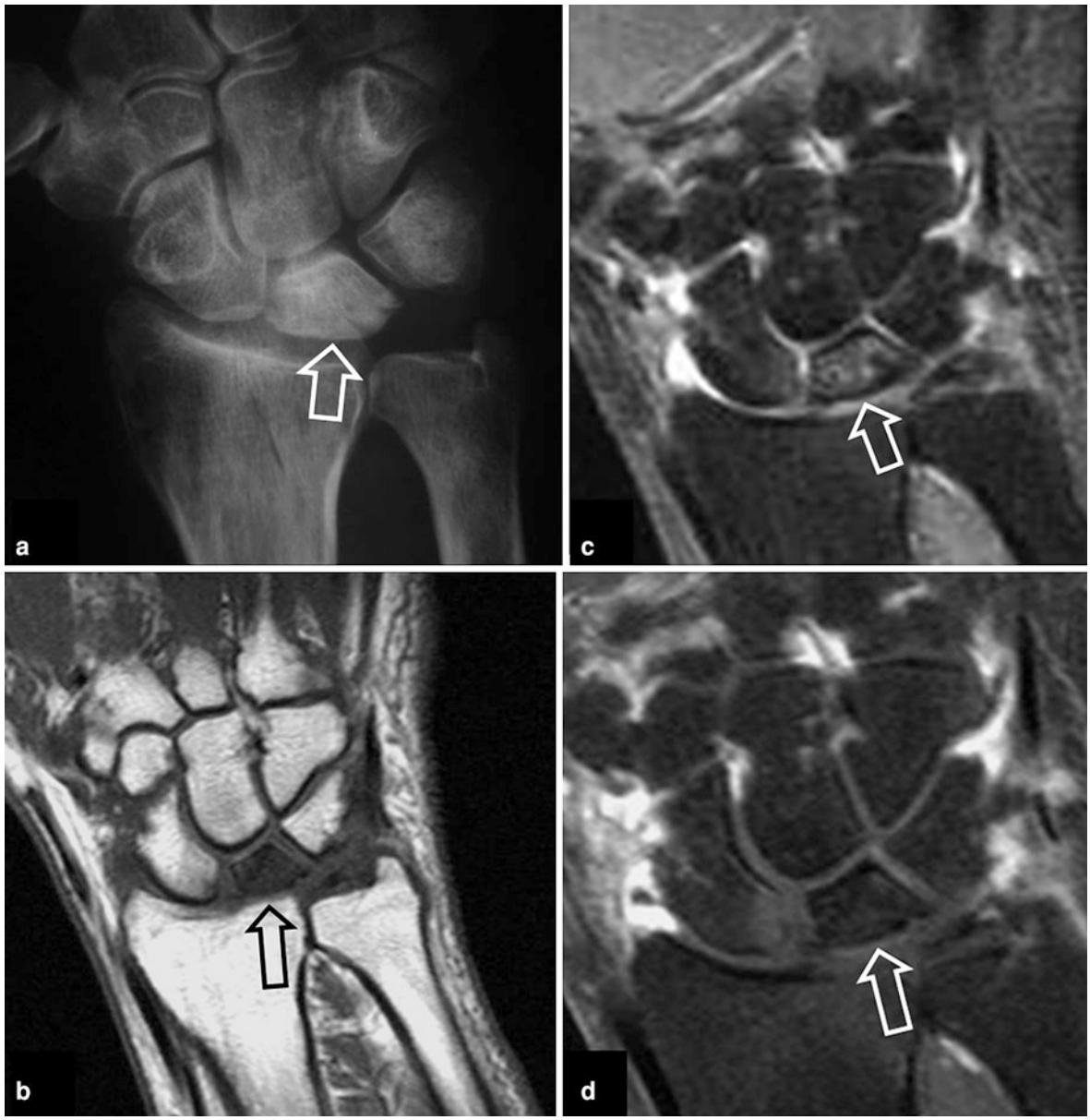

Fig. 22 A 76-year-old male patient with Kienbock's disease. The plain radiograph (**a**) shows increased sclerosis of the lunate bone (*arrow*). The coronal T1-w (**b**) and STIR (**c**) MR images show low- and high-signal intensity in the lunate respectively, in keeping with bone marrow edema (*arrows*). **d** The coronal fat suppressed contrast-enhanced T1-w MR image shows slightly lower perfusion of the lunate bone marrow as compared to surrounding bones in keeping with nonviability (*arrow*)

lesion is surrounded by extensive BME. In cases with articular collapse, a "crescent" sign, representing a subchondral fracture, may be obvious (Fig. 25).

Osteonecrosis in the postoperative knee may have a similar to the above appearance (Pape et al. 2007). Limited cases have been reported and the prognosis is currently unclear.

3.3.2.2 Ankle and Foot

Osteonecrosis of the *talus* may occur following trauma or operation. The incidence has been reported to be as high as 50% for Hawkins Type II and between 75 and 100% for Type III talar neck fracture dislocations (Hawkins 1970). Previous administration of steroids, may result in multiple and bilateral infarcts. Radiographs

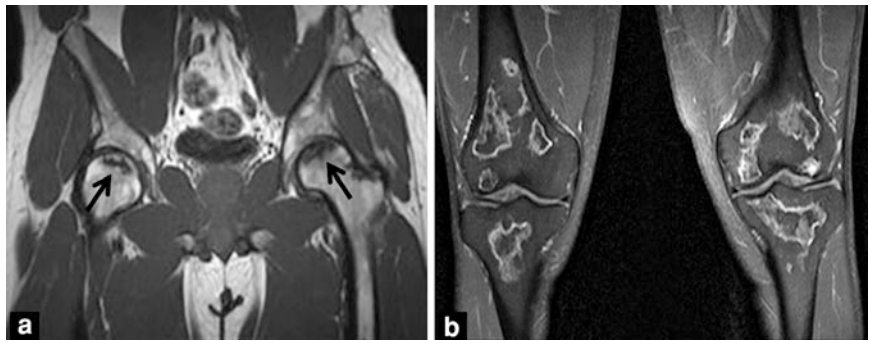

Fig. 23 A young adult patient with a history of corticosteroid administration. **a** The coronal T1-w MR image shows osteonecrosis of both femoral heads (*arrows*). **b** The coronal fat suppressed PD MR image of the knees shows multiple marrow infarcts in the distal femoral and proximal tibial bones

shown in the beginning of sclerosis is followed by deformity and articular collapse and fragmentation (Pearce et al. 2005). MRI findings do not differ as compared to other locations (Fig. 26).

A painful and osteosclerotic and fragmented tarsal *navicular*, previously normal, is suggestive of *Kohler's* disease. Navicular osteonecrosis is a self-limiting disorder with excellent prognosis, usually unilateral, affects children—most often boys—and the onset is at the age of 4–5 years. Radiographs may show osteosclerosis and collapse in advanced cases. MRI is able to depict early disease (Fig. 27). Spontaneous osteonecrosis of the tarsal navicular in adults is an uncommon entity known as *Mueller–Weiss syndrome* (Tosun et al. 2011). Bilateral involvement in female patients is usually the case.

Freiberg's disease affects usually the distal head of the second metatarsal bone in adolescent females and belongs to the group of osteochondroses. Rarely, subarticular osteonecrosis may occur in adults as well (Fig. 28).

3.3.3 Jaws

Bisphosphonates (BP) are increasingly used as antineoplastic agents in patients with metastatic bone disease in order to reduce bone pain. A recognized adverse effect of their administration is osteonecrosis of the jaws (ONJ) which is evident in up to 10% of patients receiving intravenous treatment. The diagnosis is primarily based on history and clinical presentation (Morag et al. 2009). By consensus, the syndrome is now defined by the presence of exposed bone in the mouth which fails to heal after appropriate treatment over a period of 6 or 8 weeks. The differential diagnosis of ONJ is quite narrow including only osteomyelitis and metastatic disease. Imaging is currently used to assess the initial extent and to evaluate progression and complications such as pathologic fractures. Radiographs show thickening of the lamina dura, and poor or no healing of extracted sites. Later on, there are mixed osteolytic and osteosclerotic lesions. In advanced cases, narrowing of the marrow space and mandibular canal will occur in keeping with the patient's paresthesia. CT may show better the periosteal reaction and can thus differentiate ONJ from metastatic disease which shows no periostitis (Bianchi et al. 2007). Bone scintigraphy is the most sensitive imaging modality for the detection of ONJ at an early stage, perhaps better than both the CT and MRI in establishing the diagnosis (Chiandussi et al. 2006). MRI depicts early involvement and local disease extension. The signal abnormalities follow the stage of the disease (Arce et al. 2009). The earliest MRI finding is decreased SI of the fatty marrow on the mandible and maxilla, on T1-w images. The MRI findings of more advanced disease include bone destruction, soft-tissue edema and enhancement, inferior alveolar nerve thickening, and pterygoid muscle swelling and enhancement.

3.3.4 Spine

Kummel's disease represents a failure of the fracture healing process, with development of an avascular zone below the superior endplate. Many synonymous terms have been used to describe this pathology: posttraumatic vertebral osteonecrosis or avascular necrosis, vertebral pseudarthrosis, intervertebral vacuum, cleft or gas, delayed vertebral collapse and vertebral compression fracture nonunion. The necrotic process eliminates the healing potential and results in an avascular nonunion with cavity formation (Libicher et al. 2007). The appearance of gas in a

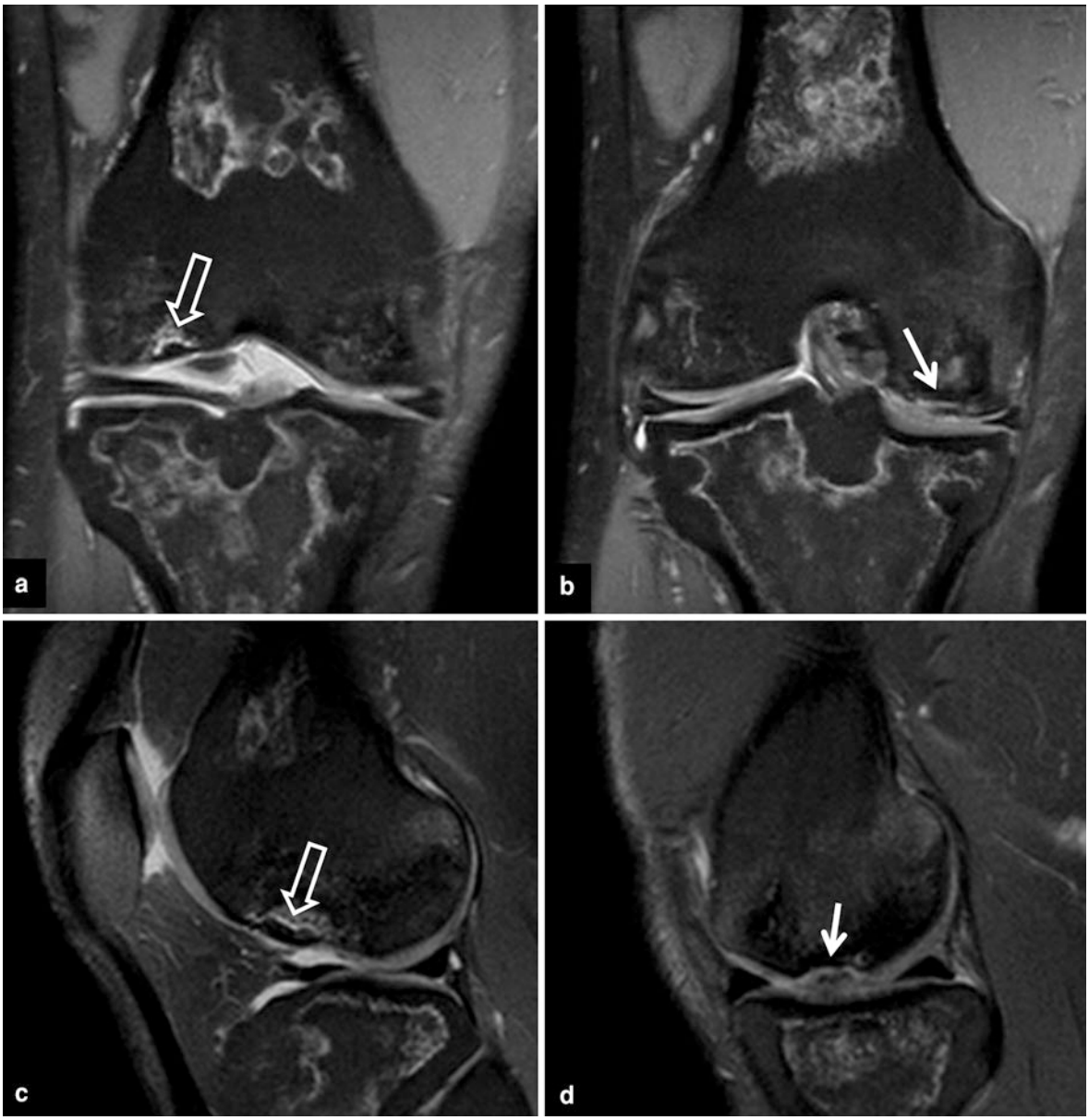

Fig. 24 A 33-year-old male patient who was involved from leukemia 20 years before and had known asymptomatic medullary infarcts in the hip and pelvis as well as around the knee joints. A recent pain without trauma appeared in the right knee. The fat suppressed PD MR images in the coronal (**a**, **b**) and sagittal (**c**, **d**) planes show multiple medullary infarcts in the metaphysis and epiphysis. In addition, there is a subchondral fracture along with articular surface collapse in the anterior lateral femoral condyle (*open arrows*) and the weight-bearing surface of the medial femoral condyle (*arrows*)

collapsed vertebral body (intravertebral vacuum cleft) is diagnostic of Kummel's disease (McKiernan and Faciszewski 2003). The osteonecrotic cavity results from trauma or osteoporotic fracture which may have occured weeks or months prior to presentation in this form. The gas migrates from a degenerated disc into the cavity and it is generally accepted that the presence of this vacuum cleft excludes infection or neoplasm. The "vacuum cleft" appears as a black linear area, usually under the upper epiphyseal plate,

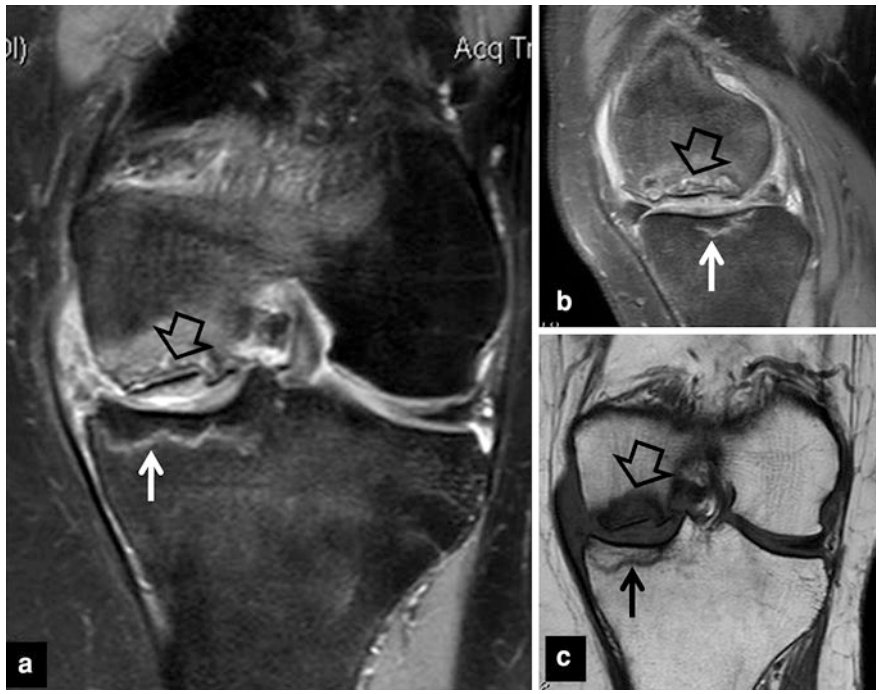

Fig. 25 Insufficiency fracture, also known as SONK, in a 72-year-old female patient with known osteopenia and medial knee joint osteoarthritis. The fat suppressed PD MR image in the coronal plane shows extensive bone marrow edema in the medial femoral condyle and proximal tibia. In addition, there is a subchondral fracture in the medial femoral condyle with associated articular surface collapse (*arrow*). A high-signal intensity linear structure in the medial tibial epiphysis (*thin arrow*) represents a second insufficiency fracture, without any collapse of the articular surface. Same findings are seen in the fat suppressed PD sagittal (**b**) and coronal T1-w (**c**) MR images

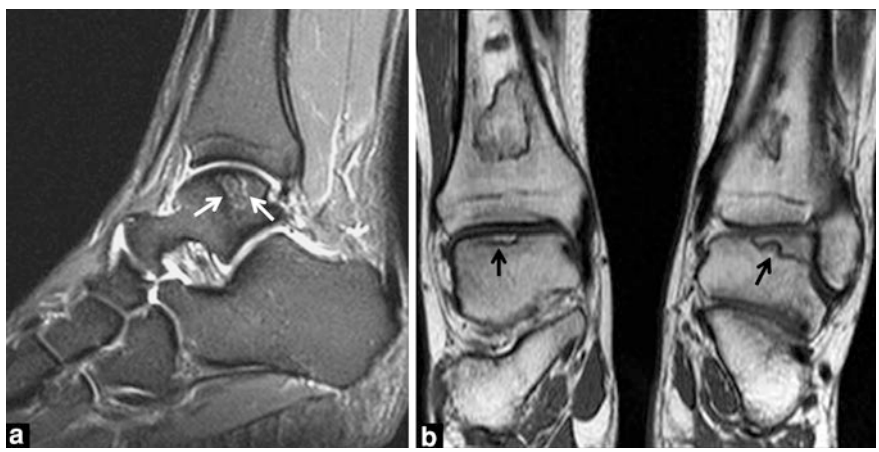

Fig. 26 Osteonecrosis of the talus. **a** The sagittal STIR MR image in this 30-year-old man, 6 months after injury in the ankle, shows the typical appearance of subarticular osteonecrosis (*arrow*s). **b** The coronal T1-w MR image in this asymptomatic 27-year-old man with a history of steroid administration shows multiple medullary infarcts in the distal tibias and osteonecrotic lesions in both tali (*arrows*)

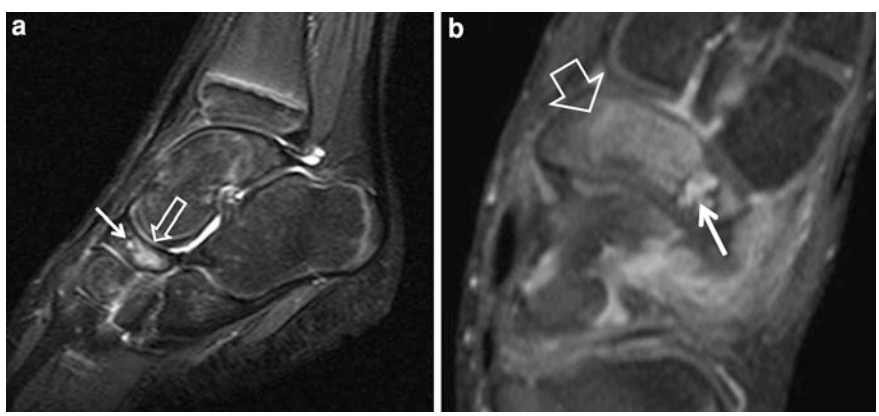

Fig. 27 Kohler's disease. The sagittal STIR image in a 7-year-old male (**a**) and the axial fat suppressed PD MR image in 7-year-old female (**b**) show bone marrow edema (*open arrow*) and some cystic changes (*thin arrow*)

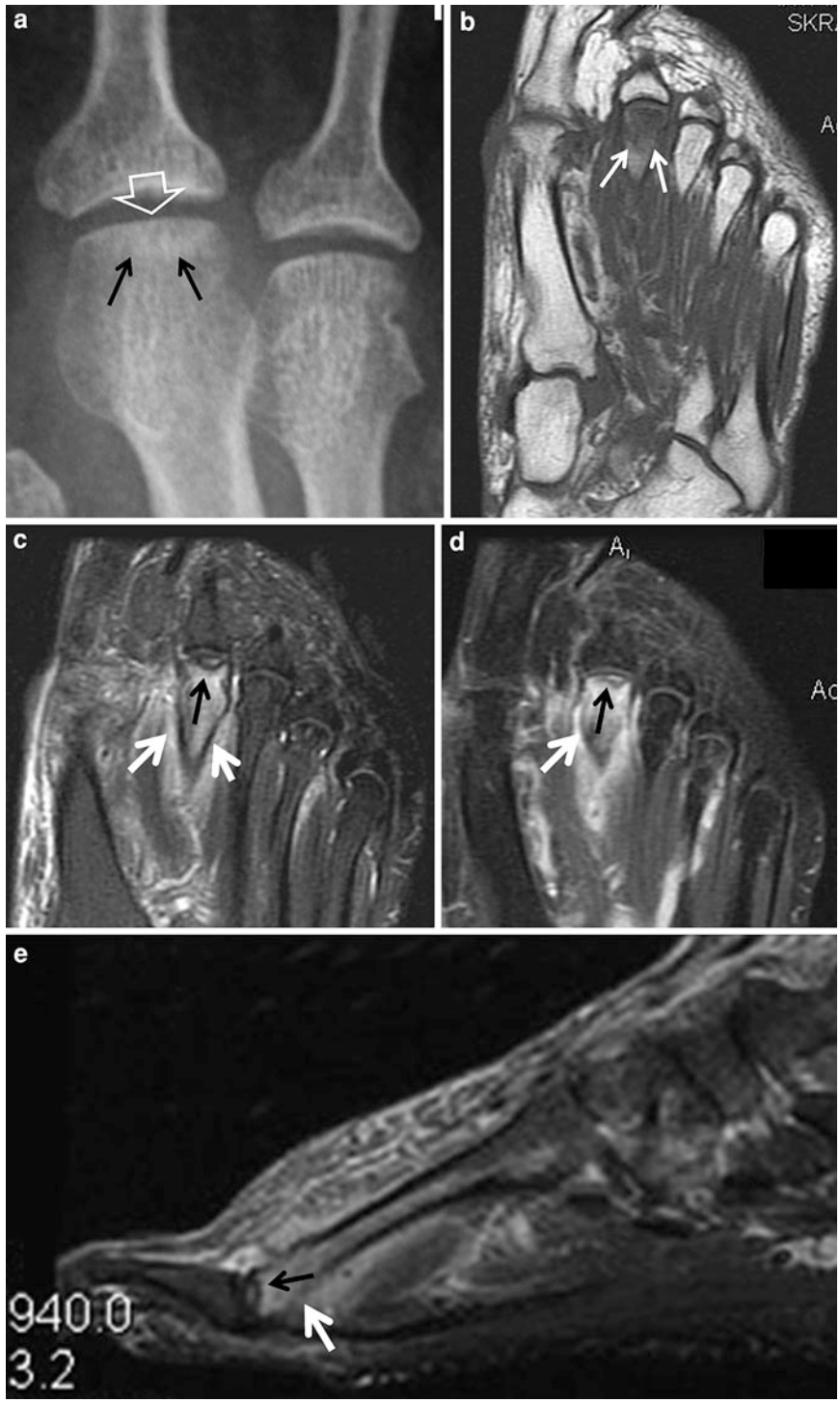

Fig. 28 Idiopathic osteonecrosis of the distal 2nd metatarsal head in a 60-year-old female patient. **a** The plain radiograph shows flattening (*open arrow*) and subarticular sclerosis (*black arrows*). **b** The T1-w MR image shows low-signal intensity corresponding to bone marrow edema (*arrows*). The fat suppressed PD (**c**) and STIR (**d**) as well as the fat suppressed contrast-enhanced T1-w (**e**) MR images show the bone marrow edema (*white arrows*) and the osteonecrotic area in the subchondral region (*black arrows*). Edema of the surrounding soft tissues is also seen.

on both CT and MRI (Fig. 29). In case that fluid migrates from the nucleus pulposus to the osteonecrotic cavity, there is a "*fluid*" sign demonstrated with high SI on STIR and T2-w MR images and again its presence stands against infection or neoplasm (Baur et al. 2002) (Fig. 29).

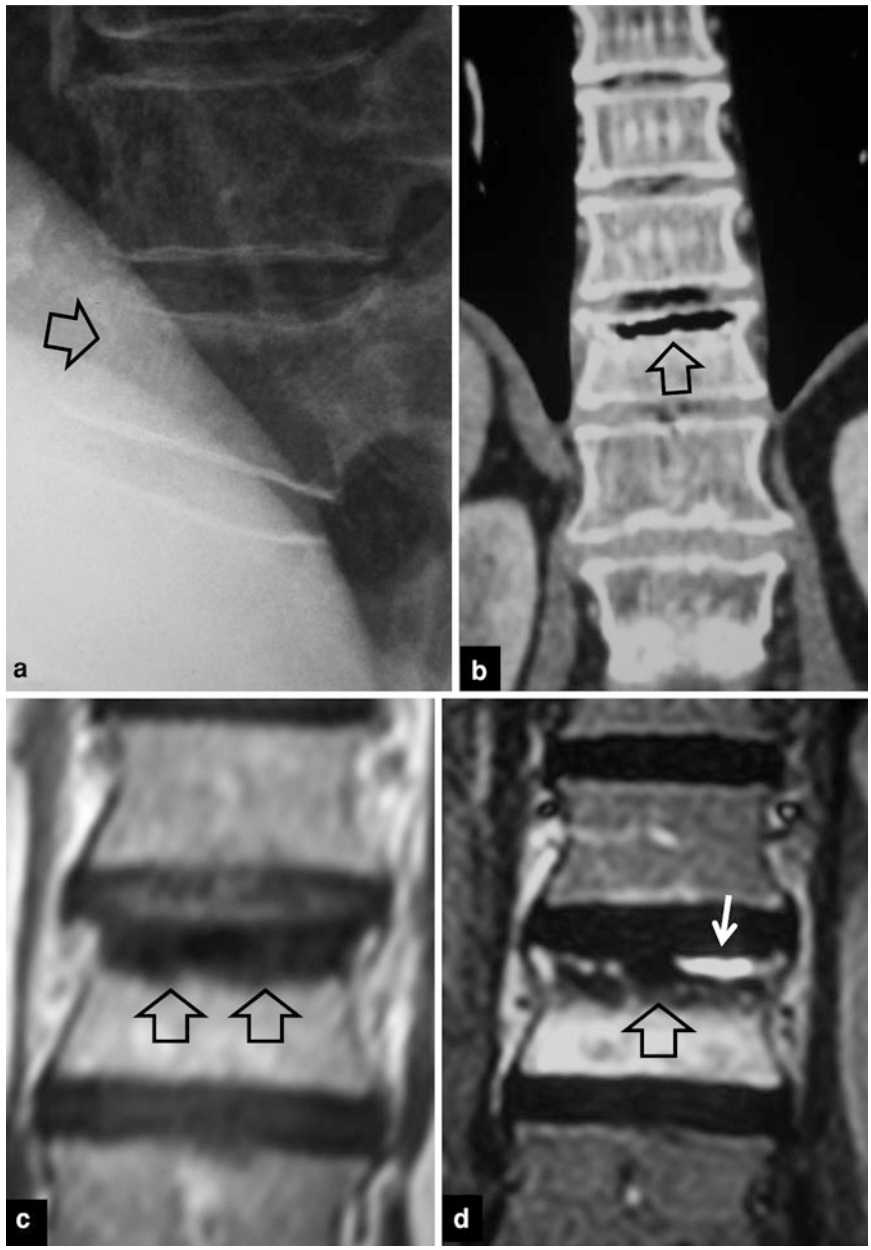

Fig. 29 Kummel's disease in a female osteoporotic 73-year-old female patient with a history of 3 weeks dorsal back pain. **a** The lateral radiograph shows a wedge-shaped deformity (*arrow*). No vacuum is seen within the fractured vertebral body. **b** The coronal CT reformation shows the "vacuum cleft" under the upper epiphyseal plate of the fractured vertebra (*arrow*). There is also vacuum within the degenerated disc above the vertebra. **c** The "vacuum cleft" is demonstrated as a low-signal intensity band on this coronal T1-w MR image (*arrows*). **d** The coronal T2-w MR image shows the "vacuum cleft" as a low-signal intensity band (*open arrow*) and in addition a "fluid" sign representing fluid within the osteonecrotic cavity (*thin arrow*)

4 Closing Remarks

Bone infarcts are in general incidental findings on radiographs and MRI. In patients with sickle cell disease, discrimination from osteomyelitis is clinically important.

FHON is a devastating disorder affecting young patients and despite treatment it normally follows a progressive course toward a destructive osteoarthropathy. MRI has gained an established role regarding accurate classification of the early stages and prognosis assessment. Evolving role of MRI includes investigation of multiple foci, depiction of the cause of pain, accurate discrimination between early and advanced disease and postoperative evaluation of the vascularized grafts. MRI is also capable of assessing osteonecrosis in other locations. The clinicians need to know if there is any ischemic lesion at all, if the lesion is indeed the cause of pain, and for the subarticular lesions, an estimation of prognosis.

References

Ahlbäck S, Bauer GC, Bohne WH (1968) Spontaneous osteonecrosis of the knee. Arthr Rheum 11:705–733

Arce K, Assael LA, Weissman JL, Markiewitcz MR (2009) Imaging findings in bisphosphonate-related osteonecrosis of jaws. J Oral Maxillofac Surg 67(1):75–84

Assouline-Dayan Y, Chang C, Greenspan A et al (2002) Pathogenesis and natural history of osteonecrosis. Semin Arthr Rheum 32:94–124

Barker DJ, Hall AJ (1986) The epidemiology of Perthes' disease. Clin Orthop Relat Res 209:89–94

Bassounas AE, Karantanas AH, Fotiadis DI, Malizos KN (2007) Femoral head osteonecrosis: volumetric MRI assessment and outcome. Eur J Radiol 63:10–15

Baur A, Stäbler A, Arbogast S, Duerr HR, Bartl R, Reiser M (2002) Acute osteoporotic and neoplastic vertebral compression fractures: fluid sign at MR imaging. Radiology 225:730–735

Beltran J, Burk JM, Herman LJ et al (1987) Avascular necrosis of the femoral head: early MRI detection and radiological correlation. Magn Reson Imaging 5:431–442

Beltran J, Herman LJ, Burk JM et al (1988) Femoral head avascular necrosis: MR imaging with clinical-pathologic and radionuclide correlation. Radiology 166:215–220

Bianchi SD, Scoletta M, Cassione FB et al (2007) Computerized tomographic findings in bisphosphonate-associated osteonecrosis of the jaw in patients with cancer. Oral Surg Oral Med Oral Pathol Oral Radiol Endod 104:249–258

Chiandussi S, Biasotto M, Dore F et al (2006) Clinical and diagnostic imaging of bisphosphonate-associated osteonecrosis of the jaws. Dentomaxillofac Radiol 35:236–243

Coleman B, Kressel H, Dalinka M et al (1988) Radiographically negative avascular necrosis: detection with MR imaging. Radiology 168:525–528

Cooney WP, Dobyns JH, Linscheid RL (1980) Fractures of the scaphoid: a rational approach to management. Clin Orthop 149:90–97

Dailiana ZH, Zachos V, Varitimidis S et al (2004) Scaphoid nonunions treated with vascularised bone grafts: MRI assessment. Eur Radiol 50:217–224

Dillman JR, Hernandez RJ (2009) MRI of Legg-Calve-Perthes disease. AJR Am J Roentgenol 193:1394–1407

Duda SH, Laniado M, Schick F, Claussen CD (1993) The double-line sign of osteonecrosis: evaluation on chemical shift MR images. Eur J Radiol 16:233–238

Fordyce M, Solomon L (1993) Early detection of avascular necrosis of the femoral head by MRI. J Bone Jt Surg Br 75:365–367

Fujioka M, Kubo T, Nakamura F et al (2001) Initial changes of non-traumatic osteonecrosis of femoral head in fat suppression images: bone marrow edema was not found before the appearance of band patterns. Magn Reson Imaging 19:985–991

Gardeniers JWM (1993) ARCO Committee on terminology and staging. Report on the committee meeting at Santiago de Compostella. ARCO Newsletter 5:79–82

Genez BM, Wilson MR, Houk RW et al (1988) Early osteonecrosis of the femoral head: detection in high-risk patients with MR imaging. Radiology 168:521–524

Hawkins LG (1970) Fractures of the neck of the talus. J Bone Jt Surg 52A:991–1002

Hadjigeorgiou GM, Karantanas AH, Zibis A et al (2004) Increased frequency of white matter lesions in patients with osteonecrosis (WMLeOn) of the femoral head. Eur J Radiol 50:278–284

Hermann G, Singson R, Bromley M et al (2004) Cystic degeneration of medullary bone infarction evaluated with magnetic resonance imaging correlated with pathologic examination. Can Assoc Radiol J 55:321–325

Huang GS, Chan WP, Chang YC et al (2003) MR imaging of bone marrow edema and joint effusion in patients with osteonecrosis of the femoral head: relationship to pain. AJR Am J Roentgenol 181:545–549

Iida S, Harada Y, Shimizu K, Sakamoto M, Ikenoue S, Akita T, Kitahara H, Moriya H (2000) Correlation between bone marrow edema and collapse of the femoral head in steroid-induced osteonecrosis. AJR Am J Roentgenol 174: 735–743

Ito H, Matsuno T, Minami A (2006) Relationship between bone marrow edema and development of symptoms in patients with osteonecrosis of the femoral head. AJR Am J Roentgenol 186:1761–1770

Karantanas AH (2007) Acute bone marrow edema of the hip: role of MR imaging. Eur Radiol 17:2225–2236

Karantanas A, Dailiana Z, Malizos K (2007) The role of MR imaging in scaphoid disorders. Eur Radiol 17:2860–2871

Karantanas AH, Drakonaki E, Karachalios T, Korompilias AV, Malizos K (2008) Acute non-traumatic marrow edema syndrome in the knee: MRI findings at presentation, correlation with spinal DEXA and outcome. Eur J Radiol 67:22–33

Karantanas AH, Drakonaki EE (2011) The role of MR imaging in avascular necrosis of the femoral head. Semin Musculoskelet Radiol 15:281–300

Kattapuram TM, Kattapuram SV (2008) Spontaneous osteonecrosis of the knee. Eur J Radiol 67:42–48

Kim YM, Ahn JH, Kang HS, Kim HJ (1998) Estimation of the extent of osteonecrosis of the femoral head using MRI. J Bone Jt Surg Br 80B:954–958

Kim YM, Oh HC, Kim HJ (2000) The pattern of bone marrow oedema on MRI in osteonecrosis of the femoral head. J Bone Jt Surg Br 82:837–841

Koo K-H, Kim R (1995) Quantifying the extent of osteonecrosis of the femoral head. A new method using MRI. J Bone Jt Surg Br 77B:875–880

Koo KH, Ahn IO, Kim R et al (1999) Bone marrow edema and associated pain in early stage osteonecrosis of the femoral head: prospective study with serial MR images. Radiology 213:715–722

Kopecky KK, Braunstein EM, Brandt KD et al (1991) Apparent avascular necrosis of the hip: appearance and spontaneous resolution of MR findings in renal allograft recipients. Radiology 179:523–527

Koren A, Garty I, Katzuni E (1984) Bone infarction in children with sickle cell disease: early diagnosis and differentiation from osteomyelitis. Eur J Pediatr 142:93–97

Kubo T, Yamazoe S, Sugano N et al (1997) Initial MRI findings of non-traumatic osteonecrosis of the femoral head in renal allograft recipients. Magn Reson Imaging 15:1017–1023

Lamer S, Dorgeret S, Khairouni A et al (2002) Femoral head vascularisation in Legg-Calvé-Perthes disease: comparison

of dynamic gadolinium-enhanced subtraction MRI with bone scintigraphy. Pediatr Radiol 32:580–585
Libicher M, Appelt A, Berger I et al (2007) The intravertebral vacuum phenomen as specific sign of osteonecrosis in vertebral compression fractures: results from a radiological and histological study. Eur Radiol 17:2248–2252
Malizos KN, Siafakas MS, Fotiadis DI, Karachalios TS, Soucacos PN (2001) An MRI-based semiautomated volumetric quantification of hip osteonecrosis. Skeletal Radiol 30:686–693
Malizos KN, Zibis AH, Dailiana Z, Hantes M, Karachalios T, Karantanas AH (2004) MR imaging findings in transient osteoporosis of the hip. Eur J Radiol 50:238–244
Malizos KN, Karantanas AH, Varitimidis SE et al (2007a) Osteonecrosis of the femoral head: etiology, imaging and treatment. Eur J Radiol 63:16–28
Malizos KN, Zachos V, Dailiana ZH, Zalavras C, Varitimidis S, Hantes M, Karantanas A (2007b) Scaphoid nonunions: management with vascularized bone grafts from the distal radius: a clinical and functional outcome study. Plast Reconstr Surg 119:1513–1525
Matsuno T, Kaneda K, Takeda N (1996) Development of angiosarcoma at the site of a bone infarct. Clin Orthop Relat Res 327:259–263
McKiernan F, Faciszewski T (2003) Intravertebral clefts in osteoporotic vertebral compression fractures. Arthr Rheum 48:14149
Merlini L, Combescure C, De Rosa V, Anooshiravani M, Hanquinet S (2010) Diffusion-weighted imaging findings in Perthes disease with dynamic gadolinium-enhanced subtracted (DGS) MR correlation: a preliminary study. Pediatr Radiol 40:318–325
Min BW, Song KS, Cho CH, Lee SM, Lee KJ (2008) Untreated asymptomatic hips in patients with osteonecrosis of the femoral head. Clin Orthop Relat Res 466:1087–1092
Mirra MJ, Gold RH, Marafiote R (1977) Malignant (fibrous) histiocytoma arising in association with a bone infarct in sickle cell disease: coincidence or cause-and -effect? Cancer 39:186–194
Mitchell DG, Rao VM, Dalinka MK et al (1987) Femoral head avascular necrosis: correlation of MR imaging, radiographic staging, radionuclide imaging, and clinical findings. Radiology 162:709–715
Mont MA, Hungerford DS (1995) Non-traumatic avascular necrosis of the femoral head. J Bone Jt Surg Am 77:459–474
Morag Y, Morag-Hezroni M, Jamadar DA et al (2009) Bisphospnonate-related osteonecrosis of the jaw: a pictorial review. Radiographics 29:1971–1986
Norman A, Steiner GC (1983) Radiographic and morphological features of cyst formation in idiopathic bone infarction. Radiology 146:335–338
Ohzono K, Saito M, Sugano N et al (1992) The fate of nontraumatic avascular necrosis of the femoral head: a radiologic classification to formulate prognosis. Clin Orthop Relat Res 277:73–78
Pape D, Seil R, Anagnostakos K, Kohn D (2007) Postarthroscopic osteonecrosis of the knee. Arthroscopy 23:428–438
Pearce DH, Mongiardi CN, Fornasier VL, Daniels TR (2005) Avascular necrosis of the talus: a pictorial essay. Radiographics 25:399–410
Radke S, Kirschner S, Seipel V, Rader C, Eulert J (2004) Magnetic resonance imaging criteria of successful core decompression in avascular necrosis of the hip. Skeletal Radiol 33:519–523
Rao VM, Fishman M, Mitchell DG et al (1986) Painful sickle cell crisis: bone marrow patterns observed with MR imaging. Radiology 161:211–215
Sagar P, Shailam R, Nimkin K (2010) Avascular necrosis of the metacarpal head: a report of two cases and review of literature. Pediatr Radiol 40:1895–1901
Saini A, Saifuddin A (2004) MRI of osteonecrosis. Clin Radiol 59:1079–1093
Saito S, Ohzono K, Ono K (1988) Minimal osteonecrosis as a segmental infarct within the femoral head. Clin Orthop Relat Res 231:35–50
Schmidt GP, Reiser MF, Baur-Melnyk A (2009) Whole-body imaging of bone marrow. Semin Musculoskelet Radiol 13:120–133
Schmitt R, Heinze A, Fellner F et al (1997) Imaging and staging of avascular osteonecroses at the wrist and hand. Eur J Radiol 25:92–103
Schmitt R, Christopoulos G, Wagner M et al (2011a) Avascular necrosis (AVN) of the proximal fragment in scaphoid nonunion: Is intravenous contrast agent necessary in MRI? Eur J Radiol 77:222–227
Schmitt R, Frohner S, van Schoonhovenb J et al (2011b) Idiopathic osteonecrosis of the scaphoid (Preiser's disease)—MRI gives new insights into etiology and pathology. Eur J Radiol 77:228–234
States LJ (2001) Imaging of metabolic bone disease and marrow disorders in children. Radiol Clin North Am 39:749–772
Steinberg ME, Brighton CT, Hayken GD, Tooze SE, Steinberg DR (1984) Early results in the treatment of avascular necrosis of the femoral head with electrical stimulation. Orthop Clin North Am 15:163–175
Steinberg ME, Bands RE, Parry S, Hoffman E, Chan T, Hartman KM (1999) Does lesion size affect the outcome in avascular necrosis? Clin Orthop Relat Res 367: 262–271
Steinberg ME, Steinberg DR (2004) Classification systems for osteonecrosis: an overview. Orthop Clin North Am 35:273–283 vii–viii
Steinberg ME, Hayken GD, Steinberg DR (1995) A quantitative system for staging avascular necrosis. J Bone Jt Surg Am 77B:34–41
Steiner RM, Mitchell DG, Rao VM et al (1990) Magnetic resonance imaging of bone marrow: diagnostic value in diffuse hematologic disorders. Magn Reson Q 6:17–34
Stevens K, Tao C, Lee SU et al (2003) Subchondral fractures in osteonecrosis of the femoral head: comparison of radiography, CT, and MR imaging. AJR Am J Roentgenol 180:363–368
Sugimoto H, Okubo RS, Ohsawa T (1992) Chemical shift and the double-line sign in MRI of early femoral avascular necrosis. J Comput Assist Tomogr 16:727–730
Theodorou DJ, Theodorou SJ, Haghighi P, Resnick D (2002) Distinct focal lesions of the femoral head: imaging features suggesting an atypical and minimal form of bone necrosis. Skeletal Radiol 31:435–444
Torres FX, Kyriakos M (1992) Bone infarct-associated osteosarcoma. Cancer 70:2418–2430

Tosun B, Al F, Tosun A (2011) Spontaneous osteonecrosis of the tarsal navicular in an adult: Mueller-Weiss syndrome. J Foot Ankle Surg 50:221–224

Turner DA, Templeton AC, Selzer PM, Rosenberg AG, Petasnick JP (1989) Femoral capital osteonecrosis: MR finding of diffuse marrow abnormalities without focal lesions. Radiology 171:135–140

Umans H, Haramati N, Flusser G (2000) The diagnostic role of gadolinium enhanced MRI in distinguishing between acute medullary bone infarct and osteomyelitis. Magn Reson Imaging 18:255–262

Yamamoto T, Bullough PG (2000) Spontaneous osteonecrosis of the knee: the result of subchondral insufficiency fracture. J Bone Jt Surg Am 82:858–866

Zhao FC, Li ZR, Zhang NF et al (2010) Lesion size changes in osteonecrosis of the femoral head: a long-term prospective study using MRI. Int Orthop 34:799–804

Zibis AH, Karantanas AH, Roidis NT et al (2007) The role of MR imaging in staging femoral head osteonecrosis. Eur J Radiol 63:3–9

Bone Marrow Edema Syndrome

Alain Blum, Sophie Lecocq, Matthias Louis,
and Pedro Teixeira

Contents

Abstract

Bone marrow edema syndrome (BMES) refers to transient clinical conditions and imaging alterations of the weight-bearing joints of the lower limbs. It usually affects middle-aged persons without a history of trauma. It usually lasts 3–9 months but can migrate to another part of the joint or to other joints. Its origin remains unclear. Transient demineralization of the hip, transient osteoporosis of the hip" (TOH) and regional migratory osteoporosis (RMO) are part of the same spectrum of disease. BMES is not an early aspect of avascular necrosis and never evolves to articular collapse. However, some clinical and imaging overlap exists between the transient and the irreversible lesions associated to bone marrow edema. MR imaging is the key technique to reach an early diagnosis. MR imaging follow-up is also necessary to demonstrate the resolution of the anomalies.

1 Introduction

Bone marrow edema syndrome (BMES) refers to transient clinical conditions and imaging alterations of the weight-bearing joints of the lower limbs. It usually affects middle-age persons without a history of trauma. It usually lasts 3–9 months but can migrate to another part of the joint or to other joints. Its origin remains unclear.

Through the numerous denomination used in the literature to describe this condition, one can approach the different clinical and imaging aspect of this disease. "Transient demineralization of the hip" was first

A. Blum (✉)
Service d'Imagerie Guilloz, CHU de Nancy,
29 av du Maréchal de Lattre de Tassigny,
54035 Nancy, France
e-mail: alain.blum@gmail.com

S. Lecocq · M. Louis · P. Teixeira
Service d'Imagerie Guilloz, Hopital Central,
CHU Nancy, 54000 Nancy, France

A. Baur-Melnyk (ed.), *Magnetic Resonance Imaging of the Bone Marrow*, Medical Radiology. Diagnostic Imaging,
DOI: 10.1007/174_2011_445, © Springer-Verlag Berlin Heidelberg 2013

described in 1959 by Curtiss and Kincaid as a self-limited disorder affecting women with hip pain in the third trimester of pregnancy (Curtiss and Kincaid 1959). The term "Transient osteoporosis of the hip" (TOH) was used in 1968 by Lequesne who described the periarticular osteopenia seen in plain radiographs 3–6 weeks after the onset of hip pain (Lequesne 1968). Wilson et al. in 1988 introduced the term "transient bone marrow edema" (TBME) considering the characteristic MRI pattern of this disease (Wilson et al. 1988).

Regional migratory osteoporosis (RMO) was described by Duncan in 1969 (Duncan et al. 1969). TOH and RMO are likely to be part of the same spectrum of disease. RMO is an uncommon disease characterized by a migrating arthralgia involving the weight-bearing joints of the lower limb. Hofmann proposed that such clinical conditions should be included under the general term BMES (Hofmann et al. 2004).

During the 1990's, the relationship between BEMS and avascular necrosis (AVN) was unclear but it is now widely accepted that BMES is a distinct entity with specific clinical and imaging features (Korompilias et al. 2009; Lakhanpal et al. 1987). BMES is not an early aspect of AVN (Fujioka et al. 2001; Guerra and Steinberg 1995; Kim et al. 2000). The relationship between BMES and insufficiency fractures, however, is still confusing and debated (Karantanas 2007; Karantanas et al. 2008a; Toms et al. 2005; Vande Berg et al. 1993, 1999). With the improvement of MRI spatial resolution, the depiction of subchondral trabecular microfractures in the femoral head of patients with TOH is very frequent but whether or not this alteration is the primary event of BMES is difficult to assess. In any case, it is important to note that in most cases, BMES is a reversible process. BMES is not expected to be complicated by articular collapse. At the hip, it may however evolve to a fracture which requires a surgical treatment. Besides, some clinical and imaging overlap exists between the transient and the irreversible lesions with bone marrow edema (Blum et al. 2009; Karantanas et al. 2008a; Vande Berg et al. 2008). Therefore, treatment should include partial weight-bearing and MR imaging follow-up is necessary to demonstrate the resolution of the anomalies.

The objective of this chapter is to discuss the characteristic pattern of BMES for each location (hip, knee, foot). We will focus on TOH which is the most frequent cause of BMES and will also discuss the imaging aspects of RMO.

2 Physiopathology

The physiopathology of BMES remains unclear. Links with ischemia, localized hyperemia, neural alterations, stress fractures and type I Complex Regional pain Syndrome (CRPS) have been suggested.

Different authors suggest that bone microdamage and consequent subchondral trabecular microfractures are the noxious stimuli responsible for BMES (Toms et al. 2005; Trevisan et al. 2002). This hypothesis is supported by different observations: the frequent coexistence of systemic osteopenia or osteoporosis with BMES, the significantly higher risk of developing transient osteoporosis in patients suffering from osteogenesis imperfecta in comparison to normal persons, the exclusive location of the bones with increased mechanical load and the fact that this disease typically affects women at the third trimester of pregnancy. At the third trimester of pregnancy, mechanical overload, osteopenia and hormonal modification may all combine to cause accumulative microdamage and consequent microfractures (McKiernan 2005; Neri et al. 1997; Spinarelli et al. 2009; Steib-Furno et al. 2007; Toms et al. 2005; Trevisan and Ortolani 2002; Trevisan et al. 2002). The frequent observation with MRI of subchondral trabecular microfractures in BMES also suggests a link between these bone alterations (Korompilias et al. 2009; Miyanishi et al. 2007).

These microfractures would generate a regional accelerated phenomenon (RAP). RAP is a process whereby local areas of normal bone metabolism, modeling and remodeling are rapidly increased (Toms et al. 2005). This RAP would explain the following transient imaging pattern: local osteopenia observed with plain film radiography or CT, marked uptake on the bone scan and bone marrow edema with MRI. Finally, induced local osteopenia might worsen the risk of fracture. This would explain the occurrence of hip fractures in pregnant women affected by TOH.

According to Hofmann, a continuous transition from migratory BMES to type I CRPS is also possible (Hofmann et al. 2004). Type I-CRPS is the current diagnostic label for the syndrome historically referred

to as reflex sympathetic dystrophy. Type I-CRPS and BMES share an unclear origin, a link with general osteoporosis, musculoskeletal disabling, some imaging features and no definite treatment. However, the epidemiologic data, the clinical findings as well as some imaging aspects differentiate BMES from type I-CRPS (Blum et al. 2008; Bruehl 2010; de Mos et al. 2007; Maihofner et al. 2010; Sandroni et al. 2003). A fracture is the most common precipitating event (44%) of type I-CRPS whereas, BMES occurs without any history of trauma (de Mos et al. 2007). Type I-CRPS mostly affects the upper limb while BMES affects the lower limbs. From an imaging point-of-view, in the early phase of type I-CRPS, MRI examination may reveal a bone marrow edema of the affected bones associated with joint effusion (Darbois et al. 1999; Graif et al. 1998; Schweitzer et al. 1995). However, BME may be missing and the sensitivity of MRI in the diagnosis of type I-CRPS is low, decreasing from 43% 2 months after the trauma to 14%, 4 months after the trauma (Schurmann et al. 2007).

Finally, "bone marrow edema" is a misnomer. It was used for the first time in 1988 by Wilson et al. who hypothesized that MR images represent a transient increase in bone marrow water content (Wilson et al. 1988). However, further studies in patients with different conditions associated with bone marrow edema at MRI showed that this pattern represents a number of non-characteristic histologic abnormalities. Edema per se is not a major constituent of MR imaging signal intensity abnormalities (Berger et al. 2003; Iwasaki et al. 2011; Thiryayi et al. 2008; Yamamoto et al. 1999, 2008; Zanetti et al. 2000; Zhao et al. 2010). In a clinicopathologic study, Yamamoto found that the most characteristic feature of TOH was focal areas of thin and disconnected bone trabeculae covered by osteoid seams and active osteoblasts. The surrounding bone marrow tissue showed edematous changes and mild fibrosis, frequently associated with vascular congestion and/or interstitial hemorrhage. No osteonecrotic region was observed in either the bone trabeculae or the bone marrow tissue (Yamamoto et al. 1999). In Berger's study, major histologic features, including osteoid seams, irregularly woven bone, dilated sinuses, and the presence of intramedullary fluid (Berger et al. 2006). Arlet observed an increased number of thin-walled vessels (Arlet et al. 1993). The progressive and gradual enhancement of the abnormal bone marrow after Gadolinium injection is compatible with the presence of fibrovascular tissue associated with vascular anomalies. For these reasons, some authors prefer the term, bone marrow edema-like pattern, to describe the MRI anomalies (Zanetti et al. 2002).

3 Transient Osteoporosis of the Hip

Transient osteoporosis of the hip is the most frequent cause of BMES.

3.1 Epidemiology

BMES is an uncommon condition but the exact incidence remains unknown because prospective studies are very scarce. Middle-aged men are more commonly affected by this condition than women. However, the third trimester of pregnancy and post-pregnancy are well-known risk periods for this disease (Curtiss and Kincaid 1959; Lequesne 1968; Wilson et al. 1988). For TOH, the male to female ratio ranges from 1.7:1 to 5:1 (Karantanas 2007). In both a 2-year prospective survey over 4,900 pregnancies and a 15-year retrospective study, Steib-Furno and al. found that transient osteoporosis of the hip and occult stress fractures of the femoral head are the main causes of hip pain in pregnant women, and that these conditions are in most cases associated with osteopenia or osteoporosis. During the 2-year prospective survey, 3 patients (4 hips) of pregnancy-related hip disease were observed: 1 case of TOH and 2 cases of occult fracture of the femoral head (Steib-Furno et al. 2007).

3.2 Clinical Presentation and Evolution

In most patients, TOH is a unilateral condition. It may be bilateral in pregnant women. Patients with TOH present with unilateral hip pain that sometimes comes on suddenly, without any history of trauma. The pain is mechanical, often severe and the patients may be unable to walk without assistance. In some cases, pain occurs at night. Physical examination may reveal mild limitation of hip movements (Lequesne 1968). The discrepancy between disability and minimal abnormalities on physical examination is indicative of TOH,

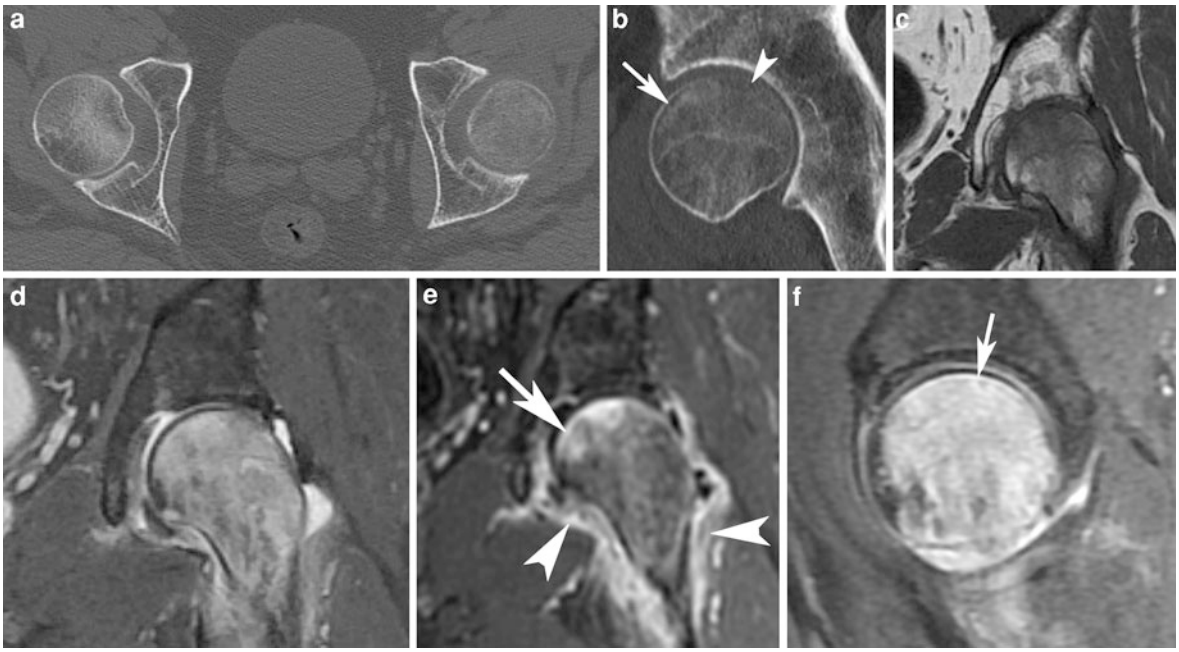

Fig. 1 Transient osteoporosis of the left hip in a 34 y.o. man. **a**, **b** Axial CT-scan and sagittal MPR showing a marked osteopenia of the left femoral head, a thinning of the bone endplate (*arrow head*) and a subchondral lucency of the left femoral head (*arrows*). **c**, **d**, **e** Coronal T1, T2 with Fat Sat and T1 after Gadolinium injection with Fat Sat showing a bone marrow edema pattern of the femoral head extending into the neck and the intertrochanteric region. Note that after gadolinium injection, the enhancement predominates in the subchondral plate (*arrow*). Note also the capsular and peri-articular enhancement (*arrow heads*). **f** Sagittal T2-weighted image with Fat Sat with increased spatial resolution compared to coronal images showing a high signal intensity subchondral line parallel to the calcified cartilage layer (*arrow*)

especially in pregnant women (Chalouhi et al. 2010). Laboratory examination is usually normal but serum vitamin D levels may be low. The condition generally follows a benign course with duration of 3–9 months, but durations up to 1 year have been described.

3.3 Plain Film Radiography and CT

Initial radiographs are normal, but osteoporosis of the femoral head with preserved joint space is seen on radiographs obtained several weeks after the onset of symptoms. Patients develop variable, often profound osteopenia of the femoral head and neck region, sometimes with mild acetabular involvement. A coarse mottled bony texture may sometimes be observed. There is a striking loss of the subchondral bone of the femoral head, which is virtually pathognomonic for transient osteoporosis. The preservation of the joint space and the absence of subchondral geodes are important negative findings (Lequesne 1968) (Figs. 1, 2).

Lequesne and Mauger described three phases in the course of TOH; the first characterized by increasing pain and disability (with normal radiographs), the second by intense symptoms and the presence of radiographic osteopenia, and the third by regression of the disease and associated radiographic resolution (Lequesne and Mauger 1982).

CT reveals the same anomalies than standard plain film radiographs with maybe a slightly higher accuracy (Horiuchi et al. 2004; Miyanishi et al. 2007; Toms et al. 2005).

3.4 Bone Scintigraphy and Hybrid Techniques

Bone scan using Tc^{99m}-MDP is a sensitive but not a specific tool in the diagnosis of TOH. It shows an increase in uptake in the affected joint, especially in the femur, which precedes radiological features and resolves progressively after the radiographic anomalies resolution. Radionuclide-increased uptake is

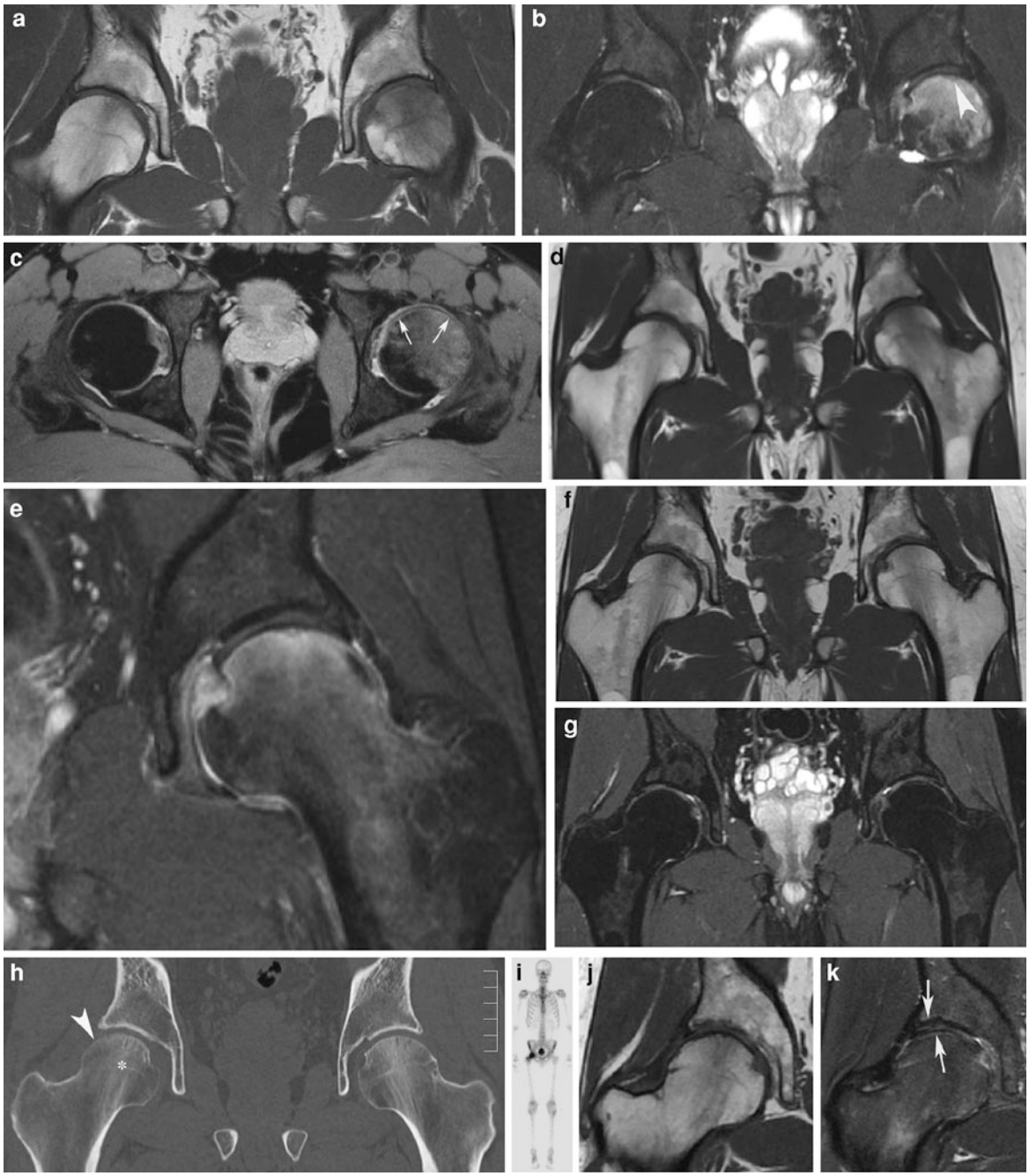

Fig. 2 Regional migratory osteoporosis in a 46 year old man. Transient osteoporosis of the left hip was the first manifestation of the disease. Transient osteoporosis of the right hip occurred 40 months after the first episode. **a**, **b**, **c** Baseline MRI with coronal T1-weighted image, coronal and axial T2-weighted images with Fat Sat showing a bone marrow edema pattern in the left femoral head. Note on the T2-weighted images a subchondral epiphyseal head irregular band in low-signal intensity (*arrow head*) probably corresponding to a trabecular microfracture and a thin and regular subchondral bright line parallel to the subchondral bone end-plate probably corresponding to an increased vascularity of the subchondral plate (*arrows*). **d**, **e** Control MRI performed 1 month later with coronal T1 weighted image and T1-weighted image with Fat Sat after Gadolinium injection showing a partial regression of the BME pattern and a thin band in *low-signal* intensity close to the subchondral plate of the *top* of the femoral head. **f**, **g** Control MRI performed 5 months after the baseline MRI with coronal T1-weighted image and T2-weighted image with Fat Sat showing a normal appearance of both hips. **h-k** CT-scan with coronal MPR, bone scan, coronal T1-weighted image and T2-weighted image with Fat Sat performed 40 months after the first episode, showing the typical pattern of transient osteoporosis of the right hip with a profound osteopenia of the femoral head (*asterisk*), a thinning of the bone end-plate (*arrow head*), an increased uptake of the femoral head on bone scintigraphy, a moderate BME pattern of the femur associated to bright subchondral lines of the femoral head and the acetabulum on T2-weighted image with Fat Sat (*arrows*)

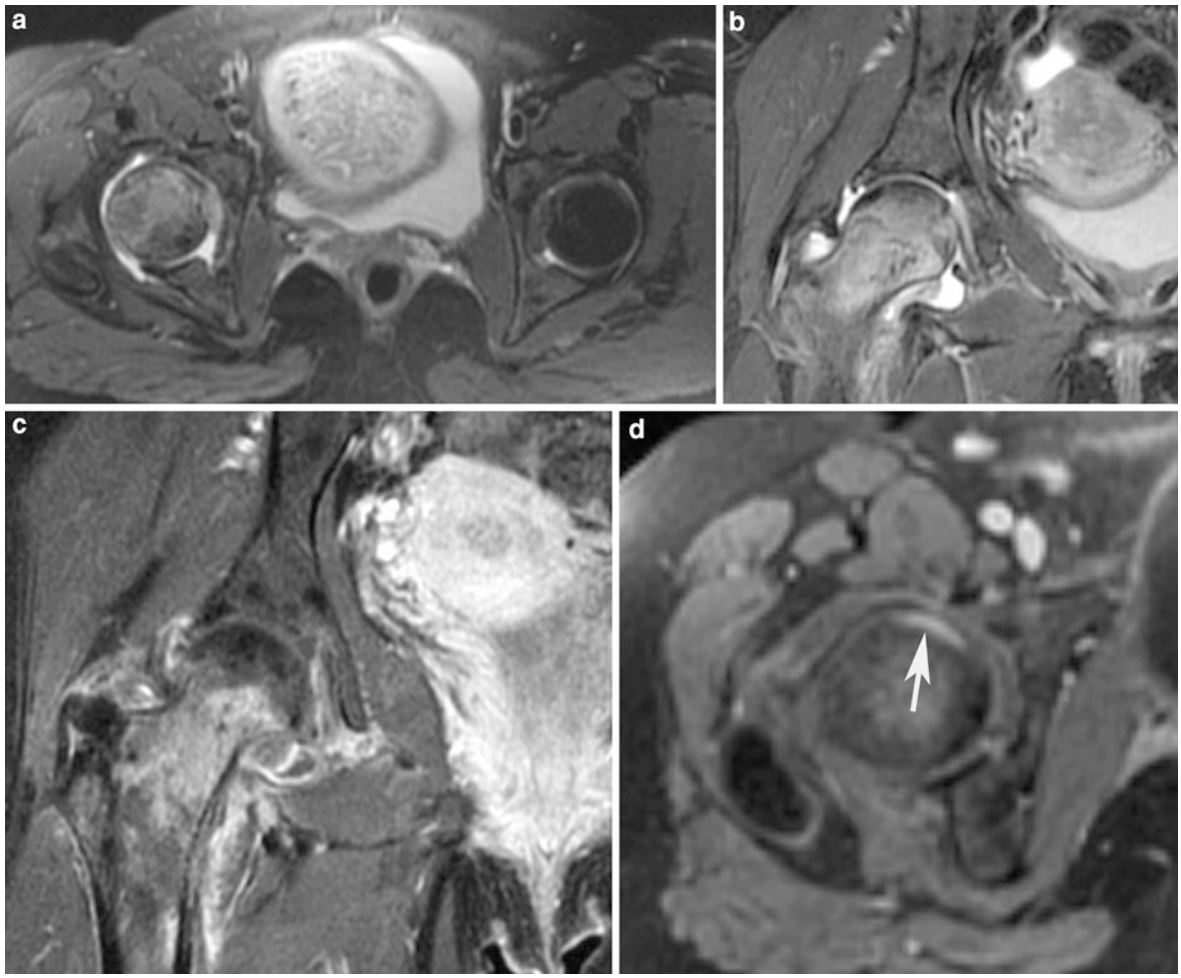

Fig. 3 Transient osteoporosis of the right hip in a 37 y.o. female patient occurring in the last week of pregnancy. MRI was performed in the post-partum period with a clinical suspicion of septic arthritis of the right hip. **a**, **b** axial and coronal T2-weighted images with Fat Sat showing an heterogenous BME pattern of the femoral head with irregular low-intensity bands. **c** Coronal T1-weighted image with Fat Sat after Gadolinium injection showing diffuse BME with subchondral sparing, capsular and peri-articular enhancement. **d** Axial dynamic acquisition after Gadolinium injection showing a hypervascularized subchondral line (*arrow*)

detected in all three-phase bone scintigram probably representing increased capillary permeability and hyperhemia as well as increased osteoblastic activity (Moreno and Ward 2001; Staudenherz et al. 1997; Tan et al. 1998) (Fig. 2).

SPECT-CT which combines the functional imaging capabilities of SPECT (Single-photon emission computed tomography) and the precise anatomical information of CT images is expected to present a better accuracy than bone scan but no study has yet been published to evaluate its diagnostic value in this condition (Gnanasegaran et al. 2009; Papathanassiou et al. 2009). In some anecdotic reports, PET-CT shows an increase in FDG uptake in the femoral head (Fabbriciani et al. 2010).

3.5 MR Imaging

MRI is the method of choice to reach an early diagnosis which is mainly based upon the identification of a bone marrow edema-like pattern of the femoral head. Even though this pattern is not specific for TOH, its aspect associated with other findings usually makes the diagnosis straightforward (Blum et al. 2009; Grimm et al. 1991; Hayes et al. 1993;

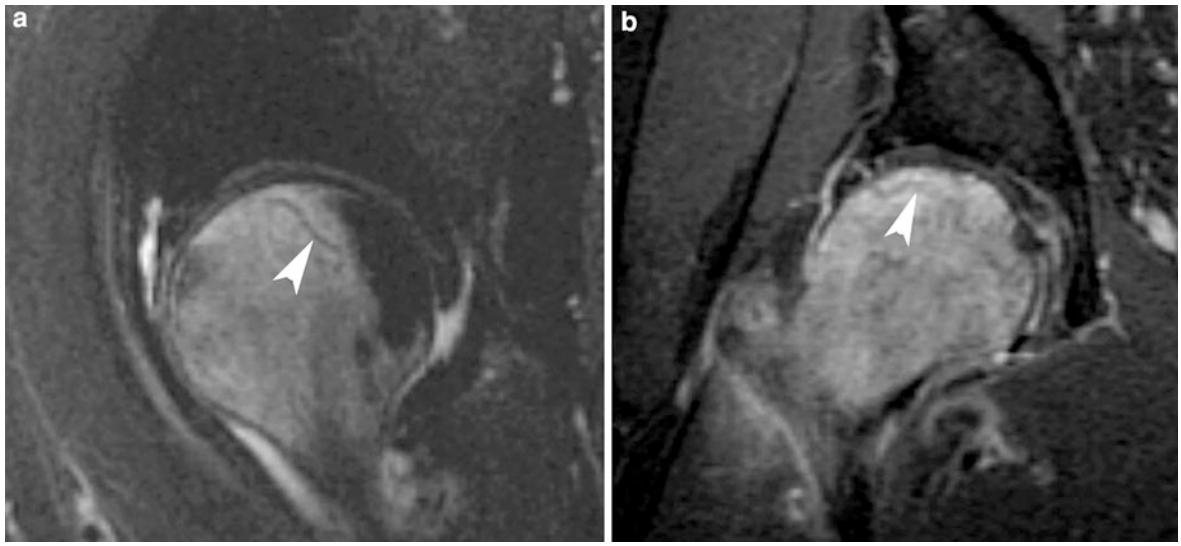

Fig. 4 Regional migratory osteoporosis in a 49 year old man. Transient osteoporosis of the left hip was the first manifestation of the disease. BME of the left knee was the second episode and transient osteoporosis of the right hip occurred 7 months after the first episode. **a**, **b** Sagittal T2-weighted image with Fat Sat and coronal T1-weighted image with Fat Sat after gadolinium injection showing a BME pattern of the right femoral head and a low-intensity band suggesting a microtrabecular fracture

Karantanas 2007; Korompilias et al. 2009; Malizos et al. 2004; Vande Berg et al. 2008) (Figs. 1, 2, 3, 4).

The bone marrow edema-like pattern is characterized by an ill-defined region with moderately reduced signal intensity on T1-weighted images and increased signal intensity on T2-weighted images with Fat Sat (or STIR images). A progressive and gradual enhancement is observed on T1-weighted dynamic acquisitions after intravenous Gadolinium injection. Visible as early as 48 h from the onset of the symptoms, the extent and location of the bone marrow is variable depending upon the course of the disease. It usually affects the femoral head including a portion of the subchondral area. In most cases, bone marrow edema extends to the femoral neck. The intertrochanteric region as well as the acetabulum may also be attained. Diffusion-weighted imaging is not useful for differentiating TOH from other conditions associated with bone marrow edema-like pattern (Karantanas et al. 2008a). However, apparent diffusion coefficient (ADC) map could be a tool to quantify and follow-up the bone marrow anomalies (Blum et al. 2009). Control MRI at the third month usually shows a partial regression of the bone marrow edema which usually migrates to the posterior portion of the femoral head or the acetabulum (Vande Berg et al. 2011).

Subchondral epiphyseal head irregular bands in low-signal intensity in all sequences may also be observed. They probably represent trabecular microfractures. Their conspicuity is probably related to the spatial resolution. The absence of any subchondral lesions favors the diagnosis of TOH with a 100% positive predictive value. The presence of small lesions, thinner than 4 mm and shorter than 12.5 mm, also favors this diagnosis and at least corresponds to transient and reversible femoral head alterations (Vande Berg et al. 1999).

A thin and regular subchondral line parallel to the subchondral bone end-plate of the femoral head which probably reflects increased vascularity in the subchondral plate, is in our experience, highly accurate for the diagnosis of TOH. It has been described in rheumatoid arthritis but the clinical presentation and the imaging pattern of these conditions are very different. The subchondral plate is a 0.6 mm thick layer of highly vascular compact bone located between the calcified cartilage layer and the trabecular bone. Its loss of integrity has been described in osteoarthritis and rheumatoid arthritis (Bae et al. 2010; Pesesse et al. 2011; Walsh et al. 2010). This line, in low-signal intensity on T1-weighted images, is hardly distinguishable from the calcified cartilage layer. It appears

bright on T2-weighted images. It is partially obscured on T2-weighted images when the bone marrow edema reaches the bone end-plate. Its conspicuity depends considerably on the spatial resolution. It is well depicted on post-Gadolinium sequences with Fat saturation and is characterized by a marked and rapid enhancement after Gadolinium injection on dynamic acquisitions. Well correlated to the presence of subchondral radiolucencies depicted on CT-scan, it should not be confused with a fracture line.

A moderate joint effusion is usually present. Finally, a capsular enhancement and peri-articular soft tissue changes have also been described (Blum et al. 2009; Karantanas 2007). No other anomalies are depicted and the negative findings are important to rule out other conditions such as osteonecrosis, fracture, osteoarthritis or infection: there is no femoral head contour deformity, no double-line nor band-like sign, no bone erosion, and no joint space narrowing.

3.6 Bone Densitometry

Many authors have reported a relationship between generalized osteoporosis or osteopenia and BMES (Fabbriciani et al. 2010; Steib-Furno et al. 2007; Toms et al. 2005; Trevisan and Ortolani 2002). It is probably advisable that patients suffering from TOH and BMES should undergo a Dual-emission X-ray absorptiometry (DXA) to measure the bone mineral density (BMD). One recent study showed that, in patients with acute non-traumatic BMES in the knee, the generalized osteopenia or osteoporosis is associated with a greater risk of articular collapse, and thus, bone mineral densitometry could stand as predictor of outcome (Karantanas et al. 2008a). DXA of the lumbar spine might be useful after delivery in women affected by TOH during pregnancy to assess bone fragility and prevent complications (Spinarelli et al. 2009; Steib-Furno et al. 2007).

3.7 Complication

Complete recovery within a few months is the rule in the majority of cases but hip fractures may occur, especially in pregnant women (Curtiss and Kincaid 1959; Karantanas 2007). In most cases, this is a subcapital femoral neck fracture (Brocq et al. 1999; Chalouhi et al. 2010; Cohen et al. 2007; Spinarelli et al. 2009). These fractures can occur during the course of pregnancy (41%), delivery (3%) or lactation (56%) (Timsit 2004). TOH is not expected to be complicated by avascular necrosis or articular collapse. Finally, TOH may be the first episode of regional migratory osteoporosis.

3.8 Differential Diagnosis

In principle, all painful conditions of the hip associated with bone marrow edema-like pattern can been discussed: inflammatory arthropathies, septic arthritis, osteoarthritis, avascular necrosis, stress fracture and osteoid osteoma (Blum et al. 2009; Hayes et al. 1993; Karantanas 2007; Krestan et al. 2011; Navas and Kassarjian 2011; Ragab et al. 2008). Considering the history of the patient, the clinical presentation as well as the imaging pattern, most of these conditions are easily ruled out (Blum et al. 2009). Their description is detailed in other chapters of this book. AVN has been for a long time the main differential diagnosis of TOH. In the 1990s, a possible transition between these two conditions was debated. However, their imaging patterns are quite different and isolated BME never evolves to AVN. AVN is characterized by a circumscribed subchondral "band-like" lesion with low-signal intensity on T1-weighted sequences and high signal intensity on T2-weighted images with Fat saturation. BME is lacking in early stages of AVN and is more common in advanced disease (Karantanas and Drakonaki 2011).

The main differential diagnosis of TOH is the subchondral insufficiency fracture of the femoral head (SIF) which appear on MRI as a low-intensity band surrounded by a focal zone of bone marrow edema-like pattern (Krestan et al. 2011) (Fig. 5). SIF may be a reversible lesion but it may also evolve to articular collapse and seem to be an important preliminary event in the development of rapidly destructive hip osteoarthritis (Boutry et al. 2002; Iwasaki et al. 2011; Watanabe et al. 2002; Yamamoto et al. 2002). Bone microfractures are probably the noxious stimuli for both conditions but their consequences probably depend on the bone regenerative capacity. Classically, SIF affects elderly patients, usually women, with poor bone quality and sometimes with insufficiency fractures in other locations (Krestan and Hojreh 2009; Rafii et al. 1997). However, in younger patients, the

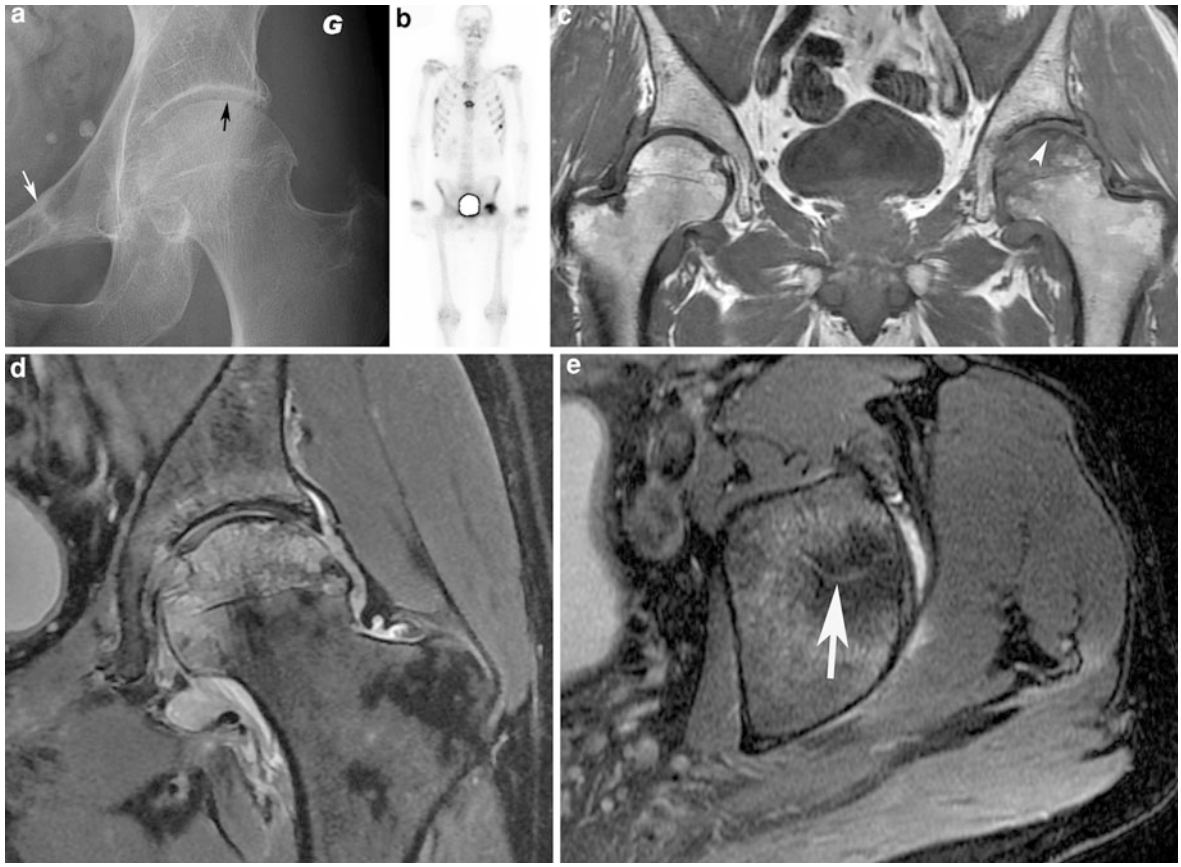

Fig. 5 Insufficiency fracture of the left femoral head in a 46 y.o. man with rheumatoid arthritis and long-term treatment with corticosteroids. **a** Standard X-rays of the left hip showing a subtle focal deformity of the subchondral bone plate of the femoral head (*black arrow*) just below the acetabular roof margin, no marked and focal osteopenia of the femur and a sequellae of insufficiency fracture of the iliopubic branch (*white arrow*). **b** Bone scan showing an increased uptake of the left femoral head and the left acetabulum and also some rib fractures. **c**, **d**, **e** Coronal T1-weighted image and coronal and axial T2-weighted images with Fat Sat showing a BME pattern in the left femoral head and the acetabulum, a small subchondral insufficiency fracture of the femoral head (*arrow head*) and a coronal fracture of the acetabular roof (*arrow*)

differentiation between TOH and SIF may appear artificial with some clinical and imaging overlap between these two entities. For Vande Berg et al. the diagnosis of TOH remains presumptive until demonstration of the complete resolution of clinical and radiological changes (Vande Berg et al. 2008). Whether or not these entities represent different aspects of the same condition, some prognostic factors have been identified. The fracture band length is predictive of the occurrence of collapse (Iwasaki et al. 2010). A length of at least 12.5 mm has a positive predictive value of greater than 73% for prediction of lesion irreversibility (Vande Berg et al. 1999). Similar to Karantanas' findings in a study of 88 patients with acute non-traumatic marrow edema syndrome in the knee, the evolution to articular collapse is probably more frequent in older female patients with low bone mineral density and longer symptoms duration before imaging (Karantanas et al. 2008a).

3.9 Treatment

The goals of the treatment are prompt relief of pain, acceleration of functional and imaging recovery of the affected joint, avoiding hip fracture and managing osteoporosis if any. The first measure to be taken is partial weight-bearing. Particular attention should be

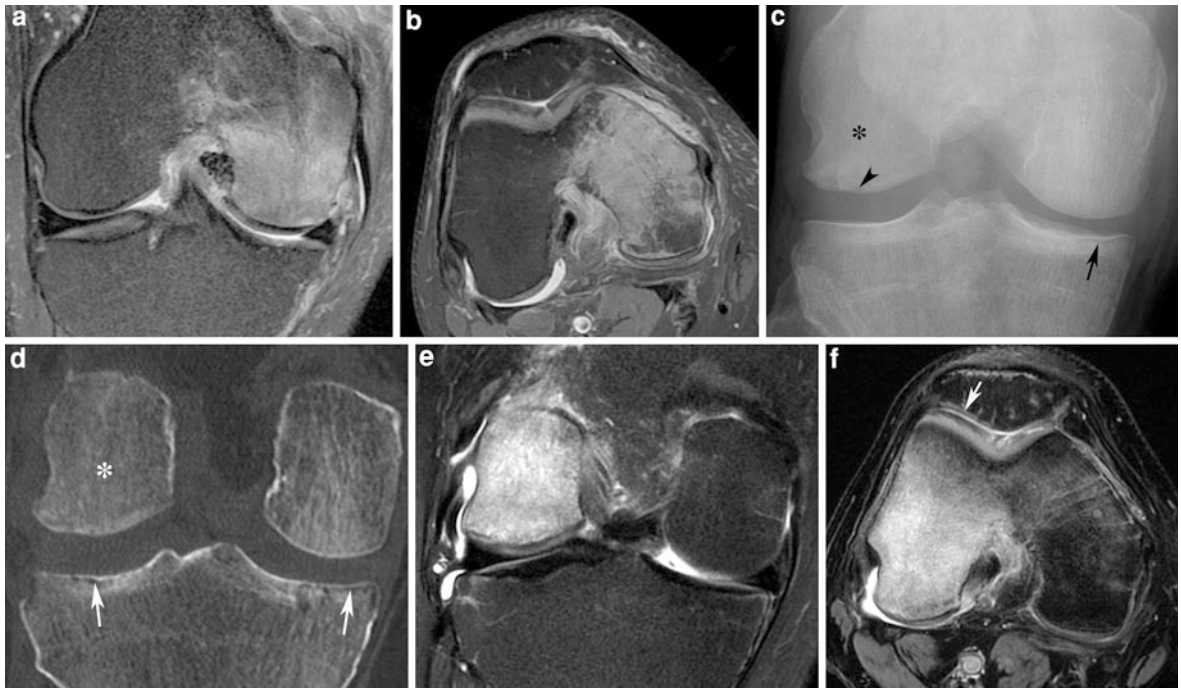

Fig. 6 Bone marrow edema syndrome of the right knee in a 56 y.o. man with intra-articular migration. **a**, **b** Baseline MRI with coronal and axial T2-weighted images showing a BME pattern of the medial condyle and soft tissue inflammation. **c** Standard X-rays taken 4 months later showing a severe osteopenia of the lateral condyle (*asterisk*) predominating in the subchondral area (*arrow head*). Note also a radiolucent line in the subchondral bone of the medial tibia plateau (*arrow*). **d** CT-scan with coronal MPR showing a profound osteopenia of the lateral condyle (*asterisk*) and lucent lines in the subchondral bone of the medial and lateral tibia plateau (*arrows*). **e**, **f** Coronal and axial T2-weighted images showing a BME pattern of the lateral condyle, an irregular low-intensity band in the subchondral bone of the lateral condyle and a bright subchondral line in the patella (*arrow*)

given to this recommendation in pregnant women who are more prone to fractures. Non-weight-bearing may be necessary in pregnant women in case of bilateral involvement as discharging only one limb accentuates contralateral weight-bearing stress, increasing the risk of stress fracture.

There is no consensus about drug prescription. Mild analgesics and non-steroidal anti-inflammatory drugs should be prescribed but they do not alter the natural course of the disease. Antiresorptive drugs such as calcitonin and bisphosphonates have been demonstrated to shorten symptom duration (Arayssi et al. 2003; La Montagna et al. 2005). The osteo-anabolic agent teriparatide and the vasoactive drug Iloprost might also reduce the duration of TOH (Aigner et al. 2009; Fabbriciani et al. 2010).

Concerning delivery, the rationale for cesarean section is that an osteoporotic hip could be at risk for fracture during vaginal delivery because of the flexed and abducted position of the lower extremities. Pain serves a protective function by limiting the patient's mobility and the stresses on the fragile bone. Regional anesthesia will increase the risk of fracture by removing the restrictive effect of the hip pain (Chalouhi et al. 2010).

4 Transient Bone Marrow Edema of the Knee

The knee joint is less frequently involved than the hip, either as a single joint or as one of the joints affected in regional migratory osteoporosis (Lakhanpal et al. 1987; Parker et al. 1997). Similarly to TOH, BME of the knee affects mainly the middle-aged males and women at the third trimester of pregnancy or in the early post-pregnancy period (Karantanas et al. 2008a; Lloyd et al. 2006; Stamp et al. 2001; Ververidis et al. 2009).

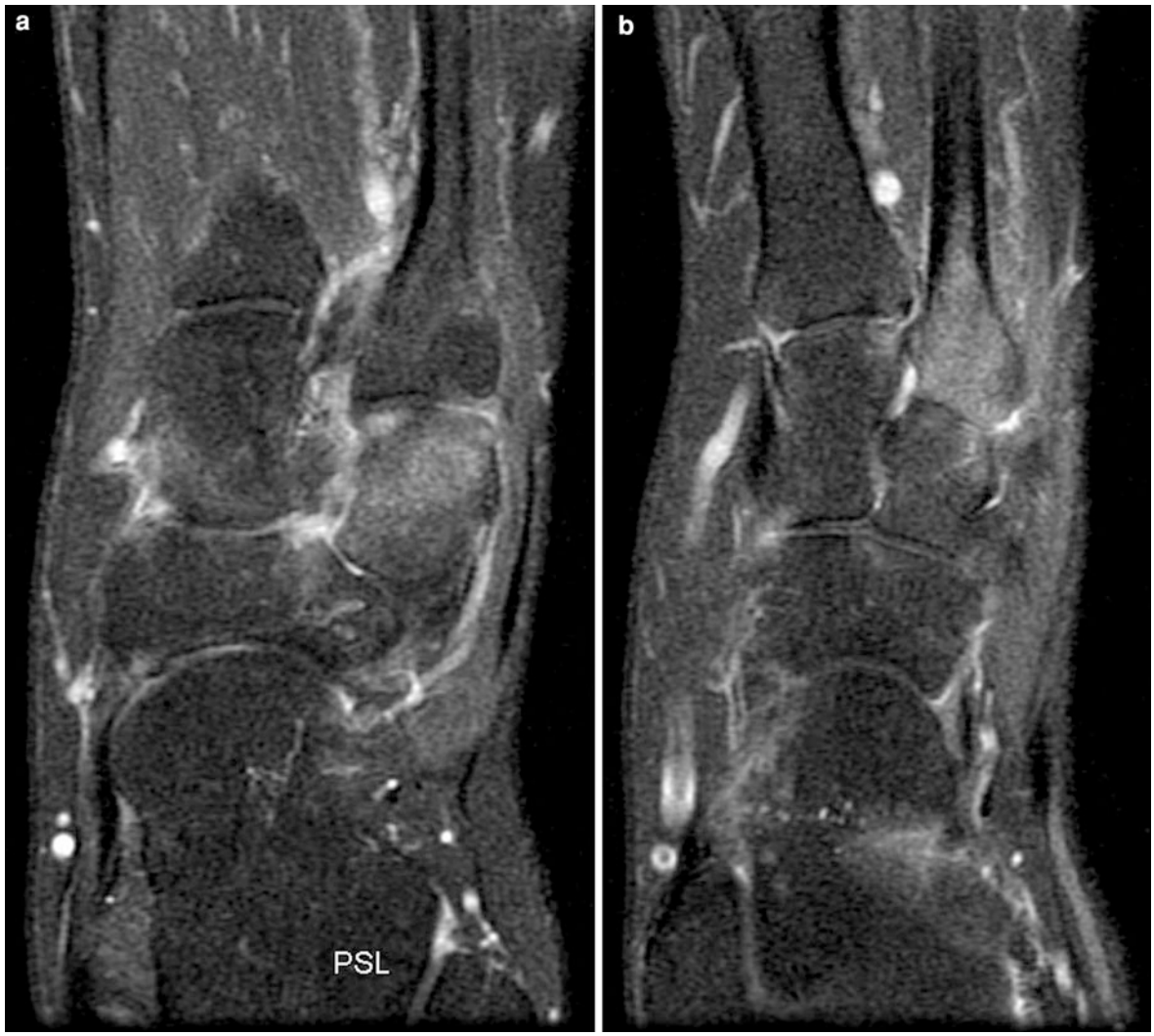

Fig. 7 Regional migratory osteoporosis in a 51 y.o. woman affecting the left knee and 7 months later the left foot. **a**, **b** Axial T2-weighted images showing a BME of different tarsal bones

The clinical and imaging pattern of BME in the knee present a lot of similarities with TOH (Karantanas et al. 2008a; Lecouvet et al. 1998, 2005; Steinbach and Suh 2011) (Fig. 6):

- the radiographs may show a focal marked osteopenia;
- a bone marrow edema-pattern is the basis of the diagnosis;
- subchondral microtrabecular fractures are depicted in about 15% of the cases (Karantanas et al. 2008a);
- a thin hypervascularized subchondral line parallel to the end-plate may be visible;
- joint fluid, capsular enhancement and peri-articular soft tissue enhancement are frequent;
- intact articular surface and no articular collapse are mandatory criteria;
- complete clinical and imaging regression is observed within a few months unless the patient suffers from regional migratory osteoporosis.

The bone marrow edema-pattern is the basis of the diagnosis. It usually corresponds to a homogeneous zone of bone marrow edema extending from the subchondral bone into a condyle or less commonly in a tibia plateau. Multiple sites are affected simultaneously

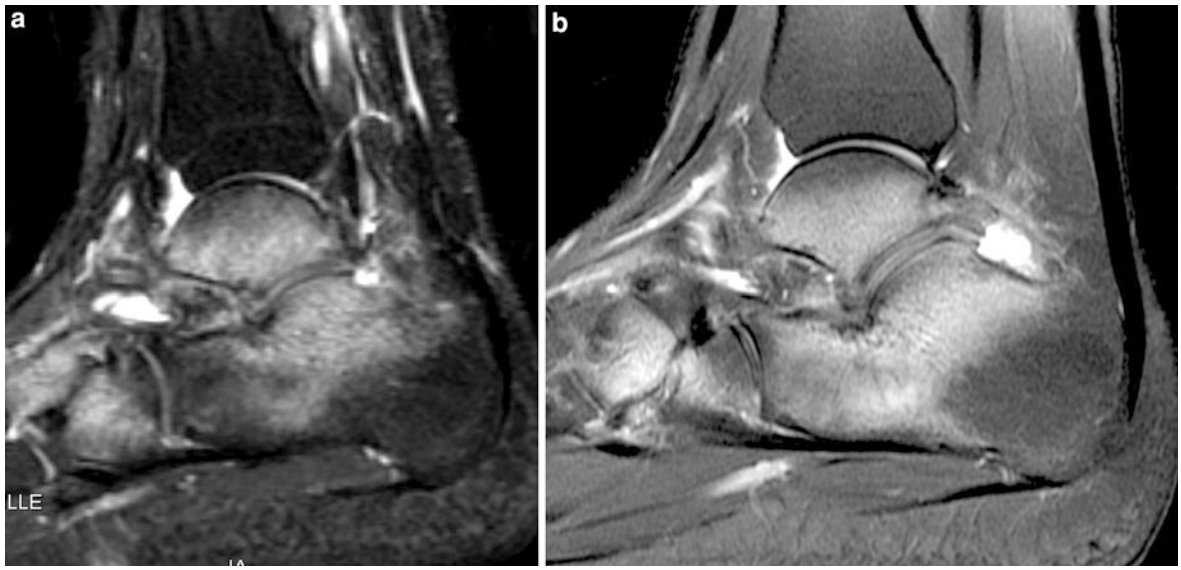

Fig. 8 Bone marrow edema syndrome of the left foot in a 16 y.o. man. **a** Baseline MRI with sagittal T2-weighted image with fat saturation showing a BME of different tarsal bones. **b** Control MRI obtained 15 months later showing a similar pattern

in about 27% of the cases. In these cases, bone marrow edema is usually uneven and predominates in a condyle. In the other locations, it may take a spotty or patchy appearance. Subchondral sparing which corresponds to a normal appearance between the cortex and the BME, is present in about 43% of the cases (Karantanas et al. 2008a).

A thin hypervascularized subchondral line parallel to the endplate may be visible, especially on post-Gadolinium sequences. This line may affect different sites of the joint and may sometimes be the only anomaly of these sites. This finding is an important imaging feature for the diagnosis of BMES. However, it has been observed in different conditions associated with hypervascularization of the bone marrow such as rheumatoid arthritis and its accuracy still have to be assessed.

The main differential diagnosis of transient bone marrow edema of the knee is the spontaneous osteonecrosis of the knee (SONK). SONK probably results from an insufficiency fracture. It may resolve spontaneously with partial weight-bearing but it may also lead to articular collapse and knee arthropathy. It is observed in the elderly, usually after the sixth decade of life, and is three times more frequent in women than in men. It has a frank predilection for the weight-bearing surface of the medial femoral condyle involved in more than 90% of the cases. It is usually associated with medial meniscal lesions, especially radial tears and root derangements of its posterior horn. Early SONK may have the same appearance as transient bone marrow edema of the knee associated with a subchondral fracture. Therefore the question is whether or not this pattern is transient and reversible (Gil et al. 2006; Lecouvet et al. 2005; Ramnath and Kattapuram 2004).

Some aspects are always associated with transient bone marrow edema. When no fracture is present, bone marrow edema never progresses to articular collapse. The sparing of the subchondral marrow by BME is also associated with transient lesions (Karantanas et al. 2008a).

The prognostic value of subchondral fractures depends upon their size and location. Lines of low-signal intensity located deep in the affected condyle may be indicative of an early irreversible lesion. In Lecouvet's study, low-intensity lines were present in 78% of cases of early irreversible lesion and 50% of cases of transient bone marrow edema. The maximal distance separating these lines from the epiphyseal cortex was significantly higher in early osteonecrosis (4 ± 2 mm) than in transient bone marrow edema (2 ± 1 mm) (Lecouvet et al. 1998). Karantanas et al. found that 45% of patients with subchondral fractures at presentation progressed to articular collapse within a period of 6.5 ± 2.3 months while the remaining patients (55%) had a favorable outcome with improvement or resolution of symptoms within 13 ± 6.5 months (Karantanas et al. 2008a).

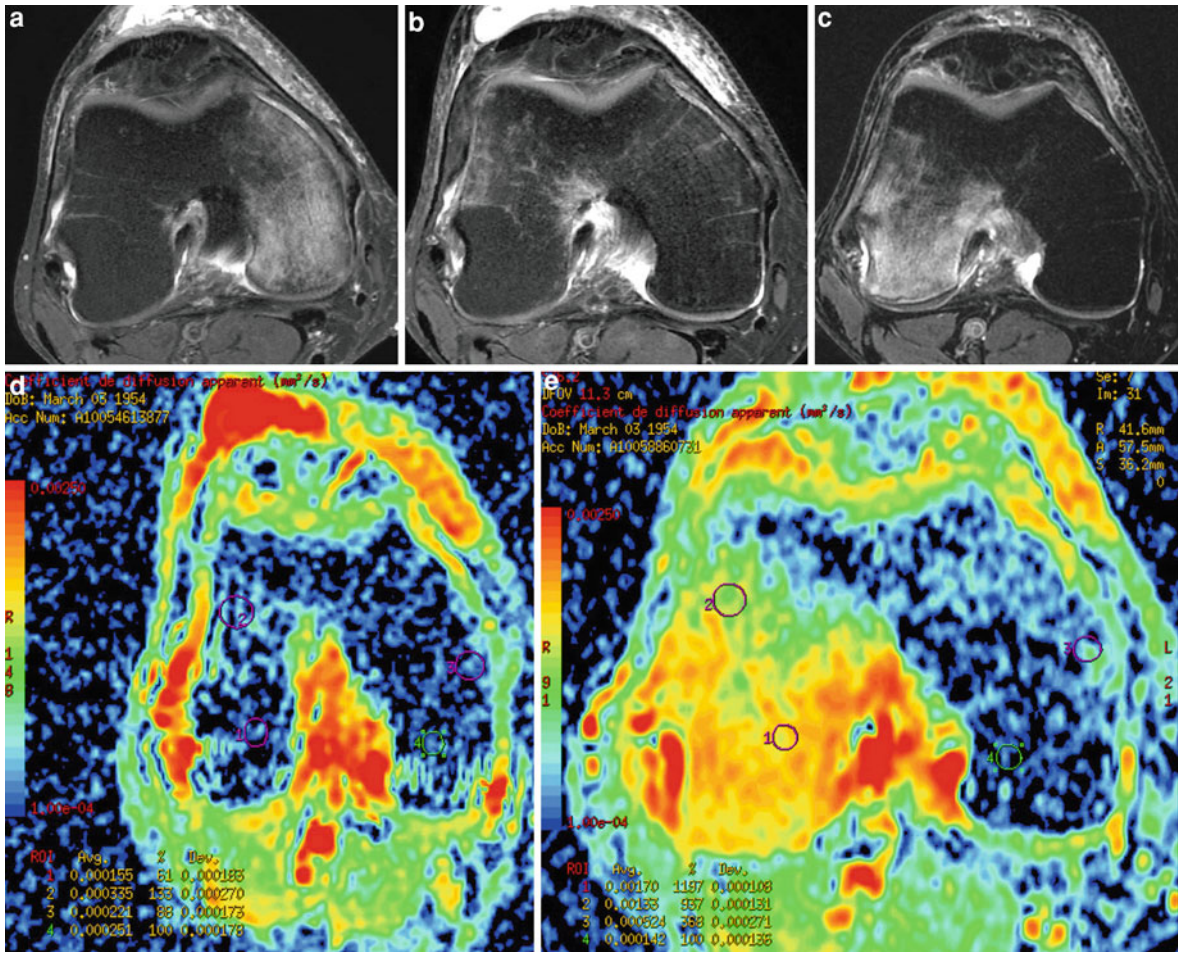

Fig. 9 Bone marrow edema syndrome of the right knee in a 55 y.o. man with intra-articular migration. **a**, **b**, **c** Axial T2-weighted images with fat saturation obtained a few weeks after the onset of the symptoms and 6 weeks and 4 months after the baseline MRI showing a BME migrating from the medial to the lateral condyle. **d**, **e** Apparent diffusion coefficient (ADC) map obtained 6 weeks and 4 months after the baseline MRI showing increasing ADC values in the lateral condyle ($b = 600$ s/mm^2)

According to this study, the evolution to articular collapse was more frequent in older female patients with low bone mineral density and longer symptoms duration before imaging.

Considering the clinical and imaging overlap between transient bone marrow edema of the knee and SONK, follow-up X-rays and MRI examinations are required to make a definite diagnosis. A DXA is also indicated to measure the bone mineral density. The treatment is however the same for both conditions and similar to the one of TOH. Partial weight-bearing is required during a few months until the resolution of pain and bone marrow edema. However, even with an articular collapse, SONK is usually well tolerated and a knee arthroplasty is rarely required.

5 Transient Bone Marrow Edema of the Foot

Transient bone marrow edema of the foot seems to be less frequent than in the hip or in the knee. Although sharing a lot of features with the other locations, transient bone marrow edema of the foot has some specific features. It usually presents with diffuse edema affecting multiple tarsal bones, sometimes with uneven intensity. The talus, the navicular, the cuneiforms and the cuboid are the bones most frequently involved but all the tarsal bones can be attained. Edema in a single bone is very uncommon. Soft tissue edema is present in all the cases. Transient bone

marrow edema of the foot does not evolve to osteonecrosis or articular collapse. However, clinical recovery may take longer than in the other locations (hip, knee) and almost one-third of patients show persistence of edema at 1 year. Intra-articular migration in the same foot occurs in about 25% of the cases at 1-year follow-up. Migration to the other foot occurs in about 25% of the cases at 1-year follow-up (Fernandez-Canton et al. 2003; Gigena et al. 2002; Sprinchorn et al. 2011; Zanetti et al. 2002) (Figs. 7, 8).

6 Regional Migratory Osteoporosis (RMO)

Regional Migratory Osteoporosis (RMO) was described by Duncan in 1969 (Duncan et al. 1969). RMO is an uncommon disease characterized by a migrating arthralgia involving the weight-bearing joints of the lower limb. TOH, bone marrow edema syndrome and RMO are likely to be part of the same spectrum of disease.

Men in their fifth and sixth decades of life are most commonly affected. In a 9-year retrospective study, Karantanas, observed 22 patients with regional migratory osteoporosis. There were 21 men for one woman and the mean age was 49 (Karantanas et al. 2008b). Migration may occur in an unpredictable time interval after the onset of the first symptoms. The migration period is usually 2–12 months with a median migration period of 4 months (Cahir and Toms 2008; Korompilias et al. 2009; Toms et al. 2005; Trevisan et al. 2002). Usually, only two sites only are attained but RMO may affect a third and even a fourth location. Since some patients demonstrate a migration period of several years, it is probable that the frequency of RMO is underestimated and that some secondary episodes are misdiagnosed.

The most common presentation is with proximal to distal spread in the lower limb. TOH is usually the first manifestation of the disease. In fact, migration occurs in 5–41% of patients with TOH. If intra-articular migration is included in the definition of RMO, then a large majority of BMES falls under the description of RMO. Patients with initial knee involvement have usually intra-articular or contralateral knee migration. Interestingly, the initial involvement in the knee is usually a condyle and when the same knee is affected twice, the secondary location is usually the other condyle. A more diffuse bone marrow edema-pattern, a tibia plateau and/or a patellar involvement are less frequent. According to Karantanas, patients initially developing bone marrow edema in one of the condyles might spontaneously shift their weight in an antalgic position, thus increasing the load on the non-affected condyle or the other knee, creating local bone microdamage (Karantanas et al. 2008a). Intra-articular migration in the foot or migration to the other foot might be related to the same phenomenon.

Considering that the imaging pattern is similar for a bone marrow edema in a single location and for multiple sites, MRI is the key technique for an early diagnosis and follow-up. Diffusion-weighted imaging with ADC map could be a tool to quantify and follow-up the bone marrow anomalies (Blum et al. 2009) (Fig. 9).

7 Conclusion

Bone marrow edema syndrome (BMES) refers to transient clinical conditions and imaging alterations of the weight-bearing joints of the lower limbs. MRI plays a major role in the positive and differential diagnosis of BMES. BMES does not evolve to articular collapse. At the hip, it may however evolve to a femoral neck fracture. Besides, some clinical and imaging overlap exists between the transient and the irreversible lesions associated with bone marrow edema. Treatment should include partial weight-bearing and a MR imaging follow-up is necessary to demonstrate the resolution of the anomalies.

References

Aigner N, Meizer R, Meraner D, Becker S, Meizer E, Landsiedl F (2009) Bone marrow edema syndrome in postpartal women: treatment with iloprost. Orthop Clin N Am 40(2):241–247

Arayssi TK, Tawbi HA, Usta IM, Hourani MH (2003) Calcitonin in the treatment of transient osteoporosis of the hip. Semin Arthritis Rheum 32(6):388–397

Arlet J, Laroche M, Soler R, Thiechart M, Pieraggi MT, Mazieres B (1993) Histopathology of the vessels of the femoral heads in specimens of osteonecrosis, osteoarthritis and algodystrophy. Clin Rheum 12(2):162–165

Bae WC, Dwek JR, Znamirowski R et al (2010) Ultrashort echo time MR imaging of osteochondral junction of the knee at 3 T: identification of anatomic structures contributing to signal intensity. Radiology 254(3):837–845

Berger CE, Kroner AH, Minai-Pour MB, Ogris E, Engel A (2003) Biochemical markers of bone metabolism in bone marrow edema syndrome of the hip. Bone 33(3):346–351

Berger CE, Kroner AH, Kristen KH et al (2006) Transient bone marrow edema syndrome of the knee: clinical and magnetic resonance imaging results at 5 years after core decompression. Arthroscopy 22(8):866–871

Blum A, Detreille R, Batch T et al (2008) Savoir reconnaître une algodystrophie en IRM. Journées Françaises de radiologie. Formation médicale continue, SFR, pp 615–625

Blum A, Roch D, Loeuille D et al (2009) Bone marrow edema: definition, diagnostic value and prognostic value. J de radiologie 90(12):1789–1811

Boutry N, Paul C, Leroy X, Fredoux D, Migaud H, Cotten A (2002) Rapidly destructive osteoarthritis of the hip: MR imaging findings. AJR 179(3):657–663

Brocq O, Simon E, Bongain A, Gillet JY, Euller-Ziegler L (1999) Femoral neck fracture complicating algodystrophy in pregnancy. Presse Med 28(22):1165–1166

Bruehl S (2010) An update on the pathophysiology of complex regional pain syndrome. Anesthesiology 113(3):713–725

Cahir JG, Toms AP (2008) Regional migratory osteoporosis. Eur J Radiol 67(1):2–10

Chalouhi GE, Harb C, Atallah D, Mansour F, Ghanem I, Dagher F (2010) Total hip replacement at thirty years. Case report of crippling complications of a transient osteoporosis of the hip during pregnancy. Eur J Obstet Gynecol Reprod Biol 149(2):226–227

Cohen I, Melamed E, Lipkin A, Robinson D (2007) Transient osteoporosis of pregnancy complicated by a pathologic subcapital hip fracture. J Trauma 62(5):1281–1283

Curtiss PH Jr, Kincaid WE (1959) Transitory demineralization of the hip in pregnancy, a report of three cases. J Bone Joint Surg Am 41-A:1327–1333

Darbois H, Boyer B, Dubayle P, Lechevalier D, David H, Ait-Ameur A (1999) MRI symptomology in reflex sympathetic dystrophy of the foot. Journal de radiologie 80(8):849–854

de Mos M, de Bruijn AG, Huygen FJ, Dieleman JP, Stricker BH, Sturkenboom MC (2007) The incidence of complex regional pain syndrome: a population-based study. Pain 129(1–2): 12–20

Duncan H, Frame B, Frost H, Arnstein AR (1969) Regional migratory osteoporosis. South Med J 62(1):41–44

Fabbriciani G, Pirro M, Manfredelli MR et al (2010) Transient osteoporosis of the hip: successful treatment with teriparatide. Rheumatol International

Fernandez-Canton G, Casado O, Capelastegui A, Astigarraga E, Larena JA, Merino A (2003) Bone marrow edema syndrome of the foot: one year follow-up with MR imaging. Skeletal Radiol 32(5):273–278

Fujioka M, Kubo T, Nakamura F et al (2001) Initial changes of non-traumatic osteonecrosis of femoral head in fat suppression images: bone marrow edema was not found before the appearance of band patterns. Magn Reson Imaging 19(7):985–991

Gigena LM, Chung CB, Lektrakul N, Pfirrmann CW, Sung MS, Resnick D (2002) Transient bone marrow edema of the talus: MR imaging findings in five patients. Skeletal Radiol 31(4):202–207

Gil HC, Levine SM, Zoga AC (2006) MRI findings in the subchondral bone marrow: a discussion of conditions including transient osteoporosis, transient bone marrow edema syndrome, SONK, and shifting bone marrow edema of the knee. Semin Musculo Skeletal Radiol 10(3):177–186

Gnanasegaran G, Barwick T, Adamson K, Mohan H, Sharp D, Fogelman I (2009) Multislice SPECT/CT in benign and malignant bone disease: when the ordinary turns into the extraordinary. Semin Nucl Med 39(6):431–442

Graif M, Schweitzer ME, Marks B, Matteucci T, Mandel S (1998) Synovial effusion in reflex sympathetic dystrophy: an additional sign for diagnosis and staging. Skeletal Radiol 27(5):262–265

Grimm J, Higer HP, Benning R, Meairs S (1991) MRI of transient osteoporosis of the hip. Arch Orthop Trauma Surg 110(2):98–102

Guerra JJ, Steinberg ME (1995) Distinguishing transient osteoporosis from avascular necrosis of the hip. J Bone Joint Surg Am 77(4):616–624

Hayes CW, Conway WF, Daniel WW (1993) MR imaging of bone marrow edema pattern: transient osteoporosis, transient bone marrow edema syndrome, or osteonecrosis. Radiographics 13(5):1001–1011, discussion 1012

Hofmann S, Kramer J, Vakil-Adli A, Aigner N, Breitenseher M (2004) Painful bone marrow edema of the knee: differential diagnosis and therapeutic concepts. Orthop Clin N Am 35(3):321–333

Horiuchi K, Shiraga N, Fujita N, Yamagishi M, Yabe H (2004) Regional migratory osteoporosis: a case report. J Orthop Sci Off J Jpn Orthop Assoc 9(2):178–181

Iwasaki K, Yamamoto T, Motomura G, et al (2010) Prognostic factors associated with a subchondral insufficiency fracture of the femoral head. British j radiol

Iwasaki K, Yamamoto T, Motomura G, Mawatari T, Nakashima Y, Iwamoto Y (2011) Subchondral insufficiency fracture of the femoral head in young adults. Clin Imag 35(3):208–213

Karantanas AH (2007) Acute bone marrow edema of the hip: role of MR imaging. Eur Radiol 17(9):2225–2236

Karantanas AH, Drakonaki EE (2011) The role of MR imaging in avascular necrosis of the femoral head. Semin Musculo Skeletal Radiol 15(3):281–300

Karantanas AH, Drakonaki E, Karachalios T, Korompilias AV, Malizos K (2008a) Acute non-traumatic marrow edema syndrome in the knee: MRI findings at presentation, correlation with spinal DEXA and outcome. Eur J Radiol 67(1):22–33

Karantanas AH, Nikolakopoulos I, Korompilias AV, Apostolaki E, Skoulikaris N, Eracleous E (2008b) Regional migratory osteoporosis in the knee: MRI findings in 22 patients and review of the literature. Eur J Radiol 67(1):34–41

Kim YM, Oh HC, Kim HJ (2000) The pattern of bone marrow oedema on MRI in osteonecrosis of the femoral head. J Bone Joint Surg 82(6):837–841

Korompilias AV, Karantanas AH, Lykissas MG, Beris AE (2009) Bone marrow edema syndrome. Skeletal Radiol 38(5):425–436

Krestan C, Hojreh A (2009) Imaging of insufficiency fractures. Eur J Radiol 71(3):398–405

Krestan CR, Nemec U, Nemec S (2011) Imaging of insufficiency fractures. Semin Musculo Skeletal Radiol 15(3): 198–207

La Montagna G, Malesci D, Tirri R, Valentini G (2005) Successful neridronate therapy in transient osteoporosis of the hip. Clin Rheum 24(1):67–69

Lakhanpal S, Ginsburg WW, Luthra HS, Hunder GG (1987) Transient regional osteoporosis a study of 56 cases and review of the literature. Ann Intern Med 106(3):444–450

Lecouvet FE, van de Berg BC, Maldague BE et al (1998) Early irreversible osteonecrosis versus transient lesions of the femoral condyles: prognostic value of subchondral bone and marrow changes on MR imaging. AJR Am J Roentgenol 170(1):71–77

Lecouvet FE, Malghem J, Maldague BE, Vande Berg BC (2005) MR imaging of epiphyseal lesions of the knee: current concepts, challenges, and controversies. Radiol Clin North Am 43(4):655–672

Lequesne M (1968) Transient osteoporosis of the hip. A nontraumatic variety of Sudeck's atrophy. Ann Rheum Dis 27(5):463–471

Lequesne M, Mauger B (1982) 100 decalcifying algodystrophies of the hip in 74 patients. Rev Rhum Mal Osteoartic 49(11):787–792

Lloyd JM, Lewis M, Jones A (2006) Transient osteoporosis of the knee in pregnancy. j knee surg 19(2):121–123

Maihofner C, Seifert F, Markovic K (2010) Complex regional pain syndromes: new pathophysiological concepts and therapies. Eur J Neurol Off J Eur Fed Neurol Soc 17(5):649–660

Malizos KN, Zibis AH, Dailiana Z, Hantes M, Karachalios T, Karantanas AH (2004) MR imaging findings in transient osteoporosis of the hip. Eur J Radiol 50(3):238–244

McKiernan FE (2005) Musculoskeletal manifestations of mild osteogenesis imperfecta in the adult. Osteoporos Int 16(12):1698–1702

Miyanishi K, Kaminomachi S, Hara T et al (2007) A subchondral fracture in transient osteoporosis of the hip. Skeletal Radiol 36(7):677–680

Moreno AJ, Ward DL (2001) Bone scan manifestation of transient osteoporosis of the hip. Clin Nucl Med 26(10): 872–873

Navas A, Kassarjian A (2011) Bone marrow changes in stress injuries. Semin Musculo Skeletal Radiol 15(3):183–197

Neri R, Martini A, Trippi D, Zampa V, Pasero G (1997) Reflex sympathetic dystrophy syndrome with microtrabecular fracture in a patient with osteogenesis imperfecta. Clin Rheumatol 16(4):363–366

Papathanassiou D, Bruna-Muraille C, Jouannaud C, Gagneux-Lemoussu L, Eschard JP, Liehn JC (2009) Single-photon emission computed tomography combined with computed tomography (SPECT/CT) in bone diseases. Jt Bone Spine Revue Du Rhumatisme 76(5):474–480

Parker RK, Ross GJ, Urso JA (1997) Transient osteoporosis of the knee. Skeletal Radiol 26(5):306–309

Pesesse L, Sanchez C, Henrotin Y (2011) Osteochondral plate angiogenesis: a new treatment target in osteoarthritis. Jt Bone Spine Revue Du Rhumatisme 78(2):144–149

Rafii M, Mitnick H, Klug J, Firooznia H (1997) Insufficiency fracture of the femoral head: MR imaging in three patients. AJR Am J Roentgenol 168(1):159–163

Ragab Y, Emad Y, Abou-Zeid A (2008) Bone marrow edema syndromes of the hip: MRI features in different hip disorders. Clin Rheumatol 27(4):475–482

Ramnath RR, Kattapuram SV (2004) MR appearance of SONK-like subchondral abnormalities in the adult knee: SONK redefined. Skeletal Radiol 33(10):575–581

Sandroni P, Benrud-Larson LM, McClelland RL, Low PA (2003) Complex regional pain syndrome type I: incidence and prevalence in Olmsted country, a population-based study. Pain 103(1–2):199–207

Schurmann M, Zaspel J, Lohr P et al (2007) Imaging in early posttraumatic complex regional pain syndrome: a comparison of diagnostic methods. Clin J Pain 23(5):449–457

Schweitzer ME, Mandel S, Schwartzman RJ, Knobler RL, Tahmoush AJ (1995) Reflex sympathetic dystrophy revisited: MR imaging findings before and after infusion of contrast material. Radiology 195(1):211–214

Spinarelli A, Patella V, Speciale D et al (2009) Hip fracture in a patient affected by transient osteoporosis of the femoral head during the last trimester of pregnancy. Orthopedics 32(5):365

Sprinchorn AE, O'Sullivan R, Beischer AD (2011) Transient bone marrow edema of the foot and ankle and its association with reduced systemic bone mineral density. Foot ankle int American Orthop Foot Ankle Soc [and] Swiss Foot Ankle Soc 32(5):S508–S512

Stamp L, McLean L, Stewart N, Birdsall M (2001) Bilateral transient osteoporosis of the knee in pregnancy. Ann Rheum Dis 60(7):721–722

Staudenherz A, Hofmann S, Breitenseher M et al (1997) Diagnostic patterns for bone marrow oedema syndrome and avascular necrosis of the femoral head in dynamic bone scintigraphy. Nucl Med Commun 18(12):1178–1188

Steib-Furno S, Luc M, Pham T et al (2007) Pregnancy-related hip diseases: incidence and diagnoses. Jt Bone Spine 74(4):373–378

Steinbach LS, Suh KJ (2011) Bone marrow edema pattern around the knee on magnetic resonance imaging excluding acute traumatic lesions. Semin Musculo Skeletal Radiol 15(3):208–220

Tan TX, Dardani M, Neal DJ, Mueller CF, Pozderac RV (1998) Atypical findings of discordant bone scan and radiographs in transient osteoporosis of the hip: case report and review of the literature. Clin Nucl Med 23(3):160–162

Thiryayi WA, Thiryayi SA, Freemont AJ (2008) Histopathological perspective on bone marrow oedema, reactive bone change and haemorrhage. Eur J Radiol 67(1):62–67

Timsit MA (2004) Pregnancy, low-back pain and pelvic girdle pain. Gynecol Obstet Fertil 32(5):420–426

Toms AP, Marshall TJ, Becker E, Donell ST, Lobo-Mueller EM, Barker T (2005) Regional migratory osteoporosis: a review illustrated by five cases. Clin Radiol 60(4):425–438

Trevisan C, Ortolani S (2002) Bone loss and recovery in regional migratory osteoporosis. Osteoporos Int J Established Result Cooperation Betw Eur Found Osteoporos Nat Osteoporos Found USA 13(11):901–906

Trevisan C, Ortolani S, Monteleone M, Marinoni EC (2002) Regional migratory osteoporosis: a pathogenetic hypothesis based on three cases and a review of the literature. Clin Rheumatol 21(5):418–425

Vande Berg BC, Malghem JJ, Lecouvet FE, Jamart J, Maldague BE (1999) Idiopathic bone marrow edema lesions of the femoral head: predictive value of MR imaging findings. Radiology 212(2):527–535

Vande Berg BC, Lecouvet FE, Koutaissoff S, Simoni P, Malghem J (2008) Bone marrow edema of the femoral head and transient osteoporosis of the hip. Eur J Radiol 67(1): 68–77

Vande Berg B, Lecouvet F, Koutaissoff S, Simoni P, Maldague B, Malghem J (2011) Transient bone marrow edema of the hip. J De Radiol 92(6):557–566

Vande Berg BE, Malghem JJ, Labaisse MA, Noel HM, Maldague BE (1993) MR imaging of avascular necrosis and transient marrow edema of the femoral head. Radiographics 13(3):501–520

Ververidis AN, Drosos GI, Kazakos KJ, Xarchas KC, Verettas DA (2009) Bilateral transient bone marrow edema or transient osteoporosis of the knee in pregnancy. Knee Surg Sports Traumatol Arthrosc 17(9):1061–1064

Walsh DA, McWilliams DF, Turley MJ et al (2010) Angiogenesis and nerve growth factor at the osteochondral junction in rheumatoid arthritis and osteoarthritis. Rheumatology 49(10):1852–1861

Watanabe W, Itoi E, Yamada S (2002) Early MRI findings of rapidly destructive coxarthrosis. Skeletal Radiol 31(1):35–38

Wilson AJ, Murphy WA, Hardy DC, Totty WG (1988) Transient osteoporosis: transient bone marrow edema? Radiology 167(3):757–760

Yamamoto T, Kubo T, Hirasawa Y, Noguchi Y, Iwamoto Y, Sueishi K (1999) A clinicopathologic study of transient osteoporosis of the hip. Skeletal Radiol 28(11):621–627

Yamamoto T, Takabatake K, Iwamoto Y (2002) Subchondral insufficiency fracture of the femoral head resulting in rapid destruction of the hip joint: a sequential radiographic study. AJR Am J Roentgenol 178(2):435–437

Yamamoto T, Iwamoto Y, Schneider R, Bullough PG (2008) Histopathological prevalence of subchondral insufficiency fracture of the femoral head. Ann Rheum Dis 67(2): 150–153

Zanetti M, Bruder E, Romero J, Hodler J (2000) Bone marrow edema pattern in osteoarthritic knees: correlation between MR imaging and histologic findings. Radiology 215(3): 835–840

Zanetti M, Steiner CL, Seifert B, Hodler J (2002) Clinical outcome of edema-like bone marrow abnormalities of the foot. Radiology 222(1):184–188

Zhao G, Yamamoto T, Ikemura S et al (2010) A histopathological evaluation of a concave-shaped low-intensity band on T1-weighted MR images in a subchondral insufficiency fracture of the femoral head. Skeletal Radiol 39(2):185–188

Bone Marrow Changes in Acute and Chronic Trauma

Filip M. Vanhoenacker, Michiel Eyselbergs, and Annick Demeyere

Contents

F. M. Vanhoenacker (✉)
Department of Radiology, General Hospital Sint-Maarten Duffel-Mechelen, Rooienberg 25, 2570 Duffel, Belgium
e-mail: filip.vanhoenacker@telenet.be

F. M. Vanhoenacker · M. Eyselbergs
University Hospital Antwerp, University of Antwerp, Rooienberg 25, 2570 Duffel, Belgium

F. M. Vanhoenacker
Faculty of Medicine and Health Sciences, University of Ghent, Rooienberg 25, 2570 Duffel, Belgium

A. Demeyere
General Hospital Imelda, Bonheiden, Belgium

Abstract

This chapter will discuss the value of medical imaging in the detection and follow-up of bone marrow edema (BME), resulting from acute and chronic trauma. The mechanisms of trauma, clinical significance and natural evolution are emphasized. Unlike plain radiography and computed tomography (CT), magnetic resonance imaging (MRI) is the only imaging technique that allows direct detection of BME. The use of fluid-sensitive sequences is particularly appropriate to evaluate BME. Apart from detection, analysis of the extent of BME may reveal the underlying mechanism of trauma. Following a single acute trauma, compressive forces between two bony structures may result in extensive areas of BME, whereas distraction forces provoke more subtle areas of BME at the insertion of supporting structures of joints. In most clinical situations, a combination of compression and distraction forces is present, causing a complex pattern of BME. A meticulous pattern approach of the distribution of these bone marrow changes around a joint can reveal in most instances the underlying mechanism of trauma. This may be helpful to analyze which joint supporting structures may be at risk. In the acute setting, plain radiography and CT may have an additional role in the detection of small avulsion fractures occurring at the site of minor areas of BME. Apart from an acute traumatic cause, BME may result from repetitive or chronic trauma. This group of lesions comprises stress fractures, chronic avulsive lesions and lesions due to altered biomechanics in certain sports activities. The clinical significance and natural history of BME is still a matter of debate.

A. Baur-Melnyk (ed.), *Magnetic Resonance Imaging of the Bone Marrow*, Medical Radiology. Diagnostic Imaging,
DOI: 10.1007/174_2011_444,

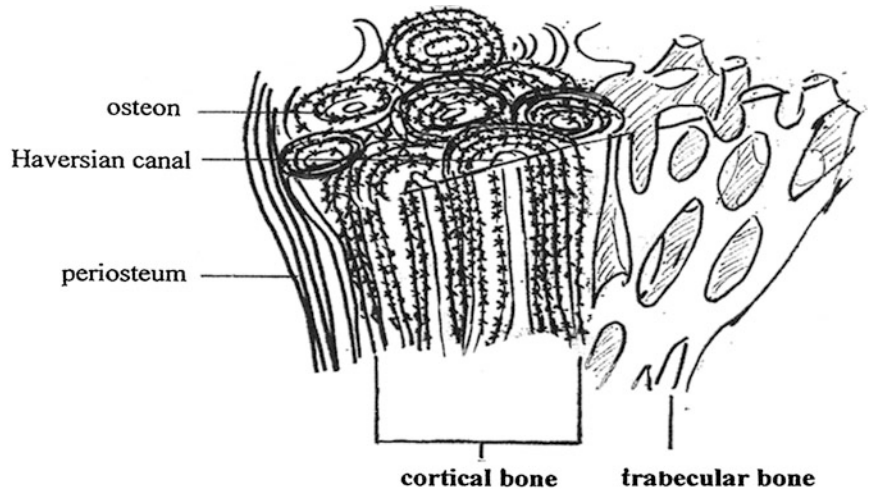

Fig. 1 Anatomy of bone. Bone is made up of cortical and trabecular bone surrounded by periosteum. The cortical bone unit is the osteon (used with permission from Demeyere and Vanhoenacker 2007)

1 Basic Anatomy

Macroscopically, living bone consists of compact bone and cancellous bone (Fig. 1). *Cancellous bone*, also designated as trabecular or spongy bone consists of a honeycomb of large cavities with an internal latticework of bars and plates (trabeculae). *Compact bone* is usually limited to the cortices of mature bones (cortical bone) and is most important in providing the strength of bone. Cancellous bone lies in the inner part of the bone, and particularly, in case of the long bones, within their expanded ends (metaphyses and epiphyses). Cancellous bone gives additional strength to cortical bone and supports the bone marrow (Soames 1995).

2 Definition and Terminology of Traumatic Bone Marrow Edema

Before the advent of Magnetic Resonance Imaging (MRI), trauma to the trabecular bone was difficult to assess on radiological examinations because the overlying cortex is often intact (Mandalia et al. 2005). 'Bone bruise' was first coined in the knee by Yao and Lee in (1988). The term "bruise" indicates the traumatic origin of these bone marrow changes. It was defined as a region of T2-hyperintensity in the absence of frank osseous fracture or subchondral cysts. MRI examination showed intraosseous areas which are hyperintense on T2-weighted imaging (WI) or STIR images and (to a lesser degree) hypointense

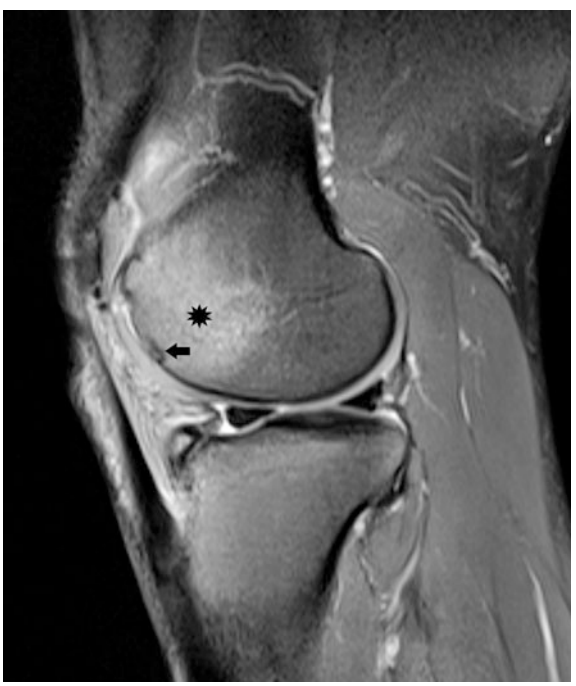

Fig. 2 Bone marrow edema (BME) due to a direct blow (impaction type BME). Sagittal fat suppressed FSE T2-WI of the knee shows extensive BME at the anterior aspect of the distal femur (*asterisk*). Notice also the subtle hypointense line at the subchondral area of the distal femur, representing a small impaction fracture (*arrow*)

on T1-WI, in acutely injured knees with no abnormalities on plain radiographs. Currently, the use of an intermediate echo time (TE) in fat suppressed (FS) T2-WI is recommended for assessment of any

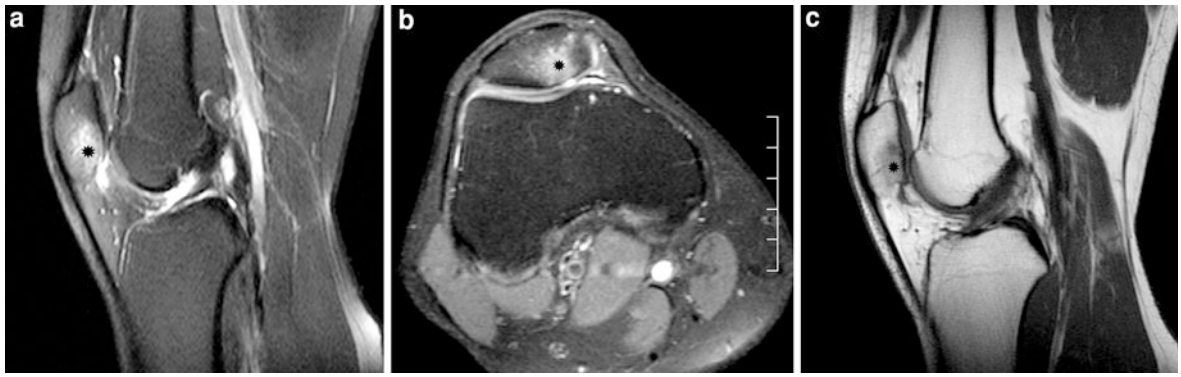

Fig. 3 BME due to a direct impact on the patella. **a** Sagittal fat suppressed FSE T2-weighted image of the knee and **b** Axial fat suppressed FSE T2-WI shows extensive BME at patella (*asterisk*). **c** Sagittal T1-WI shows the area of BME at patella as a hypointense signal (*asterisk*)

associated overlying cartilage lesions. The terms "bone bruise, bone contusion and occult fracture" are used interchangeably. Most authors use the term "occult" when plain radiography shows no abnormalities. However, current multidetector CT with isotropic multiplanar reconstructions may pick up subtle trabecular fractures more easily than plain radiographs. In this regard, the term "occult" fracture should probably be revisited. Radiologically overt fractures may be surrounded by high signal bone marrow changes on fluid-sensitive sequences. In this scenario, one can speak of accompanying bruise in the cancellous bone, adjacent to the fracture line.

3 Classification and Patterns of Injury

Traumatic BME may be due to either acute or chronic trauma.

3.1 Acute Traumatic Lesions

BME is frequently encountered on MRI after an injury to the musculoskeletal system (*S*anders et al. 2000). These osseous injuries may result from several forces acting on the joint. In general, compressive forces versus traction forces will influence the extent of BME edema around the joint (Hayes et al. 2000; Vanhoenacker and Snoeckx 2007; Vanhoenacker et al. 2007*)*.

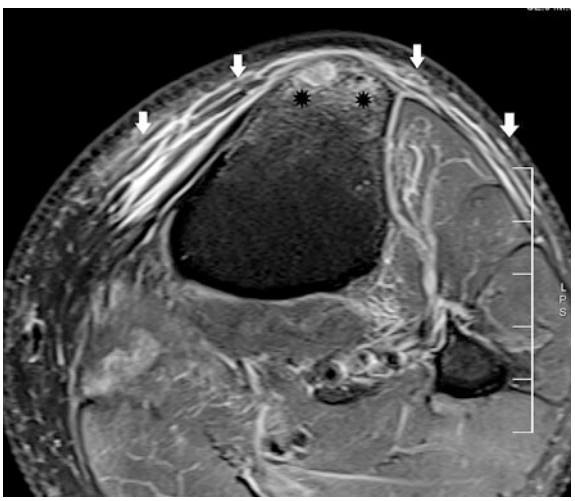

Fig. 4 Direct impact trauma on the anterior aspect of the proximal tibia. Axial fat suppressed FSE T2-WI shows focal hyperintense signal at the anterior aspect of the right proximal tibia (*asterisks*). Notice also subcutaneous hyperintense stranding due to direct impact trauma (*arrows*)

3.1.1 Impaction Injuries

Focal bruise may result from direct trauma to the bone (Figs. 2, 3, 4), but often a specific pattern of bone marrow changes on adjacent bones occurs due to impaction of one bone to another. Impaction type of BME is extensive and will involve a broad surface of the involved bony structures.

3.1.2 Avulsive Injuries

Distraction injuries are usually due to valgus, varus or rotational stress on a joint, resulting in a small

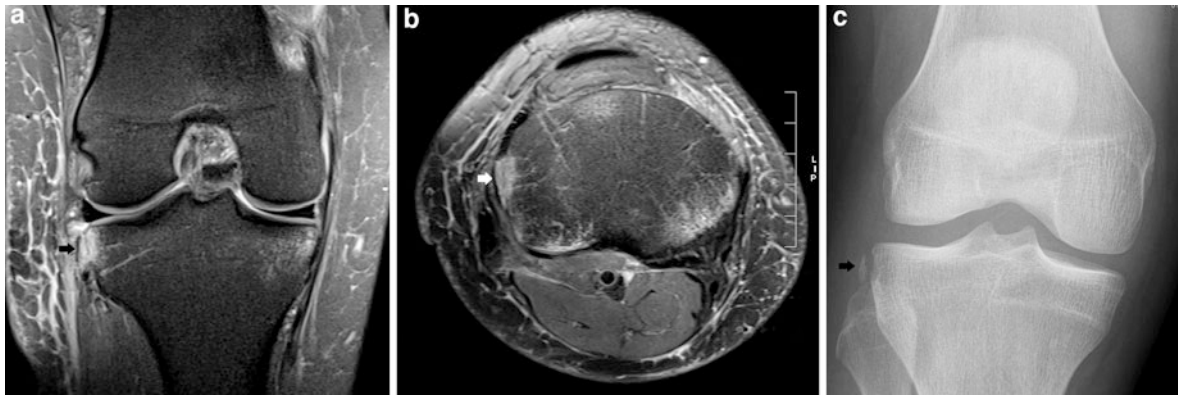

Fig. 5 Typical example of an avulsion fracture and associated BME (avulsion type BME). **a** Coronal and **b** axial fat suppressed FSE T2-WI of the right knee shows only minor focal BME at the lateral aspect of the tibia (*arrow*). The bony avulsion fracture is barely visible. **c** Standard radiograph (AP spot view) clearly shows an avulsion fracture (*arrow*) (Segond fracture)

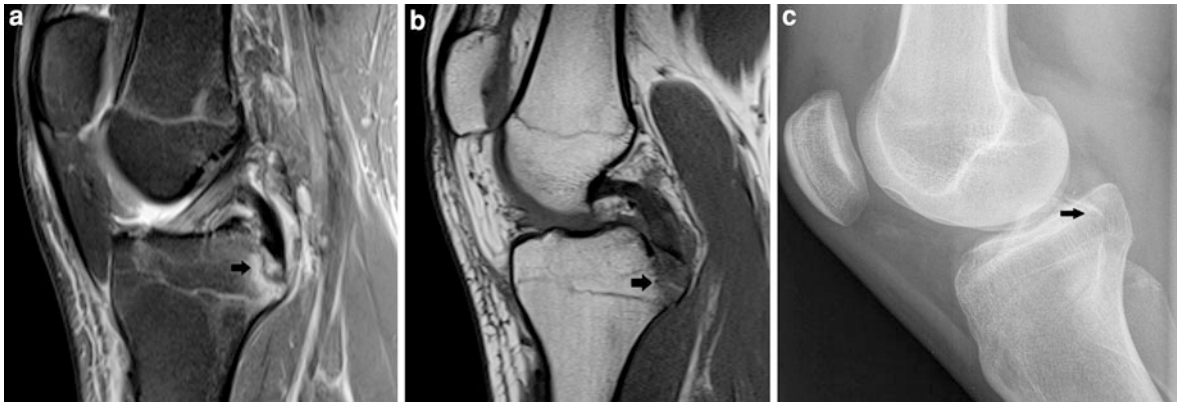

Fig. 6 Avulsion fracture at the insertion of the posterior cruciate ligament (PCL). **a** Sagittal fat suppressed FSE T2-WI reveals a focal area of increased signal distal to the insertion of the PCL at the posterior aspect of the tibia (*arrow*). Notice also the presence of a hypointense fracture line **b** Sagittal SE T1-WI. The area of BME is hypointense compared to normal fatty bone marrow (*arrow*). **c** Standard radiograph (*lateral view*) shows an avulsion fracture (*arrow*)

avulsion fracture related to a tendinous, ligamentous or capsular attachment on the bone. Because the cortical bone is involved rather than the trabecular bone, the resulting "avulsion BME pattern" is much less extensive than in impaction injuries (Figs. 5, 6). Moreover, the avulsed bony fragment may be very difficult to detect on MRI (Fig. 5a, b). In most instances, a small avulsion is far more better demonstrated on plain radiography (Fig. 5c) or CT.

3.1.3 Complex Patterns

In most clinical situations, this rigorous distinction between *"pure impaction type injuries"* and "*avulsive type injuries"* is arbitrary because both types will be seen in a single joint after acute traumatic injuries. Generally, the impaction type of BME will be encountered on the *entry site* of the force acting on a joint, whereas distraction type of BME will be seen on the *exit site* of the force. Although avulsive type BME is less extensive than the impaction type, the former is usually the witness of underlying ligamentous sprain. These soft tissue lesions are often less conspicuous than the bruises, though they are more important, at least in the short term follow-up, for stability reasons. Sprain of the supporting structures of the joint may cause instability, if not recognized and treated appropriately.

Only a minority of the studies of acute joint injuries (knee and ankle) will show isolated bruising without associated injuries. Moreover, BME around a

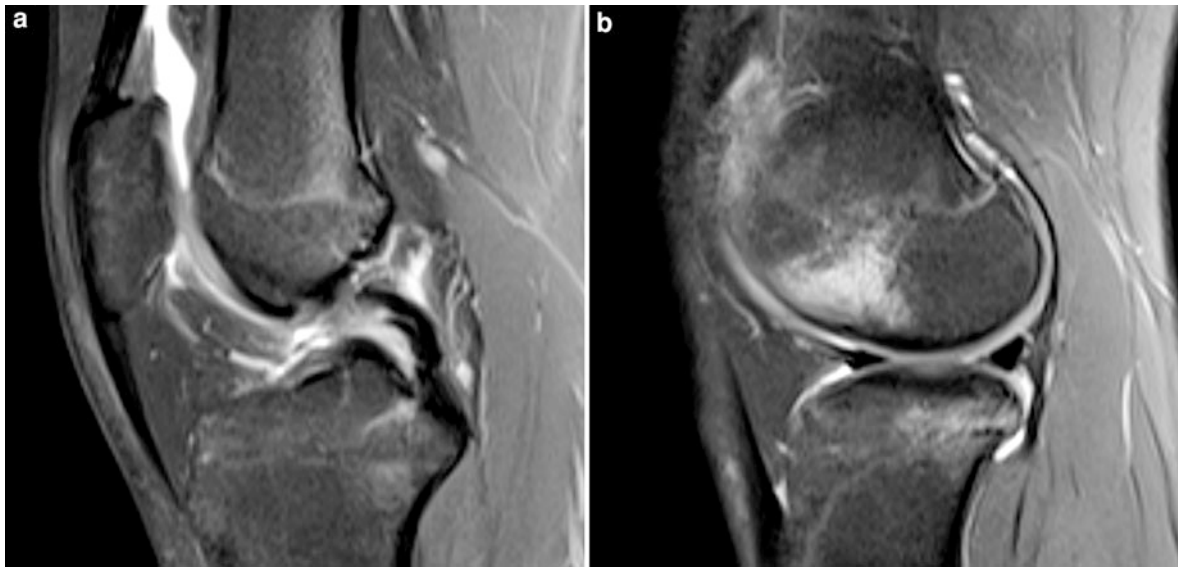

Fig. 7 Pivot shift injury due to a combination of external rotation of the tibia, valgus stress and flexion in a skier. These maneuver stress the anterior cruciate ligament (ACL), which is prone to rupture. **a** Midsagittal fat suppressed FSE T2-WI of the right knee shows absence of the ACL, in keeping with complete disruption of the ACL. **b** Sagittal fat suppressed FSE T2-WI of the right knee. Due to anterior subluxation of the tibia relative to the femur, impaction occurs between the posterolateral margin of the lateral tibial plateau and the lateral femoral condyle, resulting in extensive impaction type BME

joint is usually the result of a combination of multiple forces (instead of a single force), which all have a certain amplitude and direction. The impact of these forces may differ with the position of the joint at the moment of the trauma (e.g. degree of flexion, varus, valgus,…). Certain combinations of forces are known to cause a specific injury. Systematic analysis of the BME pattern, together with the associated soft tissue changes can often reveal the specific mechanism of injury. In this regard, the pattern and distribution of BME represents a 'footprint' of the mechanism of acute trauma (Sanders et al. 2000). In the knee for example, classic patterns which are encountered in sports injuries are pivot shift injury (Figs. 7, 8), hyperextension injury (Fig. 9), clip injury (Fig. 10), dashboard injury (Fig. 11) and (transient) lateral patellar dislocation (Fig. 12).

Pivot shift injury (Figs. 7, 8) occurs when valgus load is applied to the knee in various states of flexion, combined with external rotation of the tibia or internal rotation of the femur and results in disruption of the anterior cruciate ligament (ACL). Resulting anterior subluxation of the tibia will cause impaction of the lateral femoral condyle against the posterolateral margin of the lateral tibial plateau. Therefore, BME will be present in the posterior aspect of the lateral tibial plateau and the middle portion of the lateral femoral condyle. Associated bone bruising at the posterior lip of the medial tibial plateau may be the result of contrecoup impaction forces (Kaplan et al. 1999). According to others this medial-sided bone bruise is rather attributed to avulsion at the semimembranosus attachment (Chan et al. 1999). Concomitant soft tissue injuries of the pivot shift injury are medial collateral ligament (MCL) lesions, lesion of the posterior horn of the lateral and medial meniscus or a tear at the posterior joint capsule.

Hyperextenson injury (Fig. 9) results in a kissing contusion pattern in the anterior aspect of the distal femur and proximal tibia. Associated soft tissue lesions may include ACL or posterior cruciate ligament (PCL) tears or meniscal lesions.

Clip injury (Fig. 10) occurs when pure valgus stress is applied to the knee while the knee is in mild flexion. BME is most prominent in the lateral femoral condyle due to impaction forces, whereas a second smaller area of edema may be present in the medial femoral condyle secondary to avulsive forces at the insertion of the MCL.

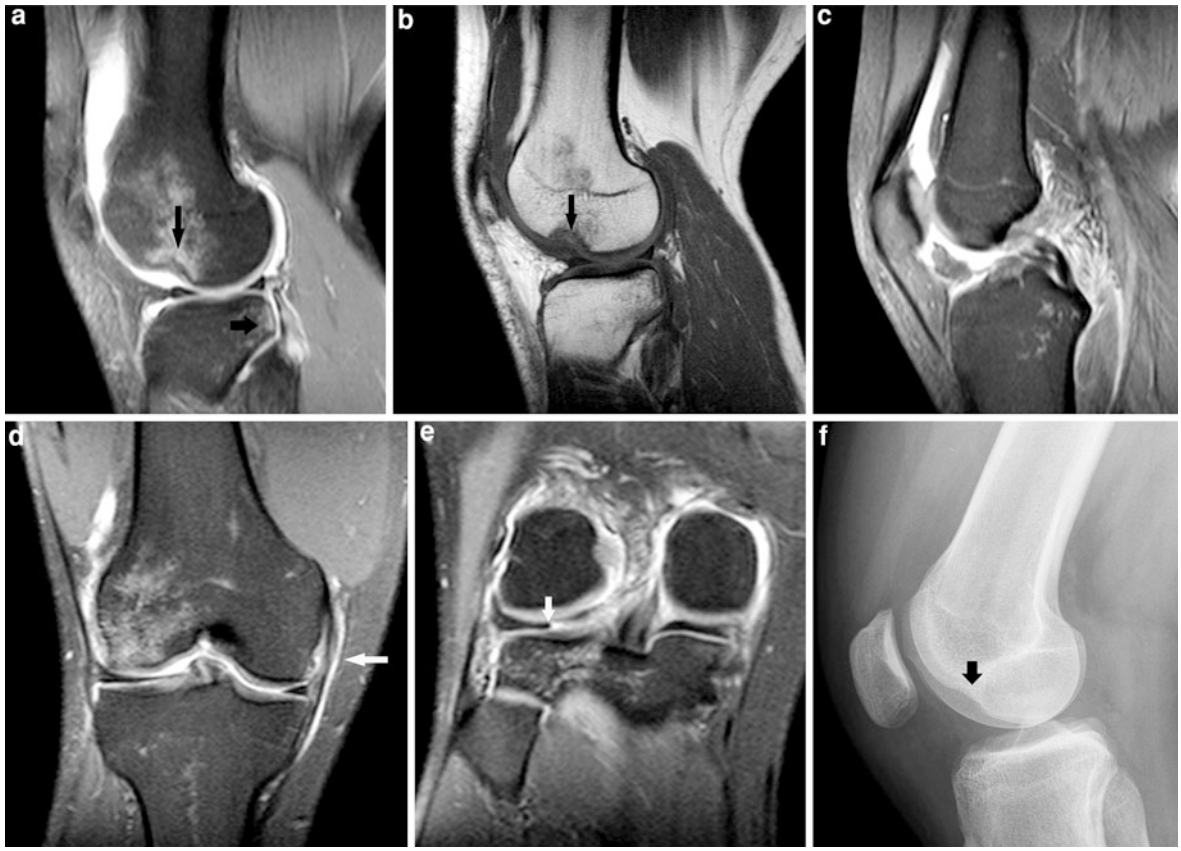

Fig. 8 Another pivot shift injury in a soccer player with associated lateral meniscus tear and medial collateral ligament (MCL) sprain. **a** Sagittal fat suppressed FSE T2-WI of the lateral aspect of the right knee. BME at the posterolateral aspect of the tibia (*short arrow*) and corresponding BME at the middle part of the lateral femoral condyle (with associated focal cortical depression; *long arrow*). **b** Sagittal SE T1-weighted image of the lateral aspect of the right knee, showing the focal cortical depression (deep femoral notch sign, *arrow*), in keeping with an impaction fracture at the lateral femoral condyle. **c** Midsagittal fat suppressed FSE T2-WI of the right knee shows complete disruption of the ACL. **d** Coronal fat suppressed FSE T2-WI of the right knee shows soft tissue edema adjacent to the medial collateral ligament, in keeping with sprain grade I of the MCL (*arrow*). **e** Coronal fat suppressed FSE T2-WI of the right knee shows a tear at the posterior horn of the lateral meniscus (*arrow*). **f** Standard radiograph (*lateral view*) clearly shows the deep femoral notch sign (*arrow*)

Dashboard injury (Fig. 11) occurs when a posteriorly directed force is applied to the anterior aspect of the proximal tibia while the knee is in a flexed position. This will result in BME at the anterior aspect of the tibia and occasionally at the posterior surface of the patella. Associated soft tissue injuries are disruption of the PCL and posterior joint capsule.

The classic bone contusion pattern seen after *lateral patellar dislocation* (Fig. 12) includes involvement of the anterolateral aspect of the lateral femoral condyle and the inferomedial aspect of the patella. Associated soft tissue injuries include sprain or disruption of the medial soft tissue restraints (medial retinaculum, medial patellofemoral ligament and the medial patellotibial ligament).

Failure of this pattern approach revealing the underlying mechanism of trauma may be due to several factors, including insufficient trauma, massive injury or pre-existing osteoarthritis associated with BME (Felson et al. 2001; MacMahon and Palmer 2011), usually encountered in older sporters. Moreover, accelerated osteoarthritis is more prevalent in sporters than in the general population, due to previous repetitive trauma.

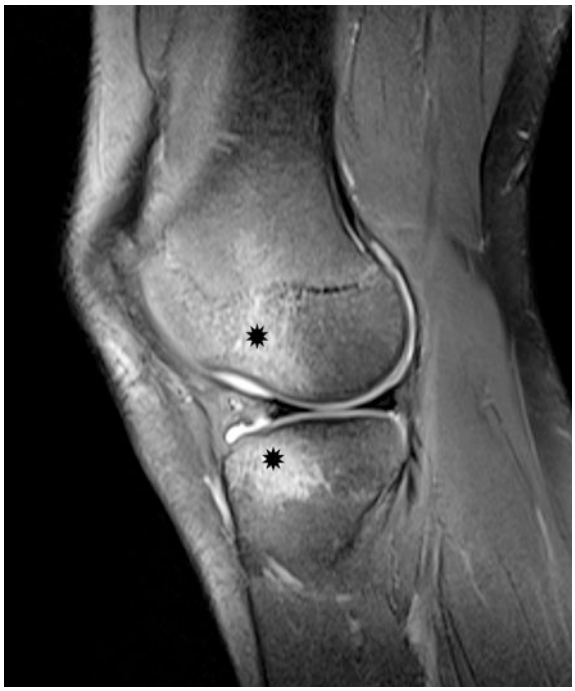

Fig. 9 Hyperextension trauma in a soccer player. Midsagittal fat suppressed FSE T2-WI of the right knee. Severe hyperextension of the knee can result in the impaction of the anterior aspect of the femoral condyle against the anterior aspect of the tibial plateau (*asterisks*)

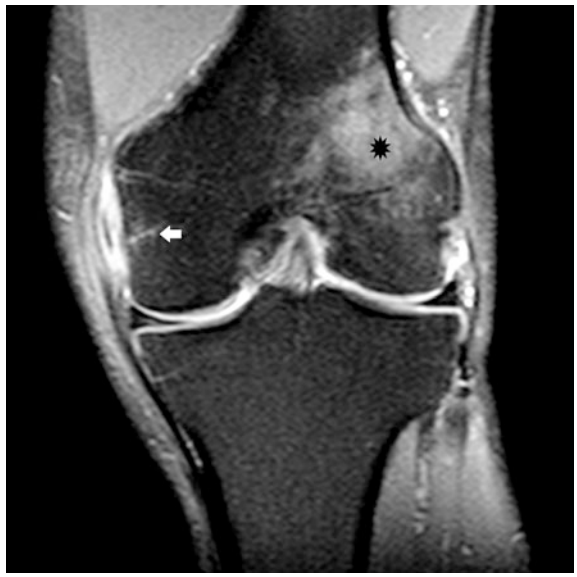

Fig. 10 Clip injury in a soccer player. Coronal fat suppressed FSE T2-WI of the left knee shows a large area of BME involving the lateral femoral condyle (*asterisk*). Minimal edema is noted within the medial femoral condyle near the proximal attachment of the MCL (*arrow*). There is partial disruption of the MCL

3.2 Chronic Traumatic Lesions (Repetitive Trauma)

Apart from pure acute traumatic causes, BME may result from repetitive or chronic trauma.

3.2.1 Stress Fractures

Chronic stress on a normally mineralized bone may result in a spectrum of MRI findings ranging from periosteal edema over severe marrow edema to a hypointense fracture line in cancellous or cortical bone. Stress-related bone injuries are common in athletes and military recruits and account for up to 10% of cases in sports medicine practice. Stress fractures have been classified into two types: fatigue and insufficiency. The fatigue fracture is caused by an abnormal stress to a normally elastic bone. Fatigue fractures are thought to occur in different sites depending on the age, gender and activity of the athlete. Insufficiency fractures arise from application of normal stress on bone that is mineral deficient or abnormally inelastic. Insufficiency fractures are most

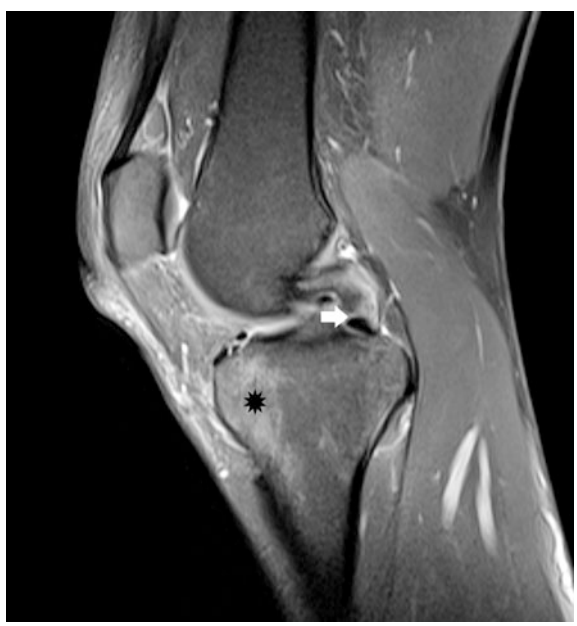

Fig. 11 Dashboard injury. Sagittal fat suppressed FSE T2-WI showing BME at the proximal tibia (*asterisk*) and associated disruption of the posterior cruciate ligament (*arrow*)

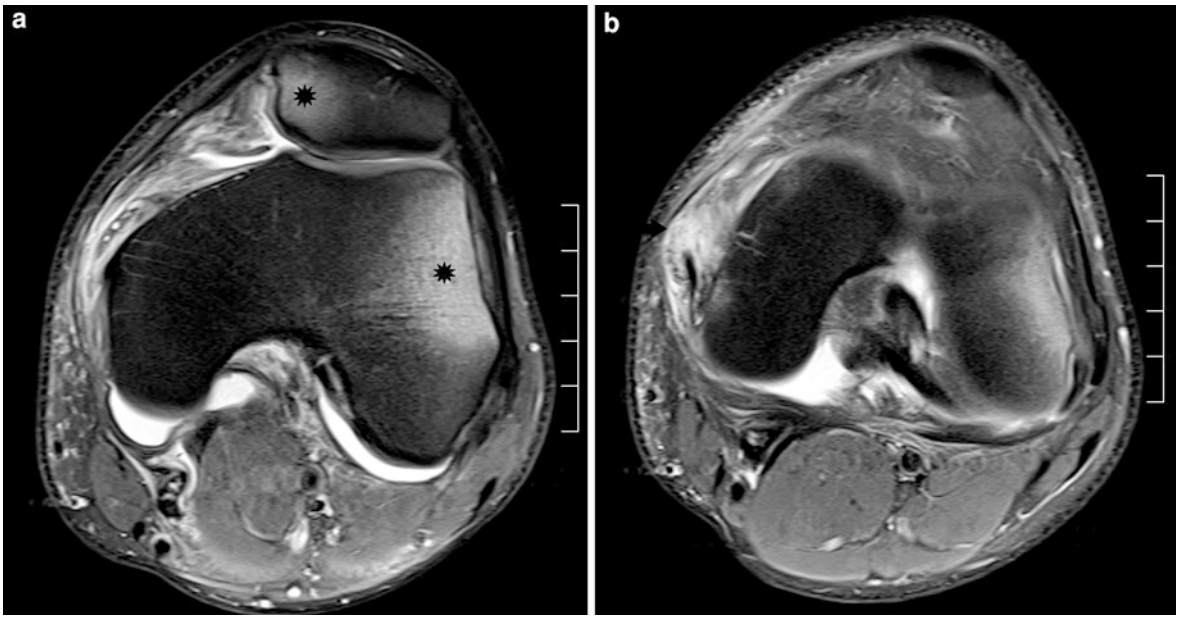

Fig. 12 Impaction type bone marrow edema, associated with lateral patellar dislocation in a soccer player. **a** axial fat suppressed FSE T2-WI of the right knee demonstrates BME involving the medial patellar facet and the anterior aspect of the lateral femoral condyle (*asterisks*). **b** Associated distraction at the medial patellofemoral ligament retinaculum results in focal disruption at its attachment at the adductor tubercle

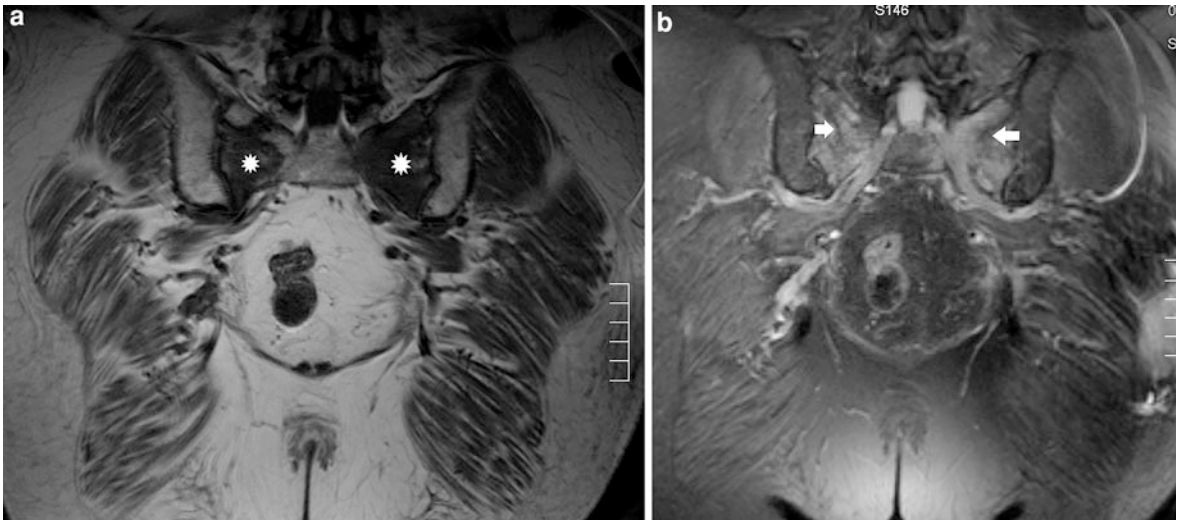

Fig. 13 Bilateral sacral insufficiency fractures in a patient with known osteoporosis. **a** Coronal T1-WI showing bandlike hypointense structures within the sacrum parallel to the sacro-iliac joints (*asterisks*). **b** Coronal fat suppressed FSE T2-WI revealing extensive BME parallel to the sacro-iliac joints. Hypo-intense fracture lines (*arrows*) are seen within these areas of BME

prevalent in nutrient deficient (osteomalacia) and older populations in whom osteoporosis (Fig. 13) and rheumatoid arthritis are more common (Romani et al. 2002; Anderson and Greenspan 1996).

Although the reported incidence of stress fractures in the general athletic population is less than 1%, the incidence in runners may be as high as 20%. But with the increasing emphasis on exercise for the elderly

Table 1 Risk factors that influence the development of (insufficiency) stress fractures (used with permission from Demeyere and Vanhoenacker 2007)

Training factors
alteration in intensity, duration or frequency of training
inadequate footwear
hard running surface
Limb malalignment
pronation of the feet
cavus foot
genu varum, subtalar or forefoot varus
limb length discrepancy
Metabolic disorders
osteoporosis
osteomalacia
hyperparathyroidism
Cushing's syndrome, hypothyroidism, renal insufficiency
rickets
scurvy
Inflammatory conditions
rheumatoid arthritis
osteomyelitis
Bone dysplasias
osteogenesis imperfecta
Neurological disorders
neurotrophic diseases
poliomyelitis
Paget's disease
Pharmacological
corticosteroids
diuretics
anticonvulsants
Nutritional deficiencies
Sleep deprivation
Smoking

and the recreational athletic population, stress fractures should not be overlooked in this population. Risk factors for development of stress injuries include training factors, limb malalignement and underlying systemic factors (Table 1). Risk factors are well described in the literature (Demeyere and Vanhoenacker 2007) and further discussion is beyond the scope of this chapter. Although stress fractures have been described in nearly every bone, they are most common in the weight-bearing bones of the lower extremities. Specific anatomic sites for stress fractures may be associated with individual sports, such as the humerus in throwing sports (Lee et al. 2006; Hoy et al. 2006), the ribs in golf and rowing, the spine in gymnastics, the lower extremities in running activities and the foot in gymnastics (Bennell and Brukner 1997). In a review of 370 athletes with stress fractures, the tibia was the most commonly involved bone (49.1% of cases), followed by the tarsals (25.3%), the metatarsals (8.8%) (Boden and Osbahr 2000) and pelvis. Bilateral stress fractures occurred in 17% of cases (Fig. 14). The potential sites of stress injuries are summarized in Table 2.

Bone response to stress is evaluated on a dynamic continuum between early remodeling and periostitis to a cortical stress fracture. These osseous changes reflect a wide spectrum of physical findings and imaging findings. This paragraph will highlight the imaging findings on different imaging modalities.

3.2.1.1 Radiography

Plain radiography plays an important role in the initial workup of a suspected stress fracture. It can be used to confirm the diagnosis at a relatively low cost. Unfortunately, initial radiographs are often normal, which is not surprising given the degree of microscopic remodeling that occurs in the early stages of stress injury. The sensitivity of early radiographs can be as low as 15% and follow-up radiographs will demonstrate diagnostic findings in only 50% of cases (Nielsen et al. 1991). The time lag between manifestation of initial symptoms and detection of radiographic findings ranges from 1 week to several months, and cessation of physical activity may impede the development of typical plain radiographic findings (Anderson and Greenspan 1996; Spitz and Newberg 2002). Initial changes in the cortical bone are the so called "gray cortex" sign seen as a subtle ill definition of the cortex (Mulligan 1995) or faint intracortical radiolucent striations, which are presumably related to the osteoclastic tunneling found early in the remodeling process (Muthukumar et al. 2005; Daffner and Pavlov 1992). These changes may be easily overlooked until periosteal new bone formation and/or endosteal thickening develops in an apparent attempt to buttress the temporarily weakened cortex. As damage increases, a true fracture line may appear (Fig. 15). These injuries typically involve the shaft of

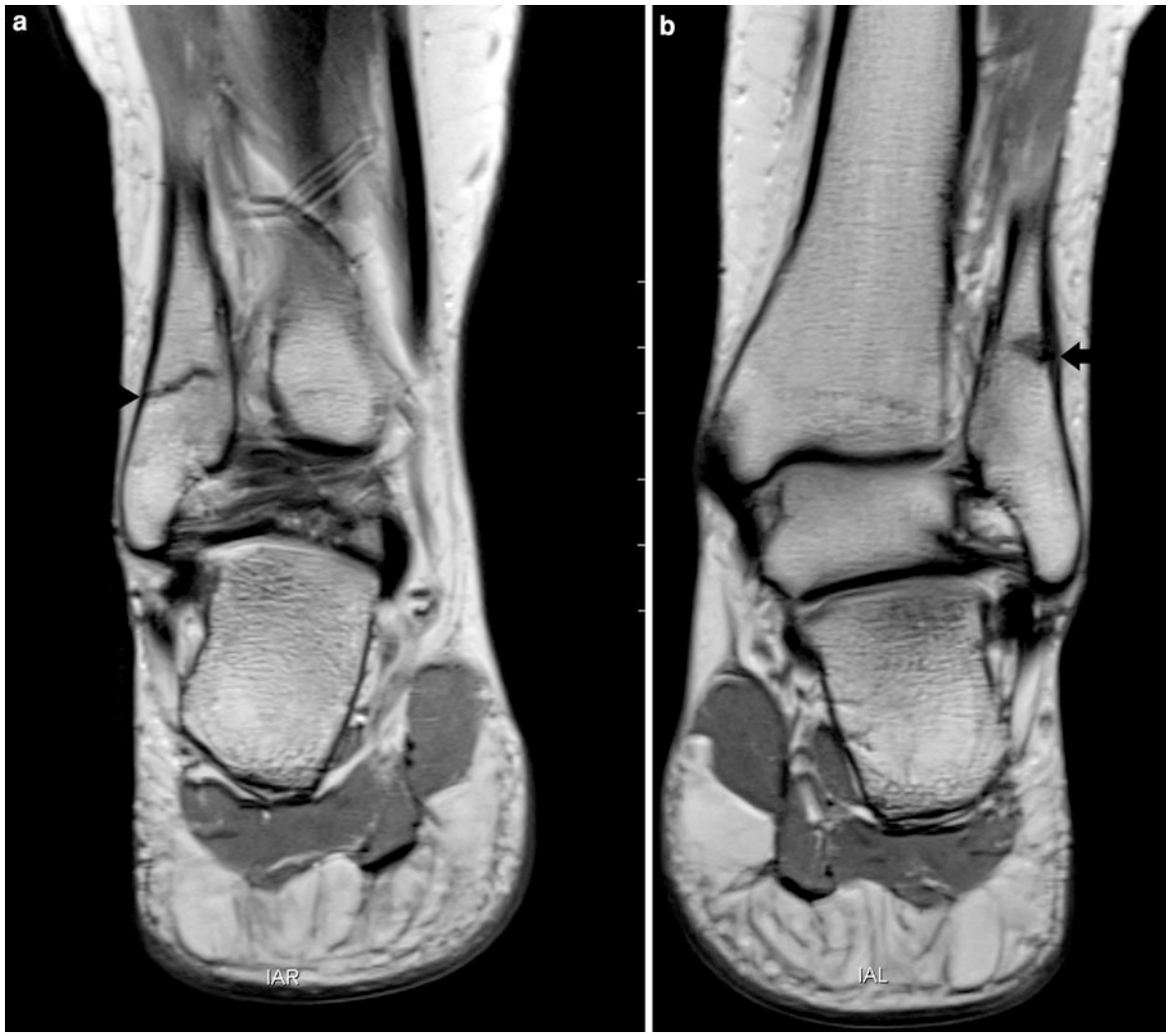

Fig. 14 Bilateral stress fractures of the distal fibula in a runner. **a** Coronal T1-WI of the right ankle. **b** Coronal T1-WI of the left ankle. Hypo-intense fractures lines are seen in the distal fibula bilaterally (*arrows*)

a long bone and are common in the posterior portion of the tibia in runners (Fig. 16).

Stress injuries in cancellous bone are notoriously difficult to detect. Subtle blurring of trabecular margins and faint sclerotic radiopaque areas may be seen secondary to peritrabecular callus, but a 50% change in bone capacity is required for these changes to be radiographically detectable. With progression, a readily apparent sclerotic band will be seen. Common sites for cancellous lesions include the calcaneal bone (Fig. 17), proximal tibia, distal tibia and fibula, pelvis and femoral neck (Anderson and Greenspan 1996; Spitz and Newberg 2002). Sometimes stress fractures may mimic tumor and tumor-like conditions.

3.2.1.2 Bone Scintigraphy

Bone scintigraphy is an effective modality in the evaluation of clinically suspected osseous stress injuries. Before the advent of MRI it had been the gold standard for evaluating stress fractures (Zwas et al. 1987). Bone scintigraphy demonstrates abnormal findings early in the continuum of the stress response in bone, by detecting the increased bone metabolism and osteoblastic activity associated with osseous remodeling. Scintigraphy is typically abnormal 1–2 weeks or more before the radiographic changes appear. Bone scintigraphy should optimally be performed using a three-phase technique. The most widely used radiopharmaceuticals for skeletal imaging are technetium-

Table 2 Possible sites of stress injuries (used with permission from Demeyere and Vanhoenacker 2007)

Upper extremity
phalangeal tufts
carpal bones: hook of hamate
ulna: coronoid, olecranon process, diaphysis
humerus: distal diaphysis
scapula: coracoid, inferior edge of glenoid fossa
Lower extremity
sesamoids
metatarsals
navicular
talus
calcaneus
tibia: mid and distal diaphysis, proximal shaft, medial malleolus
fibula: distal and proximal diaphysis
patella
femur: diaphysis, neck
pelvis: obturator ring, pubic rami, sacrum, ileum, ischium
Spine
lumbar vertebra: pars interarticularis
lower cervical, upper thoracic spinous process
Thorax
ribs
clavicle
sternum

99 m phosphate analogs which are taken up at sites of bone turnover. The degree of uptake depends primarily on the rate of bone turnover and local blood flow. The abnormal uptake may be seen within 6–72 hours of injury (Anderson and Greenspan 1996).

The three-phase technique can help to differentiate between soft tissue injury and osseous injury (Spitz and Newberg 2002). In the first phase, the blood flow phase, imaging is performed by acquiring dynamic 2–5 s images over the area of clinical concern for 60 s after the intravenous bolus injection. In the second phase, the blood pool or soft tissue phase, imaging is acquired after 5 min. The final phase of imaging is the delayed skeletal phase. These images should be acquired approximately 2–4 h after injection to maximize clearance of the radiopharmaceutical from the overlying soft tissues.

Zwas et al. (1987) described a scintigraphic classification of stress fractures ranging from grade 1 (mild) to grade 4 (severe) according to size, extent, and tracer concentration in the lesions (see Table 3; Fig. 18).

Despite its high sensitivity, the specificity of scintigraphy is slightly lower than that of radiography because other conditions such as tumors, infection, bone infarction, and shin splints or periostitis can produce similar findings. This can be improved by using the three-phase technique. The localization and distribution of the tracer accumulation and the timing can help in the differentiation (Nielsen et al. 1991; Zwas et al. 1987). For example, stress fractures are hot within all phases and have a more focal or fusiform morphology, whereas tracer uptake in shin splints is limited to the delayed phase and has a linear aspect.

On the other hand, bone scintigraphy is more sensitive than magnetic resonance especially in evaluating suspected lesions in the spine or pelvis, identifying multiple stress fractures. Additionally, scintigraphy may be helpful in depicting (multiple) stress fractures in patients with suspicion of anorexia nervosa (AN). These patients are at risk to develop stress fractures and these fractures can be the first presentation of AN. Due to the serous bone marrow changes occurring in AN, stress fractures are less conspicuous on MRI. In this regard, whole-body scintigraphy may be a useful screening examination for detecting fractures (Tins and Cassar-Pullicino 2006).

However, scintigraphy may be too sensitive; as many as 50% of scintigraphically positive findings can occur at asymptomatic sites. Areas of increased uptake may represent subclinical sites of bone remodeling or stress reactions.

Although bone scanning is good for detection of stress fractures, it is not useful for follow-up of healing because the intensity of activity decreases over 3–18 months as the bone remodels and often lags behind clinical resolution of symptoms (Boden and Osbahr 2000). Since these entities are usually treated differently, CT or MRI can be helpful for better delineation.

3.2.1.3 CT

CT is limited in its ability to detect early osseous stress injuries, and is less sensitive than bone scintigraphy and MRI. It does, however, play a role in more advanced injuries and injuries in specific

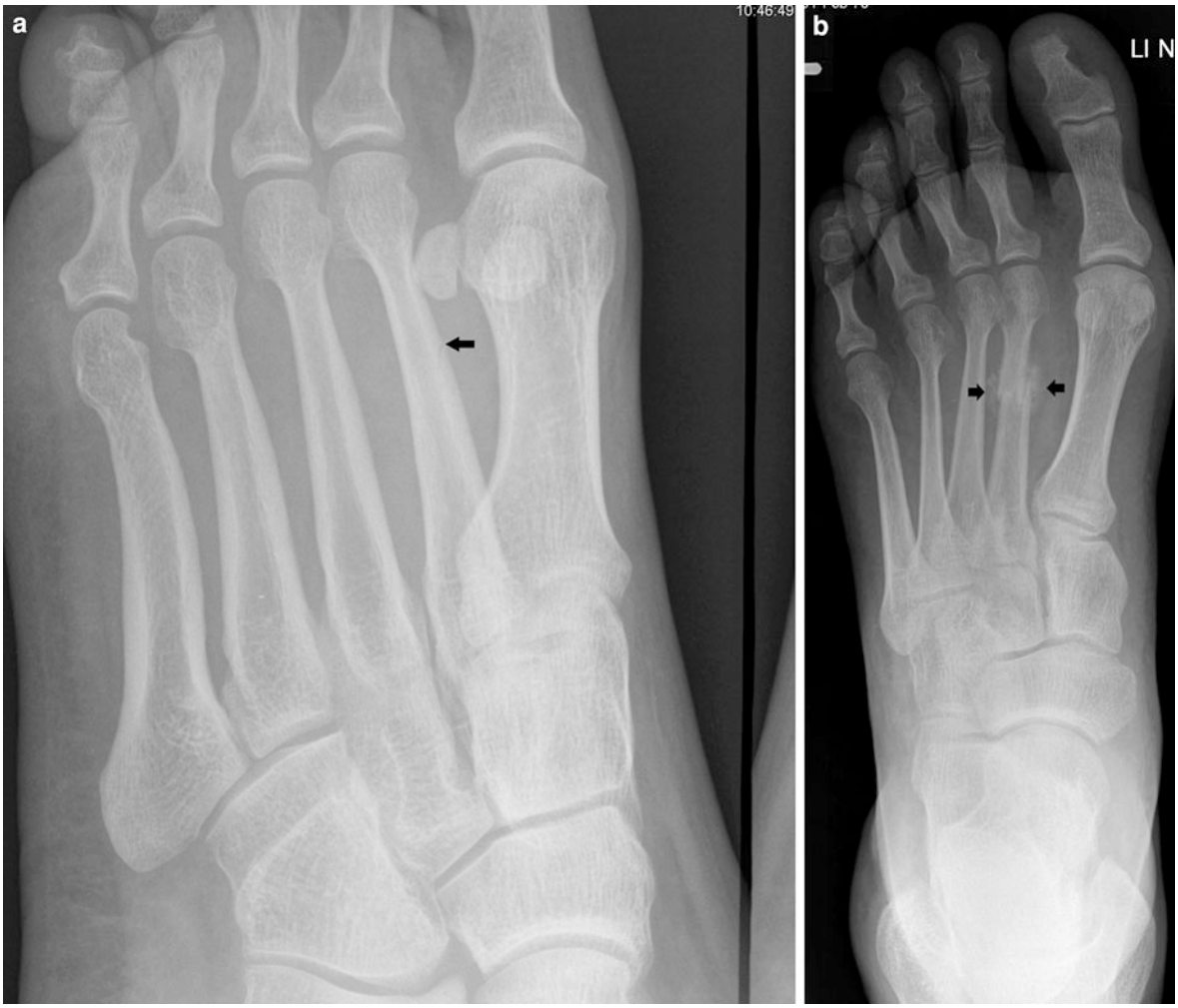

Fig. 15 Temporal radiographic changes in a metatarsal stress fracture in a 27-year-old athlete. **a** Initial plain films 1 week after the onset of pain at the left forefoot show faint intracortical lucency at the medial aspect of the diaphysis of the second metatarsal (*arrow*). **b** Follow-up radiograph 3 weeks later shows a slightly displaced fracture with surrounding periosteal callus (*arrows*)

anatomic locations where radiography fails to detect early changes due to superposition of adjacent structures. CT is particularly well suited for stress fractures of the tarsal bones (Fig. 19), longitudinal stress fracture of the tibia, pars interarticularis stress fractures (spondylolysis; Fig. 20) and stress fractures in the sacrum (Fig. 21). Whether the fracture is actually seen at CT may depend on orientation and stage in evolution of the injury. A fracture that courses longitudinally may be particularly well demonstrated with CT in comparison to one coursing transversely to the long axis of the bone. This drawback of axial CT may be overcome by multidetector CT with appropriate reformatting.

Gaeta et al. (2005) demonstrated that CT had the best performance in the identification of cortical abnormalities. Early CT changes consist of osteopenia, resorption cavities and striations within the cortical bone. They believe that these changes may precede formation of a cortical fracture. CT findings in stress fracture are sometimes nonspecific, but findings of endosteal and periosteal reaction surrounding a thin cortical translucency are diagnostic of stress fracture. In longitudinally stress fractures CT has a particular

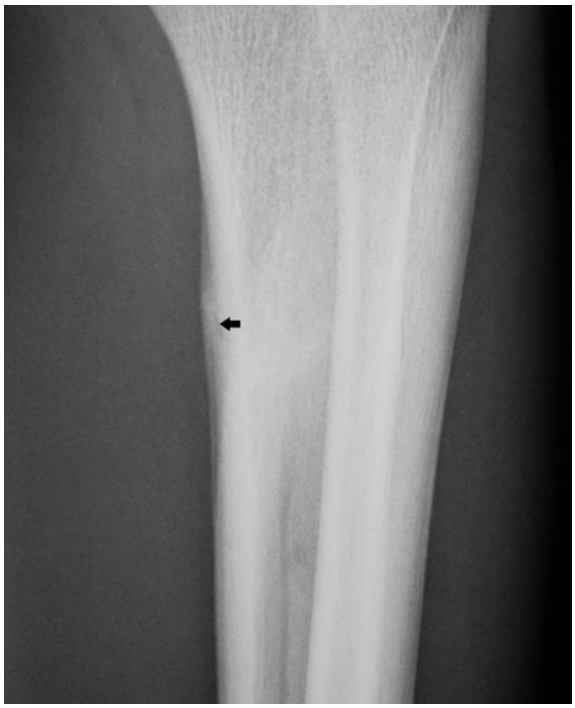

Fig. 16 Typical stress fracture at the posterior aspect of the tibia in a 14-year-old soccer player. Lateral plain film of the right tibia shows the cortical fracture line (*arrow*) as well as the surrounding periosteal and endosteal new bone formation

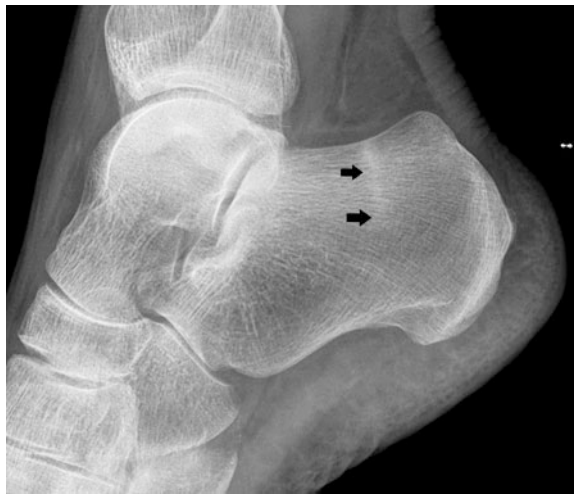

Fig. 17 Stress fracture of the calcaneal bone. Lateral plain film of the right calcaneal bone reveals a sclerotic band at the posterior calcaneus perpendicular to the stress trabeculae (*arrows*)

interest in demonstrating a fracture line that extends along the axis of the bone (Allen 1988).

Additionally, CT may be problem solving when findings are equivocal on radiographs, MRI or scintigraphy. The value of CT in this regard lies in the detection of a discrete lucent or sclerotic fracture line or periosteal reaction. CT is also extremely helpful in differentiating between a stress fracture and osteoid osteoma because both entities may be hot on bone scan, show BME at MRI and demonstrate sclerosis on radiographs. The presence of a radiolucent nidus, however, is diagnostic for osteoid osteoma. CT has also proven its value in the diagnosis of pediatric stress fractures. Initial radiographs may demonstrate marked periosteal bone formation, which may mimic tumor. Demonstration of endosteal bone formation on CT often leads to the correct diagnosis (Anderson and Greenspan 1996).

3.2.1.4 Ultrasound

Ultrasound is not recommended as imaging technique. However, ultrasound may show early changes after the onset of symptoms such as a thickened hypoechogenic periosteum (periosteal hematoma), hyperechogenic cortical irregularities in keeping with new bone formation and increased vascularity on power Doppler in the periosteal reaction (Figs. 22, 23) or cortical discontinuity, compatible with fracture. According to Boam et al. (1996), a sensitivity of 43% and a specificity of 49% were reported.

3.2.1.5 MRI

MRI is a valuable tool in identifying stress fractures in case of high index of suspicion. MRI has a comparable sensitivity and higher specificity than scintigraphy in distinguishing bone involvement from soft tissue injuries. Moreover, MRI is helpful in grading the stage of certain stress fractures (Table 3) and, therefore, predicting the time to recovery (see clinical significance). In addition, MRI avoids radiation exposure, is non-invasive and requires less time than three-phase bone scintigraphy (Boden and Osbahr 2000). MRI should also be performed in multiple orthogonal planes (Anderson and Greenspan 1996). MRI findings will differ along with the stage of the lesion and the sequences used. The MRI grading system developed by Fredericson et al. (1995) corresponds very well with the scintigraphic grading system of Zwas et al. (1987).

As discussed earlier, both resorption and replacement of bone constitute the most early histological

Table 3 Radiologic grading system for stress injuries: the correlation between histology, radiography, bone scintigraphy and MRI (used with permission from Demeyere and Vanhoenacker 2007)

	Stress reaction	Grade 1	Grade 2	Grade 3	Grade 4
Histology	–	Periosteal bone, cortical tunneling, gray cortex sign	Cortical resorption more than periosteal reaction	Extensive cortical tunneling and periosteal reaction	Trabecular microfractures, granulation tissue and necrotic areas
Radiography: cortical bone	–	–	Cortical striations, gray cortex sign	Periosteal and endosteal new bone formation	True fracture line
Radiography: cancellous bone	–	–	Blurring of trabecular margins, faint sclerotic densities	Sclerotic band	True fracture line
Scintigraphy	Amorphous lesion in the bone marrow	Small, ill-defined lesion with mildly increased cortical activity	Larger well-defined, elongated lesion with moderately increased cortical activity	Wide fusiform lesion with highly increased activity in the corticomedullary region	Wide extensive lesion with intensely increased activity in the transcorticomedullary region
MRI	Ill-defined zone of bone marrow edema (only on T2-WI)	Mild periosteal edema without BME (only on T2-WI)	Moderate to severe periosteal edema and BME (only on T2-WI)	Moderate to severe periosteal edema and BME (on both T1- and T2-WI)	Moderate to severe periosteal edema and BME, 'low signal' fracture line (on both T1- and T2-WI)

Table 4 Relationship between MR grading of stress fractures and prediction of time to recovery

MR grading	Time to recovery
Grade I	2–3 weeks
Grade II	4–6 weeks
Grade III	6–9 weeks
Grade IV	12 weeks (including 6 weeks casting)

changes of stress injury to bone. This stress reaction is accompanied by local hyperemia and edema, which is easily depicted by signal changes on MRI, especially on fluid-sensitive sequences. This is why MRI can be regarded as an excellent modality for the detection of early stress injury (Table 3) (Zanetti et al. 2002). Indeed, MRI can detect subtle cortical abnormalities on both T2- and fast STIR-WI. The resorption cavity appears as a round or oval area of high signal intensity, and striation or cortical tunneling appears as a slightly hyperintense line extending through only a part of the cortical thickness. Usually, multiple parallel striations can be seen within the cortex. Osteopenia appears as an area of intermediate signal intensity. Irregularity of subperiosteal bone can be seen as well. The appearance of resorption cavities and striations within the cortex may correlate with osteoclastic proliferation. High signal intensity depicted on T2-WI within striations and resorption cavities may be well explained by cell accumulation (osteoclasts, osteoblasts and fibroblastic cells), increased amount of blood vessels, and production of connective tissue and osteoid matrix, which all occur in osteoporotic bone (Gaeta et al. 2005). MRI also depicts periosteal and endosteal marrow edema, which are believed to be useful ancillary markers for stress injury (Fig. 24) (Schweitzer and White 1996; Fredericson et al. 1995). Especially in cancellous bone stress injuries result in non-specific bone marrow alterations similar to those described in patients with BME syndrome or bone bruise (Anderson and Greenspan 1996; Hoy et al. 2006).

The most common pattern of a frank fatigue type fracture is a fracture line that has a low signal on all pulse sequences, surrounded by a larger, ill-defined zone of edema. The fracture line is continuous with the cortex and extends into the intramedullary space oriented perpendicular to the cortex and the major weight-bearing trabeculae (Fig. 23, 25).

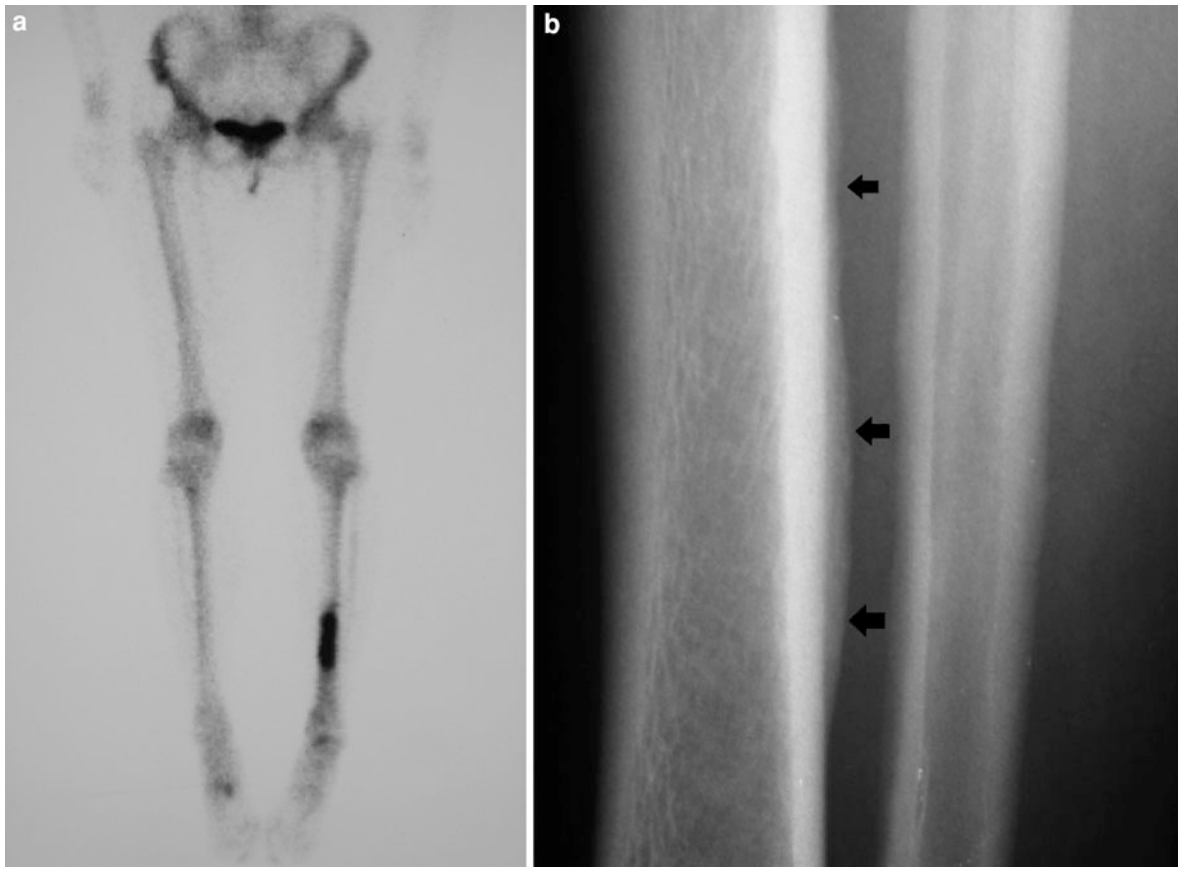

Fig. 18 Stress fracture of the left tibia. **a** Scintigraphy demonstrates a focal increased activity at the left distal tibia diaphysis. **b** Plain films show periosteal new bone formation at the lateral aspect of the tibia, in keeping with stress fracture (*arrows*)

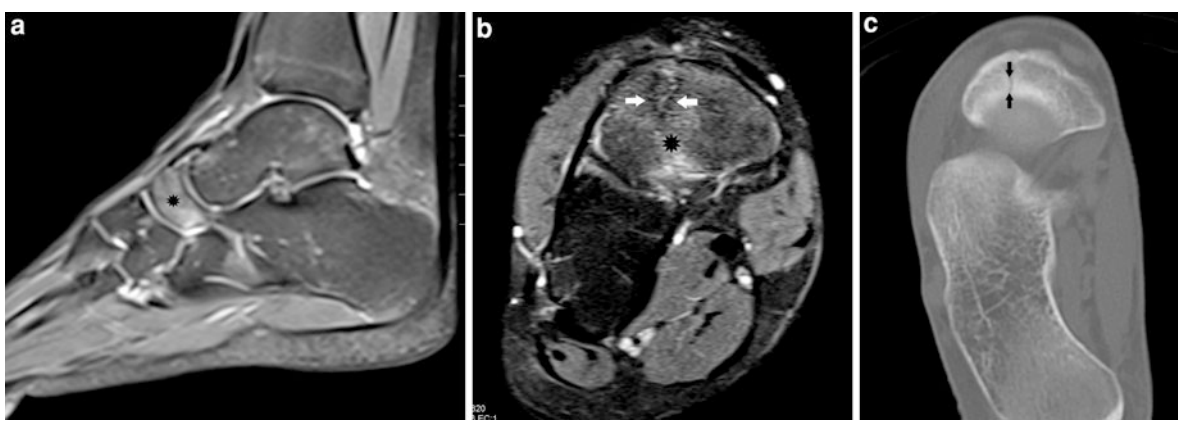

Fig. 19 Navicular stress fracture in a 17-year-old female jogger. **a** Sagittal fatsuppressed FSE T2-weighted image shows BME of the right navicular bone (*asterisk*). **b** Coronal fatsuppressed FSE T2-weighted image. A hypointense fracture line is visible (*arrows*) within the area of BME (*asterisk*). **c** Axial CT scan. The fracture line is better visible at the proximal end of the navicular bone (*arrows*)

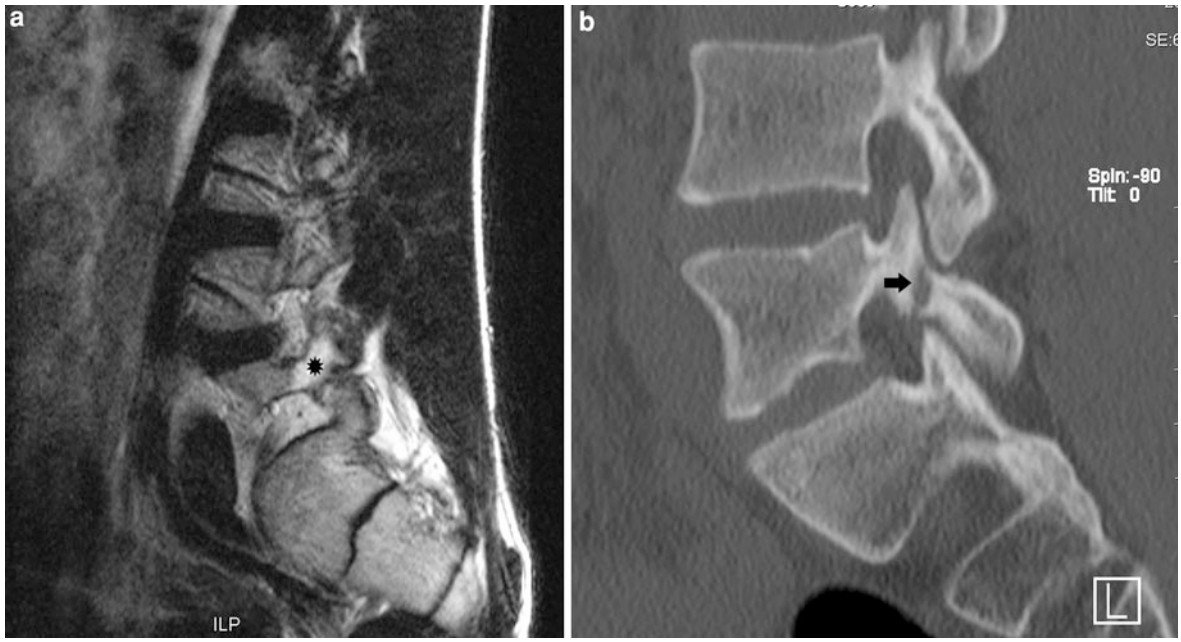

Fig. 20 Stress fracture of the left pars interarticularis L5 in a 15-year-old gymnast. **a** Sagittal FSE T2-WI shows BME at the left pars interarticularis L5 (*asterisk*). **b** Sagittal reformatted CT scan better shows the fracture line at the left pars interarticularis L5 (*arrow*). The latter is barely visible on MRI

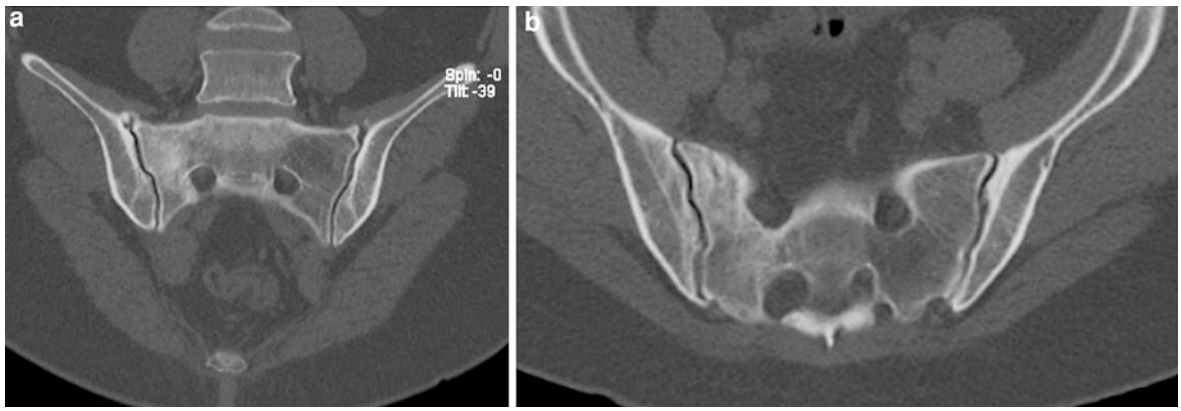

Fig. 21 Stress fracture of the sacrum. Coronal reformatted **a** CT scan **b** Axial CT scan. Notice the reactive sclerosis around the fracture line adjacent to the right sacroiliac joint

3.2.2 Chronic Avulsive Injuries

Typical examples of chronic avulsive injuries include shin splints (traction periostitis of the calf muscles along the posteromedial tibia; Fig. 26), thigh splints (distal adductor insertion avulsion syndrome, Fig. 27) and adductor-gracilis syndrome (Fig. 28).

The term shin splints has been used to describe the clinical entity of activity-related lower leg pain, typically associated with diffuse tenderness along the posteromedial tibia. A similar entity in the upper leg has been described as thigh splints or adductor insertion avulsion syndrome (Anderson et al. 2001; Van de Perre et al. 2003). Recent MRI studies have suggested that shin splints are a part of the continuum of fatigue damage in bone (Anderson et al. 1997; Fredericson et al. 1995). On T2-WI, a linear abnormal high signal is seen along the posteromedial surface of the tibia representing subperiosteal edema (Fig. 26). This implies that one cause of shin splints may be traction periostitis along the insertion of the soleus

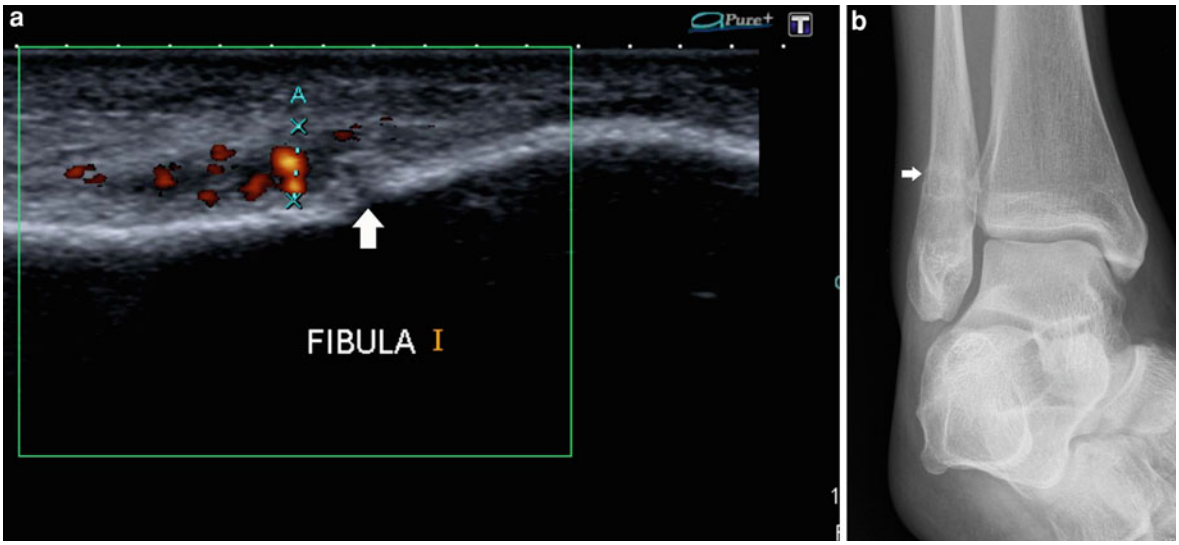

Fig. 22 Stress fracture of the right distal fibula. **a** Longitudinal ultrasound demonstrates a discontinuity of the cortex of the distal fibula (*arrow*), a thickened hypo-echogenic periosteum and increased power Doppler signal. **b** Plain films show periosteal new bone formation at the lateral aspect of the fibula in keeping with stress fracture (*arrow*). Notice also endosteal new bone formation

fascia and tibialis posterior. It can also appear as a linear high signal along the subcortical aspect of the bone marrow. This is considered to be secondary to edema or hemorrhage related to microdamage and the associated reparative response (Aoki et al. 2004). In thigh splints the periosteal reaction is located at the proximal third of the medial femoral shaft near the insertions of the adductor brevis and longus muscles (Fig. 27) (Anderson et al. 2001).

3.2.3 Altered Biomechanics and BME

Altered biomechanics due to certain sports activities (such as jogging or golf) may induce physiologic bone response to repeated stress. MRI may reveal BME in these cases, which may not necessarily correspond with severe trauma (Grampp et al. 1998; Yochum and Barry 1997).

The potential role of limb malalignment and BME was described by Felson et al. (2003). Medial bone marrow lesions can be seen in athletes with varus limb, whereas lateral lesions are associated with valgus limbs.

The importance of alignment is experimentally demonstrated by Libicher et al. (2005) in an in vivo MRI demonstration of the Pond-Nuki animal model for the evaluation of osteoarthritis. In this experimental study, 24 beagle dogs underwent transection of the anterior cruciate ligament of the left leg (modified Pond–Nuki model). The first sign on MRI was the appearance of subchondral BME at the posteromedial aspect of the tibia followed by progressive cartilage degeneration, meniscus degeneration and osteophytosis.

3.2.4 Symptomatic Accessory Bones and BME

Accessory ossicles or variations in ossification such as os trigonum (Peace et al. 2004), accessory navicular bone (Fig. 29), bipartite patella or os acromiale (Fig. 30) may become symptomatic due to chronic friction of the accessory ossicle and the adjacent host bone (Bernaerts et al. 2004; Perdikakis et al. 2011). On MRI, BME is seen on both sides of the synchondrosis between the accessory bone and the host bone.

3.2.5 Lesions of Unknown Pathogenesis

BME syndromes without any history of trauma are increasingly recognized on MRI (Mandalia et al. 2005). Distinction between bone bruising and marrow edema syndromes is primarily based on the clinical history of the patient.

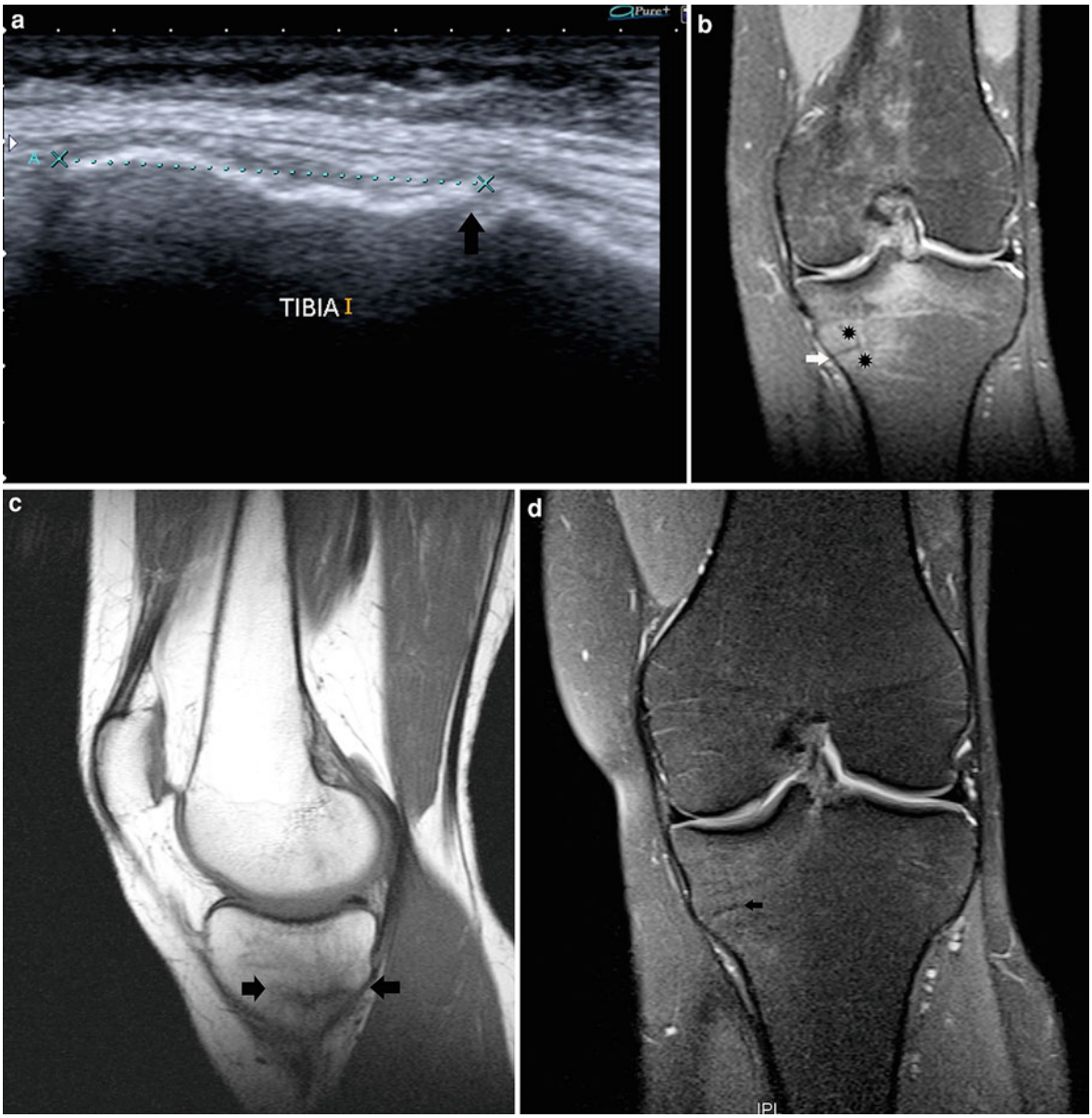

Fig. 23 Stress fracture grade four of the tibia in a 36-year-old female jogger. **a** Longitudinal ultrasound demonstrates a focal discontinuity of the cortex of the medial proximal tibia (*arrows*) and a thickened hypo-echogenic periosteum. **b** Coronal fat suppressed FSE T2-WI. A hypointense fracture line is visible (*arrow*) within surrounding hyperintense BME (*asterisks*). **c** Sagittal SE T1-WI. The fracture line (*arrows*) and surrounding BME are also visible on the T1-WI. **d** Coronal fat suppressed FSE T2-WI 6 month later. Almost complete resolution of the BME. The fracture line is only barely visible (*arrow*). The patient was free of symptoms

3.2.6 Bone Marrow Edema Syndrome

Transient bone marrow edema syndrome (BMES) is an unusual but distinct self-limiting syndrome located at the weight bearing joints of the lower limbs (Toms et al. 2005). It usually affects middle-aged men and women in the last trimester of pregnancy, but association with sports activities has been reported (Miltner et al. 2003).

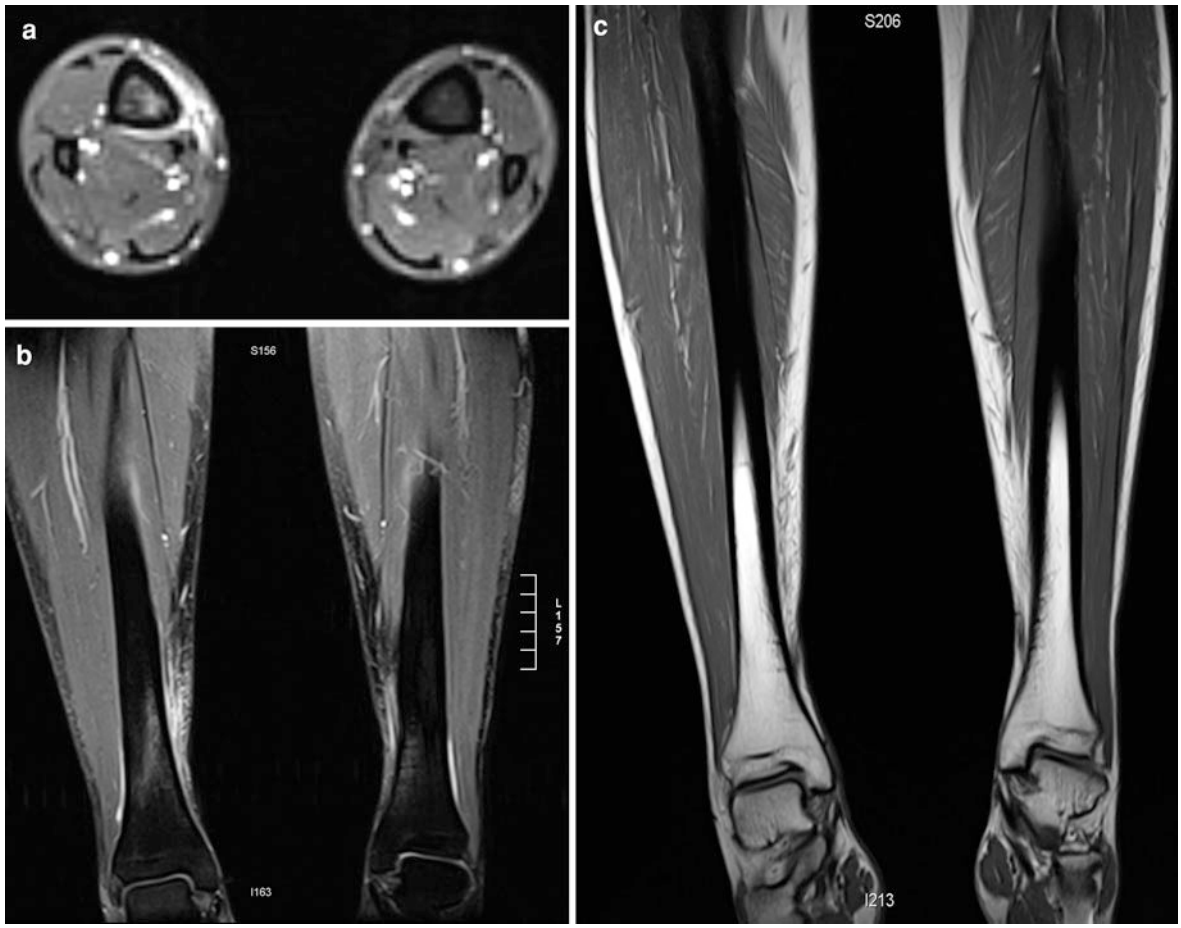

Fig. 24 Stress fracture grade 2 of the right tibia. **a** Axial fat suppressed FSE T2-WI. **b** Coronal fat suppressed FSE T2-WI demonstrates periosteal and endosteal edema. **c** Coronal SE T1-WI is unremarkable

BMES usually affects only one bone, predominantly the proximal femur. The tarsal bones and the knee joint are involved less frequently (Fig. 31) (Radke et al. 2001). Regional migratory Bone Marrow Edema Syndrome is a special form of BMES characterized by migration between the weight bearing joints. BMES will be discussed extensively in "Bone Marrow Edema Syndrome".

3.2.7 Bone Marrow Edema in Long-Distance Runners

Previous studies concerning BME about the joints in long-distance runners are highly controversial. BME has been described in recreational athletes 3 hours to 8 weeks after sports running in the knee (Krampla et al. 2001), anklel and foot (Lazzarini et al. 1997; Trappeniers et al. 2003). According to Lohman et al. (2001), the incidence of bone marrow changes in the ankle and foot is similar in marathon runners after the race, compared to age- and sex-matched asymptomatic physically active individuals without any preceding strain.

Within the knee, most of the bone marrow changes were not localized in the subchondral areas of the joint and are therefore atypical for stress-related edema. They probably represent spots of increased hematopoietic activity in asymptomatic athletes (Krampla et al. 2001). Only some cases of BME near the apex of the patella are believed to be stress-related due to forces during the run (Krampla et al. 2001).

In well-trained individuals with normal BMI however, (Schueller-Weidekamm et al. 2006) reported no incidences of new BME of the knee after

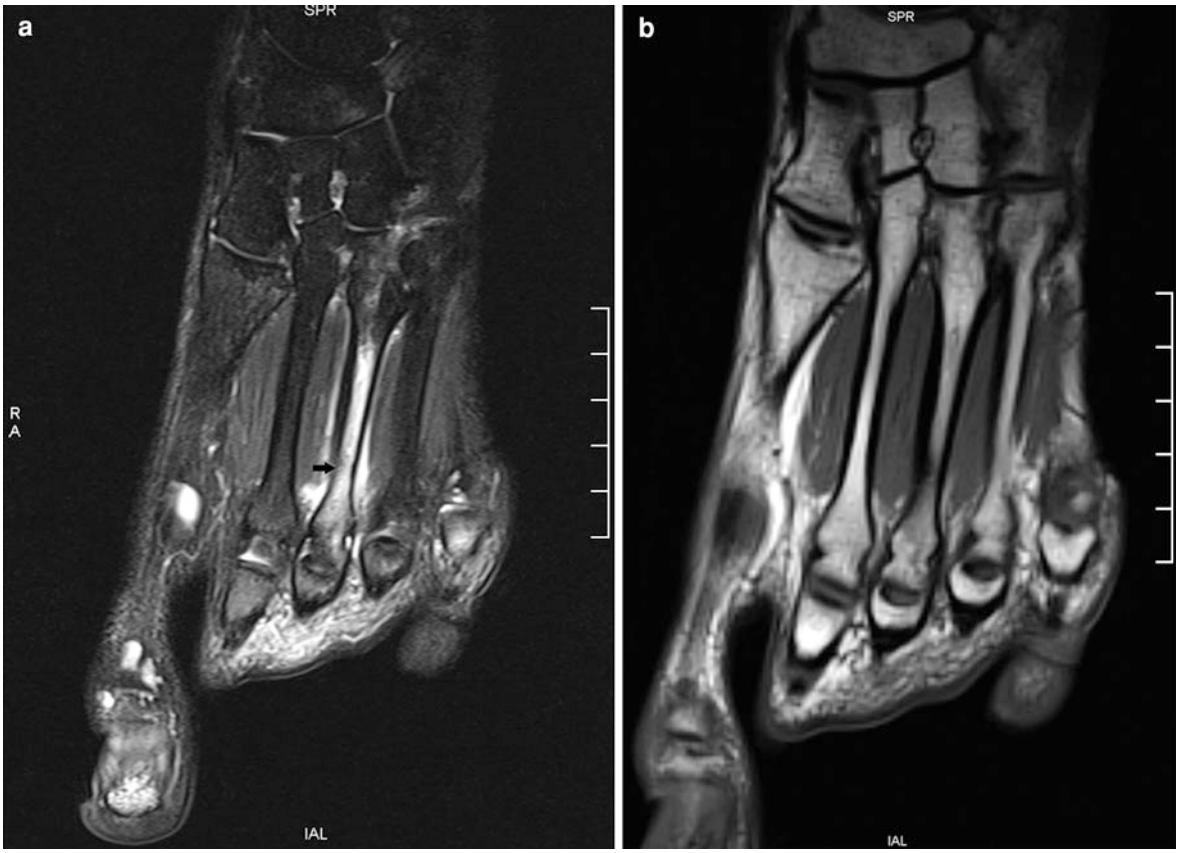

Fig. 25 Stress fracture grade 4 of the third metatarsal in a 20-year-old military recruit. **a** Axial (*long axis view*) fat suppressed FSE T2-WI. Extensive BME in the diaphysis of metatarsal 3 and adjacent soft tissue edema. The fracture line is seen a subtle transcortical hypointense line (*arrow*). **b** Axial SE T1-WI. The bone and soft tissue abnormalities are also visible on T1-WI

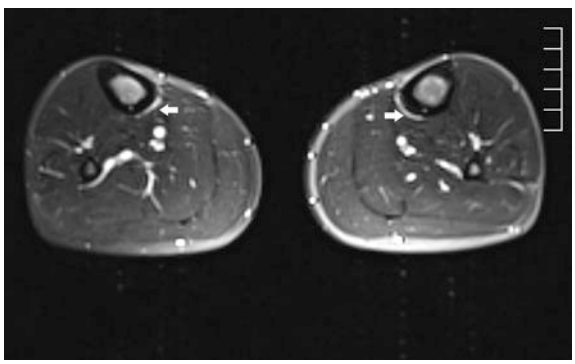

Fig. 26 Shin splints. Axial FSE T2-WI. Bilateral high signal intensity edema along the posteromedial aspect of the tibia (*arrows*)

marathon running, nor any increase in preexisting BME. STIR or T2-WI with spectral fat suppression is most sensitive to detect these edema patterns.

3.2.8 Subchondral Insufficiency Fracture

The concept of subchondral insufficiency fracture and its relationship with spontaneous osteonecrosis (SONK) and rapidly destructive osteoarthritis will be discussed briefly elsewhere in this book.

4 Histopathological Correlation

A variety of histologic studies of patients with BME have been described with different results. Some studies revealed necrosis of cellular elements in the subchondral bone, trabecular microfractures and hemorrhage and edema (Johnson et al. 1998; Ryu et al. 2000; Blankenbaker et al. 2008), whereas others demonstrated only edema with displacement of cellular elements, but absence of necrosis (Escalas and Curell 1994).

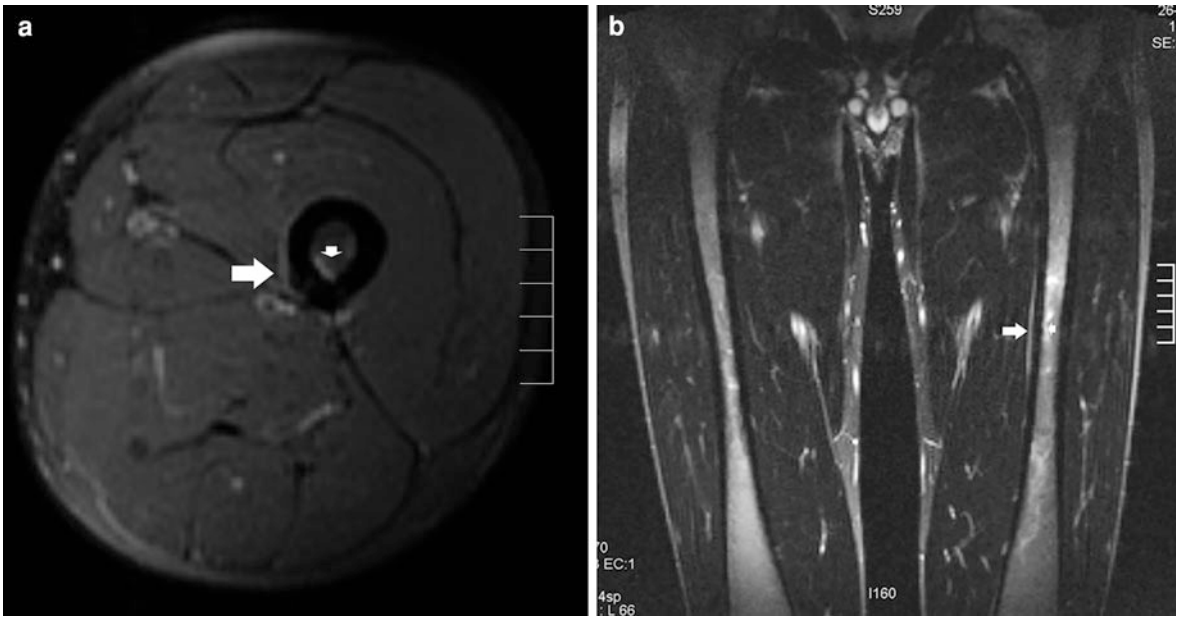

Fig. 27 Thigh splints in a 37-year-old marathon runner. **a** Axial FSE T2-WI. **b** Coronal T2-WI. Subtle high signal intensity periosteal reaction is located at the proximal third of the medial femoral shaft near the insertions of the adductor brevis (*large arrow*). Notice also some minor BME at the endosteal side of the left femoral diaphysis (*short arrow*). This finding suggests that thigh splints is part of the spectrum of stress reactions of bone

Review of the different histologic studies suggests that different degrees and severity of injuries may determine the differing histological patterns. Relatively less severe trauma causes marrow edema without obvious injury to the cellular elements, whereas with increasing severity of trauma, microfractures and hemorrhage are seen within the trabecular bone (Mandalia et al. 2005).

5 Clinical Significance

5.1 Acute BME

The clinical significance of BME has been an issue of discussion even since the first reports on bone bruise (Blum et al. 2009). It is very difficult to identify clinical signs and symptoms directly attributable to the underlying bone bruising because there are usually associated soft tissue changes (Mandalia et al. 2005). In a prospective study of 95 patients with inversion injuries of the ankle and no fracture on plain radiographs, Alanen et al. (1998) found an incidence of bone bruises of 27%. Most of the bruises were located in the talus, typically in the medial part. The authors found no statistical difference in the time to return to work, limitation in walking or physical activity and clinical outcome at three month in two groups with and without BME. These findings were in line with a previous study conducted by Zanetti et al. (1997).

Vincken et al. (2005) evaluated the clinical consequences of bone bruise on MRI around the knee in 664 consecutive patients with subacute knee complaints. They evaluated the relationship between bone bruise and (peri)articular derangement and also the impact of bone bruise at the time of MRI and 6 month thereafter. Bone bruises were diagnosed in 18.7% of patients. Indeed, prevalence of bone bruise was not significantly different between patients with (21%) and those without (16%) intraarticular pathology. Bone bruise was particularly associated with tears in the ACL, collateral ligament and lateral meniscus, whereas medial meniscal tears (although representing the most common knee lesion) were not associated with bone bruise. They concluded that bone bruise is no predictor for the presence of intraarticular pathology. On the other hand, Vincken et al. (2005) reported that patients presenting with bone bruise at the time of MRI had a significant

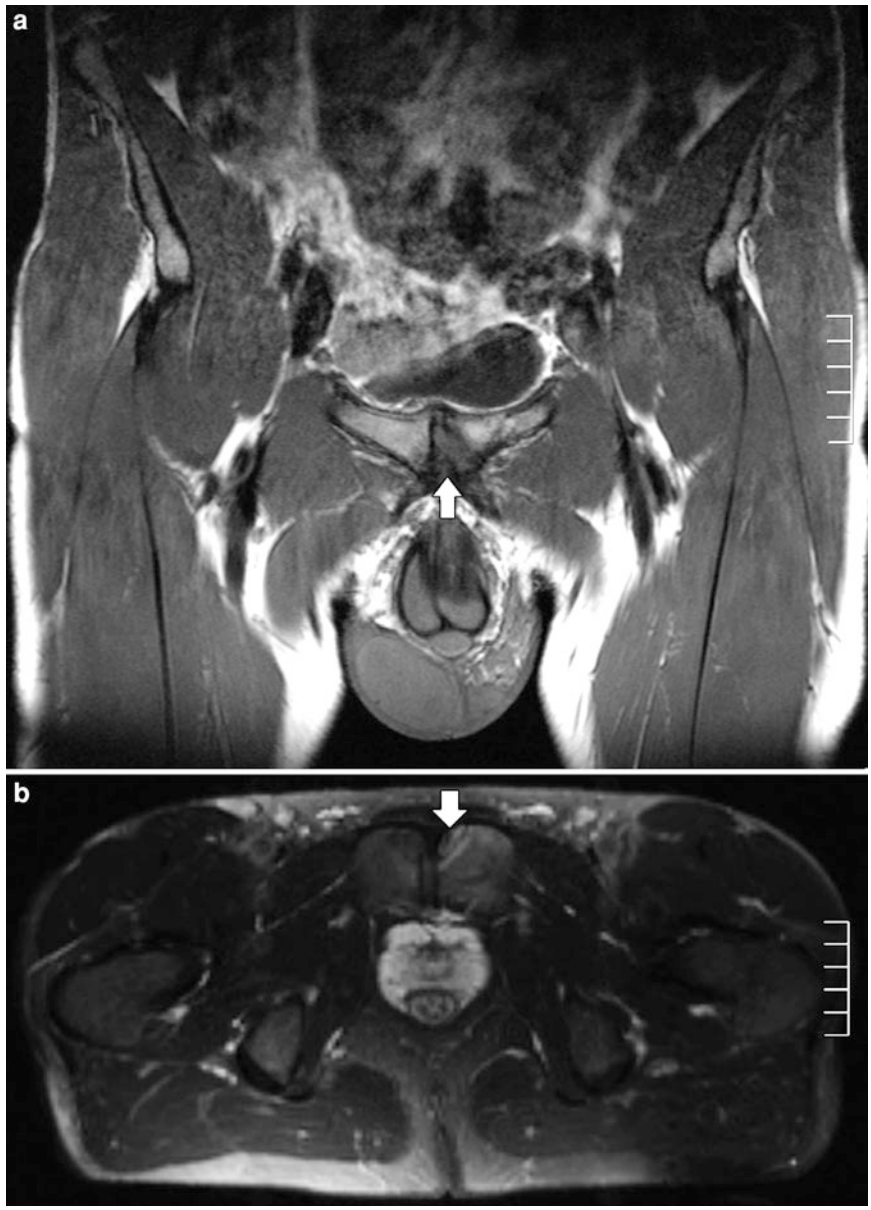

Fig. 28 Gracilis-adductor syndrome in a soccer player. **a** Coronal SE T1-WI. Irregular delineation of the inferomedial aspect of the left os pubis at the insertion of the gracilis and adductors tendons (*arrow*). **b** Axial fat suppressed FSE T2-WI. There is high signal intensity BME at the left pubic (*arrow*). The lesion represents a chronic avulsive traction injury at the proximal insertion of the gracilis and adductor tendons at the pubic bone

higher level of symptoms, functional deficit and decrease in activity. Particularly, the presence of bone bruise and MCL tear has the most impact on function and symptoms at the time of MRI. However, bone bruise did not have any effect on function, symptoms and activity at 6 month.

On the contrary, Boks et al. (2007) found no relationship between the amount of BME and pain. Future long-term prospective studies are required to clarify the question related to the clinical significance of BME. Bone marrow changes in long-distance runners and asymptomatic, physically active individuals are of no clinical significance and do not cause permanent damage (Krampla et al. 2001, 2008; Lohman et al. 2001).

5.2 Chronic Lesions

Chronic onset lesions (stress lesions) typically cause pain in the lower leg brought on by exercise but relieved by rest. Stress injuries involving the tibia

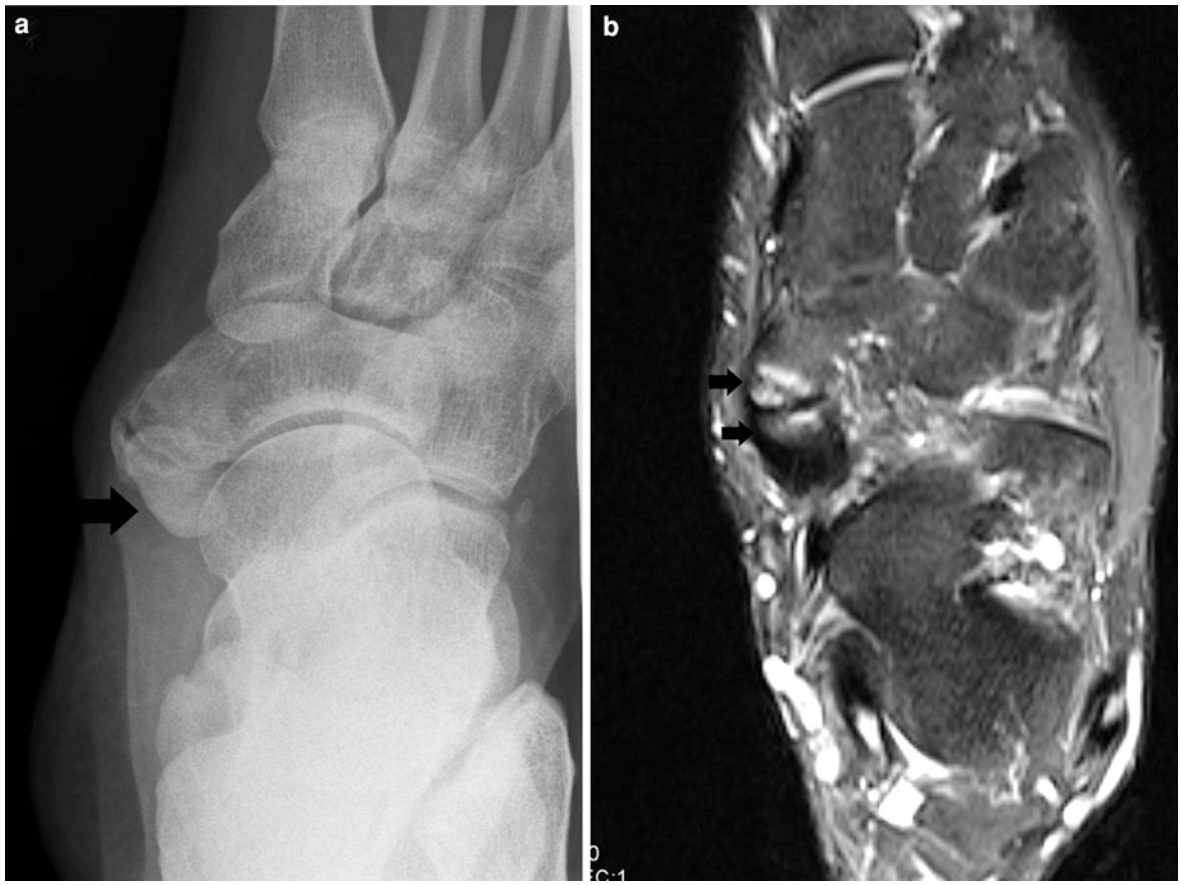

Fig. 29 Painful os naviculare syndrome. **a** Plain radiograph of the right foot shows an accessory navicular bone (type 2; large fragment with a synchondrosis between the navicular bone and the accessory fragment) (*arrow*). **b** Axial fat suppressed FSE T2-WI. There is high signal intensity BME in the accessory fragment as well as in the proximal aspect of the navicular bone (*arrows*)

account for up to 75% of exertional leg pain, and encompass several clinical syndromes such as medial tibial syndrome (shin splints), chronic compartment syndrome, soleus syndrome and stress fracture (Bhatt et al. 2000).

Grading of stress reactions along with the Fredericson MR-scoring system may influence patient management. Fredericson et al. (1995) concluded that MRI is more accurate than bone scan in correlating the degree of bone involvement with clinical symptoms, allowing for more accurate recommendations for rehabilitation and return to activity. As MRI may depict signal changes in bone marrow even before a fracture becomes apparent clinically, the use of MRI may be a powerful technique to allow early treatment and prevention of evolving higher grade stress fractures (Major 2006).

6 Natural Evolution

6.1 Follow-Up of Acute Traumatic Bone Marrow Edema

The reported time for the resolution of bone bruise is variable, ranging from as early as 3 weeks to 2 years (Mandalia et al. 2005; Roemer and Bohndorf 2002; Blum et al. 2009). This variability may be attributed to several factors, such as the severity of injury, extent of bone bruising and other associated internal knee derangement. Future large prospective studies are required to validate those factors affecting the radiological evolution of bone bruising (Mandalia et al. 2005).

Two patterns of bruise resolution have been described by Davies et al. (2004). The *centripetal* pattern is the

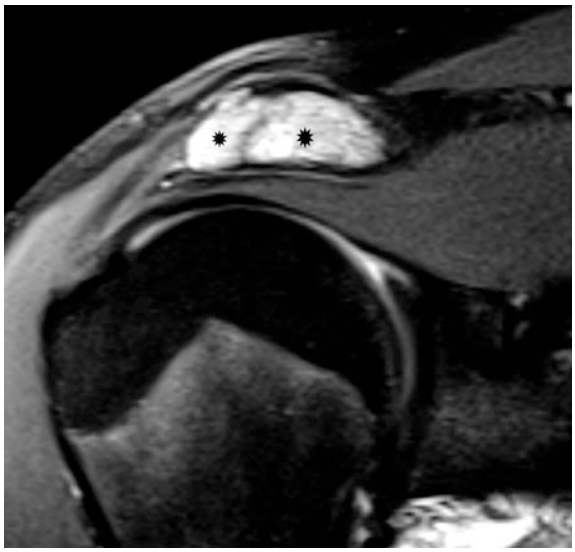

Fig. 30 Symptomatic os acromiale. Coronal fat suppressed FSE T2-WI of the right shoulder. There is high signal intensity BME in the non fused os acromiale and the adjacent acromion (*asterisks*)

most frequent (Fig. 32), while other lesions tend to resolve *toward the joint margin*. The latter generally resolves slower and probably requires longer rehabilitation because of higher risk of premature osteoarthritis. The natural history of bruises is not well known as well as whether they predispose to premature osteoarthritis. Fatty reconversion is rare (Blum et al. 2009).

Many studies have shown that bone bruising may have a deleterious effect on the overlying articular cartilage, although this concept is not generally accepted (Mandalia et al. 2005). The pathophysiological mechanisms by which the cartilage can undergo this degenerative process may be multifactorial. The initial blunt trauma might exceed a supraphysiological threshold and leads toward progressive chondral damage (Mankin 1982). Additionally, the osseous lesion might heal into a stiffer construction than the previous normal bone. The decreased compliance might then generate greater loads in the articular cartilage, leading to a progressive cartilage degeneration.

6.2 Follow-Up of Chronic Traumatic Lesions

MR grading of stress fractures (Fredericson et al. 1995) (Table 4) is helpful in predicting time to recovery. Patients with grade I stress lesions may return to athletic activity within 2–3 weeks, grade II lesions within 4–6 weeks and grade III lesions 6–9 weeks. Patients with Grade IV lesions should be treated with casting for 6 weeks, followed by another 6 weeks before return to athletic activities (Fig. 23). Apart from these general guidelines, the location of the stress injury is important. Stress injuries located at the femoral neck, the anterior tibia, medial malleolus, tarsal navicular bone, talus, fifth metatarsal, base of second metatarsal, patella and sesamoid of the hallux require a longer recovery time than those located at the posterior or medial aspect of the tibia, fibula and lateral malleolus (Karantanas 2007). Bone marrow changes in long-distance runners are transient and do not cause any permanent joint damage (Krampla et al. 2001, 2008).

6.3 Follow-Up of BMES

In BMES, the mean interval from the onset of symptoms until complete clinical resolution ranges from 4–24 month, with an average of 6 month. All patients with BMES recover completely without intervention. Therefore, the term transient BMES can be used. Recovery, however, can be speeded up with vasodilatators (Aigner et al. 2002).

7 Conclusion

MRI has proved to be the most powerful tool in assessing traumatic BME, as conventional imaging techniques are insensitive for detection of trabecular injuries. The pathogenesis of BME is variable and may be due to acute or chronic trauma or even causes without any history of obvious trauma. Distinction between traumatic and non-traumatic BME is primarily based on a clinical history of trauma, as imaging features are mostly indistinguishable. In acute trauma, the pattern of BME, however, may reveal the mechanism of underlying trauma and is often a secondary sign for detecting associated abnormalities. For assessment of chronic onset lesions, MRI has equal sensitivity to scintigraphy but a better specificity compared to any other imaging technique. Moreover, MR grading allows accurate prediction of prognosis and return to activity. The clinical significance of bone bruise is still a matter of

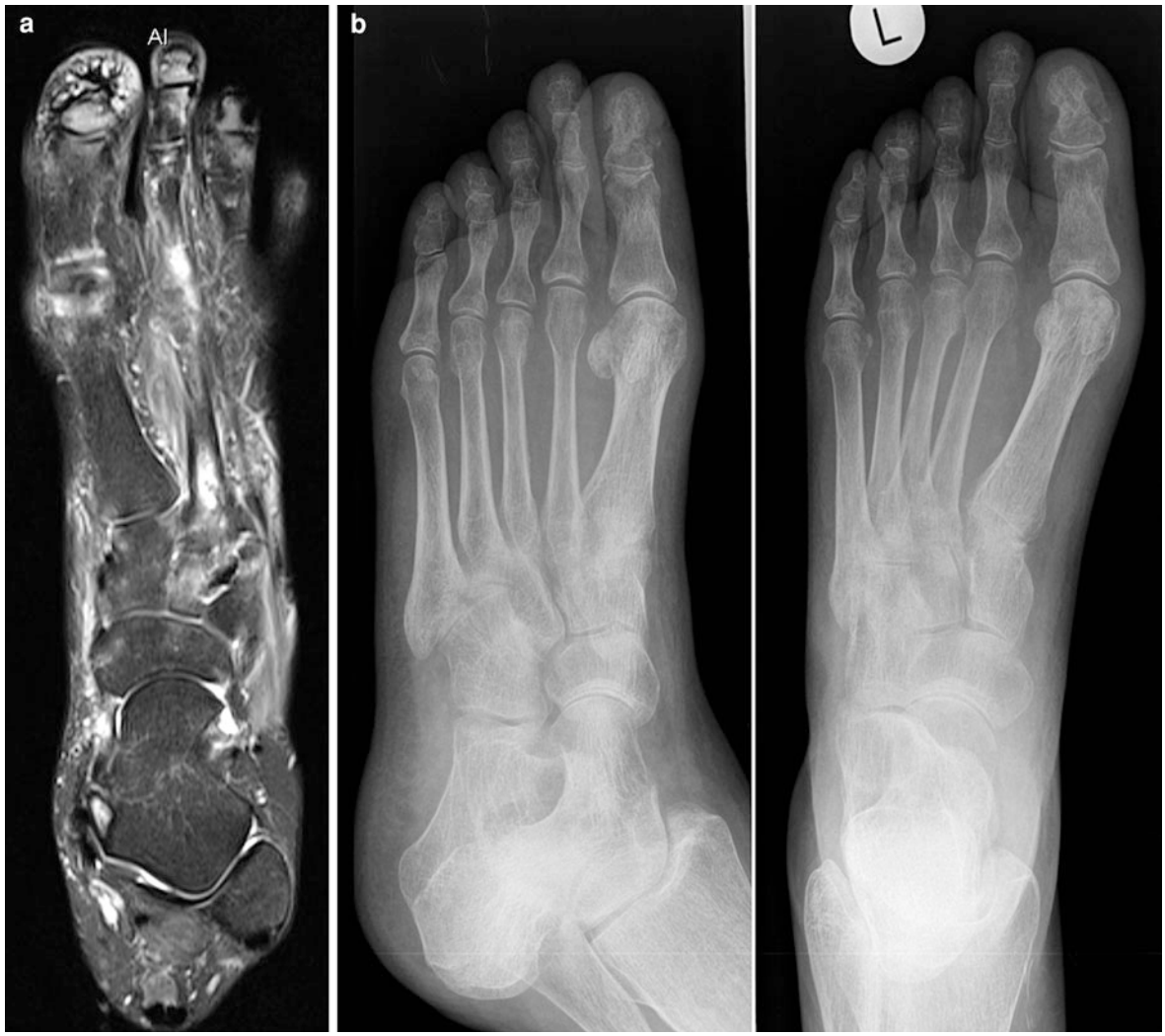

Fig. 31 Bone Marrow Edema Syndrome of the foot 2 months after onset of symptoms at the foot. **a** Axial fat suppressed FSE T2-WI showing multifocal BME at the tarsal bones and the base of metatarsal 2. **b** Plain radiograph demonstrates the presence of patchy osteopenia of the foot

debate, and long-term follow-up studies are required for further evaluation of this item.

Things to Remember

1 MRI is the imaging modality of choice to detect bone marrow lesions in sports injuries. Fat suppressed T2-WI or (S)TIR sequences are the most sensitive-ones.
2 Mostly BME in itself is benign and self limiting. Longer follow-up studies are needed to determine the clinical importance of osteochondral sequelae and to evaluate the possible evolution towards premature degeneration. Isolated bruise can be the cause of pain.
3 A systematic analysis of the BME pattern often reveals a specific underlying trauma mechanism. This can help to detect the associated soft tissue lesions, which are often less conspicuous.
4 Residual indications for conventional radiography (and/or CT) are (subtle) avulsion fractures and some stress fractures.
5 MR grading of stress fractures is helpful in predicting time to recovery.

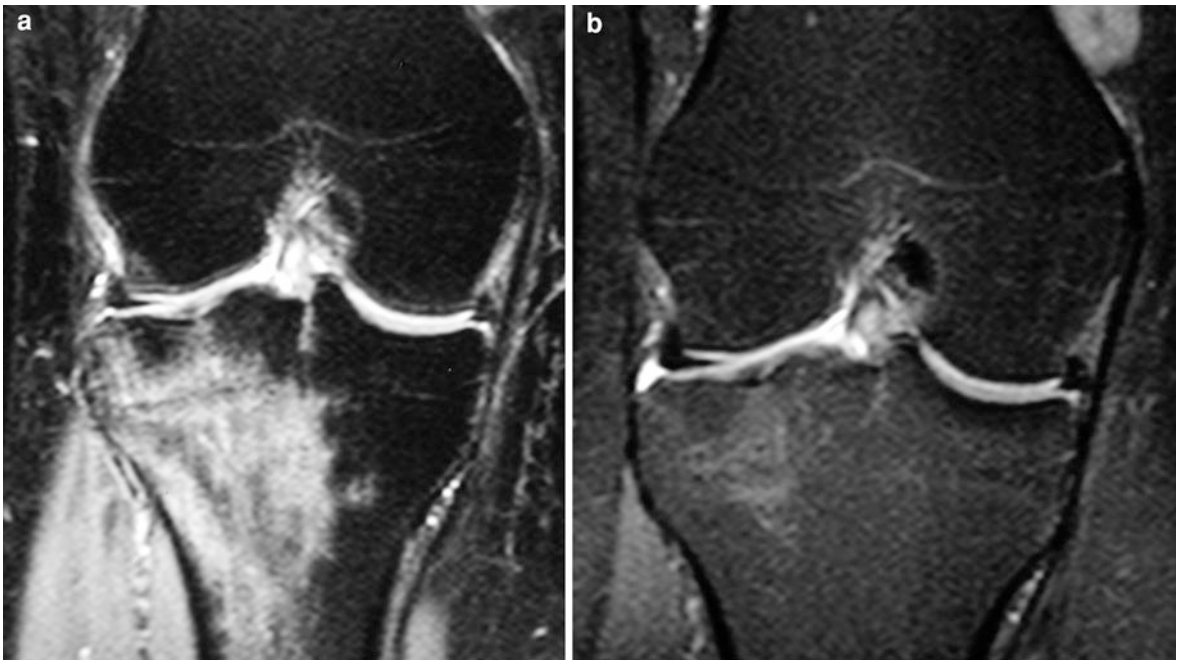

Fig. 32 Resolution pattern of BME. **a** Coronal fat suppressed FSE T2-WI of the right knee at the moment of a direct trauma at the knee (**b**) and after 3 months follow-up. **a** Extensive impaction BME at the proximal tibia. **b** There is centripetal resolution of BME, with some residual BME at the center of the original lesion (used with permission from Vanhoenacker et al. 2007)

References

Aigner N, Petje G, Schneider W et al (2002) Juvenile bone marrow oedema of the acetabulum treated by iloprost. J Bone Joint Surg Br 84:1050–1052

Alanen V, Taimela S, Kinnunen J et al (1998) Incidence and clinical significance of bone bruises after supination injury of the ankle: a double-blind prospective study. J Bone Joint Surg Br 80:513–515

Allen GJ (1988) Longitudinal stress fractures of the tibia: diagnosis with CT. Radiology 167:799–801

Anderson MW, Greenspan A (1996) Stress fractures. Radiology 199:1–12

Anderson MW, Kaplan PA, Dussault RG (2001) Adductor insertion avulsion syndrome (thigh splints). Am J Roentgenol 177:673–675

Aoki Y, Yasuda K, Tohyama H et al (2004) Magnetic resonance imaging in stress fractures and shin splints. Clin Orthop Relat Res 421:260–267

Bennell KL, Brukner PD (1997) Epidemiology and site specificity of stress fractures. Clin Sports Med 16:179–196

Bernaerts A, Vanhoenacker FM, Van de Perre S, De Schepper AM, Parizel PM (2004) Accessory navicular bone: not such a normal variant. JBR-BTR. 87(5):250–252

Blankenbaker DG, De Smet AA, Vanderby R, McCabe RP, Koplin SA (2008) MRI of acute bone bruises: timing of the appearance of findings in a swine model. Am J Roentgenol 190(1):W1–7

Bhatt R, Lauder I, Finlay DB et al (2000) Correlation of bone scintigraphy and histological findings in medial tibial syndrome. Br J Sports Med 34:49–53

Blum A, Roch D, Loeuille D, Louis M, Batch T, Lecocq S, Witte Y (2009) L'oedeme médullaire: définition, valeur diagnostique et pronostique. J Radiol 90:1789–1811

Boam WD, Miser WF, Yuill SC et al (1996) Comparison of ultrasound examination with bone scintiscan in the diagnosis of stress fractures. J Am Board Fam Pract 9:414–417

Boden BP, Osbahr DC (2000) High-risk stress fractures: evaluation and treatment. J Am Acad Orthop Surg 8: 344–353

Boks SS, Vroegindeweij D, Koes BW, Bernsen RM, Hunink MG, Bierma-Zeinstra SM (2007) Clinical consequences of posttraumatic bone bruise in the knee. Am J Sports Med 35:990–995

Chan KK, Resnick D, Goodwin D et al (1999) Posteromedial tibial plateau injury including avulsion fracture of the semimembranosus tendon insertion site: ancillary sign of anterior cruciate liagment tear at MR imaging. Radiology 211:754–758

Daffner RH, Pavlov H (1992) Stress fractures: current concepts. Am J Roentgenol 159:245–252

Davies NH, Niall D, King LJ et al (2004) Magnetic resonance of bone bruising in the acutely injured knee-short-term outcome. Clin Radiol 59:439–445

Demeyere A, Vanhoenacker FM (2007) Overuse bone trauma and stress fractures. In: Vanhoenacker FM, Maas M, Gielen JL (eds) Imaging of orthopedic sports injuries. Springer-Verlag, New York

Escalas F, Curell R (1994) Occult posttraumatic bone injury. Knee Surg Sports Traumatol Arthrosc 2:147–149

Felson DT, Chaisson CE, Hill CL et al (2001) The association of bone marrow lesions with pain in knee osteoarthritis. Ann Intern Med 134:541–549

Felson DT, McLaughlin S, Goggins J et al (2003) Bone marrow edema and its relation to progression of knee osteoarthritis. Ann Intern Med 139:330–336

Fredericson M, Bergman G, Hoffman KL et al (1995) Tibial stress reaction in runners: correlation of clinical symptoms and scintigraphy with a new magnetic resonance imaging grading system. Am J Sports Med 23:472–481

Gaeta M, Minutoli F, Scribano E et al (2005) CT and MR imaging findings in athletes with early tibial stress injuries: comparison with bone scintigraphy findings and emphasis on cortical abnormalities. Radiology 235:553–561

Grampp S, Henk CB, Mostbeck GH (1998) Overuse edema in the bone marrow of the hand: demonstration with MRI. J Comput Assist Tomog. 22:25–279

Hayes CW, Brigido MK, Jamadar DA et al (2000) Mechanism-based pattern approach to classification of complex injuries of the knee depicted at MR imaging. Radiographics 20: S121–S134

Hoy G, Wood T, Phillips N, Connell (2006) When physiology becomes pathology: the role of magnetic resonance imaging in evaluating bone marrow oedema in the humerus in elite tennis players with an upper limb pain syndrome. Br.J Sports Med 40:710–713

Johnson DL, Urban WP Jr, Caborn DNM et al (1998) Articular cartilage changes seen with magnetic resonance imaging-detected bone bruises associated with acute anterior cruciate ligament rupture. Am J Sports Med 26:409–414

Kaplan PA, Gehl RH, Dussault RG et al (1999) Bone contusions of the posterior lip of the medial tibial plateau (contrecoup injury) and associated internal derangement of the knee at MR imaging. Radiology 211:747–753

Karantanas AH (2007) Natural history and monitoring of fractures and microfractures. In: Vanhoenacker FM, Maas M, Gielen JL (eds) Imaging of orthopedic sports injuries. Springer-Verlag, Berlin Heidelberg New York, pp 467–487

Krampla W, Mayrhofer R, Malcher J et al (2001) MR imaging of the knee in marathon runners before and after competition. Skeletal Radiol 30:72–76

Krampla W, Newrkla SP, Kroener AH, Hruby WF (2008) Changes on magnetic resonance tomography in the knee joints of marathon runners: a 10-year longitudinal study. Skeletal Radiol 37:619–626

Lazzarini K, Troiana R, Smith R (1997) Can running cause the appearance of marrow edema on MR images of the foot and ankle? Radiology 202:540–542

Lee JC, Malara FA, Wood T, Hoy G, Saifuddin A, Connell DA (2006) MRI of stress reaction of the distal humerus in elite tennis players Am J Roentgenol 187:901–904

Libicher M, Ivancic M, Hoffmann M et al (2005) Early changes in experimental osteoarthritis using the Pond-Nuki dog model: technical procedure and initial results of in vivo MR imaging. Eur Radiol 15:390–394

Lohman M, Kivisaari A, Vehmas T, Kallio P, Malmivaara A, Kivisaari L (2001) MRI abnormalities of foot and ankle in asymptomatic physically active individuals. Skeletal Radiol 30:61–66

MacMahon PJ, Palmer WE (2011) A biomechanical approach to MRI of acute knee injuries. Am J Roentgenol 197: 568–577

Major NM (2006) Role of MRI in prevention of metatarsal stress fractures in collegiate basketball players. Am J Roentgenol 186:255–258

Mandalia V, Fogg AJB, Chari R et al (2005) Bone bruising of the knee. Clin Radiol 60:627–636

Mankin HJ (1982) The response of articular cartilage to mechanical injury. J Bone Joint Surg Am 65:951–957

Miltner O, Niedhart C, Piroth W et al (2003) Transient osteoporosis of the navicular bone in a runner. Arch Orthop Trauma 124:646–647

Mulligan MF (1995) The "gray cortex": an early sign of stress fracture. Skeletal Radiol 24:201–203

Muthukumar T, Butt SH, Cassar-Pullicino VN (2005) Stress fractures and related disorders in foot and ankle: plain films, scintigraphy, CT and MR imaging. Semin Musculoskelet Radiol 9:210–226

Nielsen MB, Hansen K, Holmer P et al (1991) Tibial periosteal reactions in soldiers. Acta Orthop Scand 62:531–534

Peace KAL, Hillier JC, Hulme A, Healy JC (2004) MRI features of posterior ankle impingment syndrome in ballet dancers: a review of 25 cases. Clin Radiol 59:1025–1033

Perdikakis E, Grigoraki E, Karantanas A (2011) Os naviculare: the multi-ossicle configuration of a normal variant. Skeletal Radiol 40(1):85–88

Radke S, Vispo-Seara J, Walther M et al (2001) Transient bone marrow edema of the foot. Int Orthop 25:263–267

Roemer FW, Bohndorf K (2002) Long-term osseous sequelae after acute trauma of the knee joint evaluated by MRI. Skeletal Radiol 31:615–623

Romani WA, Gieck JH, Perrin DH et al (2002) Mechanisms and management of stress fractures in physically active persons. J Athl Train 37:306–314

Ryu KM, Jin W, Ko YT et al (2000) Bone bruises: MR characteristics and histological correlation in the young pig. J Clin Imaging 24:371–380

Sanders TG, Medynski MA, Feller JF et al (2000) Bone contusion patterns of the knee at MR Imaging: footprint of mechanism of injury. Radiographics 20:S135–S151

Schueller-Weidekamm C, Schueller G, Uffmann M, Bader TR (2006) Does marathon running cause acute lesions of the knee? Evaluation with magnetic resonance imaging. Eur Radiol 16:2179–2185

Schweitzer ME, White LM (1996) Does altered biomechanics cause marrow edema? Radiology 198:851–853

Soames RW (1995) Skeletal system. In: Williams PL (ed) Gray's anatomy. Churchill Livingstone, New York, pp 425–736

Spitz DJ, Newberg AH (2002) Imaging of stress fractures in the athlete. Radiol Clin N Am 40:313–331

Tins B, Cassar-Pullicino V (2006) Marrow changes in anorexia nervosa masking the presence of stress fractures on MR imaging. Skeletal Radiol 35:657–860

Toms AP, Marshall TJ, Becker E et al (2005) Regional migratory osteoporosis: a review illustrated by five cases. Clin Radiol 60:425–438

Trappeniers L, De Maeseneer M, De Ridder F et al (2003) Can bone marrow edema be seen on STIR images of the ankle and foot after 1 week of running. Eur J Radiol 47:25–28

Van de Perre S, Vanhoenacker FM, De Schepper AM (2003) Thigh splints in a skeletally immature boy. Rofo 175:1582–1584

Vanhoenacker FM, Snoeckx A (2007) Bone marrow edema in sports: General concepts. Eur J Radiol 62:6–15

Vanhoenacker FM, Van Dyck P, Gielen JL, Geyskens W (2007) Overuse bone trauma and stress fractures. In: Vanhoenacker FM, Maas M, Gielen JL (eds) Imaging of orthopedic sports injuries. Springer-Verlag, Berlin Heidelberg New York

Vincken PW, Ter Braak BP, van Erkel AR, et al. (2005) Clinical consequences of bone bruise around the knee. Eur Radiol. doi: 10.1007/s00330-005-2735–2738

Yao L, Lee JK (1988) Occult intraosseous fracture: detection with MR imaging. Radiology 167:749–751

Yochum TR, Barry MS (1997) Bone marrow edema caused by altered pedal biomechanics. J Manipulative Physiol Ther 20:56–59

Zanetti M, Christian LS, Burkhardt S et al (2002) Clinical outcome of edema-like bone marrow abnormalities of the foot. Radiology 222:184–188

Zanetti M, De Simoni C, Wetz HH et al (1997) Magnetic resonance imaging of injuries to the ankle joint: can it predict clinical outcome? Skeletal Radiol 26: 82–88

Zwas ST, Elkanovitch R, Frank G (1987) Interpretation and classification of bone scintigraphic findings in stress fractures. J Nucl Med 28:452–457

Infective Inflammatory Bone Disease

Klaus Bohndorf and Hassan Douis

Contents

K. Bohndorf (✉)
Department of Radiology, Klinikum Augsburg, Stenglinstr. 2, 86156 Augsburg, Germany
e-mail: Klaus.bohndorf@klinikum-augsburg.de

H. Douis
Royal National Orthopaedic Hospital NHS Trust, Stanmore, UK

Abstract

Infectious inflammatory bone disease can develop via three routes: Hematogenous seeding, contiguous spread from an adjacent soft tissue or joint infection and direct implantation of microorganisms. A chronological view on osteomyelitis distinguishes acute, subacute and chronic osteomyelitis. The MR diagnosis of bone infection has to focus on (a) bone marrow inflammation, (low signal in T1, high signal in intermediate and T2-weighted TSE sequences, as well as in T1 with contrast), (b) intraosseous abscesses (similar to bone marrow inflammation but with a characteristic high signal rim in T1 with contrast), (c) sequestra (low signal in T1, low signal in intermediate and T2 and a peripheral enhancement in T1 with contrast), (d) cortical destruction (higher signal than bone in all sequences) and (e) sinus tracts into the peripheral soft tissues. In chronic post-traumatic osteomyelitis the same rules for diagnosis have to be applied, although extensive remodelling processes which include sclerosis, fibrosis and cortical thickening have to be taken into account. Sequestra and sinus tracts are regularly seen in active chronic osteomyelitis. Infections of the spine are divided into spondylitis, discitis, spondylodiscitis and spondylarthritis (septic arthritis of the facet joints) and mostly occur in the elderly. In the acute stage of the disease, spondylitis is characterised by increased signal intensity within the vertebral body in the water sensitive sequences and on the contrast-enhanced examination as well as decreased signal intensity on the T1-weighted spin echo sequence.

A. Baur-Melnyk (ed.), *Magnetic Resonance Imaging of the Bone Marrow*, Medical Radiology. Diagnostic Imaging,
DOI: 10.1007/174_2011_523,

Contrast-enhanced MRI is most sensitive in the identification of early vertebral infection. The infection typically begins at the antero-lateral aspect of the vertebral body and adjacent to the vertebral endplates. T1-weighted spin echo sequences depict the destruction of the vertebral endplates relatively well because the normal cortical signal void of the endplate changes to an intermediate signal. Disc involvement is seen early in spondylitis. T2-weighted spin echo sequences demonstrate increased signal intensity within the disc due to infection of the disc. The diagnosis of an abscess within the disc requires identification of signal intensity similar to fluid on T2-weighted spin echo sequences and lack of enhancement of this area on contrast-enhanced MRI. Osteomyelitis of the diabetic foot encounters special features based on the nature of the disease. In water sensitive sequences and after contrast an increased marrow signal is often seen in these patients and represents an unspecific finding. The diagnosis of osteomyelitis in diabetic foot has to rely mainly on the identification of an intraosseous abscess. Sinus tracts extending to bone, sequestrum formation and cortical destruction significantly help to build up a correct diagnosis.

1 Introduction

Musculoskeletal Infection, especially after acute onset, is considered a therapeutic emergency. Osteomyelitis can develop via three routes: Hematogenous seeding, contiguous spread from an adjacent soft tissue or joint infection and direct implantation of microorganisms. A chronological view on osteomyelitis distinguishes acute, subacute and chronic osteomyelitis. The MR diagnosis of bone infection has to focus on bone marrow inflammation, abscesses, sequestra, cortical destruction, cloaca and sinus tracts. Osteomyelitis of the diabetic foot encounters special features based on the nature of the disease.

2 Definition and Clinical Background of Infective Inflammatory Bone Diseases

2.1 Definition

The term osteomyelitis is used to describe an infection of the medullary cavity or an infection of the adjacent cortex (Haas and McAndrew 1996). In contrast, the term osteitis is used if the infection primarily originates from the soft tissues and the cortical bone is affected secondarily. Osteitis may subsequently develop into osteomyelitis. Another potential site which may become inoculated by pathogens is the (sub-) periosteal space (Delling 1997). Although the term "infectious periostitis" is patho-anatomically accurate, this term is rarely used. In comparison, the term "soft tissue infection" is defined as an infection of anatomical structures not involving bones or joints, namely an infection involving the skin, subcutaneous tissue, muscle, fascia, tendon or bursa. In contrast, septic arthritis represents an infection originating from the synovial membrane.

2.2 Pathogenesis

Osteomyelitis commonly is classified according to the mechanism of infection. Endogenous haematogenous osteomyelitis has to be differentiated from exogenous osteomyelitis which usually occurs due to direct inoculation of bacteria in the context of trauma or surgery or due to migration of bacteria from the surrounding soft tissues and joints.

The majority of cases of osteomyelitis are due to gram-positive bacteria with Staphylococci being the most common pathogen. In contrast, gram-negative bacteria are more commonly encountered in post-traumatic or post-surgical osteomyelitis (Munoz and Bouza 1999). Anaerobic bacteria or polymicrobial infections are usually observed in patients with a reduced blood supply such as in diabetics. Furthermore, various mycobacteria remain important pathogens, not only as a potential cause for spondylitis but also as a cause for osteomyelitis of long bones and septic arthritis.

2.3 Clinical Course of Osteomyelitis

Acute osteomyelitis is a disease of short duration with onset of symptoms occurring within days without commencement of antibiotic treatment. In contrast, *chronic* osteomyelitis is an infection where the symptoms have been present for more than 4–6 weeks, initial antibiotic therapy has been unsuccessful or in cases in which osteomyelitis is due to an open fracture or surgery (Munoz and Bouza 1999).

The term *subacute* osteomyelitis represents a clinically less severe, non-septic form of osteomyelitis. Brodie's abscess with its varying clinical presentation is a typical example that it is not always possible to differentiate subacute from chronic osteomyelitis.

Furthermore, it is important to be aware of the fact that the clinical course of osteomyelitis usually does not occur in a sequential fashion although acute osteomyelitis may subsequently develop into subacute and chronic osteomyelitis. Inadequate antibiotic treatment or resistance to commonly used antibiotics may be a cause for the development of acute osteomyelitis into subacute or chronic osteomyelitis. Furthermore, pathogens may survive in small abscesses or bone fragments, therefore leading potentially to reactivation of osteomyelitis at a later stage.

3 Acute Osteomyelitis

3.1 Definition

Acute osteomyelitis is a pathogen-induced systemic disease process with organ manifestation which primarily affects the medullary cavity.

Dependent on the age of the patient acute osteomyelitis is divided into

- Neonatal osteomyelitis
- Juvenile haematogenous osteomyelitis and
- Osteomyelitis in adulthood.

3.2 Pathologic-Anatomical Basis and Pathogenesis of Acute Osteomyelitis

Histologically, acute osteomyelitis is characterised by a leukocytic exudate, fibrin deposition and marked oedema which infiltrates the medullary cavity. The affected bone (cancellous and cortical bone) is subsequently destroyed by multi-nucleated osteoclasts and segmented neutrophils. The exudate finally spreads along preformed cavities, namely via Volkmann's canals and the Haversian system of cortical bone. A break in the cortex leads to elevation of the periosteum and ultimately to periosteal new bone formation (Delling 1997).

The transition of acute infection into chronic infection is histologically characterised by the development of granulation tissue with proliferation of connective tissue and peripheral capillary ingrowth. Bony fragments which are variable in size are separated by surrounding bone and ultimately become necrotic due to a lack in vascular supply. The destruction of larger pieces of bone therefore leads to the formation of a sequestrum. This process affects both cancellous and cortical bone (Delling 1997) (Table 1).

Staphylococcus aureus is responsible for 70–80% of all cases of acute osteomyelitis (Staubach et al. 2000). In newborns and infants, β-haemolytic Streptococci are the most common causative organisms, whereas children suffering from sickle cell disease are more prone to develop Salmonella enteridis infections (Epps et al. 1991). In adults, E. coli, Pseudomonas aeruginosa and Serratia marcescens are also associated with osteomyelitis.

Although generally speaking every bone can be affected by osteomyelitis, the lower extremity is more commonly affected than the upper extremity. The tibia and femur are most frequently affected with the distal and proximal ends of the shafts being the common sites of involvement. In children and adolescents, osteomyelitis usually affects the metaphysis of long bone whilst in infants an epimetaphyseal location is most common. The typical site affected in the upper extremities is the humerus. Less commonly involved sites are fibula, radius and ulna.

3.3 Osteomyelitis in Infancy

Osteomyelitis in infancy is a paediatric emergency. Clinically, this disease entity is characterised by an acute onset with high fever, relieving posture of the upper extremity and severe tenderness on palpation of the affected extremity. A red, hot, swollen area over the skin of the affected extremity is a further clinical

Table 1 Possible complications and consequences of acute osteomyelitis

Bone necrosis and formation of a sequestrum.
Recurrence—which can occur years after partially healed osteomyelitis with transition into chronic osteomyelitis.
Multifocal osteomyelitis—which particularly can be seen in immunocompromised patients e.g. in HIV and cancer patients, diabetics and particularly in neonates. Multifocal osteomyelitis for example is observed in 7% of all children suffering from haematogenous osteomyelitis (Nelson JD 1990).
Disruption of the cortex with development of periostitis and a subperiosteal abscess.
Extension of infection into adjacent soft tissue and development of a soft tissue phlegmon.
Change in bone growth: extension of osteomyelitis into the growth plate can lead to shortening of bone. However, hyperaemia may lead to increased cartilage proliferation and a subsequent increase in bone length.
Pathological fractures.

sign of osteomyelitis. As in all cases of osteomyelitis, the diagnosis is made by taking into account the combination of clinical findings, microbiology and imaging findings.

Usually, a joint or bone marrow aspiration is not required to identify the causative agent. It is important to note that osteomyelitis in infancy threatens the joints due to the marked blood supply of the epiphyseal cartilage.

3.4 Juvenile Haematogenous Osteomyelitis

The distinctive feature of juvenile haematogenous osteomyelitis is that it is predominantly located in the metaphysis. Juvenile haematogenous osteomyelitis demonstrates an acute onset. Diagnosis and treatment of this disease entity resemble those of osteomyelitis in infancy.

3.5 Acute Haematogenous Osteomyelitis in Adults

This form of osteomyelitis is increasingly being diagnosed, however, it primarily affects the vertebral bodies. Other sites that are affected are the pelvis and the long bones. After closure of the growth plate nutrient vessels extend again from the metaphysis into the subchondral space of the epiphysis. Joint involvement due to direct spread of the infection is therefore more frequently observed in this age group. In contrast, the cortex in the region of the metaphysis is usually strong and the periosteum is fibrosed and adherent to the cortex. Therefore, subperiosteal abscesses are rarely observed in this patient group. However, if the infection does extend through the cortex, the friable periosteum tears and the infection spreads into the soft tissue. Diagnosis and treatment of acute haematogenous osteomyelitis in adults is similar to that in children.

3.6 Magnetic Resonance Imaging Features

The basis of the examination is a STIR-sequence (short time inversion recovery), a frequency-selective fat suppressed intermediate (TE 40–50 ms) or T2-weighted (TE > 80 ms) turbo spin echo (TSE) sequence which are used as search sequences. Coil selection, patient positioning and scanning orientation have to be adjusted according to the suspected location. These technical considerations should not solely be left to the MR-technologist but should be made in conjunction with the radiologist. Skin markers at the site of suspected pathology, as far as can be clinically judged, should be placed by the radiologist. Absence of increased signal intensity on fluid-sensitive sequences excludes osteomyelitis and obviates the need for further sequences (Wunsch et al. 2001). T1-weighted spin echo sequences are important in the precise anatomic localization of osteomyelitis which has been identified on fluid-sensitive sequences. T1-weighted, fat-suppressed spin echo sequences after intravenous application of gadolinium have been proven to be particularly useful. Gadolinium application is a highly sensitive examination technique in the detection of infective musculoskeletal lesions and is a reliable method in differentiating abscesses or necrotic areas from inflammatory oedema (Hopkins et al. 1995;

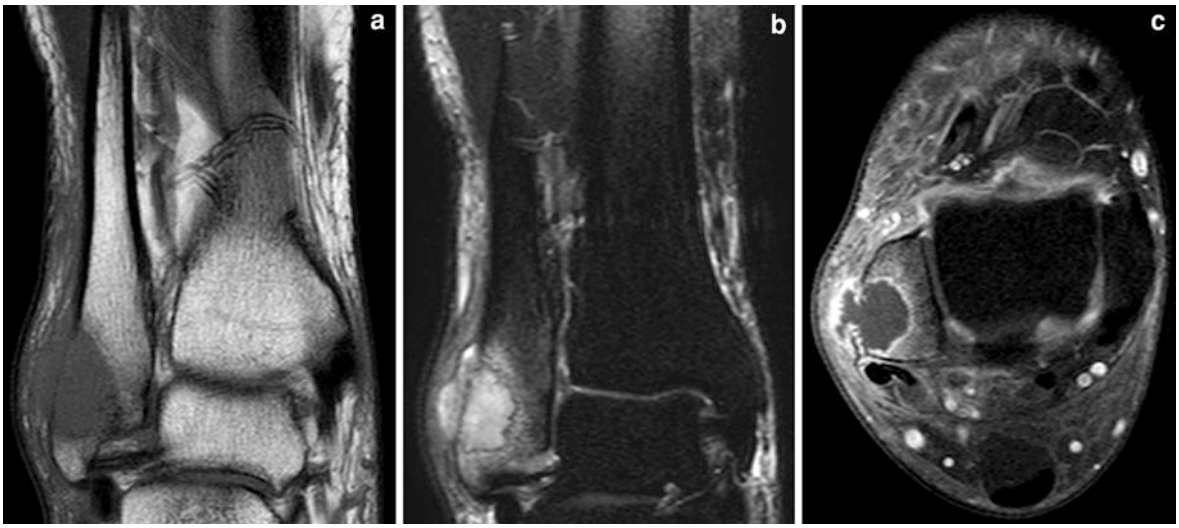

Fig. 1 Acute osteomyelitis of the distal fibula: Coronal T1-weighted (T1WI) spin echo (SE) (**a**), coronal STIR (**b**) and axial post-contrast T1W SE FS images (**c**) demonstrating an intramedullary abscess, cortical destruction, subperiosteal extension of the abscess and marked surrounding oedema. Note the rim-enhancement and lack of central enhancement of the abscess on the contrast-enhanced T1W SE FS images (**c**)

Kan et al. 2010). Furthermore, the accuracy in the diagnosis of sinus tracts and sequestra is increased. However it has to be emphasised that contrast enhancement cannot be used to reliably differentiate infectious from non-infectious conditions. Moreover, in a comparative study, Miller et al. discovered that the routine use of gadolinium in the detection of osteomyelitis (or of soft tissue infections for that matter) is not necessary (Miller et al. 1997). The diagnostic yield is only increased if there is (clinical or radiological) suspicion of an abscess or in cases where the infection is adjacent to the joints.

Involvement of osteomyelitis in bone shows in the majority of cases focal, well-described areas within the medullary cavity which are hypointense on T1-weighted SE sequences and hyperintense on fluid-sensitive sequences. The extent of the lesion on the T1-weighted sequences is virtually always smaller than on fluid-sensitive sequences or on contrast-enhanced fat-suppressed T1-weighted sequences (Jones et al. 1992). However, more extensive and ill-defined lesions which fill the medullary cavity without a well-defined focus but demonstrating the above described signal characteristics can also occur. A focal lesion is invariably associated with perifocal oedema. A good rule of thumb is that absence of perifocal oedema or very small perifocal oedema on fat suppressed sequences suggests that acute osteomyelitis is unlikely. However, the cortex can almost be normal in the early stages of osteomyelitis. During the course of the disease, well-defined or diffuse areas of increased signal intensity affecting the entire circumference of the cortex may be observed.

Subperiosteal abscesses are particularly seen in children. These types of abscesses demonstrate the same signal characteristics as abscesses described above (Fig. 1a–c). Periosteal new bone formation which is well-known from conventional radiographs, is typically demonstrated by lamellar signal voids on pre- and post contrast-enhanced MRI. Foci of acute osteomyelitis which are adjacent to joints regularly lead to a reactive synovitis of the affected joint. Intraosseous abscesses can also be detected in acute osteomyelitis. These abscesses tend to be small (less than 1.5 cm in diameter), are well demarcated, demonstrate a low signal intensity rim on T2-weighted TSE and STIR-sequences and show surrounding oedema (Fig. 2a, b). However, fluid-sensitive sequences are inadequate in differentiating fluid-filled spaces (e.g. abscesses) from soft tissue or bone marrow oedema (Boutin et al. 1998). In contrast, marked peripheral enhancement and absent or minimal central enhancement of a lesion is diagnostic of an abscess (Fig. 1a–c).

In 30–40% of all abscesses the so-called "penumbra sign" can be identified on T1-weighted imaging. This represents a high-signal intensity rim between the

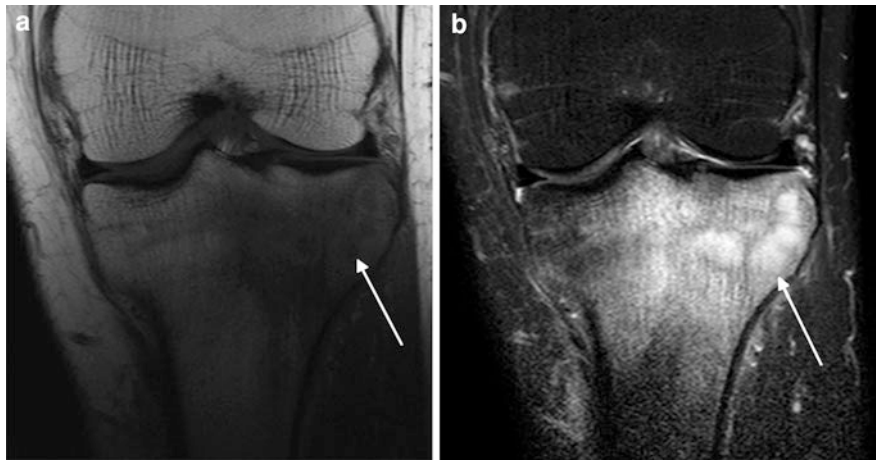

Fig. 2 Acute osteomyelitis of the proximal tibia: Coronal T1-weighted (T1WI) spin echo (SE) (**a**) and coronal T2W SE FS images (**b**) demonstrating multiple intramedullary abscesses and marked surrounding oedema

necrotic abscess cavity and the surrounding oedema. The penumbra sign is thought to be due to degradation of blood products (Grey et al. 1998) (Fig. 3a–b).

On MRI, necrotic sequestra appear as areas of signal-void on fluid-sensitive sequences which fail to demonstrate enhancement after contrast administration. The rim surrounding the areas of signal void however should demonstrate enhancement, a finding which aids in the differentiation of necrotic sequestra from calcification.

A cloaca represents a defect in the periosteum through which a subperiosteal abscess may discharge into the soft tissues. The site of rupture can occasionally, but not always, be identified as a defect in the low signal intensity line of the periosteum. The presence of a cloaca is frequently associated with infiltration of the cortex with inflammatory tissue (Fig. 4a–d).

In septic arthritis, differentiation of reactive bone marrow oedema from secondary osteomyelitis affecting adjacent bones is known to be very difficult on MR imaging. Vice versa, acute osteomyelitis which is primarily located within the epiphysis may lead to a reactive joint effusion or to secondary septic arthritis. The differentiation of these two disease entities is also challenging on MR imaging. Increased signal intensity of adjacent bones on fluid-sensitive sequences and contrast enhancement of adjacent bones is commonly but not always observed in septic arthritis (Graif et al. 1999). However, bone marrow oedema should not necessarily be interpreted as secondary osteomyelitis unless clearly demarcated adjacent joint erosions are present and therefore a direct extension of the infection into the medullary cavity can be expected (Fig. 5a, b).

Reactive joint effusions are frequently seen in cases of osteomyelitis which are in close proximity to the joint. Whereas reactive joint effusions show only mild synovial enhancement, septic arthritis demonstrates marked contrast enhancement of the joint capsule and frequently marked enhancement of the surrounding soft tissues. However, depending on the duration and extent of the disease, the imaging appearances of reactive joint effusions and septic arthritis may overlap. Therefore the above-mentioned differentiating feature is by no means a fast and hard rule and cannot be reliably used as a problem solving tool in all cases.

4 Chronic Osteomyelitis

4.1 Primary Chronic Osteomyelitis

The term chronic osteomyelitis emphasises the fact that the time course of the disease is widely used to classify osteomyelitis. However, only 6% of all cases of haematogenous osteomyelitis are primarily chronic (Munoz and Bouza 1999). The typical example of primary chronic osteomyelitis is a Brodie's abscess and will therefore be discussed separately. The term chronic haematogenous osteomyelitis also describes cases of primary acute haematogenous osteomyelitis which progress to the chronic form due to inadequate antibiotic treatment. This may be seen in patients infected with mixed pathogens where antibiotic

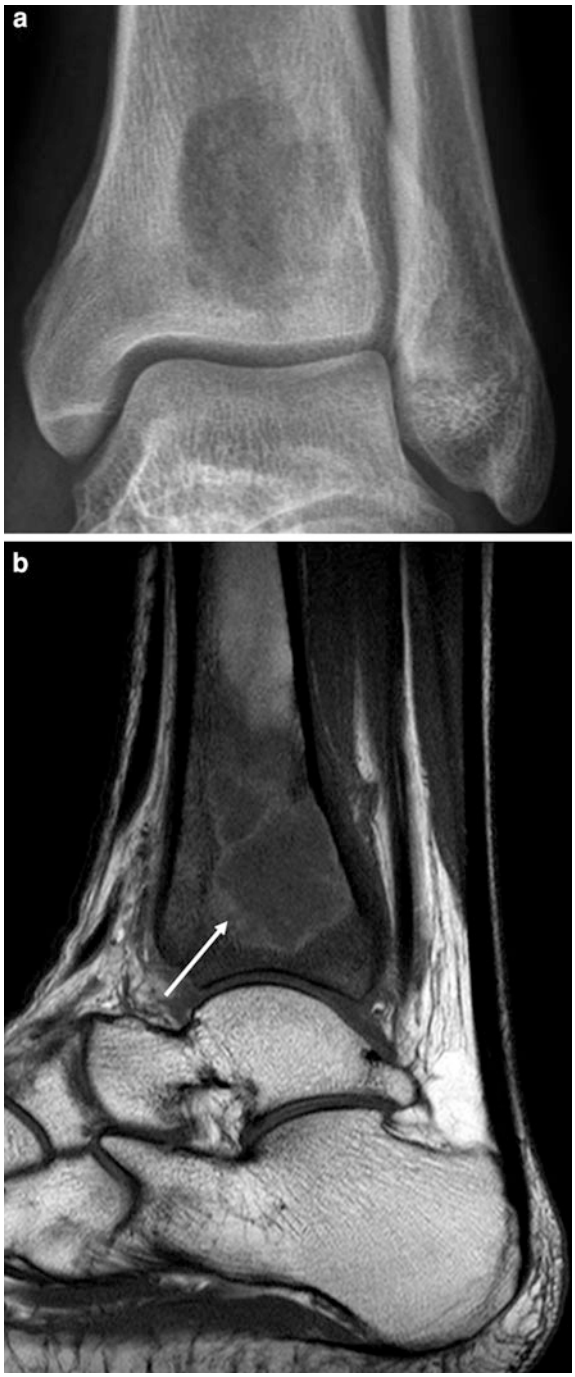

Fig. 3 **a–b** Abscess of Brodie's abscess of the distal tibia: Frontal radiograph (**a**) demonstrating well-defined radiolucency with surrounding sclerosis. Sagittal T1-weighted (T1WI) spin echo (SE) image (**b**) demonstrating a bone abscess with a penumbra sign (*arrow*). Both sagittal T1-weighted (T1WI) spin echo and sagittal STIR images depict the abscess, the marked surrounding oedema and the periosteal reaction, whereas the reactive ankle joint effusion is clearly visualised on the STIR-sequences

coverage has been insufficient or in abscesses which have not been surgically treated and almost always affects adults. The infective organisms which lie dormant within the frequently sclerotic bone may at any time lead to reactivation of the infective process.

4.1.1 Brodie's Abscess

A Brodie's abscess macroscopically represents a 1–4 cm pus-filled cavity within the spongiosa which demonstrates marked surrounding sclerosis. Histologically, a Brodie's abscess is characterised by a central abscess with a surrounding membrane of connective tissue and osteosclerosis (Delling 1997).

4.1.2 Magnetic Resonance Imaging Features

MR imaging is the imaging modality of choice to demonstrate the appearance of the abscess and to characterise a Brodie's abscess (Kornaat et al. 2010). The centre of the lesion is low signal on T1-weighted and high signal on fluid-sensitive images. This central cavity is surrounded by an inner rim which in approximately 75% of all cases is higher in signal intensity on the T1-weighted images than the central necrotic cavity (Grey et al. 1998). On T2-weighted images, this inner rim can frequently not be differentiated from the abscess cavity, however, it demonstrates marked enhancement after contrast administration. This rim is surrounded by a poorly demarcated outer layer which is hypointense in all sequences radiographically corresponding to medullary sclerosis. Brodie's abscess typically demonstrates a more or less pronounced perifocal oedema (Fig. 3a–b).

4.2 Chronic, Exogenous Osteomyelitis

Chronic exogenous osteomyelitis is a non-haematogenous induced form of osteomyelitis which after an acute onset usually develops into a chronic form with the tendency to relapse. Dependent on the pathogen, a slow, clinically insidious onset can also occur.

4.2.1 Pathologic-Anatomic Basis and Pathogenesis

Exogenous osteomyelitis can develop via three ways:

1. Penetration and migration through natural barriers:

After breaching natural barriers within the human body the infection may spread into the bone after penetrating the periosteum. Common entry sites for

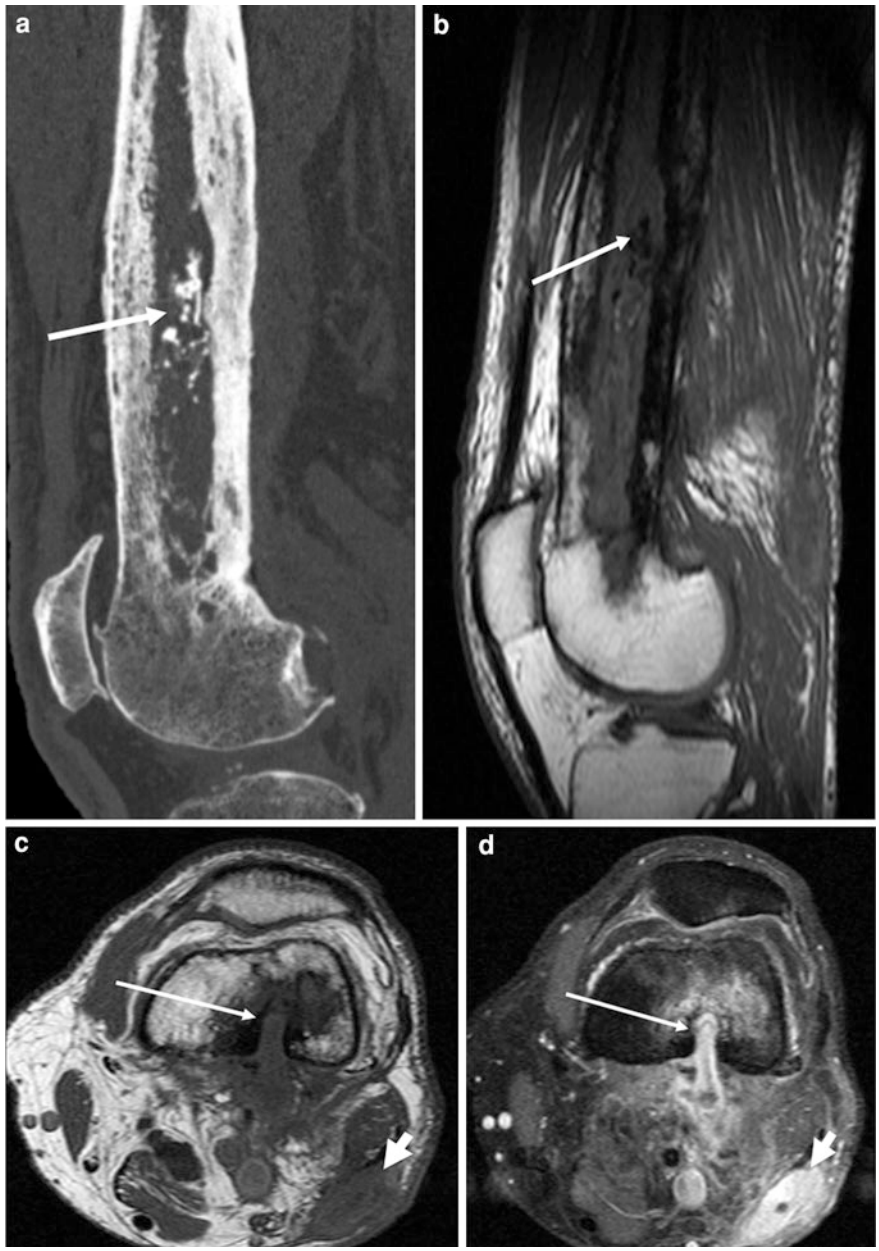

Fig. 4 Chronic osteomyelitis of the femur: Sagittal reconstruction of CT (**a**) demonstrates sequestrum (*arrow*) and surrounding hyperostosis due to solid periosteal reaction. Sagittal T1-weighted (T1WI) spin echo image (**b**) shows sequestrum (*arrow*), extensive infective tissue within the medullary cavity as well as cortical sclerosis and hyperostosis due to solid periosteal reaction. Axial T1-weighted (T1WI) spin echo (**c**) and axial contrast-enhanced T1W SE FS images (**d**) demonstrate a break in the posterior cortex in continuity with a cloaca (*long arrow*) and extension of the infection between the popliteal vessels and the lateral head of gastrocnemius via a sinus tract into the subcutaneous tissue where there is an abscess (*small arrow*)

pathogens are the skin, the sinuses, the mastoids and the teeth. It has to be emphasised however that the skin, the mucosal membranes and the epithelial lining which act as natural barriers are not obviously damaged.

2. Injury to natural barriers with subsequent soft tissue infection:

There are numerous ways through which bacteria may enter the skin e.g. through lacerations and abrasions particularly in the hands and feet, through bite wounds and iatrogenic puncture wounds and surgical procedures. Furthermore, burn injuries and pressure decubital ulcers facilitate the development of soft tissue infections which may subsequently extend into bones and joints (Borgström et al. 1988).

3. Direct inoculation of pathogens into bone:

Major trauma with open fractures has become the most common cause of exogenous osteomyelitis. Dependent on the route of infection, the pathogen and the extent and form of injury, post-traumatic osteomyelitis is observed in 2–16% of all cases of

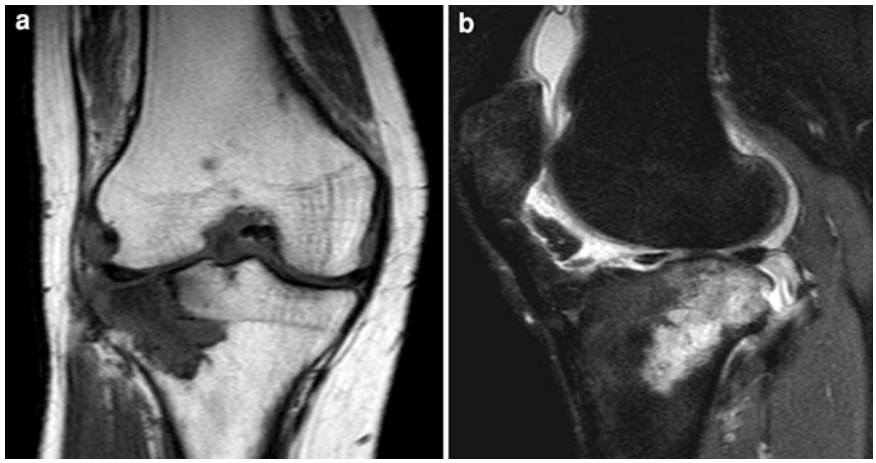

Fig. 5 **a**, **b** Acute osteomyelitis of proximal tibia with secondary septic arthritis of knee joint: Coronal T1-weighted (T1WI) spin echo (**a**) and sagittal PD FS images demonstrate acute osteomyelitis with cortical breach of proximal tibia leading to secondary septic arthritis

major trauma. In contrast, the incidence of osteomyelitis after open reduction and internal fixation of closed fractures is 0.5–2% and therefore significantly lower (Kaim et al. 2002). Percutaneous interventional procedures such as bone biopsies or vertebroplasties can in rare cases also lead to exogenous osteomyelitis. Furthermore, pathogens may enter the bone directly through penetrating injuries (e.g. nails) or injuries caused by circular saws.

4.2.2 MR Imaging

The imaging technique in post-traumatic exogenous osteomyelitis is similar to that of acute osteomyelitis. Metal artefacts may significantly impair the interpretation of MR studies due to local field inhomogeneities. This may still be the case after removal of metal implants as metal abrasions will continue to cause artefacts which can be up to 1 cm in length. The resultant signal void is surrounded by a high signal intensity semi-circle or circle. This circle is more pronounced in fat suppressed sequences. Therefore, direct comparison with T1-weighted spin echo sequences not only allows more anatomic depiction of the pathology in question but also leads to avoidance of overestimating the lesion size. Both STIR-sequence and turbo spin echo sequence are thought to be relatively reliable, the latter due to its multiple refocusing pulses. In contrast, frequency-selective fat saturation may be markedly affected by field inhomogeneities even after removal of metalware.

In post-traumatic osteomyelitis, extensive remodelling processes which include sclerosis, fibrosis and cortical thickening are the predominant pathological picture.

Nevertheless, the basic principles in the diagnosis of infective processes as described above in acute osteomyelitis remain valid. Whilst on T1-weighted imaging, infective changes within the medullary cavity manifest as areas of low signal intensity when compared to bone marrow, infection on fluid-sensitive sequences will appear as areas of high signal intensity. After contrast administration, both the membrane of an abscess and granulation tissue will demonstrate more or less pronounced enhancement whilst the abscess cavity fails to enhance or demonstrates a significantly delayed enhancement pattern.

Fistulae are usually seen as meandering, reticular areas of contrast enhancement. On T2-weighted spin echo sequences, both fluid and active infection are of high signal intensity whilst fibrosis is of low signal intensity. In contrast, a fistula will appear as linear high signal intensity (Fig. 4a–d). Using diffusion-weighted imaging patients with marked pus formation demonstrated significantly increased diffusivity in the centre of the cavity compared to patients with lesions in whom no pus formation was observed (Bitzer et al. 2002). These findings are supported by other authors, indicating that DWI has a high diagnostic value in diagnosing soft tissue abscesses and allowing differentiation from cystic, non-infected lessions (Unal et al. 2011; Harish et al. 2011). However, as reported by Khoo et al. (2011) in their review, osteomyelitis can cause hyperintensity on DWI with resulting low ADC values which may mimic malignancy.

It is important to note that in the first few weeks and months after trauma or surgery, osteomyelitis is difficult to diagnose on the basis of imaging alone

because post-traumatic oedema, granulation tissue, fibrosis and callus formation which are typically seen after trauma or orthopaedic surgery lead to signal characteristics on MR imaging which resemble those of osteomyelitis. Such non-specific post-operative changes can be seen up to 12 months after surgery and therefore hamper the diagnosis of osteomyelitis on MRI during this period (Bohndorf 1996; Kaim et al. 2000). Therefore, the diagnosis of post-traumatic bacterial osteomyelitis on MR imaging should only be made during this period if an abscess or fistula has unequivocally been detected (Ledermann et al. 2000). The role of contrast administration in case of suspected post-traumatic osteomyelitis has to be emphasised. Morrison et al. (1993) were able to significantly improve the sensitivity (from 79 to 88%) and specificity (from 53 to 93%) of MR imaging in the diagnosis of osteomyelitis using contrast-enhanced fat suppressed T1-weighted sequences when compared to unenhanced T1- and T2-weighted sequences. Of note is that their patient cohort included a large proportion of patients with chronic and post-operative osteomyelitis.

5 Osteomyelitis of the "Diabetic Foot"

5.1 Definition

Diabetic neuropathy in feet result in complete derangement of the joints, which may be subluxed or dislocated, with extensive sclerosis, bone destruction and fragmentation ("Charcot joint"). Soft tissue infection, osteomyelitis and septic arthritis often accompany the "diabetic foot". Differentiation of soft tissue infection and osteomyelitis from the sequelae of a diabetic neuroarthropathy is extremely challenging on imaging.

5.2 Pathologic-Anatomic Basis and Pathogenesis

The diabetic foot is pathogenetically due to a combination of diabetic neuropathy, macro-and microangiopathy as well as repetitive microtrauma ("Charcot joint"). Loss of proprioception leads to ataxia whilst loss of sensation of pain facilitates overload injury to tendons, capsules, muscles and subsequently bones and joints (Horowitz 1993). More than 90% of all cases of osteomyelitis in the diabetic foot are due to direct infection of the bone or joint respectively through ulcers on the sole of the foot ("Mal perforans") (Bamberger et al. 1987). This disease entity is therefore by definition an *exogenous chronic osteomyelitis*. The combination of lack of pain and decreased perfusion increases the risk of infection in comparison to injuries to the sole of the foot in non-diabetics.

Osteomyelitis in the diabetic foot is seen—in decreasing order of frequency—in the metatarsal heads, the phalanges and the calcaneus. This distribution correlates with the distribution site of foot ulcers (Milgram 1993). A study by Newman et al. (1991) revealed that in 68% of 41 diabetic feet which underwent bone biopsies bacteria were isolated. Staphylococcus aureus and Staphylococcus epidermides were the most common causative agents for osteomyelitis in this study.

5.3 MR Imaging

MRI of the diabetic foot in clinically suspected cases of superimposed infection is routinely used in daily clinical practice (Donovan and Schweitzer 2010). Ulcers, oedema and abscesses can be differentiated within the soft tissues (Ledermann et al. 2002). Signal characteristics of osteomyelitis and septic arthritis in the diabetic foot are identical to signal characteristics observed in acute and chronic osteomyelitis which have been described previously. Numerous articles have quoted a sensitivity of $\sim$100% and a specificity of $\sim$80% in the diagnosis of osteomyelitis in the diabetic foot using MR imaging (Weinstein et al. 1993; Donovan and Schweitzer 2010). However, these figures do not always correlate with the findings observed in routine clinical practice. Furthermore, Craig et al. (1997) have emphasised the fact that even contrast-enhanced MRI is not able to reliably differentiate between osteomyelitis and reactive bone marrow oedema. Non-infected diabetic neuroarthropathy can develop rapidly or insidiously. The rapid form is characterised by the development of fractures, fragmentation and by the loss of joint

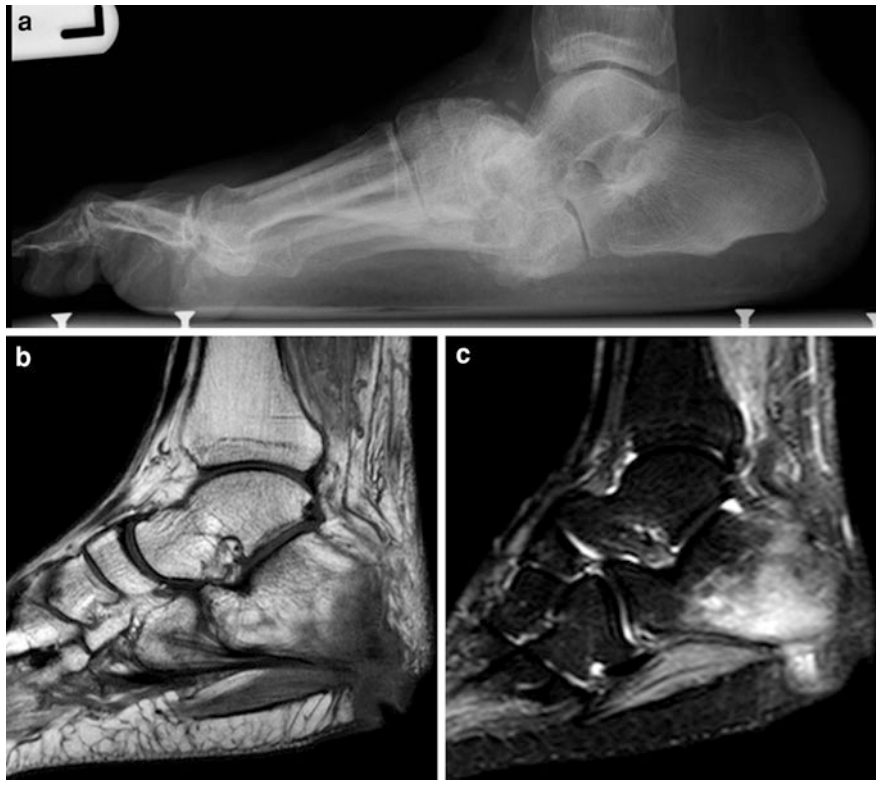

Fig. 6 **a–c** Osteomyelitis in a diabetic neuropathic foot: Lateral radiograph of the foot (**a**) shows fragmentation and destruction of the talo-navicular and intertarsal articulation in a diabetic patient with loss of the normal arch of the foot in keeping with a diabetic neuroarthropathy. Sagittal T1-weighted (T1WI) spin echo (**b**) and STIR-images demonstrate marked oedema within the calcaneus, soft tissue ulcer and oedema in the region of the heel. The bone marrow oedema in the calcaneus proved to be due to osteomyelitis

integrity which leads to marked bone marrow oedema and surrounding soft tissue oedema. This oedema is markedly hyperintense on T2-weighted fat suppressed-, STIR- and contrast-enhanced sequences. The differentiation of this bone marrow oedema and osteomyelitis is very difficult at this stage of the disease and requires great expertise (Toledano et al. 2011). Specific signs in the diagnosis of osteomyelitis in this case are the identification of an abscess and/or cortical destruction of which the diagnosis of an abscess is based on the administration of gadolinium. An important criterion in the differentiation of the two disease entities is based on T1-weighted SE sequences: in osteomyelitis the medullary cavity should be dark which corresponds to areas of high signal intensity on fluid-sensitive sequences (Fig. 6a–c). In contrast, in reactive bone marrow oedema caused by adjacent soft tissue infections or by stress reactions, the signal intensity within the affected bone marrow should only be marginally reduced on T1-weighted sequences and therefore the fat signal within the bone marrow should remain dominant. In case of an insidious onset of neuroarthropathy, sclerosis without significant oedema may be the predominant finding or the fatty bone marrow is normal in appearance. Both findings exclude osteomyelitis.

6 Infectious Spondylitis and Spondylodiscitis

6.1 Definition

Infections of the spine are divided into spondylitis, discitis, spondylodiscitis and spondylarthritis (septic arthritis of the facet joints). Pyogenic spondylitis and spondylodiscitis are relatively rare forms of skeletal infections representing ~ 2–4% of all cases of osteomyelitis. In adulthood, spondylitis and spondylodiscitis are the most common form of haematogenous osteomyelitis with Staphylococcus aureus and Mycobacterium tuberculosis being the most common pathogens worldwide. In contrast, isolated haematogenous discitis is only seen in childhood.

6.2 Pathologic-Anatomic Basis and Pathogenesis

Four sites of infection can be differentiated:

1. Spondylitis

Spondylitis is an infection of the bone marrow of the vertebral body which rapidly spreads into the

surrounding soft tissues and into adjacent discs. This is particularly the case with bacteria which produce proteolytic enzymes (e.g. Staphylococcus aureus) and therefore can lead to necrosis of disc material within 1–3 weeks (Rothman 1996).

2. Discitis

Discitis is an isolated infection of the disc and develops in adults only after surgical intervention with direct implantation of bacteria into the disc because the disc in adults does not have a blood supply. However, secondary ingrowth of vessels into the disc in patients suffering from degenerative disc disease may occur. Nevertheless, it has to be stressed that even in these circumstances primary discitis in adults remains a rarity. However, degenerative disc disease facilitates migration of infection from one vertebral body into an adjacent vertebral body (Calderone and Larson 1996). In contrast to adults, discs in children are supplied by nutrient vessels and therefore primary discitis may develop in children.

3. Spondylodiscitis

Spondylitis may spread along the anterior longitudinal ligament into the adjacent vertebral body and therefore may subsequently lead to infection of the disc causing spondylodsicitis. The infection initially leads to oedema and reactive hyperemia. Tissue necrosis occurs due to septic emboli affecting the endarteries. Subsequent activation of osteoclasts leads to bone destruction, particularly affecting the endplates which facilitates the spread of the infection into the disc. Development of fibrovascular tissue is a sign of commencement of the healing process. In non-specific spondylodiscitis, osteoblast activation and reactive sclerosis are observed 8–12 weeks after disease onset at the latest (Rothman 1996). Paravertebral abscess formation causes elevation of paraspinal ligaments which may lead to a reduction or complete disruption of blood supply to the vertebral body, subsequent vertebral body necrosis (Vaccaro et al. 1999; Moorthy and Prabhu 2002) and the development of intravertebral abscesses. (Rothman 1996). In spondylodiscitis, involvement of the epidural space is frequently observed. Direct spread into the spinal cord leading to infective myelitis may also occur (Rodiek 2001; Küker et al. 1997). Epidural abscesses are reported in 90% of cases of cervical spondylodiscitis, 33% of cases of thoracic and 24% of lumbar spondylodiscitis (Rodiek 2001). However overall, epidural abscess is most commonly seen within the lumbar spine due to the more common involvement of the lumbar spine in spondylodiscitis (Küker et al. 1997; Glazer and Hu 1996). Spread of the infection into facet joints has also been described (Vaccaro et al. 1999). However, in our experience primary infectious spondylarthritis is more likely to be iatrogenic in nature, particularly within the cervical spine, where it can occur due to therapeutic injection of the facet joint.

The causative agent depends on the route of infection. Haematogenous infections are predominantly due to Staphylococcus aureus. In particular, the elderly, diabetics, intravenous drug users and immunocompromised patients are at increased risk of developing haematogenous spondylodiscitis (Calderone and Larson 1996). In contrast, the offending organism in spondylodiscitis caused by direct implantation is dependent on the local flora at the site of origin. Iatrogenic infections are predominantly due to Staphylococccus aureus, gram-negative organisms and Mycobacterium tuberculosis (Khan et al. 1999). Polymicrobial organisms are the cause of spondylodiscitis in approximately 50% of all post-surgical cases of spondylodiscitis (Sapico 1996).

4. Spondylarthritis (septic arthritis of the facet joint)

Spondylodiscitis may also extend into the intervertebral joints. However, iatrogenic infection due to a therapeutic intervention is more commonly observed.

6.3 MR Imaging

6.3.1 Examination Technique

Sagittal T1-weighted spin echo and STIR-sequences of the area in question represent the basis of the investigation. T2-weighted turbo spin echo sequences are an adjunct to the examination. On fluid-sensitive sequences, the spinal canal appears hyperintense in comparison to the vertebral bodies. An abscess within the vertebral body, the disc or within the epidural space is clearly depicted in conjunction with the STIR-sequences. In addition, gadolinium-enhanced T1-weighted spin echo sequences with frequency selective fat-supression is routinely performed (Varma et al. 2001; Küker et al. 1997). Sagittal and axial

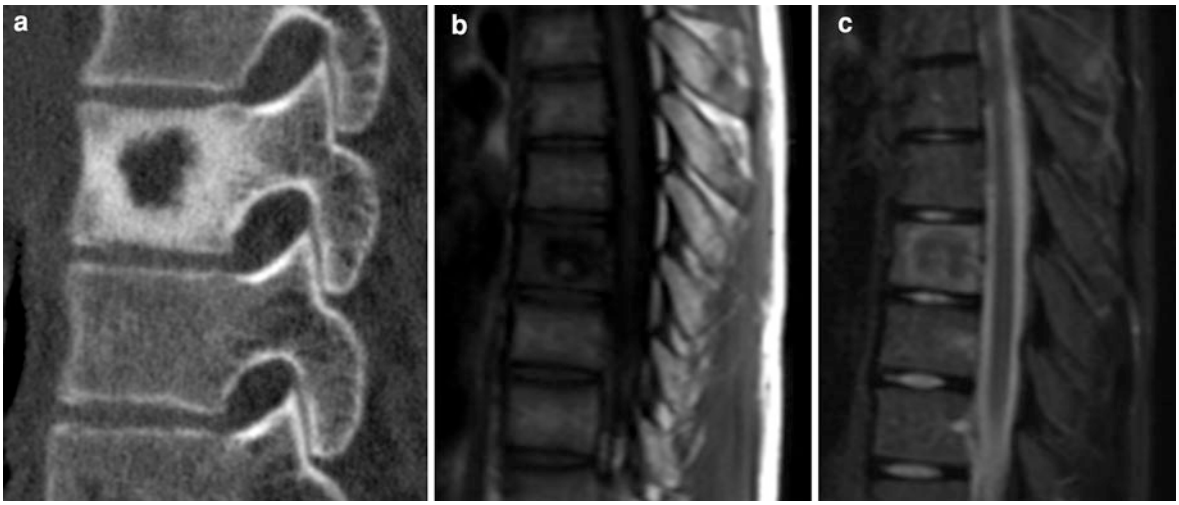

Fig. 7 **a–c** Pyogenic spondylitis of T8-vertebra with abscess formation: Sagittal CT-reconstruction (**a**), sagittal T1-weighted (T1WI) spin echo (**b**) and STIR-images reveal spondylitis with a vertebral body abscess leading to marked surrounding sclerosis and bone marrow oedema within the vertebral body. Of note is that the endplates are intact and the adjacent discs are not involved

images should routinely be performed in the assessment of spondylodiscitis. In some cases coronal images may provide further information regarding involvement of the psoas muscle or lateral ligamentous structures.

Diffusion-weighted imaging is not recommended as a worthwile additional diagnostic sequence for the diagnosis of infectious vertebral lesions at present (Khoo et al. 2011).

6.3.2 MRI Features

The signal characteristics in spondylitis are dependant on the pathologic-anatomical findings and their change over time: oedema, bone destruction, fibrosis, sclerosis and yellow marrow conversion. In the acute stage of the disease, spondylitis is characterised by increased signal intensity within the vertebral body on the STIR-sequence and on the contrast-enhanced examination as well as decreased signal intensity on the T1-weighted spin echo sequence. Contrast-enhanced MRI is most sensitive in the identification of early vertebral infection (Varma et al. 2001; Rothman 1996; Rodiek 2001). The infection typically begins at the antero-lateral aspect of the vertebral body and adjacent to the vertebral endplates. T1-weighted spin echo sequences depict the destruction of the vertebral endplates relatively well because the normal cortical signal void of the endplate changes to an intermediate signal. However, MRI cannot reliably be used for the evaluation of endplate destruction (Varma et al. 2001). The affected vertebral body demonstrates almost complete signal change at the time of diagnosis, at least on contrast-enhanced imaging. T2-weighted turbo spin echo sequences however are not suited for the assessment of signal changes within the vertebral body. It is also important to be aware of the fact that the absence of signal change within the vertebral body does not rule out infection (Dagirmanjian et al. 1996). Abscesses may develop within a vertebral body. These abscesses demonstrate high signal intensity on T2-weighted spin echo and STIR-sequences and do not show contrast enhancement or only peripheral enhancement (Vaccaro et al. 1999) (Fig. 7a–c). Vertebral body collapse leads to inhomogenous signal intensity within the deformed vertebral body with an increased amount of signal void on T2-weighted spin echo sequences. Disc involvement is seen early in spondylitis. T2-weighted spin echo sequences demonstrate increased signal intensity within the disc due to infection of the disc. At the time of diagnosis, there is loss of intervertebral disc height (Fig. 8a–d). This however can also be observed in degenerative disc disease. In case of destruction of adjacent vertebral endplates, intervertebral disc height may however also be increased (Jinkins et al. 1996). The diagnosis

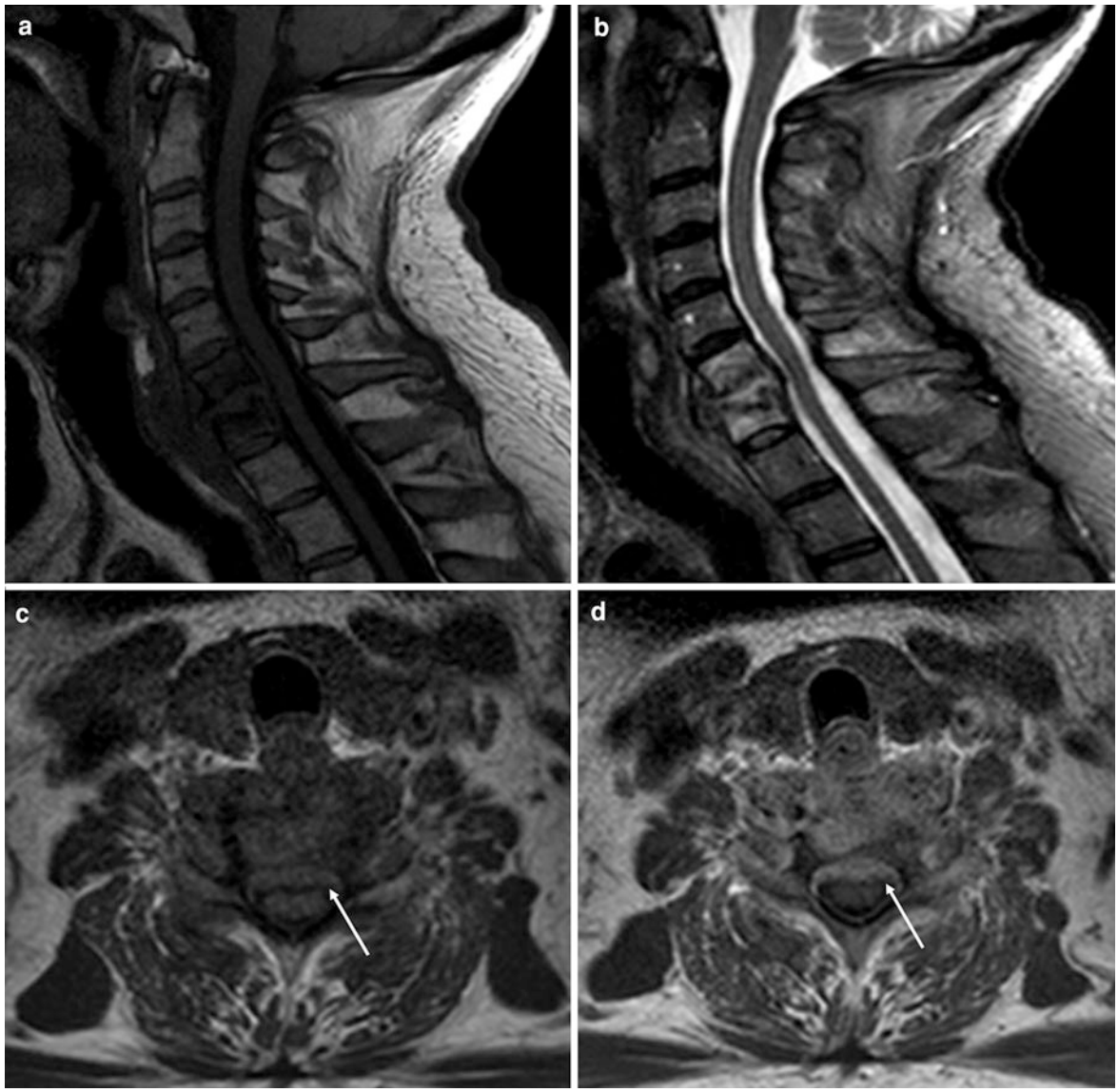

Fig. 8 Pyogenic spondylodiscitis of the cervical spine: Sagittal T1-weighted (T1WI) spin echo (**a**) and STIR-images (**b**) demonstrate increased signal intensity within the C6/7 disc on STIR-imaging, loss of disc height, destruction of adjacent endplates, oedema and sclerosis in the adjacent vertebral bodies as well as a prevertebral and epidural soft tissue mass. Axial T1-weighted (T1WI) spin echo image (**c**) clearly depicts the paravertebral and epidural (*arrow*) soft tissue mass whilst axial contrast-enhanced T1-weighted image (**d**) demonstrates diffuse enhancement of the epidural soft tissue therefore establishing the diagnosis of a phlegmon (*arrow*)

of an abscess within the disc requires identification of signal intensity similar to fluid on T2-weighted spin echo sequences and lack of enhancement of this area on contrast-enhanced MRI.

MRI is the only reliable imaging technique which allows non-invasive assessment of the contents of the spinal canal, in particular assessment of the spinal cord and the epidural space (Moorthy and Prabhu 2002; Moore and Rafii 2001). When scanning patients with suspected spondylodiscitis it is important to use the widest field of view possible because epidural abscesses may spread over a long distance in a cranio-caudal dimension. Compared to epidural fat, an epidural abscess or a phlegmon demonstrates

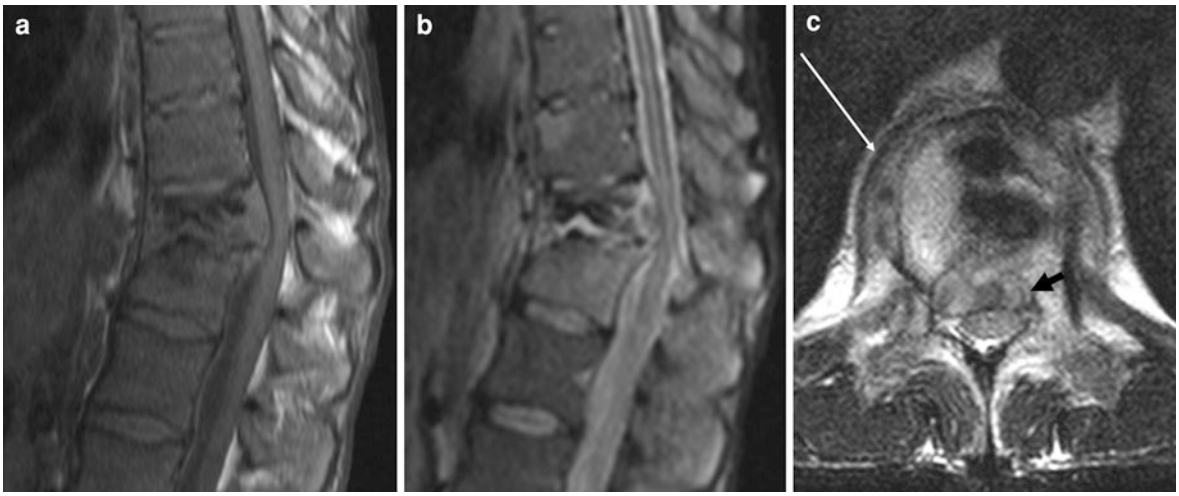

Fig. 9 a–c Tuberculous spondylodiscitis of the thoracic spine: Sagittal T1-weighted (T1WI) spin echo (**a**) and STIR-images (**b**) demonstrate almost complete T11-vertebral body collapse, endplate destruction of the T11- and T-12 vertebral bodies, marked increased oedema in both vertebral bodies, involvement of the disc, prevertebral body as well as epidural extension leading to spinal cord compression. Axial T2-weighted spin echo image (**c**) clearly depicts the paravertebral soft tissue mass (*long white arrow*) and most importantly the extent of the epidural abscess (*short black arrow*)

decreased signal intensity on T1-weighted images. In comparison to CSF, the signal intensity of an abscess is higher on T1-weighted images and lower on T2-weighted turbo spin echo sequences. The differentiation of a phlegmon from an abscess can be difficult without the application of iv-contrast. On contrast-enhanced MRI, a phlegmon demonstrates uniform, diffuse enhancement whilst an abscess reveals peripheral enhancement. The clinically vital diagnosis of an epidural abscess is made by correlating the imaging findings on unenhanced T2-weighted sequences with the contrast-enhanced T1-weighted sequences (Dagirmanjian et al. 1999; Rothman 1996; Küker et al. 1997). When reporting an epidural abscess, it is also important that the reading radiologist precisely describes the extent of the disease as an epidural abscess leading to spinal canal stenosis of more than 50% or an epidural abscess extending more than 3 cm in cranio-caudal dimension is associated with a worse prognosis (Rodiek 2001). It is important to note that an epidural abscess may also occur in the absence of spondylodiscitis in rare cases (Küker et al. 1997). Furthermore, spinal cord involvement is characterised by increased signal intensity within the spinal cord after contrast administration (Ozuna and Delamarter 1996).

Paravertebral phlegmons and abscesses are reliably identified on MRI. The characteristic features of an abscess are differently formed areas of high signal intensity on T2-weighted images which demonstrate rim-enhancement with a low signal intensity centre on contrast-enhanced T1-weighted imaging (Fig. 9a–c). In contrast, a phlegom demonstrates diffuse enhancement (Fig. 8a–d). MRI is the gold standard in the imaging diagnosis of primary spondylitis and spondylodiscitis (Glazer and Hu Glazer and Hu 1996; Varma et al. 2001). However, in patients after disc surgery, it may be challenging to diagnose spondylitis on MRI because differentiation of post-operative oedema and granulation tissue from a developing infection may be difficult or impossible. The difference between the two disease entities may only become gradually apparent unless an abscess formation is clearly observed. After uncomplicated discectomy only minor signal change within the disc and the adjacent endplates is usually observed on STIR and fat suppressed contrast-enhanced T1-weighted sequences. However, Modic type 1 changes (decreased signal intensity on T1-weighted sequences and high signal intensity on STIR-sequences within the subchondral region) after discectomy are well described. Furthermore, Modic type 1 signal changes could also have been present pre-operatively. Therefore, it may be impossible to differentiate Modic type 1 changes from early stages of post-operative spondylodiscitis (Boden et al. 1992; Khan et al. 1999).

Follow-up imaging of spondylodiscitis requires great expertise because the imaging findings may be misleading. Treatment responsive spondylodiscitis is characterised by a discrepancy between clinical improvement in symptoms and a deterioration of the imaging appearances on MRI as a progression in reduction of intervertebral disc height and a further height reduction of the infected vertebral body is usually observed despite successful antibiotic therapy. The first sign of healing on MR imaging is a reduction in signal intensity on fat suppressed contrast-enhanced T1-weighted imaging. In the experience of the authors, this is more commonly observed in the paravertebral soft tissues and the epidural space than in the vertebral bodies. A reduction in signal intensity is expected to be seen after a minimum of 6 weeks (Dagirmanjian et al. 1999; Glazer and Hu 1996; Gillams et al. 1996). However, increased signal intensity after contrast enhancement may even be observed months after spondylodiscitis on MR imaging in the abscence of clinically active infection (Dagirmanjian et al. 1999). In the long term, fatty conversion of previously infected bone marrow is observed. Fibrosis and sclerosis which is often parallel to the affected endplates appear low in signal intensity or demonstrate signal voids on T1- and T2-weighted imaging. Ultimately, spondylodiscitis may lead to loss of vertebral body height or vertebral body collapse, gibbus formation, vertebral body fusion and neurological deficits (Rodiek 2001).

Acknowledgments We acknowledge the help of Dr Asif Saifuddin (Consultant Musculoskeletal Radiologist at The Royal National Orthopaedic Hospital, Stanmore, UK) who provided cases for illustration.

References

Bamberger DM, Daus GP, Gerding DN (1987) Osteomyelitis in the feet of diabetic patients: long-term results, prognostic factors, and the role of antimicrobial and surgical therapy. Am J Med 83:653–660

Bitzer M, Schick F, Hartmann J, Geist-Barth B, Stern W, Krackhardt T, Seemann M, Morgalla M, Pereira P, Claussen CD (2002) MRT-Darstellung intraossärer Sequester und Fistelsysteme bei chronischer Osteomyelitis durch Standardsequenzen, hochselektive chemical-shift-Bildgebung, Diffusionsgewichtung and Magnetisierungstransfer. Fortschr Röntgenstr 174:1422–1429

Boden SD, Davis DO, Dina TS (1992) Postoperative diskitis: distinguishing early MR imaging findings from normal postoperative disk space changes. Radiology 184:765–771

Bohndorf K (1996) Bildgebende Diagnostik der akuten and chronischen Osteomyelitis. Radiologe 36:786–794

Borgström PS, Ekberg O, Lasson A (1988) Radiography of pressure ulcers. Acta Radiol 29:581–584

Boutin RD, Brossmann J, Sartoris DJ, Reilly D, Resnick D (1998) Update on imaging of orthopaeic infections. Orthop Clin North Am 29:41–66

Calderone RR, Larsen JM (1996) Overview and classification of spinal infections. Orthop Clin North Am 27:1–8

Craig JG, Amin MB, Wu K, Eyler WR, van Holsbeeck MT, Bouffard JA, Shirazi K (1997) Osteomyelitis of the diabetic foot: MR imaging-pathologic correlation. Radiology 203: 849–855

Dagirmanjian A, Schils J, McHenry MC (1999) MR imaging of spinal infections. Magn Reson Imaging Clin N Am 7: 525–538

Dagirmanjian A, Schils J, McHenry M, Modic MT (1996) MR Imaging of vertebral osteomyelitis revisited. Am J Roentegnol 167:1539–1543

Delling G (1997) Skelettsystem. In: Pathologie, Bd. 5. Remmele W (Hrsg.) Springer, Berlin S. 297–304

Donovan A, Schweitzer ME (2010) Use of MR imaging in diagnosing diabetes-related pedal osteomyelitis. Radiographics 30(3):723–736

Epps CH Jr, Bryant DD 3rd, Coles MJ, Castro O (1991) Osteomyelitis in patients who have sickle-cell disease: Diagnosis and management. J Bone Joint Surg 73A: 1281–1294

Gillams AR, Chaddha B, Carter AP (1996) MR appearances of the temporal evolution and resolution of infectious spondylitis. Am J Roentgenol 166:903–907

Glazer PA, Hu SS (1996) Pediatric spinal infections. Orthop Clin North Am 27:111–123

Graif M, Schweitzer ME, Deely D, Mattencci T (1999) The septic versus nonseptic inflamed joint. Skeletal Radiol 28:616–620

Grey AC, Davies AM, Mangham DC, Grimer RJ, Ritchie DA (1998) The 'penumbra sign' on T1-weighted MR imaging in subacute osteomyelitis: Frequency, cause and significance. Clin Radiol 53(8):587–592

Haas DW, McAndrew MP (1996) Bacterial osteomyelitis in adults: evolving considerations in diagnosis and treatment. Am J Med 101:550–561

Harish S, Chiavaras MM, Kotnis N, REbello R (2011) MR imaging of skeletal soft tissue infection: utility of diffusion-weighted imaging in detecting abscess formation. Skeletal Radiol 40(3):285–294

Hopkins KL, Li KC, Bergman G (1995) Gadolinium-DTPA-enhanced magnetic resonance imaging of musculoskeletal infectious processes. Skeletal Radiol 24(5):325–330

Horowitz SH (1993) Diabetic neuropathy. Clin Orthop 296: 78–85

Jinkins JR, Bazan C 3rd, Xiong L (1996) MRI of disc protrusion engendered by infectious spondylitis. J Comp Assist Tomogr 20:715–718

Jones KM, Unger EC, Granstrom P, Seeger JF, Carmody RF, Yoshino M (1992) Bone marrow imaging using STIR at 0.5 and 1.5T. Magn Reson Imaging 10(2):169–176

Kaim A, Ledermann HP, Bongartz G, Messmer P, Mueller-Brand J, Steinbrich W (2000) Chronic posttraumatic osteomyelitis of the lower extremity: comparison of

magnetic resonance imaging and combined bone scintigraphy/immunoscintrigraphy with radiolabelled monoclonal antigranulocyte antibodies. Skeletal Radiol 29:378–386
Kaim AH, Gross T, von Schulthess GK (2002) Imaging of chronic posttraumatic osteomyelitis. Eur Radiol 12: 1193–1202
Kan JH, Young RS, Yu C, Hernanz-Schulman M (2010) Clinical impact of gadolinium in the MRI diagnosis of msuculoskeletal infection in children. Pediatr Radiol 40(7): 1197–1205
Khan IA, Vaccaro AR, Zlotolow DA (1999) DA Management of vertebral diskitis and osteomyelitis. Orthopedics 22: 758–765
Khoo MM, Tyler PA, Saifuddin A, Padhani AR (2011) Diffusion-weighted imaging (DWI) in musculoskeletal MRI: a critical review. Skeletal Radiol 40(6):665–681
Kornaat PR, Cerlinck M, Vanhoenacker FM, De Praeter G, Kroon HM (2010) Brodie's abscess revisited. JBR-BTR 93(2):81–86
Küker W, Mull M, Mayfrank L, Topper R, Thron A (1997) Epidural spinal infection; variability of clinical and magnetic resonance imaging findings. Spine 22:544–551
Ledermann HP, Kaim A, Bongartz G, Steinbrich W (2000) Pitfalls and limitations of magnetic resonance imaging in chronic posttraumatic osteomyelitis. Eur Radiol 10:1815–1823
Ledermann HP, Morrison WB, Schweitzer ME (2002) Pedal abscesses in patients suspected of having pedal osteomyelitis: Analysis with MR imaging. Radiology 224:649–655
Milgram JW (1993) Osteomyelitis of the foot and ankle associated with diabetes mellitus. Clin Orthop 296:50–57
Miller TT, Randolph DA Jr, Staron RB, Feldman F, Cushin S (1997) Fat-suppressed MRI of the musculoskeletal infection: Fast T2-weighted techniques versus gadolinium-enhanced T1-weighted images. Skeletal Radiol 26:654–658
Moore SL, Rafii M (2001) Imaging of musculoskeletal and spinal tuberculosis. Radiol Clin North Am 39:329–342
Moorthy S, Prabhu NK (2002) Spectrum of MR imaging findings in spinal tuberculosis. Am J Roentgenol 179: 979–983
Morrison WB, Schweitzer ME, Bock GW, Mitchell DG, Hume EL, Pathria MN, Resnick D (1993) Diagnosis of osteomyelitis: utility of fat-suppressed contrast-enhanced MR imaging. Radiology 189(1):251–257
Munoz P, Bouza E (1999) Acute and chronic adult osteomyelitis and prothesis-related infections. Baillières Best Pract Res Clin Rheumatol 13(1):129–147
Nelson JD (1990) Acute osteomyelitis in children. Infect Dis Clin North Am 4(3):513–522
Newman LG, Waller J, Palestro CJ, Schwartz M, Klein MJ, Herrmann G, Harrington E, Harrington M, Roman SH (1991) Unsuspected osteomyelitis and diabetic foot ulcers. Diagnosis and monitoring by leukocyte scanning with indium-111 oxyquinoline. JAMA 266:1246–1251
Ozuna RM, Delamarter RB (1996) Pyogenic vertebral osteomyelitis and postsurgical disc space infections. Orthop Clin North Am 27:87–94
Rodiek SO (2001) Bildgebende Verfahren bei spinalen Infektionen. Radiologe 41:976–986
Rothman SL (1996) The diagnosis of infections of the spine by modern imaging techniques. Orthop Clin North Am 27:15–31
Sapico FL (1996) Microbiology and antimicrobial therapy of spinal infections. Orthop Clin North Am 27:9–13
Staubach KH, Bruch HP, Sobach W (2000) Osteomyelitis. In: von Mare R, Mertens T, Trautmann M, Vanek E (Hrgs) Klinische Infektiologie, Urban and Fischer, München, pp 494–499
Toledano TR, Fatone EA, Weis A, Cotton A, Beltran J (2011) MRI evaluation of bone marrow changes in the diabetic foot: a practical approach. Semin Musculoskelet Radiol. 15(3):257–268
Unal O, Koparan HI, Avcu S, Kalender AM, Kisli E (2011) The diagnostic value of diffusion-weighted magnetic resonance imaging in soft tissue abscesses. Eur J Radiol 77(3): 490–494
Vaccaro A, Shah SH, Schweitzer ME, Rosenfeld JF, Cotler JM (1999) MRI description of vertebral osteomyelitis, neoplasm, and compression fracture. Orthopedics 22:67–73
Varma R, Lander P, Assaf A (2001) Imaging of pyogenic infectious spondylodiskitis. Radiol Clin North Am 39: 203–213
Weinstein D, Wang A, Chambers R, Stuart CA, Motz HA (1993) Evaluation of magnetic resonance imaging in the diagnosis of osteomyelitis in diabetic foot infections. Foot Ankle 14:18–22
Wunsch R, Darge K, Rohrschneider W, Zieger B, Troger J (2001) Akute hämatogene Osteomyelitis – Ausschluss mit Turbo-STIR-Sequenz? Radiologe 41(5):439–441

Non-Infective Inflammatory Bone Marrow Disease

Bernhard J. Tins and Victor N. Cassar-Pullicino

Contents

Abstract

Non-infective inflammatory bone marrow disease comprises a wide variety of disorders. This chapter aims to review the current thought on the pathophysiology of inflammatory arthropathies in particular and to investigate the role of the various imaging modalities in diagnosis and follow-up. Special emphasis will be given to MR imaging as the modality best suited to assess bone marrow changes. The main imaging features and differential diagnosis of the inflammatory arthropathies will be discussed in more detail with emphasis on ankylosing spondylitis, SAPHO and Psoriasis. MRI is the modality best suited to imaging inflammatory bone marrow change. With time secondary bone changes become visible in CT and radiographic imaging and these might be the first examinations to suggest a particular pathology which was hitherto clinically not suspected/diagnosed. For this reason CT and radiographic features of non-infective inflammatory bone marrow disease will also be briefly reviewed.

1 Introduction

This chapter aims to review the most relevant conditions associated with inflammatory bone marrow changes which have not been discussed in the other chapters. Inflammatory bone marrow lesions are difficult to diagnose clinically. The classic combination of rubor, calor, dolor and tumor indicating inflammation is not found if the underlying process is limited to the intraosseous space. The presence of

B. J. Tins (✉) · V. N. Cassar-Pullicino
Department of Radiology,
Robert Jones and Agnes Hunt Orthopaedic Hospital,
Oswestry SY10 7AG, Shropshire, UK
e-mail: Bernhard.Tins@rjah.nhs.uk

A. Baur-Melnyk (ed.), *Magnetic Resonance Imaging of the Bone Marrow*, Medical Radiology. Diagnostic Imaging,
DOI: 10.1007/174_2012_575, © Springer-Verlag Berlin Heidelberg 2013

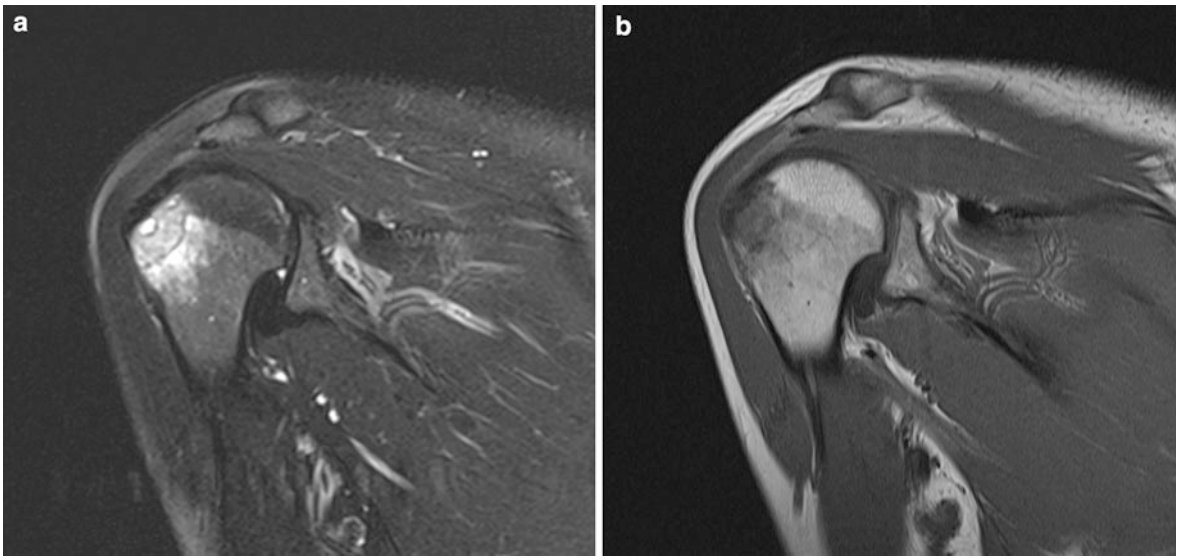

Fig. 1 A 47-year-old female with shoulder pain. Radiographs had shown calcific tendonitis. MRI demonstrates marked inflammatory change with bone marrow oedema-like signal (**a** T2 fatsat, **b** T1w). Crystal deposition can cause severe inflammatory bone reaction and pain. Plain film correlation can be extremely helpful

unexplained pain might be the only indicator of an underlying problem and triggering further examination. However, if paraosseous structures are involved, joint inflammation with synovitis or effusion, enthesitis and paraosseous soft tissue inflammation might be present.

Imagingwise a simple approach to inflammatory bone marrow lesions is to look at conditions leading to increased fluid signal in the bone marrow. This is the case for a host of often very different conditions. The underlying pathophysiology and typical imaging findings and the role of different imaging modalities are reviewed.

2 Pathophysiology

The term inflammatory bone marrow lesion is ambiguous. It might be reserved for lesions, where the underlying disease is primary inflammatory such as an inflammatory spondylarthropathy or rheumatoid arthritis. Secondary inflammatory findings can for example be seen in primary degenerative joint disease or crystal arthropathies, where inflammation is secondary to the presence of metabolites or crystals in bone marrow (Fig. 1).

Histologically the inflammatory bone marrow changes have often surprisingly minor distinguishing features despite very different underlying pathologies.

Previously it was thought that the presence of decreased MRI signal in T1-weighted and increased signal in STIR or T2-fat saturation (fatsat) sequences indicates the presence of bone marrow oedema. However, true bone marrow oedema, that is, the presence of an abnormally increased amount of fluid in tissue interstitium, is minor in most conditions so labelled based on the MRI findings. True bone marrow oedema (Fig. 2) is thought to be due to the release of cytokines especially tumor necrosis factor (TNF) alpha, interleukines, prostaglandin (espc PGE2) and leukotrienes. These mediators are thought to be the reason for the presence of true bone marrow oedema associated with bone tumors such as chondroblastoma, osteoid osteoma (Fig. 3) and Langerhans histiocytosis.

In primary inflammatory conditions histologically there are inflammatory cells infiltrates with macrophages and lymphocytes and somewhat disordered proliferation of vascular and connective tissue rather than interstitial oedema (Fig. 4). While histological differences between different primary inflammatory disorders have been reported, imaging is currently not able to definitely distinguish between these (Blum et al. 2009; Jimenez-Boj et al. 2007; McGonagle et al. 2002).

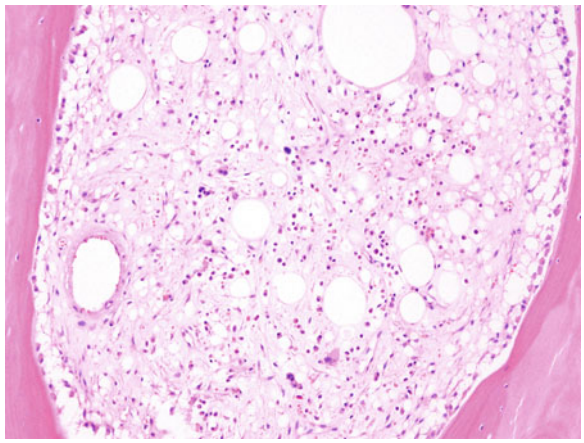

Fig. 2 Marked oedematous bone marrow change (indicated by *pink* staining of proteinaceous material) with mild reactive fibroplasia and the formation of a reactive osteoblastic rim of new bone. Some residual normal bone marrow. (Image courtesy of Dr. Mangham)

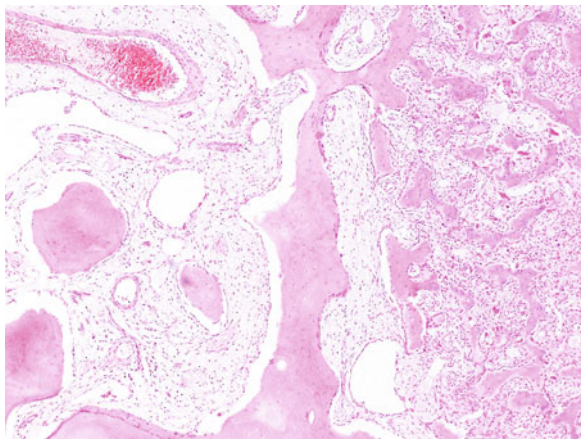

Fig. 3 Osteoid osteoma occupying the right one-third of the image. Centrally prominent bone bar, reactive bone change. Unspecific marrow change in the remaining marrow space (*left half* of the picture) with lose fibrovascular tissue replacing normal bone marrow. (Image courtesy of Dr. Mangham)

Increased water-like signal as seen in many other, not primary inflammatory conditions such as infection, trauma/microtrauma, with intraosseous disc herniations, osteoarthritis (OA), complex regional pain syndrome (CRP), osteonecrosis, metabolic disorders and tendinopathies is more due to proliferation of fibrovascular tissue and inflammatory cell infiltrates. Therefore, in most of the cases commonly called 'bone marrow oedema' it would be more accurate to talk of osteitis. (Blum et al. 2009; Zanetti et al. 2000; Taljanovic et al. 2008; Steinbach and Suh 2011; Narvaez et al. 2010).

Strictly speaking inflammatory bone marrow changes and osteitis are not the same. Bone marrow fills the space between bone trabeculae and true bone involvement is not obligatory in conditions affecting primarily the bone marrow. However, inflammatory processes in the bone marrow will secondarily involve/affect the adjacent bone trabeculae and vice versa conditions primarily affecting the bone trabeculae will secondarily involve/affect the bone marrow space.

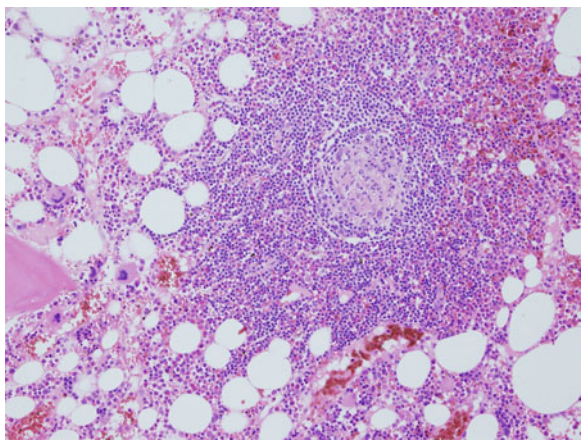

Fig. 4 Lymphoid aggregate with germinal centre formation. This is an unspecific finding seen not only in a variety of inflammatory disorders but also after any severe systemic illness, chemotherapy and at the edge of focal bone lesions. (Image courtesy of Dr. Mangham)

3 Imaging Modalities

MRI is the best tool for the imaging of inflammatory bone marrow disease. MRI can image bone marrow directly, it offers fairly high anatomical resolution and images most relevant pathologies. For many applications and clinical questions straightforward T1-weighted and water-sensitive sequences such as a short tau inversion recovery (STIR) or T2-fat saturation will be sufficient. STIR sequences have the advantage of robust suppression of fat signal. It has the disadvantage of a sometimes unpredictable signal pattern in the imaging of complex collections and after contrast medium enhancement. T2- fatsat sequences are sensitive to field inhomogeneities

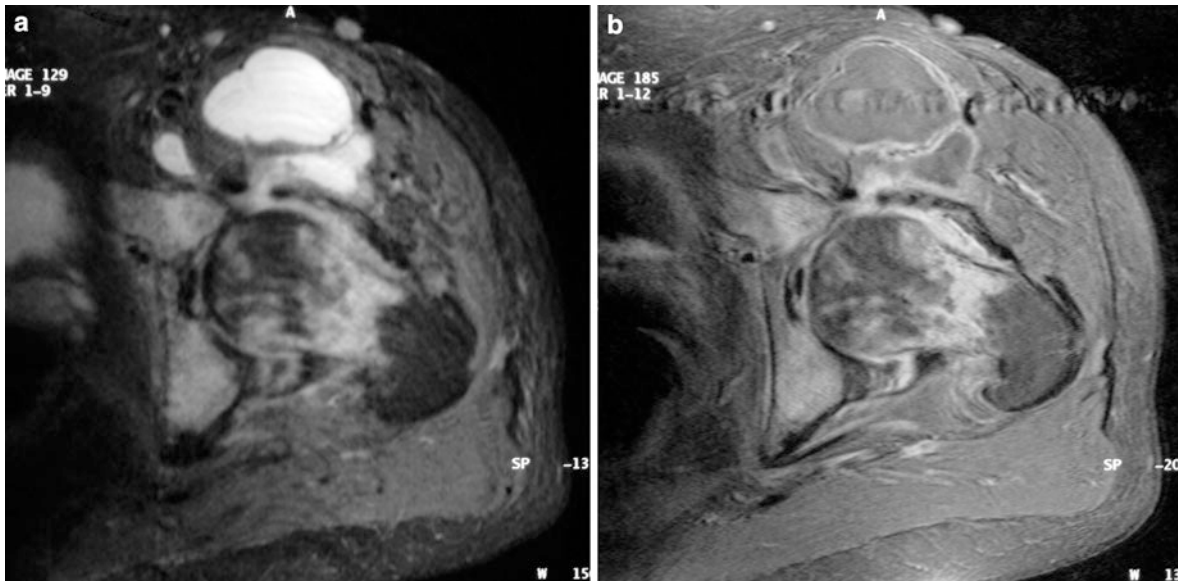

Fig. 5 A 54-year-old man with known psoriatic arthropathy. MRI shows inflammatory bone marrow changes with oedema-like signal in STIR (**a**) and contrast medium enhancement in corresponding T1-FS images (**b**) exactly mirroring the oedema-like signal. The signal change is mainly due to inflammatory infiltrates rather than true oedema. Psoriasis can lead to marked inflammatory joint changes. Contrast medium administration can distinguish fluid from inflamed tissue (synovium) and can indicate the extent of acute inflammation

resulting in incomplete or absent fat suppression. In and opposed phase imaging is not suitable for homogenous fat suppression (Delfaut et al. 1999). Dixon sequences have been suggested for the use in the diagnosis of inflammatory bone marrow changes, as they assess the water and fat content of an area of interest, (Blum et al. 2009; Delfaut et al. 1999) but their clinical usage is currently limited.

For subtle changes or difficult scenarios contrast medium enhancement (dynamic or static) and diffusion weighted imaging (DWI) might be helpful.

Contrast medium enhancement can be used to diagnose inflammation (Fig. 5). Dynamic contrast enhancement can differentiate inflammatory lesions from the normal contrast medium enhancement of normally perfused tissue. Some authors believe that contrast medium-enhanced MRI and possibly DWI are more sensitive for inflammatory bone marrow changes than conventional T1-w or STIR or T2-fat saturation (T2-FS) sequences (Bozgeyik et al. 2008; Gaspersic et al. 2008; Bredella et al. 2006; Bollow et al. 2000). However, this is not universally accepted. Baraliakos et al. compared the diagnostic performance of STIR and contrast medium-enhanced (CE) T1-FS sequences and found no major differences, STIR showed more lesions, the CE T1-FS images showed better intra- and interobserver reliability (Baraliakos et al. 2005). CE T1 imaging allows for easier differentiation between synovitis and fluid than STIR (Rudwaleit et al. 2009). Recently it has been stressed that the use of set diagnostic criteria and validated training is more relevant than the application of contrast medium enhancement (Weber et al. 2010). The use of contrast medium adds time and cost to the examination and turns a zero risk examination (if contraindications are adhered to) into an invasive and potentially harmful examination (contrast medium reactions and nephrogenic systemic fibrosis) (Baraliakos et al. 2005; Maksymowych and Weber 2011; Madsen et al. 2010; Colbert 2010).

Contrast medium enhancement can be used to assess the treatment response after drug treatment. Enhancement curves and ratios can be calculated; response quantification is important particularly in drug trials. It has been shown that the amount of contrast medium enhancement correlates to disease activity in inflammatory arthropathies (Narvaez et al. 2010; Bozgeyik et al. 2008; Gaspersic et al. 2008; Bollow et al. 2000).

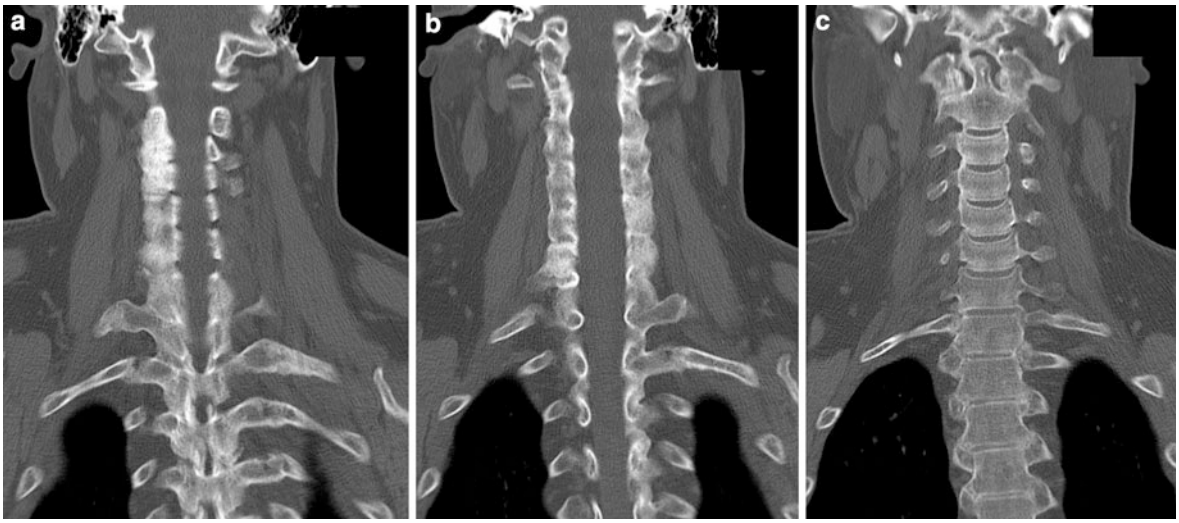

Fig. 6 A 25-year-old male with known spondyloarthropathy. Coronal reformats of a CT of the cervical and upper thoracic spine show fusion of the costovertebral and costotransverse joints (**a**). There is also fusion of the facet joints (**b**) and ossification of the atlantoaxial ligaments (**c**). Ankylosis of the spine is a serious ailment associated with respiratory impairment

The role of whole-body MRI for inflammatory arthropathies is as yet not clear. While it will detect more lesions in many cases, the impact on diagnosis or treatment is as yet not determined though this technique is currently being evaluated in clinical studies (Maksymowych and Weber 2011; Song et al. 2011a, b). Weber and colleagues in a series of 32 patients have, however, shown that the diagnostic performance of a whole-body imaging MRI protocol and a dedicated protocol for assessment of the SIJs are comparable even-though the whole-body imaging protocol offers less spatial resolution (Weber et al. 2009).

The use of (ultrasmall) superparamagnetic iron oxide particles ((U)SPIO)-containing contrast medium has been suggested for imaging of inflammatory bone marrow lesions. Macrophages take up SPIO and this should allow for the differentiation of those lesions containing macrophages and those not (Blum et al. 2009; Kotoura et al. 2011; Bierry et al. 2009). This is not a technique established for routine clinical use.

Radiographs and CT cannot image inflammatory bone marrow lesions directly. They might be able to identify secondary bone changes associated with the underlying pathology, but this can take a long time to become visible and does not assess the bone marrow as such (Fig. 6). It has been suggested that it can take up to 2–5–10 years until sacroiliitis becomes radiographically visible. MRI demonstrates significantly more erosions when compared to radiographs particularly in the early disease stages (Narvaez et al. 2010; Bozgeyik et al. 2008; Weber et al. 2010). CT is quite sensitive for secondary bone changes such as erosion, destruction, periosteal reaction, osteopenia, sclerosis and to an extent fatty bone marrow change. CT mostly appears normal when MRI shows inflammatory bone marrow changes before significant bone reaction has occurred. CT does not offer information on current disease activity (Fig. 7).

Nuclear medicine techniques can show inflammation (increased vascularity) and increased bone turnover. The anatomical resolution is not great but it is a genuine whole-body imaging technique. The standard technetium isotope examination can be combined with single photon emission computer tomography (SPECT) to increase the anatomical resolution.

To assess sacroiliitis, activity ratios can be determined. However, a review of the literature by Song and colleagues from 2008 found sensitivities of bone scintigraphy for sacroiliitis in the low 50% and concluded that bone scintigraphy is a poor tool to assess sacroiliitis in ankylosing spondylitis (Song et al. 2008). The combination of bone scintigraphy with bone marrow imaging has been described. However, there is doubt as to its usefulness (Yildiz et al. 2001).

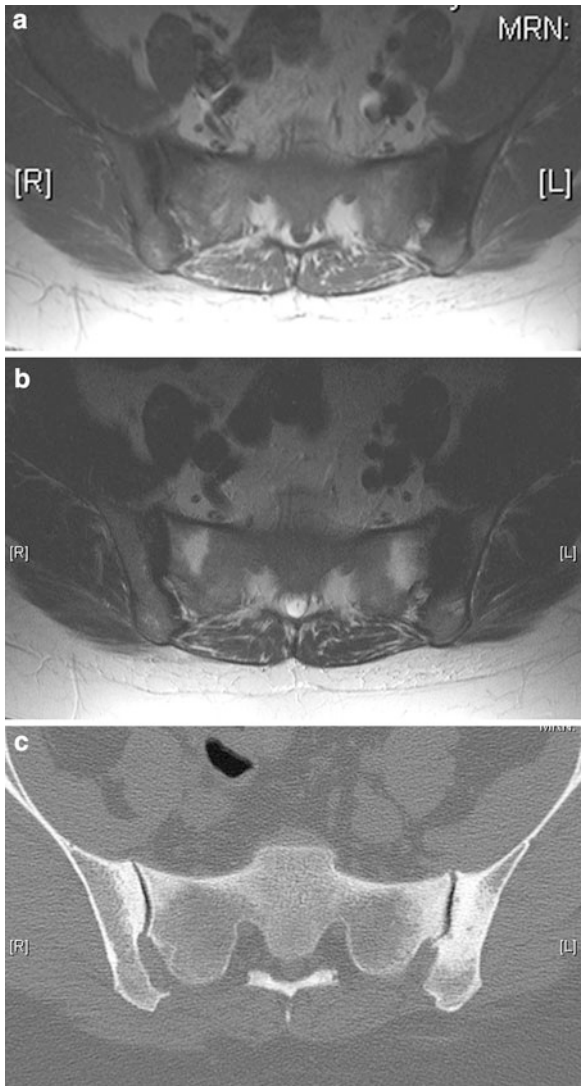

Fig. 7 A 47-year-old female with chronic low back pain. On the MRI of the lumbar spine incidental findings of marked acute on chronic sacroiliitis (**a** axial T1w image, **b** axial T2w image), the remainder of the imaged spine was almost normal. Axial (**c**) reformats of a CT of the SIJs confirm chronic sclerotic changes, the acute oedema-like changes as seen on the MRI are not appreciated. Minimal erosion on the CT images

More recently a pilot study by Roimicher and co-workers using Tc99 labelled anti-TNF alpha antibodies showed promising sensitivity (98.8%) and specificity (97.3%) when compared to MRI in 8 patients, looking at 198 joints, 49 of which showed inflammation (Roimicher et al. 2011). Clinical assessment only reached a sensitivity of 59% and specificity of 65% when compared with MRI.

PET-CT can be used for the diagnosis of inflammatory lesions such as sacroiliitis (Strobel et al. 2010) but the limited availability, cost and radiation dose restrict this to scientific interest.

Bone scintigraphy can be useful for disorders affecting potentially the whole body. It is particularly valuable in conditions with a strong bone reaction to the disease, and therefore in particular in conditions with osteitis such as Paget's disease and SAPHO. In clinically difficult to diagnose disease such as SAPHO, the bone scan can be almost pathognomonic if showing the classic bull's head sign (Depasquale et al. 2012). In Paget's disease the isotope bone scan can add prognostic and diagnostic information (Haddaway et al. 2007; Vellenga et al. 1984).

Ultrasound can be used in the assessment of inflammatory disorders. It can diagnose soft tissue inflammation and superficial bone lesions. However, it is unsuitable for the assessment of bone marrow.

4 Disease Entities

Organising disease entities with inflammatory bone marrow changes in a logical manner is not straightforward. One might organise them according to the underlying pathophysiological problem. This is not easy when the exact mechanism of disease is incompletely understood as is the case for primary inflammatory arthropathies. One might choose to organise them according to their main clinical presentation, i.e. synovitis, enthesitis or osteitis (Fig. 8). This is also unsatisfactory as there is considerable overlap and very disparate conditions are grouped together. However, the potential advantage of this approach is that it may be easier to establish the (differential) diagnosis based on imaging appearance. The disadvantage is the often marked overlap of imaging appearances in many diseases and that it is now believed that clinical manifestations such as synovitis in rheumatoid arthritis may be avoidable if the underlying disease is diagnosed and treated early enough.

Synovitis is a prominent feature in rheumatoid arthritis and related disorders, and is also seen in mechanical osteoarthritis, in crystal induced arthropathies and metabolic disorders such as in amyloid-induced arthropathy.

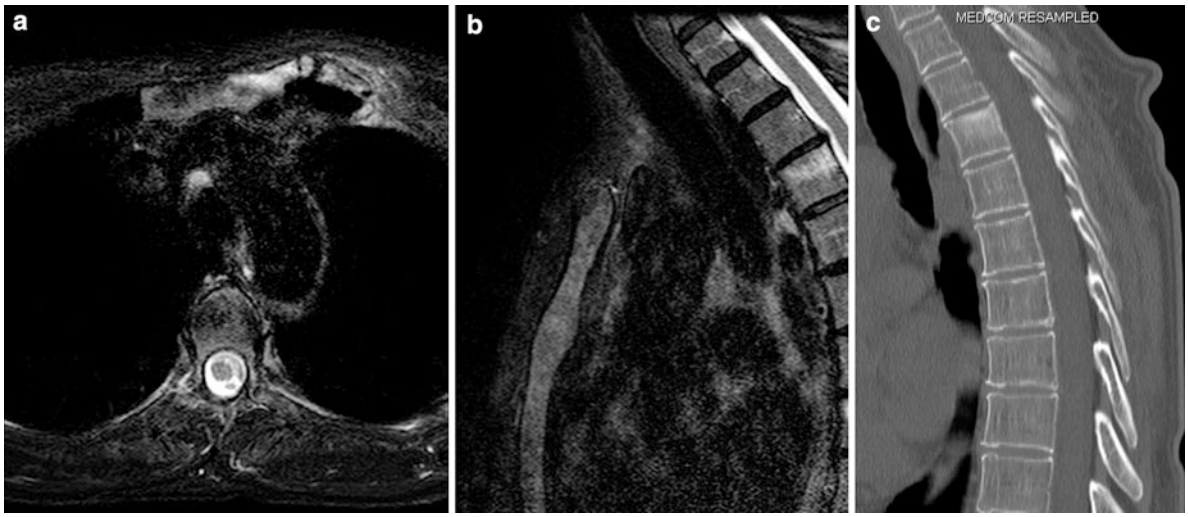

Fig. 8 A 57-year-old woman presenting with sternal pain and swelling. MRI demonstrates inflammation of the left first sternocostal joint best appreciated on the STIR images (**a** axial). Incidental finding of clinically asymptomatic inflammatory change in the upper thoracic spine at T4 indicating multifocal disease (**b** sag STIR). Distribution (in particular involvement of the sternum) and presentation suggest SAPHO. One year later T4 vertebral body demonstrates marked sclerosis on CT (**c** sagittal reformat) supporting the diagnosis of SAPHO. The primary pathological process in SAPHO is probably osteitis; bone marrow inflammation is secondary

Enthesitis is the main presenting feature of ankylosing spondylitis and related inflammatory spondyloarthropathies and in psoriatic arthropathy though this disorder in particular also often presents with prominent synovitis. Enthesitis may also prominently be seen due to mechanical stress and based on the presentation in one site only, the differentiation to inflammatory arthropathies can be difficult.

Finally *osteitis* is seen in a mixed bag of conditions such as Paget's disease, sarcoidosis, SAPHO (which also presents with a degree of (secondary?) synovitis and enthesitis) and tumoral and drug-related osteitis.

In this chapter the disease entities are laid out according to presumed underlying pathological processes to try and appreciate some causality and similarities in the presentation. However, as mentioned before there is a great degree of overlap on clinical and pathophysiological grounds and current understanding of disease processes even as common as osteoarthritis is limited.

4.1 Primary Inflammatory Arthropathies

The umbrella term primary inflammatory arthropathy contains a variety of disorders some of which is poorly understood such as the synovitis, acne, pustulosis, hyperostosis, osteitis (SAPHO) syndrome, psoriatric arthropathy and the gamut of reactive and undifferentiated arthropathies. It also covers arthritis in collagen vascular disorders such as rheumatoid arthritis and systemic lupus erythematosus (SLE). In the spine the archetypical inflammatory spondyloarthropathy is ankylosing spondylitis.

The development of disease modifying drugs, in particular the anti-tumor necrosis factor alpha (anti-TNF alpha) drugs has led to renewed interest in the imaging of disease activity and disease response to treatment for this disorder. Early treatment with these drugs might prevent the severe destructive joint and spine changes otherwise seen. As early diagnosis and disease response monitoring are imperative for good outcomes, MRI is uniquely placed to assist with both.

Inflammatory bone marrow change is a prominent feature in all of these disorders. As discussed in the paragraph on pathophysiology, actual bone marrow oedema is only a small part of this. The signal changes are mainly due to inflammatory fibrovascular and cellular infiltrates.

In the early phase of inflammatory spondylarthropathies T cells and macrophages were found to be

the predominant cellular findings in a study of biopsies taken from inflamed SIJs by Bollow et al. (2000). Another study of biopsies of inflamed entheses in patients with inflammatory spondylarthropathies by McGonagle and colleagues found macrophages as only representatives of inflammatory cells, lymphocytes were not seen. Interestingly involvement of fibrocartilage was also not seen, previously it had been suggested that inflammatory spondylarthropathies are due to or at least associated with an autoimmune response against fibrocartilage (McGonagle et al. 2002).

In patients with rheumatoid arthritis a combination of macrophages, plasma cells, CD8 positive T cells and of B cells was found in combination with an increased number of osteoclasts. This leads to bone resorption. Synovial herniations into bone, which was traditionally believed to be the mechanism primarily responsible for bone resorption, are now largely thought to be a secondary effect of the bone resorption rather than the cause of it. Bone erosions were seen when the number of inflammatory cells exceeded 50%; was it less than 50%, osteitis without bone destruction was seen (Jimenez-Boj et al. 2007; Narvaez et al. 2010; Dalbeth et al. 2009; McQueen and Ostendorf 2006).

The inflammatory bone marrow lesions in primary inflammatory disorders have a typical distribution which can help to identify the underlying disorder. As discussed, inflammatory spondyloarthropathies with ankylosing spondylitis its archetype are characterised by enthesitis, be it of muscle insertion, tendon or ligament. Rheumatoid arthritis and related diseases are primarily characterised by synovitis. Psoriatric arthropathy occupies a curious position between these archetypes with features of both, enthesitis- and synovial-based arthritis (Narvaez et al. 2010; Berthelot 2003).

4.1.1 Ankylosing Spondylitis

4.1.1.1 Diagnosis and MR Imaging

Ankylosing spondylitis (AS) typically involves the axial skeleton in particular. There is usually symmetrical involvement of the SIJs which can affect the synovial as well as the non-synovial part of the joint (Fig. 7). It might affect the non-synovial part of the SIJs first/exclusively underlining that the underlying disease process is not synovial based.

Ankylosing spondylitis usually but not always begins in the SIJs. In rare cases it can primarily affect the spine proper. In most cases AS extends to the spine at a later date (Figs. 9, 10).

Classically the diagnosis of ankylosing spondylitis was based on clinical criteria. With time, radiographic criteria were incorporated in diagnostic criteria. MRI with its ability to demonstrate bone marrow oedema such as oedema like change, synovitis, erosions and sclerosis is considered the imaging modality of choice and has become an important part of newer diagnostic criteria. The Assessment of SpondylArthritis international Society (ASAS) has published a guide for the assessment of spondylarthritis which reviews the various classifications and criteria. It is freely available on the internet and regularly updated (http://www.asas-group.org). A print version has also been published (Sieper et al. 2009). A summary of the MRI findings required to diagnose sacroiliitis according to the ASAS criteria is paraphrased as follows:

MRI findings required to diagnose sacroiliitis according to ASAS:

Active inflammatory lesions of the SIJs, i.e. bone marrow oedema (as seen on STIR) or osteitis (seen on T1-w post CE images) must be clearly present in typical anatomical areas (subchondral or periarticular bone marrow oedema). A single lesion on a single slice is not sufficient for the diagnosis for sacroiliitis. The minimum criteria are two lesions seen on one slice or one lesion seen on two adjacent slices. The presence of synovitis, enthesitis or capsulitis on their own are not sufficient to diagnose sacroiliitis on MRI. Structural changes such as fat deposition, sclerosis, erosions or ankylosis are likely to be sequelae of previous inflammation; however, in the absence of acute changes they are not diagnostic of sacroiliitis (Rudwaleit et al. 2009; Sieper et al. 2009).

Whether coronal oblique T1w and STIR images are sufficient for the diagnosis or whether axial or contrast medium enhanced images should be obtained is subject to debate (Bozgeyik et al. 2008; Gaspersic et al. 2008; Bredella et al. 2006; Rudwaleit et al. 2009; Weber et al. 2010; Maksymowych and Weber 2011; Madsen et al. 2010; Colbert 2010). Inflammatory bone marrow changes are often seen at ligament and muscle insertions as enthesopathies (Fig. 9). In the earliest stage of disease there is inflammation which on MRI manifests as contrast medium enhancement

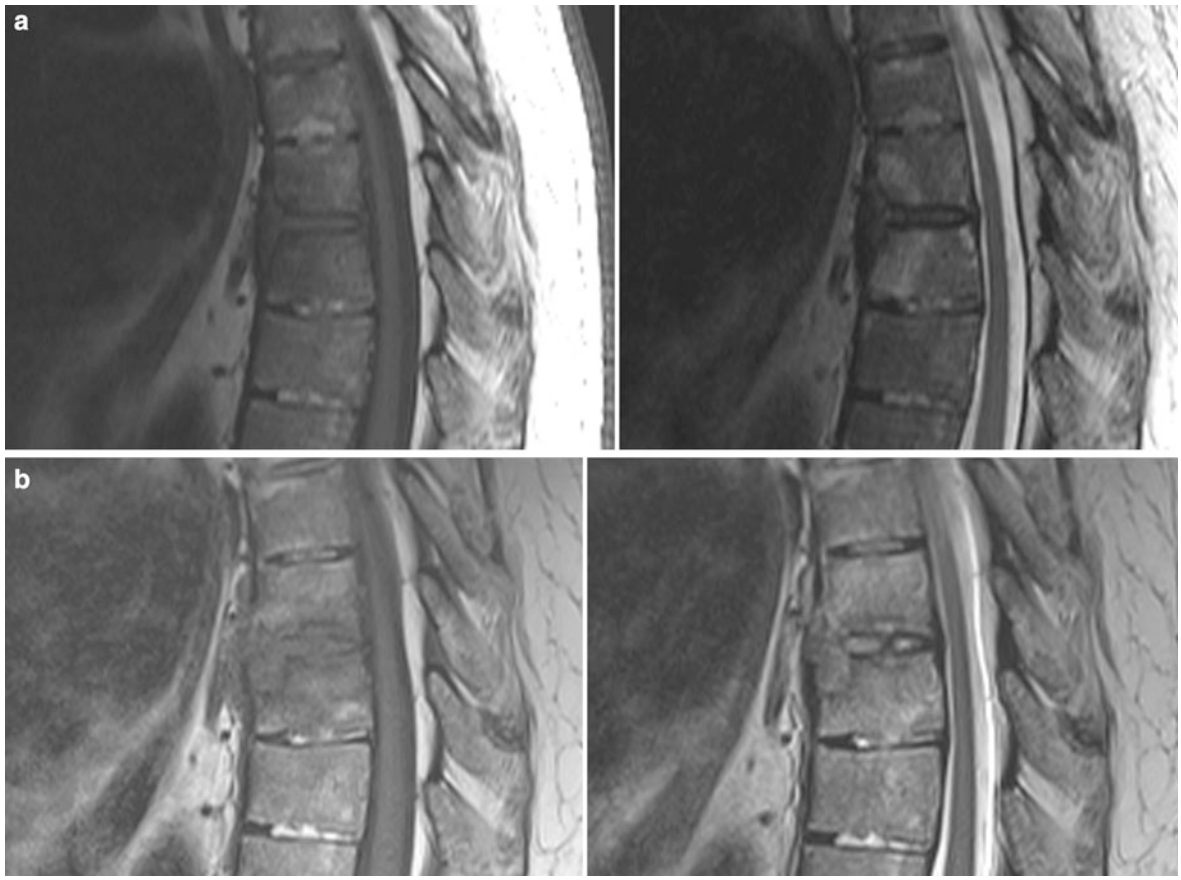

Fig. 9 A 55-year-old man with ankylosing spondylitis. Inflammatory erosive changes at the T8/9 level ventrally at the insertion of the anterior longitudinal ligament (**a** *left* T1w, *right* T2w). Two years later (**b** *left* T1w, *right* T2w) still progression of inflammation and destructive erosion. Beginning ankylosis of the intervertebral disc suggested on the T2w image

and increased water signal (increased STIR/T2 FS and decreased T1w signal). This is often followed by bone erosion. This can proceed to joint destruction or heal with fatty bone marrow change and often with productive bone change. This can have the shape of enthesophyte formation and can lead to ankylosis. It has been suggested that the apparent "fatty healing" is a necessary step before syndesmophyte formation can occur and therefore is not a finding without relevance (Song et al. 2011). Squaring of vertebral bodies and syndesmophyte formation is seen better radiographically than with MR imaging (Madsen and Jurik 2010; Horger et al. 2010).

In more severe cases of ankylosing spondylitis there is often involvement of vertebral body endplates (Figs. 9, 10) and of synovial joints, spinal and non-spinal. Spinal involvement is seen in costovertebral, costotransverse and uncovertebral joints (Appel et al. 2006). For this reason it has been advised to include the more lateral aspect of the thoracic spine on sagittal imaging (Rennie et al. 2009). The use of 3D sequences for spinal imaging has also been found useful and can assist in the assessment of these areas (Tins et al. 2012). Non-spinal involvement can be seen virtually in any joint. Non-spinal entheseal involvement is often apparent in the entheses of large structures such as the Achilles tendon insertion or the patella tendon or plantar fascia origin. In particular, in the younger patient large joints are often directly involved and show inflammatory change with bone marrow oedema, joint synovitis and effusion leading to joint destruction. This affects mainly the large joints such as shoulders, hips and knees (McGonagle et al. 2002; Horger et al. 2010).

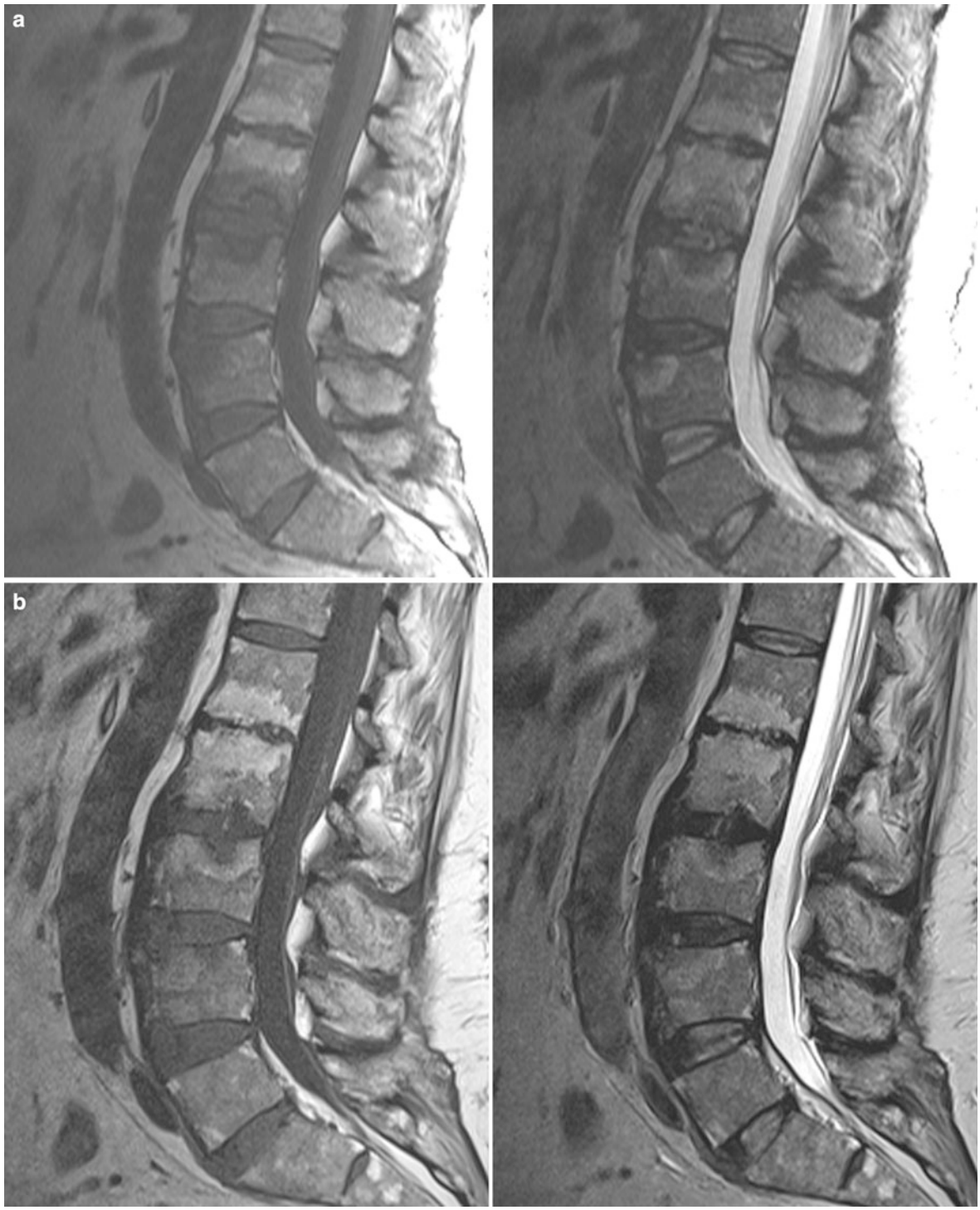

Fig. 10 A 55-year-old man with ankylosing spondylitis (same case as in Fig. 9). In the lumbar spine there are fatty endplate changes at the L1/2 level (**a** *left* T1w, *right* T2w). At L2/3 inflammatory endplate changes (Anderson lesion) and inflammatory changes at the vertebral body edges below. Two years later (**b** *left* T1w, *right* T2w) the endplate lesions at the L2/3 level have settled down. At the L4 vertebra the inferior anterior vertebral edge shows progression of inflammatory change. Ankylosing spondylitis affects primarily entheses and with this vertebral body edges and endplates. The presence of lesions in various disease stages at any given time is typical for this disease

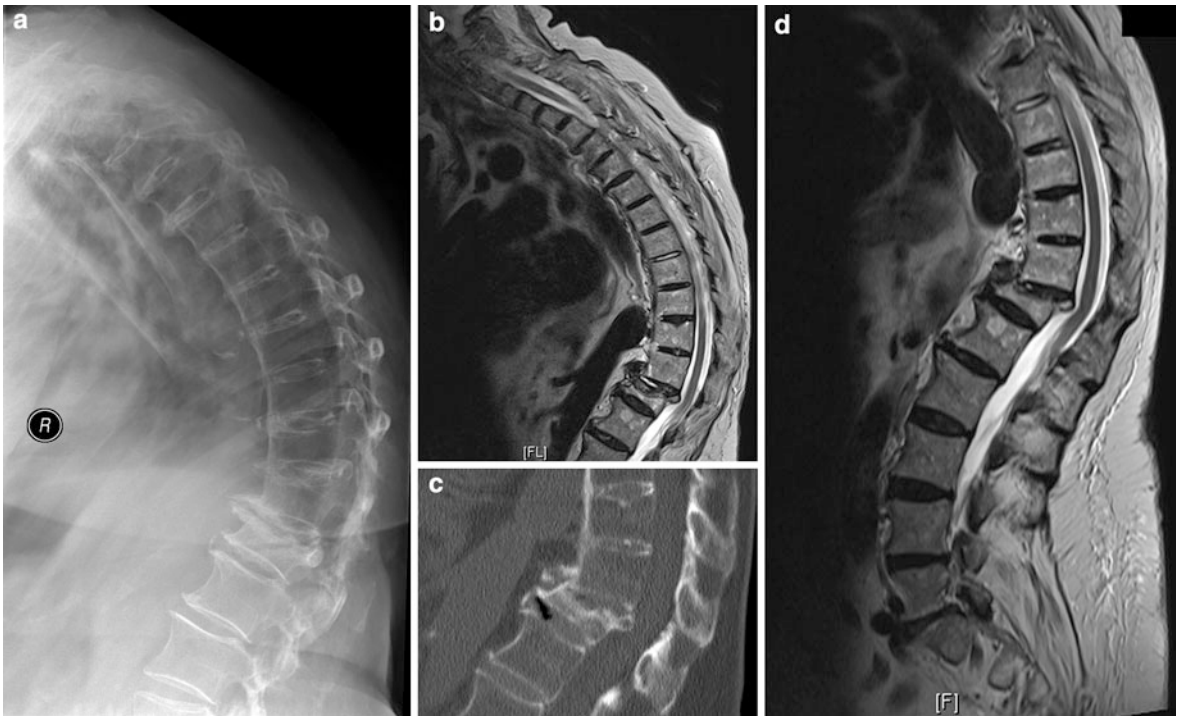

Fig. 11 A 78-year-old female with known ankylosing spondylitis. Persistent increased back pain after trauma several months earlier. A lateral radiograph (**a**) shows partial collapse of T12 vertebral body with marked endplate sclerosis adjacent to the T11/12 disc and in the adjacent posterior elements. MRI one month later (sag T2w, **b**) demonstrates a fluid cleft at the T11/12 level indicating persistent mobility here. The ankylosis is harder to appreciate compared with the radiograph. CT further eight months later shows beginning of the consolidation of the fracture (**c**). MRI three months after this shows stabilisation (**d**). Fractures in ankylosing spondylitis are often slow to heal and can result in pseudoarthrosis. Spinal ankylosis in AS is much less obvious on MRI than on plain radiographs

4.1.1.2 Radiography and CT

Nowadays, MRI is the best diagnostic tool when actively looking for active inflammatory change in AS such as sacroiliitis. However, the diagnosis of AS is often suggested based on incidental findings made on radiographs and/or CT. In addition bone erosions and ankylosis are better appreciated on CT compared with MRI.

It is of note that radiographic disease presentation in the SIJs can lag by up to 10 years and more behind the clinical presentation. CT imaging is more sensitive but still insensitive for early disease. Fundamentally the CT findings are the same as for radiographs. The anatomical resolution is of course superior and more subtle changes are easier and more confidently identified. Spinal ankylosis however can be much easier to appreciate radiographically and on CT than on MRI (Fig. 11).

Radiographic/CT findings of inflammatory arthropathies include articular bone erosions, focal deossification and reactive sclerosis as well as bone changes related to tendon and ligament insertions due to enthesitis (Fig. 6).

Ankylosing spondylitis leads with time to a number of characteristic radiographic findings secondary to the underlying inflammation. These affect the SIJs as well as the spine proper. Historically acronyms have developed to describe these findings. Inflammatory bone lesions at the anterior vertebral body edge are called Romanus lesions and bone lesions in the central part of the vertebral endplate are called Andersson lesions. Over time these lesions can persist, heal completely (restitutio ad integrum) or heal with sclerotic or fatty bone change. The reactive bone and entheseal changes can lead to ankylosis of the SIJs and spine (syndesmophyte formation). Syndesmophytes are thin ossifications aligned along ligaments and the annulus fibrosus of intervertebral discs or joints such as the syndesmosis pubis. This alignment in combination with their slender appearance differentiates them from

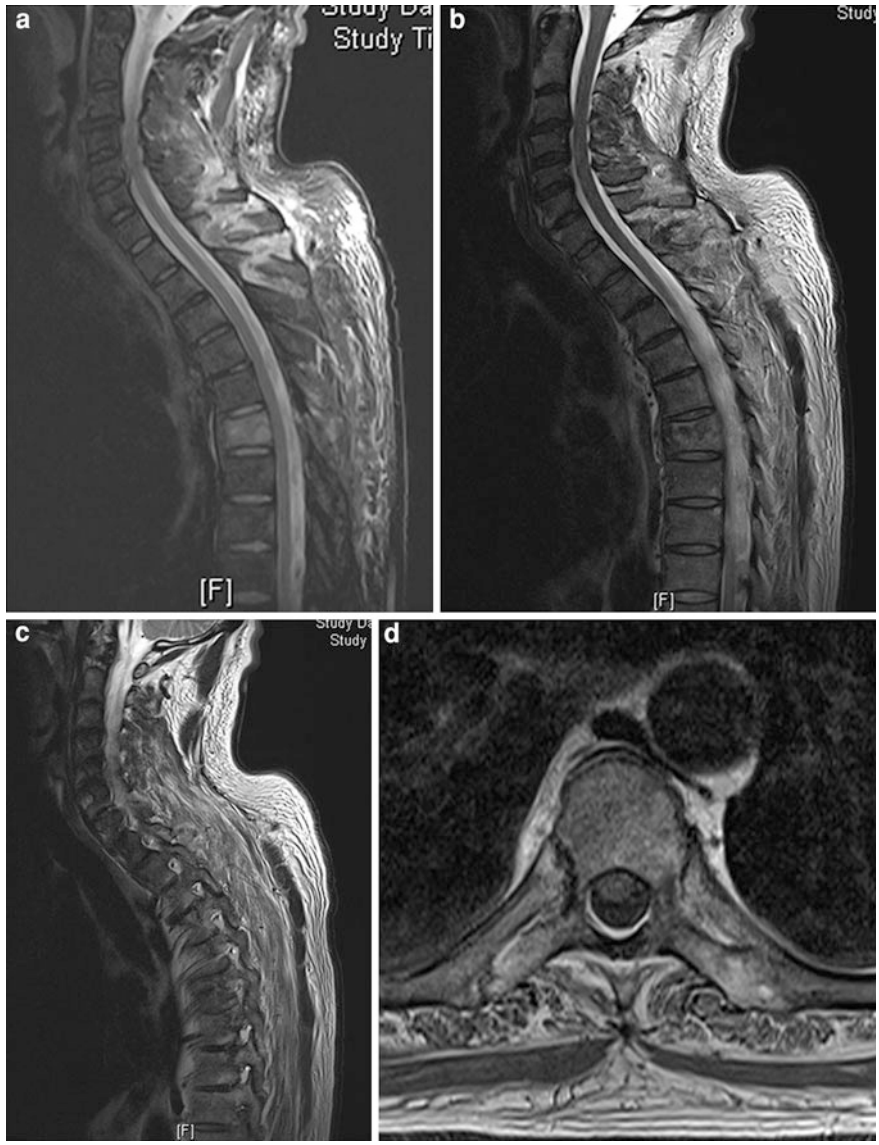

Fig. 12 A 53-year-old man with spinal injury after car accident. Sagittal MRI shows cervical and midthoracic vertebral fractures (**a** sag STIR, **b** sag T2). Parasagittal images show signal alterations at the costovertebral joints in the midthoracic spine (**c**). Axial images here (**d**, ax T1) show fusion of costovertebral and costotransverse joints. There was no ankylosis of the vertebral column. The marked bone marrow changes seen in spinal trauma can mask and distract from more subtle pre-existing signal change from an underlying abnormality (here ankylosing spondylitis). AS patients can suffer spinal injury after minor trauma. Often, as is the case here, the diagnosis of AS was not known prior to the accident and initial imaging

the coarse hypertrophic osteophytes seen in diffuse skeletal hyperostosis (DISH) or psoriatic spondyloarthritis. Here the osteophytes arise parallel to the endplate and project considerably beyond the normal outline of the spinal column. They resemble traction osteophytes seen in osteoarthritis.

Syndesmophyte formation in AS can eventually leads to ossification of the intervertebral discs themselves and with this to ankylosis of the spine. This leads to deossification of the spinal column adding to an increased fracture risk. On a frontal projection there is usually relative prominence of the ossified supraspinous ligament centrally and ankylosed facet and uncovertebral joints laterally, the so called "trolley track sign", said to resemble the track a three-wheeled trolley. On the lateral projection the ankylosed spine with the ossified discs is said to resemble bamboo, the so called "bamboo spine" sign.

4.1.1.3 Complications

Complications of AS are worth considering as separate entities due to their serious implication.

The first serious complication and starting point for later problems is ankylosis of the spine often combined with marked thoracic kyphosis. Apart from limited mobility in everyday activities breathing can be

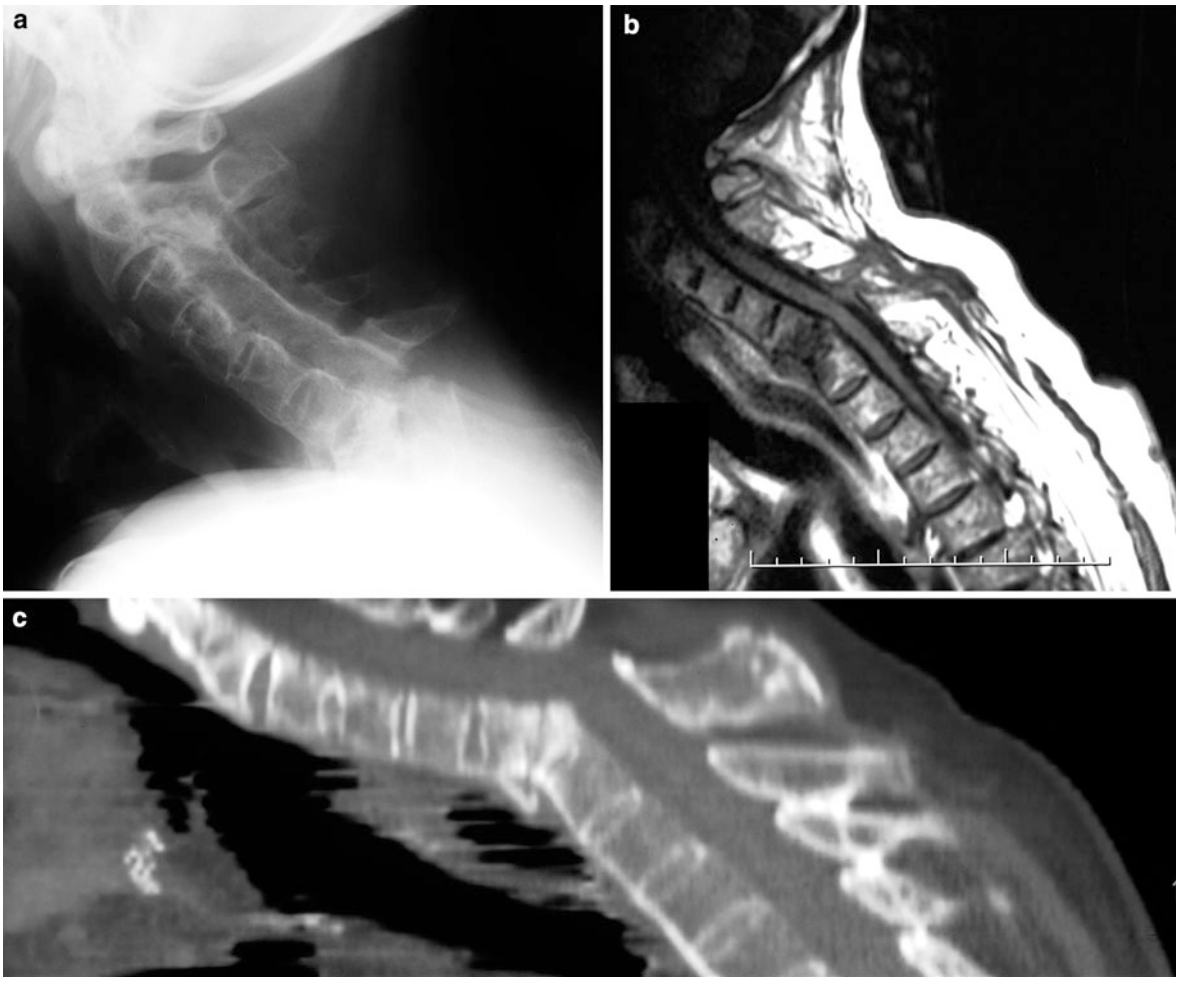

Fig. 13 A 67-year-old man with AS and established pseudoarthrosis after spine trauma (**a** lateral radiograph, note the sclerosis at the site of pseudarthrosis; **b** sag T1w, **c** sag reformat CT). No neurological deficit. Conservative treatment was unsuccessful and this patient had to undergo fusion surgery eventually (not shown) to prevent neurological deficit. Pseudoarthrosis is a common complication after spinal injury in patients with spinal ankylosis

restricted if the costovertebral and costotransverse joints are significantly involved. Mechanical lung restriction and recurrent chest infections are the consequence.

Altered bone metabolism and inflammation can lead to dural ectasia due to bone erosion of the margins of the spinal canal. Spinal nerves can become trapped in the newly formed bone recesses and cauda equine syndrome can result.

Ankylosis of the spine leads to bony deossification which in combination with the lack of elasticity, altered biomechanics (kyphosis) leads to spinal fractures even with minor trauma. Fracture might well be the first clinical presentation of AS in younger men and the authors have encountered this scenario a number of times (Fig. 12).

These fractures are frequently horizontally aligned and shear through an (ankylosed) intervertebral disc space and the posterior elements (rather than through the vertebral body). These injuries have a propensity to marked epidural or paravertebral haemorrhage due to abnormally brittle veins and the often significant distraction leading to disruption of the epidural veins. Furthermore, these fractures do not heal easily. The fracture sites often represent the only mobile segments in the spine and are therefore exposed to high mechanical stresses.

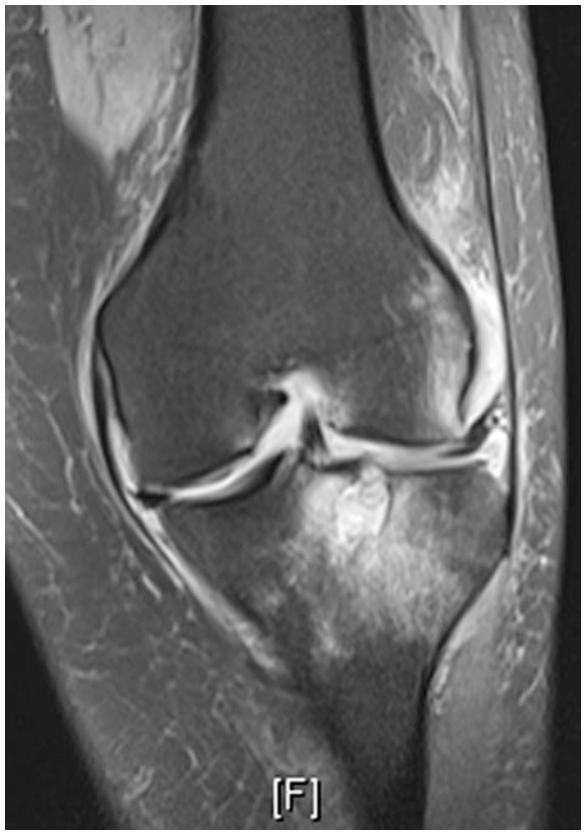

Fig. 14 A 54-year-old female with known rheumatoid arthritis. Bilateral knee pain. MRI of the left knee shows a large erosion of the lateral tibia plateau with extensive inflammatory bone marrow change (**a** cor PD-FS). Also inflammatory bone marrow change on the lateral aspect of the lateral femoral condyle, this is at the popliteus tendon insertion. Synovitis is noted in the knee joint. Bone erosions can be due to primary intra-osseous lesions as well as adjacent synovial pannus formation

This frequently leads to the formation of a pseudarthrosis (also called Andersson lesion) possibly combined with instability putting neural structures at risk which might have survived the initial trauma intact (Figs. 11, 13). The differential diagnosis to infection can be difficult as there is destructive bone change and bone marrow signal alteration and often adjacent soft tissue change. This is especially difficult if a neurological injury is present where the absence of pain sensation often leads to neuropathic appearances of the spine.

4.1.2 Rheumatoid Arthritis

Rheumatoid arthritis has traditionally been regarded as primarily synovium-based inflammatory disease with secondary cartilage and bone involvement. While it is still believed that synovitis is the hallmark feature of rheumatoid arthritis an alternative model for bone damage has been put forward. In this alternative model at least part of the inflammatory process arises primarily in the subarticular bone marrow, partly preceding any evidence of synovitis (Narvaez et al. 2010). The inflammatory infiltrate contains B- and T-lympocytes and also macrophages and leads to osteoclast activation and thereby to bone resorption (Blum et al. 2009; Dalbeth et al. 2009; McQueen and Ostendorf 2006). It has been shown that if inflammatory cells make up more than 50% of all cells bone destruction ensues. As long as the inflammatory component is less than 50% osteitis change is only seen (Jimenez-Boj et al. 2007). This raises the possibility of diagnosing and treating rheumatoid arthritis before bone destruction has occurred. There is also an association of inflammatory bone marrow change with increased pain and with worsening functional status and tendon status (McQueen and Ostendorf 2006) and also with structural disease progression despite clinical remission (Gandjbakhch et al. 2011). Apart from peripheral joints (Fig. 14), bone marrow signal change on MRI can also be observed in the spine, particularly in the cervical spine and here affects the atlantoaxial and the facet joints in particular. Again the amount of signal change is associated with pain and joint destruction (Narvaez et al. 2009).

Imagingwise synovitis is the main early disease manifestation. MRI imaging, especially if contrast medium enhanced is well suited to identify this. In rheumatoid arthritis the hands are often involved early. Unspecific wrist and MCPJ pain must be differentiated from rheumatoid arthritis with synovitis. For imaging of the hands the use of coronal and axial T1 and water-sensitive sequences have been proposed, the T1w sequences should be repeated after contrast administration. There are several synovitis scoring methods, currently most commonly used is the OMERACT RAMRIS score (outcome measures in rheumatoid arthritis clinical trials rheumatoid arthritis MRI score) (Narvaez et al. 2010).

Radiography and CT: Typical radiographic/CT changes are loss of joint space, malalignment, periarticular osteoporosis and soft tissue swelling and bone erosions. Bone lesions can heal with restitutio ad integrum but often leads on severe degenerative change including bone collapse and ankylosis.

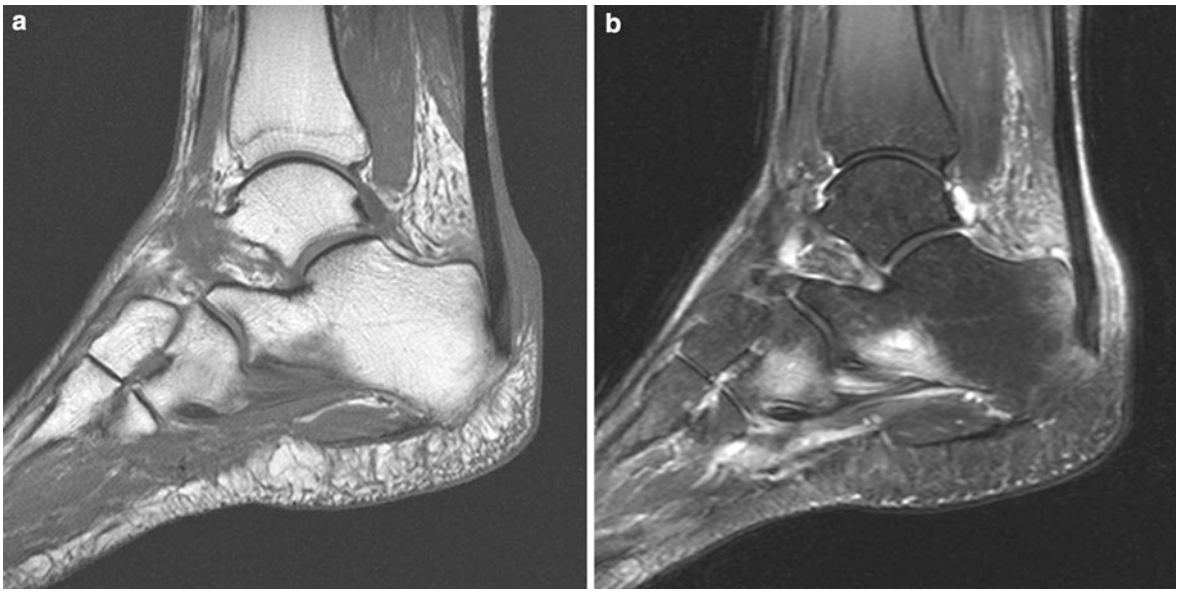

Fig. 15 A 42-year-old female with known psoriatic arthropathy, hindfoot pain. Sagittal T1 (**a**) and T2 fatsat (**b**) images show typical enthesopathy affecting the Achilles tendon insertion, the flexor digitorum brevis origin and the cuboid where the peroneus longus tendon crosses. The latter is seen as a functional enthesopathy. The imaging findings are gross, reactive bone changes. The clinical features can be surprisingly minor

4.1.3 Psoriatic Arthropathy

Psoriatic arthropathy occupies a curious middle ground between the typical spondyloarthropathies characterized by enthesitis (Fig. 15) and the typical synovitis-based diseases such as rheumatoid arthritis. Inflammatory bone marrow changes in psoriatic arthropathy can be due to synovial-based arthritis as well as enthesitis. Locally the disease can be difficult to differentiate from ankylosing spondylitis and rheumatoid arthritis though the overall pattern is different. The presence of dactylitis, the inflammation of a whole finger, is suggestive of psoriatic arthropathy. Dactylitis is characterised by a combination of tendon and tendon sheath inflammation, inflammation of the other soft tissues of the finger with often oedematous change and not rarely joint and bone involvement (Jablonka et al. 2008; McQueen et al. 2006). Spinal involvement has a preference for the cervical spine. Sacroiliitis, if present, is usually unilateral.

The diagnosis is hindered by the absence of skin manifestations in 20–30% of cases at the onset of arthritis (Jablonka et al. 2008).

MRI is particulary helpful in identifying enthesitis with often very florid bone marrow signal change. Often multiple sites are involved many of which are clinically not apparent. At any particular lesion there are no distinguishing features allowing for differentiation from ankylosing spondylitis or rheumatoid arthritis (depending on AS or rA like presentation). However, the overall distribution (see above: cranial part of the spine, dactylitis, …) and morphology of some sites (proliferative bone changes) often allow the differentiation (McQueen et al. 2006).

Disease scoring (especially to monitor treatment response) can be performed using various scores. The OMERACT Psoriatic Arthritis Magnetic Resonance Imaging Score (PsAMRIS) has been in use for a while and has been validated in a small study (Boyesen et al. 2011).

Radiography and CT: Spinal bone changes are more akin to those of diffuse idiopathic skeletal hyperostosis, DISH, than those of ankylosing spondylitis. Spinal new bone formation is flowing and in parts shows fusing osteophyte formation rather than syndesmophyte formation. This can lead to grossly hypertrophic ankylosis. In the peripheral skeleton features favouring psoriasis over rheumatoid arthritis are proliferative bone changes including ankylosis, lack of periarticular osteopenia, focal osteolysis such as

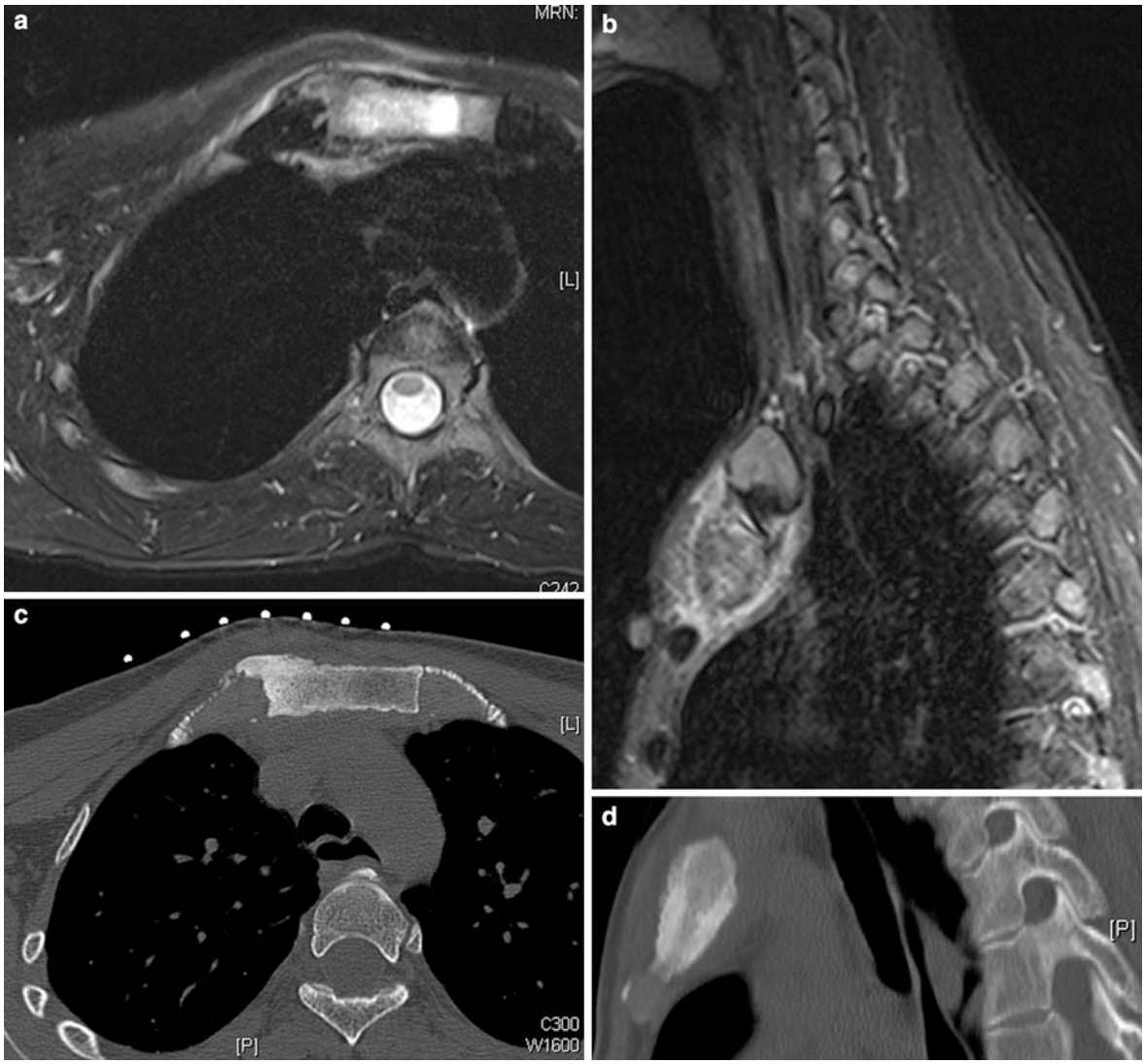

Fig. 16 A 29-year-old female presenting with sternal pain. MR imaging shows marked bone marrow oedema and soft tissue swelling around the right-sided cranial sternum (**a**, **b** axial and sagittal STIR). Radiographs (not shown) had demonstrated periosteal reaction and a malignant lesion was queried. CT prior to biopsy showed marked sclerosis related to the right first costosternal joint with associated soft tissue swelling (**c**, **d** axial and sagittal reformat). The biopsy demonstrated unspecific non-infectious inflammatory change. In conjunction with the imaging findings SAPHO was diagnosed. The patient improved with supportive treatment only. SAPHO frequently causes diagnostic difficulties and concern due to the often very florid presentation with periosteal reaction and soft tissue swelling. Biopsies should be obtained to exclude acute infection or neoplasia if in any doubt

pencil in cup joint destruction or acroosteolysis, extensive DIPJ involvement, asymmetrical involvement in the hand, periostitis, osteitis away from the immediate joint surface and flexor rather than extensor tenosynovitis and dactylitis (Blum et al. 2009; Narvaez et al. 2010; Berthelot 2003; McQueen et al. 2006).

4.1.4 SAPHO

4.1.4.1 Definition, Diagnostic Criteria and Differential Diagnosis

SAPHO is a complex disorder of uncertain etiology (Figs. 8, 16, 17). SAPHO is an umbrella term which is now commonly believed to unify disorders such

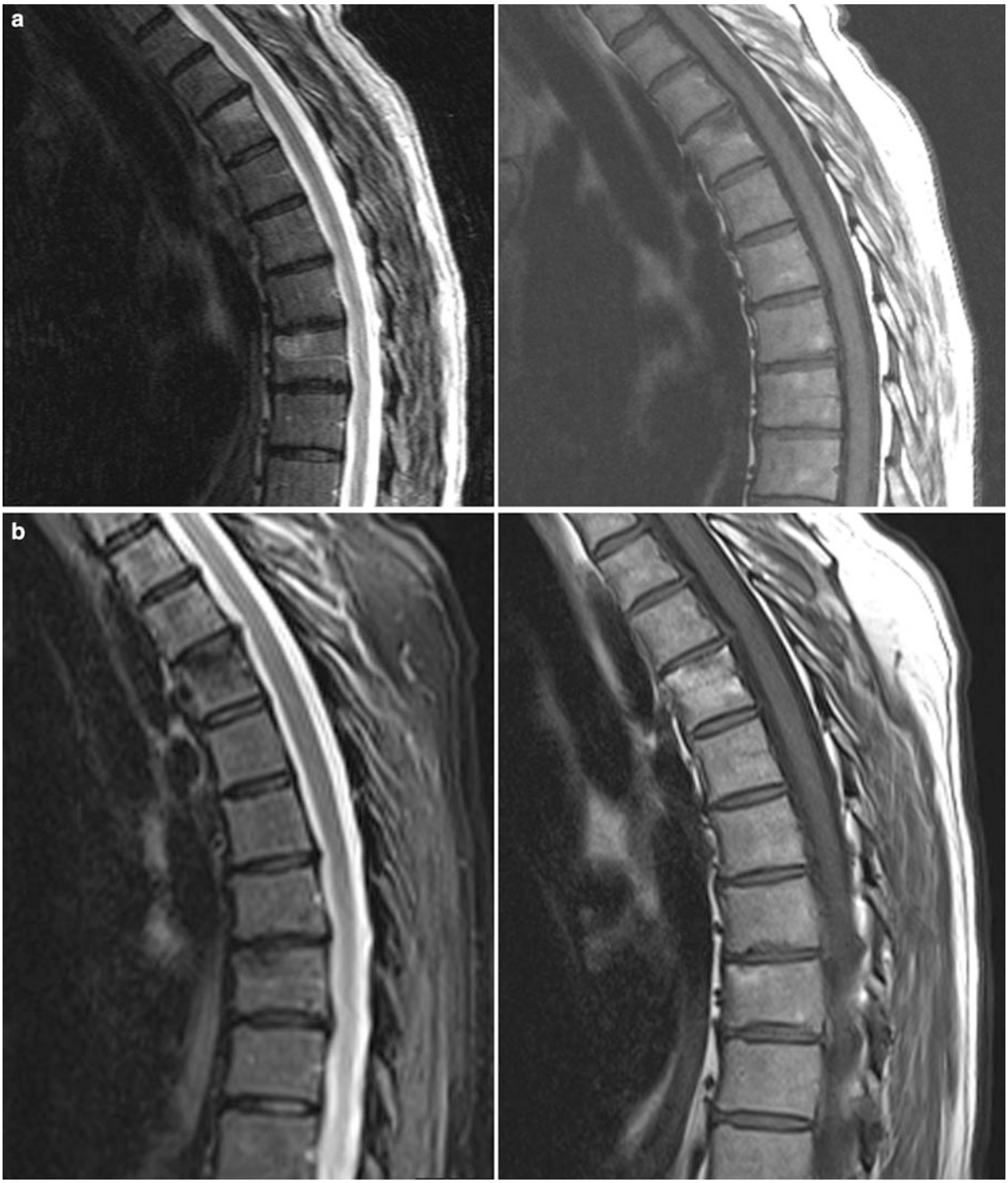

Fig. 17 A 57-year-old woman presenting with sternal pain and swelling, SAPHO involving sternum and spine (same patient as Fig. 8). MRI at the time of the CT shown in Fig. 8 demonstrates a further lesion in T8 vertebral body, invisible on CT as there is no reactive bone change and in and T1w MRI. Both the T4 and the T8 lesions show bone marrow oedema, the T4 lesion also shows sclerosis and adjacent fatty change on MRI (**a** *left* T2w, *right* T1w). A year later both lesions demonstrate fatty change only in STIR (**b** *left*) and T1w (**b** *right*). This reflects the natural history of SAPHO with spontaneous healing, the duration of lesion activity can vary as in this case. Without the costosternal involvement the exact diagnosis would remain unclear, undifferentiated spondyloarthropathy can present in the same manner as the spinal lesions

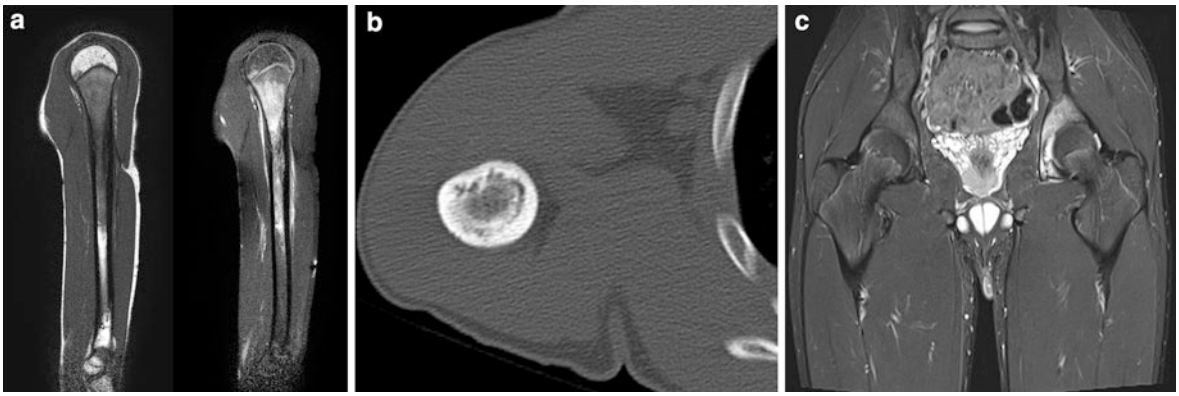

Fig. 18 A 14-year-old boy presenting with right arm pain. MRI (**a** left sagittal T1, right T1w FS post CE) demonstrates marked inflammatory change in and around the humerus shaft involving the proximal epiphysis. A STIR sequence (not shown) demonstrated exactly the same involvement pattern as the T1-FS sequence post contrast medium enhancement, the signal changes are due to inflammation rather than true oedema. CT (**b**) demonstrates disorganised new bone formation. Ewing sarcoma in particular has to be excluded. Biopsy revealed unspecific inflammatory and reactive bone change. The bone texture with multiple small bone defects was suggestive of SAPHO. On further questioning a history of suspected osteomyelitis of the left hip several years ago was obtained. MRI (**c** cor PD-FS) demonstrated persistent inflammatory change in the left acetabulum, this was clinically asymptomatic. Chronic recurrent multifocal osteomyelitis (CRMO) was diagnosed (a subtype of SAPHO). Supportive treatment was initiated. The lesions gradually matured over the next few years with minimal clinical symptoms. The diagnosis of CRMO is very difficult acutely, careful history taking and examination often reveal other areas of involvement or previous disease episodes

as acquired hyperostosis syndrome, anterior thoracic wall inflammatory syndrome, recurrent relapsing symmetrical clavicular osteitis, sterno-costo-clavicular hyperostosis, inter-sterno-costo-clavicular ossification, pustular arthro-osteitis, pustulo-psoriatic hyperostotic spondylarthritis, chronic recurrent multifocal osteomyelitis (CRMO) (Fig. 18), recurrent multifocal parostosis, chronic mandibular osteitis, sclerosing osteomyelitis, follicular occlusive triad, enteropathic spondyloarthritis and acne spondyloarthritis.

The primary pathology in SAPHO is probably osteitis but inflammatory bone marrow change will follow. There are no specific histological features to these inflammatory changes making SAPHO a clinical radiological diagnosis and most often the diagnosis is reached by exclusion of other inflammatory disorders.

The original description by Chamot et al. in 1987 gave four criteria for the diagnosis of SAPHO, any of which is diagnostic: (1) bone involvement with acne, (2) bone involvement with palmoplantar pustulosis, (3) sterno-costo-clavicular hyperostosis, (4) aseptic osteomyelitis (Laredo et al. 2007).

Recurrent multifocal involvement with negative microbiology and involvement of the anterior chest wall are further helpful features (Depasquale et al. 2012). Whole-body imaging is useful to identify these features. Whole-body MRI and nuclear medicine techniques are particularly helpful here (Fritz et al. 2009).

The diagnosis is based on a typical disease distribution particularly anterior chest wall involvement, associated skin changes and in children often a remitting recurrent pattern. The sternoclavicular joints, the sternum and the clavicles are often affected in the adult (Fig. 16). Increased activity of the sternoclavicular joints and the adjacent sternum on isotope bone scanning is said to resemble the head of a bull, the so-called bull's head sign. In children long bone involvement (often metaphyseal) is often seen and here usually part of CRMO, a subcategory of SAPHO. This will be discussed in more detail below.

MRI, radiography, CT findings: SAPHO is not limited to joints and can affect any part of any bone. Spinal involvement with vertebral endplate erosions with inflammation can be seen as well as hyperostotic non-marginal enthesophytes which morphologically resemble more the appearance of DISH than those of ankylosing spondylitis (Depasquale et al. 2012; Colina et al. 2009). In this SAPHO bears similarities to psoriatic arthropathy. Peripheral skeletal involvement (hands, fingers, feet) is not typical for SAPHO and is more suggestive of psoriatic arthropathy.

Imaging shows mottled bone lysis in the early phase with florid bone marrow oedema such as change, periostitis and adjacent soft tissue change. The periostitis leads to marked new bone formation which gradually matures. MRI is much more sensitive for early lesions than radiographs (Fritz et al. 2009; Iyer et al. 2011). Generally the presence of skin changes is helpful to consider this group of disorders.

The involvement of soft tissue adjacent to the inflammatory bone changes as well as the bone changes themselves can be striking. This often leads to significant concern about malignancy such as an osteosarcoma, Ewing sarcoma or, rarer, metastases.

4.1.4.2 CRMO

In children in addition to considering a malignancy the combination of metaphyseal inflammatory change and the soft tissue involvement can also lead to the erroneous diagnosis of infection (osteomyelitis). To complicate matters, the lesions can also histologically display features of infection (neutrophile infiltration) in the acute stage though this is not very pronounced and non-specific inflammatory infiltration by lymphocytes and plasma cells is the rule. The acuity of radiological findings should be correlated with the histology to avoid misdiagnosis. Nevertheless, frequently conservative (antibiotic) treatment for infection is instituted. Usually the patient gets better under this. However, this is not due to successful treatment but reflects the natural course of the disease. Often the diagnosis of CRMO is only made when after an asymptomtic interval the findings recur at the original location or similar findings occur in a new location. Gikas et al. found that in their orthopaedic specialist centre about half the cases of CRMO were diagnosed after recurring. In their series of 41 patients just under two-third of lesions occurred in clavicle, femur or tibia (Gikas et al. 2009). Skin manifestation as seen in SAPHO are rare in CRMO making the diagnosis more challenging (Gikas et al. 2009). As mentioned above whole body imaging is very valuable in patients with suspected CRMO/SAPHO as often additional lesions in perhaps more typical locations are seen supporting the diagnosis. In a study of 13 children with CRMO, Fritz et al. (2009) have found multifocal lesions in all children, often symmetric lesions were seen. There was a predilection for the knee, ankle and hindfoot area. However, CRMO can manifest almost anywhere in the skeletal system (Depasquale et al. 2012; Iyer et al. 2011).

4.1.5 Other Inflammatory Arthropathies

The other inflammatory disorders form clinically and morphologically a rather mixed bag and usually exhibit features of the diseases discussed above. Reactive and unspecified arthropathies form part of this as well as collagen vascular disorders such as systemic lupus erythematosus (SLE). Locally there can be bone marrow involvement either subarticular, related to the SIJs, the spine in various locations or entheses. The local imaging features are not specific.

4.2 Mechanical

Mechanically induced inflammatory bone marrow changes are extremely common. Most people with significant degenerative joint disease demonstrate oedema like signal change in the bone marrow deep to the areas of degenerative change (Fig. 19). However, it has been shown that true bone marrow oedema forms a negligible part of these changes. The main cause for the signal change is a fibrovascular infiltrate (Zanetti et al. 2000; Link and Li 2011; Phan et al. 2006). Depending on the severity of degeneration, bone marrow necrosis with trabecular change might also be seen. Similar bone marrow signal change might be seen after mechanical stress such as excessive running or due to avascular necrosis or stress/insufficiency fracture. These changes can wax and wane with time (Taljanovic et al. 2008; Steinbach and Suh 2011).

Excessive mechanical force can also cause reactive bone marrow changes around entheses.

4.3 Metabolic

The group of metabolic disorders is vast. Insufficiency or stress fractures or avascular necrosis have already been discussed in the paragraph on mechanically induced inflammatory bone marrow changes. Whatever the cause, once mechanical disruption of bone trabecles occurs there will be an inflammatory healing response.

Crystal arthropathies are different to the pathologies discussed so far, in that the inflammatory response is not mechanical but due to the presence of metabolites. Gout and calcium pyrophosphate dehydrate disease (CPPD) are the commonest representatives of this group.

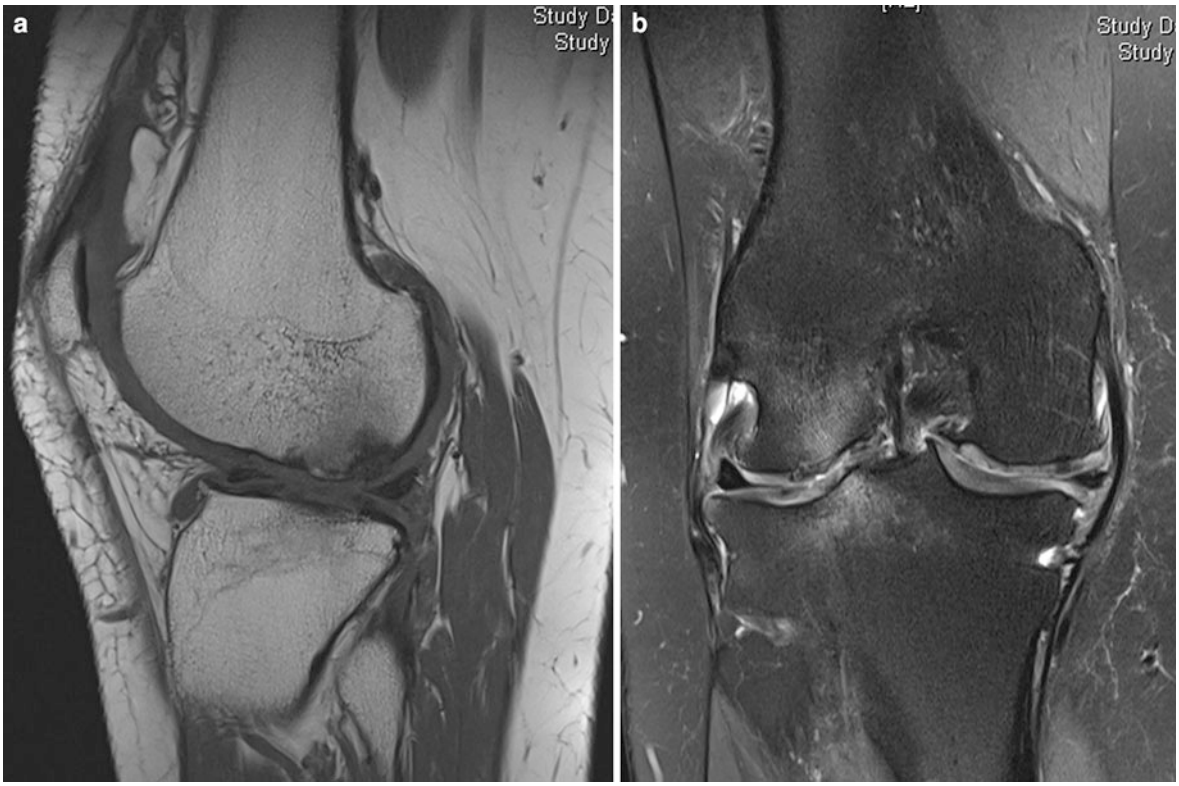

Fig. 19 A 33-year-old female. Complex OA changes with cartilage defects, central osteophyte formation and small bone cyst-like areas (**a** sagittal T1w, **b** cor PD-FS). Associated bone marrow oedema-like change. Degenerative change can be associated with inflammatory bone marrow changes

The gout tophus itself usually demonstrates vascular ingrowth and inflammatory changes adjacent to the tophus. If the tophus is intraosseous, inflammatory bone marrow oedema may sometimes result. The gout tophus itself usually has intermediate signal intensity in T1w, the T2w signal is highly variable. It can be inhomogenous within a lesion, low signal, intermediate or high signal. In most cases it will be low signal (Fig. 20) (Yu et al. 1997; Paparo et al. 2010).

CPPD can also incite an intense inflammatory response. This is usually limited to soft tissue, intraosseous inflammatory change is not typical but can be florid and extremely painful.

Amyloidosis is a further complex and multifaceted disease that can lead to spondyloarthropathy and with that to inflammatory bone marrow changes. Amyloidosis is a complex group of disorders all leading to deposition of insoluble proteins within the body. Amyloidosis can be primary or secondary. Secondary amyloidosis is more common due to a range of chronic inflammatory conditions. In some disorders such as rheumatoid arthritis, chronic dialysis amyloidosis frequently develops. In these cases joint and soft tissue involvement can be due to the primary underlying disease or the secondary amyloidosis. More confusingly some types of amyloidosis can clinically present like rheumatoid arthritis (Katoh et al. 2008; Jennings et al. 2008).

Whatever the cause amyloidosis can lead to joint involvement. The commonest presentation in the extra-axial skeleton are synovial and intra-osseous deposits of amyloid. Amyloid masses typically demonstrate low to intermediate signal in T1w and T2w. Adjacent inflammatory bone marrow change is not common (Jennings et al. 2008; Otake et al. 1998; Sheldon and Forrester 2003).

The reverse is true for axial involvement. Primary (very rare) as well as secondary amyloidosis such as in chronic dialysis (much more common) frequently leads to an inflammatory, erosive spondylodiscitis which imagingwise is very similar to infective spondylodiscitis. However, often the changes are seen

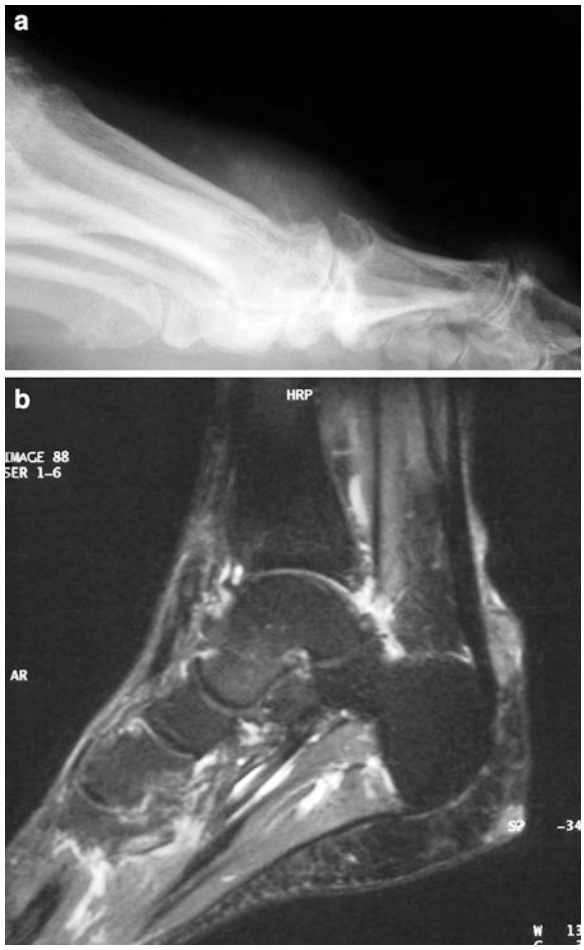

Fig. 20 A 49-year-old man with known gout. A lateral radiograph (**a**) shows a punched out lesion of the first MTPJ with an associated soft tissue mass. MRI demonstrates further gout tophi in the hindfoot (**b** STIR), the bone marrow as such is normal. Intra-osseous gout does not usually cause inflammatory bone marrow changes, even in case of bone erosion

at multiple levels and there are usually no significant paravertebral inflammatory masses and there is no abscess formation. The clinical presentation is also usually different and there is a suggestive clinical history. Nevertheless biopsy can be necessary (Ito et al. 1976; Parmar et al. 2010).

4.4 Paget

Paget's disease is a modelling abnormality of bone of unknown etiology usually affecting middle aged and older patients. Although it seems to have become less prevalent and there is a trend to monoosseous rather than polyosseous involvement in more recent years, the morbidity can be significant (Haddaway et al. 2007; Vellenga et al. 1984). In the lytic phase there is intense fibrovascular ingrowth which causes inflammation like bone marrow signal changes on MRI. Strictly speaking Paget's disease is a primary bony abnormality with secondary bone marrow involvement and this is the reason that it is well visualised with often pathognomonic radiographs. On MR imaging, however, the bone marrow changes are dominant and they can be difficult to interpret if unfamiliar with the MRI features. MRI is better suited than any other imaging technique to assess for disease-related complications such as neural impingement (Stacy and Dixon 2007; Roberts et al. 1989; Dell'Atti et al. 2007).

Radiographs and CT show initial lytic change and at a later date the classic findings of bone expansion and coarsened medullary trabecles.

4.5 Tumoral

Inflammatory bone marrow changes can sometimes be seen as perilesional signal change in malignant primary bone tumours. They represent an inflammatory response to the primary lesion and are usually quite limited in extent. They can make it hard to assess the extent of the primary lesion and affect treatment planning.

Extensive inflammatory bone marrow changes are however seen in some aggressive primarily benign bone tumours. These are particularly osteoid osteoma (Fig. 21), chondroblastoma and Langerhans histiocytosis. The inflammatory changes are thought to be due to the release of proinflammatory mediators such as TNF alpha, interleukin, prostaglandins and leukotrienes (Blum et al. 2009; James et al. 2008; Yamamura et al. 1997).

Bizarre parosteal osteochondromatous proliferation (BPOP) is a further disorder which is believed to be a benign neoplastic tumour by some authors and in which inflammatory bone marrow changes have been described. However, other authors favour the continuum theory of progression from florid reactive periostitis over BPOP to turret exostosis. Inflammatory bone marrow changes are probably present in only a limited number of BPOP cases (Joseph et al. 2011).

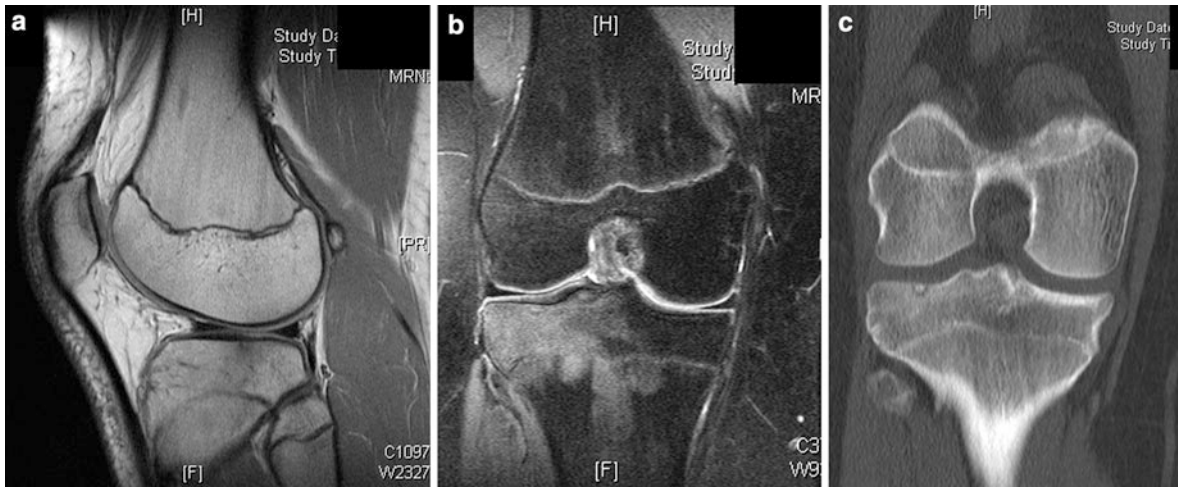

Fig. 21 A 19-year-old man with knee pain. MRI shows bone marrow oedema-like change with a subtle focal bone abnormality seen only on a single T1w (**a**) and PD-FS (**b**) image. They were not seen on the corresponding sagittal PD-FS and coronal T1w images. CT (**c** coronal reformat) demonstrates the nidus typical for osteoid osteoma much better, sublte bone sclerosis is noted. Extensive oedema-like change can mask the underlying abnormality, a well-known pitfall in imaging of osteoid osteomas. The size of the underlying lesion often bears no relation to the size of inflammatory bone marrow changes

4.6 Sarcoidosis

Sarcoidosis is an inflammatory granuloma forming disorder of unclear etiology. It is one of the chameleon diseases that can be very difficult to diagnose. Inflammatory bone marrow infiltration is part of the disease spectrum. If the fingers are involved, radiographically lace-like lytic bone changes may suggest the disease. MRI shows inflammatory bone marrow infiltration, in small bones regularly with cortical bone involvement. In large bones and the spine cortical involvement is not typical. The findings here are varied and can be multi or unifocal, discrete and well defined or diffused and ill-defined. Morphologically metastases, multiple myeloma/plasmacytoma, lymphoma, osseous haemangioma and disseminated granulomatous infection can be considered (Moore et al. 2005).

4.7 Drug Related

Bone changes related to drug intake have been described for many drugs, inflammatory bone marrow changes related to drug use are however rare. Most drugs affecting the bone metabolism affect the bone marrow and the periosteum. Inflammatory changes in the bone marrow have been suggested to occur in hypervitaminosis A and in treatment with retinoids, synthetic vitamin A derivates (Jennings et al. 2008). Certain prostaglandins can cause inflammatory bone marrow change (Blum et al. 2009; Yamamura et al. 1997) but some are used to treat patients with bone marrow oedema syndrome to reduce the bone marrow changes and pain (Jager et al. 2008).

4.8 Differential Diagnosis

The differential diagnosis of inflammatory bone marrow changes is vast. Particularly for the more florid and larger bone lesions with soft tissue involvement malignancy and infection need to be excluded. The pattern of disease distribution and lesion morphology should be diagnostic in most cases of classic ankylosing spondylitis and rheumatoid arthritis. For psoriasis and SAPHO this can be much harder. Often there is soft tissue involvement and marked periosteal reaction. Single-level involvement is more common and make it hard to narrow the differential diagnosis. Whole-body imaging and careful history taking often are of great help here. However, biopsy will still often be necessary. Histology showing unspecific inflammatory changes does

not equate to a failed biopsy. As long as clearly lesional tissue was sampled the radiologist has to argue the case for an inflammatory spondyloarthropathy and investigate further clinical assessment and workup rather than further or more invasive procedures.

5 Conclusions

Inflammatory bone marrow changes are seen in a large number of very disparate conditions. Primary inflammatory disorders encompass inflammatory spondyloarthropathies, rheumatoid arthritis and similar disorders and the large group of undifferentiated arthropathies and SAPHO.

The commonest disorder leading to inflammatory bone marrow changes is however osteoarthritis though commonly and somewhat lazily the bone marrow changes here are called “bone marrow oedema”.

Imaging has a great deal to offer in the diagnosis of most of these disorders while the exact histological diagnosis is often not possible. MR imaging is the imaging modality of choice for diagnosis and to assess the response to treatment and to identify possible complications. Contrast medium administration can be useful in selecting cases/circumstances but is usually not routinely indicated.

References

Appel H, Kuhne M, Spiekermann S et al (2006) Immunohistologic analysis of zygapophyseal joints in patients with ankylosing spondylitis. Arthritis Rheum 54(9):2845–2851

Baraliakos X, Hermann KG, Landewe R et al (2005) Assessment of acute spinal inflammation in patients with ankylosing spondylitis by magnetic resonance imaging: a comparison between contrast enhanced T1 and short tau inversion recovery (STIR) sequences. Ann Rheum Dis 64(8): 1141–1144

Berthelot JM (2003) Psoriatic arthritis as a mountain. Reumatismo 55(1):6–15

Bierry G, Jehl F, Boehm N et al (2009) Macrophage imaging by USPIO-enhanced MR for the differentiation of infectious osteomyelitis and aseptic vertebral inflammation. Eur Radiol 19(7):1604–1611

Blum A, Roch D, Loeuille D et al (2009) Bone marrow edema: definition, diagnostic value and prognostic value. J Radiol 90(12):1789–1811

Bollow M, Fischer T, Reisshauer H et al (2000) Quantitative analyses of sacroiliac biopsies in spondyloarthropathies: T cells and macrophages predominate in early and active sacroiliitis- cellularity correlates with the degree of enhancement detected by magnetic resonance imaging. Ann Rheum Dis 59(2):135–140

Boyesen P, McQueen FM, Gandjbakhch F et al (2011) The OMERACT psoriatic arthritis magnetic resonance imaging score (PsAMRIS) is reliable and sensitive to change: results from an OMERACT workshop. J Rheumatol 38(9):2034–2038

Bozgeyik Z, Ozgocmen S, Kocakoc E (2008) Role of diffusion-weighted MRI in the detection of early active sacroiliitis. Am J Roentgenol 191(4):980–986

Bredella MA, Steinbach LS, Morgan S et al (2006) MRI of the sacroiliac joints in patients with moderate to severe ankylosing spondylitis. Am J Roentgenol 187(6):1420–1426

Colbert RA (2010) Early axial spondyloarthritis. Curr Opin Rheumatol 22(5):603–607

Colina M, Govoni M, Orzincolo C et al (2009) Clinical and radiologic evolution of synovitis, acne, pustulosis, hyperostosis, and osteitis syndrome: a single center study of a cohort of 71 subjects. Arthritis Rheum 61(6):813–821

Dalbeth N, Smith T, Gray S et al (2009) Cellular characterisation of magnetic resonance imaging bone oedema in rheumatoid arthritis; implications for pathogenesis of erosive disease. Ann Rheum Dis 68(2):279–282

Delfaut EM, Beltran J, Johnson G et al (1999) Fat suppression in MR imaging: techniques and pitfalls. Radiographics 19(2): 373–382

Dell’Atti C, Cassar-Pullicino VN, Lalam RK et al (2007) The spine in Paget’s disease. Skeletal Radiol 36(7):609–626

Depasquale R, Kumar N, Lalam RK et al (2012) SAPHO: what radiologists should know. Clin Radiol 67(3): 195–206

Fritz J, Tzaribatchev N, Claussen CD et al (2009) Chronic recurrent multifocal osteomyelitis: comparison of whole-body MR imaging with radiography and correlation with clinical and laboratory data. Radiology 252(3):842–851

Gandjbakhch F, Foltz V, Mallet A et al (2011) Bone marrow oedema predicts structural progression in a 1-year follow-up of 85 patients with RA in remission or with low disease activity with low-field MRI. Ann Rheum Dis 70(12): 2159–2162

Gaspersic N, Sersa I, Jevtic V et al (2008) Monitoring ankylosing spondylitis therapy by dynamic contrast-enhanced and diffusion-weighted magnetic resonance imaging. Skeletal Radiol 37(2):123–131

Gikas PD, Islam L, Aston W et al (2009) Nonbacterial osteitis: a clinical, histopathological, and imaging study with a proposal for protocol-based management of patients with this diagnosis. J Orthop Sci 14(5):505–516

Haddaway MJ, Davie MW, McCall IW et al (2007) Effect of age and gender on the number and distribution of sites in Paget’s disease of bone. Br J Radiol 80(955):532–536

Horger M, Schmalzing M, Ioanoviciu SD et al (2010) Ankylosing spondylitis: imaging findings in the axial skeleton. Rofo 182(8):639–643

Ito M, Abumi K, Takeda N et al (1998) Pathologic features of spinal disorders in patients treated with long-term hemodialysis. Spine 23(19):2127–2133 (Phila Pa 1976)

Iyer RS, Thapa MM, Chew FS (2011) Chronic recurrent multifocal osteomyelitis: review. Am J Roentgenol 196(Suppl 6): S87–S91

Jablonka K, Freyschmidt J (2008) Psoriatic arthritis and psoriatic spondylarthropathy. In: Pope et al (eds) Imaging of the Musculoskeletal System. Saunders, Philadelphia, pp 1113–1119

Jager M, Tillmann FP, Thornhill TS et al (2008) Rationale for prostaglandin I2 in bone marrow oedema–from theory to application. Arthritis Res Ther 10(5):R120

James SL, Panicek DM, Davies AM (2008) Bone marrow oedema associated with benign and malignant bone tumours. Eur J Radiol 67(1):11–21

Jennings BT, Gibson MS, Murphey MD et al (2008) Amyloidosis. In: Pope et al (eds) Imaging of the musculoskeletal system. Saunders, Philadelphia, pp 1524–1529

Jimenez-Boj E, Nobauer-Huhmann I, Hanslik-Schnabel B et al (2007) Bone erosions and bone marrow edema as defined by magnetic resonance imaging reflect true bone marrow inflammation in rheumatoid arthritis. Arthritis Rheum 56(4): 1118–1124

Joseph J, Ritchie D, MacDuff E et al (2011) Bizarre parosteal osteochondromatous proliferation: a locally aggressive benign tumor. Clin Orthop Relat Res 469(7):2019–2027

Katoh N, Tazawa K, Ishii W et al (2008) Systemic AL amyloidosis mimicking rheumatoid arthritis. Intern Med 47(12):1133–1138

Kotoura N, Sakamoto K, Fukuda Y et al (2011) Evaluation of magnetic resonance signal intensity in bone marrow after administration of super paramagnetic iron oxide (SPIO). Nihon Hoshasen Gijutsu Gakkai Zasshi 67(3):212–220

Laredo JD, Vuillemin-Bodaghi V, Boutry N et al (2007) SAPHO syndrome: MR appearance of vertebral involvement. Radiology 242(3):825–831

Link TM, Li X (2011) Bone marrow changes in osteoarthritis. Semin Musculoskelet Radiol 15(3):238–246

Madsen KB, Jurik AG (2010) MRI grading method for active and chronic spinal changes in spondyloarthritis. Clin Radiol 65(1):6–14

Madsen KB, Egund N, Jurik AG (2010) Grading of inflammatory disease activity in the sacroiliac joints with magnetic resonance imaging: comparison between short-tau inversion recovery and gadolinium contrast-enhanced sequences. J Rheumatol 37(2):393–400

Maksymowych WP, Weber U (2011) Diagnostic utility of MRI in early spondyloarthritis. Curr Rheumatol Rep 13(5):402–408

McGonagle D, Marzo-Ortega H, O'Connor P et al (2002) Histological assessment of the early enthesitis lesion in spondyloarthropathy. Ann Rheum Dis 61(6):534–537

McQueen FM, Ostendorf B (2006) What is MRI bone oedema in rheumatoid arthritis and why does it matter? Arthritis Res Ther 8(6):222

McQueen F, Lassere M, Ostergaard M (2006) Magnetic resonance imaging in psoriatic arthritis: a review of the literature. Arthritis Res Ther 8(2):207

Moore SL, Teirstein A, Golimbu C (2005) MRI of sarcoidosis patients with musculoskeletal symptoms. Am J Roentgenol 185(1):154–159

Narvaez JA, Narvaez J, de Albert M et al (2009) Bone marrow edema in the cervical spine of symptomatic rheumatoid arthritis patients. Semin Arthritis Rheum 38(4):281–288

Narvaez JA, Narvaez J, De Lama E et al (2010) MR imaging of early rheumatoid arthritis. Radiographics 30(1):143–163 (discussion 163–165)

Otake S, Tsuruta Y, Yamana D et al (1998) Amyloid arthropathy of the hip joint: MR demonstration of presumed amyloid lesions in 152 patients with long-term hemodialysis. Eur Radiol 8(8):1352–1356

Paparo F, Sconfienza LM, Muda A et al (2010) Multimodality imaging of chronic tophaceous gout. Reumatismo 62(4): 286–291

Parmar H, Rath T, Castillo M et al (2010) Imaging of focal amyloid depositions in the head, neck, and spine: amyloidoma. Am J Neuroradiol 31(7):1165–1170

Phan CM, Link TM, Blumenkrantz G et al (2006) MR imaging findings in the follow-up of patients with different stages of knee osteoarthritis and the correlation with clinical symptoms. Eur Radiol 16(3):608–618

Rennie WJ, Dhillon SS, Conner-Spady B et al (2009) Magnetic resonance imaging assessment of spinal inflammation in ankylosing spondylitis: standard clinical protocols may omit inflammatory lesions in thoracic vertebrae. Arthritis Rheum 61(9):1187–1193

Roberts MC, Kressel HY, Fallon MD et al (1989) Paget disease: MR imaging findings. Radiology 173(2):341–345

Roimicher L, Lopes FP, de Souza SA et al (2011) 99mTc-anti-TNF-{alpha} scintigraphy in RA: a comparison pilot study with MRI and clinical examination. Rheumatol (Oxford) 50(11):2044–2050

Rudwaleit M, Jurik AG, Hermann KG et al (2009) Defining active sacroiliitis on magnetic resonance imaging (MRI) for classification of axial spondyloarthritis: a consensual approach by the ASAS/OMERACT MRI group. Ann Rheum Dis 68(10):1520–1527

Sheldon PJ, Forrester DM (2003) Imaging of amyloid arthropathy. Semin Musculoskelet Radiol 7(3):195–203

Sieper J, Rudwaleit M, Baraliakos X et al (2009) The assessment of spondyloarthritis international society (ASAS) handbook: a guide to assess spondyloarthritis. Ann Rheum Dis 68(Suppl 2): ii1–ii44

Song IH, Carrasco-Fernandez J, Rudwaleit M et al (2008) The diagnostic value of scintigraphy in assessing sacroiliitis in ankylosing spondylitis: a systematic literature research. Ann Rheum Dis 67(11):1535–1540

Song IH, Hermann K, Haibel H et al (2011a) Effects of etanercept versus sulfasalazine in early axial spondyloarthritis on active inflammatory lesions as detected by whole-body MRI (ESTHER): a 48-week randomised controlled trial. Ann Rheum Dis 70(4):590–596

Song IH, Hermann KG, Haibel H et al (2011b) Relationship between active inflammatory lesions in the spine and sacroiliac joints and new development of chronic lesions on whole-body MRI in early axial spondyloarthritis: results of the ESTHER trial at week 48. Ann Rheum Dis 70(7): 1257–1263

Stacy GS, Dixon LB (2007) Pitfalls in MR image interpretation prompting referrals to an orthopedic oncology clinic. Radiographics 27(3):805–826 (discussion 827-828)

Steinbach LS, Suh KJ (2011) Bone marrow edema pattern around the knee on magnetic resonance imaging excluding acute traumatic lesions. Semin Musculoskelet Radiol 15(3): 208–220

Strobel K, Fischer DR, Tamborrini G et al (2010) 18F-fluoride PET/CT for detection of sacroiliitis in ankylosing spondylitis. Eur J Nucl Med Mol Imaging 37(9):1760–1765

Taljanovic MS, Graham AR, Benjamin JB et al (2008) Bone marrow edema pattern in advanced hip osteoarthritis: quantitative assessment with magnetic resonance imaging and correlation with clinical examination, radiographic findings, and histopathology. Skeletal Radiol 37(5):423–431

Tins B, Cassar-Pullicino V, Haddaway M (2012) The 3d SPACE sequence for routine imaging of the spine—preliminary experience. British J Radiol (BJR Advance)

Vellenga CJ, Pauwels EK, Bijvoet OL et al (1984) Untreated Paget disease of bone studied by scintigraphy. Radiology 153(3):799–805

Weber U, Maksymowych WP, Jurik AG et al (2009) Validation of whole-body against conventional magnetic resonance imaging for scoring acute inflammatory lesions in the sacroiliac joints of patients with spondylarthritis. Arthritis Rheum 61(7):893–899

Weber U, Lambert RG, Ostergaard M et al (2010) The diagnostic utility of magnetic resonance imaging in spondylarthritis: an international multicenter evaluation of one hundred eighty-seven subjects. Arthritis Rheum 62(10):3048–3058

Yamamura S, Sato K, Sugiura H et al (1997) Prostaglandin levels of primary bone tumor tissues correlate with peritumoral edema demonstrated by magnetic resonance imaging. Cancer 79(2):255–261

Yildiz A, Gungor F, Tuncer T et al (2001) The evaluation of sacroiliitis using 99mTc-nanocolloid and 99mTc-MDP scintigraphy. Nucl Med Commun 22(7):785–794

Yu JS, Chung C, Recht M et al (1997) MR imaging of tophaceous gout. Am J Roentgenol 168(2):523–527

Zanetti M, Bruder E, Romero J et al (2000) Bone marrow edema pattern in osteoarthritic knees: correlation between MR imaging and histologic findings. Radiology 215(3):835–840

Part IV

Technical Aspects in Bone Marrow Imaging

Techniques for Diffusion and Perfusion Assessment in Bone-Marrow MRI

Olaf Dietrich

Contents

Abstract

In addition to conventional magnetic resonance imaging (MRI) approaches of bone marrow such as T_1-weighted or short-tau inversion-recovery (STIR) MRI, newer techniques are available today allowing the visual and also quantitative assessment of several microstructural and physiological tissue parameters. The most important of these new techniques are MRI of hemodynamic parameters ("perfusion MRI") and MRI of molecular water diffusion ("diffusion MRI"). Both techniques are aimed at tissue parameters beyond proton density, relaxation properties, or fat content. They allow the (absolute) quantification of properties such as the diffusion coefficient of water molecules in tissue or hemodynamic parameters including the blood volume and the blood flow. In this chapter, the physical and physiological basics of diffusion and perfusion MRI are introduced and discussed with respect to their application in bone-marrow MRI. Non-quantitative and quantitative approaches for the analysis of diffusion-weighted images and semi-quantitative and quantitative approaches for the analysis of dynamic contrast-enhanced perfusion MRI are discussed.

1 Introduction

Magnetic resonance imaging (MRI) is well established for the examination of bone-marrow disorders. Conventional MRI techniques, in particular T_1-weighted MRI with and without contrast-agent administration as well as techniques with fat-signal

O. Dietrich (✉)
Josef Lissner Laboratory for Biomedical Imaging, Department of Clinical Radiology-Großhadern, Ludwig Maximilian University (LMU) of Munich, Munich, Germany
e-mail: od@dtrx.net

A. Baur-Melnyk (ed.), *Magnetic Resonance Imaging of the Bone Marrow*, Medical Radiology. Diagnostic Imaging,
DOI: 10.1007/174_2012_549, © Springer-Verlag Berlin Heidelberg 2013

suppression such as short-tau inversion-recovery (STIR) sequences or fat-saturated proton density-weighted MRI are useful for either the direct visualization of bone marrow or for the sensitive depiction of pathological changes (Glaser et al. 2008). The image contrast of these techniques is based predominantly on the relaxation times (T_1 and T_2) of the magnetization of different types of tissues. Apart from the relaxation properties, the relative fat content of tissue is highly relevant in bone-marrow MRI; therefore, techniques that are sensitive to the fat signal are frequently applied. Examples are techniques which suppress either the fat or the water signal as well as opposed-phase gradient-echo techniques, in which the signal is modulated depending on the relative fat and water content of the tissue (Vanel 2004; Gerdes et al. 2007).

In addition to these conventional approaches, newer techniques are available today allowing the visual and also quantitative assessment of several microstructural and physiological tissue parameters. The most important of these new techniques are MRI of hemodynamic parameters (frequently termed *perfusion MRI*) and MRI of molecular water diffusion (or, shorter, *diffusion MRI*).

Both techniques (diffusion as well as perfusion MRI) are aimed at tissue parameters beyond proton density, relaxation properties, or fat content. They allow the (absolute) quantification of tissue properties such as the diffusion coefficient of water molecules in tissue (in units of mm^2/s) or hemodynamic parameters including the blood (plasma) volume (mL/(100 g)) and the blood (plasma) flow (mL/(min 100 g)). Although both techniques are frequently mentioned and discussed together, it should be noted that they are in fact fundamentally different in their relation to tissue physiology: Diffusion MRI is focused on *physical* parameters (e.g., the diffusion coefficient and its spatial anisotropy), which generally depend in a complicated way on tissue microstructure (such as the cell density and cell types), but can be determined relatively directly from MR measurements. In contrast, perfusion MRI is focused on *physiological* parameters (e.g., plasma volume and flow, tissue transit times), the determination of which is substantially more complicated and generally requires several simplifying assumptions as well as extensive data post-processing. Interestingly, in spite of these principal differences, a suitably performed diffusion MRI measurement can be used to acquire both, diffusion- and perfusion-related tissue parameters together and, thus, reunites both approaches to a certain extent as described below.

In this chapter, the physical and physiological basics of diffusion and perfusion MRI are introduced and discussed with respect to their application in bone-marrow MRI.

2 Principles of Diffusion-Weighted MRI

2.1 Physics of Molecular Diffusion

2.1.1 Diffusion Coefficient

In the context of diffusion MRI, the term *diffusion* refers to the stochastic motion of water molecules in the tissue (Dietrich 2008). It can be directly observed in the form of the Brownian motion of minute particles floating in the liquid. The molecular motion is caused by the thermal kinetic energy and is an undirected random process resulting in a time-varying displacement of each molecule (Fig. 1). Averaged over a large number of molecules, the mean displacement after a certain diffusion time, τ, is 0; i.e., there is no macroscopic (bulk) flow of molecules. However, the standard deviation of the molecular displacements increases with time and, thus, molecular diffusion can be quantified using the statistical variance of displacements $\langle s^2 \rangle$ normalized to the diffusion time to define the diffusion coefficient:

$$D = \frac{\langle s^2 \rangle}{6\tau}.$$

The diffusion coefficient, D, is given in units of mm^2/s, $\mu m^2/ms$, or $\mu m^2/s$. Typical values for biological tissues or liquids are in the order of 1×10^{-3} $mm^2/s = 1$ $\mu m^2/ms = 1{,}000$ $\mu m^2/s$; e.g., pure water has a diffusion coefficient of about 2×10^{-3} mm^2/s at room temperature and of about 3×10^{-3} mm^2/s at body temperature. The diffusion coefficient can be used to estimate the diameter of the spatial range, d, accessible to a water molecule in a given diffusion time, $d \approx 2\sqrt{\langle s^2 \rangle} = 2\sqrt{6D\tau}$. That is, for diffusion times in milliseconds, the diameter given in micrometers can be obtained as $\frac{d}{\mu m} \approx 5\sqrt{\frac{\tau}{ms}}$ based on a diffusion coefficient of 1×10^{-3} mm^2/s. Hence, in vivo, this diameter is in the order of 20–70 μm for typical diffusion times (used in MRI) between 20 and

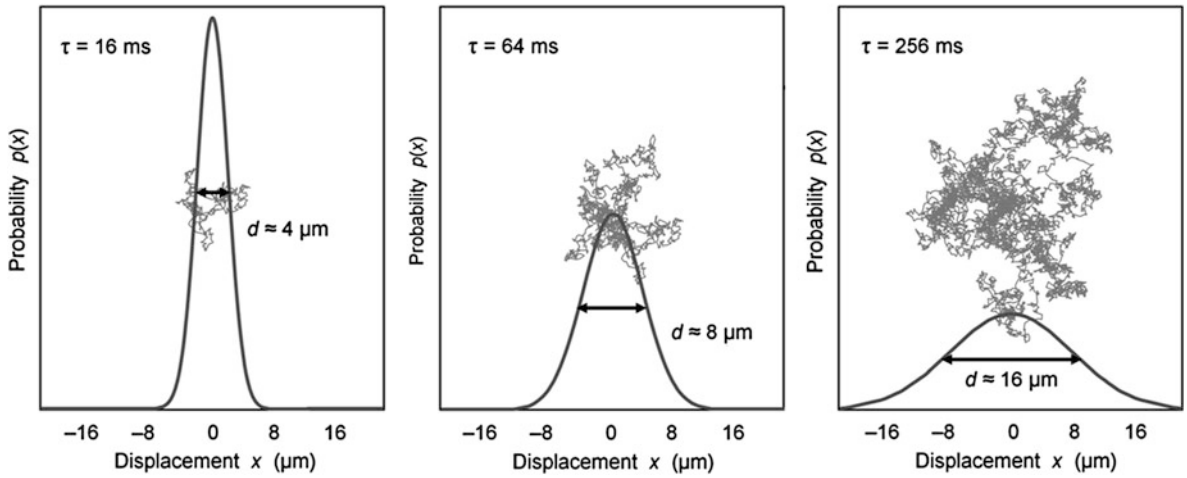

Fig. 1 Molecular diffusion as a microscopic stochastic process. A typical molecular motion of a spin in a liquid (obtained by a random-walk simulation) is illustrated in the background. The probability distribution, $p(x)$, for the resulting displacement is a normal distribution centered at 0. Diffusion times τ increase quadratically from 16 over 64 to 256 ms while the "range", d, of the molecular motion increases linearly from 4 over 8 to 16 µm

200 ms. In other words, an average water molecule in biological tissue will move (stochastically) in a spherical environment with a diameter of about 20 µm during a time interval of 20 ms.

Diffusion coefficients in biological tissue vary between approximately 0 and the value of free water at body temperature depending on the tissue microstructure. This reduction of the measured diffusion coefficient relative to the one of pure water is caused by the interaction of the water molecules with the tissue; e.g., with cell membranes, cell organelles, or biological macromolecules. The motion of the water molecules is hindered to a certain degree by these obstacles and, thus, the molecular displacement is reduced. This effect can increase with the diffusion time, since the number of obstacles hit by a water molecules increases as well. The reduced, effective diffusion coefficient observed in a measurement is called *apparent diffusion coefficient* (ADC). Some typical ADCs are summarized in Table 1.

The value of the ADC depends, thus, on the tissue microstructure; tissues with high cellularity generally exhibit lower ADCs because of the decreased mobility of the water molecules. In contrast, liquids such as the cerebrospinal fluid or necrotic tissues without remaining cell structures exhibit high ADCs similar to the one of pure water.

As mentioned above, the measured ADC of tissue can depend (at least to a certain degree) on the measurement parameters, in particular on the diffusion time, τ, during which the molecules diffuse in the measurement process, but potentially also on other measurement parameters such as the echo time or the application of fat saturation. A closer analysis of the distribution of molecular displacements in tissue for different diffusion times will typically exhibit a more complex form than the originally assumed normal (Gaussian) distribution. Approaches to probe these more complex diffusion properties are, e.g., q-space diffusion analysis (Cohen and Assaf 2002) or diffusional kurtosis

Table 1 Apparent diffusion coefficients (ADCs) of liquids and biological tissues

	ADC (10^{-3} mm^2/s)
Water, 5°C	1.31
Water, 20°C	2.02
Water, 35°C	2.92
Brain, white matter	0.70
Brain, gray matter	0.89
Liver	1.83
Kidney, cortex	2.43
Kidney, medulla	2.16
Vertebral bone marrow	0.2…0.6
Malignant vertebral fracture	0.7…1.0
Osteoporotic vertebral fracture	1.0…2.0

Values from Dietrich (2008), Dietrich et al. (2010) and Dietrich and Baur-Melnyk (2011)

analysis (Jensen and Helpern 2010), which, however, are both beyond the scope of this chapter.

2.1.2 Diffusion Tensor

The stochastic motion of molecules in a liquid is isotropic; i.e., the properties of the motion are independent of the orientation in space. In particular, the standard deviation of the displacement (used for the definition of D) is the same for all directions; e.g., the diffusion coefficient observed along the x direction is the same as the one observed along the y or z or any other oblique direction. However, spatial diffusion anisotropy may be observed in vivo: Anisotropic cell structures, in particular strongly directed tissues such as nerve fibers or muscle fibers, influence the diffusion properties of the water molecules. In such tissues, water diffusion is less restricted parallel to the fiber direction than perpendicular to it and, hence, the measured ADC will be greater along the fiber direction. In this case, the diffusion cannot longer be described by a single diffusion coefficient, but several diffusion coefficients in different spatial orientations are required; this collection of diffusion coefficients is mathematically summarized within the *diffusion tensor*, **D** (Basser et al. 1994a, b). This tensor is described by a symmetric 3×3 matrix and can be obtained in the framework of diffusion tensor imaging (DTI) from a series of diffusion measurements as described below.

While the diffusion tensor itself is a relatively complex entity, certain easily interpretable quantitative parameters can be derived if the tensor is known. These include the mean diffusion coefficient (describing the diffusion averaged over all spatial orientations), different measures of the diffusion anisotropy (e.g., the fractional or relative anisotropy), or the predominant orientation of the diffusion (which typically corresponds to the direction of the cell fibers in the tissue). Many of these parameters are most easily calculated after a process called diagonalization of the diffusion tensor; in this mathematical process, the symmetric 3×3 matrix is transformed to a diagonal matrix with 3 eigenvalues, D_1, D_2, D_3, and to three eigenvectors, $\mathbf{v}_1$, $\mathbf{v}_2$, $\mathbf{v}_3$:

$$\mathbf{D} = \begin{pmatrix} D_{xx} & D_{xy} & D_{xz} \\ D_{xy} & D_{yy} & D_{yz} \\ D_{xz} & D_{yz} & D_{zz} \end{pmatrix} \xrightarrow{\text{diagonalization}} \begin{pmatrix} D_1 & 0 & 0 \\ 0 & D_2 & 0 \\ 0 & 0 & D_3 \end{pmatrix}, \mathbf{v}_1, \mathbf{v}_2, \mathbf{v}_3.$$

The mean diffusivity, D, is then given by the mean value of the three eigenvalues (a third of the *trace* of the diffusion tensor, i.e., of the sum of the eigenvalues or of the diagonal elements):

$$D = \frac{1}{3}(D_1 + D_2 + D_3),$$

the fractional anisotropy (FA), a_F, by (Basser and Pierpaoli 1996)

$$a_{\mathrm{F}} = \sqrt{\frac{3}{2}} \frac{\sqrt{(D_1 - D)^2 + (D_2 - D)^2 + (D_3 - D)^2}}{\sqrt{D_1^2 + D_2^2 + D_3^2}},$$

the relative anisotropy (RA), a_{R}, by

$$a_{\mathrm{R}} = \sqrt{\frac{1}{3}} \frac{\sqrt{(D_1 - D)^2 + (D_2 - D)^2 + (D_3 - D)^2}}{D},$$

and the predominant diffusion direction by the eigenvector belonging to the largest eigenvalue (e.g., by $\mathbf{v}_1$ if $D_1 \geq D_2 \geq D_3$). Both anisotropy measures are dimensionless numbers (i.e., they have no physical units). FA and RA exhibit only minor differences for the description of tissue; they are zero in the case of isotropic diffusion (e.g., in a pure liquid) and increase with growing diffusion anisotropy. The maximum value of the FA (for purely one-dimensional diffusion in a three-dimensional tissue)−− is 1 whereas the maximum value of the RA is $\sqrt{2} \approx 1.414$. (Sometimes, the normalized RA is defined as the RA divided by $\sqrt{2}$; thus also ranging between 0 and 1.)

In particular, for bone marrow or other bone structures, only very few DTI results have been published demonstrating a certain variability of the anisotropy in the spongy bone and a potential of DTI for studying bone architecture (Capuani et al. 2005; Rossi et al. 2005).

2.2 Diffusion-Weighted MRI

2.2.1 Diffusion Weighting of MRI Pulse Sequences

Diffusion MRI is based on the diffusion-related signal attenuation acquired with specifically modified MR pulse sequences: this attenuation increases at higher diffusion coefficients and is caused by a pair of additional gradient pulses (called *diffusion gradients*) in the

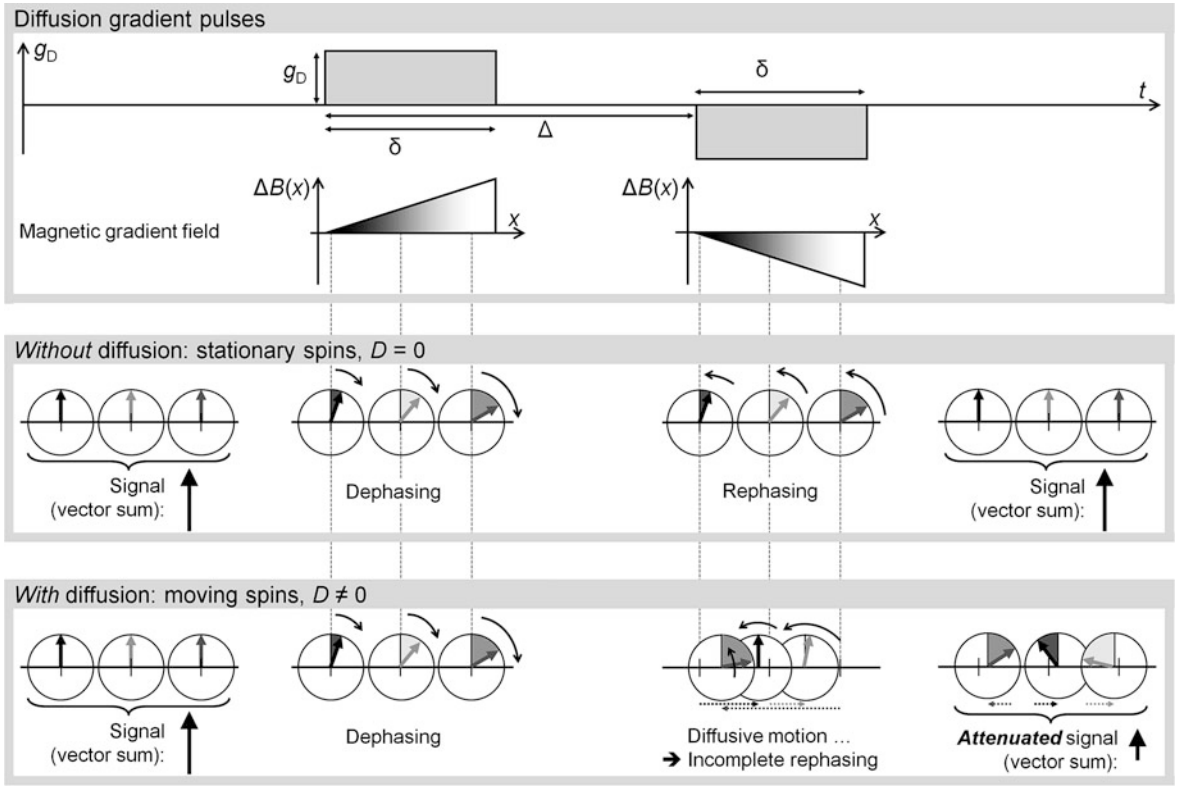

Fig. 2 Signal attenuation by diffusion-weighting gradient pulses. Two gradient pulses, g_D, of duration δ and with an interval of Δ between their onsets cause a spatially varying magnetic field and, thus, influence the phase angle of the precessing spins. Only stationary spins are completely rephased by the second gradient pulse while diffusing spins are rephased incompletely, which is observed as diffusion-attenuated signal intensity

pulse sequence (Hahn 1950; Stejskal and Tanner 1965). The underlying concept is a position-dependent dephasing and rephasing of the nuclear spins: a first gradient pulse modifies the phases of the spins (i.e., the spins are rotated by a certain angle) depending on their position, and a second gradient pulse after the diffusion time, τ, applies exactly the opposite rotation to the spins—if the spins have not moved, but stayed at the same position. If, however, spins have been moving due to the diffusional motion, the applied rephasing cannot fully compensate the initial dephasing and a stochastic phase dispersion remains. This incoherent phase distribution results in a reduced vector sum of individual magnetizations and, hence, in a reduced signal (Fig. 2).

The strength of this attenuation effect is called *diffusion weighting* or *b-value* of the sequence and depends (in the case of two identical gradient pulses) on the gradient amplitude, g_D, the gradient duration, δ, and the interval between the onsets of the gradients, Δ. The diffusion weighting for the pulses shown in Fig. 2 is

$$b = \gamma^2 g_D^2 \delta^2 \left(\Delta - \frac{\delta}{3}\right),$$

where $\gamma = (2\pi) \times 42.58 \times 10^6\ \mathrm{s}^{-1}/\mathrm{T}$ is the gyromagnetic ratio of the precessing nuclei (the given number is the gyromagnetic ratio for protons). The diffusion time, τ, is approximately equal to the interval, Δ, between the onsets of the diffusion gradients; in the case of relatively long diffusion gradients, the gradient duration, δ, needs to be considered as well, yielding a corrected diffusion time of $\tau = \Delta - \frac{\delta}{3}$. More generally, for arbitrary gradient shapes $g(t)$ in a given orientation applied between times $t = 0$ and $t = T$, the b-value is given by the integral:

$$b = \gamma^2 \int_{t=0}^{T} \left(\int_{t'=0}^{t} g(t')\mathrm{d}t' \right)^2 \mathrm{d}t.$$

Typical (maximum) b-values for conventional clinical diffusion MRI are in the range of 500–1500 s/mm^2.

The signal attenuation of a diffusion-weighted acquisition depends exponentially on the b-value and the diffusion coefficient, D (similarly as the signal attenuation in a T_2-weighted acquisition depends on the echo time, TE, and on the relaxation rate $R_2 = 1/T_2$). The attenuation $S(b)/S_0$ (relative to the original signal amplitude S_0) is

$$\frac{S(b)}{S_0} = \exp(-b \cdot D).$$

Higher attenuations correspond to larger diffusion coefficients and vice versa; thus, diffusion-weighted images show regions with reduced ADCs (such as ischemic brain tissue in stroke patients or tumor tissue with increased cellularity) hyperintense compared to normal-appearing tissue.

The diffusion coefficient can be determined quantitatively by measuring the attenuation, $S(b)/S_0$, for two or more different b-values and then fitting the exponential function to the measured signals. In the simplest case of only two measurements with b-values 0 and b, the ADC can also be calculated directly from the logarithm of the signal attenuation as

$$D = \frac{-1}{b} \ln \frac{S(b)}{S_0}.$$

Areas with reduced ADC that appear hyperintense in diffusion-weighted images are hypointense in the ADC map.

With the technique described above, the diffusion coefficient can be measured in the orientation of the applied diffusion gradient. The components of the diffusion tensor are measured by applying the diffusion gradient in several different spatial orientations (measurements in at least 6 non coplanar diffusion directions are required to estimate all 6 independent components of the tensor (Basser and Pierpaoli 1998)).

2.2.2 Pulse Sequences for Diffusion-Weighted MRI

Diffusion gradients as described above can be inserted in many different MRI pulse sequence types as summarized, e.g., in Dietrich et al. (2010) or Dietrich and Baur–Melnyk (2011). Historically, the first diffusion-weighted MR images were acquired with (single-echo) stimulated-echo and spin-echo sequences (Merboldt et al. 1985; Taylor and Bushell 1985; Le Bihan et al. 1986), which, however, were very slow and prone to motion artifacts. Today, the most important sequence type for diffusion-weighted imaging (DWI) is the single-shot spin-echo echo-planar imaging (EPI) sequence, in which the diffusion gradients can be easily inserted at both sides of the 180° refocusing radio-frequency (RF) pulse (Turner et al. 1990). EPI acquisitions are fast (a complete image can be acquired in about 0.2 s) and, hence, relatively insensitive to motion. On the other hand, EPI sequences are very sensitive to susceptibility variations and eddy currents, both potentially resulting in geometrically gross distortions of the images. Diffusion-weighted EPI sequences have been established for many years for imaging of the brain (where only moderate susceptibility artifacts occur); but only relatively recent improvements of MRI hardware and in particular of the gradient system and the fat-suppression techniques enabled the general robust application of diffusion-weighted MRI in many other parts of the body and, in fact, also for whole-body applications (Takahara et al. 2004; Lambregts et al. 2011; Wu et al. 2011).

Other fast techniques for diffusion MRI are single-shot fast-spin-echo (or turbo-spin-echo) sequences with additional diffusion gradients such as diffusion-weighted half-Fourier-acquisition single-shot turbo-spin-echo (HASTE) or rapid acquisition with relaxation enhancement (RARE) sequences (Norris et al. 1992). These approaches avoid the high sensitivity to susceptibility variations of EPI sequences, but they exhibit certain other disadvantages including lower signal-to-noise ratio (SNR) or image artifacts due to unwanted stimulated echoes. Several detail improvements have been proposed to increase the image quality and robustness of these pulse sequences for diffusion-weighted MRI (Alsop 1997; Le Roux 2002; Norris 2007).

Further and less frequently applied approaches include segmented (multi-shot) EPI techniques (Robson et al. 1997; Brockstedt et al. 2000), non-Cartesian k-space trajectories with radial acquisition or with the "periodically rotated overlapping parallel lines with enhanced reconstruction" (PROPELLER) technique (Pipe et al. 2002), diffusion-sensitized fast spoiled gradient-echo (turbo-FLASH or snapshot-FLASH) sequences (Lee and Price 1994) or line-scan diffusion-weighted imaging sequences (Gudbjartsson et al. 1996).

A somewhat different approach for diffusion-weighted imaging is obtained by inserting a single diffusion gradient in a steady-state free-precession

(SSFP) sequence. SSFP sequences can be differentiated in three different basic types: those that acquire a free-induction-decay(-FID)-like signal such as the "Fourier-acquired steady-state" (FAST) or "fast imaging with steady precession" (FISP) sequences; those with a spin-echo-like signal such as the contrast-enhanced FAST (CE-FAST) or the reversed FISP (PSIF) sequences; and finally those with fully balanced gradients that acquire a combination of both signals such as the TrueFISP or balanced SSFP (bSSFP) sequences (Oppelt et al. 1986; Bruder et al. 1988; Gyngell 1988). To obtain a reasonable diffusion weighting at short repetition times (TR), particularly the spin-echo-like approaches have proven useful (Le Bihan 1988; Merboldt et al. 1989). Inserting a single (monopolar) diffusion gradient in each TR provides a spin dephasing that is rephased at a later TR (not necessarily at the immediately successive one since the magnetization is switched around between transversal and longitudinal contributions). The delayed rephasing is advantageous in that it provides an increased diffusion weighting—however, it becomes extremely complicated to exactly quantify the diffusion weighting, since it depends not only on the properties of the diffusion gradient, but also on the flip angle, the TR, and the relaxation times of the tissue (Wu and Buxton 1990; Buxton 1993; Deoni et al. 2004). Therefore, diffusion-sensitized SSFP sequences can be used to acquire diffusion-weighted image data (which qualitatively visualize increased ADCs as attenuated signal), but not for the exact quantification of diffusion coefficients. This approach has been demonstrated to be particularly valuable in vertebral bone marrow, since a differentiation of pathological (neoplastic) and benign (osteoporotic) vertebral compression fractures is possible based on the contrast of the diffusion-weighted PSIF sequence (Baur et al. 1998, 2001; Dietrich et al. 2009; Biffar et al. 2011a, b; Dietrich and Baur-Melnyk 2011).

2.3 Diffusion-Weighted MRI in Bone Marrow

When diffusion-sensitive MR techniques are to be applied in bone marrow, the choice of the pulse sequence type and of several sequence parameters should, in general, be different from those used, e.g., for diffusion-weighted MRI of the brain. While echo-planar imaging is the standard technique for diffusion measurements in the brain, a broader spectrum of techniques is applied in body applications. Typically, the homogeneity of the static magnetic field (B_0) is lower in body applications than in the brain, resulting in severer geometrical distortions and image artifacts due to impaired fat suppression when using echo-planar imaging. Thus, pulse sequences with reduced sensitivity to field inhomogeneities have often been applied for bone-marrow imaging such as diffusion-weighted RARE or line-scan diffusion-weighted imaging sequences (Dietrich et al. 2009; Dietrich and Baur-Melnyk 2011).

The transversal relaxation times (T_2) are typically shorter in the musculoskeletal system than in the brain and, hence, the signal intensity is frequently low due to the relatively long echo times required for diffusion-weighted sequences. To obtain sufficient signal, multiple averaging and shorter echo times should be used implying also a reduced maximum diffusion weighting of, e.g., only $b = 600$ s/mm^2 instead of 1,000 s/mm^2.

On the other hand, typical ADCs of normal bone marrow are substantially lower (by a factor of 2–3) than of the brain or of abdominal organs; published values range between about 0.2 and 0.6 $\times$ 10^{-3} mm^2/s. Due to these low ADCs and the technical constraints mentioned above, it is very difficult to measure the ADCs of bone marrow accurately in a reasonable scan time. This is also reflected by the considerable variation of published ADCs of bone marrow as summarized in (Dietrich et al. 2009; Dietrich and Baur-Melnyk 2011). Apart from image noise, these varying results are also influenced by the choice of applied b-values as well as by the application fat saturation. Fortunately, ADCs of most bone-marrow pathologies are generally significantly higher (cf. Table 1) and, thus, can be detected much more accurately even at low b-values.

3 Principles of Perfusion MRI

3.1 Hemodynamic Tissue Properties

In the context of perfusion MRI, the term *perfusion* is frequently used (pars pro toto) to summarize several hemodynamic parameters associated with the (capillary) blood supply of biological tissue. These include the blood volume in the tissue, the blood flow and typical transit time constants. Depending on the physiology, these parameters can be defined and measured

for a single physiological compartment or for multiple tissue compartments with certain exchange properties (Brix et al. 2010; Sourbron 2010; Sourbron and Buckley 2012). In a narrower definition, perfusion is used as synonym for the blood flow parameter and is, thus, one of several hemodynamic parameters.

The hemodynamic parameters mentioned above were traditionally defined (and measured) on a per-organ basis by considering the total blood flow through an organ (in units of mL/min) or the corresponding total blood volume (in mL). For instance, typical organ perfusion values (in rest) are about 250 mL/min for the myocardium, 750 mL/min for the brain, and 1200 mL/min for the kidneys. Dividing these values by the mass (or the volume) of the organ, the average specific tissue perfusion is calculated. Typical values are 4 mL/(min g) = 400 mL/(min 100 g) for the kidney parenchyma or 0.5 mL/(min g) =50 mL/(min 100 g) for brain tissue (Silbernagl and Despopoulos 2008).

With imaging methods, hemodynamic parameters can be determined spatially resolved for the tissue of an organ. These values are defined as before normalized to the mass or volume of perfused tissue, but may now exhibit regional differences, e.g., for gray and white matter of the brain or for the renal cortex and the medulla. In this case, the regional flow is also given in units of mL/(min 100 g) or mL/(min 100 mL) and the regional blood volume in units of mL/(100 g) or mL/(100 mL). The conversion factor between both conventions (normalization to mass or volume) is the specific tissue mass density, ρ, in units of g/cm^3 = g/mL, which is relatively close to 1 g/mL for several soft tissues (with certain exceptions such as the lung). Thus, a regional kidney perfusion of about 400 mL/(min 100 g) based on the mass of the tissue is approximately equivalent to a flow value of 400 mL/(min 100 mL) if normalized to the volume.[1]

3.2 Techniques for Perfusion MRI

Perfusion MRI can be performed qualitatively or quantitatively with several fundamentally different techniques. The most important approaches are either based on the administration of intravenous contrast-media or—employing blood as an endogenous contrast-agent—on the labeling of arterial blood by appropriate magnetization preparation RF pulses, the so-called arterial spin labeling (ASL) techniques (Luypaert et al. 2001; Petersen et al. 2006). A third approach is based on diffusion-weighted acquisitions: The signal attenuation of diffusion-weighted images at very low *b*-values between 0 and about 150 s/mm^2 is influenced by the microcapillary perfusion as well as by normal diffusive processes. This additional influence results in a bi-exponential signal attenuation instead of the mono-exponential dependence described above. By analyzing the bi-exponential signal, two characteristic parameters, the perfusion fraction (in percent) and the perfusion-related pseudo diffusion coefficient, D^*, can be determined. This technique is frequently called *intravoxel incoherent motion* (IVIM) MRI and was already proposed in the 1980s (Le Bihan et al. 1988), but only recently, the general interest in this kind of acquisition has grown substantially (Koh et al. 2011).

Perfusion techniques that are based on the administration of an exogenous contrast-agent can be grouped into those that acquire the signal attenuation in T_2^*-weighted acquisitions due to the contrast-agent susceptibility ("dynamic susceptibility-contrast-enhanced MRI", DSC-MRI) (Ostergaard 2004) and those that acquire the contrast-media-induced signal increase in T_1-weighted acquisitions (Jackson et al. 2005). For bone-marrow MRI, only the last approach has been applied in a relevant number of studies; hence, the remaining parts of this introduction focus on these contrast-enhanced T_1-based techniques.

Depending on the specific acquisition parameters of the T_1-weighted measurement, particularly on the number of acquisitions and their temporal resolution, the evaluation of tissue perfusion can be performed either only qualitatively, semiquantitatively, or fully quantitatively yielding absolute hemodynamic parameters. The acquisition requirements are lowest if only a qualitative evaluation is intended. Even a single T_1-weighted acquisition after contrast-media injection will reflect certain perfusion-related properties: contrast enhancement is generally associated with blood volume and flow, and regions without perfusion are not enhanced at all. However, even a qualitative evaluation of perfusion properties is usually based on the signal development in several

[1] If normalized to the volume, the regional blood volume can also be given in % = mL/(100 mL) and the regional flow-related quantities in %/min = mL/(100 mL min).

subsequent acquisitions with temporal resolutions ranging from seconds to some minutes. Techniques that acquire such T_1-weighted signal-time courses are referred to as dynamic contrast-enhanced MRI (DCE-MRI) (Dyke and Aaron 2010; Sourbron 2010).

Only at high temporal resolutions of ideally about 1–3 s per acquisition, the details of the contrast-media passage through the vasculature can be analyzed, which is required for an accurate evaluation of the associated blood-flow parameters. Acquisitions with lower temporal resolutions, i.e., with reduced data acquisition rate, can be used to evaluate only a subset of hemodynamic parameters such as the contrast-media extravasation into the tissue if the total acquisition duration is sufficiently long.

By far the most commonly used sequence type for T_1-weighted perfusion MRI is the fast spoiled gradient-echo technique or, synonymously, fast low-angle shot (FLASH) or fast field-echo (FFE) sequence (Sourbron 2010). This sequence type can be used either for two-dimensional or three-dimensional acquisitions and with or without magnetization preparation such as inversion or saturation pulses. Frequently found combinations are saturation-recovery turbo-FLASH (snapshot-FLASH) sequences with short saturation times of 100–200 ms and two-dimensional readout, or three-dimensional gradient-echo sequences without magnetization preparation. Of particular importance for (semi)quantitative evaluations is a high temporal resolution of the acquisition in the order of about 1–3 s per acquisition. In two-dimensional approaches, this is achieved by relatively low spatial resolutions, high receiver bandwidth and very short TRs, a low number of acquired slices, and several acceleration techniques such as partial-Fourier acquisitions or parallel imaging. Fast, dynamic three-dimensional imaging is optimized similarly with relatively low spatial resolutions and parallel-imaging approaches; in addition, with view-sharing techniques (e.g., "time-resolved imaging of contrast kinetics", TRICKS, or "time-resolved imaging with stochastic trajectories", TWIST) that update the center of k-space more frequently than the periphery can be employed (Korosec et al. 1996; Lim et al. 2008). The sequence parameters, in particular the saturation time and the flip angle, should be chosen such that the resulting signal enhancement is approximately proportional to the contrast-agent concentration for those concentrations typically found in arteries and perfused tissue.

Apart from the pulse sequence, the contrast-media injection protocol needs to be considered and optimized for perfusion MRI. Typically, a standard dose of contrast-agent (0.1 mmol/kg body weight) is injected as a short bolus followed by a saline flush of about 20–30 mL. Injection rates are about 3 mL/s resulting in an injection duration of approximately 5 s for a typical contrast-agent.

3.3 Evaluation of Perfusion MRI

3.3.1 Qualitative and Semiquantitative DCE-MRI

A simple qualitative evaluation of the tissue perfusion can be based on the visual inspection of the signal-time course in a dynamic series of T_1-weighted images. A regionally increased signal enhancement indicates hyperperfused tissue, while a decreased enhancement is associated with hypoperfused tissue; a typical example of the latter is the locally reduced visual enhancement of lung parenchyma after thromboembolic arterial occlusion. If a series of several dynamic phases (e.g. 6–10) is acquired with a temporal resolution between 15 s and 1 min, it might be possible to differentiate qualitatively several enhancement patterns (in particular slowly increasing enhancement associated with the extravasation of the contrast-agent vs. fast contrast-agent wash-out in later phases). For instance, two enhancement types, namely one with a considerable wash-out after the initial rise of contrast and the other one with a plateau at the later phase, were differentiated in a study of degenerative endplate marrow changes based on a series of nine acquisitions with a temporal resolution of 16.4 s (Savvopoulou et al. 2011). The analysis of enhancement patterns or time-intensity curve (TIC) patterns can also be applied at higher temporal resolutions: e.g., in a perfusion study of vertebral lesions, five evaluated TIC patterns were "nearly no enhancement", "slow enhancement", "rapid contrast wash-in followed by an equilibrium phase", "rapid contrast wash-in followed by early wash-out", and "rapid contrast wash-in with a second slower-rising slope" (Chen et al. 2002).

Qualitative evaluations can be performed visually without the need for any dedicated software; however, the results are generally difficult to compare inter- or intra-individually (e.g., between baseline and follow-up examinations). The requirements with respect to

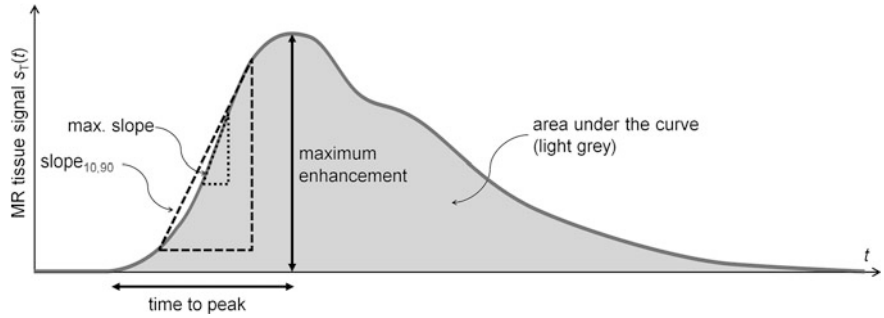

Fig. 3 Descriptive (semi-quantitative) perfusion parameters. Shown is the (idealized) signal-time curve of the tissue of interest obtained, e.g., by evaluating the mean signal of a region of interest. Important descriptive parameters of this curve are the maximum (or peak) enhancement, the time to peak, the area under the curve, or the slope which can be determined either by evaluating the difference between 10 and 90% of the maximum signal enhancement ($slope_{10,90}$) or by estimating the maximum slope

the applied imaging technique (in particular, to the temporal resolution and to signal linearity) are relatively low.

More information than by visual inspection can be obtained from DCE-MRI measurements with sufficient temporal resolution by deriving several descriptive or semiquantitative parameters from the acquired signal-time curves (Fig. 3). The most important of these parameters are the maximum of the curve (peak enhancement), the time to peak, the area under the curve, or the (maximum) slope of the signal increase. There are several options for the calculation of the slope; e.g., it can be estimated from the enhancement rate between 10 and 90% of the total enhancement (from baseline to maximum signal). Semiquantitative parameters were evaluated in several recent publications on bone-marrow perfusion (Griffith et al. 2009; Chan et al. 2011; Courcoutsakis et al. 2011; Li et al 2012).

The two main disadvantages of these descriptive parameters are their obvious dependence on the experimental parameters such as the pulse sequence contrast and, in particular, on the contrast-agent injection protocol as well as their unclear interpretation in terms of physiological hemodynamic terms. Depending on the tissue and the pathology (e.g. tumor or ischemia), the relationship between the descriptive parameters and the physiological parameters such as the blood flow into the tissue or the diffusion of fluid into the extracellular space can be very different. In studies based on these semiquantitative (descriptive) parameters, it is frequently left open exactly which hemodynamic tissue property is examined.

On the other hand, obvious advantages of many of these descriptive parameters are that they are reasonably easy to calculate and relatively robust even in the presence of noise.

3.3.2 Quantitative DCE-MRI

Apart from the descriptive indices mentioned above, it is also possible to estimate several quantitative hemodynamic parameters such as the regional blood volume (RBV), the regional blood flow (RBF), or the permeability-surface-area product (PS) describing the vascular permeability (i.e., the extraction flow) from a detailed analysis of the measured contrast-agent dynamics. To obtain parameters that do not depend on the (variable) injection and circulation parameters and, thus, on the individual shape of the contrast bolus, this analysis has to be based on the contrast-agent dynamics in two regions: (1) in the tissue of interest and (2) in the tissue-feeding artery. The background of this procedure in the framework of indicator-dilution theory (Meier and Zierler 1954; Zierler 1962, 1965; Sourbron and Buckley 2012) is explained in Fig. 4: The contrast-agent concentration-time curve in the tissue, $c_T(t)$, is a complex combination of a tissue-response function (or impulse-response function), $f_T(t)$, and the arterial input function (AIF), $c_A(t)$. In the case of an idealized extremely short contrast-agent input as in Fig. 4a, the tissue-response, i.e., the concentration-time curve in the tissue, is directly given by the tissue-response function. The tissue-response function contains all hemodynamic information related to the tissue: Its initial value, $f_T(0)$, is the blood flow through the tissue and the area

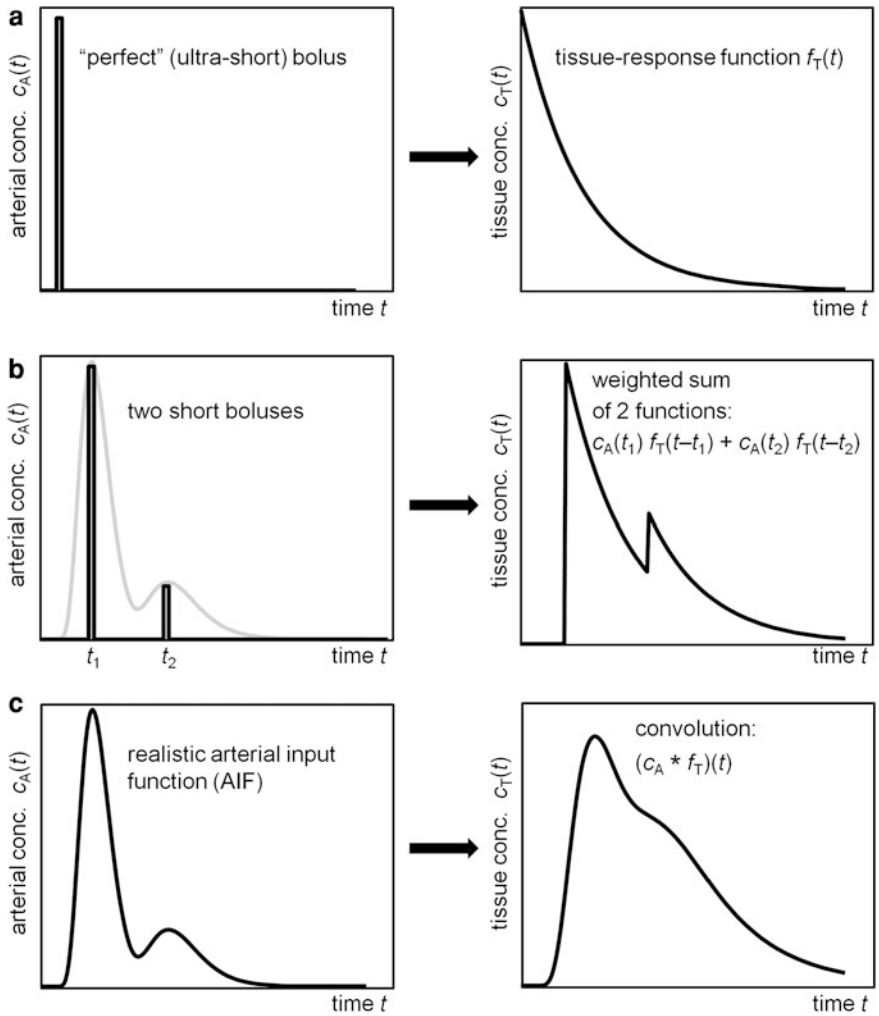

Fig. 4 Tissue concentration-time curve as a convolution of arterial concentration and tissue-response function. **a** The tissue-response function describes the contrast-agent concentration in the tissue after a "perfect" (extremely short) arterial bolus. **b** If the arterial input function (AIF, gray) is approximated by two boluses for the first pass and the re-circulation, the tissue concentration is obtained by the sum of two shifted tissue-response functions. **c** In the case of a realistic AIF, the sum is replaced by an integral, i.e., by the convolution of AIF and tissue-response function

under the curve, $\int_{-\infty}^{\infty} f_T(t)\mathrm{d}t$, is the blood volume in the tissue. A third important parameter, the mean transit time (MTT) is given by the quotient $\int_{-\infty}^{\infty} f_T(t)\mathrm{d}t / f_T(0)$. Depending on the tissue physiology, further parameters such as the permeability-surface-area product (extraction flow) or the extravascular, extracellular volume may also be required to describe the tissue-response function, and, thus, may be derived from this function. Hence, the tissue-response function may be written as $f_T(t; A,B,C,\ldots)$, where A, B, C, … describe several hemodynamic tissue parameters that influence the tissue response.

If the tissue-response function is normalized to the initial value 1, i.e., divided by the blood flow, $f_T(0)$, the resulting function, $R(t) = f_T(t) / f_T(0)$, is called the tissue-residue function. This function (and thus, practically, the tissue-response function itself as well) has the following simple interpretation: the residue functions describes what fraction of the blood (or contrast-agent) pool present in the tissue at $t = 0$ is still there at the time t. I.e., if we label the blood in the tissue at an arbitrary point of time and then wait the interval, t, exactly the fraction $R(t)$ (< 1) of the originally labeled blood is still there. Consequently, the residue function is always a positive and monotonically decreasing function.

An important approach to measure the above-mentioned hemodynamic parameters is the determination of the tissue-response function in an organ. However, if the bolus is not an ideal, ultra-short

impulse but a realistic bolus, then the influence of the bolus shape has to be removed from the concentration-time curve in the tissue. To understand this influence, one can imagine a sequence of short pulses with amplitude $c_A(t_i)$ at time t_i as approximation to the realistic arterial bolus shape as shown in Fig. 4b. The resulting concentration-time curve is then a superposition of several shifted tissue-response functions scaled by the amplitude of the individual impulses:

$$c_T(t) = c_A(t_1) \cdot f_T(t - t_1) + c_A(t_2) \cdot f_T(t - t_2) + \cdots = \sum_{i=1}^{N} c_A(t_i) \cdot f_T(t - t_i)$$

The transition to a smooth arterial input function (see Fig. 4c) is now equivalent to an integral calculation (instead of the sum of functions), called the *convolution* of the arterial input function and the tissue-response function (denoted by the symbol *):

$$c_T(t) = \int_{-\infty}^{\infty} c_A(s) \cdot f_T(t - s)ds = (c_A * f_T)(t).$$

In a typical perfusion measurement, the tissue concentration $c_T(t)$ and the arterial input concentration $c_A(t)$ are measured and the tissue-response function, $f_T(t)$ (or the parameters $A, B, C, \ldots$ defining $f_T(t)$), are to be determined from these; i.e., the convolution process has to be inverted. This calculation is termed deconvolution and sometimes denoted by the symbol $*^{-1}$:

$$f_T(t) = \left(c_T *^{-1} c_A\right)(t).$$

Unfortunately, the direct deconvolution is a numerically difficult and not very robust process (also called a numerically ill-posed problem) and several so-called regularization strategies have been proposed to improve the deconvolution such as truncated singular-value decomposition or the standard-form Tikhonov regularization (Kind et al. 2010).

An alternative to the direct deconvolution approach is based on a tissue model with a number of hemodynamic parameters A, B, C, … that imply a certain mathematical form of the tissue-response function, $f_T(t; A,B,C,\ldots)$. By varying these parameters, the convolution $(c_A * f_T)(t; A, B, C, \ldots)$ can be calculated and compared with the actual concentration, $c_T(t)$, in the tissue. By minimizing the difference

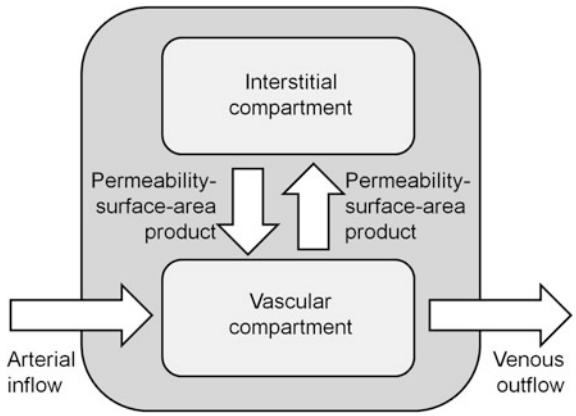

Fig. 5 Two-compartment exchange model with vascular and interstitial compartment. Four parameters that can be used to describe this model quantitatively are the (arterial) blood flow into the vascular compartment, the blood volumes of each compartment, and the flow (extraction flow or, synonymously, permeability-surface-area product) between the two compartments

(defined as the sum of squared differences) between the calculated convolution and the measured concentration-time curve, the hemodynamic parameters A, B, C, … are determined. This least-squares fitting procedure is frequently performed with the Levenberg–Marquardt algorithm.

The tissue model can comprise one or more (frequently two) compartments with certain individual properties such as specific blood volumes or specific mean transit times. A tissue compartment is generally defined as a space in which the contrast-agent is distributed instantly and uniformly and which has an inlet and an outlet connected to other compartments. A typical two-compartment model includes, e.g., the vascular compartment with arterial inflow and venous outflow as well as an extravascular, extracellular (i.e., interstitial) compartment to which blood (and contrast-agent) is transported via the permeable vascular surface, described by the permeability-surface-area product. A frequently used quite general model is the two-compartment exchange model with bidirectional flow between both compartments (Fig. 5).

Under certain conditions, the blood volume and flow can also be estimated directly from the tissue concentration and the AIF without the need for numerical deconvolution. E.g., the blood volume is given by $\int_0^\infty c_T(t)\mathrm{d}t / \int_0^\infty c_A(t)\mathrm{d}t$, if the concentration-time curves return to zero within the acquisition window.

All considerations above were based on the *concentration*-time curves (in the artery or the tissue); these, however, are not directly accessible in MRI but must be derived from the measured *signal*-time curves. Depending on the pulse sequence type and other parameters such as the flip angle distribution, different relationships between either the absolute or relative signal enhancement due to the contrast-media and the contrast-media concentration can be established. In most situations, additional calibration measurements of the pre-contrast T_1 values and the B_1 (flip angle) homogeneity are required (Sourbron 2010).

3.4 Perfusion Parameters in Bone Marrow

Perfusion properties of bone marrow have been assessed at least qualitatively or semiquantitatively in a relatively large number of studies as summarized, e.g., in (Biffar et al. 2010a). Early examinations of contrast-media uptake dynamics in bone tumors were already performed in the late 1980s demonstrating higher slopes of enhancement in malignant than in benign bone tumors (Erlemann et al. 1989). Further semiquantitative analyses demonstrated, e.g., decreasing bone-marrow perfusion with age (Chen et al. 2001; Montazel et al. 2003) or with osteoporosis (Shih et al. 2004; Griffith et al. 2005). Increasing perfusion indices were demonstrated, e.g., in bone marrow with diffuse tumor infiltration (Rahmouni et al. 2003), in myeloproliferative neoplasms (Courcoutsakis et al. 2011), in idiopathic osteonecrosis of the femoral head (Chan et al. 2011), and in rheumatoid arthritis (Li et al. 2011); increasing contrast enhancement and lower slopes were reported for degenerative endplate changes (Savvopoulou et al. 2011). Reduced perfusion indices at baseline were shown to predict increased reduction of the bone mineral density in the femoral neck after 4 years (Griffith et al. 2011). Significantly different semiquantitative perfusion parameters were found in neoplastic and normal bone (D'Agostino et al. 2010) as well as in osteoporotic and neoplastic vertebral compression fractures (Tokuda et al. 2005); for the latter differentiation, time-intensity-curve patterns were also reported to be valuable (Chen et al. 2002). Another recent study showed a generally good reproducibility of the measurement of these perfusion-related indices in the bone (Griffith et al. 2009).

Only few results have been published with fully quantitative perfusion evaluation of the bone marrow. Permeability-related quantitative parameters of bone marrow evaluated in patients with multiple myeloma yielded increased values for the contrast-agent exchange rate constant of tissue with (high-degree) infiltration (Moehler et al. 2001; Nosas-Garcia et al. 2005). Permeability constants, elimination rates, and the perfusion amplitude were found to be reduced in osteoporotic subjects using a modified Brix model (Ma et al. 2010) and increased in bone marrow edema relative to normal bone (Lee et al. 2009). Typical blood flow and volume parameters in normal-appearing vertebral bone marrow are reported to be about 15 mL/(100 mL min) and about 5 mL/100 mL, respectively, with a very low permeability-surface-area product (Biffar et al. 2010b, 2011b). These values are significantly increased in osteoporotic vertebral fractures as summarized in Table 2. An improved analysis of bone-marrow perfusion data has been proposed to include effects of the fat fraction within the tissue which is about 30–50 % in healthy bone marrow (Biffar et al. 2010c). Assuming that the contrast-agent influences only the T_1 relaxation of the water protons and considering the different baseline relaxation rates of the fat and water fraction in bone marrow, this more sophisticated perfusion analysis yielded a significantly increased value of plasma volume in healthy bone marrow and a significantly decreased value of plasma flow in vertebral fractures (Table 2).

4 Conclusions

Both diffusion and perfusion MRI have been successfully employed for bone-marrow imaging studies in a multitude of different pathologies. A large number of these studies apply conventional diffusion-weighted imaging in order to determine apparent diffusion coefficients in bone marrow or, alternatively, to assess pathologies based on relative signal attenuations, e.g., using diffusion-weighted SSFP techniques. Frequently employed approaches for perfusion MRI are based on descriptive perfusion indices such as peak enhancement or slope derived directly from the signal-time

Table 2 Quantitative perfusion parameters in vertebral bone marrow

	Plasma flow (mL/(min 100 mL))	Plasma volume (mL/100 mL)	Permeability-surface-area product (mL/(min 100 mL))	Interstitial volume (mL/100 mL)	Ref.
Normal-appearing bone marrow	15	5	–	–	[a]
	18	6	0.1	–	[b]
	17	10	0.3	–	[c]
Osteoporotic fractures	71	25	20	28	[a]
	69	24	10	20	[b]
Osteoporotic or malignant fractures	41	21	6	19	[c]
	67	20	7	19	[d]

[a] Biffar et al. (2010b)
[b] Biffar et al. (2011b)
[c] Perfusion quantification considering the fat fraction in bone marrow (Biffar et al. 2010c)
[d] Perfusion quantification without considering the fat fraction (Biffar et al. 2010c)

curves of dynamic contrast-enhanced T_1-weighted acquisitions in different tissues of interest.

Newer diffusion techniques including diffusion tensor imaging, intravoxel incoherent motion MRI, or generalized non-Gaussian diffusion methods may be promising, but are not yet systematically evaluated in bone-marrow applications. Similarly, a fully quantitative perfusion assessment with appropriate multi-compartment models has been evaluated only in a very small number of recent studies. These techniques still promise improved diagnostic accuracy and superior tissue characterization in several applications in the near future.

References

Alsop DC (1997) Phase insensitive preparation of single-shot RARE: application to diffusion imaging in humans. Magn Reson Med 38(4):527–533

Basser PJ, Pierpaoli C (1996) Microstructural and physiological features of tissues elucidated by quantitative-diffusion-tensor MRI. J Magn Reson B 111(3):209–219

Basser PJ, Pierpaoli C (1998) A simplified method to measure the diffusion tensor from seven MR images. Magn Reson Med 39(6):928–934

Basser PJ, Mattiello J et al (1994a) Estimation of the effective self-diffusion tensor from the NMR spin echo. J Magn Reson B 103(3):247–254

Basser PJ, Mattiello J et al (1994b) MR diffusion tensor spectroscopy and imaging. Biophys J 66(1):259–267

Baur A, Stabler A et al (1998) Diffusion-weighted MR imaging of bone marrow: differentiation of benign versus pathologic compression fractures. Radiology 207(2):349–356

Baur A, Huber A et al (2001) Diagnostic value of increased diffusion weighting of a steady-state free precession sequence for differentiating acute benign osteoporotic fractures from pathologic vertebral compression fractures. AJNR Am J Neuroradiol 22(2):366–372

Biffar A, Dietrich O et al (2010a) Diffusion and perfusion imaging of bone marrow. Eur J Radiol 76(3):323–328

Biffar A, Sourbron S et al (2010b) Combined diffusion-weighted and dynamic contrast-enhanced imaging of patients with acute osteoporotic vertebral fractures. Eur J Radiol 76(3):298–303

Biffar A, Sourbron S et al (2010c) Measurement of perfusion and permeability from dynamic contrast-enhanced MRI in normal and pathological vertebral bone marrow. Magn Reson Med 64(1):115–124

Biffar A, Baur-Melnyk A et al (2011a) Quantitative analysis of the diffusion-weighted steady-state free precession signal in vertebral bone marrow lesions. Invest Radiol 46(10):601–609

Biffar A, Schmidt GP et al (2011b) Quantitative analysis of vertebral bone marrow perfusion using dynamic contrast-enhanced MRI: initial results in osteoporotic patients with acute vertebral fracture. J Magn Reson Imaging 33(3):676–683

Brix G, Griebel J et al (2010) Tracer kinetic modelling of tumour angiogenesis based on dynamic contrast-enhanced CT and MRI measurements. Eur J Nucl Med Mol Imaging 37(Suppl 1):S30–S51

Brockstedt S, Moore JR et al (2000) High-resolution diffusion imaging using phase-corrected segmented echo-planar imaging. Magn Reson Imaging 18(6):649–657

Bruder H, Fischer H et al (1988) A new steady-state imaging sequence for simultaneous acquisition of two MR images with clearly different contrasts. Magn Reson Med 7(1):35–42

Buxton RB (1993) The diffusion sensitivity of fast steady-state free precession imaging. Magn Reson Med 29(2):235–243

Capuani S, Rossi C et al (2005) Diffusion tensor imaging to study anisotropy in a particular porous system: the trabecular bone network. Solid State Nucl Magn Reson 28(2–4):266–272

Chan WP, Liu YJ et al (2011) Relationship of idiopathic osteonecrosis of the femoral head to perfusion changes in

the proximal femur by dynamic contrast-enhanced MRI. Am J Roentgenol 196(3):637–643
Chen WT, Shih TT et al (2001) Vertebral bone marrow perfusion evaluated with dynamic contrast-enhanced MR imaging: significance of aging and sex. Radiology 220(1): 213–218
Chen WT, Shih TT et al (2002) Blood perfusion of vertebral lesions evaluated with gadolinium-enhanced dynamic MRI: in comparison with compression fracture and metastasis. J Magn Reson Imaging 15(3):308–314
Cohen Y, Assaf Y (2002) High *b*-value q-space analyzed diffusion-weighted MRS and MRI in neuronal tissues—a technical review. NMR Biomed 15(7–8):516–542
Courcoutsakis N, Spanoudaki A et al (2011) Perfusion parameters analysis of the vertebral bone marrow in patients with Ph(1-) chronic myeloproliferative neoplasms (Ph(neg) MPN): a dynamic contrast-enhanced MRI (DCE-MRI) study. J Magn Reson Imaging. doi:10.1002/jmri.22870 [Epub ahead of print]
D'Agostino F, Dell'Aia P et al (2010) Differentiation of normal and neoplastic bone tissue in dynamic gadolinium-enhanced magnetic resonance imaging: validation of a semiautomated technique. Radiol Med 115(5):804–814
Deoni SC, Peters TM et al (2004) Quantitative diffusion imaging with steady-state free precession. Magn Reson Med 51(2):428–433
Dietrich O (2008) Diffusion-weighted imaging and diffusion tensor imaging. In: Reiser MF, Semmler W, Hricak H (eds) Magnetic Resonance Tomography. Springer, Heidelberg, pp. 130−152
Dietrich O, Biffar A et al (2009) Diffusion-weighted imaging of bone marrow. Semin Musculoskelet Radiol 13(2):134–144
Dietrich O, Biffar A et al (2010) Technical aspects of MR diffusion imaging of the body. Eur J Radiol 76(3):314–322
Dietrich O, Baur-Melnyk A (2011) Diffusion-weighted MR imaging of the bone marrow and the spine. In: Taouli B (ed) Extra-cranial applications of diffusion-weighted MRI. Cambridge University Press, Cambridge, pp 144–161
Dyke JP, Aaron RK (2010) Noninvasive methods of measuring bone blood perfusion. Ann N Y Acad Sci 1192:95–102
Erlemann R, Reiser MF et al (1989) Musculoskeletal neoplasms: static and dynamic Gd-DTPA–enhanced MR imaging. Radiology 171(3):767–773
Gerdes CM, Kijowski R et al (2007) IDEAL imaging of the musculoskeletal system: robust water fat separation for uniform fat suppression, marrow evaluation, and cartilage imaging. AJR Am J Roentgenol 189(5):W284–W291
Glaser C, Weckbach S et al (2008) Musculoskeletal system. In: Reiser MF, Semmler W, Hricak H (eds) Magnetic resonance tomography. Springer, Heidelberg, pp 1079–1176
Griffith JF, Yeung DK et al (2005) Vertebral bone mineral density, marrow perfusion, and fat content in healthy men and men with osteoporosis: dynamic contrast-enhanced MR imaging and MR spectroscopy. Radiology 236(3):945–951
Griffith JF, Yeung DK et al (2009) Reproducibility of MR perfusion and (1)H spectroscopy of bone marrow. J Magn Reson Imaging 29(6):1438–1442
Griffith JF, Yeung DK et al (2011) Prediction of bone loss in elderly female subjects by MR perfusion imaging and spectroscopy. Eur Radiol 21(6):1160–1169
Gudbjartsson H, Maier SE et al (1996) Line scan diffusion imaging. Magn Reson Med 36(4):509–519
Gyngell ML (1988) The application of steady-state free precession in rapid 2DFT NMR imaging: FAST and CE-FAST sequences. Magn Reson Imaging 6(4):415–419
Hahn EL (1950) Spin echoes. Phys Rev 80(4):580–594
Jackson A, Buckley DL et al (eds) (2005) Dynamic contrast-enhanced magnetic resonance imaging in oncology. Medical radiology—diagnostic imaging. Springer, Heidelberg
Jensen JH, Helpern JA (2010) MRI quantification of non-Gaussian water diffusion by kurtosis analysis. NMR Biomed 23(7):698–710
Kind T, Houtzager I et al (2010) Evaluation of model-independent deconvolution techniques to estimate blood perfusion. Conf Proc IEEE Eng Med Biol Soc 2602–2607
Koh DM, Collins DJ et al (2011) Intravoxel incoherent motion in body diffusion-weighted MRI: reality and challenges. AJR Am J Roentgenol 196(6):1351–1361
Korosec FR, Frayne R et al (1996) Time-resolved contrast-enhanced 3D MR angiography. Magn Reson Med 36(3): 345–351
Lambregts DM, Maas M et al (2011) Whole-body diffusion-weighted magnetic resonance imaging: current evidence in oncology and potential role in colorectal cancer staging. Eur J Cancer 47(14):2107–2116
Le Bihan D (1988) Intravoxel incoherent motion imaging using steady-state free precession. Magn Reson Med 7(3): 346–351
Le Bihan D, Breton E et al (1986) MR imaging of intravoxel incoherent motions: application to diffusion and perfusion in neurologic disorders. Radiology 161(2):401–407
Le Bihan D, Breton E et al (1988) Separation of diffusion and perfusion in intravoxel incoherent motion MR imaging. Radiology 168(2):497–505
Le Roux P (2002) Non-CPMG Fast Spin Echo with full signal. J Magn Reson 155(2):278–292
Lee H, Price RR (1994) Diffusion imaging with the MP-RAGE sequence. J Magn Reson Imaging 4(6):837–842
Lee JH, Dyke JP et al (2009) Assessment of bone perfusion with contrast-enhanced magnetic resonance imaging. Orthop Clin North Am 40(2):249–257
Li X, Yu A et al (2012) Quantitative characterization of bone marrow edema pattern in rheumatoid arthritis using 3 Tesla MRI. J Magn Reson Imaging 35(1):211–217
Lim RP, Shapiro M et al (2008) 3D time-resolved MR angiography (MRA) of the carotid arteries with time-resolved imaging with stochastic trajectories: comparison with 3D contrast-enhanced Bolus-Chase MRA and 3D time-of-flight MRA. AJNR Am J Neuroradiol 29(10):1847–1854
Luypaert R, Boujraf S et al (2001) Diffusion and perfusion MRI: basic physics. Eur J Radiol 38(1):19–27
Ma HT, Griffith JF et al (2010) Modified brix model analysis of bone perfusion in subjects of varying bone mineral density. J Magn Reson Imaging 31(5):1169–1175
Meier P, Zierler KL (1954) On the theory of the indicator-dilution method for measurement of blood flow and volume. J Appl Physiol 6(12):731–744
Merboldt KD, Hanicke W et al (1985) Self-Diffusion NMR Imaging Using Stimulated Echoes. J Magn Reson 64(3): 479–486
Merboldt KD, Bruhn H et al (1989) MRI of "diffusion" in the human brain: new results using a modified CE-FAST sequence. Magn Reson Med 9(3):423–429

Moehler TM, Hawighorst H et al (2001) Bone marrow microcirculation analysis in multiple myeloma by contrast-enhanced dynamic magnetic resonance imaging. Int J Cancer 93(6):862–868

Montazel JL, Divine M et al (2003) Normal spinal bone marrow in adults: dynamic gadolinium-enhanced MR imaging. Radiology 229(3):703–709

Norris DG (2007) Selective parity RARE imaging. Magn Reson Med 58(4):643–649

Norris DG, Bornert P et al (1992) On the application of ultra-fast RARE experiments. Magn Reson Med 27(1): 142–164

Nosas-Garcia S, Moehler T et al (2005) Dynamic contrast-enhanced MRI for assessing the disease activity of multiple myeloma: a comparative study with histology and clinical markers. J Magn Reson Imaging 22(1):154–162

Oppelt A, Graumann R et al (1986) FISP—a new fast MRI sequence. Electromedica 54:15–18

Ostergaard L (2004) Cerebral perfusion imaging by bolus tracking. Top Magn Reson Imaging 15(1):3–9

Petersen ET, Zimine I et al (2006) Non-invasive measurement of perfusion: a critical review of arterial spin labelling techniques. Br J Radiol 79(944):688–701

Pipe JG, Farthing VG et al (2002) Multishot diffusion-weighted FSE using PROPELLER MRI. Magn Reson Med 47(1): 42–52

Rahmouni A, Montazel JL et al (2003) Bone marrow with diffuse tumor infiltration in patients with lymphoproliferative diseases: dynamic gadolinium-enhanced MR imaging. Radiology 229(3):710–717

Robson MD, Anderson AW et al (1997) Diffusion-weighted multiple shot echo planar imaging of humans without navigation. Magn Reson Med 38(1):82–88

Rossi C, Capuani S et al (2005) DTI of trabecular bone marrow. Magn Reson Imaging 23(2):245–248

Savvopoulou V, Maris TG et al (2011) Degenerative endplate changes of the lumbosacral spine: dynamic contrast-enhanced MRI profiles related to age, sex, and spinal level. J Magn Reson Imaging 33(2):382–389

Shih TT, Liu HC et al (2004) Correlation of MR lumbar spine bone marrow perfusion with bone mineral density in female subjects. Radiology 233(1):121–128

Silbernagl S, Despopoulos A (2008) Color atlas of physiology. Thieme, Stuttgart

Sourbron S (2010) Technical aspects of MR perfusion. Eur J Radiol 76(3):304–313

Sourbron SP, Buckley DL (2012) Tracer kinetic modelling in MRI: estimating perfusion and capillary permeability. Phys Med Biol 57(2):R1–R33

Stejskal EO, Tanner JE (1965) Spin diffusion measurements: spin echoes in the presence of a time-dependent field gradient. J Chem Phy 42(1):288–292

Takahara T, Imai Y et al (2004) Diffusion weighted whole body imaging with background body signal suppression (DWIBS): technical improvement using free breathing, STIR and high resolution 3D display. Radiat Med 22(4):275–282

Taylor DG, Bushell MC (1985) The spatial-mapping of translational diffusion-coefficients by the NMR imaging technique. Phys Med Biol 30(4):345–349

Tokuda O, Hayashi N et al (2005) Dynamic contrast-enhanced perfusion MR imaging of diseased vertebrae: analysis of three parameters and the distribution of the time-intensity curve patterns. Skeletal Radiol 34(10):632–638

Turner R, Le Bihan D et al (1990) Echo-planar imaging of intravoxel incoherent motion. Radiology 177(2):407–414

Vanel D (2004) MRI of bone metastases: the choice of the sequence. Cancer Imaging 4(1):30–35

Wu EX, Buxton RB (1990) Effect of diffusion on the steady-state magnetization with pulsed field gradients. J Magn Reson 90(2):243–253

Wu LM, Gu HY et al (2011) Diagnostic value of whole-body magnetic resonance imaging for bone metastases: a systematic review and meta-analysis. J Magn Reson Imaging 34(1):128–135

Zierler KL (1962) Theoretical basis of indicator-dilution methods for measuring flow and volume. Circ Res 10(3):393–407

Zierler KL (1965) Equations for measuring blood flow by external monitoring of radioisotopes. Circ Res 16:309–321

Magnetic Resonance Imaging of the Bone Marrow Contrast Media for Bone Marrow Imaging

Daniel Golovko, Elizabeth Sutton, and Heike E. Daldrup-Link

Contents

Abstract

Non-enhanced MR scans provide information about the presence and extent of bone marrow pathologies. However, for specific indications, contrast agents can provide additional functional and metabolic information. Both gadolinium (Gd)-based low molecular weight contrast agents as well as ultrasmall superparamagnetic iron oxide (USPIO) achieve MR signal enhancement by decreasing T1- and T2-relaxation times. However, both classes of contrast agents have very different properties and pharmacokinetics. Low molecular weight Gd-chelates have a relatively short blood half life and provide early, brief tissue enhancement, whereas USPIO have a long blood half life, provide delayed tissue enhancement, and are actively taken up by phagocytic myeloid cells. Nephrogenic systemic fibrosis (NSF) is a known side effect of Gd-based agents and occurs in patients with chronic kidney disease. USPIO are metabolized by cells of the reticuloendothelial system, that have been proven to be safe in patients with chronic kidney disease, and thus may be an alternative in this patient population. Contrast-enhanced MRI can also improve the detection and characterization of bone marrow pathologies, guide biopsies, and monitor treatment effects. This chapter will provide an overview over various Gd-chelates and USPIO compounds as well as their respective applications for bone marrow imaging.

D. Golovko
Department of Internal Medicine,
University of Colorado Hospital,
Aurora, CO, USA

E. Sutton
Department of Radiology,
Memorial Sloan-Kettering Cancer Center,
New York, USA

H. E. Daldrup-Link (✉)
Department of Radiology,
Lucile Packard Children's Hospital,
Stanford University, 725 Welch Road,
Stanford, CA 94305, USA
e-mail: H.E.Daldrup-Link@stanford.edu

A. Baur-Melnyk (ed.), *Magnetic Resonance Imaging of the Bone Marrow*, Medical Radiology. Diagnostic Imaging,
DOI: 10.1007/174_2012_577,

1 Introduction

This chapter provides an overview of MR contrast agents in the realm of current contrast agents research, development, and recent trends in MRI. Gadolinium (Gd) and iron oxide-based contrast agents have improved both the sensitivity and specificity in MRI based on differential accumulation and differential T1- and/or T2-signal effects in normal and pathologic bone marrow. While plain MRI sequences can provide insight into morphological features of the bone marrow, the obtained information is limited to the cell, water, and/or fat content of the bone marrow. Contrast agents can provide useful additional information related to functional characteristics of the bone marrow, such as information regarding bone marrow metabolism, angiogenesis, and phagocytic activity of myeloid cells. We will provide an overview of Gd- and Fe-based contrast agents available for bone marrow imaging, provide practical examples where contrast enhancement may be particularly useful, and provide an outlook on new developments in the contrast agent arena.

2 Basic Principles of MR Contrast Agents

Intrinsic tissue contrast on MR images is characterized by the T1- and T2-relaxation times of that tissue. T1- and T2-relaxation times of bone marrow are determined by many factors, the most clinically relevant being concentration of fat and cell density for T1-weighted sequences, and concentration of water for fat-saturated T2-weighted sequences. Contrast agents shorten both T1- and T2-relaxation times of bone marrow, which results in net signal gain on T1-weighted sequences and net signal loss on T2-weighted sequences. Contrast agents are molecules with unpaired electrons in their orbitals, which lead to a net electron spin and a strong local magnetic field. Changes in the magnetic field can be transferred to neighboring water molecules, via dipole–dipole interactions (Lauffer 1987). Contrast agents can also change imaging properties based on their propensity to cause magnetic susceptibility. Clinically relevant contrast agents represent Gd-chelates, which are T1-predominant agents (mostly used for positive enhancement of target tissues on T1-weighted MR scans) and iron oxide nanoparticles, which are T2-predominant agents (mostly used for negative enhancement of target tissues on T2-weighted MR scans).

2.1 Gadolinium-Based Contrast Agents

2.1.1 Gadopentate Dimeglumine (Gd-DTPA) or Gadolinium Diethylene Triamine Penta-Acetic Acid

This was the first commercially available contrast agent for MRI. Its structure is that of a linear ligand (DTPA; charge: −5) that envelops and tightly binds the gadolinium-ion (Gd; charge: +3). The metal chelate possesses a net charge of −2, which is counterbalanced by two *N*-methyl glucamines each having a charge of +1. This contrast agent is manufactured as a clear, colorless solution, largely for intravenous injection available at a concentration of 0.5 mol/l (469.01 mg of Gd-DTPA/ml). It has a molecular weight of 938 ($C_{28}H_{54}GdN_5O_{20}$) and size of 1 nm. In addition, the formulation contains an excess of the free ligand, DTPA (0.1% of weight), which guarantees the stability of the complex during synthesis and storage in such a way that no free Gd is present in the formulation. Gd-DTPA forms a solution of high stability and low viscosity, which is hyperosmolar and displays an osmolality of 1.96 osmol/kg. It is a hydrophilic substance with a partition coefficient between butanol and water (<0.001). Its stability constant has been determined to be approximately 10^{22} and its effective stability constant Ke_{eff} at pH 7.4 is $10^{18.3}$.

These constants are values that reflect the Gd-chelate in its fully dissociated state without considering in vivo interactions with H^+ and OH^-ions. Nevertheless, biochemical tests have proven that Gd-DTPA is stable under physiological conditions. Measurements by highly sensitive analytical methods did not detect a release of the metal ion from its bond through supplantation or a long-term accumulation of Gd^+ or Gd-DTPA in the body. Finally, the pharmaceutical stability of the formulation is excellent. A shelf-life of five years has been reported. Intravenous bolus administration of Gd-DTPA leads to a rapid and early enhancement of the bone marrow, with an early peak enhancement and a subsequent wash-out due to a rapid elimination by the kidneys.

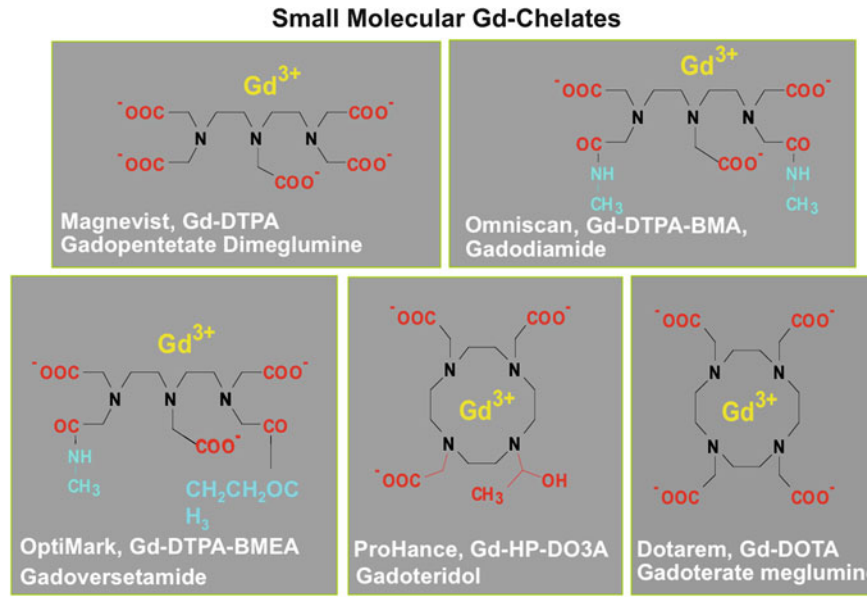

Fig. 1 Molecular structures of common small molecular Gd-chelates

2.1.2 Other Small Molecular Gd-Chelates

In addition to Magnevist (gadopentate dimeglumine; Bayer-Schering-Pharma AG, Berlin, Germany) the following are other small molecular Gd-chelates currently available (Fig. 1).

2.1.3 ProHance (Gadoteridol/Gd-HP-DO3A; Bracco, Milan, Italy)

This was the second Gd-chelate approved for intravenous injection in 1992. Its structure is that of a rigid macrocylic ligand (HP-DO3A; charge: −3) which overlies and tightly binds the gadolinium ion (Gd; charge: +3). The net charge for this complex is thus neutral or nonionic. Its macrocyclic nature increases its stability in vivo and thus decreases its release of free Gd.

2.1.4 Omniscan (Gadodiamide/Gd-DTPA-BMA; GE Healthcare, US)

This Gd-chelate is approved for intravenous injection in 1993. Its structure is that of a linear ligand (DTPA-BMA; charge: −3) that envelops and tightly binds the gadolinium ion (Gd; charge: +3). Two methyl amides differentiate the chelate from DTPA and change the charge from −5 to −3. The net charge for this complex is thus neutral or nonionic.

2.1.5 Dotarem (Gadoterate Meglumine/Gd-DOTA; Guerbet, Aulnay-sous-Bois, France)

This agent has widespread international clinical approval with the exception of Germany and the United States. Its structure is that of a rigid macrocylic ligand (DOTA; charge: −4). The metal chelate thus has a net charge of −1, yet is counterbalanced by a methyl glucamine (charge: +1).

2.1.6 OptiMark (Gadoversetamide/Gd-DTPA-BMEA; Mallinkrodt, St. Louis, Mo)

Its structure is that of a linear ligand (DTPA-BMEA; charge: −3). The net charge of this complex is thus neutral or nonionic. Its properties are similar to that of gadodiamide with intended use in whole-body MR.

2.1.7 Gadovist (Gadobutrol/Gd-DO3A-butriol; Bayer-Schering-Pharma AG, Berlin, Germany)

This agent has been approved for use in several countries. Its structure is that of a rigid macrocylic ligand. This agent is formulated at 1.0 M which offers advantages in the realm of angiographic and perfusion imaging.

2.1.8 Primovist (Gadoxetic Acid Disodium/ Gd-EOB-DTPA; Bayer-Schering-Pharma AG, Berlin, Germany)

This agent has been approved for use in several countries. It has two elimination pathways with approximately 50% renal and 50% hepatobiliary excretion. Therefore, it is primarily used for liver MR imaging. However, the dual excretion pathway has been utilized for evaluation of patients with borderline renal function. Due to some protein binding, the T1 plasma relaxivity is approximately double that of Magnevist and the agent is typically administered at lower doses compared to other Gd-chelates.

2.1.9 Multihance (Gadobenate Dimeglumine/Gd-BOPTA; Bracco, Milan, Italy)

This agent has also been approved for use in several countries. It also has two elimination pathways with approximately 90% renal and 5–10% hepatobiliary excretion. Multihance has similar relaxation properties as Primovist.

Since all of the aforementioned agents, with the exception of Primovist and Multihance (both of which will not be discussed further), are hydrophilic, extracellular non-specific (i.e. do not bind to plasma proteins or receptors) Gd-chelates with low molecular masses that are excreted unmetabolized in urine, they tend to be equally effective as they have comparable biodistribution and relaxivities (Fig. 2). In essence, their T1-and T2-relaxivity profiles are virtually identical. Thus MR enhancement will be the same regardless of the agent providing the same dose is used. Consequently, their clinical applications are also broadly similar; however, pertinent physiochemical properties vary as a result of their structural design and need to be recognized. They differ in two structural features: linear versus macrocyclic cores and ionic versus non-ionic charge types. The stability of a macrocyclic core (gadoteridol and gadoterate meglumine) is greater than a linear core (gadopentetate dimeglumine and gadodiamide), and as a result these complexes dissociate free Gd less frequently. The thermodynamic stability of macrocyclic agents is comparable to the open chain complexes, however, the thermodynamic stability is not the critical parameter within this class of complexes. The kinetic stability is the key as the dissociation and formation of the Gd complexes is extremely slow and thus the

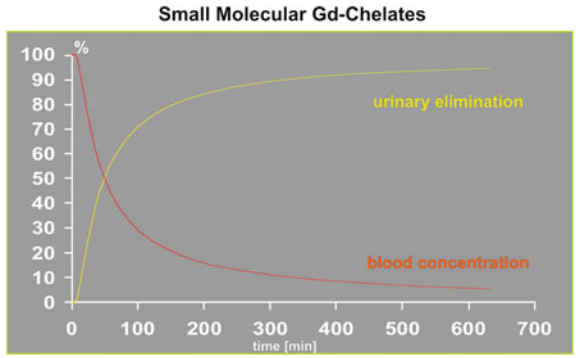

Fig. 2 Biodistribution of small molecular Gd-Chelates (blood concentration vs. urinary elimination) as a function of time

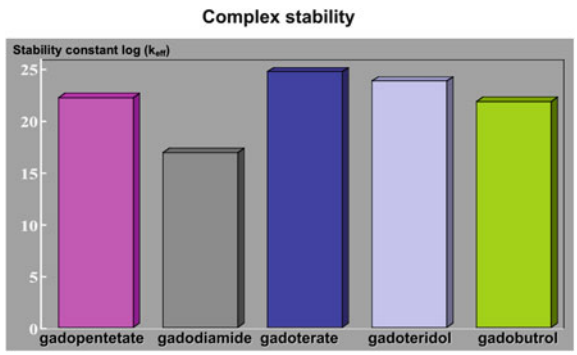

Fig. 3 Complex stability ($\log(k_{eq})$) of five commonly used small molecular Gd-chelates whereby gadoterate is the most and gadodiamide the least stable

organism does not 'see' any Gd outside the chelator. Chemical properties determined on the basis of kinetic and thermodynamic stability demonstrate that gadoteridol is the most stable and gadodiamide the least stable contrast agent (Fig. 3). The viscosity and osmolality of non-ionic molecules (gadoteridol and gadodiamide) is lower than ionic molecules (gadopentetate dimeglumine > gadoterate meglumine) thus enabling the development of these contrast agents at higher concentrations. Low viscosity and osmolality also allows for the safe administration of higher doses at a more rapid rate (e.g. faster bolus). Agents with relatively high osmolality may cause pain and tissue necrosis following extravasation, though this is not often appreciated.

In patients with unimpaired renal function, Gd-based contrast agents have an excellent safety profile. In a study, reporting 45 million administrations of

Gd-DTPA, the rate of adverse effects was 0.018% (Knopp et al. 2006). The most common adverse effects included subjective symptoms, urticaria, and local reactions around the site of injection. However, Gd-based contrast agents have been implicated in nephrogenic system fibrosis (NSF), discussed in more detail below.

2.2 Nephrogenic Systemic Fibrosis

Since December 2006, the FDA has investigated reports of NSF, a rare but debilitating disease which presents primarily in patients with decreased renal function with symptoms of focal and multifocal skin fibrosis of various extent. Extensive skin fibrosis can lead to joint contractures (Grobner 2006; Sadowski et al. 2007; Marckmann et al. 2006). NSF was first described in the medical literature in 2000. The first case of NSF was identified in 1997. The etiology of the disease is thought to be secondary to deposition of free Gd ion into subcutaneous tissue with resultant inflammation and fibrosis. Linear Gd-based contrast agents with low thermodynamic stability and low kinetic stability, such as gadodiamide (Omniscan, GE Medical) has been implicated the most with NSF (Frenzel et al. 2008). Onset has occurred 2–75 days following exposure and clinical course was marked by subacute swelling of the extremities, skin induration, serious physical disability, and possibly multi-organ involvement. Other, more stable agents, such as the linear, ionic (gadopentetate dimeglumine [Magnevist], gadobenate dimeglumine [MultiHance]), and macrocyclic agents (gadoteridol [Prohance]), have been associated with NSF with less frequency (Broome 2008). Kidney dysfunction appears to be a prerequisite for NSF. With normal kidney function, the half-life of typical Gd contrast agents is typically <1 h and thus, the Gd-chelate complex simply does not have much time to dissociate and deposit into tissue (Rofsky et al. 2008). With significant kidney disease, however, the half-life can be prolonged substantially. Kidney dysfunction may also increase transmetallation (that is, replacement of Gd from its complex by another metal ion) through acidosis, hyperphosphatemia, and likely other metabolic alterations, so that the likely etiology of NSF is multifactorial. Many published series have suggested an increased risk of NSF development in patients exposed to high doses and multiple doses of Gd; however, cases with single doses (0.1 mmol/kg) have also been reported.

Based on this data, many institutions have limited administration of Gd-based contrast agents to patients with confirmed unimpaired kidney function. Screening questions for renal disease include the following: medical history, hypertonia, protein in urine, diabetes, gout, or status post-kidney surgery. The U.S. Food and Drug Administration currently warns against using Gd-based contrast agents in patients with a glomerular filtration rate <30 ml/min/1.73 m^2, or any acute renal insufficiency related to the hepatorenal syndrome or perioperative organ transplantation. Many institutions have imposed stringent indications for imaging patients with mildly impaired kidney function and have switched to more stable Gd-chelates (Prince et al. 2008). Cases in the literature have been described of NSF developing even with patients on dialysis (Idee et al. 2006), and thus even prompt dialysis should not be viewed as a means of NSF prevention, because hemodialysis is not suited to efficiently eliminate released Gd-atoms from blood or even tissues.

2.3 Effect of Gd-chelates on Lab Tests

The current medical literature has suggested that Gd-chelates possibly interfere with laboratory tests, in particular, the colorimetric determination of calcium. A subsequent study demonstrated that this effect is dependent on the type of contrast agent: gadodiamide and gadoversetamide do cause the misleading appearance of reduced serum calcium levels, but this interference was not seen with Gd-DTPA. In addition, Niendorf and Seifert reported transient changes in serum iron, bilirubin, and transaminase levels following Gd-DTPA administration. Preclinical and clinical data demonstrate that Gd-chelates do not significantly influence cardiovascular and hemodynamic parameters even after rapid intravenous injection of high doses.

2.4 Iron Oxide Nanoparticles

Iron oxide nanoparticle-based contrast agents have been applied for bone marrow imaging by some investigators, including our own group. Iron oxide

nanoparticle-based MR contrast agents typically consist of an iron oxide core and a hydrophilic coating (Thorek et al. 2006). They are further classified based on their size as superparamagnetic iron oxide nanoparticles (SPIO) with a hydrodynamic diameter >50 nm and ultrasmall superparamagnetic iron oxide (USPIO) with a hydrodynamic diameter of <50 nm.

SPIO nanoparticles are effectively 80–150 times larger than the small molecular Gd-chelates such as Gd-DTPA. Upon intravenous injection, these large SPIO particles are rapidly recognized and phagocytosed by macrophages in liver and spleen, leading to clearance from the blood with a half-life of 10–20 min, too rapid to be useful for evaluation of other organs and/or pathologies outside the reticuloendothelial system. However, the smaller USPIO are not as rapidly recognized by the RES, leading to prolonged intravascular half-life of many hours or even days, depending on dose, resulting in strong, long-lasting blood-pool enhancement, and subsequent uptake by bone marrow macrophages. The USPIO blood-pool enhancement can be utilized for MR angiographies, the prolonged tissue enhancement can be used for evaluation of multiple sites of pathologies with one single contrast agent injection (e.g. multifocal inflammations of multifocal tumor infiltration), and the bone marrow macrophage uptake can be utilized for the differentiation of normal, hypercellular hematopoetic marrow from bone marrow inflammations, or neoplasms. Historically, three USPIO compounds have been tested in clinical trials, namely Ferumoxtran-10 (Sinerem, Guerbet and Combidex, Advanced Magnetics), Ferucarbotran (Resovist S, Schering AG), and Feruglose (Clariscan, GE Healthcare). These compounds are currently not being developed further for clinical use due to marketing and safety considerations.

Currently, the only clinically applicable iron oxide nanoparticle is ferumoxytol (FeraHeme, AMAG Pharmaceuticals). Ferumoxytol is a USPIO, which has been FDA-approved as an intravenous iron supplement, for treatment of chronic kidney disease-induced anemia (Spinowitz et al. 2008). However, a number of investigators use ferumoxytol "off label" as an MR contrast agent, via investigator-initiated INDs (investigational new drug applications). Compared to the much smaller Gd-based agents, ferumoxytol displays a vastly different biodistribution and MR signal enhancement profile. Ferumoxytol shows a blood half-life of 9.3–14.5 h, depending on the dose, followed by RES phagocytosis in liver, spleen, bone marrow, and lymph nodes (Weissleder et al. 1990; Turetschek et al. 2001; Landry et al. 2005; Raynal et al. 2004). The normal hematopoietic bone marrow shows strong T2-enhancement within 15–20 min after ferumoxytol administration. However, due to the large size of the nanoparticles, extravasation into neoplasms and tumors occurs much slower. The interstitial USPIO exerts a combined positive (bright) signal effect on T1-weighted MR images and a negative (dark) signal effect on T2-weighted MR scans. Once the nanoparticles are compartimentalized in cells, the T1-signal effect vanishes due to lack of USPIO interaction with protons. T2- and T2*-signal effects persist. The diminishing T1-effect allows a non-invasive diagnosis of intracellular compartimentalization. Timing and degree of intracellular compartimentalization can be utilized to differentiate normal bone marrow from bone marrow pathologies. For tumor imaging, USPIO like ferumoxytol offers certain distinct advantages over other contrast agents; in addition to potentially defining vascular status of target tissues they can also be used to detect metastatic spread to lymph nodes, liver, and bone marrow. Thus, dynamic plus delayed USPIO-enhanced MR imaging may be suited as a "one-stop-shop" diagnostic tool for staging of cancer patients.

Ferumoxytol is slowly metabolized in the RES and not excreted via the kidneys. Patients with known iron overload should not receive iron-based contrast. In patients with normal iron stores, administration of ferumoxytol leads to transient reduction of iron absorption from the gut. Ferumoxytol has been shown to be safe in patients with chronic renal failure and may represent a potential alternative contrast agent to Gd-chelates, which cannot be applied in these patients. However, it should be noted that NSF was an entity only described after millions of Gd-based contrast agent applications. Thus, it is certainly conceivable that iron-based contrast agents could potentially display another rare adverse reaction, which has not been recognized yet.

Data-to-date report few side effects of USPIO, such as temporary hypotension, flush, or swelling at the injection site. It should be noted that even intravenously injectable USPIO should be administered very slowly rather than as rapid bolus injections, in order to avoid a potentially serious hypotension. For ferumoxytol, a relatively high frequency of allergic

reactions, including severe anaphylaxis or anaphylactoid reactions were reported (Neuwelt et al. 2009). Third-generation USPIO with improved safety profiles are currently under development and are expected to become available within the next few years.

3 Practical Applications

Contrast enhancement is not always required for bone marrow MR imaging (Verstraete and Lang 2000). Contrast-enhanced MRI can however provide additional information when plain film radiography and plain MRI scans are inconclusive. In this setting, contrast agent administration can help differentiating normal and abnormal marrow, characterizing focal lesions, monitoring treatment effects, and assisting with biopsy planning (Fig. 4).

3.1 Lesion Characterization

Typically, solid malignant lesions will display higher permeability and vascularity compared to benign lesions; however, there is a significant overlap of this feature (Erlemann et al. 1989). Bone cysts are usually well delineated with a typical appearance on T2-weighted imaging. In cases where questions arise, administration of contrast can help to detect or exclude solid tumor components. Contrast agent administration can also aid in determining whether an aneurysmal cyst is a candidate for elective arterial embolization (Rossi et al. 2011). Contrast agent administration can similarly aid in distinguishing hemangiomas from lymphangiomas (Schepper et al. 1999). Some authors reported that the differentiation between enchondromas and chondrosarcomas can be improved with contrast (Verstraete and Lang 2000). On dynamic, contrast-enhanced MR imaging studies, inactive enchondromas displayed a slow enhancement and perfusion whereas active enchondromas and low grade chondrosarcomas displayed earlier and faster enhancement. Thus, while addition of contrast was not able to differentiate these entities fully, it was able to assist in determining clinically significant lesions in need of further intervention.

Infectious processes can be determined with corroborating laboratory or historical clinical information; however, these are not always present at the time of read. Granulation tissue surrounding an abscess or osteomyelitis is strongly enhancing whereas necrotic tissue display no enhancement. Additionally, surrounding tissue edema is typically seen.

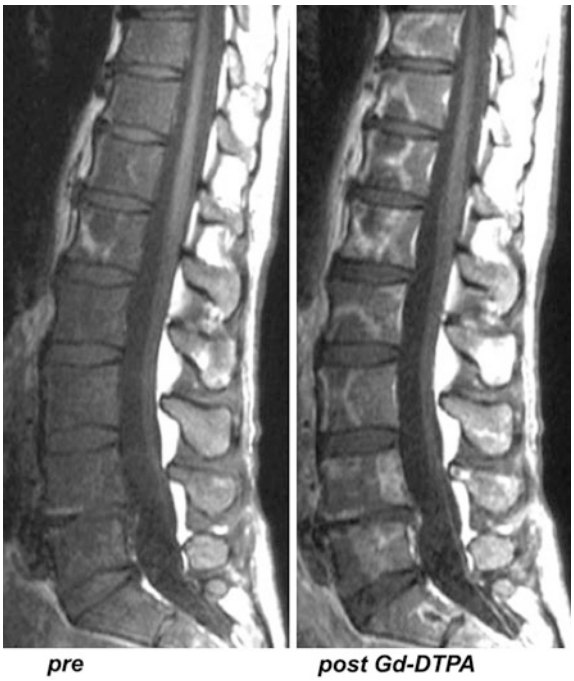

Fig. 4 Sagittal T1-weighted spin echo images of the lumbar spine in a patient with sickle cell anemia. The hypercellular hematopoietic marrow is relatively hypointense on plain images before contrast media administration. Following intravenous injection of Gd-DTPA, multiple bone infarcts are delineated

Differentiation between physiological hypercellular bone marrow after treatment with granulocyte colony stimulating factor (GCSF) and neoplastic marrow is improved with contrast agents. Owing to their larger blood volume, neoplasia will display earlier and faster enhancement to Gd-chelates (Bollow et al. 1997). While, there is a overlap between the imaging characteristics of both entities, an increase of signal intensity >40% indicated diffuse neoplastic infiltration (Stabler et al. 1996).

3.2 Monitoring Neoplasm Response to Treatment and Recurrence

Without contrast, imaging the response to treatment for neoplasms typically is limited to measuring tumor size and surrounding edema (Holscher et al. 1995).

Diffusion-weighted imaging can provide additional information as this technique can depict loss of membrane integrity in response to chemotherapy; however, the addition of contrast agents can greatly assist in monitoring response to treatment. This is especially important for bone sarcomas in the pre-operative/neo-adjuvant setting in evaluating the indications for limb sparing surgery (Erlemann et al. 1989; Lawrence et al. 1993; Erlemann 1990). Typically, contrast enhanced dynamic imaging should be performed before initiation of chemotherapy, 4–6 cycles into chemotherapy and prior to surgery. Dynamic imaging will depict a component of quick enhancement that is dependent on the amount of blood flow the tumor receives (more blood flow leads to more enhancement) and a component of slow decline in enhancement that is dependent on the size of the extracellular space around the tumor (more extracellular space leads to longer retention and a slower decline of enhancement). Areas that show enhancement correlate with viable tumor (van der Woude et al. 1995). Dynamic imaging differentiates between viable tumor and surrounding bone marrow edema as tumor will have more blood supply, and thus a strongly increased early enhancement compared to bone marrow edema that will only slowly accumulate contrast. Similarly, tumor necrosis will result in little to no enhancement after administration of contrast and is thus differentiated from viable tumor tissue. After chemotherapy, tumor tissue can transform into well-perfused inflammatory granulation tissue. Thus, waiting 4–6 cycles into chemotherapy is prudent as by that time, the blood flow of the granulation tissue will have subsided, whereas the blood flow to tumor will stay the same (Shapeero et al. 1999).

After treatment, unenhanced imaging can display lesions where the differential consideration is broad and includes not only inflammation, seromas, bone marrow reconversion but also tumor recurrence. Contrast enhanced dynamic MRI can aid in distinguishing between these lesions. Not all post-treatment surveillance MRI needs to be done with contrast. However, if a new suspicious lesion is seen, administration of contrast should be performed (Davies and Vanel 1998). Again, characteristics of tumor tissue on dynamic imaging are strong blood supply leading to a strong early increase of signal intensity with a slow decline afterwards. Once an equilibrium state has been reached between the intravascular space and interstitium (about 3 min after injection), signal intensities will be about the same and thus a single static post-contrast image will not suffice in differentiating tumor recurrence (Verstraete et al. 1996). Other lesions will typically not display a quick rise in signal intensity. After radiation therapy, however, neovascularization and granulation tissue can occur. This tissue can have dynamic characteristics similar to tumor, however, close follow-up with repeat imaging of 1–2 months afterwards should show decreased perfusion with granulation tissue whereas tumor should show increased perfusion. Slopes from signal intensity versus time plots of ROIs of suspected recurrences should be compared to the same plots from the initial tumor; however, tumor that has recurred may have somewhat different (and more aggressive) properties than the original primary.

Sometimes with treatment, complications such as bone infarction or avascular necrosis can occur. These can be easily differentiated with contrast as no or only little enhancement will occur given the disruption of the blood supply.

3.3 Biopsy Planning

For obvious reasons, obtaining biopsy specimens of viable tumor tissue is of much more clinical value than obtaining a specimen of necrotic, hemorrhagic, or myxoid regions. Tumor growth can be quite heterogenous with areas of rapid, slow, and no growth. In areas of no growth and sluggish perfusion, necrosis can be found which is of little diagnostic value (Vaupel et al. 1989). Areas of high enhancement will typically correlate to areas of active and rapid growth and thus these should be targeted on biopsy. Appropriate areas of tumor are well depicted on dynamic sequences by a rapid onset of contrast enhancement. The potential pitfall of using a single-static post-contrast image to guide biopsy is that enhancement of active and inactive areas within the tumor could be equal thus making the distinction between the two difficult. Contrast to active tumor will not only perfuse and diffuse quickly but will also wash out quickly, whereas contrast to inactive tumor or necrosis will perfuse slowly but over time diffuse into the interstitium. In the time course of a few minutes the signal intensities of these different portions of the tumor can become equal and thus a single-static post-contrast image will give a false certainty of targeting active tumor. Nevertheless, if only a single

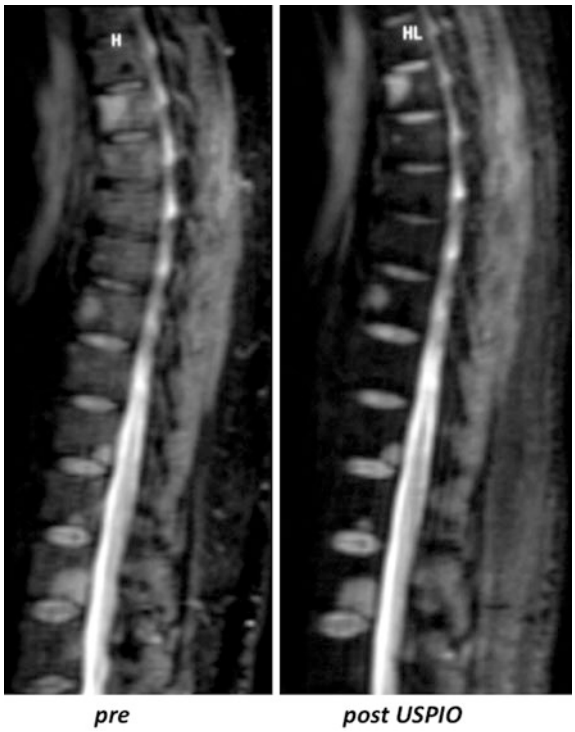

Fig. 5 Sagittal STIR images of the thoracic spine of a patient with focal bone marrow lesions due to lymphoma. Following intravenous injection of USPIO, the normal bone marrow shows significant T2-enhancement, in which focal neoplastic lesions stand out as unenhancing, T2-hyperintense areas

post-contrast image is available then the highest yield area to biopsy will likely be the region with the highest contrast enhancement. (Verstraete and Lang 2000).

4 USPIO

In some settings, the property of USPIO to be taken up by reticuloendothelial cells in the bone marrow can be useful. Hypercellular bone marrow can be found in the pediatric population or as a reactive response after chemotherapy. It can be difficult to distinguish between this physiological hypercellularity and neoplastic infiltration (Baur et al. 1997). Hypercellular bone marrow will slowly take up and phagocytose USPIO after administration. Neoplasms contain "tumor-associated macrophages", which take up USPIO slowly compared to macrophages in normal bone marrow. Thus, "early" MR scans after USPIO injection, 15 min—1 h post injection, will delineate "non-enhancing" neoplastic areas from "enhancing" normal marrow on T2-weighted MR images (Daldrup-Link et al. 2002). USPIO-enhanced imaging of bone marrow depicted significantly more focal lesions compared to non-enhanced scans (Metz et al. 2006) (Fig. 5). To visualize this, STIR or T2-weighted fat saturated sequences are best suited (Reimer et al. 2004; Simon et al. 2005). If concomitant T1-enhancement of vessels of pathologies is desired, T1-weighted gradient echo sequences with minimized TE are recommended in order to minimize confounding T2-effects. Delayed post-contrast scans, 24 h p.i., can be utilized to detect and quantify macrophages in bone marrow pathologies. This can be used to differentiate tumors from inflammations and to grade malignant tumors. USPIO-enhanced bone marrow imaging has also been used to characterize inflammatory processes, such as arthritis, osteomyelitis, or abscesses (Lutz et al. 2004; Kaim et al. 2003; Bierry et al. 2008). As USPIOs have a lengthy blood half-life, administration of these agents may be useful in global inflammatory processes, such as rheumatoid arthritis, if multiple joints are to be examined in the same session.

5 Conclusion

In summary, MRI provides excellent characterization of bone marrow without the addition of contrast agents. For selected indications, however, contrast agents can provide additional, clinically useful information. Standard small molecular Gd-chelates provide specific information about the functional status of normal bone marrow and bone marrow pathologies that otherwise are not depicted. However, Gd-chelates have been recently associated with the risk of NSF. Third-generation USPIO contrast agents may provide an alternative which provide potentially extended information about vascularity, cellularity, and macrophage content of target tissues.

References

Baur A, Stabler A, Bartl R, Lamerz R, Scheidler J, Reiser M (1997) MRI gadolinium enhancement of bone marrow: age-related changes in normals and in diffuse neoplastic infiltration. Skeletal Radiol 26(7):414–418

Bierry G, Jehl F, Prevost G, Mohr M, Meyer N, Dietemann JL, Kremer S (2008) Percutaneous inoculated rabbit model of intervertebral disc space infection: magnetic resonance imaging features with pathological correlation. Joint Bone Spine 75(4):465–470. doi:10.1016/j.jbspin.2007.06.018

Bollow M, Knauf W, Korfel A, Taupitz M, Schilling A, Wolf KJ, Hamm B (1997) Initial experience with dynamic MR imaging in evaluation of normal bone marrow versus malignant bone marrow infiltrations in humans. J Magn Reson Imaging 7(1):241–250

Broome DR (2008) Nephrogenic systemic fibrosis associated with gadolinium based contrast agents: a summary of the medical literature reporting. Eur J Radiol 66(2):230–234. doi:10.1016/j.ejrad.2008.02.011

Daldrup-Link HE, Rummeny EJ, Ihssen B, Kienast J, Link TM (2002) Iron-oxide-enhanced MR imaging of bone marrow in patients with non-hodgkin's lymphoma: differentiation between tumor infiltration and hypercellular bone marrow. Eur Radiol 12(6):1557–1566. doi:10.1007/s00330-001-1270-5

Davies AM, Vanel D (1998) Follow-up of musculoskeletal tumors I local recurrence. Eur Radiol 8(5):791–799

Erlemann R, Reiser MF, Peters PE, Vasallo P, Nommensen B, Kusnierz-Glaz CR, Ritter J, Roessner A (1989) Musculoskeletal neoplasms: static and dynamic Gd-DTPA-enhanced MR imaging. Radiology 171(3):767–773

Erlemann R, Sciuk J, Bosse A, Ritter J, Kusnierz-Glaz CR, Peters PE, Wuisman P (1990) Response of osteosarcoma and ewing sarcoma to preoperative chemotherapy: assessment with dynamic and static MR imaging and skeletal scintigraphy. Radiology 175(3):791–796

Frenzel T, Lengsfeld P, Schirmer H, Hutter J, Weinmann HJ (2008) Stability of gadolinium-based magnetic resonance imaging contrast agents in human serum at 37 degrees C. Invest Radiol 43(12):817–828. doi:10.1097/RLI.0b013e3181852171

Grobner T (2006) Gadolinium—a specific trigger for the development of nephrogenic fibrosing dermopathy and nephrogenic systemic fibrosis? Nephrol Dial Transplant 21(4):1104–1108. doi:10.1093/ndt/gfk062

Holscher HC, Bloem JL, van der Woude HJ, Hermans J, Nooy MA, Taminiau AH, Hogendoorn PC (1995) Can MRI predict the histopathological response in patients with osteosarcoma after the first cycle of chemotherapy? Clin Radiol 50(6):384–390

Idee JM, Port M, Raynal I, Schaefer M, Le Greneur S, Corot C (2006) Clinical and biological consequences of transmetallation induced by contrast agents for magnetic resonance imaging: a review. Fundam Clin Pharmacol 20(6):563–576. doi:10.1111/j.1472-8206.2006.00447.x

Kaim AH, Jundt G, Wischer T, O'Reilly T, Frohlich J, von Schulthess GK, Allegrini PR (2003) Functional-morphologic MR imaging with ultrasmall superparamagnetic particles of iron oxide in acute and chronic soft-tissue infection: study in rats. Radiology 227(1):169–174. doi:10.1148/radiol.2272020490

Knopp MV, Balzer T, Esser M, Kashanian FK, Paul P, Niendorf HP (2006) Assessment of utilization and pharmacovigilance based on spontaneous adverse event reporting of gadopentetate dimeglumine as a magnetic resonance contrast agent after 45 million administrations and 15 years of clinical use. Invest Radiol 41(6):491–499. doi:10.1097/01.rli.0000209657.16115.42

Landry R, Jacobs PM, Davis R, Shenouda M, Bolton WK (2005) Pharmacokinetic study of ferumoxytol: a new iron replacement therapy in normal subjects and hemodialysis patients. Am J Nephrol 25(4):400–410. doi:10.1159/000087212

Lauffer RB (1987) Paramagnetic metal complexes as water proton relaxation agents for NMP imaging: theory and design. Chem Rev 87(5):901–927. doi:10.1021/cr00081a003

Lawrence JA, Babyn PS, Chan HS, Thorner PS, Pron GE, Krajbich IJ (1993) Extremity osteosarcoma in childhood: prognostic value of radiologic imaging. Radiology 189(1):43–47

Lutz AM, Seemayer C, Corot C, Gay RE, Goepfert K, Michel BA, Marincek B, Gay S, Weishaupt D (2004) Detection of synovial macrophages in an experimental rabbit model of antigen-induced arthritis: ultrasmall superparamagnetic iron oxide-enhanced MR imaging. Radiology 233(1):149–157. doi:10.1148/radiol.2331031402

Marckmann P, Skov L, Rossen K, Dupont A, Damholt MB, Heaf JG, Thomsen HS (2006) Nephrogenic systemic fibrosis: suspected causative role of gadodiamide used for contrast-enhanced magnetic resonance imaging. J Am Soc Nephrol 17(9):2359–2362. doi:10.1681/ASN.2006060601

Metz S, Lohr S, Settles M, Beer A, Woertler K, Rummeny EJ, Daldrup-Link HE (2006) Ferumoxtran-10-enhanced MR imaging of the bone marrow before and after conditioning therapy in patients with non-hodgkin lymphomas. Eur Radiol 16(3):598–607. doi:10.1007/s00330-005-0045-9

Neuwelt EA, Hamilton BE, Varallyay CG, Rooney WR, Edelman RD, Jacobs PM, Watnick SG (2009) Ultrasmall superparamagnetic iron oxides (USPIOs): a future alternative magnetic resonance (MR) contrast agent for patients at risk for nephrogenic systemic fibrosis (NSF)? Kidney Int 75(5):465–474. doi:10.1038/ki.2008.496

Prince MR, Zhang H, Morris M, MacGregor JL, Grossman ME, Silberzweig J, DeLapaz RL, Lee HJ, Magro CM, Valeri AM (2008) Incidence of nephrogenic systemic fibrosis at two large medical centers. Radiology 248(3):807–816. doi:10.1148/radiol.2483071863

Raynal I, Prigent P, Peyramaure S, Najid A, Rebuzzi C, Corot C (2004) Macrophage endocytosis of superparamagnetic iron oxide nanoparticles: mechanisms and comparison of ferumoxides and ferumoxtran-10. Invest Radiol 39(1):56–63. doi:10.1097/01.rli.0000101027.57021.28

Reimer P, Bremer C, Allkemper T, Engelhardt M, Mahler M, Ebert W, Tombach B (2004) Myocardial perfusion and MR angiography of chest with sh u 555 c: results of placebo-controlled clinical phase i study. Radiology 231(2):474–481. doi:10.1148/radiol.2312021251

Rofsky NM, Sherry AD, Lenkinski RE (2008) Nephrogenic systemic fibrosis: a chemical perspective. Radiology 247(3):608–612. doi:1148/radiol.2473071975

Rossi G, Mavrogenis AF, Rimondi E, Ciccarese F, Tranfaglia C, Angelelli B, Fiorentini G, Bartalena T, Errani C, Ruggieri P, Mercuri M (2011) Selective arterial embolisation for bone tumours: experience of 454 cases. Radiol Med 116 (5):793–808. doi:10.1007/s11547-011-0670-0

Sadowski EA, Bennett LK, Chan MR, Wentland AL, Garrett AL, Garrett RW, Djamali A (2007) Nephrogenic systemic fibrosis: risk factors and incidence estimation. Radiology 243(1):148–157. doi:10.1148/radiol.2431062144

Schepper AM, De Beuckeleer LH, Vandevenne JE (1999) Imaging of soft tissue tumors in the pediatric patient. Semin Musculoskelet Radiol 3(1):59–80. smr00073

Shapeero LG, Vanel D, Verstraete KL, Bloem JL (1999) Dynamic contrast-enhanced MR imaging for soft tissue

sarcomas. Semin Musculoskelet Radiol 3(2):101–114. doi: 10.1055/s-2008-1080055

Simon GH, Raatschen HJ, Wendland MF, von Vopelius-Feldt J, Fu Y, Chen MH, Daldrup-Link HE (2005) Ultrasmall superparamagnetic iron-oxide-enhanced MR imaging of normal bone marrow in rodents: original research original research. Acad Radiol 12(9):1190–1197. doi:10.1016/j.acra.2005.05.014

Spinowitz BS, Kausz AT, Baptista J, Noble SD, Sothinathan R, Bernardo MV, Brenner L, Pereira BJ (2008) Ferumoxytol for treating iron deficiency anemia in CKD. J Am Soc Nephrol 19(8):1599–1605. doi:10.1681/ASN.2007101156

Stabler A, Baur A, Bartl R, Munker R, Lamerz R, Reiser MF (1996) Contrast enhancement and quantitative signal analysis in mr imaging of multiple myeloma: assessment of focal and diffuse growth patterns in marrow correlated with biopsies and survival rates. AJR Am J Roentgenol 167(4): 1029–1036

Thorek DL, Chen AK, Czupryna J, Tsourkas A (2006) Superparamagnetic iron oxide nanoparticle probes for molecular imaging. Ann Biomed Eng 34(1):23–38. doi: 10.1007/s10439-005-9002-7

Turetschek K, Huber S, Floyd E, Helbich T, Roberts TP, Shames DM, Tarlo KS, Wendland MF, Brasch RC (2001) MR imaging characterization of microvessels in experimental breast tumors by using a particulate contrast agent with histopathologic correlation. Radiology 218(2):562–569

van der Woude HJ, Bloem JL, Verstraete KL, Taminiau AH, Nooy MA, Hogendoorn PC (1995) Osteosarcoma and ewing's sarcoma after neoadjuvant chemotherapy: value of dynamic MR imaging in detecting viable tumor before surgery. AJR Am J Roentgenol 165(3):593–598

Vaupel P, Kallinowski F, Okunieff P (1989) Blood flow, oxygen and nutrient supply, and metabolic microenvironment of human tumors: a review. Cancer Res 49(23): 6449–6465

Verstraete KL, Lang P (2000) Bone and soft tissue tumors: the role of contrast agents for MR imaging. Eur J Radiol 34(3):229–246. doi:S0720-048X(00)00202-3

Verstraete KL, Van der Woude HJ, Hogendoorn PC, De-Deene Y, Kunnen M, Bloem JL (1996) Dynamic contrast-enhanced MR imaging of musculoskeletal tumors: basic principles and clinical applications. J Magn Reson Imaging 6(2):311–321

Weissleder R, Elizondo G, Wittenberg J, Rabito CA, Bengele HH, Josephson L (1990) Ultrasmall superparamagnetic iron oxide: characterization of a new class of contrast agents for MR imaging. Radiology 175(2):489–493

Index

A. Baur-Melnyk (ed.), *Magnetic Resonance Imaging of the Bone Marrow*, Medical Radiology. Diagnostic Imaging,
DOI: 10.1007/978-3-642-17860-3, © Springer-Verlag Berlin Heidelberg 2013